

New Applications of Amorphous $\text{Si}_3\text{B}_3\text{N}_7$ Ceramics and a Novel Production Method for Crystalline Nitridosilicates

Von der Fakultät Chemie der Universität Stuttgart
zur Erlangung der Würde eines Doktors der
Naturwissenschaften (Dr. rer. nat.) genehmigte Abhandlung

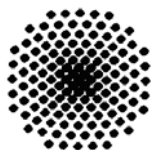
Vorgelegt von
Hasan Çakmak
aus Sakarya, Türkei

Hauptberichter: Prof. Dr. Dr. h. c. Martin Jansen
Mitberichter: Prof. Dr. Thomas Schleid

Tag der Einreichung: 10.06.2009
Tag der mündlichen Prüfung: 27.07.2009

Max-Planck-Institut für Festkörperforschung, Stuttgart
Universität Stuttgart

2009



to Güliz,

Contents

I. Introduction	1
1. Introduction	3
II. General Part	5
2. Preparative Working Methods	7
2.1. Vacuum and Inert Gas Apparatus	7
2.2. Vacuum Devices	7
2.3. Purifying and Drying the Solvents and Gases	8
2.4. Handling of Air-sensitive Substances	8
2.5. Pyrolysis Devices	9
3. Analytical Methods	11
3.1. Fluorescence Spectroscopy	11
3.2. Diffuse Reflection Spectroscopy	13
3.3. Fourier Transform Infrared Spectroscopy (FT-IR)	14
3.4. Gas Chromatography / Mass Spectroscopy	15
3.5. Nuclear Magnetic Resonance (NMR) Spectroscopy	16
3.6. X-ray Analysis	17
3.6.1. Powder X-ray Diffraction Analysis	17
3.6.2. Single Crystal Analysis	18
3.7. Thermal Analysis	18
3.8. Magnetic Measurements	19
3.9. Scanning Electron Microscopy and Energy Dispersive X-ray Analysis	20
3.10. Quantitative Elemental Analysis	21
3.10.1. Carrier Gas Heat Extraction	21
3.10.2. Inductively Coupled Plasma Optical Emission Spectroscopy (ICP-OES)	22

III. Special Part	23
4. Literature Overview	25
4.1. Multinary Amorphous Non-oxide Ceramics	25
4.2. Luminescence	34
4.3. Luminescent Materials for LED-based Lighting Devices	40
4.4. Ceramic Foams	46
4.5. General Objectives and Strategies	47
5. Phosphors Based on Amorphous $\text{Si}_3\text{B}_3\text{N}_7$ Matrix	51
5.1. Intrinsic Properties of Amorphous $\text{Si}_3\text{B}_3\text{N}_7$	51
5.2. Eu Doped Amorphous $\text{Si}_3\text{B}_3\text{N}_7$ Matrix	62
5.3. Eu Doped Amorphous Si_3N_4 Matrix	70
5.4. Ce Doped Amorphous $\text{Si}_3\text{B}_3\text{N}_7$ Matrix	74
5.5. Ce/Eu Codoped Amorphous $\text{Si}_3\text{B}_3\text{N}_7$ Matrix	77
5.6. Nd Doped Amorphous $\text{Si}_3\text{B}_3\text{N}_7$ Matrix	80
5.7. Nd/Eu Codoped Amorphous $\text{Si}_3\text{B}_3\text{N}_7$ Matrix	83
5.8. Sm Doped Amorphous $\text{Si}_3\text{B}_3\text{N}_7$ Matrix	86
5.9. Sm/Eu Codoped Amorphous $\text{Si}_3\text{B}_3\text{N}_7$ Matrix	89
5.10. Gd Doped Amorphous $\text{Si}_3\text{B}_3\text{N}_7$ Matrix	91
5.11. Gd/Eu Codoped Amorphous $\text{Si}_3\text{B}_3\text{N}_7$ Matrix	94
5.12. Tb Doped Amorphous $\text{Si}_3\text{B}_3\text{N}_7$ Matrix	95
5.13. Tb/Eu Codoped Amorphous $\text{Si}_3\text{B}_3\text{N}_7$ Matrix	99
5.14. Tb/Ce Codoped Amorphous $\text{Si}_3\text{B}_3\text{N}_7$ Matrix	103
5.15. Ho Doped Amorphous $\text{Si}_3\text{B}_3\text{N}_7$ Matrix	107
5.16. Ho/Eu Codoped Amorphous $\text{Si}_3\text{B}_3\text{N}_7$ Matrix	112
5.17. Tm Doped Amorphous $\text{Si}_3\text{B}_3\text{N}_7$ Matrix	114
5.18. Tm/Eu Codoped Amorphous $\text{Si}_3\text{B}_3\text{N}_7$ Matrix	118
5.19. Yb Doped Amorphous $\text{Si}_3\text{B}_3\text{N}_7$ Matrix	119
5.20. Yb/Eu Codoped Amorphous $\text{Si}_3\text{B}_3\text{N}_7$ Matrix	124
5.21. Sn Doped Amorphous $\text{Si}_3\text{B}_3\text{N}_7$ Matrix	126
5.22. Sn/Eu Codoped Amorphous $\text{Si}_3\text{B}_3\text{N}_7$ Matrix	130
5.23. M Doped Amorphous $\text{Si}_3\text{B}_3\text{N}_7$ Matrices, where M = Sr, Ba, Y and La . . .	131
5.24. M/Eu Codoped Amorphous $\text{Si}_3\text{B}_3\text{N}_7$ Matrices, where M = Sr, Ba, Y and La	135
5.25. Dependence of Luminescence on the Concentration of Activators in Amorphous $\text{Si}_3\text{B}_3\text{N}_7$	140
5.26. Conclusions	145
6. Ferromagnetic $\text{Si}_3\text{B}_3\text{N}_7$ Ceramics	149

6.1. Fe Doped Amorphous $\text{Si}_3\text{B}_3\text{N}_7$ Matrix	149
6.2. Co Doped Amorphous $\text{Si}_3\text{B}_3\text{N}_7$ Matrix	152
6.3. Ni Doped Amorphous $\text{Si}_3\text{B}_3\text{N}_7$ Matrix	158
6.4. Conclusions	160
7. A Novel Production Method for Crystalline Nitridosilicates	161
7.1. Synthesis and Characterization of $\text{M}_{2-x}\text{Eu}_x\text{Si}_5\text{N}_8$, where $\text{M} = \text{Ca}$ and Sr	162
7.2. Synthesis and Characterization of $\text{M}_{2-2x}\text{Ce}_x\text{Li}_x\text{Si}_5\text{N}_8$, where $\text{M} = \text{Ca}$ and Sr	172
7.3. Synthesis and Characterization of $\text{M}_{2-2x}\text{Tb}_x\text{Li}_x\text{Si}_5\text{N}_8$, where $\text{M} = \text{Ca}$ and Sr	176
7.4. Synthesis and Characterization of $\text{Sr}_{2-x}\text{Mn}_x\text{Si}_5\text{N}_8$	180
7.5. Synthesis and Characterization of $\text{Ba}_{1-2x}\text{Ce}_x\text{Li}_x\text{Si}_7\text{N}_{10}$	183
7.6. Synthesis and Characterization of $\text{Ba}_{1-2x}\text{Tb}_x\text{Li}_x\text{Si}_7\text{N}_{10}$	186
7.7. Synthesis and Characterization of CeSi_3N_5	190
7.8. Conclusions	192
8. A New Silaborazine-type Single Source Precursor for Si/B/N/C Ceramics	193
8.1. 1,1,3,5-tetrachloro-2,6-dimethyl-4-hydride-1-silaborazine (TDSB)	193
8.2. Preceramic Polymers from TDSB	204
8.3. New Si/B/N/(C) Ceramics	209
8.4. Conclusions	215
9. Open Cell SiBNC Ceramic Foams	217
10. General Experimental Methods	221
10.1. Preparation of Phosphors Based on Amorphous $\text{Si}_3\text{B}_3\text{N}_7$ Ceramic	221
10.1.1. Metal Route	222
10.1.2. Organometallic Route	224
10.2. Preparation of Ferromagnetic $\text{Si}_3\text{B}_3\text{N}_7$ Ceramics	231
10.2.1. Preparation of Fe Doped $\text{Si}_3\text{B}_3\text{N}_7$ Ceramics	231
10.2.2. Preparation of Co Doped $\text{Si}_3\text{B}_3\text{N}_7$ Ceramics	231
10.2.2.1. Reactions with $\text{Co}(\text{NH}_3)_6\text{Cl}_3$	231
10.2.2.2. Reactions with $\text{Co}[\text{N}(\text{Si}(\text{CH}_3)_3)_2]_2$	232
10.2.3. Preparation of Ni Doped $\text{Si}_3\text{B}_3\text{N}_7$ Ceramics	232
10.3. Preparation of Crystalline Nitridosilicate Phosphors	233
10.3.1. Metal Route	233
10.3.2. Organometallic Route	235
10.4. Preparation of New Si/B/N/(C) Ceramics	237
10.4.1. Synthesis of TDSB	237
10.4.2. Preparation of Preceramic Polymers from TDSB	238

Contents

10.4.2.1. Preparation of P-TDSB-1 Polymer	238
10.4.2.2. Preparation of P-TDSB-2 Polymer	238
10.4.3. Preparation of Si/B/N/(C) Ceramics	238
10.5. Preparation of Open Cell SiBNC Ceramic Foams	239
11. Summary	241
12. Zusammenfassung	247
Bibliography	253
13. Acknowledgments	285
14. List of Publication	287
15. Curriculum Vitae	291
16. Explanation	293

List of Figures

2.1. Vacuum and argon manifold.	7
2.2. Set up for purification of argon.	8
3.1. Schematic representation of a double grating fluorescence spectrometer. . .	13
3.2. Schematic representation of a triple-quadrupole mass spectrometer.	15
4.1. Representation of a configurational coordinate model.	36
4.2. Representation of five main radiative recombination processes in semiconductors: 1) band-to-band recombination, 2) free exciton recombination, 3) bound exciton recombination, 4) band-to-impurity recombination, 5) donor-acceptor pair transition [193].	37
4.3. Observed energy levels of trivalent lanthanide ions in LaCl_3 [194].	39
5.1. Powder X-ray diffractogram of undoped amorphous $\text{Si}_3\text{B}_3\text{N}_7$ ceramic.	54
5.2. Photoluminescence spectra of undoped amorphous $\text{Si}_3\text{B}_3\text{N}_7$ ceramic at different excitation and emission wavelengths.	54
5.3. Three-dimensional representation of photoluminescence spectra for undoped amorphous $\text{Si}_3\text{B}_3\text{N}_7$ ceramic.	55
5.4. Emission spectra of undoped amorphous $\text{Si}_3\text{B}_3\text{N}_7$ ceramic excited between 254 nm and 335 nm light.	55
5.5. Emission spectra of undoped amorphous $\text{Si}_3\text{B}_3\text{N}_7$ ceramic in blue region excited between 254 nm and 330 nm light.	56
5.6. Emission spectra of undoped amorphous $\text{Si}_3\text{B}_3\text{N}_7$ ceramic excited between 335 nm and 462 nm light.	56
5.7. Maximum emission intensities and wavelengths for various excitation wavelengths of undoped amorphous $\text{Si}_3\text{B}_3\text{N}_7$ ceramic for intrinsic blue emissions.	58
5.8. Maximum emission intensities and wavelengths for various excitation wavelengths of undoped amorphous $\text{Si}_3\text{B}_3\text{N}_7$ ceramic for intrinsic violet emissions. The peak at 400 nm due to the light from the source was deleted (*).	59
5.9. Maximum emission intensities and wavelengths for various excitation wavelengths of undoped amorphous $\text{Si}_3\text{B}_3\text{N}_7$ ceramic for intrinsic red emissions.	59

5.10. Representation of a configurational coordinate model for the absorption of UV light to higher excited state and the emission from lower excited state.	60
5.11. Representation of a configurational coordinate model for the reabsorption and the reemission (red shift).	60
5.12. Diffuse reflection spectra of undoped and some selected doped amorphous $\text{Si}_3\text{B}_3\text{N}_7$ ceramics.	61
5.13. Powder X-ray diffractograms of Eu^{2+} doped amorphous $\text{Si}_3\text{B}_3\text{N}_7$ ceramics via the metal and organometallic routes.	63
5.14. Diffuse reflection spectra of undoped, 0.5 % (wt), 3.8 % (wt) and 11.4 % (wt) Eu^{2+} doped amorphous $\text{Si}_3\text{B}_3\text{N}_7$ ceramics.	63
5.15. Photoluminescence spectra of Eu^{2+} doped (0.47 % wt) amorphous $\text{Si}_3\text{B}_3\text{N}_7$ ceramic via the metal route at different excitation and emission wavelengths.	64
5.16. Photoluminescence spectra of Eu^{2+} doped (0.57 % wt) amorphous $\text{Si}_3\text{B}_3\text{N}_7$ ceramic via the organometallic route at different excitation and emission wavelengths.	64
5.17. Photoluminescence spectra of Eu^{2+} doped amorphous $\text{Si}_3\text{B}_3\text{N}_7$ ceramics via both the metal and organometallic routes.	65
5.18. Representation of energy level diagrams of Eu^{2+} and Eu^{3+} ions (for reasons of clarity not all levels have been shown).	65
5.19. Maximum emission intensities and wavelengths for various excitation wavelengths of Eu^{2+} doped amorphous $\text{Si}_3\text{B}_3\text{N}_7$ ceramic.	66
5.20. Photoluminescence spectra of Eu^{2+} doped (3.76 % wt) amorphous $\text{Si}_3\text{B}_3\text{N}_7$ ceramic via the metal route at different excitation and emission wavelengths.	67
5.21. Magnetic susceptibility of Eu^{2+} doped (1.14 % wt) amorphous $\text{Si}_3\text{B}_3\text{N}_7$ ceramic prepared via the metal route represented as χ_{mol} vs. T (squares) and χ_{mol}^{-1} vs. T (circles) in an applied field of 3 Tesla.	69
5.22. Magnetic susceptibility of Eu^{2+} doped (0.57 % wt) amorphous $\text{Si}_3\text{B}_3\text{N}_7$ ceramic prepared via the organometallic route represented as χ_{mol} vs. T (squares) and χ_{mol}^{-1} vs. T (circles) in an applied field of 3 Tesla.	69
5.23. Powder X-ray diffractograms of Eu^{2+} doped amorphous Si_3N_4 ceramics.	71
5.24. Diffuse reflection spectra of Eu^{2+} doped amorphous Si_3N_4 ceramics.	72
5.25. Photoluminescence spectra of Eu^{2+} doped (1 % wt) amorphous Si_3N_4 ceramic (a- Si_3N_4 :Eu-1) at different excitation and emission wavelengths.	72
5.26. Photoluminescence spectra of Eu^{2+} doped (2 % wt) amorphous Si_3N_4 ceramic (a- Si_3N_4 :Eu-2) at different excitation and emission wavelengths.	73
5.27. Comparison of the emission spectra of approximately 1 % by weight Eu^{2+} doped amorphous Si_3N_4 and $\text{Si}_3\text{B}_3\text{N}_7$ ceramics.	73

5.28. Powder X-ray diffractograms of Ce ³⁺ doped and Ce ³⁺ /Eu ²⁺ codoped amorphous Si ₃ B ₃ N ₇ ceramics.	74
5.29. Diffuse reflection spectra of undoped, 0.66 % (wt), 1.7 % (wt) and 3.36 % (wt) Ce ³⁺ doped amorphous Si ₃ B ₃ N ₇ ceramics.	75
5.30. Photoluminescence spectra of Ce ³⁺ doped sample at different excitation and emission wavelengths.	76
5.31. Representation of energy level diagram of Ce ³⁺ ions.	76
5.32. Maximum emission intensities and wavelengths for various excitation wavelengths of Ce ³⁺ doped amorphous Si ₃ B ₃ N ₇ ceramic.	77
5.33. Diffuse reflection spectra of undoped, Ce ³⁺ doped, Eu ²⁺ doped and Ce ³⁺ /Eu ²⁺ codoped amorphous Si ₃ B ₃ N ₇ ceramics.	78
5.34. Comparison of the energy level diagrams of Ce ³⁺ and Eu ²⁺ ions.	78
5.35. Photoluminescence spectra of Ce ³⁺ /Eu ²⁺ codoped amorphous Si ₃ B ₃ N ₇ ceramic at different excitation and emission wavelengths.	79
5.36. Photoluminescence spectra of Ce ³⁺ doped, Eu ²⁺ doped and Ce ³⁺ /Eu ²⁺ codoped amorphous Si ₃ B ₃ N ₇ ceramics (Excitation spectra are measured at maximum emission wavelengths and emission spectra are measured at 365 nm excitation wavelength).	79
5.37. Representation of energy level diagram of Nd ³⁺ ions (for reasons of clarity not all levels have been shown).	80
5.38. Powder X-ray diffractograms of Nd ³⁺ doped and Nd ³⁺ /Eu ²⁺ codoped amorphous Si ₃ B ₃ N ₇ ceramics.	81
5.39. Diffuse reflection spectra of undoped, Nd ³⁺ doped, Eu ²⁺ doped and Nd ³⁺ /Eu ²⁺ codoped amorphous Si ₃ B ₃ N ₇ ceramics.	82
5.40. Photoluminescence spectra of Nd ³⁺ doped amorphous Si ₃ B ₃ N ₇ ceramic at different excitation and emission wavelengths.	82
5.41. Emission spectra of undoped and Nd ³⁺ doped amorphous Si ₃ B ₃ N ₇ ceramics at 330 nm excitation wavelength.	83
5.42. Energy transfer mechanism from Eu ²⁺ ions to Nd ³⁺ ions in Nd ³⁺ /Eu ²⁺ codoped amorphous Si ₃ B ₃ N ₇ ceramic.	84
5.43. Photoluminescence spectra of Nd ³⁺ /Eu ²⁺ codoped amorphous Si ₃ B ₃ N ₇ ceramic at different excitation and emission wavelengths.	85
5.44. Emission spectra of undoped, Eu ²⁺ doped, Nd ³⁺ doped and Nd ³⁺ /Eu ²⁺ codoped amorphous Si ₃ B ₃ N ₇ ceramics measured at 365 nm excitation wavelength.	85
5.45. Representation of energy level diagrams of Sm ²⁺ and Sm ³⁺ ions (for reasons of clarity not all levels have been shown).	86

List of Figures

5.46. Powder X-ray diffractograms of Sm^{3+} doped and $\text{Sm}^{3+}/\text{Eu}^{2+}$ codoped amorphous $\text{Si}_3\text{B}_3\text{N}_7$ ceramics.	87
5.47. Diffuse reflection spectra of undoped, Sm^{3+} doped, Eu^{2+} doped and $\text{Sm}^{3+}/\text{Eu}^{2+}$ codoped amorphous $\text{Si}_3\text{B}_3\text{N}_7$ ceramics.	88
5.48. Photoluminescence spectra of Sm^{3+} doped amorphous $\text{Si}_3\text{B}_3\text{N}_7$ ceramic at different excitation and emission wavelengths.	88
5.49. Photoluminescence spectra of $\text{Sm}^{3+}/\text{Eu}^{2+}$ codoped amorphous $\text{Si}_3\text{B}_3\text{N}_7$ ceramic at different excitation and emission wavelengths.	89
5.50. Emission spectra of Eu^{2+} doped, Sm^{3+} doped and $\text{Sm}^{3+}/\text{Eu}^{2+}$ codoped amorphous $\text{Si}_3\text{B}_3\text{N}_7$ ceramics measured at 365 nm excitation wavelength.	90
5.51. Energy transfer mechanism from Eu^{2+} ions to Sm^{3+} ions in $\text{Sm}^{3+}/\text{Eu}^{2+}$ codoped amorphous $\text{Si}_3\text{B}_3\text{N}_7$ ceramic.	91
5.52. Representation of energy level diagram of Gd^{3+} ions (for reasons of clarity not all levels have been shown).	92
5.53. Powder X-ray diffractograms of Gd^{3+} doped, and $\text{Gd}^{3+}/\text{Eu}^{2+}$ codoped amorphous $\text{Si}_3\text{B}_3\text{N}_7$ ceramics.	93
5.54. Diffuse reflection spectra of undoped, Gd^{3+} doped, Eu^{2+} doped and $\text{Gd}^{3+}/\text{Eu}^{2+}$ codoped $\text{Si}_3\text{B}_3\text{N}_7$ ceramics.	93
5.55. Photoluminescence spectra of Gd^{3+} doped amorphous $\text{Si}_3\text{B}_3\text{N}_7$ ceramic at different excitation and emission wavelengths.	94
5.56. Photoluminescence spectra of $\text{Gd}^{3+}/\text{Eu}^{2+}$ codoped amorphous $\text{Si}_3\text{B}_3\text{N}_7$ ceramic at different excitation and emission wavelengths.	95
5.57. Powder X-ray diffractograms of Tb^{3+} doped, $\text{Tb}^{3+}/\text{Eu}^{2+}$ codoped and $\text{Tb}^{3+}/\text{Ce}^{3+}$ codoped amorphous $\text{Si}_3\text{B}_3\text{N}_7$ ceramics.	96
5.58. Representation of energy level diagram of Tb^{3+} ions (for reasons of clarity not all levels have been shown).	96
5.59. Diffuse reflection spectra of undoped, Tb^{3+} doped, Eu^{2+} doped, Ce^{3+} doped, $\text{Tb}^{3+}/\text{Eu}^{2+}$ codoped and $\text{Tb}^{3+}/\text{Ce}^{3+}$ codoped amorphous $\text{Si}_3\text{B}_3\text{N}_7$ ceramics.	97
5.60. Photoluminescence spectra of Tb^{3+} doped amorphous $\text{Si}_3\text{B}_3\text{N}_7$ ceramic at different excitation and emission wavelengths.	98
5.61. Photos of Tb^{3+} doped amorphous $\text{Si}_3\text{B}_3\text{N}_7$ ceramic under day light and under 254 nm, 320 nm and 365 nm lights.	98
5.62. Three-dimensional representation of photoluminescence spectra for Tb^{3+} doped amorphous $\text{Si}_3\text{B}_3\text{N}_7$ ceramic.	99
5.63. Photoluminescence spectra of $\text{Tb}^{3+}/\text{Eu}^{2+}$ codoped amorphous $\text{Si}_3\text{B}_3\text{N}_7$ ceramic at different excitation and emission wavelengths.	101

5.64. Excitation spectra of Tb ³⁺ doped, Eu ²⁺ doped and Tb ³⁺ /Eu ²⁺ codoped amorphous Si ₃ B ₃ N ₇ ceramics measured at maximum emission wavelengths.	101
5.65. Emission spectra of Tb ³⁺ doped, Eu ²⁺ doped and Tb ³⁺ /Eu ²⁺ codoped amorphous Si ₃ B ₃ N ₇ ceramics measured at 280 nm excitation wavelength.	102
5.66. Emission spectra of Tb ³⁺ doped, Eu ²⁺ doped and Tb ³⁺ /Eu ²⁺ codoped amorphous Si ₃ B ₃ N ₇ ceramics measured at 365 nm excitation wavelength.	102
5.67. Energy transfer mechanism from Eu ²⁺ ions to Tb ³⁺ ions in Tb ³⁺ /Eu ²⁺ codoped amorphous Si ₃ B ₃ N ₇ ceramic.	103
5.68. Photoluminescence spectra of Tb ³⁺ /Ce ³⁺ codoped amorphous Si ₃ B ₃ N ₇ ceramic at different excitation and emission wavelengths.	104
5.69. Emission spectra of Tb ³⁺ /Ce ³⁺ codoped amorphous Si ₃ B ₃ N ₇ ceramic at some selected excitation wavelengths.	106
5.70. Emission spectra of Tb ³⁺ doped, Ce ³⁺ codoped and Tb ³⁺ /Ce ³⁺ codoped amorphous Si ₃ B ₃ N ₇ ceramics measured at 420 nm excitation wavelength.	106
5.71. Tb ³⁺ emissions obtained by subtracting the emission spectrum of Ce ³⁺ doped amorphous Si ₃ B ₃ N ₇ ceramic (blue line) from the emission spectrum of Tb ³⁺ /Ce ³⁺ codoped amorphous Si ₃ B ₃ N ₇ ceramic (black line) in Figure 5.70 measured at 420 nm excitation wavelength.	107
5.72. Representation of energy level diagram of Ho ³⁺ ions (for reasons of clarity not all levels have been shown).	108
5.73. Powder X-ray diffractograms of Ho ³⁺ doped and Ho ³⁺ /Eu ²⁺ codoped amorphous Si ₃ B ₃ N ₇ ceramics.	108
5.74. Diffuse reflection spectra of undoped, Ho ³⁺ doped, Eu ²⁺ doped and Ho ³⁺ /Eu ²⁺ codoped amorphous Si ₃ B ₃ N ₇ ceramics.	109
5.75. Photoluminescence spectra of Ho ³⁺ doped amorphous Si ₃ B ₃ N ₇ ceramic at different excitation and emission wavelengths.	110
5.76. Excitation spectra of undoped and Ho ³⁺ doped amorphous Si ₃ B ₃ N ₇ ceramics measured at 400 nm (black), 440 nm (blue) and 480 nm (red) emissions (solid lines = Ho ³⁺ doped ceramic, dash lines = undoped ceramic).	111
5.77. Emission spectra of undoped and Ho ³⁺ doped amorphous Si ₃ B ₃ N ₇ ceramics measured at 280 nm (black), 365 nm (blue), 385 nm (red) and 400 nm (green) excitations (solid lines = Ho ³⁺ doped ceramic, dash lines = undoped ceramic).	111
5.78. Photoluminescence spectra of Ho ³⁺ /Eu ²⁺ codoped amorphous Si ₃ B ₃ N ₇ ceramic at different excitation and emission wavelengths.	112
5.79. Excitation spectra of Eu ²⁺ doped and Ho ³⁺ /Eu ²⁺ codoped amorphous Si ₃ B ₃ N ₇ ceramics measured at 545 nm emission wavelength.	113

List of Figures

5.80. Emission spectra of Ho^{3+} doped, Eu^{2+} doped and $\text{Ho}^{3+}/\text{Eu}^{2+}$ codoped amorphous $\text{Si}_3\text{B}_3\text{N}_7$ ceramics measured at 365 nm excitation wavelength.	114
5.81. Representation of energy level diagram of Tm^{3+} ions (for reasons of clarity not all levels have been shown).	115
5.82. Powder X-ray diffractograms of Tm^{3+} doped and $\text{Tm}^{3+}/\text{Eu}^{2+}$ codoped amorphous $\text{Si}_3\text{B}_3\text{N}_7$ ceramics.	116
5.83. Diffuse reflection spectra of undoped, Tm^{3+} doped, Eu^{2+} doped and $\text{Tm}^{3+}/\text{Eu}^{2+}$ codoped amorphous $\text{Si}_3\text{B}_3\text{N}_7$ ceramics.	116
5.84. Photoluminescence spectra of Tm^{3+} doped amorphous $\text{Si}_3\text{B}_3\text{N}_7$ ceramic at different excitation and emission wavelengths.	117
5.85. Emission spectra of undoped and Tm^{3+} doped amorphous $\text{Si}_3\text{B}_3\text{N}_7$ ceramics measured at 400 nm excitation.	118
5.86. Photoluminescence spectra of $\text{Tm}^{3+}/\text{Eu}^{2+}$ codoped amorphous $\text{Si}_3\text{B}_3\text{N}_7$ ceramic at different excitation and emission wavelengths.	119
5.87. Powder X-ray diffractograms of Yb doped and Yb/Eu codoped amorphous $\text{Si}_3\text{B}_3\text{N}_7$ ceramics obtained via both the metal and organometallic routes.	120
5.88. Representation of energy level diagrams of Yb^{2+} and Yb^{3+} ions.	120
5.89. Diffuse reflection spectra of undoped, Yb doped and Yb/Eu codoped amorphous $\text{Si}_3\text{B}_3\text{N}_7$ ceramics.	121
5.90. Photoluminescence spectra of Yb doped amorphous $\text{Si}_3\text{B}_3\text{N}_7$ ceramic via the metal route at different excitation and emission wavelengths.	122
5.91. Photoluminescence spectra of Yb doped amorphous $\text{Si}_3\text{B}_3\text{N}_7$ ceramic via the organometallic route at different excitation and emission wavelengths.	123
5.92. Photoluminescence spectra of Yb/Eu codoped amorphous $\text{Si}_3\text{B}_3\text{N}_7$ ceramic prepared via the metal route at different excitation and emission wavelengths.	125
5.93. Photoluminescence spectra of Yb/Eu codoped amorphous $\text{Si}_3\text{B}_3\text{N}_7$ ceramic prepared via the organometallic route at different excitation and emission wavelengths.	125
5.94. Emission spectra of Eu doped and Yb/Eu codoped amorphous $\text{Si}_3\text{B}_3\text{N}_7$ ceramics measured at 365 nm excitation wavelength.	126
5.95. Powder X-ray diffractograms of Sn^{2+} doped and $\text{Sn}^{2+}/\text{Eu}^{2+}$ codoped amorphous $\text{Si}_3\text{B}_3\text{N}_7$ ceramics.	127
5.96. Diffuse reflection spectra of undoped, Sn^{2+} doped, Eu^{2+} doped and $\text{Sn}^{2+}/\text{Eu}^{2+}$ codoped amorphous $\text{Si}_3\text{B}_3\text{N}_7$ ceramics.	128
5.97. Photoluminescence spectra of Sn^{2+} doped amorphous $\text{Si}_3\text{B}_3\text{N}_7$ ceramic at different excitation and emission wavelengths.	128
5.98. Excitation spectra of undoped and Sn^{2+} doped amorphous $\text{Si}_3\text{B}_3\text{N}_7$ ceramics at 480 nm emission.	129

5.99. Excitation spectrum at 500 nm emission wavelength (black line) and emission spectra at 340 nm (red line) and 365 nm (blue line) excitation wavelengths of Sn ²⁺ doped amorphous Si ₃ B ₃ N ₇ ceramic.	129
5.100. Photoluminescence spectra of Sn ²⁺ /Eu ²⁺ codoped amorphous Si ₃ B ₃ N ₇ ceramic at different excitation and emission wavelengths.	130
5.101. Excitation spectra at maximum emission wavelengths and emission spectra at 365 nm excitation wavelength of Eu ²⁺ doped, Sn ²⁺ doped and Sn ²⁺ /Eu ²⁺ codoped amorphous Si ₃ B ₃ N ₇ ceramics.	131
5.102. Powder X-ray diffractograms of Sr ²⁺ doped, Ba ²⁺ doped, Y ³⁺ doped and La ³⁺ doped amorphous Si ₃ B ₃ N ₇ ceramics.	132
5.103. Diffuse reflection spectra of undoped, Sr ²⁺ doped, Ba ²⁺ doped, Y ³⁺ doped and La ³⁺ doped amorphous Si ₃ B ₃ N ₇ ceramics.	132
5.104. Photoluminescence spectra of Sr ²⁺ doped amorphous Si ₃ B ₃ N ₇ ceramic at different excitation and emission wavelengths.	133
5.105. Photoluminescence spectra of Ba ²⁺ doped amorphous Si ₃ B ₃ N ₇ ceramic at different excitation and emission wavelengths.	134
5.106. Photoluminescence spectra of Y ³⁺ doped amorphous Si ₃ B ₃ N ₇ ceramic at different excitation and emission wavelengths.	134
5.107. Photoluminescence spectra of La ³⁺ doped amorphous Si ₃ B ₃ N ₇ ceramic at different excitation and emission wavelengths.	135
5.108. Powder X-ray diffractograms of M/Eu ²⁺ codoped amorphous Si ₃ B ₃ N ₇ ceramics, where M = Sr ²⁺ , Ba ²⁺ , Y ³⁺ and La ³⁺	136
5.109. Diffuse reflection spectra of undoped, Eu ²⁺ doped and M/Eu ²⁺ codoped amorphous Si ₃ B ₃ N ₇ ceramics, where M = Sr ²⁺ , Ba ²⁺ , Y ³⁺ and La ³⁺	137
5.110. Photoluminescence spectra of Sr ²⁺ /Eu ²⁺ codoped amorphous Si ₃ B ₃ N ₇ ceramic at different excitation and emission wavelengths.	137
5.111. Photoluminescence spectra of Ba ²⁺ /Eu ²⁺ codoped amorphous Si ₃ B ₃ N ₇ ceramic at different excitation and emission wavelengths.	138
5.112. Photoluminescence spectra of Y ³⁺ /Eu ²⁺ codoped amorphous Si ₃ B ₃ N ₇ ceramic at different excitation and emission wavelengths.	138
5.113. Photoluminescence spectra of La ³⁺ /Eu ²⁺ codoped amorphous Si ₃ B ₃ N ₇ ceramic at different excitation and emission wavelengths.	139
5.114. Emission spectra of Eu ²⁺ doped and M/Eu ²⁺ codoped amorphous Si ₃ B ₃ N ₇ ceramics, where M = Sr ²⁺ , Ba ²⁺ , Y ³⁺ and La ³⁺ , at 365 nm excitation wavelength.	139

5.115. Photoluminescence spectra of Eu^{2+} doped amorphous $\text{Si}_3\text{B}_3\text{N}_7$ ceramics having various Eu^{2+} concentration (Excitation spectra were measured at maximum emission wavelengths and emission spectra were measured at 365 nm excitation wavelength).	141
5.116. Effect of the Eu^{2+} concentration on the maximum emission wavelength and intensities.	142
5.117. Representation of a configurational coordinate model for the energy transfer followed by reabsorption and reemission (red shift) processes between two neighboring luminescent active centers.	142
5.118. Photos of Eu^{2+} doped amorphous $\text{Si}_3\text{B}_3\text{N}_7$ ceramics having various Eu^{2+} concentration under day light and 366 nm light.	143
5.119. Photoluminescence spectra of Ce^{3+} doped amorphous $\text{Si}_3\text{B}_3\text{N}_7$ ceramics at various Ce^{3+} concentration (Excitation spectra are measured at maximum emission wavelengths and emission spectra are measured at 365 nm excitation wavelength).	143
5.120. Effect of the Ce^{3+} concentration on the maximum emission wavelength and intensities.	144
5.121. Photoluminescence spectra of $\text{Ce}^{3+}/\text{Eu}^{2+}$ codoped amorphous $\text{Si}_3\text{B}_3\text{N}_7$ ceramics at various Ce^{3+} and Eu^{2+} concentrations (Excitation spectra are measured at maximum emission wavelengths and emission spectra are measured at 365 nm excitation wavelength).	144
5.122. Photoluminescence spectra of 2.25 % (wt) Tb^{3+} doped amorphous $\text{Si}_3\text{B}_3\text{N}_7$ ceramic at different excitation and emission wavelengths.	145
6.1. Powder X-ray diffractograms of a) Fe_2O_3 nanoparticles, b) Fe_2O_3 doped SiBN polymer after 210 °C and c) Fe doped $\text{Si}_3\text{B}_3\text{N}_7$ ceramic after 1200 °C.	150
6.2. SEM images of Fe_2O_3 nanoparticles (a and b) and $\text{Si}_3\text{B}_3\text{N}_7:\text{Fe}$ ceramic (c and d) at different magnifications.	150
6.3. Hysteresis loops of Fe doped $\text{Si}_3\text{B}_3\text{N}_7$ ceramic at 5 K and 300 K (The inset is an expanded region of the hysteresis loops depicting the small coercivity and remanence values).	151
6.4. Powder X-ray diffractograms of a) SiBN:Co-1 polymer after 210 °C, $\text{Si}_3\text{B}_3\text{N}_7:\text{Co}$ -1 ceramics after b) 900 °C with NH_3 flow and c) 1200 °C with N_2 flow, starting with $\text{Co}(\text{NH}_3)_6\text{Cl}_3$ as Co source.	153
6.5. Powder X-ray diffractograms of a) SiBN:Co-2 polymer after 210 °C, $\text{Si}_3\text{B}_3\text{N}_7:\text{Co}$ -2 ceramics b) after 900 °C and c) 1200 °C with Ar flow, starting with $\text{Co}(\text{NH}_3)_6\text{Cl}_3$ as Co source.	153

6.6. Powder X-ray diffractograms of a) SiBN:Co-3 polymer after 210 °C, Si ₃ B ₃ N ₇ :Co-3 ceramic after b) 900 °C with NH ₃ flow and c) 1200 °C with N ₂ flow, starting with Co[N(SiMe ₃) ₂] ₂ as Co source.	154
6.7. The SEM images of SiBN:Co-1 (a and b), SiBN:Co-2 (c and d) and SiBN:Co-3 (e and f) ceramics after 1200 °C at different magnifications.	155
6.8. Hysteresis loops for Si ₃ B ₃ N ₇ :Co-1 ceramic at 5 K and 300 K (The inset is an expanded region of the hysteresis loops depicting the small coercivity and remanence values).	156
6.9. Hysteresis loops for Si ₃ B ₃ N ₇ :Co-2 ceramic at 5 K and 300 K (The inset is an expanded region of the hysteresis loops depicting the small coercivity and remanence values).	156
6.10. Hysteresis loops for Si ₃ B ₃ N ₇ :Co-3 ceramic at 5 K and 300 K (The inset is an expanded region of the hysteresis loops depicting the small coercivity and remanence values).	157
6.11. Powder X-ray diffractograms of a) SiBN:Ni polymer after 210 °C, Si ₃ B ₃ N ₇ :Ni ceramics after b) 900 °C with NH ₃ flow and c) 1200 °C with N ₂ flow. . . .	159
6.12. The SEM images of Si ₃ B ₃ N ₇ :Ni ceramic after 1200 °C at different magnifications.	159
6.13. Hysteresis loops of Ni doped Si ₃ B ₃ N ₇ ceramic at 5 K and 300 K (The inset is an expanded region of the hysteresis loops depicting the small coercivity and remanence values).	160
7.1. Powder X-ray diffractogram of Ca ₂ Si ₅ N ₈	163
7.2. Powder X-ray diffractogram of Sr ₂ Si ₅ N ₈	163
7.3. Diffuse reflection spectra of Ca ₂ Si ₅ N ₈ , Eu ²⁺ doped Ca ₂ Si ₅ N ₈ and Eu ₂ Si ₅ N ₈	164
7.4. Diffuse reflection spectra of Sr ₂ Si ₅ N ₈ , Eu ²⁺ doped Sr ₂ Si ₅ N ₈ and Eu ₂ Si ₅ N ₈	164
7.5. Powder X-ray diffractogram of Eu ²⁺ doped Ca ₂ Si ₅ N ₈	165
7.6. Emission spectra of Eu ²⁺ doped Ca ₂ Si ₅ N ₈ at different excitation wavelengths (Inset: Excitation spectrum at 602 nm emission wavelength).	166
7.7. Powder X-ray diffractogram of Eu ²⁺ doped Sr ₂ Si ₅ N ₈	168
7.8. Emission spectra of Eu ²⁺ doped Sr ₂ Si ₅ N ₈ at different excitation wavelengths (Inset: Excitation spectrum at 632 nm emission wavelength).	168
7.9. Powder X-ray diffractogram of Eu ₂ Si ₅ N ₈ synthesized via the metal route.	169
7.10. Powder X-ray diffractogram of Eu ₂ Si ₅ N ₈ synthesized via the organometallic route.	169
7.11. Emission spectra of Eu ₂ Si ₅ N ₈ synthesized via the metal route at different excitation wavelengths (Inset: Excitation spectrum at 684 nm emission wavelength).	170

List of Figures

7.12. Emission spectra of $\text{Eu}_2\text{Si}_5\text{N}_8$ synthesized via organometallic route at different excitation wavelengths (Inset: Excitation spectrum at 681 nm emission wavelength).	170
7.13. Comparison of the emission spectra of Eu^{2+} doped $\text{Ca}_2\text{Si}_5\text{N}_8$ and $\text{Sr}_2\text{Si}_5\text{N}_8$, $\text{Eu}_2\text{Si}_5\text{N}_8$ synthesized via both the metal and the organometallic route, and Eu^{2+} doped amorphous $\text{Si}_3\text{B}_3\text{N}_7$ at 365 nm excitation wavelength.	171
7.14. Powder X-ray diffractogram of $\text{Ce}^{3+}/\text{Li}^+$ codoped $\text{Ca}_2\text{Si}_5\text{N}_8$	173
7.15. Diffuse reflection spectra of $\text{Ca}_2\text{Si}_5\text{N}_8$, $\text{Ce}^{3+}/\text{Li}^+$ codoped $\text{Ca}_2\text{Si}_5\text{N}_8$, $\text{Sr}_2\text{Si}_5\text{N}_8$, and $\text{Ce}^{3+}/\text{Li}^+$ codoped $\text{Sr}_2\text{Si}_5\text{N}_8$	174
7.16. Photoluminescence spectra of $\text{Ce}^{3+}/\text{Li}^+$ codoped $\text{Ca}_2\text{Si}_5\text{N}_8$ at different excitation and emission wavelengths.	174
7.17. Powder X-ray diffractogram of $\text{Ce}^{3+}/\text{Li}^+$ codoped $\text{Sr}_2\text{Si}_5\text{N}_8$	175
7.18. Photoluminescence spectra of $\text{Ce}^{3+}/\text{Li}^+$ codoped $\text{Sr}_2\text{Si}_5\text{N}_8$ at different excitation and emission wavelengths.	175
7.19. Powder X-ray diffractogram of $\text{Tb}^{3+}/\text{Li}^+$ codoped $\text{Ca}_2\text{Si}_5\text{N}_8$	176
7.20. Diffuse reflection spectra of $\text{Ca}_2\text{Si}_5\text{N}_8$, $\text{Tb}^{3+}/\text{Li}^+$ codoped $\text{Ca}_2\text{Si}_5\text{N}_8$, $\text{Sr}_2\text{Si}_5\text{N}_8$, and $\text{Tb}^{3+}/\text{Li}^+$ codoped $\text{Sr}_2\text{Si}_5\text{N}_8$	177
7.21. Excitation spectra of $\text{Tb}^{3+}/\text{Li}^+$ codoped $\text{Ca}_2\text{Si}_5\text{N}_8$ at different emission wavelengths (Inset represents the zoomed spectra).	177
7.22. Emission spectra of $\text{Tb}^{3+}/\text{Li}^+$ codoped $\text{Ca}_2\text{Si}_5\text{N}_8$ at different excitation wavelengths.	178
7.23. Powder X-ray diffractogram of $\text{Tb}^{3+}/\text{Li}^+$ codoped $\text{Sr}_2\text{Si}_5\text{N}_8$	179
7.24. Excitation spectra of $\text{Tb}^{3+}/\text{Li}^+$ codoped $\text{Sr}_2\text{Si}_5\text{N}_8$ at different emission wavelengths (Inset represents the zoomed spectra).	179
7.25. Emission spectra of $\text{Tb}^{3+}/\text{Li}^+$ codoped $\text{Sr}_2\text{Si}_5\text{N}_8$ at different excitation wavelengths.	180
7.26. Powder X-ray diffractogram of Mn^{2+} doped $\text{Sr}_2\text{Si}_5\text{N}_8$	181
7.27. Representation of the energy levels of Mn^{2+} ions.	182
7.28. Diffuse reflection spectra of $\text{Sr}_2\text{Si}_5\text{N}_8$ and Mn^{2+} doped $\text{Sr}_2\text{Si}_5\text{N}_8$	182
7.29. Photoluminescence spectra of Mn^{2+} doped $\text{Sr}_2\text{Si}_5\text{N}_8$ at different excitation and emission wavelengths.	183
7.30. Powder X-ray diffractogram of $\text{Ce}^{3+}/\text{Li}^+$ codoped $\text{BaSi}_7\text{N}_{10}$	185
7.31. Diffuse reflection spectrum of $\text{Ce}^{3+}/\text{Li}^+$ codoped $\text{BaSi}_7\text{N}_{10}$	185
7.32. Photoluminescence spectra of $\text{Ce}^{3+}/\text{Li}^+$ codoped $\text{BaSi}_7\text{N}_{10}$ at different excitation wavelengths.	186
7.33. Powder X-ray diffractogram of $\text{Tb}^{3+}/\text{Li}^+$ codoped $\text{BaSi}_7\text{N}_{10}$	187
7.34. Diffuse reflection spectrum of $\text{Tb}^{3+}/\text{Li}^+$ codoped $\text{BaSi}_7\text{N}_{10}$	187

7.35. Excitation spectra of Tb ³⁺ /Li ⁺ codoped BaSi ₇ N ₁₀ at different emission wavelengths (Inset represents the zoomed spectra).	188
7.36. Emission spectra of Tb ³⁺ /Li ⁺ doped BaSi ₇ N ₁₀ at different excitation wavelengths.	189
7.37. Powder X-ray diffractogram of CeSi ₃ N ₅	191
7.38. Diffuse reflection spectra of CeSi ₃ N ₅	191
7.39. Photoluminescence spectra of CeSi ₃ N ₅ at different excitation and emission wavelengths.	192
8.1. Synthesis of TDSB (a) and a proposed mechanism (b).	194
8.2. Mass spectrum of TDSB.	195
8.3. a) ¹ H-NMR, b) ¹³ C-NMR, c) ²⁹ Si-NMR, d) ¹¹ B-NMR spectra and e) numbering scheme of TDSB molecule.	196
8.4. FT-IR spectrum of TDSB.	197
8.5. Molecular structure of TDSB.	203
8.6. A view of TDSB molecules along the [001] direction (<i>c</i> -axis).	203
8.7. Powder X-ray diffractograms of P-TDSB-1 and P-TDSB-2.	205
8.8. FT-IR spectrum of P-TDSB-1.	205
8.9. FT-IR spectrum of P-TDSB-2.	206
8.10. DTA/TG/MS thermogram of P-TDSB-1 polymer.	208
8.11. DTA/TG/MS thermogram of P-TDSB-2 polymer.	208
8.12. Powder X-ray diffractograms of C-TDSB-1, C-TDSB-2 and C-TDSB-3 after 1400 °C.	210
8.13. FT-IR spectrum of C-TDSB-1.	211
8.14. FT-IR spectrum of C-TDSB-2.	211
8.15. FT-IR spectrum of C-TDSB-3.	212
8.16. High-temperature-DTA/TG thermogram (heating cycles) of of C-TDSB-1.	212
8.17. High-temperature-DTA/TG thermogram (heating cycles) of C-TDSB-2.	213
8.18. High-temperature-DTA/TG thermogram (heating cycles) of C-TDSB-3.	213
8.19. Powder X-ray diffractogram of C-TDSB-1 after 1970 °C.	214
8.20. Powder X-ray diffractogram of C-TDSB-2 after 1970 °C.	214
8.21. Powder X-ray diffractogram of C-TDSB-3 after 1970 °C.	215
9.1. TGA/DTA thermograms of pristine open cell Basotect [®] foam.	218
9.2. SEM picture of pristine Basotect [®] foam.	218
9.3. SEM picture of the SiBNC ceramic foam obtained from preceramic polymer which is coated on the open cell walls of Basotect [®] foam once.	219
9.4. SEM picture of the SiBNC ceramic foam obtained from preceramic polymer which is filled in the open cell volume of Basotect [®] foam.	219

List of Figures

9.5. SEM picture of the SiBNC ceramic foam obtained from preceramic polymer coated on the open cell walls of Basotect[®] foam twice. 220

List of Tables

3.1. NMR characteristics of some selected isotopes.	16
4.1. Reactions to generate E-N bonds (E= Si, B and R=Alkyl)	28
4.2. Reactions to generate E-C bonds (E=Si, B and R=Alkyl)	29
8.1. NMR spectroscopic data of TDSB.	195
8.2. IR absorptions of TDSB.	197
8.3. Crystal data and structure refinement for TDSB at 273 K.	199
8.4. Atomic coordinates ($\times 10^4$) and equivalent isotropic displacement parameters ($\text{\AA}^2 \times 10^3$) for TDSB. U_{eq} is defined as one third of the trace of the orthogonalized U^{ij} tensor.	200
8.5. Anisotropic displacement parameters ($\text{\AA}^2 \times 10^3$) for TDSB. The anisotropic displacement factor exponent takes the form: $-2\pi[h^2a^{*2}U^{11} + \dots + 2hka^*b^*U^{12}]$	201
8.6. Torsion angles ($^\circ$) of TDSB.	201
8.7. Bond lengths (pm) of TDSB.	202
8.8. Bond angles ($^\circ$) of TDSB.	202
8.9. IR absorptions of P-TDSB-1.	206
8.10. IR absorptions of P-TDSB-2.	207
8.11. Chemical compositions (% weight) of ceramics from TDSB after 1400 $^\circ\text{C}$.	210
8.12. IR absorptions of ceramics derived from P-TDSB polymers.	210
10.1. Commercially supplied chemicals.	222
10.2. Experimental details, maximum emission wavelengths and full width at half maximum (FWHM) values for doped amorphous $\text{Si}_3\text{B}_3\text{N}_7$ ceramics.	225
10.3. Chemical compositions (weight %) of some luminescent rare earth doped amorphous $\text{Si}_3\text{B}_3\text{N}_7$ and Si_3N_4 ceramics.	230
10.4. Experimental details, maximum emission wavelengths and full width at half maximum (FWHM) values for crystalline nitridosilicate-type ceramics.	236

List of Tables

Part I.

Introduction

1. Introduction

Ceramics have always been a part of daily life since the beginning of the human civilization and still play a crucial role to improve the quality of our lives, both in conventional applications and in innovative products. Among others, high performance ceramics are one of the most fascinating materials of our age which allow previously unachieved combinations of mechanical, electrical, thermal and chemical properties to be attained [1, 2]. Therefore, these materials find easily new structural and functional applications which innovate new technologies.

In recent years, amorphous multinary non-oxide ceramics such as $\text{Si}_3\text{B}_3\text{N}_7$ and SiBN_3C have attracted great attentions both in academy and industry [1, 3]. They exhibit surprisingly outstanding mechanical, chemical and thermal stabilities even under oxidizing conditions compared to binary non-oxide ceramics such as BN, Si_3N_4 and SiC, although amorphous materials are considered to be thermodynamically unstable with respect to transformation or decomposition to the crystalline phases. The three-dimensional networks of these amorphous ceramics contain both strong covalent bonds between the elements silicon, boron, nitrogen and carbon and different coordination geometry of the cationic functions, which make rearrangements of the chemical bonds difficult, and thus these materials resist the crystallization even at higher temperatures [1, 3].

Unlike multinary oxide ceramics, silicon boron carbonitrides (Si/B/N/C) can not be produced via conventional solid state reactions (powder route), starting from the pure elements and/or respective binary compounds. Since nitrides and carbides of silicon and boron are melting incongruently, and cations of silicon and boron have very low self-diffusion coefficients, the only feasible approach for the production of Si/B/N/C known so far is the “*polymer route*”. Many ideas for the synthesis of new single source precursors and an excellent insight in multinary non-oxide amorphous ceramics can be found in a detailed review by Jansen et. al. and references therein [4].

A wide variety of application areas, mainly under extreme conditions, for amorphous Si/B/N/C ceramics are expected such as in heat engines (in particular turbines) and aerospace. This is due to having not only the attractive properties such as low density, low thermal coefficient of expansion, low thermal conductivity, high thermal shock resistivity, and good mechanical properties, especially at high temperatures, but also a broad choice in processing. Preceramic molecules and polymers can be obtained virtually any physical

1. Introduction

state so that chemical vapour deposition can be applied for gaseous or volatile single source precursors, injection molding, microstructuring, coating, infiltration and fiber spinning can be applied for liquid or meltable preceramic polymers and finally conventional powder processing can be applied for the solid precursors and the derived ceramics. Among others, the most promising application of amorphous SiBN_3C are fibers due to having superior performance as compared to crystalline SiC in the market, and these are the only fibers which fulfill the specifications of the European aircraft engine manufacturers for the second generation turbines [1]. It is proved by the successful application of amorphous SiBN_3C ceramics in fiber technology that amorphous $\text{SiBN}(\text{C})$ ceramics can play a crucial role in other emerging technologies as well. Therefore, it appears to be particularly beneficial to explore further fields of application and, of course, new single source precursors for improved properties in final ceramics. In this respect, the present study has aimed to apply the amorphous $\text{Si}_3\text{B}_3\text{N}_7$ ceramic as a host matrix for new functional materials, e.g., luminescent (Chapter 5) and ferromagnetic (Chapter 6) ceramics, and the amorphous SiBN_3C ceramic for a new structural material, e.g., open-cell ceramic foam (Chapter 9). Moreover, synthesis of new cyclic single source precursor molecules has also been aimed at (Chapter 8). In addition to the research on ternary and quaternary amorphous ceramics, a novel production method for nitridosilicate-type crystalline ceramics has been developed (Chapter 7).

In the present work, fluorescence spectroscopy, diffuse reflection spectroscopy, Fourier transform infrared (FT-IR) spectroscopy, single crystal analysis, powder X-ray diffraction, magnetic measurements, gas chromatography / mass spectroscopy (GC/MS), nuclear magnetic resonance (NMR) spectroscopy, scanning electron microscopy (SEM), inductively coupled plasma optical emission spectroscopy (ICP-OES), differential thermal analysis / thermal gravimetry / mass spectroscopy (DTA/TG/MS), and high temperature differential thermal analysis (HT-DTA) were applied as main analytical methods.

Part II.
General Part

2. Preparative Working Methods

2.1. Vacuum and Inert Gas Apparatus

All manipulations during syntheses were performed under inert conditions due to having air and moisture sensitive starting materials. Desired inert conditions were achieved with a vacuum and inert gas apparatus which is made from Duran glass (Figure 2.1).

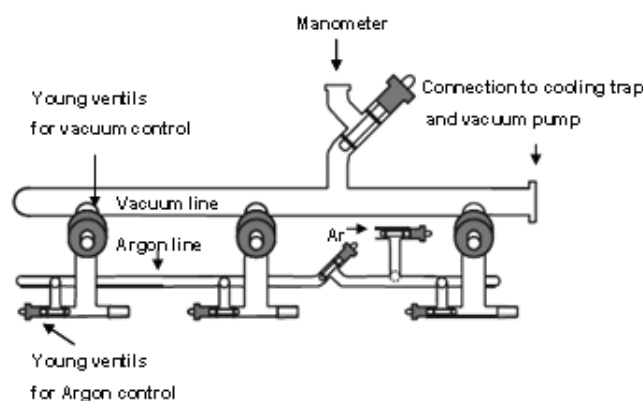


Figure 2.1.: Vacuum and argon manifold.

This apparatus is connected to a rotary valve oil pump with a liquid nitrogen cold trap in between. Argon (purity grade 4.8, Messer-Griesheim, Krefeld, Germany) is chosen as the inert gas and is directly supplied to the all laboratories by the low temperature service department (Max-Planck-Institute, Stuttgart, Germany) through the copper pipe infrastructure, and is used after a further purification process. Teflon valves (Young ventil) are used for main vacuum and argon flow controlling.

2.2. Vacuum Devices

The desired fine vacuum is achieved by using a rotary vane vacuum pump (Trivac D4B, Oerlikon Leybold Vacuum GmbH, Köln, Germany) which is connected to the vacuum and inert gas apparatus with a flexible metal tube. The quality of vacuum is controlled by a manometer (Thermovac TM 20, Leybold) within a range of 10^{-3} - 10^3 mbar. Intermediate pressures up to 10 mbar is adjusted with a membrane pump (MZ 2C, Vacuubrand GmbH, Wetheim, Germany), especially for vacuum distillation.

2.3. Purifying and Drying the Solvents and Gases

Solvents such as hexane, pentane, tetrahydrofurane (THF) and ethers are dried by refluxing them with the presence of sodium metal and benzophenone up to get a bluish color. And then, they are distilled and stored under argon atmosphere in the presence of sodium wires.

Argon, which is received from the common lines, needs further purification in order to remove any contamination of moisture and oxygen (Figure 2.2). First of all, it is entered into a silicon oil bubbler which is used as flow controller. Then, it is passed through four successive drying towers of blue gel, potassium hydroxide, molecular sieves (3 Å mesh size) and phosphorous pentoxide on an inert substrate (Sicapent, Merck), respectively. After that, it is connected to a pressure regulator (e.g. a mercury bubbler). Finally, it is passed through a titanium sponge (Sigma-Aldrich, USA) filled in a quartz tube, which is heated to 700 °C with a furnace (Loba, HTM Reetz GmbH, Berlin, Germany).

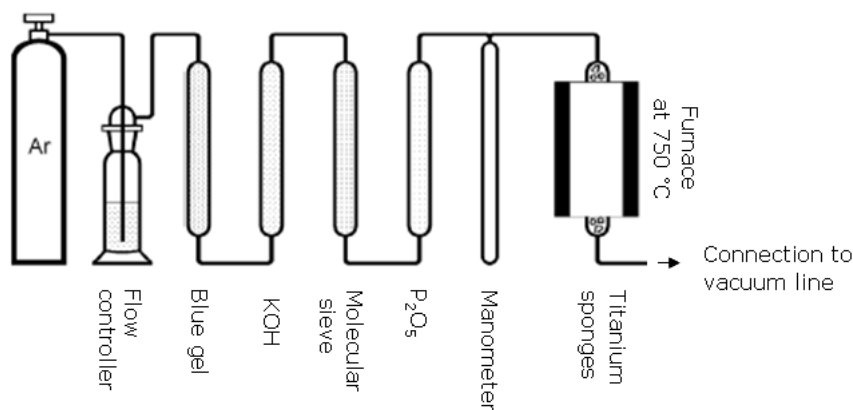


Figure 2.2.: Set up for purification of argon.

2.4. Handling of Air-sensitive Substances

All of the present work have been performed as much as possible only with glassware systems, which can be connected from their joints and sealed with silicon grease (Wacker, München, Germany). Before any manipulation, glassware systems, which are connected to the vacuum and inert gas apparatus, are several times evacuated up to 10^{-3} mbar regime, heated with a Bunsen burner under vacuum and filled with dried argon in order to ensure that the apparatus is completely inert and free of moisture. Standard Schlenk techniques have been applied for handling air and moisture sensitive substances [5, 6]. Any filling or removing processes of these substances are done under argon flow. Liquids are transferred by a single-use syringe (Norm-Ject, Henke Sass Wolf GmbH, Tuttlingen,

Germany) connected with a single-use needle (Supra, Ehrhardt MMedizinprodukte, Geislingen, Germany), which are several times flushed with dried argon. Substances, which can not be handled with vacuum and inert gas apparatus, are handled in argon-filled glove-boxes (MT 200, MB 150BG-II, MB 200B, M.Braun GmbH, Garching, Germany), which have water and oxygen levels less than 0.1 ppm.

2.5. Pyrolysis Devices

The pyrolysis of preceramic polymers is usually performed in two steps. Before each of the pyrolysis process, an empty boron nitride (BN) crucible (Henze Boron Nitride Products GmbH, Kempten, Germany) is loaded into the quartz tube in a horizontal furnace (max. 1200 °C, LOBA, HTM Reetz GmbH, Berlin, Germany) which is connected to the vacuum and inert gas apparatus. Then, it is heated with 100 °C/h to 600 °C under vacuum, kept at that temperature for 5 hours and cooled down to room temperature with 100 °C/h in order to make the system inert. The first step after loading the sample is heating the furnace to 300 °C with 100 °C/h and keeping at that temperature for 3 hours in order to remove organic impurities. Afterwards, it is further heated to 900 °C with 100 °C/h, kept at that temperature for 3 hours and finally cooled down to room temperature with 100 °C/h. The first step can be done under N₂, Ar or NH₃ atmospheres. The second step is calcination of the sample at higher temperatures, e.g. 1200 °C or higher, for 3 to 5 hours in an alumina tube furnace (LORA 1800, HTM Reetz GmbH, Berlin, Germany and Carbolite STF 15/50, Carbolite, Hope Walley, UK), which has constant N₂ or Ar flow.

2. *Preparative Working Methods*

3. Analytical Methods

3.1. Fluorescence Spectroscopy

Fluorescence is the optical emission from a sample that is excited to higher energy levels by absorption of electromagnetic radiation. Therefore, in fluorescence spectroscopy, the sample is first excited, by absorbing a photon, from its ground electronic state to one of the various vibrational states in the excited electronic state. Then, the excited species immediately relaxes nonradiatively to the lowest vibrational state of the excited electronic state by losing the vibrational energy due to the collisions with other molecules. The excited species then relax radiatively (by emitting a photon) to one of the various vibrational levels of the ground electronic state again, after which they immediately relax nonradiatively to the lowest vibrational state of the ground electronic state.

Generally, excitation and emission spectra are measured by fluorescence spectrometer. An *emission spectrum* is the wavelength distribution of an emission at a single constant excitation wavelength. Conversely, an *excitation spectrum* is the dependence of emission intensity, measured at a single emission wavelength, upon scanning the excitation wavelength [7]. Unlike the other spectroscopy techniques, the fluorescence is most often measured at a 90° angle relative to the excitation light in order to avoid interference of the transmitted excitation light. No monochromator is perfect and transmits some stray light. On the other hand, measuring at a 90° angle, only the light scattered by the sample causes the stray light, resulting in a better signal-to-noise ratio, and lowering the detection limit. Furthermore, the fluorescence can also be measured from the front, which is often done for turbid and powder samples. In a typical experiment, a light source of radiation produces photons. The beam of light is filtered by an excitation spectrometer that allows a single wavelength of light to reach the sample. In the sample compartment, the sample responds to the incoming radiation. The resulting radiation is filtered by an emission spectrometer that feeds the signal to a photomultiplier detector. By stepping either or both spectrometers through a wavelength region, and recording the variation in intensity as a function of wavelength, a spectrum is produced.

During the measurements of excitation and emission spectra, the most common source of unwanted light is higher-order light diffraction by the monochromator [7]. Light diffraction at grating can occur as a first, second- or third-order process. These diffraction orders

3. Analytical Methods

frequently overlap and can result in extraneous light passing through the both excitation and emission monochromators. Therefore, the emission spectrum of a sample can have peak at twice the excitation wavelength due to the second-order transmission through the emission monochromator. In order to avoid the second-order peak in emission spectrum either the emission monochromator is scanned up to the wavelengths less (usually 10 nm) than twice the excitation wavelength or a bandpass excitation filters are used.

Photoluminescence spectra have been obtained by using a Fluorolog[®]-3 Model FL3-22 (Horiba Jovin Yvon, Bensheim, Germany) equipped with a 450-W xenon light source, two double grating monochromators in the excitation and emission paths in an “L” configuration (Czerny Turner design), a T-box sample compartment module with a flat sample holder and a front face emission collector, and a photomultiplier detector (room temperature R928P detector) (Figure 3.1). A black anodized aluminum sample holder was used, which has in the middle $12 \times 6 \times 1.6$ mm³ space, in which powder samples can be fixed with the help of a 0.2 mm thick suprasil glass.

The excitation and emission spectra were recorded in the range of 240 nm - 490 nm and 385 nm - 750 nm, respectively. To illustrate, an emission spectrum at 365 nm excitation wavelength was obtained as follow: First of all, 365 nm light was created by the excitation monochromator. Then, the 365 nm light was exposed on the sample and the emission monochromator was scanned through 385 nm and 750 nm, during which the amount of the emitted photons were counted by the photomultiplier detector (i.e., the emission intensity was recorded as count per second, cps). In a similar manner, an excitation spectrum at 570 nm emission wavelength was obtained as follow: In this case, the emission monochromator was fixed to 570 nm; in other words, only the 570 nm light could pass through the emission monochromator and reach to the detector. Then the excitation monochromator was scanned through 240 nm and 490 nm, during which the amount of the emitted photons at 570 nm were counted by the photomultiplier detector (i.e., the emission intensity was recorded as count per second, cps, for 570 nm created by each of the excitation wavelength).

The excitation and emission slit widths were adjusted between 0.55 nm and 0.68 nm in order not to exceed the linear range of the R928P detector, that is $2 \cdot 10^6$ count per second. In order to avoid the second-order peak in emission spectrum, a 385 nm bandpass excitation filter was used. All emission spectra were corrected with regard to detector sensitivity and all excitation spectra were corrected with regard to the intensity of xenon lamp. Data acquisition and analysis were performed by the software FluorEssenceTM, created by Horiba Jobin Yvon. The photoluminescence spectra were plotted by using the program Origin 8G. Inside the present thesis, the abbreviations “em” and “ex” in photoluminescence spectra refer to which wavelength the excitation and emission spectrum, respectively, are recorded.

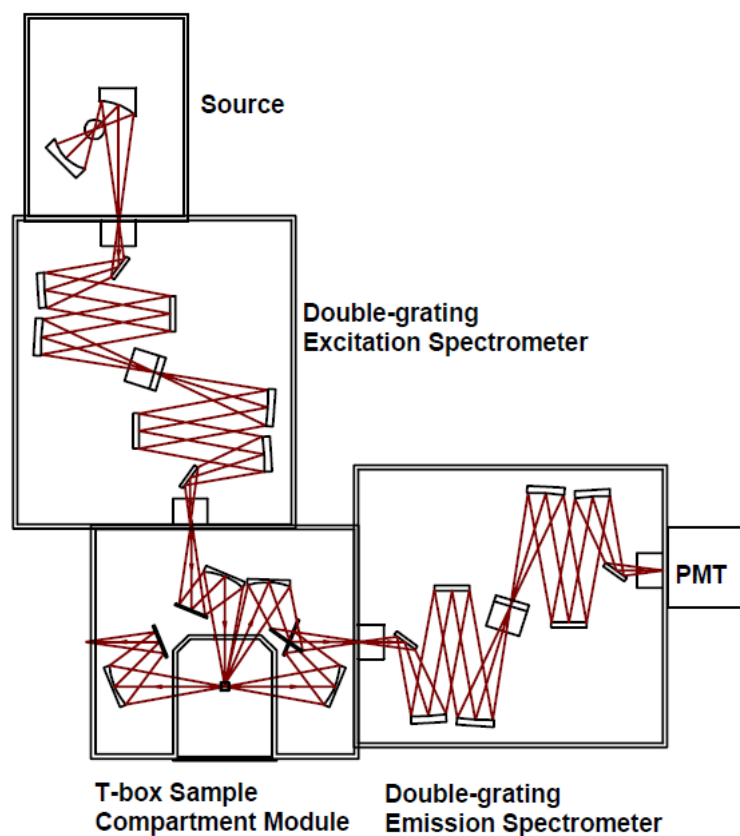


Figure 3.1.: Schematic representation of a double grating fluorescence spectrometer.

3.2. Diffuse Reflection Spectroscopy

Diffuse reflection spectroscopy is based on the focused projection of the spectrometer beam into the sample where it is reflected, scattered and transmitted through the sample. The back reflected, or diffusely scattered light, is then collected by the accessory (e.g., an integrating sphere) and directed to the detector optics. Only the part of the beam that is scattered within a sample and returned to the surface is considered to be diffuse reflection. Diffuse reflection spectra of the samples were obtained with a double beam Perkin Elmer Lambda 19 UV/VIS/NIR Spectrometer (Bodenseewerk Perkin Elmer & Co GmbH, Überlingen, Germany) equipped with a deuterium lamp for UV/VIS range and a Tungsten-Halogen lamp for NIR range, prealigned sources with automatic switch-over, two double beam holographic grating monochromators (1440 lines/mm in UV/VIS range and 360 lines/mm in NIR range) and a 60 mm integrating sphere (B013-9941, Perkin Elmer). A black anodized aluminum sample holder was used, which has in the middle $20 \times 12 \times 1.5 \text{ mm}^3$ space in which powder samples are fixed with the help of 0.5 mm thick suprasil glass. Integration sphere was internally coated with BaSO_4 , which was also used as reference material and equipped with a side-on photomultiplier and a PbS cell, permitting the measurements in the spectral range from 200 nm to 2600 nm with

3. Analytical Methods

wavelength accuracy of 0.2 nm in UV/VIS range and 0.8 nm in NIR range. The sample and reference ports on integration sphere were configured such that the respective materials were angled at 8° to the plane of incident radiation. The specular component reflected from the surface of the sample was thus directed to the specular component aperture covered with a specular component trap. By this configuration, the specular radiation was absorbed in this trap and could not enter the sphere, so that only the diffuse component reflected from the surface was measured. Acquisition of the data was performed by using UV Winlab 2.70.01 (Perkin Elmer), and saved as ASCII file, which was converted to graphics by using the Origin 8G.

3.3. Fourier Transform Infrared Spectroscopy (FT-IR)

Infrared spectroscopy utilizes the specific frequencies at which molecules rotate or vibrate corresponding to discrete energy levels (vibrational modes). The shape of the molecular potential energy surfaces, the masses of the atoms and the associated vibronic coupling determine the resonant frequencies. A permanent dipole moment change is the main requirement in order for a vibrational mode in a molecule to be IR active. The mid-infrared, approximately $4000\text{--}400\text{ cm}^{-1}$ ($30\text{--}1.4\text{ }\mu\text{m}$) may be used to study the fundamental vibrations and associated rotational-vibrational structure. In a Fourier transform infrared (FTIR) spectrometer, the IR light is guided through an interferometer instead of recording the amount of energy absorbed when the frequency of the infra-red light is varied (monochromator), after which a mathematical Fourier transform is performed on this signal to result in a spectrum identical to that from conventional (dispersive) infrared spectroscopy. The infrared spectra of the present work have been obtained with a Fourier Transform Infrared Spectrometer IFS 113v (Bruker Optik, Karlsruhe, Germany) equipped with vacuum optic and Genzel Interferometer in between 400 cm^{-1} and 4000 cm^{-1} wavenumbers with a resolution of 2 cm^{-1} . A silicon carbide globar was used as a radiation source and a DTGS (deuterated triglycine sulphate) detector was used for detection. Spectra were analyzed with OPUS program [8], and saved as ASCII file, which is converted to graphics by using the Origin 8G. Moisture or air sensitive substances were prepared in a glove box and transported in an argon filled desiccator. Roughly between 1 and 2 mg of the solid substances together with 500 mg of dried KBr (99 % + f.d. IR-Spectroscopy, Aldrich) are finely ground in an agate mortar and pestle, and pressed about 10 minutes with a hydraulic press at 0.8 GPa to obtain transparent pellets with 13 mm diameter.

3.4. Gas Chromatography / Mass Spectroscopy

A Triple-Quadrupole Mass Spectrometry (TSQ 700, Finnigan MAT, Bremen, Germany) was used for mass spectroscopy analysis. Schematic representation is given in Figure 3.2.

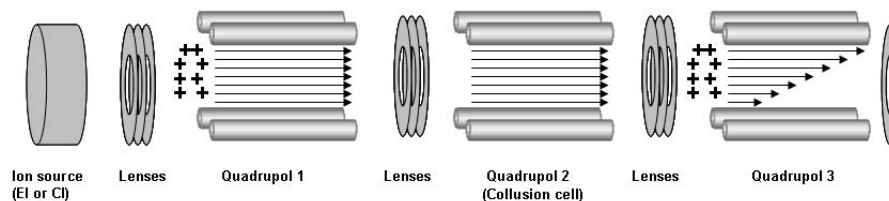


Figure 3.2.: Schematic representation of a triple-quadrupole mass spectrometer.

The ionization was achieved by electron ionization with 70 eV. Quadrupole 3 is adjusted as mass analyzer, whereas quadrupole 1 was adjusted as mass filter and transmitter and quadrupole 2 was adjusted as only transmitter modes. Three electrostatic lenses were used to focus the ions in between the quadrupoles. The ion source, the three quadrupoles and the detector (Channeltron multiplier with conversion dynode) were fixed in a high vacuum system at around $3 \cdot 10^{-6}$ mbar. Ion source was kept at 150 °C and the quadrupoles and the detector at 70 °C. The sensitivity of the measurement is 0.1 mass-to-charge (m/z) ratio. The analyses of the mass spectra were done by using ICIS program, and saved as ASCII file, which was converted to graphics by using the Origin 8G. Mass spectra of liquid and low volatile samples were obtained by coupling of a gas chromatography (Varian 3400, Varian, Darmstadt, Germany) to the Mass Spectrometer. A 30 m x 0.25 mm capillary column (J&W Scientific, Folsom, CA, USA) and helium (99.996 %, Westfalen AG, Münster, Germany) as carrier gas were used. A Y-shaped quartz glass short-cut was adjusted just before the entrance of the capillary column to the mass spectrometer in order to analyze the reactive liquid substances, especially containing -BCl groups, which are reacting with and damaging the stationary phase of the column. One end of the Y-shaped quartz short-cut was connected to the end of the capillary column and the other end was connected to the mass spectrometer with 70 cm long same capillary column. A shorter capillary column (around 15 cm long) was connected to the last exit of the short-cut, which was kept closed by a rubber septum. Air sensitive reactive liquid samples were prepared under inert conditions in a glass container having screw cap with rubber septum sealing. They were measured by inserting the short exit of the short-cut glass like a needle through the rubber septum on the cap and inserted just above the liquid in order to allow the vapours to go directly into the mass spectrometer. By this way, contamination and degradation of the all column are avoided. Air sensitive solid samples were sealed into a glass capillary which is fitting the space on the heatable sample insertion rod. This glass capillary was broken just before the analysis and inserted into the direct insertion unit and evacuated

3. Analytical Methods

as fast as possible. After evacuation, the sample was directly moved into the ionization chamber and measured subsequently.

3.5. Nuclear Magnetic Resonance (NMR) Spectroscopy

Nuclear magnetic resonance (NMR) spectroscopy exploits a physical resonance phenomenon involving the observation of specific quantum mechanical magnetic properties of an atomic nucleus in the presence of an applied external magnetic field. A key feature of NMR is that the resonance frequency of a particular substance is directly proportional to the strength of the applied magnetic field. NMR usually involves two sequential steps: the alignment (polarization) of the magnetic nuclear spins in a constant applied magnetic field and the perturbation of this alignment of the nuclear spins by employing an electromagnetic, usually radio frequency (RF) pulse. The required perturbing frequency is dependent upon the static magnetic field (H_0) and the nuclei of observation.

Table 3.1.: NMR characteristics of some selected isotopes.

Property	^1H	^{11}B	^{13}C	^{29}Si
Spin	1/2	3/2	1/2	1/2
Natural abundance (%)	99.985	80.42	1.108	4.70
Gyromagnetic constant (γ) $10^7 \text{ rad T}^{-1} \text{ s}^{-1}$	26.751	8.58	6.726	-5.314
External standard	SiMe_4	$\text{BF}_3 \cdot \text{OEt}_2$	SiMe_4	SiMe_4
NMR frequency in MHz at 7.05 T	300.13	96.25	75.46	59.63
Receptivity relative to ^1H at natural abundance	1	0.133	1.76×10^{-4}	3.69×10^{-4}
Receptivity relative to ^{13}C at natural abundance	5680	754	1	2.09

The NMR spectroscopic analysis of liquid samples were performed by using a AVANCE DPX-300 SB spectrometer (Bruker Analytik, Karlsruhe) equipped with a 300 MHz magnet ($B_0 = 7.05 \text{ T}$) and a 5 mm broad band sampling head (^1H , ^{109}Ag , ^{31}P) which could be heated between $-80 \text{ }^\circ\text{C}$ and $100 \text{ }^\circ\text{C}$ by using XWIN-NMR program. The graphics of the spectra were plotted via XWIN-PLOT program. In this work, ^1H , ^{11}B , ^{13}C , ^{29}Si nuclei were analyzed. NMR spectrometric characteristics of these nuclei were presented in Table 3.1. The ^{13}C -NMR spectra were recorded by coupling with broad band ^1H . The samples

were measured in a borosilicate glass tube (WG-5 mm Economy 8, Rototec Spintec GmbH, Biebesheim, Germany) which could be closed with a plastic cap. Deuterated benzene (C_6D_6) with a deuteration amount at least 99.5 % (Merck, Darmstadt, Germany) was used as a solvent. Roughly 5 mg of sample was dissolved in 0.5 ml deuterated solvent for measurements. Air sensitive samples were prepared under inert conditions and the cap was additionally sealed with parafilm.

3.6. X-ray Analysis

Crystals are regular arrays of atoms, and X-rays can be considered waves of electromagnetic radiation. Atoms scatter X-ray waves, primarily through the electrons of the atoms. To illustrate, a lighthouse produces secondary circular waves when an ocean wave strikes. This phenomenon is known as elastic scattering, and the lighthouse is considered as the scatterer. In the same way, an electron in a crystal produces secondary spherical waves when an X-ray strikes. Therefore, a regular array of scatterers produces a regular array of spherical waves. Although these waves cancel one another out in most directions through destructive interference, they add constructively in a few specific directions, determined by Bragg's law:

$$2d \cdot \sin \theta = n \cdot \lambda$$

where d is the spacing between diffracting planes, θ is the incident angle, n is any integer, and λ is the wavelength of the beam. These specific directions appear as spots on the diffraction pattern, often called reflections. Thus, X-ray diffraction results from an electromagnetic wave (the X-ray) impinging on a regular array of scatterers (the repeating arrangement of atoms within the crystal). X-ray crystallography is a method of determining the arrangement of atoms within a crystal, in which a beam of X-rays strikes a crystal and scatters into many different directions. A three-dimensional picture of the density of electrons within the crystal can be deduced from the angles and intensities of these scattered beams, by which various informations such as the mean positions of the atoms in the crystal, the chemical bonds and the disorderness can be determined.

3.6.1. Powder X-ray Diffraction Analysis

Crystallinity of the powder samples were analyzed at ambient conditions either by a transmission diffractometer Stadi P (Stoe & Cie, Darmstadt) or a laboratory diffractometer D8 in the Bragg-Brentano geometry (Bruker, USA). The X-rays were generated in a fine focus tube with Cu anode by using a germanium [111] single crystal as a monochromator (Cu- $K_{\alpha 1}$ radiation, $\lambda=1.5406 \text{ \AA}$) and focused on goniometer. For Stadi P, a position

3. Analytical Methods

sensitive image plate detector with a high angle low resolution (PSD1 – Position Sensitive Detector, angle range 35° , $\Delta 2\theta = 0.15^\circ$) was used for routine analyzes, whereas a high resolution linear detector with an effective range of 6° and a resolution of 0.06° (PSD2) was used for high resolution measurements. Elementary silicon (cubic, $Fd\bar{3}m$, $a = 543.08(8)$ pm) was used as an external standard for calibration. For D8, a LynxEye position sensitive detector with a 3.5° opening angle was used. Air sensitive samples were measured in a glass capillary ($\varnothing=0.1-0.7$ mm) in Debye-Scherrer geometry. Other samples were measured either with Stadi P in transmission geometry with a flat sample holder on which powder sample was distributed in a silicone grease and kept in between two X-ray amorphous polyethylene foils, or with D8 in the Bragg-Brentano geometry with a Si(911)-zero-background sample holder on which powder sample was distributed with ethanol. In all cases, the sample was spun during measurement for better particle statistics. The obtained powder X-ray patterns were analyzed by using the WinXPow program [9]. The substances were identified by comparing their powder diffraction pattern with previously recorded diffractograms, stored in databases such as ICSD [10] and JCPDS [11].

3.6.2. Single Crystal Analysis

For single crystal structure analysis, a crystal was picked and glued on a thin capillary. For air sensitive samples, this thin capillary with the crystal fixed at the tip was put in a wider capillary in a glove box. Then, it was fixed onto a goniometer head for adjustment into the X-ray beam. The measurements were performed with a dual plane detector diffractometer IPDS II (Stoe & Cie, Darmstadt, Germany) and a three circle diffractometer AXS Smart with CCD 1000 detector (Bruker, Karlsruhe, Germany), both equipped with a fine focus tube with Mo-anode (Mo- $K_{\alpha 1}$ radiation $\lambda=71.073$ pm) as source of the X-rays and graphite single crystal as monochromator. From the experimentally measured reflections and intensities the data were processed by using the program SMART32 [12]. Further data reductions and absorption corrections were carried out with the program SADABS [13]. The structures were solved with the help of direct methods using SHELXTL version 6.12 [14]. The refinements of structures were carried out by the least squares refinement procedure with the help of the SHELXTL program package [14].

3.7. Thermal Analysis

Thermal analysis exploits the properties of materials upon changing the temperature. Several methods are commonly used, which are distinguished from one another by the measured property. Differential thermal analysis (DTA) is a technique, in which a sample and an inert reference experience an identical thermal cycles, while recording any tem-

perature difference between sample and reference. This differential temperature is then plotted against time, or against temperature (DTA curve or thermogram). Changes in the sample, either exothermic or endothermic, can be detected relative to the inert reference. Thus, a DTA curve provides data on the transformations that have occurred, such as glass transitions, crystallization, melting and sublimation. The area under a DTA peak is the enthalpy change and is not affected by the heat capacity of the sample. Thermogravimetric analysis (TGA) is method to determine changes in weight in relation to change in temperature. Therefore, a high degree of precision in weight, temperature, and temperature change are required. As many weight loss curves look similar, a transformation may be required to interpret the results; i.e., a derivative weight loss curve can be used to tell the point at which weight loss is most apparent.

DTA / TG analysis up to 1350 °C were performed simultaneously by a thermal analyzer STA 409 C (Netzsch, Selb, Germany). By this method, the change in the mass of the sample due to its decomposition was studied by heating the sample to a controlled temperature program in oxygen or argon atmosphere. The decomposition products were detected with a quadrupole mass spectrometer QMS 421(Balzers, Hudson, USA) with a Skimmer[®] coupling system from corundum, connected to DTA / TG system. For the measurement, between 5 and 30 mg samples were placed (in glove box for air sensitive samples) in a corundum sample holder and heated with 10 K/min heating rate up to desired temperature under oxygen or argon flow. Thermal analysis up to 2000 °C was performed with a thermal analyzer STA 409 C (Netzsch, Selb, Germany), equipped with a special high temperature oven unit under He atmosphere. Only ceramic samples, which were previously heated in another furnace at least up to the 1200 °C, were measured with this machine in order to prevent the damaging of the thermo elements by the reactive gases outcoming during the heat treatment.

3.8. Magnetic Measurements

Magnetic measurements are performed in order to have an idea about the presence of the unpaired electrons in a substance. It is possible to distinguish between diamagnetic, paramagnetic, ferromagnetic, ferrimagnetic and anti-ferromagnetic substances, depending on the magnetic moment and the kind of magnetic interaction. Magnetic measurements in this work were achieved by using a superconducting *quantum interference device* (SQUID), MPMS 5.5 (Quantity Design, San Diego, USA), which can operate between 1.7 K and 800 K in a homogeneous magnetic field up to 7 T. Powder samples were measured in a gelatin capsule; therefore, magnetic contribution of the capsule was corrected. All other diamagnetic contributions were considered according to the literature data [15].

3.9. Scanning Electron Microscopy and Energy Dispersive X-ray Analysis

The scanning electron microscope (SEM) is a type of electron microscope that images the sample surface by scanning it with a high-energy beam of electrons in a raster scan pattern, in which an image is subdivided into a sequence of (usually horizontal) strips known as "scan lines". The electrons interact with the atoms that make up the sample producing signals (including secondary electrons (SE), back scattered electrons (BSE), characteristic X-rays) that contain information about the sample's surface topography and composition. In a typical SEM, an electron beam is thermoionically emitted from an electron gun fitted with a tungsten filament cathode. When the primary electron beam interacts with the sample, the electrons lose energy by repeated random scattering and absorption within a teardrop-shaped volume of the specimen known as the interaction volume. The energy exchange between the electron beam and the sample results in the reflection of high-energy electrons by elastic scattering, emission of secondary electrons by inelastic scattering and the emission of electromagnetic radiation, each of which can be detected by specialized detectors. The beam current absorbed by the specimen can also be detected and used to create images of the distribution of specimen current. Electronic amplifiers of various types are used to amplify the signals which are displayed as variations in brightness on a cathode ray tube. The raster scanning of the CRT display is synchronised with that of the beam on the specimen in the microscope, and the resulting image is therefore a distribution map of the intensity of the signal being emitted from the scanned area of the specimen. In an SEM, magnification results from the ratio of the dimensions of the raster on the specimen and the raster on the display device and is, therefore, controlled by the current supplied to the scanning coils, and not by objective lens power. The most common imaging mode collects low-energy (<50 eV) secondary electrons that are ejected from the k-orbitals of the specimen atoms by inelastic scattering interactions with beam electrons. Due to their low energy, these electrons originate within a few nanometers from the sample surface and are detected by a scintillator-photomultiplier detector system. Backscattered electrons (BSE) consist of high-energy electrons originating in the electron beam, that are reflected or back-scattered out of the specimen interaction volume by elastic scattering interactions with specimen atoms. Since heavy elements (high atomic number) backscatter electrons more strongly than light elements (low atomic number), and thus appear brighter in the image, BSE are used to detect contrast between areas with different chemical compositions and are usually detected either by scintillator or semiconductor type detectors. X-rays, which are also produced by the interaction of electrons with the sample, may also be detected in an SEM equipped for energy-dispersive X-ray (EDX) spectrometer. When a sample is bombarded with electrons via SEM device,

a high-energy electron ejects an electron from the inner-shell of the atom and leaves a vacancy behind in the shell. Afterwards, the excited electrons return immediately to their initial state (radiative recombination) by emitting X-rays, characteristic of the elements in the sample.

The morphology of the samples in this study was characterized by a SEM XL 30 TMP (Philips Electron Optics, Eindhoven, The Netherlands), with a tungsten cathode. Even though the size of the accelerating voltages applied to the filament was infinitely variable up to 30 kV, most of the measurements were performed at 25 kV accelerating voltage. SEM device was integrated with an EDX spectrometer (EDAX, Traunstein-Neuhof, Germany) with a S-UTW-Si(Li) detector (Super Ultra Thin window technology, Polymer window, active detection area of 10 mm², resolution < 135 eV for Mn-K_α / 100 cps and 65 eV for Cu-K_α / 100 cps). The qualitative and the quantitative analyses of the X-rays were performed by the program Phoenix (EDAX, Traunstein-Neuhof, Germany) [16].

3.10. Quantitative Elemental Analysis

Elemental analysis is a method to determine the amounts (typically in weight percent) of elements in a compound. This method is particularly useful in determining the elemental composition and thus the empirical formula of the compound.

3.10.1. Carrier Gas Heat Extraction

The quantitative analyzes of nitrogen and oxygen were obtained by using a carrier gas heat extraction analyzer TC-436 (LECO, St. Joseph, MI, USA). About 10-20 mg of sample were weighed in a Sn capsule and about 0.9 g of Ni powder and 0.35 g of granulated Sn were added. The compressed capsule, which serves as a metallic flux, was transferred into a preheated graphite crucible and heated about 2500 °C under helium flow in the chamber of the analyser. Under this reduced condition, bonded oxygens are converted to CO and then all are oxidized to CO₂, which is quantified by infrared absorption. Nitrogen was detected in a heat conductivity cell. The carbon content was determined by using a carrier gas heat extraction analyzer C-200 (LECO, St. Joseph, MI, USA). Approximately 20 mg sample together with 1 g of Cu and 0.8 g of Fe powders were mixed, put into a Mullit crucible and heated inductively to about 2200 °C under O₂ flow. The CO₂ formed was detected by IR absorption. Calibration standards used for O, N and C are SiO₂, Si₃N₄ and SiC, respectively.

3.10.2. Inductively Coupled Plasma Optical Emission Spectroscopy (ICP-OES)

Inductively Coupled Plasma Optical Emission Spectroscopy (ICP-OES) is used for quantitative and qualitative determination of metals and certain non-metals in solution. The liquid sample is nebulised into a plasma where the temperature is sufficiently high to break the chemical bonds, liberate elements present and transform them into a gaseous atomic state. Certain number of atoms pass immediately into the excited state and then emit radiation when they return the ground state. The frequency of the emitted radiation is characteristic for the element that is used for identification purposes. The intensity of this radiation is proportional to the concentration of that element within the solution that is used for quantitative purposes.

The B and Si in digestion solutions were determined with an optical emission spectrometer ARL 3580 B (ARL, EcuBlens, Switzerland) equipped with inductively coupled plasma [17]. Digestion solutions were prepared by dissolving samples at elevated temperatures in a mixture of HNO₃/HF under pressure by using a steel pressure digestion vessel DAB-1 (Berghof, Eningen, Germany) equipped with a 10 ml PTFE liner. A multi channel analyzer is configured together with a conventional grating monochromator as a vacuum spectrometer in a Paschen-Runge mounting. It allows to measure simultaneous light intensities in addition to sequential determination of emission lines of up to 50 elements in a wavelength range between 170 nm and 810 nm. A low energy plasma chamber was used as plasma source in which an argon plasma was obtained in order to quantize the elements to analyze. In addition to these measurements, some measurements were obtained by using a Vista Pro Simultaneous ICP-OES (Varian, Darmstadt, Germany) equipped with an axial plasma, an Echelle-polychromator and a CCD detector. The data analyzes were done by ICP Expert Software. Calibration of Si and B were carried out by standard addition method.

Part III.
Special Part

4. Literature Overview

4.1. Multinary Amorphous Non-oxide Ceramics

Oxide ceramics have extensively been explored since almost the beginning of modern chemistry due to availability of multinary systems obtained from their binary compounds, mostly via conventional solid state synthesis. Various structural and functional multinary oxide ceramics were developed such as lead zirconate titanates (PZTs) as ferroelectrics [18, 19] and cuprates as high temperature superconductors [20, 21, 22]. It has been demonstrated that fine tuning in chemical composition resulted in optimization of desired properties in multinary systems. To illustrate, the maximum T_c for $\text{YBa}_2\text{Cu}_3\text{O}_{7-x}$ is obtained when x is close to 0.4; however, no transition to the superconducting state at all is achieved when $x > 0.5$ [23]. Even though the scientific community has realized the versatility of the multinary systems like in oxides, in the field of non-oxide ceramics, currently only binaries such as Si_3N_4 , SiC and BN are in use, and potentially more capable multinary non-oxide nitrides and carbides seem to have remained essentially unexplored. Attempts to obtain multinary non-oxide ceramics from their binary compounds via conventional solid state reactions - so called powder route - have always failed and only composites of the binary compounds have been obtained, which exhibit better properties than pure binary compounds. The main reason of these failures is the extremely low self diffusion coefficients of silicon or boron in their nitrides or carbides. In addition to this, binary silicon or boron carbides or nitrides have high melting points such that at least one of the reactants decomposes at the temperature required to complete the solid state reaction [24, 25, 26]. Due to these thermodynamic considerations, no solid state synthesis of the multinary compounds within the system Si/B/N/C from the binary compounds has been successful so far; therefore, it was extremely urgent to find an alternative approach for the synthesis.

Fortunately, considerable progress has been achieved in the past decades in the syntheses of multinary non-oxide materials by applying the only alternative synthetic approach which is based on molecular and polymeric intermediates. Based on the basic idea to construct a solid material from molecular or polymeric precursors, the Sol-Gel process was the first route to apply for the production of multinary oxides [27, 28, 29, 30, 31, 32]. The classical Sol-Gel technique allows at room temperature successful synthesis of homogeneous

4. Literature Overview

multinary oxide materials in various shapes generated in the gel state, i.e., monoliths, films, fibers, and mono-sized powders. They are used for many specific applications including protective and porous films, optical coatings, window insulators, dielectric and electronic coatings, high temperature superconductors, reinforcement fibers, fillers, and catalysts. This technique involves the generation of inorganic networks through the formation of a colloidal suspension (sol) via hydrolysis and polycondensation reactions of precursors such as metal alkoxides and metal chlorides and gelation of the sol via evolving to form a network in a continuous liquid phase (gel). This synthesis route has already been applied for the synthesis binary non-oxide ceramics such as SiC [33, 34, 35], BN [36, 37] and Si₃N₄ [38, 39, 40, 41, 42] not only as powders but also, for the first time, as fibers. Most recent and rather successful approach has aimed to produce multinary non-oxide ceramics along with the “Polymer Route” for the systems such as ternary Si/B/N [1, 43], Si/C/N [44, 45, 46, 47, 48, 49, 50, 51, 52], B/N/C [53, 54, 55, 56, 57] and quaternary Si/B/N/C [1, 4, 43]. The main idea behind the polymer route is to produce multinary ceramics from preceramic polymers. However, a special way to produce a Si/B/N/C polymers through crosslinking of a Si/N/C polymers with a borane adduct has been interpreted as polymer route which is not the way of thinking in this work [58]. Actually, the idea of polymer route was first proposed in 1964 by Chantrell and Popper [59] for preparation of ceramics starting from inorganic polymers even though, in 1961, Nöth et al. published a borazine-based SiBNC polymer without reporting any investigations of this polymer related to its use as a ceramic precursor [60]. Ten years after this proposal, a pioneering work by Winter et al. [49, 61, 62] appeared in the literature for the production of Si/C/N fibers via the pyrolysis of a spinnable inorganic polymer which is synthesized by the ammonolysis or aminolysis of methylchlorosilanes. One year after, in 1975, Yajima et al. [33, 34] developed a method for the production of SiC fibers (Nicalon) in industrial scale via pyrolysis of polycarbosilanes, which is obtained by polymerization of dichlorodimethylsilane through Wurtz-analogous synthesis with subsequent rearrangement. In 1984, Seyfert et al. [38, 39, 40, 41, 63, 64] succeeded in producing of Si₃N₄ in industrial scale via pyrolysis of polysilazanes which is obtained by ammonolysis of chlorosilanes. In addition to these pioneering studies, Si, B, N and C containing inhomogeneous polymers have been obtained by either polymer mixing such as co-condensation of polysila(za)nes and polyboranes or by polymer modification such as copolymerization of polysila(za)nes with boranes. In 1985, Takamizawa et al. modified polysilanes with molecular borazine derivatives and pyrolysed them between 800 and 1500 °C, yielding SiC, BN and B₄C composite fibers in which Si:B ratio were between 13:1 and 46.3:1 [65, 66, 67]. These composite fibers were reported to have improved mechanical and thermal properties as compared to Nicalon SiC fibers. In 1990, Seyfert et al. published a modification of (CH₃SiH₂NH)_n oligomer mixture with H₃B.S(CH₃)₃ to obtain a borosilazane polymeric precursor [68]. Pyrolysis of this

polymer at 1500 °C was reported to give BN and Si₃N₄ composite without mentioning any X-ray data. Even though the authors announced to discuss amorphous borosilicon carbonitride and borosilicon nitride and their conversion to crystalline nanocomposites of Si₃N₄ and BN in further publications, such reports have never appeared in the literature. All these works and following efforts employing polymer mixing or polymer modifications resulted in heterogeneous final ceramics with a composite type microstructure [69]. On the other hand, many researchers preferred to produce crystalline composites of non-oxide ceramics. However, in 1992, Jansen et al. [43] developed a novel synthesis method for producing amorphous and homogeneous ternary Si₃B₃N₇ and quaternary SiBN₃C ceramics which is based on polymerization of a molecular single source precursor. The main idea behind aiming at amorphous network rather than crystalline materials was the realization of the major drawback in mechanical durability at higher temperatures of non-metallic crystalline inorganic materials due to being inherently brittle. Since all crystalline materials are preferably cleaved along the lowly indexed lattice plane, a promising approach to overcome this problem appeared to resort to amorphous inorganic networks, which possess no lattice planes and additionally can absorb the fracture energy via reorientation of dangling bonds [1]. At the beginning, this idea seemed to contradict with its nature because amorphous materials are thermodynamically unstable with respect to the transformation to crystalline phases. However, proper selection of elements such as silicon, boron, nitrogen and carbon, possessing binding energies derived from strong and local covalent bonds, makes them less dependent on long range crystalline order. On the other hand, having different coordination geometries of the cationic functions makes the rearrangement of the chemical bonds difficult, and such networks may resist crystallization even at higher temperatures. All these factors of influence would allow to produce amorphous materials with remarkable thermal and mechanical durability. The only elegant way for such “*molecular design*” of the ceramics is to use molecular single source precursors [1]. In this context, as the main requirements of single source precursors, they should contain the elements with “cationic” structural chemical function in the same ratios as desired in the final ceramic and should include the same structural bridging elements as in the targeted crystalline or amorphous ceramics. This had been achieved, for the first time, for the amorphous ceramics obtained by the single source precursor, (trichlorosilylamino)-dichloroborane (TADB). This precursor is obtained via two step reaction starting from hexamethyldisilazane, SiCl₄ and BCl₃. Ammonolysis or aminolysis of TADB yields polyborosilazanes, and further pyrolysis gives amorphous Si₃B₃N₇ or SiBN₃C ceramics [43]. This sensational achievement through the single source precursor by Jansen et al. attracted great attention among the researchers in both academy and industry [1, 4, 70, 71]. After this invention, an extensive research has been performed to find new single source precursors, to improve thermal and mechanical properties of Si/B/N/C ceramics and, of course, to find potential applications

4. Literature Overview

of the ceramics.

There is a certain number of chemical reactions suited to synthesize single source precursors for non-oxide ceramics. Single source precursors generally contain two different elements such as silicon and boron linked by a nitrogen or a carbon atom, and the resulting molecule should be functionalized enabling for polycondensation reactions following aminolysis or transamination. The main reactions for generating E-N bonds are given in Table 4.1, and for E-C bonds in Table 4.2, where E=Si, B.

Table 4.1.: Reactions to generate E-N bonds (E= Si, B and R=Alkyl)

Dehydrohalogenation
$\text{E-Cl} + 2 \text{H-NR}_2 \longrightarrow \text{E-NR}_2 + \text{NH}_2\text{R}_2 \text{ Cl}$
Salt Elimination
$\text{E-Cl} + \text{Li-NR}_2 \longrightarrow \text{E-NR}_2 + \text{LiCl}$
Silazane and Stannazane Cleavage
$\text{E-Cl} + \text{R}_3\text{M-NR}_2 \longrightarrow \text{E-NR}_2 + \text{R}_3\text{MCl} , \text{ M=Si,Sn}$
Aminolysis or Transamination
$\text{E-NR}_2 + \text{H-NR}'_2 \longrightarrow \text{E-NR}'_2 + \text{H-NR}_2$
Hydrogen Elimination
$\text{E-H}^{\delta^-} + \text{H}^{\delta^+}\text{-NR}_2 \longrightarrow \text{E-NR}_2 + \text{H}_2$

Silazane cleavage reactions appeared to be the most convenient and versatile approach for preparing precursors containing nitrogen bridging between the electropositive elements such as silicon and boron. A significant number of important precursors have been synthesized via this method including (trichlorosilylamino)-dichloroborane (TADB) [43], so far the most successful precursor, B,B,B-tris-[trichlorosilylmethyl]-borazin (TSMB) [72], the first cyclic single source precursor, and some others [73, 74, 75, 76, 77, 78]. The major advantage of the respective reaction sequences is that easily recyclable volatile adducts are evolving, which is of particular interest for economical and environmental reasons. In addition, ceramic yields are usually high and heat of reactions are low, which all in all makes this approach very attractive to scale up for mass production. Alternative to silazane cleavage, stannazane cleavage is also widely applied and especially preferred when the reactivity of silazanes is not sufficiently high [79, 80]. Even though this reaction path works well in the laboratory for basic research, the major drawback of it is being toxic, and thus has not been considered for scaling up.

Dehydrohalogenation was applied for the synthesis of dichloroboryl-methyl-trichlorosilylamine (DMTA) and dichloroboryl-dichloro-(methyl)silyl- methyl-amine (DDMA) through

Table 4.2.: Reactions to generate E-C bonds (E=Si, B and R=Alkyl)

Metathesis or Transmetallation
$E-Cl + M-CR_3 \longrightarrow E-CR_3 + MCl$, $M=Li, MgCl$
$B(OR)_3 + 2 MgCl-CR_3 \longrightarrow (RO)_2B-CR_3 + Mg(OR)Cl$
Hydrosilylation and Hydroboration
$R_2-C=C-R_2 + H-E \longrightarrow R_2H-C-C-ER_2$
Organotin route
$SnR_4 + 2 BCl_3 \longrightarrow R_2SnCl_2 + 2 BCl_2R$
Kumada Rearrangement
$R_2(CH_3)Si-SiR_3 \longrightarrow R_2HSi-CH_2-SiR_3$
Wurtz Analogous Dehalogenation
$R_2(CH_3)Si-Cl + Cl-SiR_3 \longrightarrow R_2(CH_3)Si-SiR_3$
Müller-Rochow Synthesis
$2 R-Cl + Si + Cu \text{ (catalyst)} \longrightarrow R_2SiCl_2$

a gas phase reaction in high yields [81]. Even though separation of the salts is generally a problem in this reaction path, having available continuous processes for production of DMTA and DDMA with cheap starting compounds makes them particularly well suited for scaling up. Transmetallation is also widely applied reaction path for creating especially boron-nitrogen bonds [80, 82]. Starting compounds containing acidic NH functional unit is metallated by organolithium compounds like n-butyllithium and subsequent reaction of readily formed lithium amide with a suitable element halide like borontrichloride gives the desired precursor compound together with lithium halide [80, 82]. Using organolithium reagents and difficulties of separation of the salt make this path unfeasible in scaling up. In this respect, transamination and hydrogen elimination reactions can be a promising technique due to generally obtaining gaseous side products such as amines and hydrogen gas [83]. However, both reaction paths give highly reactive compounds which makes the control of process quite difficult.

Hydroboration and transmetallation (salt elimination) are two major reaction paths to obtain carbon boron bonds. By hydroboration, not only new single source precursors but also polymers for Si/B/N and Si/B/C/N ceramics can be prepared. This method basically includes the addition of boranes to carbon-carbon double bonds. In contrast to hydrosilylation [84, 85, 86], hydroboration reactions usually does not require any catalyst [87, 88]. This method had first been employed by Jones and Myers [89] to produce silylorganoboranes by the reaction of unsaturated methylchlorosilylalkenes with dibo-

4. Literature Overview

ranes. Later, Riccitiello et al. reported to synthesize polyborosilanes via hydroboration of methylvinylsilanes by boranes or diboranes [90]. Based on these results, Aldinger et al. [91] and Riedel et al. [92] applied hydroboration reactions of different borane adducts with various vinylsilanes to obtain single source precursors with a carbon bridge between silicon and boron. As a major drawback of this route, a mixture of single source precursors is obtained with different regioisomers resulting in a complex mixture of molecules with different chemical and physical properties. Reports on isolation of the individual isomers prior to polymerization has never appeared so far in the literature, most probably due to being very laborious and costly. Fortunately, a more elegant method has been inspired from the work of Soundararajan and Matteson, who obtained highly reactive intermediate HBCl_2 in situ by mixing trichloroborane and trialkylsilane [93, 94]. In 1997, Jansen and Jünger mann used HBCl_2 for the hydroboration of vinylchlorosilanes and obtained a new family of single source precursors containing a branched carbon bridge between boron and silicon like $\text{Cl}_3\text{Si}-\text{CH}(\text{CH}_3)-\text{BCl}_2(\text{TSDE})$ [95, 96]. More interestingly, reacting TSDE with hexamethyldisilazane gave corresponding borazine derivative $[\text{B}\{\text{CH}(\text{CH}_3)(\text{SiCl}_3)\}\text{NH}_3]_3$ (TSEB) in an almost quantitative yields [97]. Organotin routes can also be applied to obtain boron carbon bonds, however, this route is usually avoided due to having toxic products after the reactions.

Transmetallation reactions have been widely applied to form silicon-carbon bonds [98]. First organosilicon compounds were synthesized by Friedel and Crafts by heating Et_2Zn and SiCl_4 [99]. Shortly after the discovery of Grignard reagents [100], Kipping synthesized a mixture of EtSiCl_3 , Et_2SiCl_2 , Et_3SiCl , Et_4Si by reacting SiCl_4 and EtMgI [101]. In 1941, E. G. Rochow [102, 103] and R. Müller [104] discovered independently the direct process of organosilicon compounds which have had a high impact in silicon industry. This is known as Müller-Rochow process (also known as Direct Synthesis or Direct Process) that involves a copper-catalyzed reaction of alkyl halides with silicon metal [105, 106, 107, 108, 109, 110]. Kumada, in 1953, had accidentally observed, on a very cold day, the formation of hexamethyldisilanes during the fractional distillation of undesired high-boiling-point side-products of Müller-Rochow process, and thermal treatment of $\text{Me}_3\text{SiSiMe}_3$ yielded $\text{Me}_3\text{SiCH}_2\text{SiHMe}_2$ [111, 112, 113, 114]. This is now known as Kumada rearrangement, which later served as a model reaction for Yajima's process for the production of SiC fibers from methylpolysilanes obtained via Wurtz-analogous dehalogenation of Me_2SiCl_2 [33, 34, 35]. Since both Müller-Rochow reactions and Kumada rearrangements yield always mixed products which are laborious to separate, these reactions are not the preferred ones for the synthesis of single source precursors. Moreover, silicon-carbon bonds are formed in the final ceramic not only due to existing in the structure of single source precursor but also observed that carbon in crosslinking agent, e.g. methyl amine, is spontaneously incorporated into network upon pyrolysis.

Alternatively, boron-carbon and silicon-carbon bonds can be created, even intramolecularly, by transmetallation reactions via lithiation or Grignard reagents. An elegant Grignard reagent for synthesis of Si-C-B containing compounds is obtained from the reaction between haloalkylsilanes and magnesium. In principle, desired organoboranes can be obtained by the reaction between a haloborane and a silicon Grignard reagent. However, a big conflict had been faced with these reactions such that the preparation of silicon Grignard reagents can only be carried out in ethers, such as diethylether or THF, in which trihaloboranes act as strong Lewis acids and react rapidly with the solvent [115]. Fortunately, this problem was overcome by Jansen et al. by using a haloborane with low Lewis acidity like dialkoxyhaloborane, and a subsequent halogenation of organoborane dialkylesters yielded new class of single source precursor molecules, having a methylene bridge between B and Si, i.e. $\text{Cl}_3\text{Si-CH}_2\text{-BCl}_2$ (TSDM) and $(\text{CH}_3)\text{Cl}_3\text{Si-CH}_2\text{-BCl}_2$ (DSDM). Reacting these precursors with hexamethyldisilazane gives corresponding borazine derivatives $[\text{B}\{\text{CH}_2(\text{SiCl}_3)\}\text{NH}]_3$ (TSMB) and $[\text{B}\{\text{CH}_2(\text{SiCl}_2(\text{CH}_3))\}\text{NH}]_3$ (DSMB), respectively [72, 116].

Substituents of the cationic elements, e.g. silicon and boron, of single source precursor molecule are chosen so that they allow the molecule to convert to polymer easily. Halogens (predominantly chlorides) or amino ($-\text{NR}_2$) leaving groups are frequently preferred as substituents. Amino substituents have significant advantages over halogen ones because polycondensation via transamination of amino groups typically forms volatile products whereas dehydrohalogenation of halogen groups forms salt. Alkoxy groups, $-\text{OR}$, should not be considered as substituent in order to avoid possible incorporation of oxygen into polymer, and finally into ceramic. Single source precursors with hydride substituents have the advantage that polymerization can be carried out without any crosslinking agents, such as ammonia or (alkyl)amine, rather via hydrogen gas removal. Unsaturated substituents can also be used in single source precursors, and polymerization of them can be achieved either radicalic and ionic polymerization, or addition reactions such as hydroboration and hydrosilylation. It is crucially essential that reactive crosslink sites of all the cationic functional elements should not allow only one component to be preferably carried out during pyrolysis.

Composition and properties of final ceramic are governed not only by molecular precursor applied but also by crosslinking reagent used for polymerization. The number of crosslinkable functional sites in monomeric precursor molecule together with thermal treatment of the polymer, after removal of solvent, affect the degree of crosslinking, therefore rheological properties of polymer [117, 118]. To illustrate, a carbon-rich crosslinking agent results in ceramics with increased carbon content [119]. Two fundamentally different approaches are generally applied to get multinary preceramic polymers: either co-condensation of mixture of molecules, each containing only one cationic element or

4. Literature Overview

polymerization of single-source precursors, containing all cations in a ratio required for the final ceramic.

Pre-ceramic polymers by co-condensation have widely been applied for Si/B/N, Si/B/C and Si/B/N/C ceramics. Dietz et al. have obtained a polymer via co-ammonolysing mixtures of SiCl_4 and BCl_3 for Si/B/N ceramics, which was a composite of BN and Si_3N_4 [120]. Hydrogen elimination is an attractive method to obtain polymers by co-condensation. However, the crucial precondition for this is that the precursor molecule and crosslinking agent have to bear differently polarized hydrogen atoms. The Sol-Gel process for the synthesis of oxides has been adapted for the production of polyborosilazanes and has been named as Ammono-Sol-Gel process. In the latter, metal alkoxides are replaced by alkylamides and water by ammonia as the solvolysing agent [121, 122, 123, 124]. Among others, hydroboration is the most widely applied in order to obtain polymers via co-condensation. Boranes have been reacted with (poly)silanes for Si/B/N [125] or Si/B/C [126] and (poly)silazanes for Si/B/N/C [127] polymers. (Poly)alkylsila(z)anes have been reacted with borane adducts to obtain various polyboro(carbo)sila(z)anes [91, 128, 129, 130, 131, 132, 133]. SiBNC polymers can also be obtained by direct bonding of borazine units on to (poly)organosilazanes [134, 135, 136, 137]. Moreover, Funayama et al. have modified various hydropolysilazanes with boron alkoxides, boron halides and aminoboranes [138, 139, 140, 141].

In contrast to co-condensation route, reaction control on a molecular level for pre-ceramic polymers via crosslinking of single source precursors seems to be possible. A large number of nitrogen containing crosslinking agents are available, i.e. ammonia and primary or secondary amines [1, 43, 69, 73, 76, 80, 95]. Thus, choosing the crosslinking reagents in this route is very crucial in order to tailor the properties of polymers and ceramics. Among these, ammonia and methylamine are the most versatile and preferred ones. Polycondensation via ammonia yields highly crosslinked insoluble and unmeltable solid polymers together with the formation of ammonium chloride salt, which can be removed from the polymer by washing with liquid ammonia (laborious) or by sublimation (relatively expensive) [142, 143]. Employing methyl amine instead of ammonia yields liquid, or dissolved, polymer and an ammonium salt which can easily be removed by filtration. By appropriate heat treatment, the polymer can be tailored as liquid, meltable, soluble or unmeltable for any desired application. Other than ammonia and amines, hexamethyldisilazane, cyanamide, bis(trimethylsilyl)carbodiimide, formamide, cyanoguanidine, guanidine or melamine can also be used as crosslinking agents [58, 83, 91, 130, 144, 145, 146, 147, 148].

After the polymerization, an additional heat treatment process is applied to polymer for further polycondensation. Upon increasing the temperature to several hundred degrees, organic fragmentations take place, indicating the transition to "pyrolysis". All volatile

compounds (mainly organics) are removed during the pyrolysis until a pure inorganic solid residuum is obtained. In the first step of the heating process, depending on nature of polymer, polycondensation is usually completed between 200 °C and 500 °C by releasing the products such as methylamine, hydrogen, ammonia or trimethylsilyl. In the second step, at about 600 °C, the biggest weight loss occurs and mostly methane, hydrogen, hydrogen cyanide, methylamine, acetonitrile, dimethylamine are evolved. Finally, at about 1100 °C, residual hydrogen and a small amount of nitrogen are lost [1, 149]. Depending on composition, way of synthesis and especially on the oxygen content, Si/B/N/(C) ceramics start to crystallize between 1500 °C and 1900 °C into composites consisting of α/β -SiC and α/β -Si₃N₄ [1, 58].

It has been shown that increasing the carbon content in the final ceramic improved significantly the thermal durability of Si/B/N random networks [150]. Moreover, the hardness, stiffness and thermal durability of Si/B/N/C ceramics increase with incorporation of rigid structural elements into the amorphous network like borazine rings [97, 151]. It is attributed that the covalent Si/B/N/C network is strengthened by the highly inflexible borazine rings as a rigid backbone. As a result, reorientation of atoms (e.g. on upcoming decomposition) is significantly suppressed, making the whole network stiffer and stronger.

Since there is no long-range order in these amorphous ceramics, structural investigations of them are still quite challenging. Apart from theoretical studies [152, 153, 154, 155, 156, 157, 158], only a few analytical techniques have been applied such as XANES [159, 160, 161, 162, 163], IR, Raman, TEM [164], and solid state NMR spectroscopy [76, 151, 165, 166, 167, 168, 169, 170, 171, 172]. Among those, solid state NMR spectroscopy had already been proved to be one of the most versatile techniques to investigate short or medium range ordering in amorphous networks.

Since the preceramic molecules and polymers are available in virtually any physical states, a wide variety of processing techniques, therefore applications, are possible. Chemical vapour deposition is a convenient technique for gaseous or volatile single source precursors [173, 174, 175]. Liquid or meltable polymers are applicable for injection molding, coating [176], infiltration [177, 178, 179, 180], micro-structuring [181] or fiber spinning [3, 182, 183, 184, 185, 186]. Solid precursors and ceramics, of course, can be processed via conventional powder route [187, 188]. Even though only a few of those techniques so far have been explored extensively, extremely promising potential fields of high-tech application in this novel class of materials clearly has become urgent and apparent.

4.2. Luminescence

Luminescence is defined as a phenomenon in which the electronic state of a substance is excited by some kind of external energy and the excitation energy is given off as electromagnetic radiation, usually in the visible region but also in the near-ultraviolet and near-infrared regions. In luminescence, some energy source kicks an electron of an atom out of its "ground" (lowest-energy) state into an "excited" (higher-energy) state; then the electron gives back the energy in the form of light while it falls back to its "ground" state [189]. Luminescence can be excited by many types of energy. Electroluminescence is luminescence caused by electric current, e.g. Light Emitting Diodes (LEDs) and laser diodes. Cathodoluminescence is luminescence caused by energetic electron beams, e.g. cathode ray tubes (television screens). Triboluminescence is excited by mechanical energy, for example, some minerals glow when hit or scratched. X-ray luminescence is caused by X-ray. Sonoluminescence is the emission of short bursts of light from imploding bubbles in a liquid when excited by sound. Chemiluminescence is luminescence where the energy is supplied by chemical reactions. Those glow-in-the-dark plastic tubes sold in amusement parks are examples of chemiluminescence. Bioluminescence, a form of chemiluminescence, is luminescence caused by chemical reactions in living things, e.g. fireflies glow by bioluminescence. Radioluminescence is the phenomenon by which luminescence is produced in a material by the bombardment of ionizing radiation such as beta particles, e.g. tritium-excited luminous paints used on watch dials. Photoluminescence is luminescence where the energy is supplied by electromagnetic radiation (often ultraviolet). In this context, light emission occurring during excitation with a delay of 10^{-8} s is called fluorescence, while the glow continuing longer than 10^{-8} is known as afterglow or phosphorescence [190]. Optically stimulated luminescence is phosphorescence triggered by visible light or infrared. In this case red or infrared light is only a trigger for release of previously stored energy. Thermoluminescence is phosphorescence triggered by temperatures above a certain point. This should not be confused with incandescence, which is light from heat energy such that when a solid is heated to about 600 °C, it emits (infra)red radiation, e.g. glowing of a tungsten filament of an ordinary incandescent light bulb, which is heated at around 2700 K. In thermoluminescence, heat is not the primary source of the energy, it is only the trigger for the release of energy that originally came from another source. In contrast to incandescence, luminescence is "cold light", that is the light from other sources of energy, which can take place at normal and lower temperatures.

Luminescent materials or phosphors are mainly solid inorganic materials which are composed of an intentionally doped host lattice with impurities, i.e. activators and sensitizers. The energy for exciting the luminescence is absorbed by either the host lattice or by the intentionally doped "impurities". On the other hand, the emission mostly takes place from

activator ions. However, if the activator ions exhibit too weak absorption, other type of “impurities”, called sensitizers, are included, which absorb the energy and subsequently transfer the energy to the activator ions. The emission color can be usually adjusted by choosing the proper “impurity” ions, without changing the host lattice [191].

Most phosphors have localized luminescent centers and can be classified by their electronic transitions as follow (below, an arrow to the right indicates optical absorption and to the left emission) [192]:

- $1s \rightleftharpoons 2p$, e.g. F-centers.
- $ns^2 \rightleftharpoons nsnp$, e.g. Ga^+ , In^+ , Tl^+ , Ge^{2+} , Sn^{2+} , Pb^{2+} , Sb^{3+} , Bi^{3+} , Cu^- , Ag^- , Au^- .
- $3d^{10} \rightleftharpoons 3d^9 4s$, e.g. Ag^+ , Cu^+ , Au^+ .
- $3d^n \rightleftharpoons 3d^n$, $4d^n \rightleftharpoons 4d^n$, e.g. the first and second row transition-metal ions.
- $4f^n \rightleftharpoons 4f^n$, $5f^n \rightleftharpoons 5f^n$, e.g. lanthanide and actinide ions.
- $4f^n \rightleftharpoons 4f^{n-1} 5d$, e.g. Ce^{3+} , Pr^{3+} , Sm^{2+} , Eu^{2+} , Tm^{2+} and Yb^{2+} (only absorption transitions are observed for Tb^{3+}).
- A charge-transfer transition or a transition between an anion p electron and an empty cation orbital. Examples are intramolecular transitions in complexes such as VO_4^{3-} (transition from the 2p orbital of O^{2-} to the 3d orbital of V^{5+}), WO_4^{3-} , and MoO_4^{2-} .
- $\pi \rightleftharpoons \pi^*$ and $n \rightleftharpoons \pi^*$, e.g. organic molecules having π electrons (n indicates a nonbonding electron).

Luminescence of a localized center is often explained by the configurational coordinate model. This model explains optical properties based on potential curves, each of which corresponds to total energy of the molecule in its ground and excited state as a function of configurational coordinate (Figure 4.1) [189, 192].

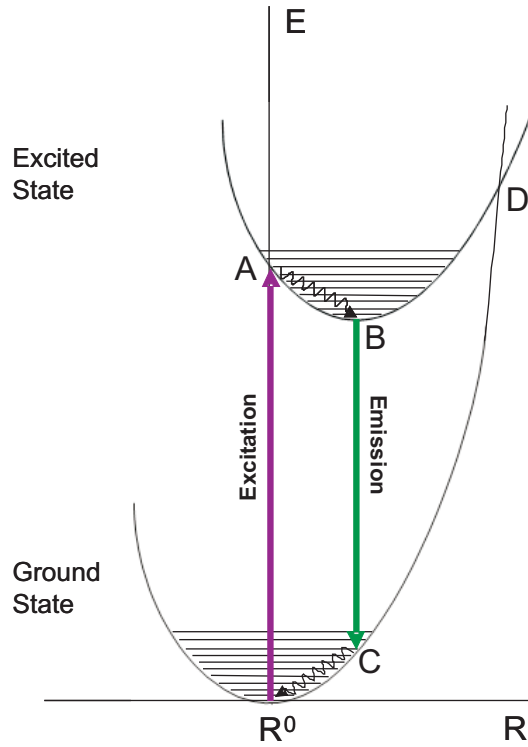


Figure 4.1.: Representation of a configurational coordinate model.

In Figure 4.1, the lower and the upper curves represent the potential energy curves (including the vibrational levels) of a luminescent center in ground state and excited state, respectively. The optical absorption (or excitation) proceeds from the equilibrium position of the ground state, as indicated by arrow $R^0 \rightarrow A$. When an electron reaches the excited state (A), it mostly prefers to relax nonradiatively to the lowest excited vibrational level because the probability for an excited electron to lose energy by generating lattice vibration is about $10^{-12} - 10^{-13} \text{ s}^{-1}$, whereas the probability for light emission is at most 10^{-9} s^{-1} [192]. Therefore, the excited electron in position A relaxes nonradiatively to the equilibrium position B. This is followed by the emission process $B \rightarrow C$ and another nonradiative relaxation process, $C \rightarrow R^0$, completing the cycle. Since the equilibrium positions of the ground and the excited states are different from each other due to the spatial distribution of the electron orbitals, the energy of emission process is different than that of excitation process, which is usually lower and known as Stokes' shift. During the absorption (excitation) and emission processes, the nucleus of an emitting ion does not change significantly its position because an atomic nucleus is $10^3 - 10^4$ times heavier than an electron. In addition, when two configurational coordinate curves intersect (D), an electron in the excited state can cross the intersection D assisted by thermal energy and can reach the ground state nonradiatively. Therefore, luminescence quantum yield is reduced at higher temperatures.

In semiconductors, impurities or defects distort the lattices and affect significantly the energy level structures. The impurities that supply electrons to be freed easily are called *donors*, whereas those that supply free holes easily are called *acceptors*. Light absorption in semiconductors takes place between valence band and impurity levels, or between impurity level and conduction band. Although all electrons are specified by the energy band states, they occupy a characteristic excited state, called *exciton*. They exist in almost all semiconductors or ionic crystals and play an important role in luminescence. When an electron is excited to a higher energy level, it leaves behind a hole with opposite charge, to which the electron is attracted by Coulombic force (binding of an electron with its hole creates an exciton). Excitons can be created by photons (photoluminescence), electron-beam (cathodoluminescence) or carrier injection (electroluminescence). The main radiative recombination of excitons are presented in Figure 4.2 as: 1) band-to-band recombination, 2) free exciton recombination, 3) bound exciton recombination, 4) band-to-impurity recombination and 5) donor-acceptor pair transition. The created excitons relax promptly and nonradiatively to their respective bands, where they have their lowest energy, and afterward they can recombine radiatively or nonradiatively to ground state [193].

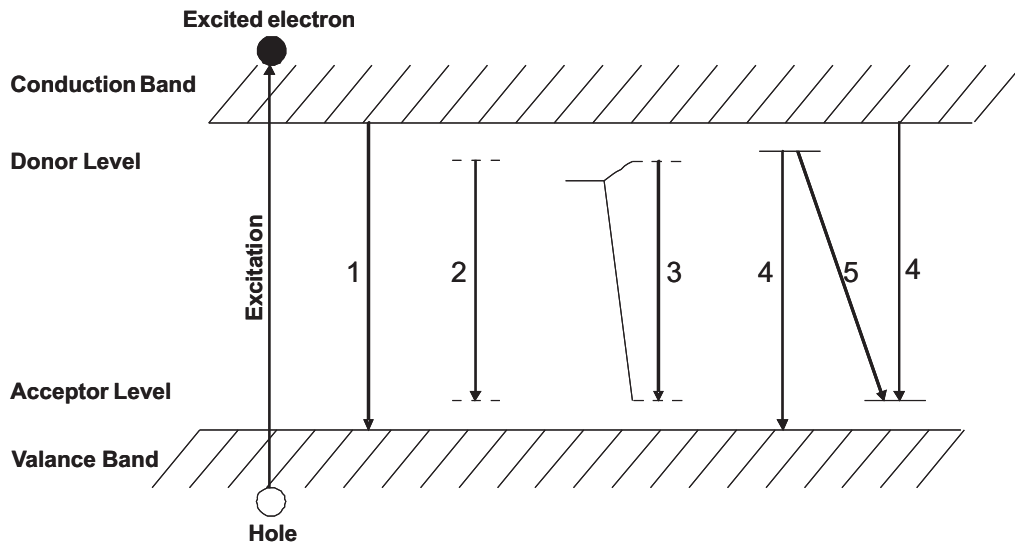


Figure 4.2.: Representation of five main radiative recombination processes in semiconductors: 1) band-to-band recombination, 2) free exciton recombination, 3) bound exciton recombination, 4) band-to-impurity recombination, 5) donor-acceptor pair transition [193].

Most of the inorganic phosphors constitute rare earth elements. The electronic configuration of all lanthanides can be written as $[\text{Xe}]4f^m6s^2$. The most stable oxidation state of the rare-earth ions is trivalent. The 4f electronic energy levels of lanthanide ions are characteristic for each ion. These levels are not affected much by the environment because 4f electrons are shielded from external electric fields by the outer $5s^2$ and $5p^6$ electrons, which is in strong contrast with transition metal ions such that outer orbit d electrons

4. Literature Overview

are heavily affected by the environment or crystal electric field. The characteristic energy levels of 4f electrons of trivalent lanthanide ions have been experimentally determined by considering the optical spectra of individual ions incorporated in different crystals [194, 195] and reported as a diagram for LaCl_3 host lattice by Dieke et. al, which is now known as Dieke diagram (Figure 4.3). This diagram is applicable for trivalent lanthanide ions in almost any environment because the maximum variation of the energy levels is, at most, on the order of several hundred cm^{-1} .

The $4f^{n-1}5d^1$ states, resulted by transferring an electron from 4f level to 5d level, and the charge transfer states (CTSs), resulted by transferring a 4f electron to a 4f level of the neighboring anion, are located in the energy region spanned by 4f levels. Both of these processes are allowed and result in a broad absorption and emission bands. The energies of $4f^{n-1}5d^1$ and CTSs are more dependent on their environments than that of 4f states. In addition to Ce^{3+} , $4f^{n-1}5d^1 \rightarrow 4f$ transitions are mainly observed for Eu^{2+} , Sm^{2+} , Tm^{2+} and Yb^{2+} [196].

Almost all phosphors have quantum efficiency less than unity due to some quenching and degradation processes [191]. First, the energy may not reach the luminescent ion if both the luminescent ions and host matrix have absorption at the excitation wavelength, or if probability of energy transfer from host matrix to activator ions is less than unity. Second, the absorbed energy arrives at the luminescent ion but there might be some nonradiative paths to return to its ground state. This can happen mainly in two ways. When the energy curves of excited and ground state meet an energy which is thermally accessible from the relaxed excited state, the luminescent ion can return to the ground state via thermal radiation, known as thermal quenching. Therefore, the quantum efficiencies generally drop when temperature is increased.

Another quenching process is related to energy transfer among the activator ions, known as concentration quenching. Activator ions beyond the optimum concentration interact with each other by overlapping of their wave functions. This results in decreasing the luminescent intensity (favoring non-radiative emission) by allowing energy to be transferred back and forth between activator ions. Thus, the activator concentration is generally low, between 0.005 % and 10 % [197]. In most cases, the energy of absorption is higher than emission and this energy difference is called as Stokes shift or quantum deficit. A large Stokes shift reduces energy transfer and therefore concentration quenching, whereas a very large Stokes shift increases the probability for thermal quenching. Energy can also be transferred to centers for nonradiative recombination or killing centers, degrading the luminescent property of materials. Such centers are vacancies and activators or sensitizers that change their valance during operation of the device. Lastly, the generated luminescence can be absorbed by the activator ions, which is known as self-absorption. This results in an ineffective scattering of the luminescence light [191].

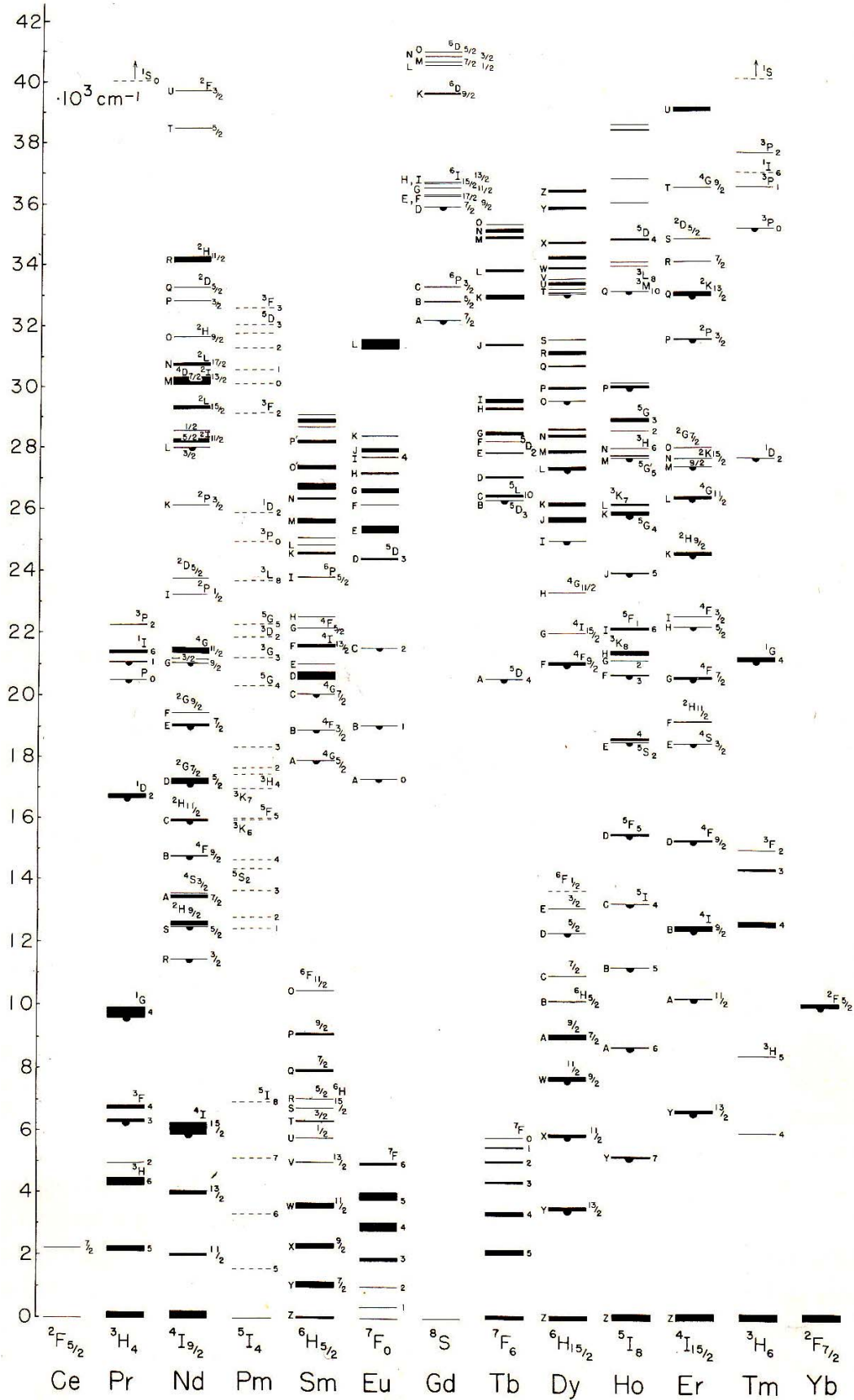


Figure 4.3.: Observed energy levels of trivalent lanthanide ions in LaCl₃ [194].

Phosphors are generally employed in light sources (e.g. fluorescent lamps and white LEDs), display devices (e.g. cathode-ray tubes), detector systems (X-ray screens and scintillators) and other basic applications like luminous paints with long persistent phosphorescence [192]. Since the phosphors in the present study are potential candidates for LED-based solid state lighting devices, lamp phosphors and white emitters will be discussed in the following parts.

4.3. Luminescent Materials for LED-based Lighting Devices

In comparison with the conventional lighting technologies, e.g. incandescent and fluorescent lamps, LED-based solid state lighting devices show remarkable improvements in terms of long lifetime, compactness, designability, environmental friendliness and, most importantly, energy efficiency [191]. This revolution in lighting technology is spreading all over the world and is improving our everyday life. Multi-chip light emitting diodes (mc-LEDs) and phosphor-converted LEDs (pc-LEDs) are two basic concepts to generate white light. mc-LEDs are obtained by combining at least three, most often red, green and blue (RGB) LEDs [198]. pc-LEDs use phosphors to convert the radiation of UV or blue LEDs. Although mc-LEDs have the advantageous of potentially higher efficiency and electronically control of the color, they require a more complex design, i.e. a power source for each LED increasing the cost dramatically, and are not applicable for small sizes. In addition, LEDs having different emission wavelengths have different working lifetimes, which results in different aging of LEDs. And even worse, individual lighting character of each LED leads to an uneven color mixing and results in insufficient illumination due to the lack of good external quantum efficiency values in the deep green to yellow region of the spectrum (known as “green window problem”) [199]. Therefore, without doubt, in this revolution, wavelength conversion phosphors play a crucial role.

In white light emission, two parameters are usually discussed in applications. The first one is color rendering index (CRI), which is defined as a quantitative measure of the ability of a light source to reproduce the colors of various objects faithfully in comparison with an ideal or natural light source by the International Commission on Illumination (CIE for its French name Commission Internationale de l'éclairage). The other one is color temperature, which is defined as the absolute temperature of a Planckian radiator (black body) that has the same color or the same colorimetric coordinates as that of the light source. When the chromaticity coordinates of a light source are not exactly on the locus of the Planckian radiator, the absolute temperature of the Planckian radiator closest to the light source is taken, which is called correlated color temperature (CCT) and usually

measured in Kelvin (K) [192]. Counterintuitively, higher Kelvin temperatures (5000 K or more) are "cool" (green–blue) colors, and lower color temperatures (2700–3000 K) are "warm" (yellow–red) colors. In white light illumination technology, it is important to match the requirements of the consumers. If white light is required to view colored objects, consumers will better comply with a light source having the superior color rendering index. In a specific case, a surgeon prefers a light source with as high CRI as possible in a medical operation in order to see as much contrast and detail of internal tissues as possible. However, if the light is necessary only to read a black and white page of a book, then color rendering is not so important. Usually CRIs of 80 % is acceptable for domestic use. On the other hand, cool-colored light is considered better for visual tasks whereas warm-colored light is preferred for living spaces, because it is considered more flattering to skin tones and clothing. Color temperatures in the 2700–3600 K range are recommended for most general indoor and task lighting [199].

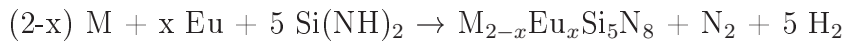
After the discovery of efficient blue-LEDs by Nakamura [200, 201, 202, 203, 204, 205, 206, 207, 208, 209], phosphors for pc-LEDs have gained more technological importance; therefore, a lot of research activities have been carried out especially in industry [210, 211, 212, 213, 214, 215, 216, 217, 218, 219, 220, 221, 222, 223, 224, 225, 226, 227, 228, 229, 230, 231, 232]. Almost all inorganic phosphors were synthesized by solid state reactions from very pure inorganic starting materials at high temperatures and pressures. Currently available color conversion phosphors for pc-LEDs are mainly divided in to three groups: oxide-based, sulphide-based and nitride-based phosphors. Metal oxide-based phosphors are dominated by the garnet-type. A representative host lattice is $\text{Y}_3\text{Al}_5\text{O}_{12}$ (YAG) and this versatile host matrix can be doped with various elements [233, 234, 235]. The most prominent example is $\text{Y}_3\text{Al}_5\text{O}_{12}:\text{Ce}^{3+}$ (YAG:Ce, yellow emission, 540 nm). A replacement of Y^{3+} with Gd^{3+} or Lu^{3+} results in a red shift to 585 nm or a blue shift to 510 nm, respectively. Moreover, an additional peak at 620 nm is obtained when Pr^{3+} ions are codoped on those system [236, 237]. Some other oxide-based phosphors are $\text{Ca}_3\text{Sc}_2\text{Si}_3\text{O}_{12}:\text{Ce}^{3+}$ (yellow emission, 570 nm) [238], $(\text{Ba}_{1-x-y}\text{Sr}_x\text{Ca}_y)_2\text{SiO}_4:\text{Eu}^{2+}$ (emission between 525 and 595 nm) [239, 240] and $\text{Y}_{2-x-y}\text{Eu}_x\text{Bi}_y\text{O}_3$ (red emission) [241]. Another class of phosphors which can be pumped with blue LEDs are metal sulphides. Some representatives are $(\text{Sr}_x\text{Ca}_{1-x})\text{S}:\text{Eu}^{2+}$ (red emission) [242] and $\text{SrGa}_2\text{S}_4:\text{Eu}^{2+}$ (green emission, 535 nm) [243]. The main drawback of this class of phosphors is the rather low stability of sulphides in a moist environment due to hydrolytic and oxidative decomposition.

The third main class of phosphors for pc-LEDs is metal nitride-based. Especially, nitridosilicate type phosphors are being studied extensively all over the world due to having outstanding thermal, chemical, and mechanical stabilities and structural diversities. Various M-Si-N phases have been investigated as host lattices for color conversion phosphors such as MSiN_2 , $\text{M}_5\text{Si}_2\text{N}_6$, $\text{M}_2\text{Si}_4\text{N}_7$, $\text{M}_3\text{Si}_6\text{N}_{11}$, M_4SiN_4 , MSi_3N_5 , $\text{M}_2\text{Si}_5\text{N}_8$ and $\text{MSi}_7\text{N}_{10}$,

4. Literature Overview

where M= Mg, Ca, Sr, Ba, Ln and Y [199]. One reason behind those superior properties in nitridosilicate type phosphors is the presence of nitrogen atoms coordinating the dopant ions [244]. Higher formal charge and covalency of N³⁻ ion compared to, for example, O²⁻ ion affect drastically the luminescent properties of rare earth ions. This increases the crystal field strength, which leads to a shift in gravity center of 5d energy levels to lower values (nephelauxetic effect). Therefore, nitridosilicate type phosphors exhibit longer excitation and emission wavelengths compared to oxide counterparts. In addition, incorporation of N into a host matrix increases rigidity due to forming more extended network, e.g. SiN₄ units, resulting in a smaller Stokes shift. This results in a higher efficiency (due to lower energy loss) and smaller thermal quenching.

Among the host lattices of nitridosilicate type, M₂Si₅N₈ (M=Ca, Sr, Ba) is the most intensively explored system both in industry and academy. It consist of a three dimensional network of crosslinked SiN₄ tetrahedra in which alkaline earth ions, i.e. Ca, Sr and Ba, are incorporated. Such lattices were first synthesized by Schnick and co-workers [245, 246, 247, 248, 249, 250] and some prominent examples are Ca₂Si₅N₈ [251], Sr₂Si₅N₈ and Ba₂Si₅N₈ [252]. The phosphors utilizing M₂Si₅N₈ (M=Ca, Sr, Ba) host lattices, particularly Eu²⁺ doped ones, show orange to red emissions with a high quantum efficiency and very low thermal quenching, which makes them very promising red phosphors in white LEDs to improve the color rendering properties. For the first time, these type of phosphors were prepared by Schnick et al. via reacting a stoichiometric amount of metals M (M=Ca, Sr, Ba) and Eu metal with silicon diimide (Si(NH)₂) in a tungsten crucible using a radio frequency furnace at extreme temperatures and usually with long reaction times [246]. To illustrate, Ba₂Si₅N₈:Eu²⁺ was prepared by multi-step heating under nitrogen atmosphere: First heating to 800 °C within 30 min with a dwelling at this temperature for 1 hour, then heating within 25 hours to 1600 °C with dwelling at this temperature for 40 hours, afterwards heating to 1650 °C within 2 hours and finally quenching to room temperature within 30 minutes [253]. For this method, the following reaction was proposed:



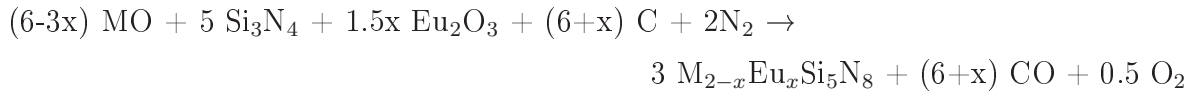
The same research group has recently prepared M_{2-x}Eu_xSi₅N₈, where M= (Ca, Sr, Ba), with the same method by employing Eu(NH₂)₂ instead of Eu metal, which resulted in a lower reaction temperatures, between 1150 °C and 1400 °C [254]. Although these orange-to-red phosphors show the best properties ever achieved, the original synthesis method was not applicable to industrial scale. First of all the raw materials, such as Eu(NH₂)₂ and Si(NH)₂, are not commercially available and have to be synthesized separately. Furthermore, all reactants are very sensitive to oxygen and moisture and have to be ground in a dry-box, which makes the handling quite laborious. And even worse,

preparation of them are performed in a radio frequency furnace in a tungsten crucible mostly at extreme temperatures with long reaction times, making the cost very high and the spatial yield very low. Therefore, this multistep and complex procedure is not suitable for an industrial scale production. Moreover, different groups tried to find more efficient ways to synthesize these compounds. An alternative route has been proposed by Hintzen et al. They have reacted metal nitride (Ca_3N_2 , SrN_x and BaN_x ($x \approx 0.6 - 0.66$)) and europium nitride (EuN_x ($x \approx 0.94$)) with silicon nitride ($\alpha\text{-Si}_3\text{N}_4$) in a Mo crucible in a horizontal tube or graphite furnace under a nitrogen atmosphere [255, 256, 257, 258]. The appropriate amounts of starting materials were ground in an agate mortar and fired twice with a medium grinding in between at 1300 °C and 1400 °C for 12 and 16 hours, respectively. They proposed the following reaction:



Nitridation of Eu, Ba and Sr were done separately and the nitrides obtained ground together with the other reactants in an agate mortar in a dry-box, which again makes the handling difficult and tedious. This method again includes a multistep and complex procedure for mass production. Nevertheless, it is regarded as a method superior to the previous one.

Carbothermal reduction and nitridation (CRN) was also considered as an alternative route to produce $\text{M}_{2-x}\text{Eu}_x\text{Si}_5\text{N}_8$, where $\text{M}=\text{Ca}$ and Sr . The synthesis was performed in a graphite crucible and heated in a radio frequency furnace under N_2 flow according to the following chemical equation [259, 260, 261, 262]:



In this reaction, the reactants initially contain MCO_3 and heating to 1200 °C for two hours decomposes MCO_3 to MO . Further heating to 1550 °C for 6 hours lead to obtain the desired compound. The same authors have recently synthesized $\text{CaSr}_{1-x}\text{Eu}_x\text{Si}_5\text{N}_8$ with the same procedure by using CaCN_2 instead of graphite powder according to following equation [263]:

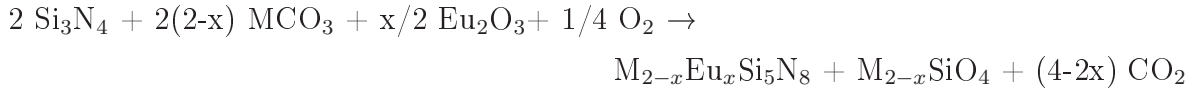


The big disadvantage of the CRN route is that it seems to be unavoidable to have residual carbon in final phosphors, which significantly reduces its absorption and emission. Annealing at temperatures above 600 °C in air or oxygen atmosphere can be applied

4. Literature Overview

in order to remove the residual carbon but Krevel et al. have reported that after a heat treatment at 600 °C in air for 2 hours, the red emission of $\text{Sr}_2\text{Si}_5\text{N}_8:\text{Eu}^{2+}$ was killed completely due to oxidation of Eu^{2+} to Eu^{3+} [264]. Therefore, the problem of complete removal of residual carbon in final phosphors makes this method unlikely to be used for mass production. The same authors mentioned in another publication that the CRN method can not be applied for Ba analogue because carbon does not work as an effective reducing agent due to having higher affinity to barium than to oxygen [265]. Therefore, they have proposed self-propagating high temperature synthesis (SHS) process for $\text{Ba}_2\text{Si}_5\text{N}_8:\text{Eu}^{2+}$. This method has widely been used for the preparation of alloy compounds, e.g borides and nitrides. The precursor was a $\text{Ba}_{2-x}\text{Eu}_x\text{Si}_5$ alloy powder synthesized from Si, Ba and Eu metal shots. These raw materials were arc-melted several times to form a homogeneous alloy ingot, and was carefully ground to fine powder. The alloy powder was loaded into a BN crucible and heated in a radio frequency furnace under a pure N_2 flow. After the self-propagating reaction had started at 1060 °C, the temperature was increased to 1350–1450 °C and maintained for 8 h for further nitridation. Quite obviously this method is also not convenient for mass production.

Lastly, Xie and co-workers have proposed a direct solid state reaction among metal carbonates (MCO_3 , where $\text{M}=\text{Ca}$, Sr), Eu_2O_3 and Si_3N_4 in a gas-pressure sintering furnace with a graphite heater at 1600 °C for 2 hours under a 0.5 MPa N_2 according to the following equation [266, 267]:



However, the major problem of this process is that an undesired side product, M_2SiO_4 , is formed during the solid state reaction:



Therefore, the synthesized phosphor is a complex mixture of $\text{M}_2\text{Si}_5\text{N}_8:\text{Eu}^{2+}$ (~64 wt %) and $\text{M}_2\text{SiO}_4:\text{Eu}^{2+}$ (~36 wt %). The authors, on the other hand, claimed that the latter does not give emissions under the blue light excitation, making the complex phosphor resembling a single phase $\text{M}_2\text{Si}_5\text{N}_8:\text{Eu}^{2+}$ phosphor. Nevertheless, one can not obtain pure, single phase phosphors with this method.

In addition $\text{M}_2\text{Si}_5\text{N}_8$, two other widely studied nitridosilicate-type host lattices for phosphors are MSiN_2 [268] and MAlSiN_3 [269, 270, 271], where $\text{M}=\text{Ca}$ and Sr . Le Toquin and Cheetham prepared a red emitting $\text{CaSiN}_2:\text{Ce}^{3+}$ phosphor via a solid state reactions of Ca_3N_2 , Si_3N_4 and CeO_2 between 1300 °C and 1500 °C [268]. The authors tuned the emission color of $\text{CaSiN}_2:\text{Ce}^{3+}$ from yellow to red by partial substitution of Ca with Sr

or Mg, and Si with Al. Uheda et al. synthesized $\text{CaAlSiN}_3:\text{Eu}^{2+}$ phosphors by reacting stoichiometric amount of EuN , AlN , Ca_3N_2 and Si_3N_4 at $1800\text{ }^\circ\text{C}$ [269]. These phosphors show a broad orange to red emission with a wide excitation window between 300 nm and 600 nm. The authors claim that these phosphors are more efficient than $\text{M}_2\text{Si}_5\text{N}_8:\text{Eu}^{2+}$ and $\text{MSiN}_2:\text{Ce}^{3+}$, where $\text{M} = \text{Ca}$ and Sr , due to having both $[\text{SiN}_4]$ and $[\text{AlN}_4]$ tetrahedra, forming more rigid network and resulting smaller thermal quenching.

Alkaline-earth metal oxynitrides are also considered as promising phosphors due to having good thermal behavior, broad excitation bands and emission light from green to red [272]. However, main drawbacks are difficulties in manufacturing and having broad red emissions with low luminous efficiency. β -SiAlON is a representative compound in this class and derived from β - Si_3N_4 by substitution of Al-O by Si-N. β -SiAlON: Eu^{2+} phosphors give intense green emission at 538 nm when excited at 405 nm [192, 273]. Similarly, α -SiAlONs are derived from α - Si_3N_4 by substituting $m+n$ Si-N bonds by m Al-N and n Al-O and charge is compensated by metal cations [274]. An example is $(\text{Sr,Ca})_{p/2}\text{Al}_{p+q}\text{Si}_{12-p-q}\text{O}_q\text{N}_{16-q}:\text{Eu}^{2+}$, which can be excited between 350 nm and 490 nm with an emission maximum at 575 nm. A combination of this phosphor with a blue-LED and a red nitride phosphor has been reported to yield a warm white at 3200 K [199]. Other oxynitride phosphors are $\text{MSi}_2\text{O}_2\text{N}_2:\text{Eu}^{2+}$ ($\text{M} = \text{Ca}, \text{Sr}, \text{Ba}$) which emit a broad yellow light at 562 nm when $\text{M} = \text{Ca}$, a green light at 543 nm when $\text{M} = \text{Sr}$ and a blue-green light at 491 nm when $\text{M} = \text{Ba}$ [192, 275, 246].

Although the general approaches for pc-LEDs have been widely explored, there are still serious problems with the phosphors that need to be addressed [199]. At first, the excitation spectrum of the color conversion phosphor needs to overlap with the emission wavelength range of the LED. At the present, there is but a small number of phosphors that can be excited with blue/violet light and emit efficiently at longer wavelengths in visible range. Loss of light should be minimized via optimizing the particle size of the phosphors. The light that is emitted backwards in LED chip required to be redirected into forward direction in order to maximize the light output of pcLEDs. Compared to phosphors, LEDs have angle dependent emissions. Thus, phosphors need to be coated directly on the LED chip in order to minimize any angle dependent shift of the color point of the pc-LEDs. At the same time, phosphors need to be deposited homogeneously on the LED chip or other remote substrate. Moreover, the binder, in which phosphors are suspended, should not be photodegradable by the LED light. Another very crucial parameter to be controlled is color rendering index and this problem has been solved by red-emitting nitride phosphors. However, as it was mentioned above, mass production of nitride phosphors has not yet been attained due to problems in current manufacturing processes. Therefore, it is extremely urgent to develop a new process to synthesize required phosphors in a simple and economical way and on a large scale, in order to meet the

predicted large demand for such LEDs. Last but not least, a single phosphor having efficient and broad-band emission excited by UV- or blue-LED with lower CCTs and higher CRIs is urgently required for white light pc-LEDs that have warmer white in order to satisfy consumers preferences.

4.4. Ceramic Foams

Ceramic foams are a class of porous materials with large voids (10 μm – 5 mm) which are known as cells [276, 277, 278]. If cells are fully surrounded by ceramic walls, the ceramic is addressed as closed cell foam. On the other hand, if cells contain solid material at only cell edges (struts), which creates an interconnected structure, the ceramic is called an open cell foam. Ceramic foams have low density, low thermal conductivity, high thermal stability, high specific strength and high resistance to chemical attacks. Therefore, they can be used in a wide range of engineering applications such as molten metal, hot gas and diesel exhaust filters, catalyst carriers, biomaterials, thermal insulators for furnaces, aerospace applications, gas combustion burners and light weight structures. Various processing routes have been proposed for the production of ceramic foams [279], including immersion of an open cell polymeric foam into a ceramic slurry or a preceramic polymer and subsequent pressureless sintering at elevated temperatures (replica method) [280, 281, 282, 283, 284], direct foaming of ceramic slurry or a sol-gel solution with or without the aid of a sacrificial polymeric backbone [285], incorporation of a fugitive phase which is removed by heating (sacrificing template method), CVD or electrospraying of refractory materials on a foamed skeleton [276], sintering of hollow spheres and siliciding of carbon preforms [282]. Due to having high thermal and mechanical strength and toughness, non-oxide ceramic foams of SiC [286, 287], Si₃N₄ [288, 289] and SiCN [282] and their composites [290] have received a great attention.

The most common processes for producing open cell non-oxide ceramic foams are soaking polyurethane foam into any appropriate precursor polymer (polysilanes, polycarbosilanes or polysilazanes) [282, 290, 285] or mixing precursor polymers with polyol-isocyanate mixture which yields polyurethane foam spontaneously [291, 292]. Another method is direct foaming of preceramic polymers with a liquid physical blowing agent. The biggest advantageous of applying preceramic polymers is that several fillers (ceramic powders, metal powders and short fibers) can be incorporated easily in order to tailor electrical, thermal, mechanical and magnetic properties of final ceramic foams [293, 294].

4.5. General Objectives and Strategies

Most of the available luminescent materials are crystalline. In these materials, the desired luminescent properties are achieved by replacing an available ion from the crystal lattice with another ion which is called activator ion. The cations, as well as its lattice space, of the crystalline host matrix must provide such properties that they correspond to the chemical and structural requirements of the activator ion and therefore allow the corresponding substitution. These conditions, in this respect, make strong limitations that for each activator ion a specific host lattice must be found. Moreover, accessible doping concentrations are limited due to an unavoidable mismatch between the substituted and activator ions in the host lattice. For all aliovalent doping together with electronic defects have negative effects like quenching on luminescence. An additional disadvantageous consequence of using crystalline matrices is that in case to obtain a desired broad emission, e.g. white light from the combination of the green, red and blue emissions, two or more different luminescent materials must be used which increase the cost and expenditure of manufacturing. Furthermore, all previously described luminescent materials are produced via solid state reactions at extreme temperatures and sometimes also pressures. Among them, rare-earth doped silicon-nitride based materials have recently been extensively studied due to having outstanding chemical, thermal and mechanical properties as compared to oxide, sulphide and halide based phosphors or their combinations. The reason having such superior properties is possessing nitrogen atoms as network-formers of host lattice, which make strong covalent bonds in the highly crosslinked structure. Therefore, high covalency of N^{3-} ion affects drastically the luminescent properties of rare earth ions by lowering the gravity center of the 5d levels (nephelauxetic effect), improving crystal field strength and decreasing the Stokes shift. In the light of the extensive research performed in rare earth doped silicon nitride-based crystalline phosphors, it is aimed to obtain not only mechanically, thermally and chemically more stable phosphors, but also to introduce an amorphous host matrix, which can allow various activators and sensitizers to be incorporated at the same time without considering any lattice symmetry or charges. Fortunately, in the present dissertation, rare-earth doped amorphous silicon-boron-nitride luminescent ceramics have been successfully synthesized for the first time by using a very easy and versatile method. Quite obviously, as it was proposed, amorphous $Si_3B_3N_7$ provides a rather versatile matrix that is able to host various activator and/or sensitizer atoms, irrespective of their sizes and charges. Avoiding the conventional solid state route, rare earth ions are successfully incorporated into the amorphous $Si_3B_3N_7$ ceramics by employing the polymer route. For that purpose, a single source precursor ($Cl_3SiN(H)BCl_2$, (trichlorosilylamino)-dichloroborane, TADB) was ammonolyzed with liquid ammonia in which activators and/or sensitizers were involved. This involvement was achieved mainly

4. Literature Overview

along two routes. The first route is based on dissolving Eu, Yb, Sr and Ba metals or their mixtures in liquid ammonia and, we call it “the metal route”. Along the second route metal complexes $\text{RE}[\text{N}(\text{Si}(\text{CH}_3)_3)_2]_3$, where $\text{RE} = \text{Ce}, \text{Nd}, \text{Sm}, \text{Eu}, \text{Gd}, \text{Tb}, \text{Ho}, \text{Tm}$ and Yb , and $\text{Sn}[\text{N}(\text{Si}(\text{CH}_3)_3)_2]_2$ or their mixtures are suspended with liquid ammonia and, we call it “the organometallic route”. In both cases, solvents like hexane can be added in order to increase the homogeneity at mixing. After removal of excess ammonia and solvent by distillation, and NH_4Cl by sublimation, almost salt-free rare earth doped polyborosilazane is obtained. Further pyrolysis of the doped polymer to 1200 °C yields homogeneous amorphous luminescent ceramics. Surprisingly, rare-earth doped amorphous $\text{Si}_3\text{B}_3\text{N}_7$ ceramics show well developed emissions in the visible range by excitation with UV and/or blue light, which makes them very promising novel class of phosphors to obtain white light by combining them with UV- and blue-LEDs.

In solid state lighting community, there is a tremendous demand for efficient red and green phosphors in order to obtain higher color rendering index for indoor illumination applications. Up to know, the best results for red phosphors in terms of efficiency and stability were achieved by $\text{M}_{2-x}\text{Si}_5\text{N}_8:\text{Eu}_x$, where $\text{M}=\text{Ca}, \text{Sr}, \text{Ba}$. However, the production methods reported in the literature include time-consuming multistep and complex solid state reactions that require extreme temperatures and pressures which make them unfeasible in mass production. Therefore, the present study also aims to develop an easy and versatile method for production of rare earth doped crystalline nitridosilicate phosphors. This novel method was inspired from the method which was applied to produce rare earth doped amorphous $\text{Si}_3\text{B}_3\text{N}_7$ phosphors, as described above. The well known polymer route has been applied for the production of crystalline nitridosilicate-type phosphors including CeSi_3N_5 , $\text{M}_{2-x}\text{Eu}_x\text{Si}_5\text{N}_8$, $\text{M}_{2-2x}\text{R}_x\text{Li}_x\text{Si}_5\text{N}_8$, and $\text{Ba}_{1-2x}\text{R}_x\text{Li}_x\text{Si}_7\text{N}_{10}$, where $\text{M} = \text{Ca}$ and Sr , and $\text{R} = \text{Ce}$ and Tb . To the best of our knowledge, $\text{Ca}_{2-2x}\text{Tb}_x\text{Li}_x\text{Si}_5\text{N}_8$, $\text{Sr}_{2-2x}\text{Tb}_x\text{Li}_x\text{Si}_5\text{N}_8$, $\text{Ba}_{1-2x}\text{Ce}_x\text{Li}_x\text{Si}_7\text{N}_{10}$ and $\text{Ba}_{1-2x}\text{Tb}_x\text{Li}_x\text{Si}_7\text{N}_{10}$ systems have been synthesized for the first time. In order to obtain the desired phosphors, SiCl_4 was ammonolyzed with liquid NH_3 in which Eu, Ca, Sr and Ba were dissolved or $\text{RE}[\text{N}(\text{Si}(\text{CH}_3)_3)_2]_3$, where $\text{RE} = \text{Eu}, \text{Ce}$ and Tb were suspended in hexane medium. Similarly, after removal of excess ammonia and solvent by distillation, and NH_4Cl by sublimation, almost salt-free rare earth doped silicon-nitride-based polymers were obtained. Further pyrolysis of the doped polymers to 1500 °C yielded crystalline nitridosilicate phosphors.

This versatile “polymer route” is aimed to be extended for incorporating some transition metals in a host matrix in order to obtain more functional properties in the final ceramic. For that purpose, Fe, Co and Ni were doped into amorphous $\text{Si}_3\text{B}_3\text{N}_7$ matrix through the polymer route in order to obtain ferromagnetic ceramics. Powder X-ray analysis exhibited typical amorphous behavior of $\text{Si}_3\text{B}_3\text{N}_7$ ceramics together with the Bragg reflections of elemental Fe, Co and Ni in respective ceramics. Magnetic measurements revealed the

ferromagnetic behavior in the final ceramics. SEM images presented the homogeneous distribution of the metallic Fe, Co and Ni domains in amorphous $\text{Si}_3\text{B}_3\text{N}_7$ host matrix. Hence, the polymer route was successfully applied for Fe, Co and Ni doping into the amorphous $\text{Si}_3\text{B}_3\text{N}_7$ host matrix for preparing ferromagnetic ceramics.

Intrinsic properties of single source precursor compounds are one of the major factors which determine properties and performances of the final ceramic; therefore, there are always requirements to discover new single source precursors having different functionality and structures. It has already been proven that single source precursors having cyclic structures significantly improve the thermal durability of amorphous ceramics. In this respect, it is also aimed to synthesize a new cyclic single source precursor in the present work. Thus, a monocyclic and halo-substituted silaborazine-type single source precursor, 1,1,3,5-tetrachloro-2,6-dimethyl-4-hydride-1-silaborazine (TDSB) has been synthesized. The precursor TDSB is a particularly attractive compound, because it contains for the first time Si:B in the ratio of 1:2 in a monocyclic molecule, which is interesting to see the effects in the final ceramic.

Ceramic foams are widely used materials in various engineering applications. However, to best of our knowledge, there is no study to obtain SiBNC ceramic foams having regular pores which could be used in engineering applications. Therefore, it is aimed to obtain open cell SiBNC ceramic foams by employing the replica method. For that purpose, polyborocarbosilazane, which is obtained from the reaction of single source precursor TADB and methyl amine, was used as a polymer source and commercially available melamine-based open cell Basotect[®] foam was used as a replica template. For preparation, a piece of Basotect[®] foam was soaked into polyborocarbosilazane. Then, excess polymer was removed by centrifuging to allow coating of the open cell walls only with a thin layer of the polymer. Afterward, it was carefully tempered in order to crosslink the polymers on the cell walls well enough before the template was removed. Further heating to 1400 °C yielded open cell SiBNC ceramic foams.

4. *Literature Overview*

5. Phosphors Based on Amorphous $\text{Si}_3\text{B}_3\text{N}_7$ Matrix

In the present work, amorphous $\text{Si}_3\text{B}_3\text{N}_7$ ceramic has been considered as a host matrix for various activator ions, such as Ce^{3+} , Nd^{3+} , Sm^{3+} , Eu^{2+} , Gd^{3+} , Tb^{3+} , Ho^{3+} , Tm^{3+} , Yb^{3+} and Sn^{2+} , and sensitizer and/or charge compensator ions, such as Sr^{2+} , Ba^{2+} , Y^{3+} and La^{3+} . From this diverse list, Ce^{3+} , Eu^{2+} and Tb^{3+} ions in particular have been investigated in more detail due to promising photoluminescence properties. For producing the desired luminescent amorphous $\text{Si}_3\text{B}_3\text{N}_7$ ceramics, a novel method based on a single source precursor or polymer route has been applied [295]. Firstly, the single source precursor (trichlorosilylamino)dichloroborane (TADB) has been synthesized by the conventional method via a two step reaction [43]. Then, TADB has been ammonolysed with liquid ammonia, in which either Eu, Yb, Sr and Ba metals or mixtures of them were dissolved (the metal route), or $\text{RE}[\text{N}(\text{Si}(\text{CH}_3)_2)_3]$, where $\text{RE} = \text{Ce}, \text{Nd}, \text{Sm}, \text{Eu}, \text{Gd}, \text{Tb}, \text{Ho}, \text{Tm}, \text{Yb}, \text{Y}$ or La , and $\text{Sn}[\text{N}(\text{Si}(\text{CH}_3)_2)_2]$ or mixtures of them were suspended (the organometallic route). In a broader sense, these two routes have also been combined in a single reaction. After successive purification and pyrolysis steps, the desired amorphous luminescent $\text{Si}_3\text{B}_3\text{N}_7$ ceramics were obtained. Details of the experimental work are given in Section 10.1. As implied, this novel versatile method allows easy incorporation of more than one element at the same time. Therefore, in this study various ions, including Ce^{3+} , Nd^{3+} , Sm^{3+} , Gd^{3+} , Tb^{3+} , Ho^{3+} , Tm^{3+} , Yb^{2+} , Yb^{3+} , La^{3+} , Y^{3+} , Sn^{2+} , Sr^{2+} and Ba^{2+} have been codoped with Eu^{2+} into amorphous $\text{Si}_3\text{B}_3\text{N}_7$ matrix in order to study the effect of codoping on luminescent properties of Eu^{2+} in amorphous $\text{Si}_3\text{B}_3\text{N}_7$. In addition, codoping of Tb^{3+} with Ce^{3+} in amorphous $\text{Si}_3\text{B}_3\text{N}_7$ matrix has been investigated.

5.1. Intrinsic Properties of Amorphous $\text{Si}_3\text{B}_3\text{N}_7$

The properties of compounds depend ultimately on their geometry and electronic structure. From this point of view, it is not surprising that peculiar magnetic, electrical and optical properties are observed in amorphous materials due to the disordered atomic structures, including “defects”, e.g. dangling bonds. A dangling bond occurs when an atom is missing a neighbor to which it would be able to bind, and gives rise to interface states

5. Phosphors Based on Amorphous $\text{Si}_3\text{B}_3\text{N}_7$ Matrix

within the energy band gap of the system [296, 297, 298, 299]. In addition to the disordered structure and defects in amorphous materials, interaction with external fields, e.g. light, induces deep gap states, which make it even more difficult to explain the resulting peculiar phenomena [300]. When light interacts with matter, an electron can be excited from the ground state level into a higher energy level. The missing electron in the valence band leaves a hole (of opposite electric charge) behind, to which the electron is attracted by a Coulombic force. The *exciton* (bound electron-hole pair) results from the binding of the electron with its hole. Once an exciton is created in a material, the energy of excitation can be dissipated in three ways: by conversion into heat, by ionizing to give free electron and hole, and by emission of light. It is essential for luminescence that the exciton should be in a stationary energy state, known as a *trapping* centers, which can be provided by the imperfections or dislocations in the structure [301]. In most cases, the excited electron and hole spontaneously create a localized distortion which lowers their total energy and localizes and traps them at the distortion. This results in formation of so-called self-trapped excitons [302, 303]. Many unusual physical properties are explained by the existence of free and self-trapped excitons. One of the most interesting defect-dependent property was reported by Staebler and Wronski such that the defect density of hydrogenated amorphous silicon (a-Si:H) increased with light exposure (due to the formation of dangling bonds), which resulted in an increase in the recombination current and, therefore, a decrease in the sunlight-to-electricity conversion efficiency in solar cells (known as the *Staebler-Wronski Effect*) [304, 305]. Another unusual spectroscopic behavior is known as the *Red-Edge Effect* (REE, also known as red-edge excitation shift, edge-excited red shift and bathochromic luminescence effect), which is the dependence of emission spectra on excitation wavelength [306]. This violates commonly accepted concepts based on the independence of emission energy on excitation energy within the absorption band (Vavilov's law [307]) and the occurrence of emission irrespective of excitation band, always from the lowest electronic and vibrational state of the same multiplicity (Kasha's rule [308]). The REE was reported independently in 1970 by three different laboratories [309, 310, 311] for organic fluorophores in low-temperature glasses and, later, has been reported for a variety of fluorophores in different media with frozen or relatively slow structural dynamics, from vitrified and highly viscous solutions (including proteins and ionic liquids) to polymer matrices. The existence of an excited-state distribution of organic fluorophores based on their interaction energy with the environment and the slow rate of dielectric relaxation of its environment were the accepted mechanisms responsible for the REE [306]. Two conclusions are generally drawn for materials exhibiting REE: (1) heterogeneity in the micro-environments of the fluorophores and (2) relaxation times of the excited-state that are longer than or, at least, compatible to the emission lifetime [312].

The structure of amorphous Si₃B₃N₇ ceramic corresponds to some random covalent network and has been characterized by its short range, medium range and long range order. According to the short range order analyses (e.g. IR, Raman, NMR, XANES, EXAFS and etc.), the local environment of the atoms in amorphous Si₃B₃N₇ ceramic has been described as follows [1, 313]: The boron atoms are approximately threefold planar coordinated by nitrogen atoms, that is, coordinated as in hexagonal BN. The local environment of silicon atoms is similar to that in Si₃N₄ (α or β phases), that is, approximately tetrahedrally coordinated by four nitrogen atoms. The local environment of nitrogen is threefold (planar), and consists a mixture of N-B and N-Si bonds. According to the given synthetic method and the structure of the molecular precursor, formation of Si-Si, B-B, N-N and Si-B bonds are highly unlikely [158]. The medium range order analyses (e.g. advanced double resonance NMR techniques (REDOR and REAPDOR) and pair correlation function analyses via X-ray, neutron or electron diffraction) have revealed an agglomeration of B-N-B linkages and Si-N-Si linkages to form boron-rich and silicon-rich domains, which were well fitted to the heterogeneous fragment model [4]. The high resolution mapping of the elements Si, B and N via TEM showed highly homogeneous distribution of the elements above the lateral resolution of the method applied in the range of 0.8 - 1.0 nm [164]. To summarize, the amorphous Si₃B₃N₇ ceramic has 1) homogeneous elemental distribution down to the nanometer scale, 2) no vacancies greater than those on a nanometer scale, 3) cationic islands of silicon and boron inside an anionic nitrogen matrix below the nanometer length scale and 4) SiN₄ tetrahedral and BN₃ triangular units on the Angstrom length scale.

The powder X-ray diffractogram of the undoped amorphous Si₃B₃N₇ ceramic is presented in Figure 5.1. Intrinsic photoluminescence properties of undoped amorphous Si₃B₃N₇ ceramic are given in Figure 5.2 (2-D plot) and Figure 5.3 (3-D plot). According to those figures, there are three intrinsic emission regions (depending on the excitation wavelength), violating the Vavilov-Kasha rule. Defect centers are assigned as the cause of the photoluminescence in amorphous Si₃B₃N₇. The following photoluminescence characteristics have been observed: When the sample was excited with wavelengths between 254 nm to 330 nm, intense blue emissions with peak maxima ranging from 447 nm to 479 nm were observed (Figure 5.4). Especially, excitation with 305 nm light has yielded intense blue emission at 460 nm, which was consistent with the strong absorption noticeable between 254 nm to 330 nm in excitation and diffuse reflection spectra. This intrinsic blue emission has also been observed for most of the rare earth doped amorphous Si₃B₃N₇ ceramics, when they were excited with the same range of light as mentioned above. Excitation between 315 nm and 420 nm resulted in two broad emission peaks (Figure 5.6). The first one was in the range between 400 nm (excitation by 315 nm) and 440 nm (excitation by 390 nm). The second peak was observed between 560 nm (excitation by 315 nm) and

5. Phosphors Based on Amorphous $\text{Si}_3\text{B}_3\text{N}_7$ Matrix

690 nm (excitation by 400 nm). Of these two peaks, the one in the violet region was always dominant over the one in the red region, thus a violet color was perceived with the eye via excitation with 330 nm or higher wavelengths.

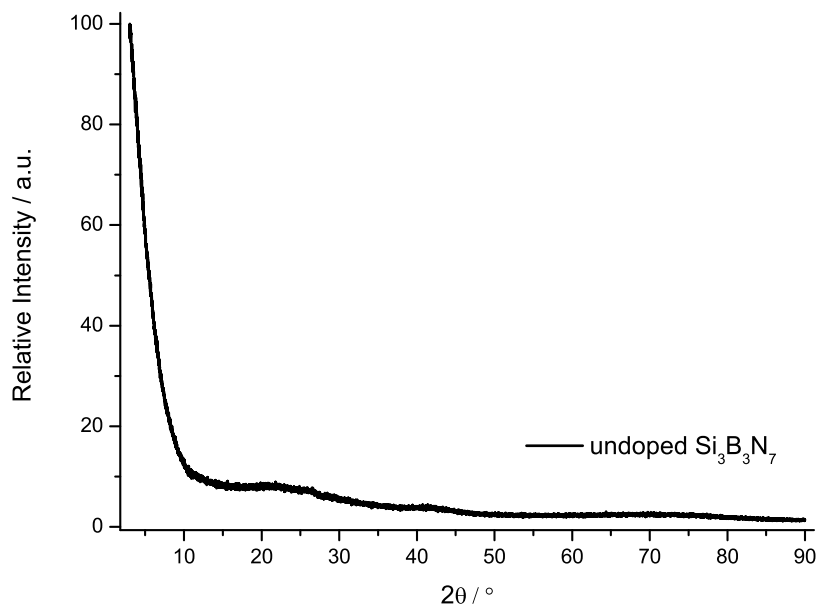


Figure 5.1.: Powder X-ray diffractogram of undoped amorphous $\text{Si}_3\text{B}_3\text{N}_7$ ceramic.

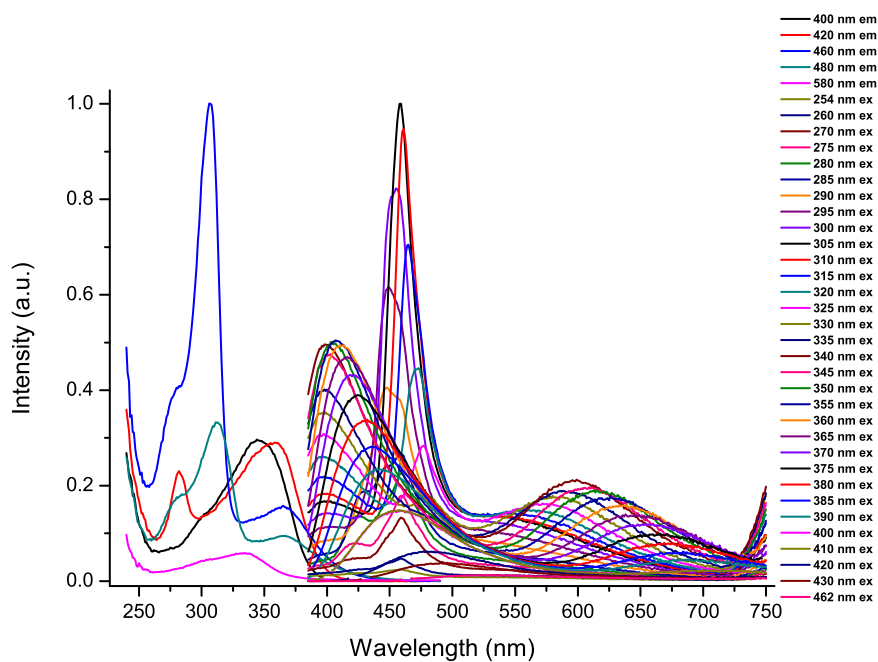


Figure 5.2.: Photoluminescence spectra of undoped amorphous $\text{Si}_3\text{B}_3\text{N}_7$ ceramic at different excitation and emission wavelengths.

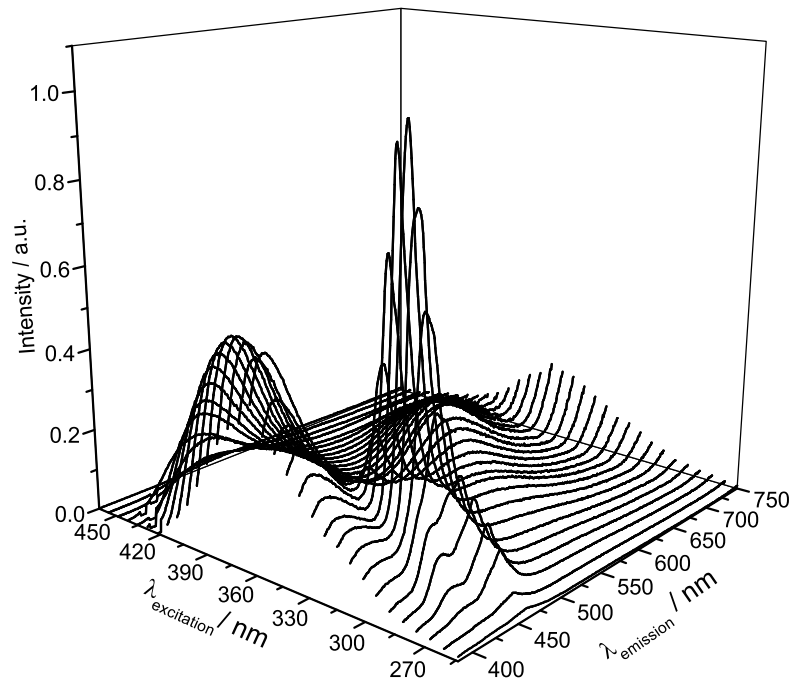


Figure 5.3.: Three-dimensional representation of photoluminescence spectra for undoped amorphous $\text{Si}_3\text{B}_3\text{N}_7$ ceramic.

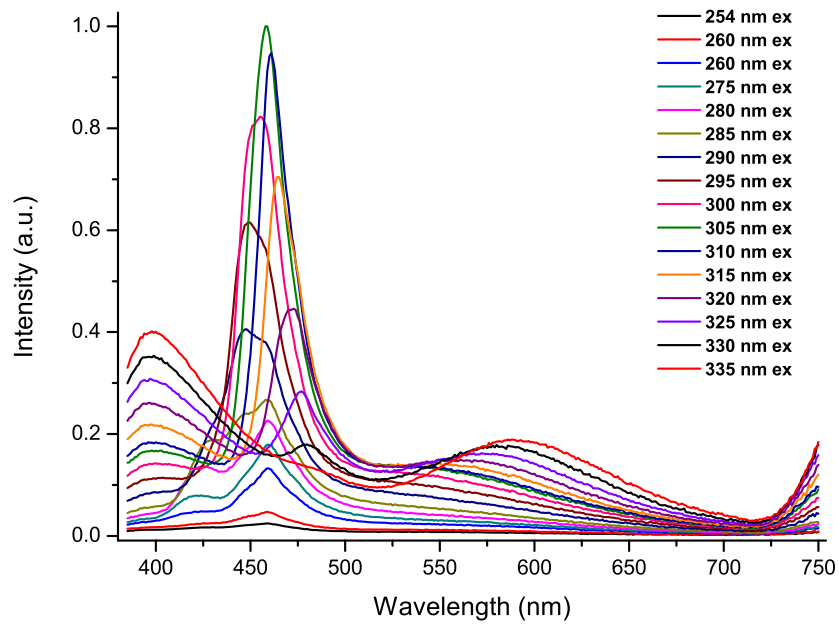


Figure 5.4.: Emission spectra of undoped amorphous $\text{Si}_3\text{B}_3\text{N}_7$ ceramic excited between 254 nm and 335 nm light.

5. Phosphors Based on Amorphous $\text{Si}_3\text{B}_3\text{N}_7$ Matrix

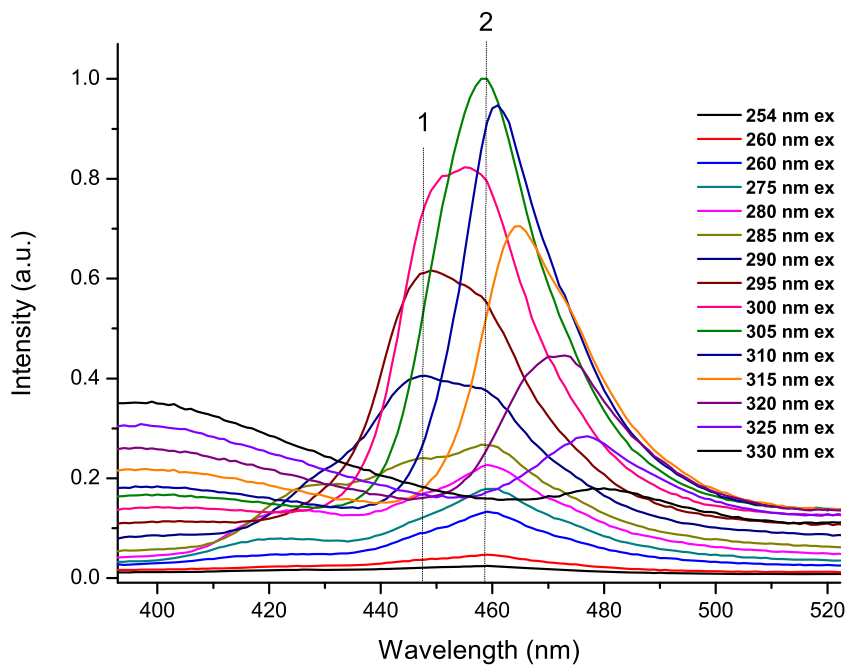


Figure 5.5.: Emission spectra of undoped amorphous $\text{Si}_3\text{B}_3\text{N}_7$ ceramic in blue region excited between 254 nm and 330 nm light.

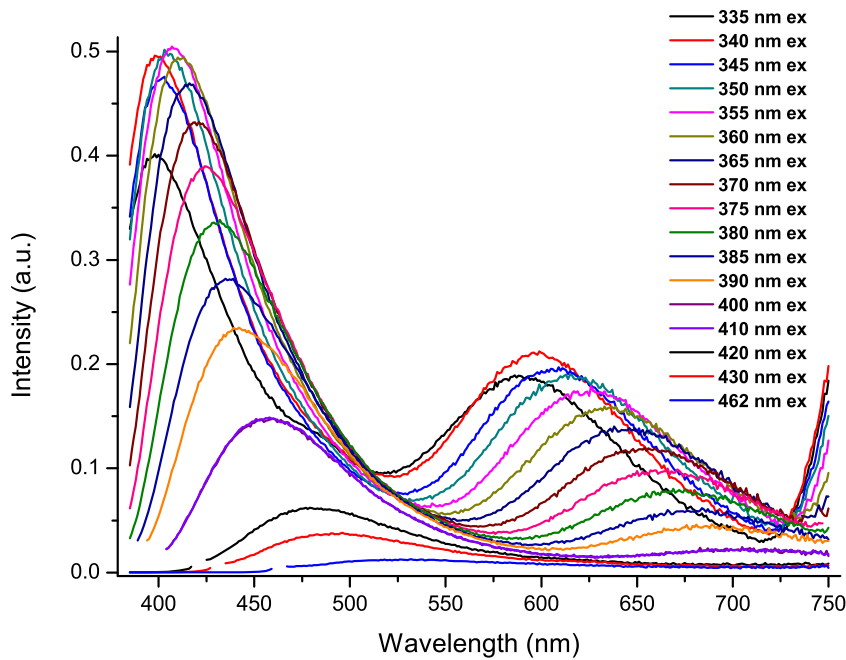


Figure 5.6.: Emission spectra of undoped amorphous $\text{Si}_3\text{B}_3\text{N}_7$ ceramic excited between 335 nm and 462 nm light.

The three distinct intrinsic emission regions in photoluminescence spectrum of undoped amorphous Si₃B₃N₇ ceramic are related to the three different topological regions in the structure of the amorphous Si₃B₃N₇ ceramic. Firstly, the intrinsic emission in the violet region is believed to occur due to the boron rich domains. This assumption is based on the fact that the boron rich domains contain boron atoms coordinated by nitrogen atoms as in hexagonal BN. It is known that hexagonal BN exhibits a wide band gap around 5.7 eV (215 nm) and has photoluminescent emission around 400 nm [314, 315, 316]. Secondly, the intrinsic emission in the red region is attributed to the silicon rich domains. This assumption is justified as the silicon rich domains contain silicon atoms which have a local environment similar to that in Si₃N₄. It is known that Si₃N₄ has a wide band gap around 5.3 eV (234 nm) and shows photoluminescent emission in the range between 400 nm and 620 nm depending on the defect energy levels [317, 318, 319, 320, 321, 322, 323]. Finally, the intrinsic emission in blue region is assigned to the remaining border region between the boron and silicon rich domains, containing significant amount of atoms N atoms directly connected to B and Si. Similar to phenomena giving rise to the Staebler-Wronski Effect and Red-Edge Effect, it is believed that all of the intrinsic luminescence of amorphous Si₃B₃N₇ ceramic in the visible region is due to the presence of excitons that are trapped in the defect energy levels resulted from the dangling bonds such as ≡Si•, = N• and = B•. The red shift in emission via a decrease in the excitation energy is similar to the Red-Edge Effect and is assigned to the spontaneous formation of localized energy levels by excitons depending on the energy of the incident light and the interactions between the excitons and their local environments. The mechanism of this red shift phenomenon can be explained by the configurational coordinate model. As there are three different intrinsic emission regions, they are considered separately.

Maximum emission intensities and wavelengths for various excitation wavelengths of the undoped amorphous Si₃B₃N₇ ceramic in the intrinsic blue, violet and red emission regions are presented in Figure 5.7, Figure 5.8 and Figure 5.9, respectively. In all those figures, the graphs of the maximum emission intensities appear similar to the excitation spectra for the respective regions. The slopes of the graphs for the maximum emission wavelength versus excitation wavelength in Figure 5.7 (for intrinsic blue emission region) and Figure 5.8 (for intrinsic violet emission region) showed dramatic changes at the edges of the corresponding excitation bands. Similar behavior was reported for Eu²⁺ doped Ca-α-SiAlON ceramic phosphors [324]. In the blue emission region of the spectrum, two broad emission peaks appeared at 448 nm and 459 nm (1 and 2, respectively in Figure 5.5), especially when excited between 285 nm and 300 nm. This implies that there are two very close higher energy levels for defect centers resulting in blue emission. The excitation between 285 nm and 300 nm resulted in the emission at 448 nm to become more favorable than that at 459 nm. The emission at 448 nm disappears at longer excitation wavelength

5. Phosphors Based on Amorphous $\text{Si}_3\text{B}_3\text{N}_7$ Matrix

because the energy for excitation seems not to be enough to populate the higher excitation level and thus emission at 460 nm becomes dominant. This can be explained in the configurational coordinate diagram in Figure 5.10. The emissions at 448 nm and 460 nm were assigned to the transitions from F to C and from B to C, respectively.

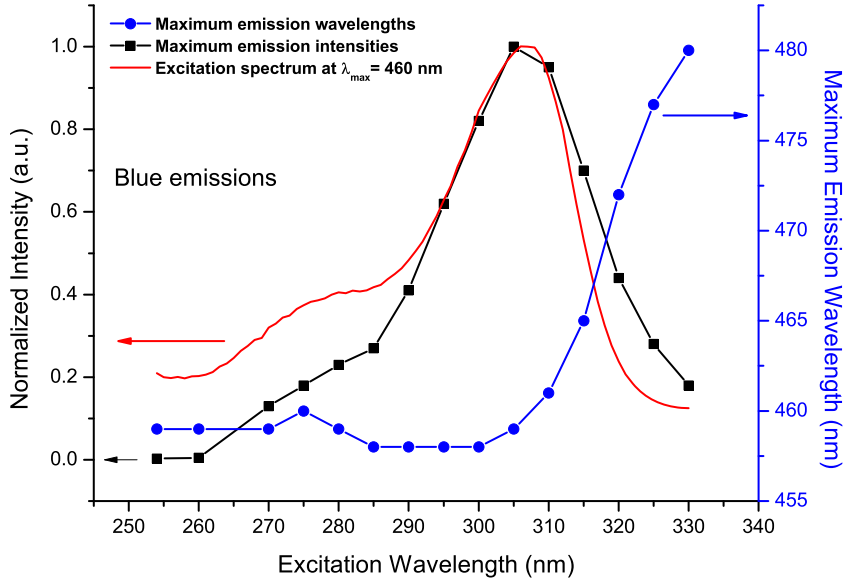


Figure 5.7.: Maximum emission intensities and wavelengths for various excitation wavelengths of undoped amorphous $\text{Si}_3\text{B}_3\text{N}_7$ ceramic for intrinsic blue emissions.

In order to emphasize the red shift due to the excitation with light at the absorption edge, the maximum emission wavelengths between 285 nm and 300 nm were chosen as 459 nm (on line 2 in Figure 5.5). Even though the red shift in the undoped amorphous $\text{Si}_3\text{B}_3\text{N}_7$ ceramic, when excited with light at the absorption edge, appears similar to the Red-Edge Effect observed for organic fluorophores in rigid or viscous media, reabsorption of the emitted light was also believed to play a significant role [324]. The reabsorption and reemission (red shift) can be explained in the configurational coordinate diagram in Figure 5.11. In a typical excitation and emission process, an electron in the ground state absorbs the energy of a photon and jumps to the excited state ($\text{R}_0 \rightarrow \text{A}$). This is followed by the nonradiative relaxation to the lowest vibration level of the excited state ($\text{A} \rightarrow \text{B}$) from which the emission ($\text{B} \rightarrow \text{C}$) and nonradiative relaxation ($\text{C} \rightarrow \text{R}_0$) take place to complete the cycle. However, some number of electrons in the ground state can be populated, in a certain probability, at the position C assisted by the thermal energy at room temperature and can absorb the emitted light (reabsorption) and reach the point B. The electrons in point B which are excited from point C by reabsorption can move to the position E with the assistance of thermal energy. From the position E, reemission (red shift) occurs at a

longer wavelength ($G \rightarrow H$), which is followed by the nonradiative relaxation to the lowest vibrational level in the ground state ($G \rightarrow R_0$) to complete the cycle.

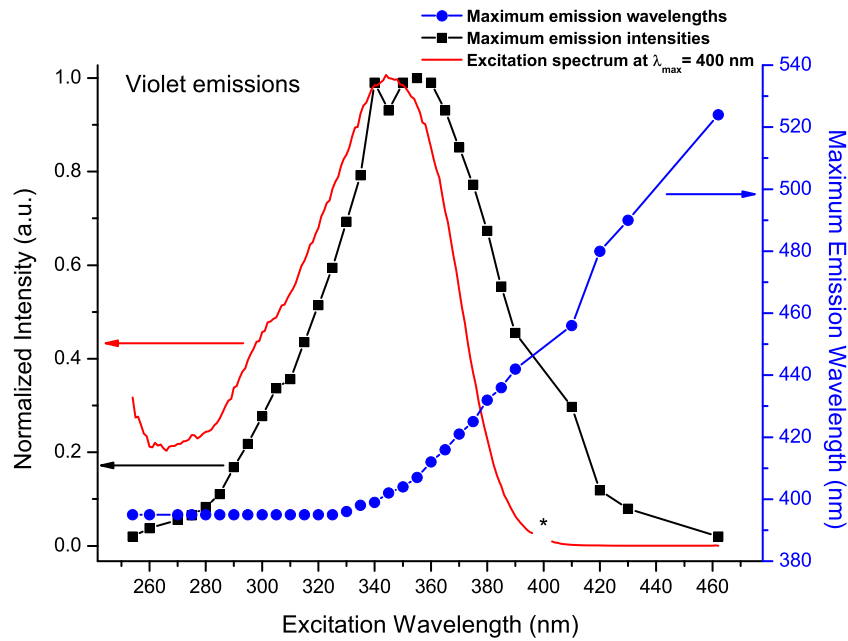


Figure 5.8.: Maximum emission intensities and wavelengths for various excitation wavelengths of undoped amorphous $\text{Si}_3\text{B}_3\text{N}_7$ ceramic for intrinsic violet emissions. The peak at 400 nm due to the light from the source was deleted (*).

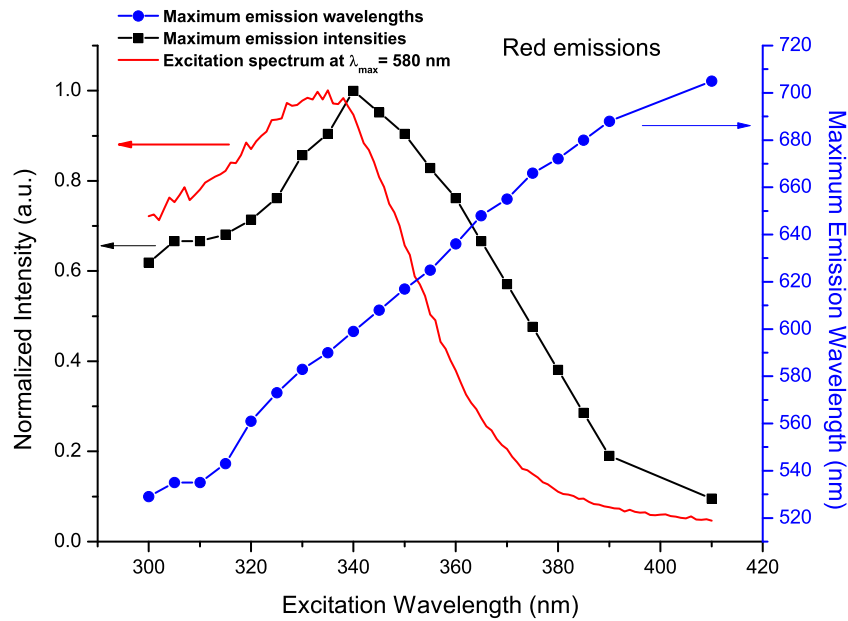


Figure 5.9.: Maximum emission intensities and wavelengths for various excitation wavelengths of undoped amorphous $\text{Si}_3\text{B}_3\text{N}_7$ ceramic for intrinsic red emissions.

5. Phosphors Based on Amorphous $Si_3B_3N_7$ Matrix

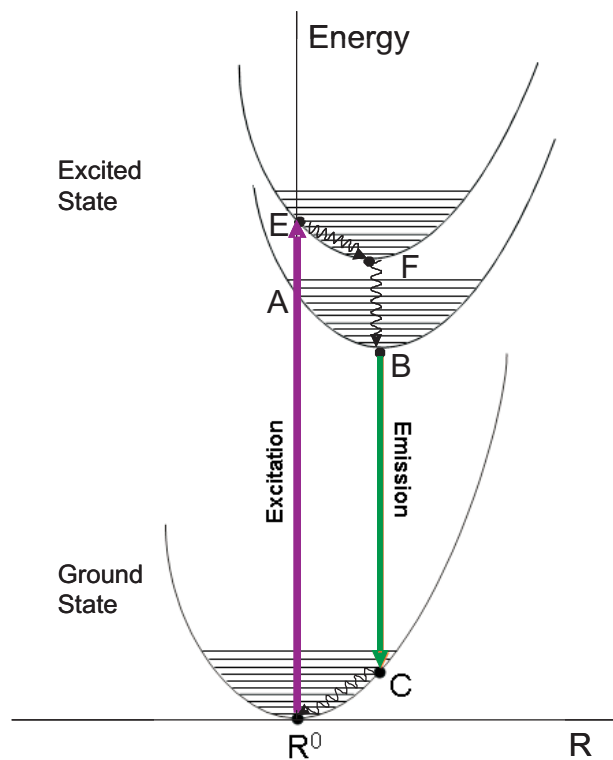


Figure 5.10.: Representation of a configurational coordinate model for the absorption of UV light to higher excited state and the emission from lower excited state.

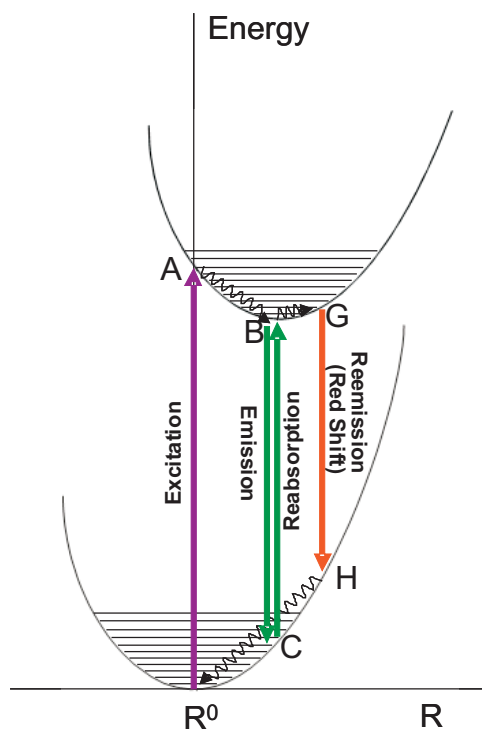


Figure 5.11.: Representation of a configurational coordinate model for the reabsorption and the reemission (red shift).

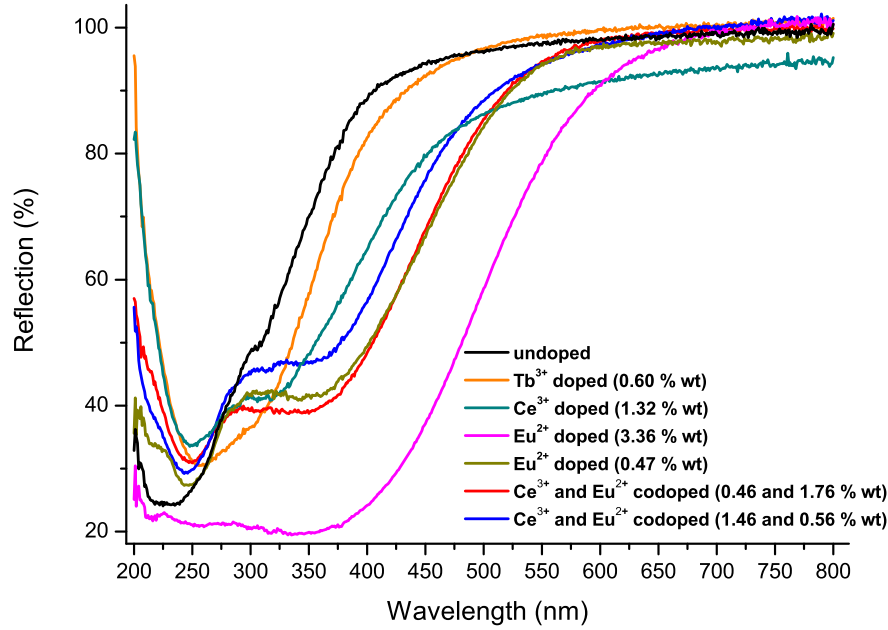


Figure 5.12.: Diffuse reflection spectra of undoped and some selected doped amorphous $\text{Si}_3\text{B}_3\text{N}_7$ ceramics.

The reabsorption and reemission processes has been reported to occur at the excitation wavelengths which are in the range where the excitation band overlaps with the emission band (that is the side of low energies in absorption band or the *red excitation edge*) [324]. It is obvious in Figure 5.2 that intrinsic violet emission overlaps with the excitation spectra up to about 320 nm (by extrapolating the emission peaks to the wavelength axis). Therefore, it is reasonable to assume that the red shifts in undoped amorphous $\text{Si}_3\text{B}_3\text{N}_7$ ceramic mainly result from the reabsorption mechanism. In Figure 5.7, the maximum emission wavelength values were almost constant at around 460 nm when excited between 254 nm and 315 nm wavelengths, and a significant red shift appeared at excitation wavelengths higher than 315 nm, which corresponded to the side of low energies in the absorption band. Similarly, in Figure 5.8, the maximum emission wavelength values were almost constant at around 400 nm when excited between 254 nm and 365 nm wavelengths, and a significant red shift appeared at excitation wavelengths higher than 365 nm, which corresponded to the side of low energies in the absorption band. Considering the intrinsic emissions in the red region of the spectrum (Figure 5.6), very broad emissions with low intensities were almost indistinguishable when the excitation wavelengths were 315 nm or lower. A steep increase in the maximum emission wavelength values were observed when the sample was excited with light between 315 nm and 462 nm, which covered not only the red excitation edge but also the high energy side in the absorption band. This peculiar behavior can

be explained by the inhomogeneous broadening of the bands arising from the dynamics of redistribution of the active centers (i.e., defects) between different local environments. As the intensities of the intrinsic red emissions in amorphous $\text{Si}_3\text{B}_3\text{N}_7$ ceramic are always lower than the blue and the violet emissions, the inhomogeneous broadening of spectra is more probable. To summarize the intrinsic photoluminescence properties of undoped amorphous $\text{Si}_3\text{B}_3\text{N}_7$: excitation with shorter wavelengths (around 305 nm) yields intense blue emission, whereas excitation with longer wavelengths (around 340 nm) results in an intense violet emission.

The undoped amorphous $\text{Si}_3\text{B}_3\text{N}_7$ ceramic has been synthesized as a white powder. Therefore, it shows a high reflection in the visible range of the spectrum (400 nm - 750 nm) as shown in Figure 5.12. Besides the main reflection edge, there is a significant drop in the reflection between 250 nm and 400 nm, which is ascribed to intrinsic absorption of the amorphous $\text{Si}_3\text{B}_3\text{N}_7$ network. When rare-earth ions are incorporated into amorphous $\text{Si}_3\text{B}_3\text{N}_7$ host matrix, the absorption in the reflection spectrum due to rare-earth ions is superimposed with the absorption of the host matrix, and extends up to around 650 nm, depending on type and concentration of rare-earth ions (Figure 5.12). This explains, for example, the dark yellow color observed for samples having higher Eu^{2+} concentrations.

5.2. Eu Doped Amorphous $\text{Si}_3\text{B}_3\text{N}_7$ Matrix

Various amounts of Eu^{2+} ions have been incorporated into amorphous $\text{Si}_3\text{B}_3\text{N}_7$ matrix by applying both the metal and organometallic routes. Figure 5.13 shows powder X-ray diffractograms for Eu^{2+} doped amorphous $\text{Si}_3\text{B}_3\text{N}_7$ ceramics prepared via both the metal and organometallic routes. Diffuse reflection spectra of Eu^{2+} doped amorphous $\text{Si}_3\text{B}_3\text{N}_7$ ceramics are given in Figure 5.12 and Figure 5.14. In these spectra, the strong drop in the reflection between 250 nm and 400 nm due to $\text{Si}_3\text{B}_3\text{N}_7$ host matrix was extended significantly to the longer wavelengths up to around 650 nm due to the absorption of Eu^{2+} ions, depending on the concentration. Samples prepared by both routes exhibit similar photoluminescence properties as shown in Figure 5.15 and 5.16 for the metal and organometallic routes, respectively. For clarity, photoluminescence spectra of the Eu^{2+} doped amorphous $\text{Si}_3\text{B}_3\text{N}_7$ ceramics prepared via both routes were compared in Figure 5.17. All Eu^{2+} doped samples exhibit broad and structureless excitation spectra, which were measured at the emission maxima, and cover a wide range in the UV-to-visible region. This broad excitation band shows a maximum between 340 nm and 365 nm, corresponding to the $4f^7 \rightarrow 4f^65d^1$ transition of Eu^{2+} (Figure 5.18).

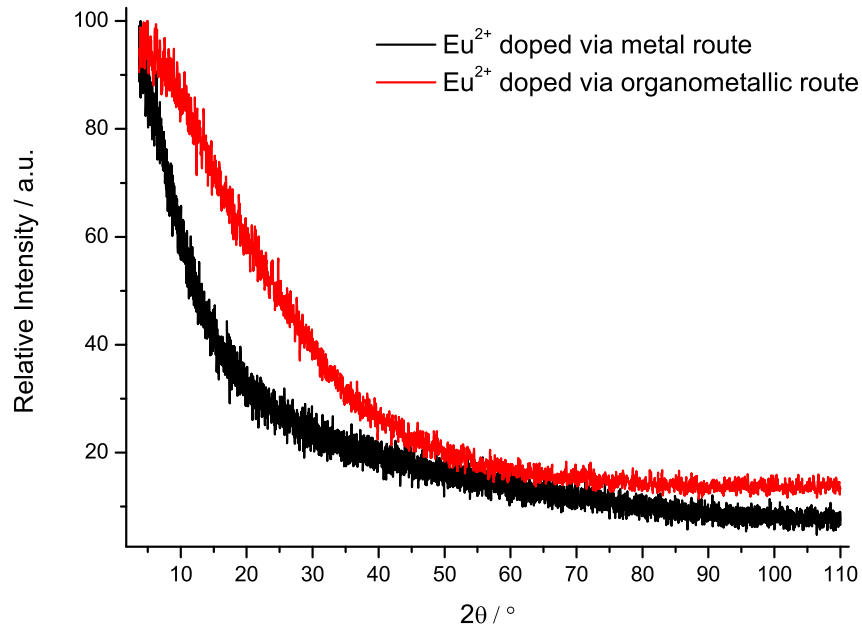


Figure 5.13.: Powder X-ray diffractograms of Eu^{2+} doped amorphous $\text{Si}_3\text{B}_3\text{N}_7$ ceramics via the metal and organometallic routes.

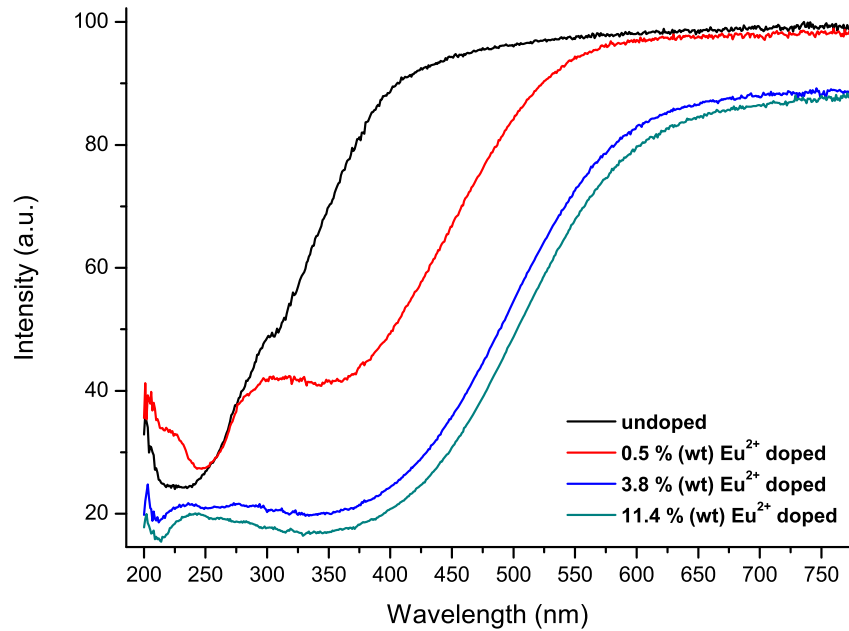


Figure 5.14.: Diffuse reflection spectra of undoped, 0.5 % (wt), 3.8 % (wt) and 11.4 % (wt) Eu^{2+} doped amorphous $\text{Si}_3\text{B}_3\text{N}_7$ ceramics.

5. Phosphors Based on Amorphous $\text{Si}_3\text{B}_3\text{N}_7$ Matrix

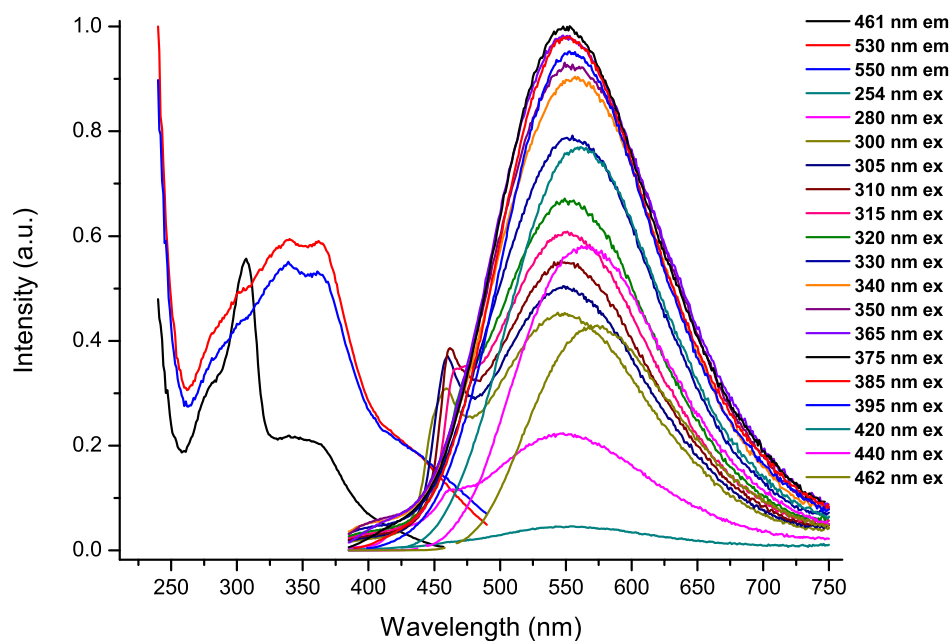


Figure 5.15.: Photoluminescence spectra of Eu^{2+} doped (0.47 % wt) amorphous $\text{Si}_3\text{B}_3\text{N}_7$ ceramic via the metal route at different excitation and emission wavelengths.

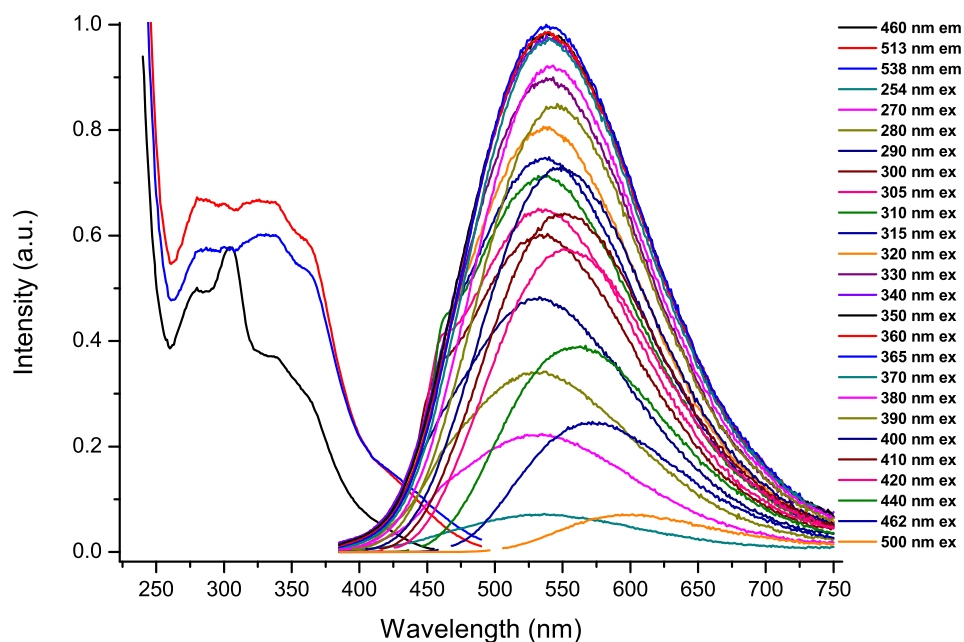


Figure 5.16.: Photoluminescence spectra of Eu^{2+} doped (0.57 % wt) amorphous $\text{Si}_3\text{B}_3\text{N}_7$ ceramic via the organometallic route at different excitation and emission wavelengths.

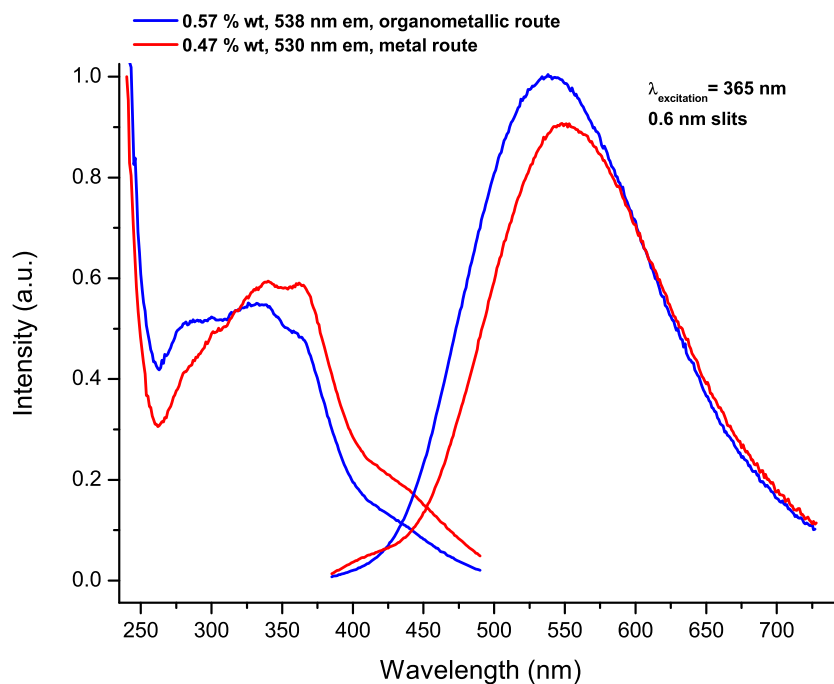


Figure 5.17.: Photoluminescence spectra of Eu^{2+} doped amorphous $\text{Si}_3\text{B}_3\text{N}_7$ ceramics via both the metal and organometallic routes.

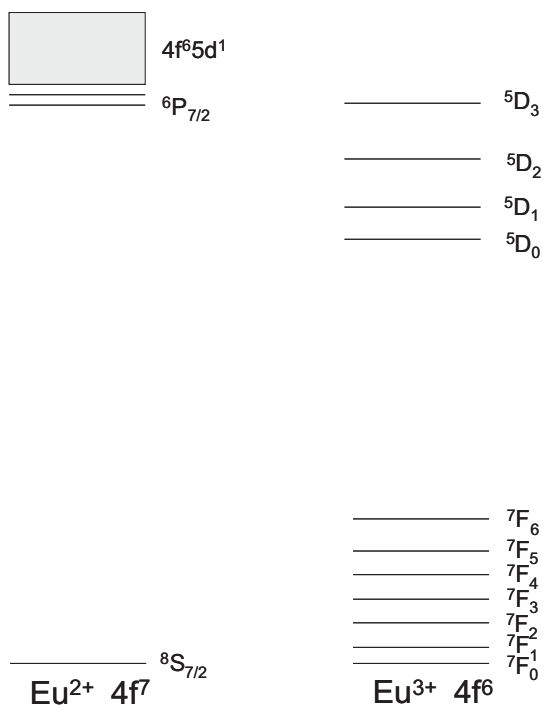


Figure 5.18.: Representation of energy level diagrams of Eu^{2+} and Eu^{3+} ions (for reasons of clarity not all levels have been shown).

5. Phosphors Based on Amorphous $\text{Si}_3\text{B}_3\text{N}_7$ Matrix

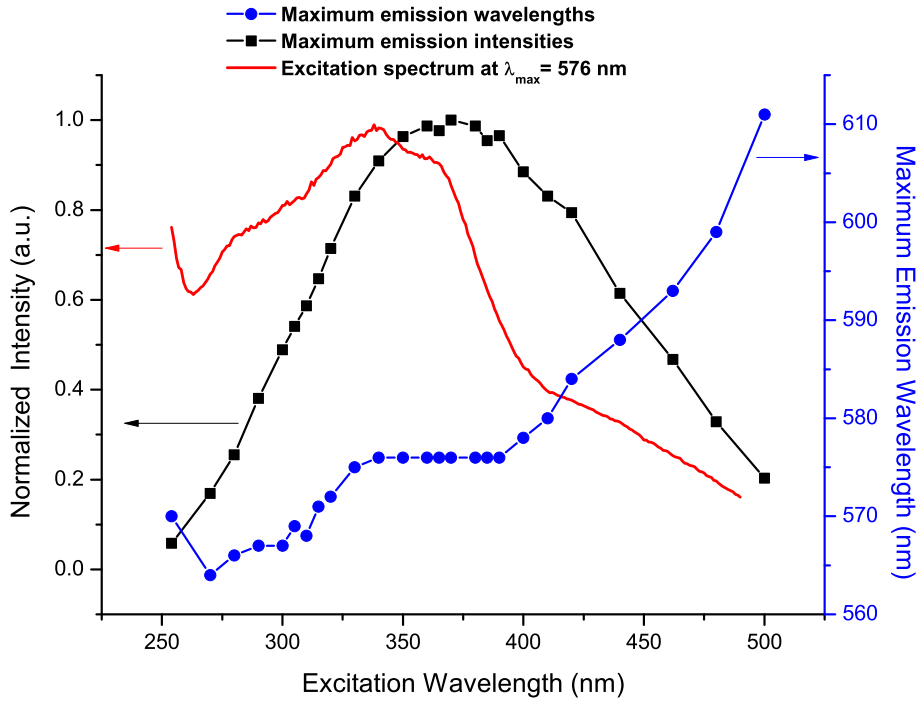


Figure 5.19.: Maximum emission intensities and wavelengths for various excitation wavelengths of Eu^{2+} doped amorphous $\text{Si}_3\text{B}_3\text{N}_7$ ceramic.

Eu^{2+} doped samples have broad emission bands, which were assigned to the allowed $4f^65d^1 \rightarrow 4f^7$ transition of Eu^{2+} ions. The maximum values of the broad emission bands were observed in the range between 540 nm and 640 nm, depending on the concentration of Eu^{2+} ions, which will be discussed in detail in Section 5.25. In addition to the dependence of the emission on the concentration of Eu^{2+} , individual Eu^{2+} doped amorphous $\text{Si}_3\text{B}_3\text{N}_7$ ceramics showed unusual photoluminescence properties such as the Red-Edge Effect, where the broad emission band was shifted towards longer wavelengths upon excitation with lower energy light [306]. When Eu^{2+} doped amorphous $\text{Si}_3\text{B}_3\text{N}_7$ ceramics (regardless of the Eu^{2+} concentration) were excited with light of wavelengths between 254 nm and 400 nm, no significant red shift was observed (Figure 5.19). However, when the Eu^{2+} doped samples were excited with light of wavelength greater than 400 nm, a significant red shift, about 35 nm (e.g. maximum emission values at 390 nm and 500 nm excitation are 575 nm and 611 nm, respectively), was observed. According to excitation spectra of Eu^{2+} doped amorphous $\text{Si}_3\text{B}_3\text{N}_7$ ceramics (e.g. in Figure 5.15), wavelengths greater than 400 nm correspond to the longer wavelength edge (red-edge) of the spectrum. The same phenomenon has been reported for organic fluorophores in low-temperature glasses and highly viscous media (see Section 5.1 and [306]) and for Eu^{2+} doped $\text{Ca-}\alpha\text{-SiAlON}$ ceramic phosphors [324]. This peculiar behavior is assigned to the different interaction that the excited state particles of Eu^{2+} ions experience with the local

environments (different defect sites) of the amorphous $\text{Si}_3\text{B}_3\text{N}_7$ matrix, which is believed to enhance the reabsorption and reemission mechanisms (see Figure 5.11), as discussed previously. This can be explained by the configurational coordinate model as already discussed in Section 5.1. For comparison, the REE has not been observed in the crystalline $\text{Eu}_2\text{Si}_5\text{N}_8$ luminescent ceramics, in which Eu^{2+} ions always experience the same local environment (see Figure 7.12).

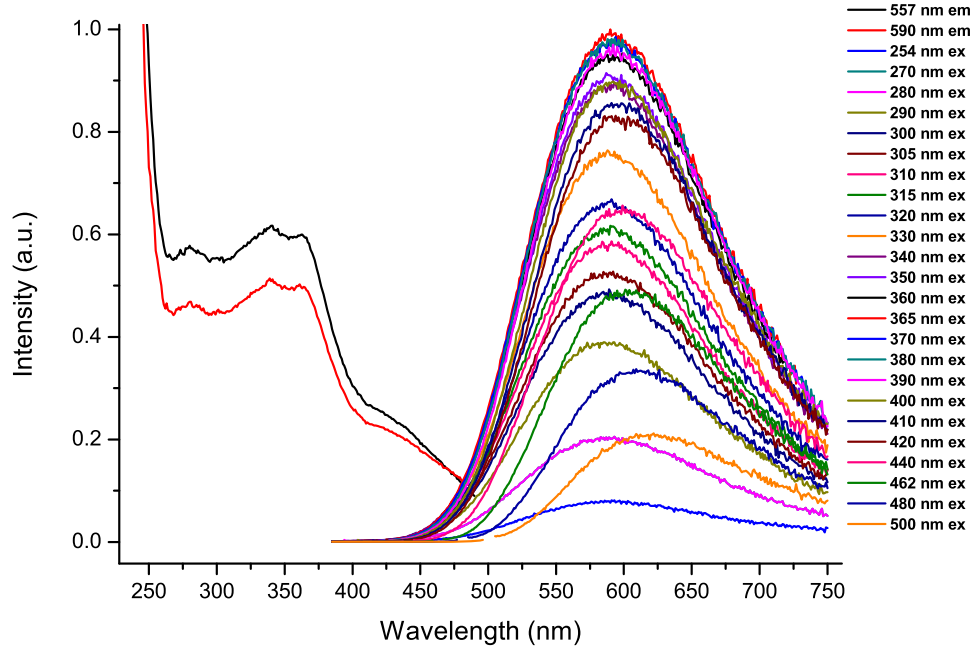


Figure 5.20.: Photoluminescence spectra of Eu^{2+} doped (3.76 % wt) amorphous $\text{Si}_3\text{B}_3\text{N}_7$ ceramic via the metal route at different excitation and emission wavelengths.

On the other hand, the emission spectra of the samples having Eu^{2+} concentration up to around 2 % by weight showed additional less intense peaks in the blue region of the spectrum, around 460 nm, while at higher Eu^{2+} concentrations, this blue emission disappeared (Figure 5.20). These blue emissions were obtained by exciting the samples with light of wavelength between 280 nm and 330 nm. This excitation wavelength range corresponds exactly to the same range that resulted in blue emissions in the undoped amorphous $\text{Si}_3\text{B}_3\text{N}_7$ ceramic. Therefore, the blue emission in Eu^{2+} doped samples has to be assigned to the intrinsic emission of the amorphous $\text{Si}_3\text{B}_3\text{N}_7$ host matrix as in Figure 5.3. This can also be proven by comparing the excitation spectra of the undoped and the Eu^{2+} doped amorphous $\text{Si}_3\text{B}_3\text{N}_7$ ceramics measured at the emission maximum value of 460 nm in Figure 5.2 and Figure 5.15, respectively. It is obvious that the excitation band of the Eu^{2+} doped sample for an emission maximum value of 461 nm appears different from the one for an emission maximum value of 530 nm and 550 nm, and it is similar

5. Phosphors Based on Amorphous $\text{Si}_3\text{B}_3\text{N}_7$ Matrix

to the one obtained for undoped amorphous $\text{Si}_3\text{B}_3\text{N}_7$ ceramic at an emission maximum value of 460 nm. The possible explanation for this phenomenon is that at the low Eu^{2+} concentrations, Eu^{2+} ions are distributed such that the interatomic distances between the neighboring Eu^{2+} ions are long enough and thus undoped regions in the network are still able to emit the blue light. However, at higher Eu^{2+} concentrations, the interatomic distances between the neighboring Eu^{2+} ions are so close that they most probably absorb the intrinsic blue emission of the matrix, which, therefore, is no longer visible.

In the present study, the characteristic sharp line emissions for Eu^{3+} ions between 580 nm and 650 nm due to $4f \rightarrow 4f$ transition have not been observed (Figure 5.18). This suggests that all Eu ions in amorphous $\text{Si}_3\text{B}_3\text{N}_7$ host matrices are in the divalent state. The broad emission, which is typical for Eu^{2+} ions, is expected for samples synthesized via the metal route, as Eu^{2+} ions are obtained when Eu metal is dissolved in liquid ammonia before the reaction. On the other hand, one could expect to see the typical Eu^{3+} sharp emission lines for the samples obtained via the organometallic route, due to the presence of Eu^{3+} ions in the starting compound, which is $\text{Eu}[\text{N}(\text{Si}(\text{CH}_3)_3)_2]_3$. However, it was previously shown that Eu^{3+} ions are easily reduced to Eu^{2+} ions by the reducing nitrogen environment during synthesis [264]. This phenomenon has additionally been proven by magnetic measurements where Eu^{2+} doped amorphous $\text{Si}_3\text{B}_3\text{N}_7$ ceramics synthesized via both routes showed the typical paramagnetic behavior of Eu^{2+} ions.

Magnetic susceptibility and inverse magnetic susceptibility as a function of temperature in a 3 T external magnetic field are shown for samples prepared via the metal route in Figure 5.21 and the organometallic route in Figure 5.22. It is clearly visible that Eu doped amorphous $\text{Si}_3\text{B}_3\text{N}_7$ ceramics via both routes exhibited Curie behavior. The experimental magnetic moment values were derived from the fitted $1/\chi_{mol}$ versus T dependence and found to be $8.77 \mu_B$ for the metal route and $9.03 \mu_B$ for the organometallic route. These values are in fair agreement with the theoretical value of $7.94 \mu_B$ for free Eu^{2+} ions. Therefore, these results, together with emission spectra, confirm that Eu ions are in the divalent state regardless of the synthetic route. The slight differences in experimental and theoretical magnetic moment values resulted from the difficulties in assigning the exact amount of Eu^{2+} ions during the magnetic measurements. As the samples are amorphous and the amount of Eu^{2+} ions are determined via elemental analysis, such deviations are unavoidable. On the other hand, the samples synthesized via two different routes exhibited very similar magnetic properties. No magnetic ordering was detected down to 10 K for both routes. In fact, the Weiss temperatures for metal and organometallic routes were determined from the fit of $1/\chi_{mol}$ versus T as -1 K and 0.9 K, respectively, suggesting that any magnetic interactions were very weak indeed.

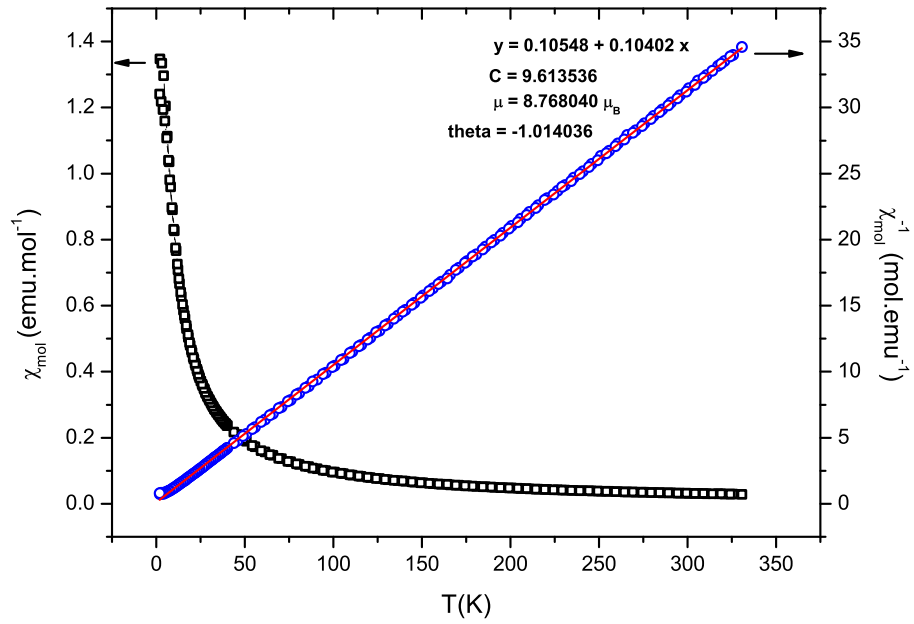


Figure 5.21.: Magnetic susceptibility of Eu^{2+} doped (1.14 % wt) amorphous $\text{Si}_3\text{B}_3\text{N}_7$ ceramic prepared via the metal route represented as χ_{mol} vs. T (squares) and χ_{mol}^{-1} vs. T (circles) in an applied field of 3 Tesla.

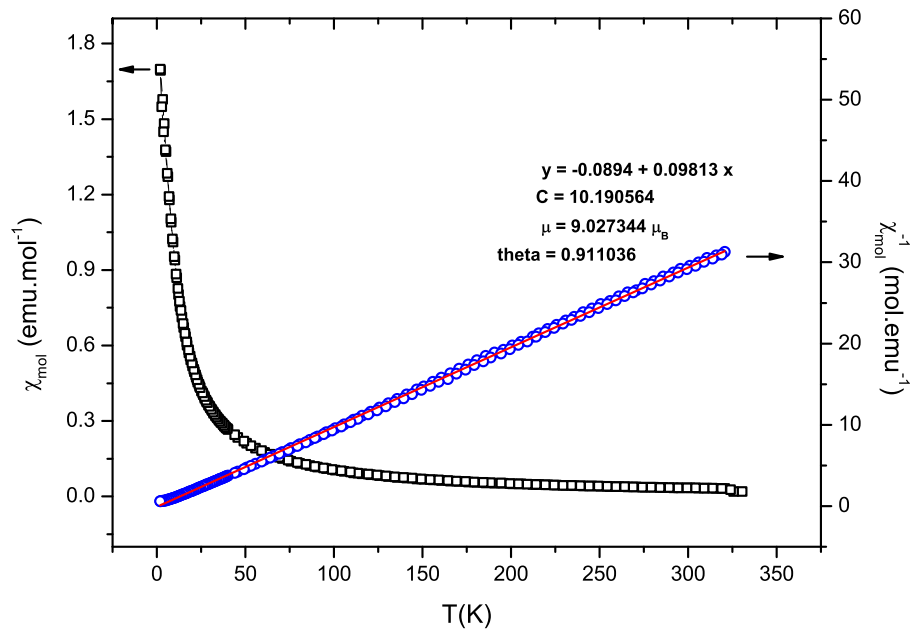


Figure 5.22.: Magnetic susceptibility of Eu^{2+} doped (0.57 % wt) amorphous $\text{Si}_3\text{B}_3\text{N}_7$ ceramic prepared via the organometallic route represented as χ_{mol} vs. T (squares) and χ_{mol}^{-1} vs. T (circles) in an applied field of 3 Tesla.

5. Phosphors Based on Amorphous $\text{Si}_3\text{B}_3\text{N}_7$ Matrix

Another very challenging result is that emission spectra of Eu^{2+} doped amorphous $\text{Si}_3\text{B}_3\text{N}_7$ ceramics have relatively high Full Width at Half Maximum (FWHM) values. In fact, FWHM values indicate how much of the visible light is emitted efficiently by the sample and, therefore, the larger the FWHM, the better the CRI values. Eu^{2+} doped amorphous $\text{Si}_3\text{B}_3\text{N}_7$ ceramics have FWHM values mainly between 140 and 180 nm, depending on Eu^{2+} concentration and excitation wavelength. In literature, the FWHM values of YAG:Ce, which is used as a conversion phosphor in commercially available white-LEDs, were reported to be 105 ± 10 nm [325, 326]. Therefore, it is quite obvious that Eu^{2+} doped amorphous $\text{Si}_3\text{B}_3\text{N}_7$ ceramics are very promising candidates as a replacement conversion phosphor as they may have much better CRI values than YAG:Ce and produce a superior white light that covers a wider range of visible spectrum.

5.3. Eu Doped Amorphous Si_3N_4 Matrix

Analogous to Eu^{2+} doped amorphous $\text{Si}_3\text{B}_3\text{N}_7$ ceramics, Eu^{2+} doped amorphous Si_3N_4 ceramics have been prepared via the polymer route. In this case, instead of TADB, SiCl_4 has been ammonolysed with liquid ammonia in which Eu metal is dissolved. After purification and heating processes, luminescent amorphous Si_3N_4 ceramics have been obtained. Two different samples have been prepared containing approximately 1 % and 2 % Eu (determined by elemental analysis, see Table 9.3) and named as a- Si_3N_4 :Eu-1 and a- Si_3N_4 :Eu-2, respectively. Details for experiments are presented in Section 10.1.1. The amorphous nature of the samples was confirmed with powder X-ray analysis (Figure 5.23). Diffuse reflection spectra of both samples are presented in Figure 5.24. Similar to the Eu^{2+} doped amorphous $\text{Si}_3\text{B}_3\text{N}_7$ ceramics, Eu^{2+} doped amorphous Si_3N_4 samples exhibit broad absorption bands between 280 nm and 450 nm, which are consistent with the excitation spectra of the corresponding samples. Obviously, the strong absorption at around 210 nm has to be attributed to the amorphous Si_3N_4 matrix. Photoluminescence properties of the Eu^{2+} doped amorphous Si_3N_4 ceramics are shown in Figure 5.25 for a- Si_3N_4 :Eu-1 and Figure 5.26 for a- Si_3N_4 :Eu-2. The photoluminescence spectra of both samples are very similar to those for the Eu^{2+} doped amorphous $\text{Si}_3\text{B}_3\text{N}_7$ ceramics. This is to be expected because Eu^{2+} ions experience a very similar local surrounding: in one case it is an amorphous Si-N network and in the other case it is an amorphous Si-B-N network. A structureless broad excitation band in the UV region of the spectrum and a broad emission band in the visible region of the spectrum due to the $5d \leftrightarrow 4f$ transitions of Eu^{2+} ions have been observed. Figure 5.27 compares the emission spectra of approximately 1 % (weight) Eu^{2+} doped amorphous Si_3N_4 and $\text{Si}_3\text{B}_3\text{N}_7$ matrices. According to this figure, Eu^{2+} doped amorphous Si_3N_4 sample has the emission maximum value at a considerably shorter wavelength, as compared to Eu^{2+} doped amorphous $\text{Si}_3\text{B}_3\text{N}_7$ (528 nm for amor-

phous $\text{Si}_3\text{N}_4:\text{Eu}^{2+}$ and 574 nm for amorphous $\text{Si}_3\text{B}_3\text{N}_7:\text{Eu}^{2+}$). Obviously, this red shift in the amorphous $\text{Si}_3\text{B}_3\text{N}_7$ host matrix results from the additional boron atoms bonded to nitrogen in the network structure. This phenomenon can be explained by the inductive effect [327]. The net negative charge on nitrogen atoms in B-N-Si (in amorphous $\text{Si}_3\text{B}_3\text{N}_7$) is less compared to Si-N-Si (in amorphous Si_3N_4) due to more electronegative character of B atoms (2.04 in Pauling scale) compared to Si atoms (1.90 in Pauling scale). This leads to have less net positive charge on Eu^{2+} ions in amorphous $\text{Si}_3\text{B}_3\text{N}_7$ network (inductive effect) and thus increases the 4f levels of Eu^{2+} resulting in a decrease in 4f-5d gap; that means a red shift in emission. Similar phenomena were reported for Eu^{2+} ions in BaLiF_3 and BaSiF_6 [327, 328], and for Ce^{3+} ions in Ce_2Si_5 , $\text{Ce}_6\text{Si}_4\text{S}_{17}$ and $\text{Ce}_4\text{Si}_3\text{S}_{12}$ [329] matrices. In addition, increasing the Eu^{2+} concentration in amorphous Si_3N_4 results in a red shift in emission maximum wavelength, i.e 528 nm for a- $\text{Si}_3\text{N}_4:\text{Eu}$ -1 (FWHM = 151 nm) and 552 nm for a- $\text{Si}_3\text{N}_4:\text{Eu}$ -2 (FWHM = 166 nm). Furthermore, similar to the Eu^{2+} doped amorphous $\text{Si}_3\text{B}_3\text{N}_7$ ceramics, red-edge effect has been observed, which most probably occurs due to the similar reasoning as mentioned in Chapters 5.1 and 5.2. All these results imply that amorphous Si_3N_4 is also a potential candidate to host various ions for different functional materials, including phosphors, magnetic materials, pigments and etc.

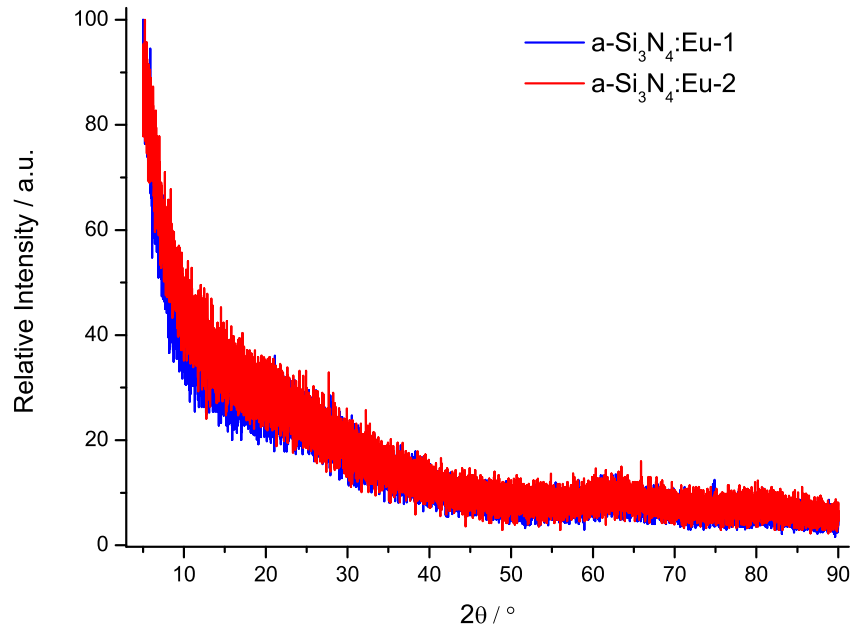


Figure 5.23.: Powder X-ray diffractograms of Eu^{2+} doped amorphous Si_3N_4 ceramics.

5. Phosphors Based on Amorphous $\text{Si}_3\text{B}_3\text{N}_7$ Matrix

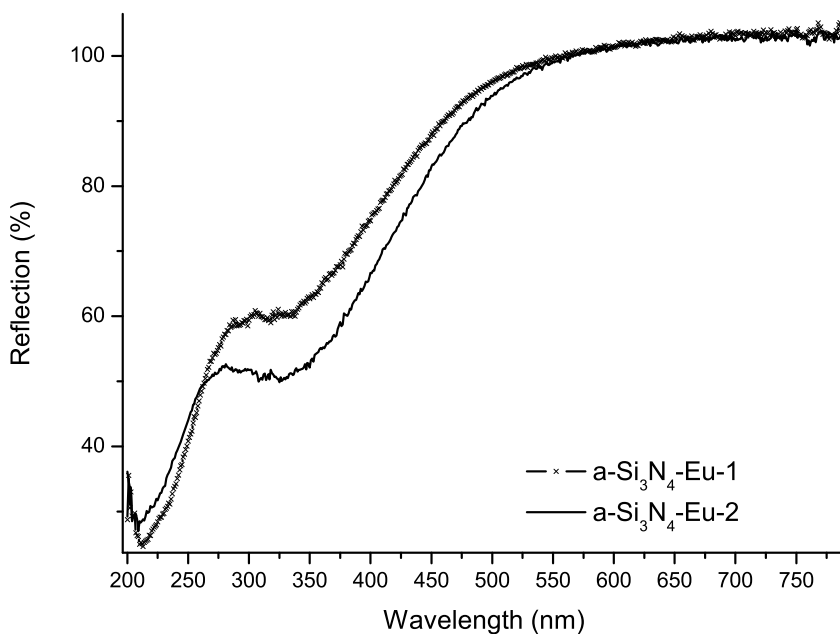


Figure 5.24.: Diffuse reflection spectra of Eu^{2+} doped amorphous Si_3N_4 ceramics.

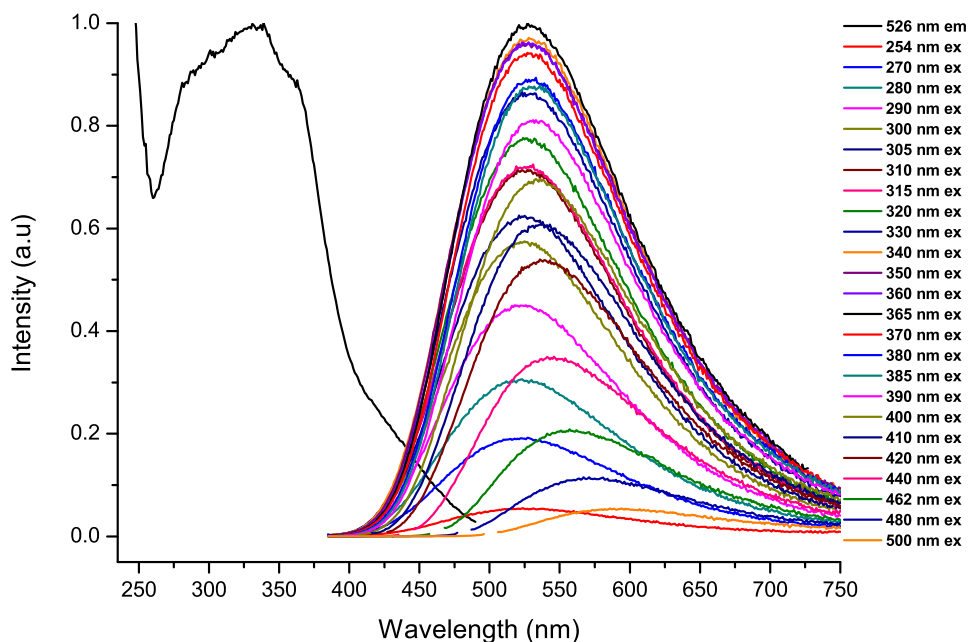


Figure 5.25.: Photoluminescence spectra of Eu^{2+} doped (1 % wt) amorphous Si_3N_4 ceramic ($\text{a-Si}_3\text{N}_4:\text{Eu-1}$) at different excitation and emission wavelengths.

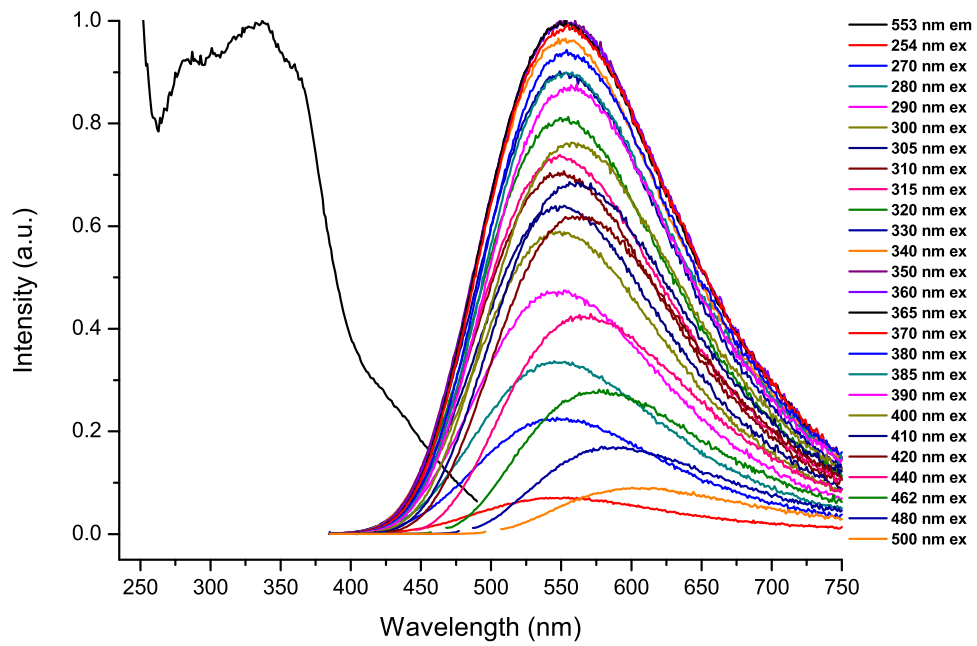


Figure 5.26.: Photoluminescence spectra of Eu^{2+} doped (2 % wt) amorphous Si_3N_4 ceramic ($\text{a-Si}_3\text{N}_4:\text{Eu-2}$) at different excitation and emission wavelengths.

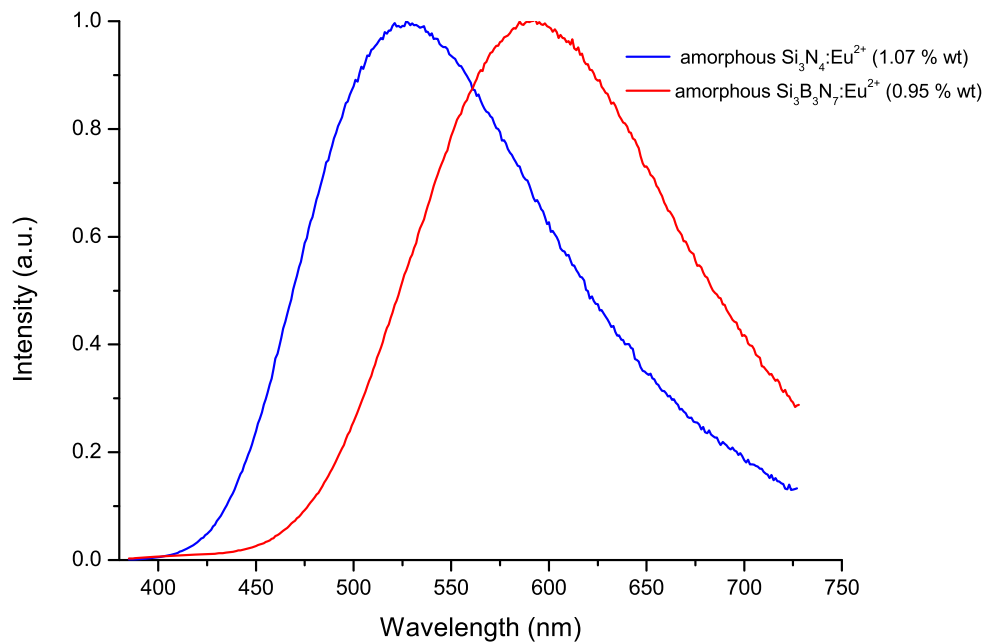


Figure 5.27.: Comparison of the emission spectra of approximately 1 % by weight Eu^{2+} doped amorphous Si_3N_4 and $\text{Si}_3\text{B}_3\text{N}_7$ ceramics.

5.4. Ce Doped Amorphous $\text{Si}_3\text{B}_3\text{N}_7$ Matrix

Ce^{3+} doping into amorphous $\text{Si}_3\text{B}_3\text{N}_7$ matrix has been achieved via the organometallic route by using $\text{Ce}[\text{N}(\text{Si}(\text{CH}_3)_3)_2]_3$. Powder X-ray pattern and diffuse reflection spectrum of Ce^{3+} doped amorphous $\text{Si}_3\text{B}_3\text{N}_7$ ceramic are shown in Figure 5.28 and Figure 5.29, respectively. In the diffuse reflection spectra, the strong drop in reflection between 250 nm and 400 nm due to $\text{Si}_3\text{B}_3\text{N}_7$ host matrix was shifted towards longer wavelengths up to 550 nm with an additional absorption band between 340 nm and 400 nm due to Ce^{3+} ions for Ce^{3+} doped amorphous $\text{Si}_3\text{B}_3\text{N}_7$ ceramics, depending on the Ce^{3+} concentration. Typical photoluminescence properties of Ce^{3+} doped amorphous $\text{Si}_3\text{B}_3\text{N}_7$ ceramic are given in Figure 5.30. The Ce^{3+} doped samples exhibit broad and structureless excitation spectra, measured at emission maxima, and cover a wide range in the UV and visible regions. This broad excitation band has a maximum between 340 nm and 365 nm, corresponding to the $4f^1 \rightarrow 4f^05d^1$ transition of Ce^{3+} (Figure 5.31). Ce^{3+} doped samples have broad emission bands with maximum values in the range between 520 nm and 550 nm depending on the concentration of Ce^{3+} ions, which will be discussed in detail in Section 5.25. These emission bands have been assigned to the allowed $4f^05d^1 \rightarrow 4f^1$ transition of Ce^{3+} ions. The excitation band at 305 nm (measured at emission maximum value of 462 nm) and the less intense blue emission peaks in Figure 5.30 resulted from the intrinsic emission of $\text{Si}_3\text{B}_3\text{N}_7$ host matrix, which were also observed in the Eu^{2+} doped samples.

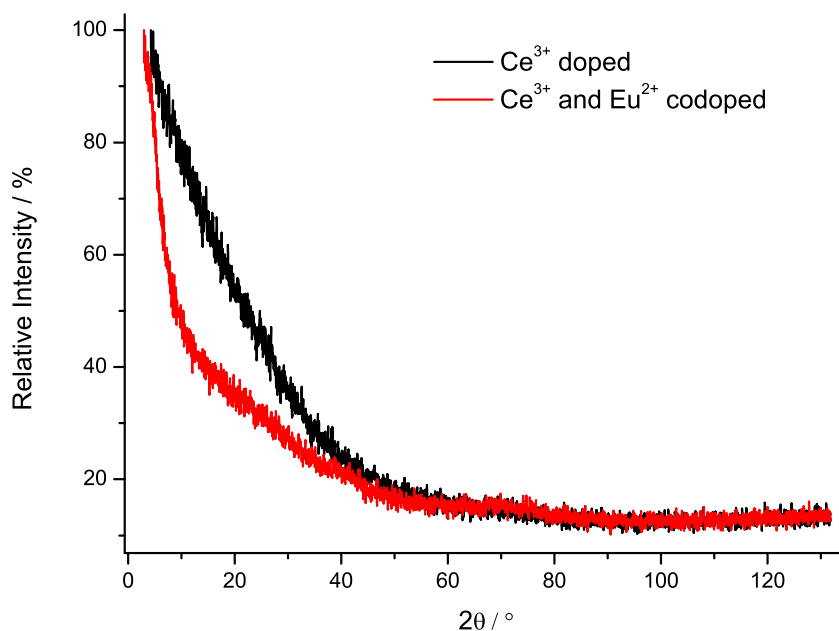


Figure 5.28.: Powder X-ray diffractograms of Ce^{3+} doped and $\text{Ce}^{3+}/\text{Eu}^{2+}$ codoped amorphous $\text{Si}_3\text{B}_3\text{N}_7$ ceramics.

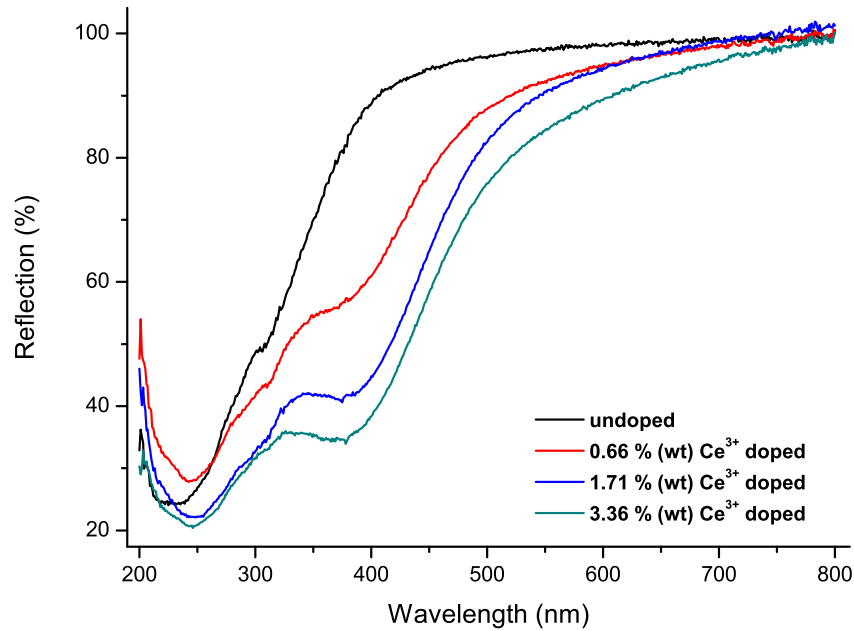


Figure 5.29.: Diffuse reflection spectra of undoped, 0.66 % (wt), 1.7 % (wt) and 3.36 % (wt) Ce^{3+} doped amorphous $\text{Si}_3\text{B}_3\text{N}_7$ ceramics.

Similar to the Eu^{2+} doped samples, Ce^{3+} doped samples also show red shift in emission spectra (see Section 5.1 and Section 5.2); however, in contrast to Eu^{2+} doped samples, Ce^{3+} doped samples show a significant intermediate red shift (about 20 nm) when the samples are excited with the light between 315 nm and 340 nm (Figure 5.32), which are not on the low energy side of the absorption band (red excitation edge). Therefore, this intermediate red shift cannot be simply explained by the classical Red-Edge Effect but most probably results from the dynamic local interactions between the luminescent active species (i.e., Ce^{3+} ions and defects of the host matrix) with their environment at the specified energies. Emission peak maximum values shifted back to 546 nm when samples were excited with the light between 340 nm and 365 nm (Figure 5.32). Afterwards, the maximum emission values exhibited no red shift up to the excitation wavelength of 420 nm, after which a significant red shift, about 54 nm, was observed (e.g. maximum emission values at 420 nm and 500 nm excitation are 546 nm and 600 nm, respectively). The same reasons giving rise to red shifts in Eu^{2+} doped amorphous $\text{Si}_3\text{B}_3\text{N}_7$ ceramics are thought to be responsible for the red shifts in Ce^{3+} doped samples, too.

The samples with Ce^{3+} concentrations up to around 2 % by weight showed additional less intense emission peaks in the blue region of the spectrum, around 460 nm. Similar to Eu^{2+} doped samples, these blue emissions are attributed to the intrinsic emission of $\text{Si}_3\text{B}_3\text{N}_7$ matrix. The Ce^{3+} doped amorphous $\text{Si}_3\text{B}_3\text{N}_7$ ceramics also possess high FWHM

5. Phosphors Based on Amorphous $\text{Si}_3\text{B}_3\text{N}_7$ Matrix

values between 180 and 205 nm, depending on the Ce^{3+} concentration and excitation wavelength, which also makes them very promising candidates for white LEDs.

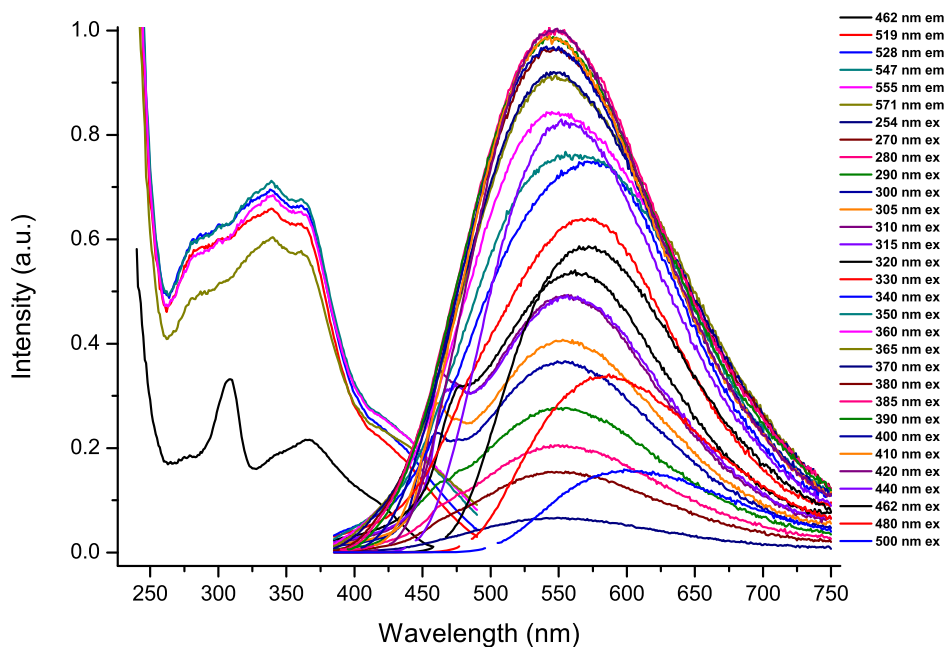


Figure 5.30.: Photoluminescence spectra of Ce^{3+} doped sample at different excitation and emission wavelengths.

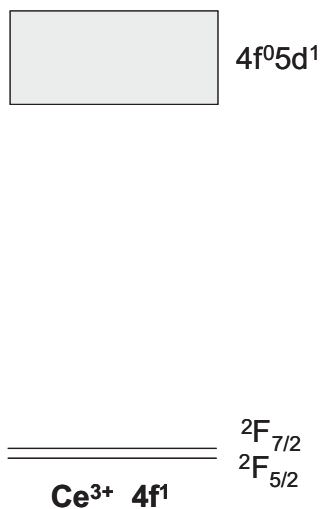


Figure 5.31.: Representation of energy level diagram of Ce^{3+} ions.

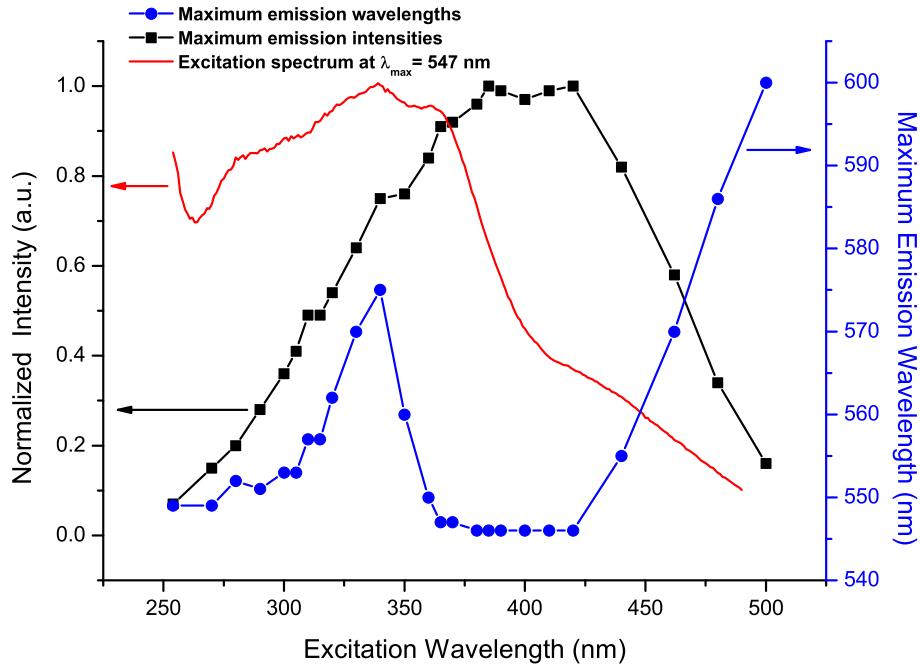


Figure 5.32.: Maximum emission intensities and wavelengths for various excitation wavelengths of Ce^{3+} doped amorphous $\text{Si}_3\text{B}_3\text{N}_7$ ceramic.

5.5. Ce/Eu Codoped Amorphous $\text{Si}_3\text{B}_3\text{N}_7$ Matrix

Powder X-ray pattern and diffuse reflection spectrum of $\text{Ce}^{3+}/\text{Eu}^{2+}$ codoped amorphous $\text{Si}_3\text{B}_3\text{N}_7$ ceramic are shown in Figure 5.28 and Figure 5.33, respectively. In previous sections, photoluminescence properties of Ce^{3+} doped and Eu^{2+} doped amorphous $\text{Si}_3\text{B}_3\text{N}_7$ ceramics were discussed. As the energy level diagrams of $\text{Ce}^{3+}(4f^1)$ and $\text{Eu}^{2+}(4f^7)$ are very similar (Figure 5.34), these ions share common photoluminescence characteristics such that the broad $5d \rightarrow 4f$ emission band in the visible region dominates the corresponding emission spectra. The $4f^65d^1$ band of Eu^{2+} is usually located at lower position in energy than the $4f^05d^1$ band of Ce^{3+} , which results in emission at slightly longer wavelengths. Therefore, broad emission bands for $\text{Ce}^{3+}/\text{Eu}^{2+}$ codoped amorphous $\text{Si}_3\text{B}_3\text{N}_7$ ceramics are also expected, which would resemble the emission spectra of single ion doped samples with emission maximum values in between that of the single doped ones. The photoluminescence spectra of $\text{Ce}^{3+}/\text{Eu}^{2+}$ codoped amorphous $\text{Si}_3\text{B}_3\text{N}_7$ ceramic at different excitation and emission wavelengths shown in Figure 5.35 indicate that this is indeed the case. As the energy difference between the $5d4f$ band and $4f$ level of Ce^{3+} and Eu^{2+} ions are very similar, the broad emission band in $\text{Ce}^{3+}/\text{Eu}^{2+}$ codoped amorphous $\text{Si}_3\text{B}_3\text{N}_7$ ceramic is attributed to simultaneous $5d4f \rightarrow 4f$ emissions of both Ce^{3+} and Eu^{2+} ions. Depending on the concentration of Ce^{3+} and Eu^{2+} ions, emission maximum values of

5. Phosphors Based on Amorphous $\text{Si}_3\text{B}_3\text{N}_7$ Matrix

$\text{Ce}^{3+}/\text{Eu}^{2+}$ codoped samples were obtained between 525 nm and 575 nm, which will be discussed in Section 5.25. Not surprisingly, the Red-Edge Effect was also detected for $\text{Ce}^{3+}/\text{Eu}^{2+}$ codoped samples. Figure 5.36 compares the excitation and emission spectra of Ce^{3+} doped, Eu^{2+} doped and $\text{Ce}^{3+}/\text{Eu}^{2+}$ codoped amorphous $\text{Si}_3\text{B}_3\text{N}_7$ ceramics. The same emission maximum value was obtained for single ion doped and codoped samples, which is, in principle, possible because the emission maximum value is strongly dependent on the concentration of Ce^{3+} and Eu^{2+} ions. As expected, the FWHM value in emission spectrum of $\text{Ce}^{3+}/\text{Eu}^{2+}$ codoped $\text{Si}_3\text{B}_3\text{N}_7$ ceramic was observed between the values for single ion doped ceramics: larger than the Eu^{2+} doped ceramic but smaller than the Ce^{3+} doped one.

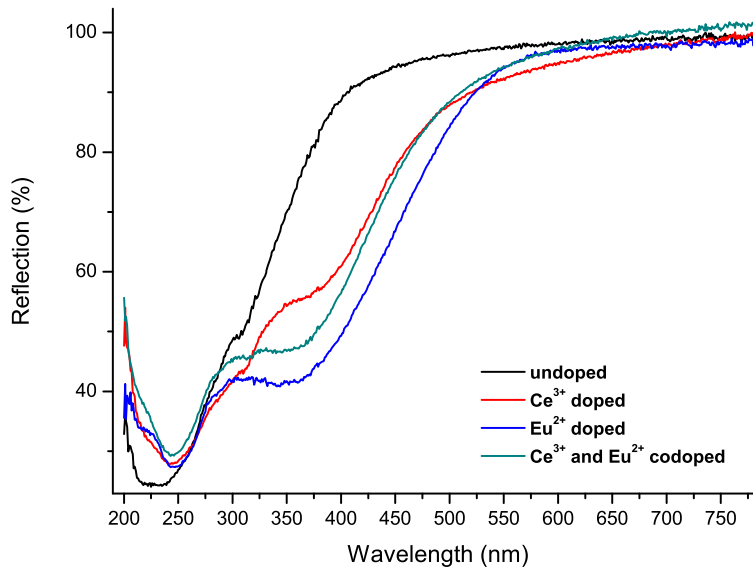


Figure 5.33.: Diffuse reflection spectra of undoped, Ce^{3+} doped, Eu^{2+} doped and $\text{Ce}^{3+}/\text{Eu}^{2+}$ codoped amorphous $\text{Si}_3\text{B}_3\text{N}_7$ ceramics.

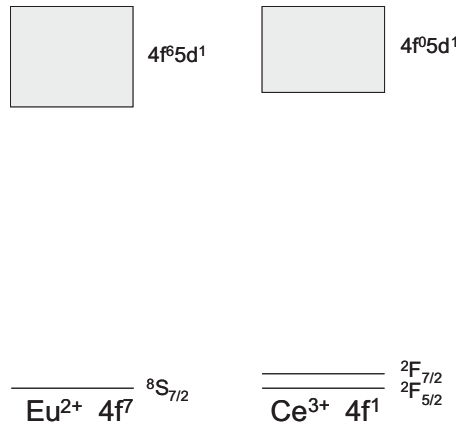


Figure 5.34.: Comparison of the energy level diagrams of Ce^{3+} and Eu^{2+} ions.

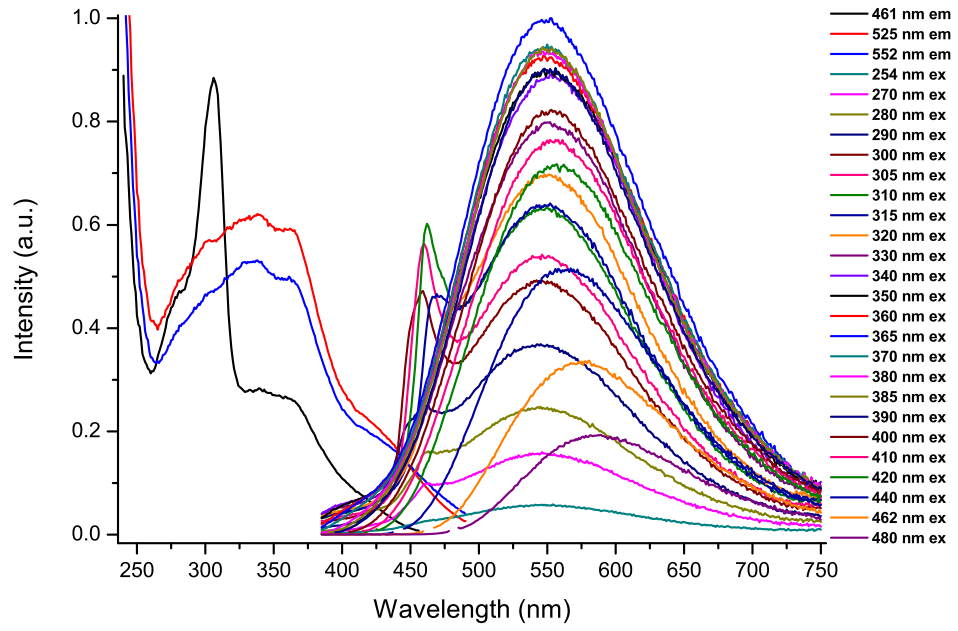


Figure 5.35.: Photoluminescence spectra of Ce³⁺/Eu²⁺ codoped amorphous Si₃B₃N₇ ceramic at different excitation and emission wavelengths.

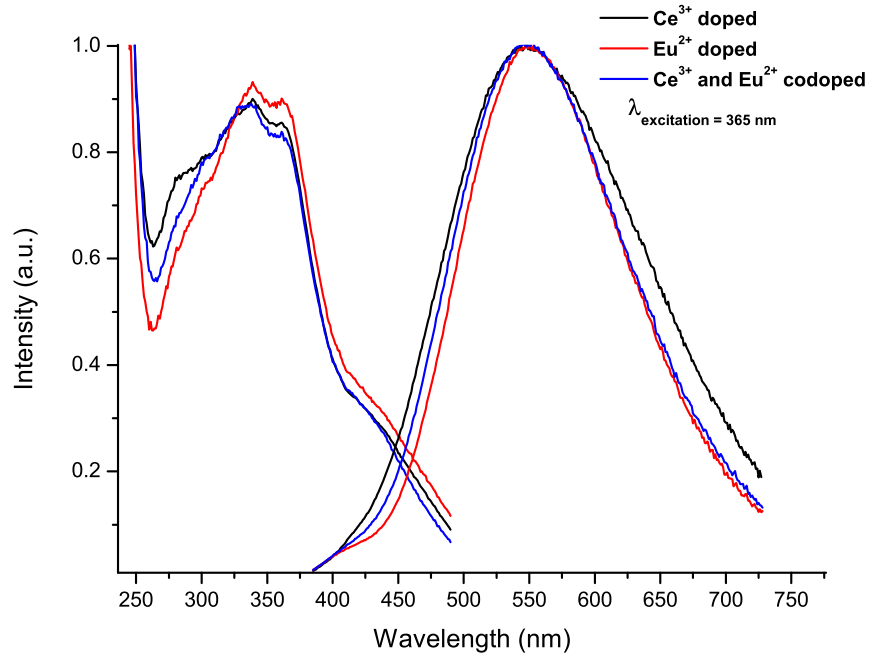


Figure 5.36.: Photoluminescence spectra of Ce³⁺ doped, Eu²⁺ doped and Ce³⁺/Eu²⁺ codoped amorphous Si₃B₃N₇ ceramics (Excitation spectra are measured at maximum emission wavelengths and emission spectra are measured at 365 nm excitation wavelength).

5.6. Nd Doped Amorphous $\text{Si}_3\text{B}_3\text{N}_7$ Matrix

The trivalent lanthanide ions including Pr^{3+} , Nd^{3+} , Er^{3+} and Yb^{3+} have been widely studied for near-infrared (NIR) luminescence [330]. There are three particular driving forces for this interest in NIR luminescence [331]. First, the most popular application of infrared luminescent materials is laser systems (the common Nd-containing 1064 nm laser). Second, telecommunication optical networks based on silica fibers use NIR radiation to send information because in this region silica has a high transparency. Third, human tissue is relatively transparent at around 800-1000 nm and metal ions which are luminescent in this region are ideal candidates for in-vivo luminescent imaging.

Even though Nd^{3+} containing materials are potential candidates for NIR luminescence, in the present study, the photoluminescence properties in visible region via near-UV to VIS excitation have been studied. Energy levels of Nd^{3+} ions are presented in Figure 5.37. Powder X-ray diffractograms of amorphous $\text{Si}_3\text{B}_3\text{N}_7$ ceramics, in which Nd^{3+} ions are incorporated, are shown in Figure 5.38. Incorporation of Nd^{3+} ions into the amorphous $\text{Si}_3\text{B}_3\text{N}_7$ matrix has been proven via diffuse reflection spectroscopy (Figure 5.39). In the diffuse reflection spectrum, in addition to the strong drop in the reflection between 250 nm and 400 nm due to the $\text{Si}_3\text{B}_3\text{N}_7$ host matrix, typical absorption bands of Nd^{3+} ions have been observed and the absorptions from the ground state $^4\text{I}_{9/2}$ level to the higher energy levels are depicted.

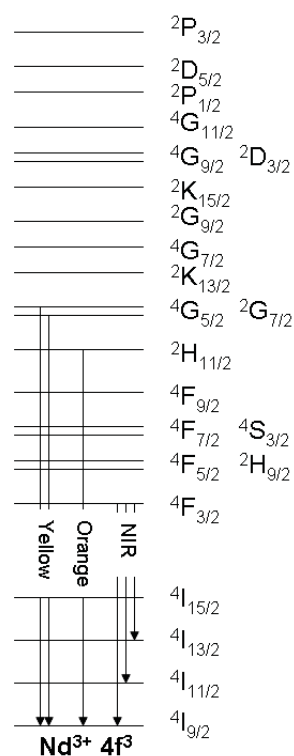


Figure 5.37.: Representation of energy level diagram of Nd^{3+} ions (for reasons of clarity not all levels have been shown).

The absorption bands due to Nd^{3+} ions in Figure 5.39 were ascribed to the following transitions: at 886 nm due to the $^4\text{I}_{9/2} \rightarrow ^4\text{F}_{3/2}$, at 810 nm due to $^4\text{I}_{9/2} \rightarrow ^4\text{F}_{5/2}$ and $^4\text{I}_{9/2} \rightarrow ^4\text{H}_{9/2}$, at 748 nm due to $^4\text{I}_{9/2} \rightarrow ^4\text{F}_{7/2}$ and $^4\text{I}_{9/2} \rightarrow ^4\text{S}_{3/2}$, at 686 nm due to $^4\text{I}_{9/2} \rightarrow ^4\text{F}_{9/2}$, at 589 nm due to $^4\text{I}_{9/2} \rightarrow ^4\text{G}_{5/2}$ and $^4\text{I}_{9/2} \rightarrow ^2\text{G}_{7/2}$, at 530 nm due to $^4\text{I}_{9/2} \rightarrow ^2\text{K}_{13/2}$, at 517 nm due to $^4\text{I}_{9/2} \rightarrow ^4\text{G}_{7/2}$, at 477 nm due to $^4\text{I}_{9/2} \rightarrow ^2\text{K}_{15/2}$, at 432 nm due to $^4\text{I}_{9/2} \rightarrow ^2\text{P}_{1/2}$ and at 363 nm due to $^4\text{I}_{9/2} \rightarrow ^2\text{P}_{3/2}$ transitions. As a result of these absorptions, the Nd^{3+} doped amorphous $\text{Si}_3\text{B}_3\text{N}_7$ ceramic appeared as light cyan.

Photoluminescence spectra of Nd^{3+} doped amorphous $\text{Si}_3\text{B}_3\text{N}_7$ ceramic at different excitation and emission wavelengths are displayed in Figure 5.40. The sample mainly exhibited similar excitation and emission profiles as the undoped amorphous $\text{Si}_3\text{B}_3\text{N}_7$ matrix (see Figure 5.2) with a slight difference of having two distinguished broad weak emission peaks at 557 nm and 616 nm. These peaks were assigned to the emissions from $^4\text{G}_{5/2}$ and $^2\text{G}_{7/2}$ levels to $^4\text{I}_{9/2}$ ground state level and from $^2\text{H}_{11/2}$ level to $^4\text{I}_{9/2}$ ground state level, respectively. For clarity, in Figure 5.41, the emission spectra of undoped and Nd^{3+} doped amorphous $\text{Si}_3\text{B}_3\text{N}_7$ ceramics at 330 nm excitation wavelength are compared and $^2\text{K}_{13/2} \rightarrow ^4\text{I}_{9/2}$, $^4\text{G}_{5/2}$ and $^2\text{G}_{7/2} \rightarrow ^4\text{I}_{9/2}$, and $^2\text{H}_{11/2} \rightarrow ^4\text{I}_{9/2}$ transitions were presented. For the same reasons discussed in Section 5.1 for undoped amorphous $\text{Si}_3\text{B}_3\text{N}_7$ ceramic, red shifts were also observed for Nd^{3+} doped sample. On the other hand, Nd^{3+} doped amorphous $\text{Si}_3\text{B}_3\text{N}_7$ ceramics might show NIR luminescence. During relaxation, some of the excited Nd^{3+} can decay nonradiatively to the $^4\text{F}_{3/2}$ level, from which they can decay radiatively to the $^4\text{I}_{11/2}$ and the $^4\text{I}_{9/2}$ levels by emitting at around 890 nm and 1064 nm, respectively. Thus, further NIR investigations are required.

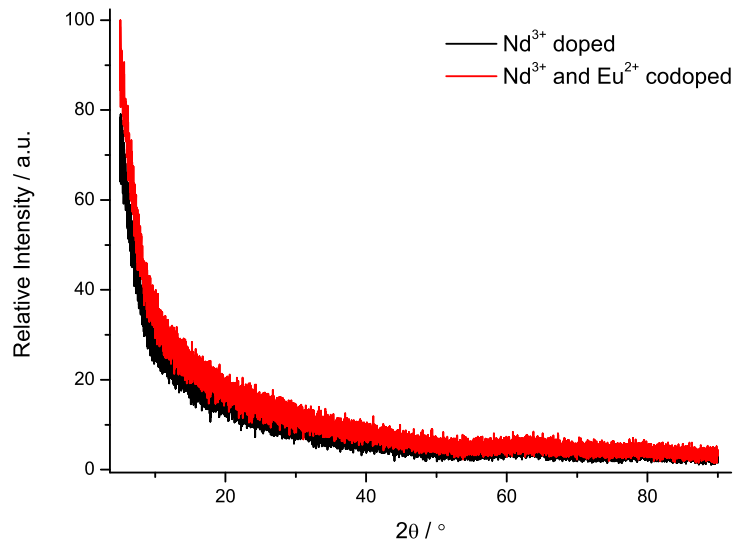


Figure 5.38.: Powder X-ray diffractograms of Nd^{3+} doped and $\text{Nd}^{3+}/\text{Eu}^{2+}$ codoped amorphous $\text{Si}_3\text{B}_3\text{N}_7$ ceramics.

5. Phosphors Based on Amorphous $\text{Si}_3\text{B}_3\text{N}_7$ Matrix

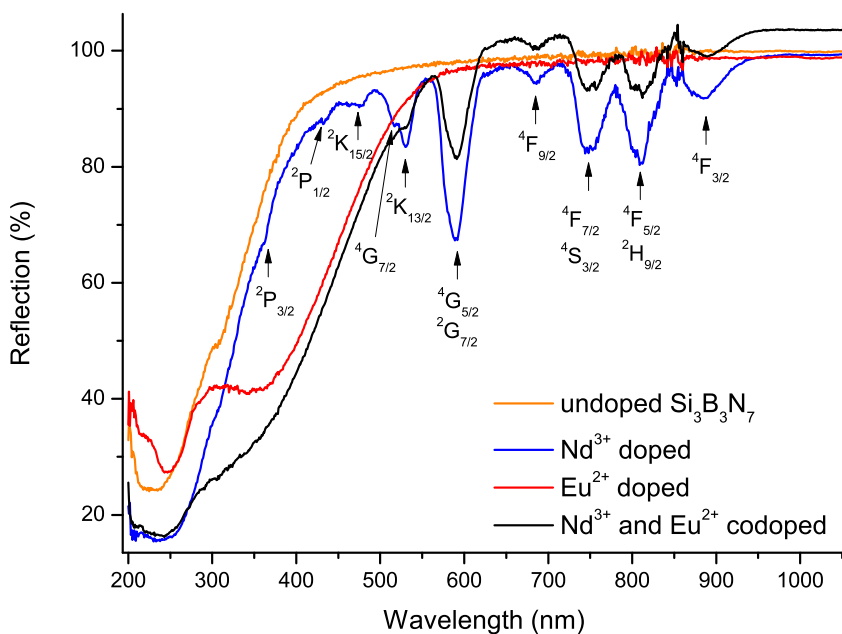


Figure 5.39.: Diffuse reflection spectra of undoped, Nd^{3+} doped, Eu^{2+} doped and $\text{Nd}^{3+}/\text{Eu}^{2+}$ codoped amorphous $\text{Si}_3\text{B}_3\text{N}_7$ ceramics.

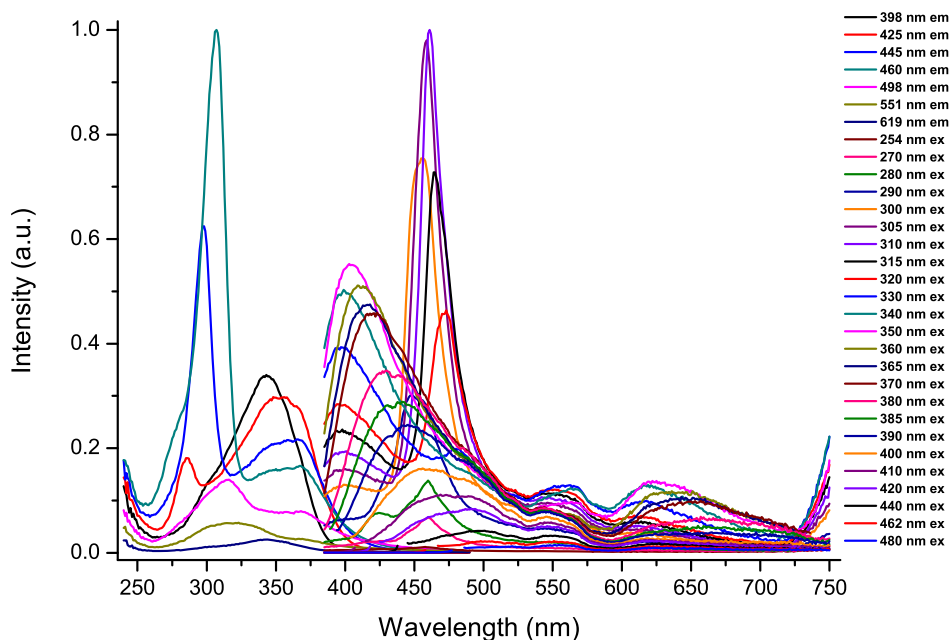


Figure 5.40.: Photoluminescence spectra of Nd^{3+} doped amorphous $\text{Si}_3\text{B}_3\text{N}_7$ ceramic at different excitation and emission wavelengths.

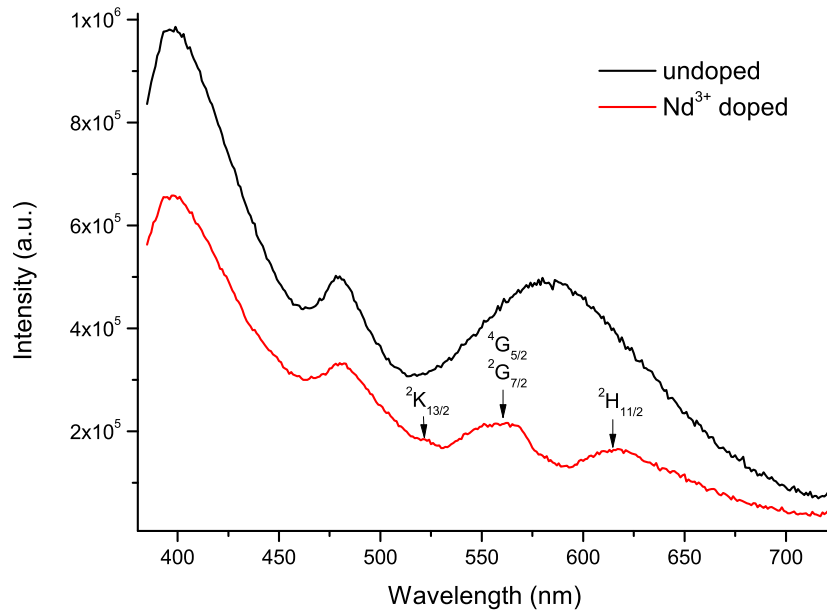


Figure 5.41.: Emission spectra of undoped and Nd^{3+} doped amorphous $\text{Si}_3\text{B}_3\text{N}_7$ ceramics at 330 nm excitation wavelength.

5.7. Nd/Eu Codoped Amorphous $\text{Si}_3\text{B}_3\text{N}_7$ Matrix

Amorphous X-ray pattern of $\text{Nd}^{3+}/\text{Eu}^{2+}$ codoped amorphous $\text{Si}_3\text{B}_3\text{N}_7$ ceramic is given in Figure 5.38. In the diffuse reflection spectrum (Figure 5.39), typical Nd^{3+} absorption bands were observed, proving the incorporation of Nd^{3+} ions into the matrix. On the other hand, as expected, codoping of Eu^{2+} ions together with Nd^{3+} into amorphous $\text{Si}_3\text{B}_3\text{N}_7$ matrix resulted in a shift in the reflection spectrum of the intrinsic strong drop due to the host matrix up to around 520 nm. Therefore, absorptions below 520 nm belonging to the Nd^{3+} were overlapped by the stronger absorption of the Eu^{2+} ions, resulting a light greenish yellow body color in the final ceramic.

Photoluminescence spectra of $\text{Nd}^{3+}/\text{Eu}^{2+}$ codoped amorphous $\text{Si}_3\text{B}_3\text{N}_7$ ceramic are given in Figure 5.43. The emission profile of $\text{Nd}^{3+}/\text{Eu}^{2+}$ codoped sample appears significantly different than Eu^{2+} doped one (see Figure 5.15). For $\text{Nd}^{3+}/\text{Eu}^{2+}$ codoped sample, broad emission band at 550 nm, which is typical for Eu^{2+} ions, contains two distinguished broad peaks due to Nd^{3+} ions at 564 nm and 613 nm and are assigned to the emissions due to ${}^4G_{5/2}$, ${}^2G_{7/2} \rightarrow {}^4I_{9/2}$ and ${}^2H_{11/2} \rightarrow {}^4I_{9/2}$ transitions, respectively (Figure 5.44). The peak appeared as a shoulder at 524 nm is assigned to the ${}^2K_{13/2} \rightarrow {}^4I_{9/2}$ transition.

As these corresponding emission bands appeared relatively weak in Nd^{3+} doped amorphous $\text{Si}_3\text{B}_3\text{N}_7$ ceramic (see also Figure 5.40), one could expect these peaks to overlap

5. Phosphors Based on Amorphous $\text{Si}_3\text{B}_3\text{N}_7$ Matrix

with the strong and broad Eu^{2+} emission band. However, these weak emission bands were not overlapped by the strong and broad Eu^{2+} emission band and are observed for all excitation wavelengths; this behaviour was ascribed to an efficient energy transfer from Eu^{2+} ions to Nd^{3+} ions. An energy transfer mechanism is proposed with an energy level diagram shown in Figure 5.42.

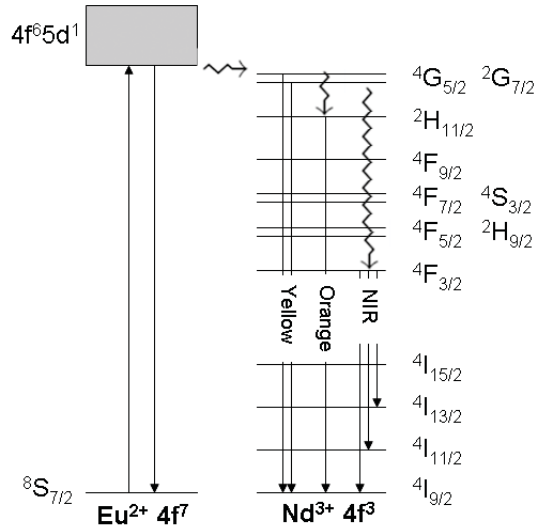


Figure 5.42.: Energy transfer mechanism from Eu^{2+} ions to Nd^{3+} ions in $\text{Nd}^{3+}/\text{Eu}^{2+}$ codoped amorphous $\text{Si}_3\text{B}_3\text{N}_7$ ceramic.

Excitations of Nd^{3+} ions were believed to occur mainly via energy transfer from the $4\text{f}^65\text{d}^1$ level of Eu^{2+} ions to the $2\text{G}_{7/2}$ level of Nd^{3+} ions, which are expected to have almost the same energy. After excitation of the $4\text{f}^65\text{d}^1$ state of Eu^{2+} ions, some of the electrons could relax radiatively to the 4f^7 ground state of Eu^{2+} ions, which produced the broad emission band at around 550 nm, while the other electrons were transferred to the $2\text{G}_{7/2}$ level of Nd^{3+} ions. Then, some of the electrons in the $2\text{G}_{7/2}$ level of Nd^{3+} ions would decay radiatively to the $4\text{I}_{9/2}$ ground state level of Nd^{3+} ions by emitting at 564 nm. The other electrons in the $2\text{G}_{7/2}$ level could then relax nonradiatively to the $2\text{H}_{11/2}$ from which they could decay radiatively to the $4\text{I}_{9/2}$ ground state level of Nd^{3+} ions by emitting at 613 nm. In addition, some nonradiative relaxation from $2\text{G}_{7/2}$ level to the $4\text{F}_{3/2}$ level, from which NIR emissions can occur, is possible and thus this phenomenon needs to be further analyzed. Furthermore, the excitation band at 305 nm (measured at emission maximum value of 460 nm) and the less intense blue emission peaks in Figure 5.40 result from the intrinsic emission of $\text{Si}_3\text{B}_3\text{N}_7$ host matrix. Even though the Red-Edge Effect was observable for the broad emission band due to the Eu^{2+} ions in $\text{Nd}^{3+}/\text{Eu}^{2+}$ codoped samples, the $4\text{f} \rightarrow 4\text{f}$ emission bands belonging to Nd^{3+} ions appeared to have no significant red shift. This implies that excited states of the Nd^{3+} ions were not affected significantly by the local environment of the amorphous $\text{Si}_3\text{B}_3\text{N}_7$ host matrix. This was expected as it is well known that the 4f shell in lanthanides are better shielded than the

5d shell; hence, $4f \rightarrow 4f$ transitions are not significantly affected by the local environment as compared to $5d \rightarrow 4f$ transitions.

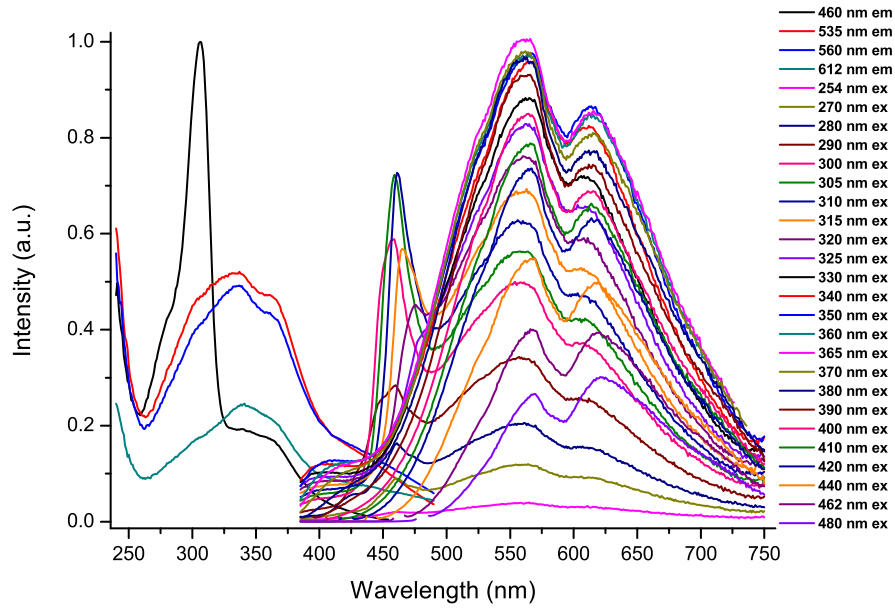


Figure 5.43.: Photoluminescence spectra of Nd³⁺/Eu²⁺ codoped amorphous Si₃B₃N₇ ceramic at different excitation and emission wavelengths.

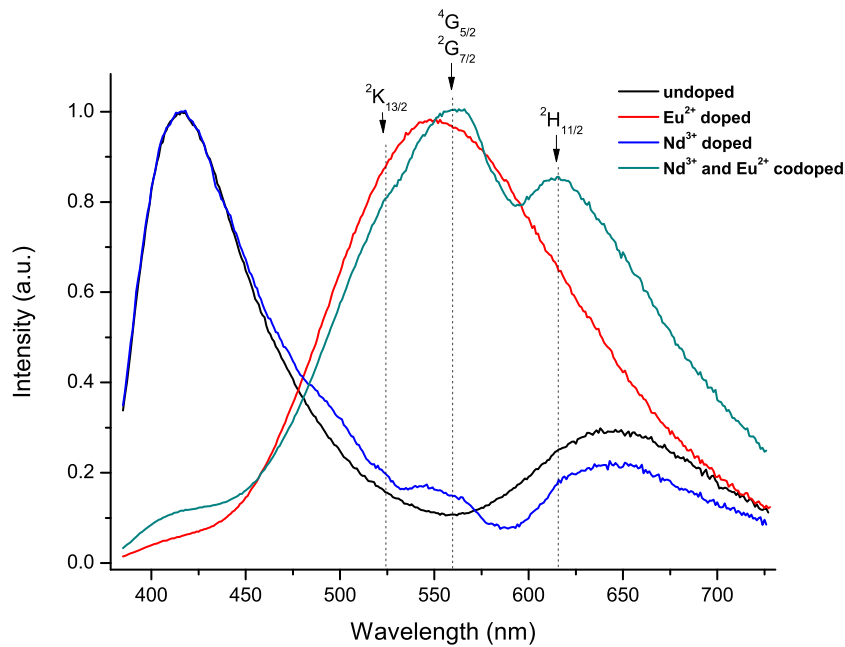


Figure 5.44.: Emission spectra of undoped, Eu²⁺ doped, Nd³⁺ doped and Nd³⁺/Eu²⁺ codoped amorphous Si₃B₃N₇ ceramics measured at 365 nm excitation wavelength.

5.8. Sm Doped Amorphous $\text{Si}_3\text{B}_3\text{N}_7$ Matrix

Sm^{2+} ($4f^6$) and Sm^{3+} ($4f^5$) are both luminescent ions and characteristic emissions can be seen in the red part of the visible spectrum, between 550 and 750 nm [192, 332]. As the 4f energy levels of both divalent and trivalent Sm ions are well known, 4f \rightarrow 4f emission lines for these ions can be easily discriminated. Energy level diagrams for both Sm^{2+} and Sm^{3+} are given in Figure 5.45. Sm^{2+} ions, which are isoelectronic with Eu^{3+} ions, usually have a $4f^55d^1$ level above its 4f levels and this results in line emissions rather than band emission from the $^5\text{D}_0$ level to $^7\text{F}_0$, $^7\text{F}_1$ and $^7\text{F}_2$ levels at around 680 nm, 700 nm and 725 nm, respectively [333, 334]. On the other hand, Sm^{3+} ions show line emissions from $^4\text{G}_{5/2}$ level to $^6\text{H}_{5/2}$, $^6\text{H}_{7/2}$, $^6\text{H}_{9/2}$ and $^6\text{H}_{11/2}$ levels at around 565 nm, 600 nm, 650 nm and 710 nm, respectively [335]. In the present work, photoluminescence and diffuse reflection spectra of Sm doped amorphous $\text{Si}_3\text{B}_3\text{N}_7$ ceramics have revealed that a significant amount of the incorporated Sm ions were in trivalent states.

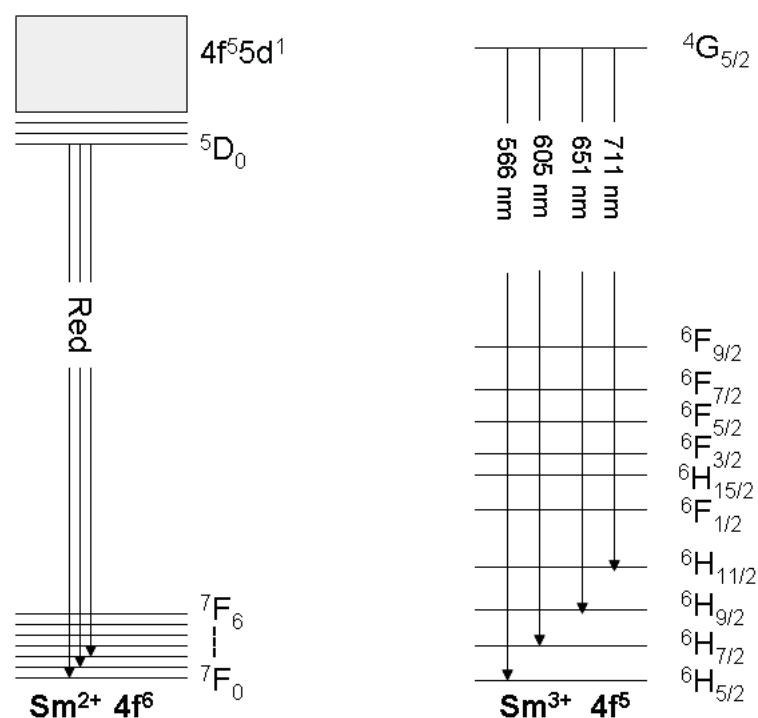


Figure 5.45.: Representation of energy level diagrams of Sm^{2+} and Sm^{3+} ions (for reasons of clarity not all levels have been shown).

Amorphous properties of Sm^{3+} doped and $\text{Sm}^{3+}/\text{Eu}^{2+}$ codoped $\text{Si}_3\text{B}_3\text{N}_7$ ceramics were investigated by powder X-ray diffractometry, as shown in Figure 5.46. The diffuse reflection spectra of undoped and Sm^{3+} doped samples were compared in Figure 5.47. The strong absorption at around 230 nm due to the $\text{Si}_3\text{B}_3\text{N}_7$ host matrix was shifted about 50 nm towards longer wavelengths. In addition, characteristic 4f \rightarrow 4f transitions of Sm^{3+} were observed. All absorption bands in the visible and near-IR regions in the diffuse re-

flexion spectrum can be assigned to the transition from the ground level $^6\text{H}_{5/2}$ to higher energy levels of Sm^{3+} ions, which are well consistent with the literature data [335]. These transitions are from the $^6\text{H}_{5/2}$ ground state level to the $^6\text{P}_{3/2}$ level at 410 nm, to $^6\text{F}_{9/2}$ level at 1070 nm, to $^6\text{F}_{7/2}$ level at 1210 nm, to $^6\text{F}_{5/2}$, $^6\text{F}_{3/2}$ and $^6\text{H}_{11/2}$ levels between 1340 nm and 1450 nm, and to $^6\text{F}_{1/2}$ level at 1600 nm.

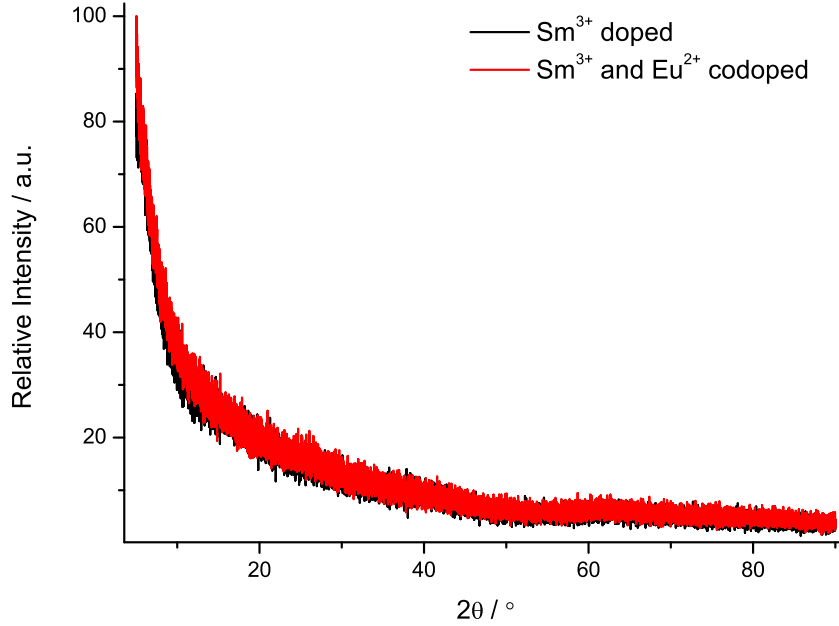


Figure 5.46.: Powder X-ray diffractograms of Sm^{3+} doped and $\text{Sm}^{3+}/\text{Eu}^{2+}$ codoped amorphous $\text{Si}_3\text{B}_3\text{N}_7$ ceramics.

Figure 5.48 shows the photoluminescence properties of Sm^{3+} doped amorphous $\text{Si}_3\text{B}_3\text{N}_7$ ceramic. The spectra clearly indicates that almost all Sm ions are trivalent due to obtaining typical Sm^{3+} emissions at 567 nm, 605 nm, 651 nm and 711 nm. No emissions due to Sm^{2+} ions were obtained. The first three emissions of Sm^{3+} ions are clearly observed in Figure 5.48 but the emission at 711 nm is barely visible. This might be due to a low concentration of Sm^{3+} ions within the amorphous $\text{Si}_3\text{B}_3\text{N}_7$ host matrix, which could be concluded by observing the typical intrinsic emission profile of the undoped amorphous $\text{Si}_3\text{B}_3\text{N}_7$ host matrix together with the characteristic Sm^{3+} emission lines. Even though the Red-Edge Effect were easily observed in the emission spectra from the bands which were assigned to amorphous $\text{Si}_3\text{B}_3\text{N}_7$ host matrix, no any red shift was detected for the $4f \rightarrow 4f$ emission lines which were assigned to Sm^{3+} ions. This is due to the stronger shielding of 4f shell such that $4f \rightarrow 4f$ transitions are not significantly affected by the local environment in the amorphous $\text{Si}_3\text{B}_3\text{N}_7$ host matrix, as in Nd^{3+} doped sample.

5. Phosphors Based on Amorphous $\text{Si}_3\text{B}_3\text{N}_7$ Matrix

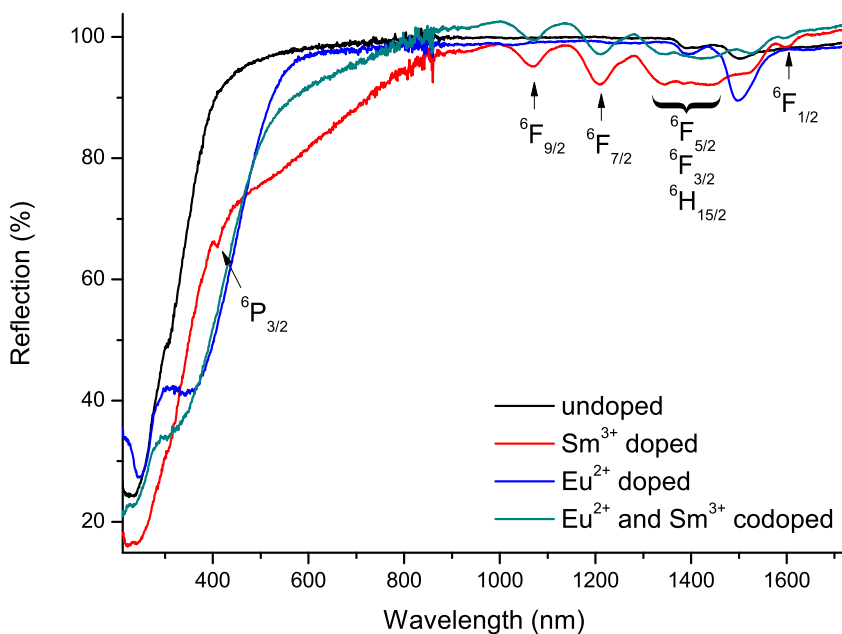


Figure 5.47.: Diffuse reflection spectra of undoped, Sm^{3+} doped, Eu^{2+} doped and $\text{Sm}^{3+}/\text{Eu}^{2+}$ codoped amorphous $\text{Si}_3\text{B}_3\text{N}_7$ ceramics.

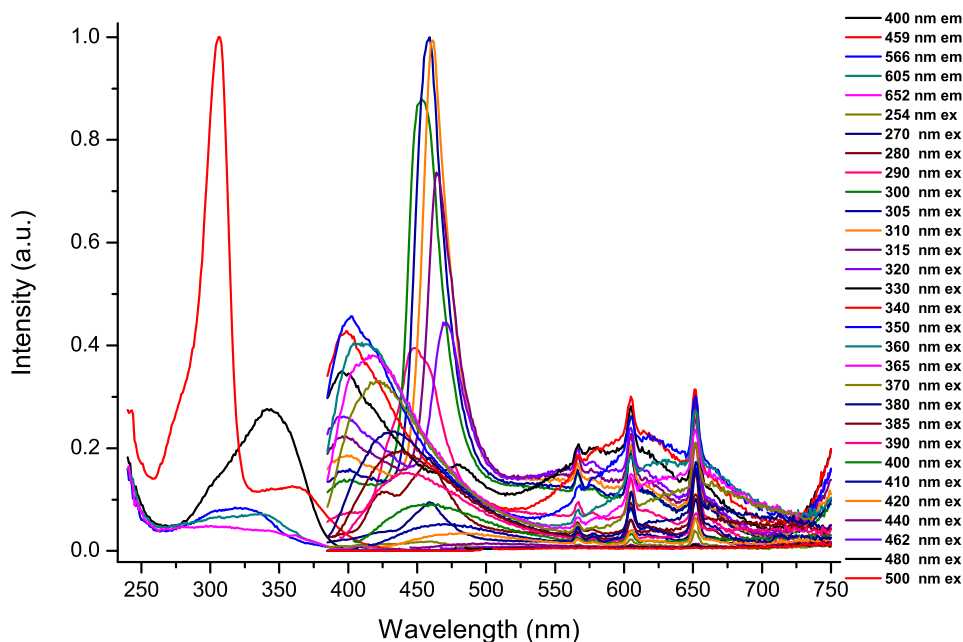


Figure 5.48.: Photoluminescence spectra of Sm^{3+} doped amorphous $\text{Si}_3\text{B}_3\text{N}_7$ ceramic at different excitation and emission wavelengths.

Similar to trivalent Eu and Yb ions, trivalent Sm ions have been found in literature to be reduced fully or partially to Sm²⁺ in the presence of nitrogen during synthesis [332]. However, in the case of Sm doped amorphous Si₃B₃N₇ ceramics, there is no evidence in the emission spectrum for such a reduction. Excitation spectra of Sm doped amorphous Si₃B₃N₇ ceramic exhibited typical excitation behavior of undoped amorphous Si₃B₃N₇ matrix, which was consistent with the emission spectra. Additionally, a broad excitation peak for Sm³⁺ was observed at 320 nm, which was measured at a maximum emission wavelength of 605 nm.

5.9. Sm/Eu Codoped Amorphous Si₃B₃N₇ Matrix

Powder X-ray pattern of Sm³⁺/Eu²⁺ codoped amorphous Si₃B₃N₇ ceramic is given in Figure 5.46. In the reflection spectrum (Figure 5.47), typical Sm³⁺ absorption bands were observed, proving the incorporation of Sm³⁺ ions into the Si₃B₃N₇ matrix. On the other hand, as expected, codoping of Eu²⁺ ions together with Sm³⁺ ions into Si₃B₃N₇ matrix resulted in a shift of the intrinsic strong drop due to the absorption of the host matrix between 250-400 nm in the reflection spectrum to around 520 nm. Therefore, ⁶H_{5/2} → ⁶P_{3/2} absorption of Sm³⁺ ions below 520 nm was overlapped by the stronger absorption of Eu²⁺ ions and is not visible in the reflection spectrum.

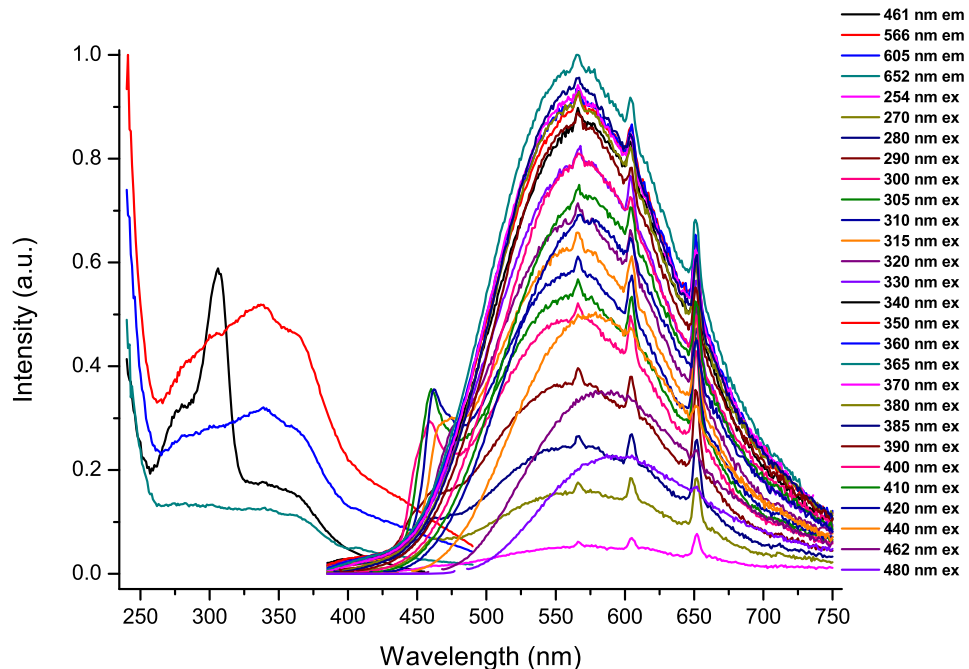


Figure 5.49.: Photoluminescence spectra of Sm³⁺/Eu²⁺ codoped amorphous Si₃B₃N₇ ceramic at different excitation and emission wavelengths.

5. Phosphors Based on Amorphous $\text{Si}_3\text{B}_3\text{N}_7$ Matrix

Photoluminescence spectra of $\text{Sm}^{3+}/\text{Eu}^{2+}$ codoped amorphous $\text{Si}_3\text{B}_3\text{N}_7$ ceramic are depicted in Figure 5.49. It is clearly seen that the emission profile of $\text{Sm}^{3+}/\text{Eu}^{2+}$ codoped sample were significantly different from that of Eu^{2+} doped sample (see Figure 5.15). For $\text{Sm}^{3+}/\text{Eu}^{2+}$ codoped sample, a broad emission band at 566 nm, which is typical for Eu^{2+} ions, also has three additional emission lines at 566 nm, 605 nm and 651 nm, which were assigned to the emissions of Sm^{3+} ions from the $^4\text{G}_{5/2}$ level to the $^6\text{H}_{5/2}$, $^6\text{H}_{7/2}$ and $^6\text{H}_{9/2}$ levels, respectively (see Figure 5.50). As these corresponding peaks are relatively weak in Sm^{3+} doped amorphous $\text{Si}_3\text{B}_3\text{N}_7$ ceramic compared to the intrinsic emissions of undoped sample (see Figure 5.48), one could expect that these peaks were overlapped by the strong and broad Eu^{2+} emission band. However, these peaks were observed for all excitation wavelengths, which could be explained by an efficient energy transfer from Eu^{2+} ions to Sm^{3+} ions, as also observed in $\text{Nd}^{3+}/\text{Eu}^{2+}$ codoped sample.

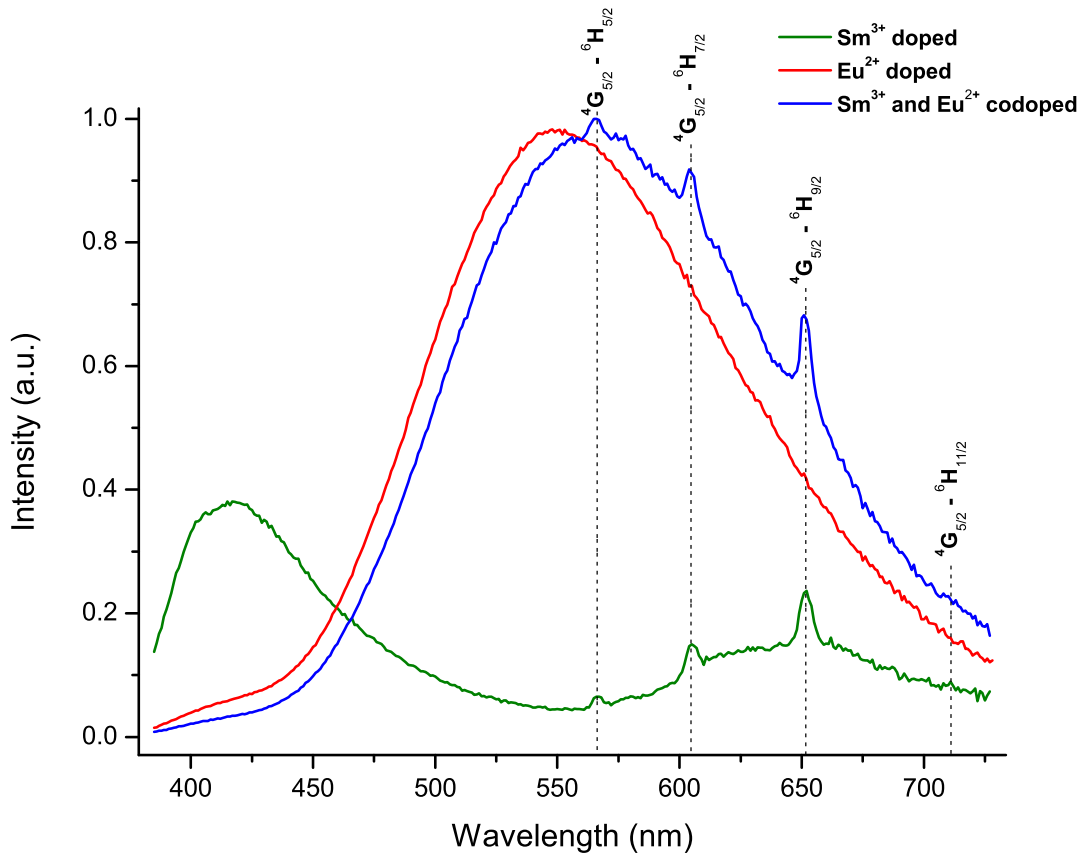


Figure 5.50.: Emission spectra of Eu^{2+} doped, Sm^{3+} doped and $\text{Sm}^{3+}/\text{Eu}^{2+}$ codoped amorphous $\text{Si}_3\text{B}_3\text{N}_7$ ceramics measured at 365 nm excitation wavelength.

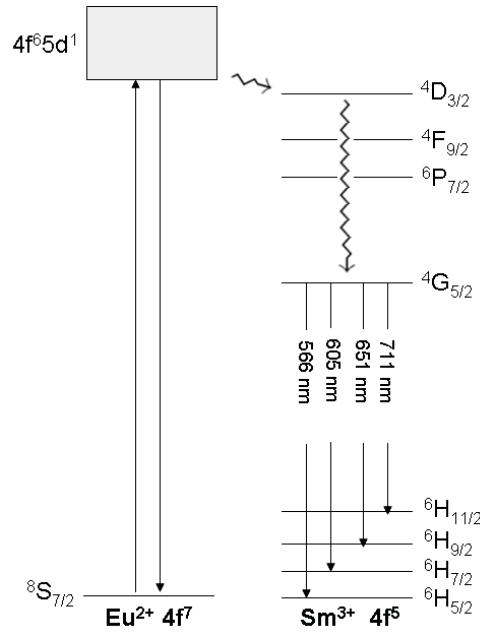


Figure 5.51.: Energy transfer mechanism from Eu^{2+} ions to Sm^{3+} ions in $\text{Sm}^{3+}/\text{Eu}^{2+}$ codoped amorphous $\text{Si}_3\text{B}_3\text{N}_7$ ceramic.

A proposed energy transfer mechanism from Eu^{2+} ions to Sm^{3+} ions is shown in Figure 5.51. Excitation of Sm^{3+} ions are suggested to occur mainly via energy transfer from the $4\text{f}^65\text{d}^1$ level of Eu^{2+} ions to the $4\text{D}_{3/2}$ level of Sm^{3+} ions, which are expected to have almost the same energy. After excitation of the $4\text{f}^65\text{d}^1$ state of Eu^{2+} ions, some of the electrons may relax radiatively to the 4f^7 ground state of Eu^{2+} ions, which results in a broad emission band at around 560 nm, while the other electrons are transferred to the $4\text{D}_{3/2}$ level of Sm^{3+} ions. Then, these electrons in the $4\text{D}_{3/2}$ level of Sm^{3+} decay nonradiatively to the $4\text{G}_{5/2}$ level, from which they can decay radiatively to the $6\text{H}_{5/2}$, $6\text{H}_{7/2}$ and $6\text{H}_{9/2}$ levels at 566 nm, 605 nm and 651 nm, respectively (see Figure 5.50). In addition to these emissions, $4\text{G}_{5/2} \rightarrow 6\text{H}_{11/2}$ emission is also expected to occur at 710 nm but is barely visible in the spectra. Even though the Red-Edge Effect was observed for the broad emission band due to the Eu^{2+} ions in $\text{Sm}^{3+}/\text{Eu}^{2+}$ codoped sample, the $4\text{f} \rightarrow 4\text{f}$ emissions of Sm^{3+} ions show no red shift due to the strong shielding of 4f shell.

5.10. Gd Doped Amorphous $\text{Si}_3\text{B}_3\text{N}_7$ Matrix

Gd^{3+} ions have a very stable $8\text{S}_{7/2}$ ground state due to a half-filled 4f shell. The excited energy levels of Gd^{3+} ions appear at energies higher than 32000 cm^{-1} (312 nm) (Figure 5.52). Therefore, Gd^{3+} ions have emissions only in the ultraviolet region and can sensitize the luminescence of the other rare earth ions. Among the rare earth ions, Gd^{3+} ions have the highest energy level between the ground and excited states, so that they have no quenching effect on the other rare earth ions. This property make them a very good

5. Phosphors Based on Amorphous $\text{Si}_3\text{B}_3\text{N}_7$ Matrix

candidate as constituent cations, even better than Y^{3+} , in host materials substituted by luminescent rare earth ions.

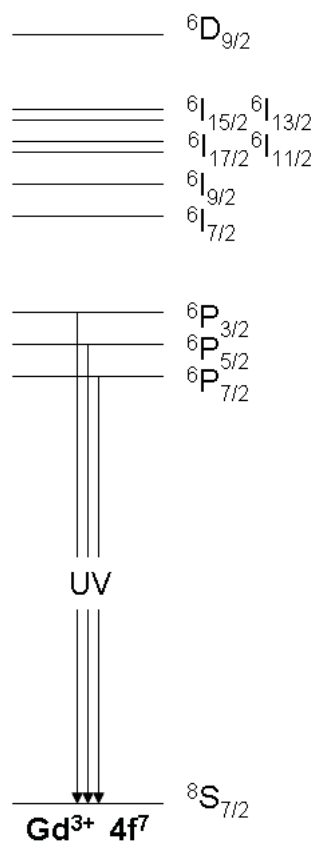


Figure 5.52.: Representation of energy level diagram of Gd^{3+} ions (for reasons of clarity not all levels have been shown).

Gd^{3+} ions were incorporated into the amorphous $\text{Si}_3\text{B}_3\text{N}_7$ matrix by applying the organometallic route. Figure 5.53 shows the powder X-ray diffractogram for Gd^{3+} doped amorphous $\text{Si}_3\text{B}_3\text{N}_7$ ceramic. Figure 5.54 presents the diffuse reflection spectra of Gd^{3+} doped amorphous $\text{Si}_3\text{B}_3\text{N}_7$ ceramic compared to undoped, Eu^{2+} doped, and $\text{Gd}^{3+}/\text{Eu}^{2+}$ codoped samples. Since both Gd^{3+} ions and amorphous $\text{Si}_3\text{B}_3\text{N}_7$ host matrix have absorptions in the UV region, no absorption bands could be distinguished specifically for Gd^{3+} ions. Furthermore, Gd^{3+} doped amorphous $\text{Si}_3\text{B}_3\text{N}_7$ ceramic resulted in the same reflection profile with the undoped amorphous $\text{Si}_3\text{B}_3\text{N}_7$ ceramic. Typical photoluminescence properties of Gd^{3+} doped amorphous $\text{Si}_3\text{B}_3\text{N}_7$ ceramic were shown in Figure 5.55. It is clear that the Gd^{3+} doped sample exhibits the same excitation and emission behavior as the undoped $\text{Si}_3\text{B}_3\text{N}_7$ host matrix. Therefore, it is inferred that the same discussions for the photoluminescence properties of the undoped amorphous $\text{Si}_3\text{B}_3\text{N}_7$ ceramic are valid for Gd^{3+} doped sample (see Section 5.2). Attempts to obtain emissions from Gd^{3+} ions in the UV region of the spectrum have thus far failed. This is most probably due to a simultaneous absorption of any UV light emitted by Gd^{3+} ions the $\text{Si}_3\text{B}_3\text{N}_7$ matrix.

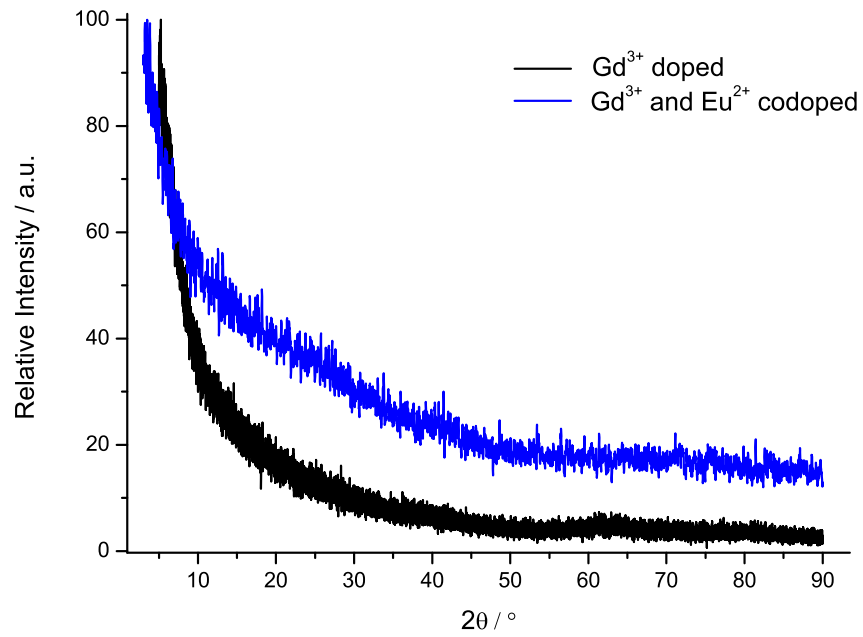


Figure 5.53.: Powder X-ray diffractograms of Gd^{3+} doped, and $\text{Gd}^{3+}/\text{Eu}^{2+}$ codoped amorphous $\text{Si}_3\text{B}_3\text{N}_7$ ceramics.

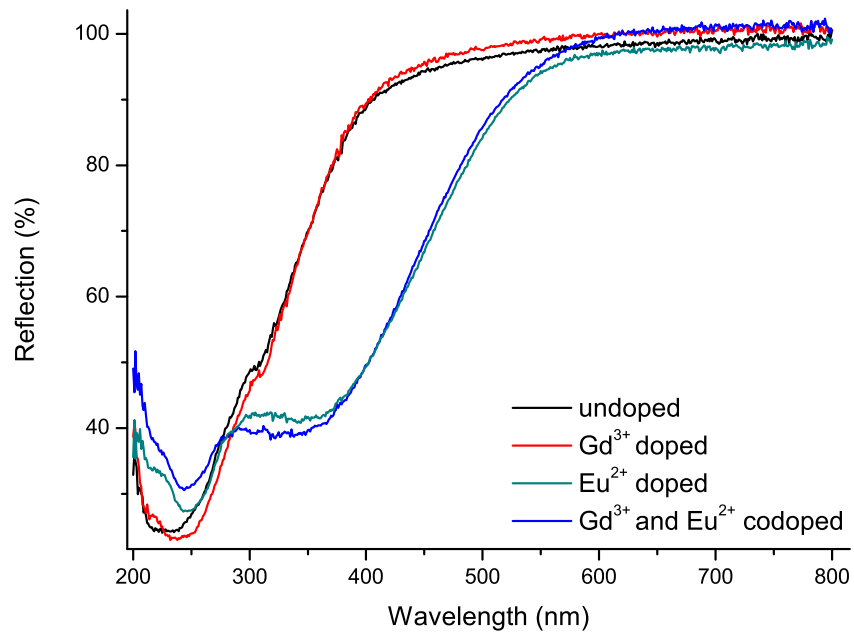


Figure 5.54.: Diffuse reflection spectra of undoped, Gd^{3+} doped, Eu^{2+} doped and $\text{Gd}^{3+}/\text{Eu}^{2+}$ codoped $\text{Si}_3\text{B}_3\text{N}_7$ ceramics.

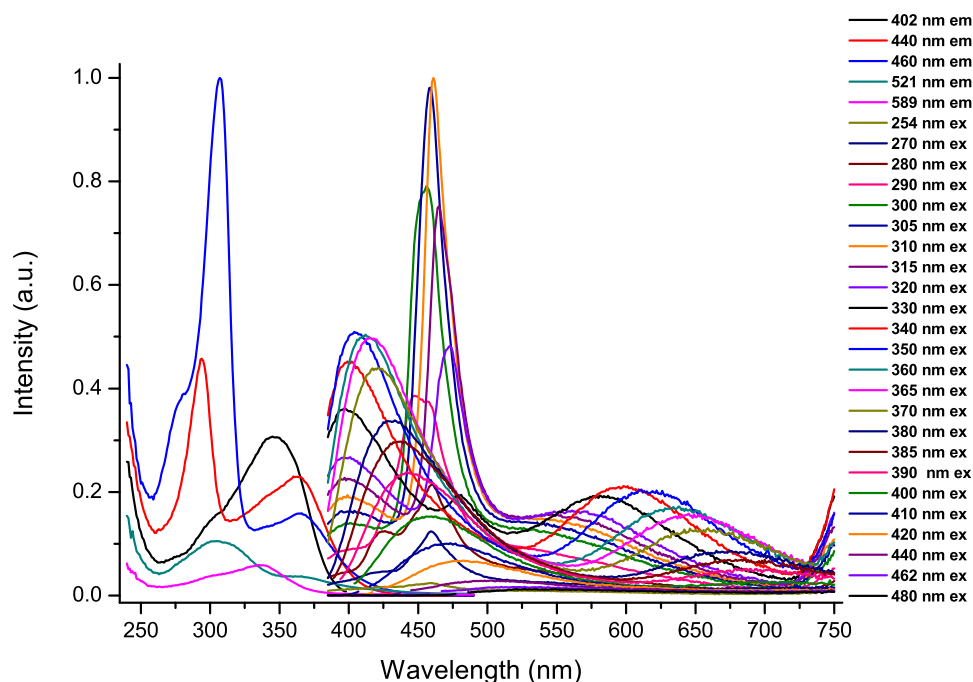


Figure 5.55.: Photoluminescence spectra of Gd^{3+} doped amorphous $\text{Si}_3\text{B}_3\text{N}_7$ ceramic at different excitation and emission wavelengths.

5.11. Gd/Eu Codoped Amorphous $\text{Si}_3\text{B}_3\text{N}_7$ Matrix

Powder X-ray pattern of $\text{Gd}^{3+}/\text{Eu}^{2+}$ codoped amorphous $\text{Si}_3\text{B}_3\text{N}_7$ ceramic is given in Figure 5.53. As discussed in Section 5.10, both Gd^{3+} ions and amorphous $\text{Si}_3\text{B}_3\text{N}_7$ host matrix have strong absorption properties in the UV region, and thus no absorption band belonging to Gd^{3+} ions can be distinguished in excitation and diffuse reflection spectra. Furthermore, Gd^{3+} ions have emission in the UV region only around 312 nm, which is most probably absorbed simultaneously by the amorphous $\text{Si}_3\text{B}_3\text{N}_7$ host matrix so that no emission has been observed for Gd^{3+} ions in the amorphous $\text{Si}_3\text{B}_3\text{N}_7$ host matrix. The same behavior is also expected and observed for $\text{Gd}^{3+}/\text{Eu}^{2+}$ codoped amorphous $\text{Si}_3\text{B}_3\text{N}_7$ ceramics. As given in the diffuse reflection spectrum in Figure 5.54, the same absorption profile with the Eu^{2+} doped sample has been obtained for $\text{Gd}^{3+}/\text{Eu}^{2+}$ codoped samples. Furthermore, photoluminescence spectra of $\text{Gd}^{3+}/\text{Eu}^{2+}$ codoped amorphous $\text{Si}_3\text{B}_3\text{N}_7$ ceramic are shown in Figure 5.56. Clearly, the same emission profile with Eu^{2+} doped sample (see Figure 5.15) has been obtained for the $\text{Gd}^{3+}/\text{Eu}^{2+}$ codoped sample. Therefore, the same discussions for the photoluminescence properties of Eu^{2+} doped amorphous $\text{Si}_3\text{B}_3\text{N}_7$ ceramic are valid for $\text{Gd}^{3+}/\text{Eu}^{2+}$ codoped samples (see Section 5.2).

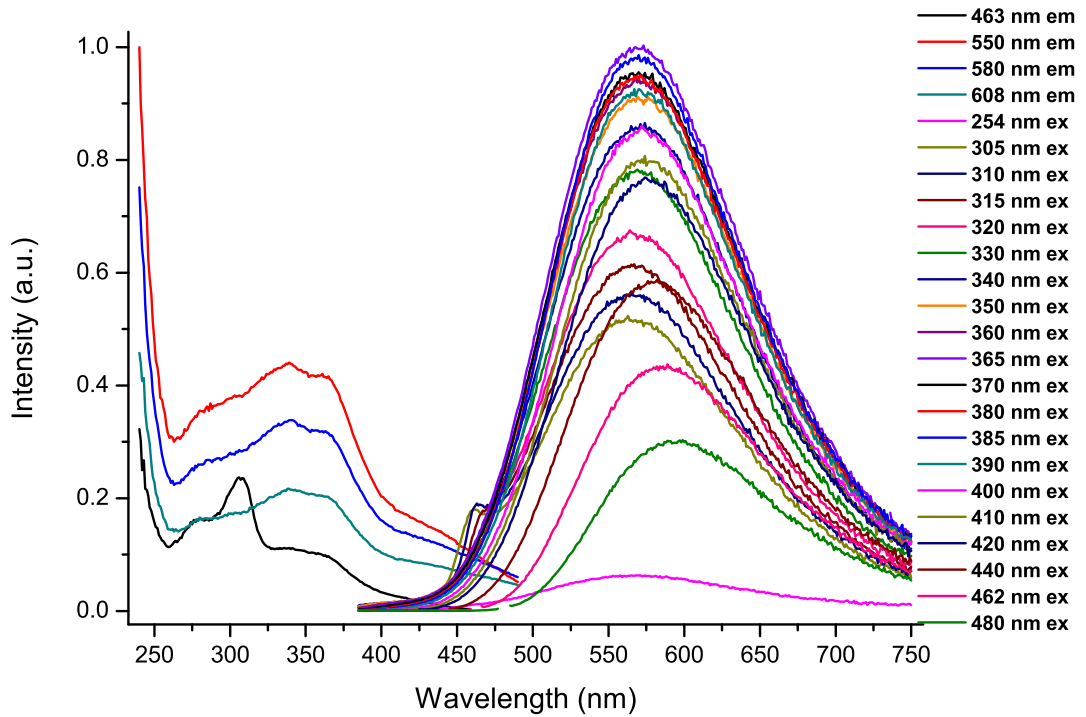


Figure 5.56.: Photoluminescence spectra of $\text{Gd}^{3+}/\text{Eu}^{2+}$ codoped amorphous $\text{Si}_3\text{B}_3\text{N}_7$ ceramic at different excitation and emission wavelengths.

5.12. Tb Doped Amorphous $\text{Si}_3\text{B}_3\text{N}_7$ Matrix

Various amounts of Tb^{3+} ions have been incorporated into amorphous $\text{Si}_3\text{B}_3\text{N}_7$ matrices by applying the organometallic route. Figure 5.57 includes powder X-ray diffractograms for Tb^{3+} doped samples. Photoluminescence properties of Tb^{3+} doped samples are given in Figure 5.60. Typical emissions of Tb^{3+} ions are shown in the energy level diagram in Figure 5.58. Violet emissions are obtained by transitions from $^5\text{D}_3$ to $^7\text{F}_6$ and $^7\text{F}_5$ levels. Blue emissions are obtained by transitions from $^5\text{D}_3$ to $^7\text{F}_4$, $^7\text{F}_3$, $^7\text{F}_2$, $^7\text{F}_1$ and $^7\text{F}_0$ together with a $^5\text{D}_4 \rightarrow ^7\text{F}_6$ transition. The $^5\text{D}_4 \rightarrow ^7\text{F}_5$ transition results in a very intense green emission. On the other hand, $^5\text{D}_4 \rightarrow ^7\text{F}_4$ and $^5\text{D}_4 \rightarrow ^7\text{F}_3$ transitions result in yellow and red emissions, respectively. In general, cross-relaxation occurs when excitation from the $^7\text{F}_6$ to $^7\text{F}_0$ level of Tb^{3+} ion promotes the non-radiative drain from the $^5\text{D}_3$ to the $^5\text{D}_4$ level of a neighboring Tb^{3+} ion and the probability of this process is strongly dependent on the distance between the two neighboring ions [336].

5. Phosphors Based on Amorphous $\text{Si}_3\text{B}_3\text{N}_7$ Matrix

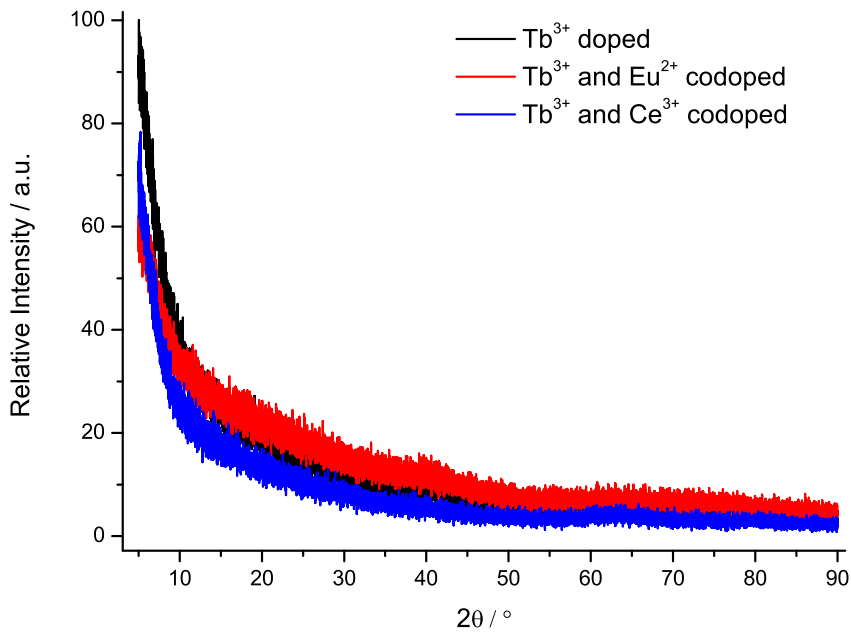


Figure 5.57.: Powder X-ray diffractograms of Tb^{3+} doped, $\text{Tb}^{3+}/\text{Eu}^{2+}$ codoped and $\text{Tb}^{3+}/\text{Ce}^{3+}$ codoped amorphous $\text{Si}_3\text{B}_3\text{N}_7$ ceramics.

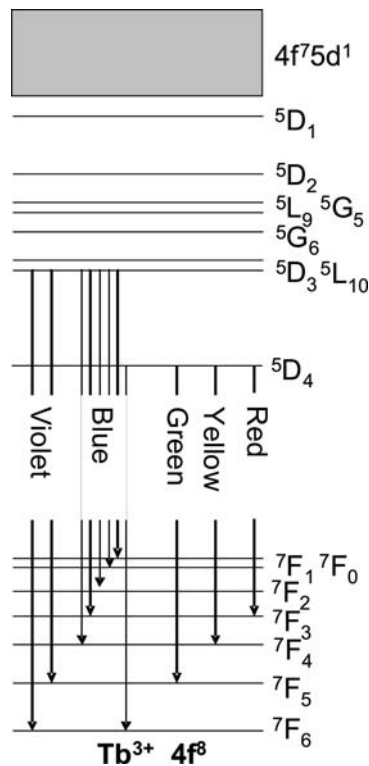


Figure 5.58.: Representation of energy level diagram of Tb^{3+} ions (for reasons of clarity not all levels have been shown).

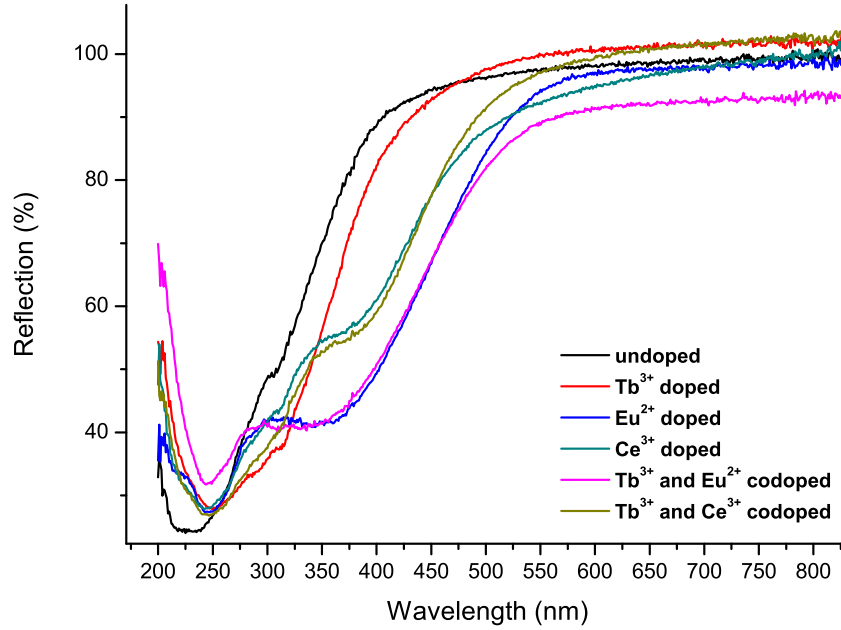


Figure 5.59.: Diffuse reflection spectra of undoped, Tb^{3+} doped, Eu^{2+} doped, Ce^{3+} doped, $\text{Tb}^{3+}/\text{Eu}^{2+}$ codoped and $\text{Tb}^{3+}/\text{Ce}^{3+}$ codoped amorphous $\text{Si}_3\text{B}_3\text{N}_7$ ceramics.

As seen from Figure 5.60, Tb^{3+} doped amorphous $\text{Si}_3\text{B}_3\text{N}_7$ ceramic exhibited strong green emission due to a $^5\text{D}_4 \rightarrow ^7\text{F}_5$ transition, whereas blue emissions from the $^5\text{D}_3$ level were not well distinguished. The invisibility of the blue emissions from the $^5\text{D}_3$ level of Tb^{3+} can be attributed to quenching via the well-known cross-relaxation between the Tb^{3+} ions or to the signal being masked by the intrinsic blue emission of the undoped amorphous $\text{Si}_3\text{B}_3\text{N}_7$ host matrix. Excitation spectrum measured with an emission maximum at 544 nm showed a half peak which had a peak maximum at around 250 nm, which is the minimum measurement limit. This can be confirmed by the diffuse reflection spectra in Figure 5.59, which depicts a strong absorption between 254 nm and 320 nm. Therefore, very intense green Tb^{3+} emissions were obtained by exciting with shorter wavelengths, e.g. between 254 nm and 290 nm. In emission spectra, this green emission peak at 544 nm was observed when the sample was excited with any light up to 430 nm. In addition, excitation between 290 nm and 330 nm resulted in the intrinsic blue emission of the $\text{Si}_3\text{B}_3\text{N}_7$ host matrix as strong as the green emission. Therefore, excitation especially at around 310 nm resulted in a very intense white light due to the combination of the intrinsic blue emission of the $\text{Si}_3\text{B}_3\text{N}_7$ host matrix at 460 nm and typical Tb^{3+} green emission at 544 nm, orange emission at 591 nm and red emission at 623 nm in almost equal ratios (Figure 5.62 and Figure 5.61). On the other hand, exciting the samples the light between 330 nm to 350 nm significantly decreased the green emission and

5. Phosphors Based on Amorphous $\text{Si}_3\text{B}_3\text{N}_7$ Matrix

the intrinsic violet emission of $\text{Si}_3\text{B}_3\text{N}_7$ host matrix became dominant. Even though the Red-Edge Effect were easily observed in the emission spectra from the bands assigned to the amorphous $\text{Si}_3\text{B}_3\text{N}_7$ host matrix, no red shift was detected for the $4f \rightarrow 4f$ emission bands assigned to Tb^{3+} ions. This is again due to the strong shielding of $4f$ shell such that $4f \rightarrow 4f$ transitions are not affected by the local environment of the amorphous $\text{Si}_3\text{B}_3\text{N}_7$ host matrix.

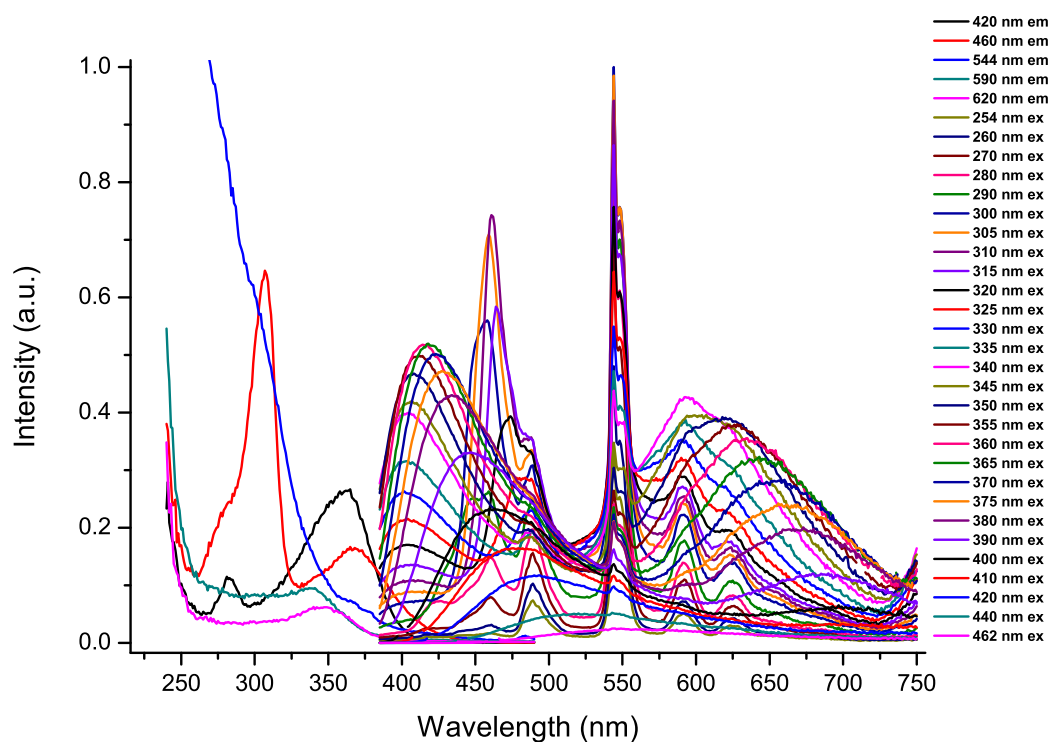


Figure 5.60.: Photoluminescence spectra of Tb^{3+} doped amorphous $\text{Si}_3\text{B}_3\text{N}_7$ ceramic at different excitation and emission wavelengths.

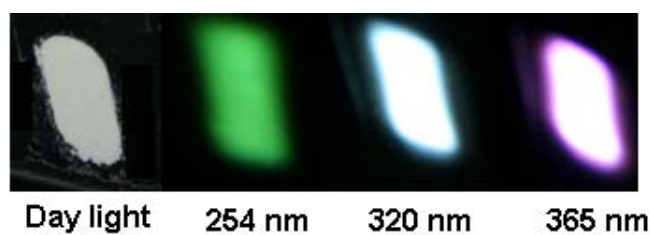


Figure 5.61.: Photos of Tb^{3+} doped amorphous $\text{Si}_3\text{B}_3\text{N}_7$ ceramic under day light and under 254 nm, 320 nm and 365 nm lights.

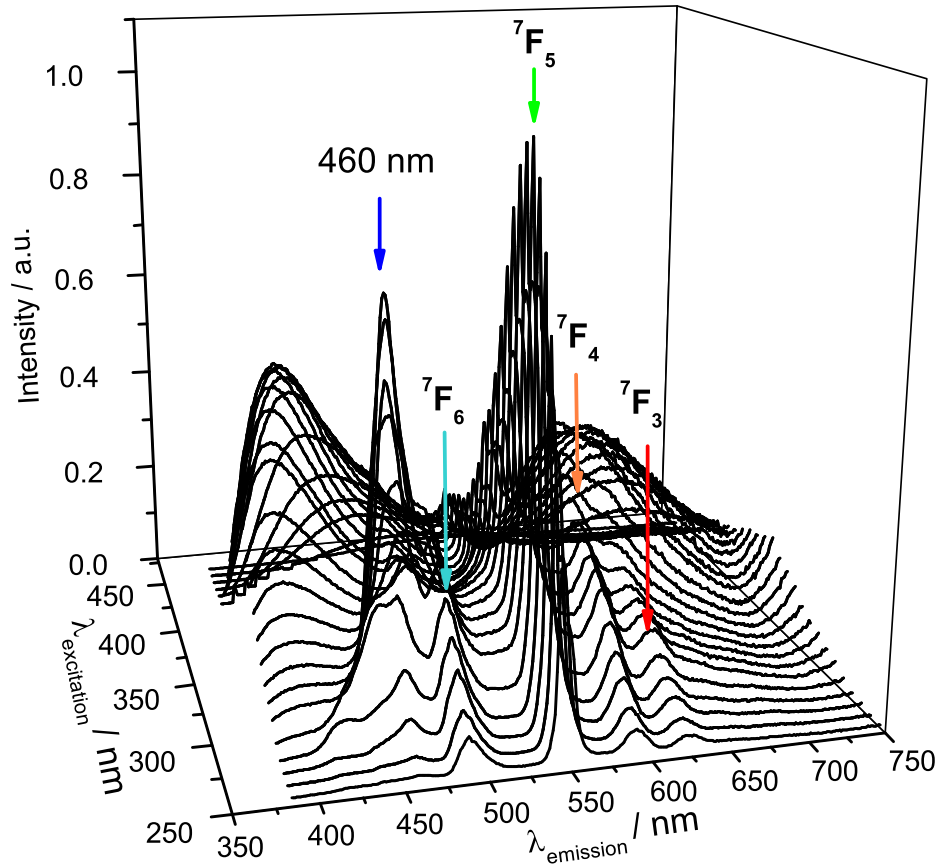


Figure 5.62.: Three-dimensional representation of photoluminescence spectra for Tb^{3+} doped amorphous $\text{Si}_3\text{B}_3\text{N}_7$ ceramic.

5.13. Tb/Eu Codoped Amorphous $\text{Si}_3\text{B}_3\text{N}_7$ Matrix

Powder X-ray pattern and diffuse reflection spectrum of $\text{Tb}^{3+}/\text{Eu}^{2+}$ codoped amorphous $\text{Si}_3\text{B}_3\text{N}_7$ ceramic are shown in Figure 5.57 and Figure 5.59, respectively. In the diffuse reflection spectrum of the $\text{Tb}^{3+}/\text{Eu}^{2+}$ codoped sample, the intrinsic strong drop in the reflection between 250 nm and 400 nm due to $\text{Si}_3\text{B}_3\text{N}_7$ host matrix has shifted up to 520 nm due to the absorption of Eu^{2+} ions. Photoluminescence spectra of $\text{Tb}^{3+}/\text{Eu}^{2+}$ codoped amorphous $\text{Si}_3\text{B}_3\text{N}_7$ ceramic are exhibited in Figure 5.63. Clearly, the emission profile of $\text{Tb}^{3+}/\text{Eu}^{2+}$ codoped samples are different from that of Eu^{2+} doped samples (see Figure 5.15). For the $\text{Tb}^{3+}/\text{Eu}^{2+}$ codoped sample, broad emission at 570 nm, which is typical for Eu^{2+} ions, contained additional peaks, which are typical for Tb^{3+} ions. The emission at 488 nm is assigned to the $^5\text{D}_4 \rightarrow ^7\text{F}_6$ transition, whereas at 544 nm to the $^5\text{D}_4 \rightarrow ^7\text{F}_5$

5. Phosphors Based on Amorphous $\text{Si}_3\text{B}_3\text{N}_7$ Matrix

transition, at 591 nm to the $^5\text{D}_4 \rightarrow ^7\text{F}_4$ transition and at 624 nm to the $^5\text{D}_4 \rightarrow ^7\text{F}_3$ transition. Among them, emission at 544 nm was the most intense and observed with any excitation wavelength up to 440 nm. The other emissions were observed as separated peaks at shorter excitation wavelengths and as shoulders at longer excitation wavelengths. Even though the Red-Edge Effect was obvious for the broad emission band due to the Eu^{2+} ions in $\text{Tb}^{3+}/\text{Eu}^{2+}$ codoped samples, the $4f \rightarrow 4f$ emissions belonging to Tb^{3+} ions have appeared to show no any red shift due to the strong shielding of $4f$ shell.

In Figure 5.64, the excitation spectra of Tb^{3+} doped, Eu^{2+} doped, and $\text{Tb}^{3+}/\text{Eu}^{2+}$ codoped samples measured at maximum emission wavelengths are compared. The Tb^{3+} doped sample has very strong absorption at shorter wavelengths between 254 nm and 310 nm, which resulted in very intense green emission at 544 nm, and had almost no absorption above 350 nm, resulting the intrinsic violet emission of the $\text{Si}_3\text{B}_3\text{N}_7$ host matrix (see Section 5.12). On the other hand, the Eu^{2+} doped sample has stronger absorption between 330 nm and 380 nm and relatively weak absorption between 254 - 330 nm and 380 - 480 nm. In the case of $\text{Tb}^{3+}/\text{Eu}^{2+}$ codoped sample, a hybrid absorption character has been obtained. The codoped sample had absorptions significantly higher than Eu^{2+} doped sample but lower than Tb^{3+} doped one at excitation wavelengths between 254 nm and 310 nm. Moreover, the codoped sample had absorptions significantly higher than Tb^{3+} doped sample but lower than the Eu^{2+} doped one at excitation wavelengths higher than 350 nm.

In Figure 5.65 and 5.66, the emission spectra of Tb^{3+} doped, Eu^{2+} doped, and $\text{Tb}^{3+}/\text{Eu}^{2+}$ codoped samples are compared, when excited with 280 nm and 365 nm wavelengths, respectively. In Figure 5.65, it can be observed that Tb^{3+} doped samples had very intense green emission at 544 nm together with emissions at 488 nm, 591 nm and 624 nm when excited with 280 nm light. All these peaks were also clearly observed in the $\text{Tb}^{3+}/\text{Eu}^{2+}$ codoped sample together with the broad emission at 570 nm due to the Eu^{2+} ions. Furthermore, when excited with 365 nm wavelength light, the Tb^{3+} doped sample showed mostly intrinsic violet emission due to the $\text{Si}_3\text{B}_3\text{N}_7$ host matrix but only very weak green emission at 544 nm due to Tb^{3+} ions (see Figure 5.66).

As the corresponding Tb^{3+} emission peaks are relatively weak in Tb^{3+} doped amorphous $\text{Si}_3\text{B}_3\text{N}_7$ ceramic when measured at excitation wavelengths of 330 nm or higher (see Figure 5.60), one can expect that these peaks should overlapped by the strong and broad Eu^{2+} emission in $\text{Tb}^{3+}/\text{Eu}^{2+}$ codoped sample. On the other hand, $\text{Tb}^{3+}/\text{Eu}^{2+}$ codoped sample had green emission at 544 nm as a separate peak together with the broad emission peak at 570 nm due to Eu^{2+} ions. In addition, the emissions at 488 nm, 591 nm and 624 nm due to Tb^{3+} ions appear as shoulders. As Tb^{3+} emission peaks were observed up to 440 nm excitation wavelength in codoped samples, this phenomenon can be described with an energy transfer from Eu^{2+} ions to Tb^{3+} ions.

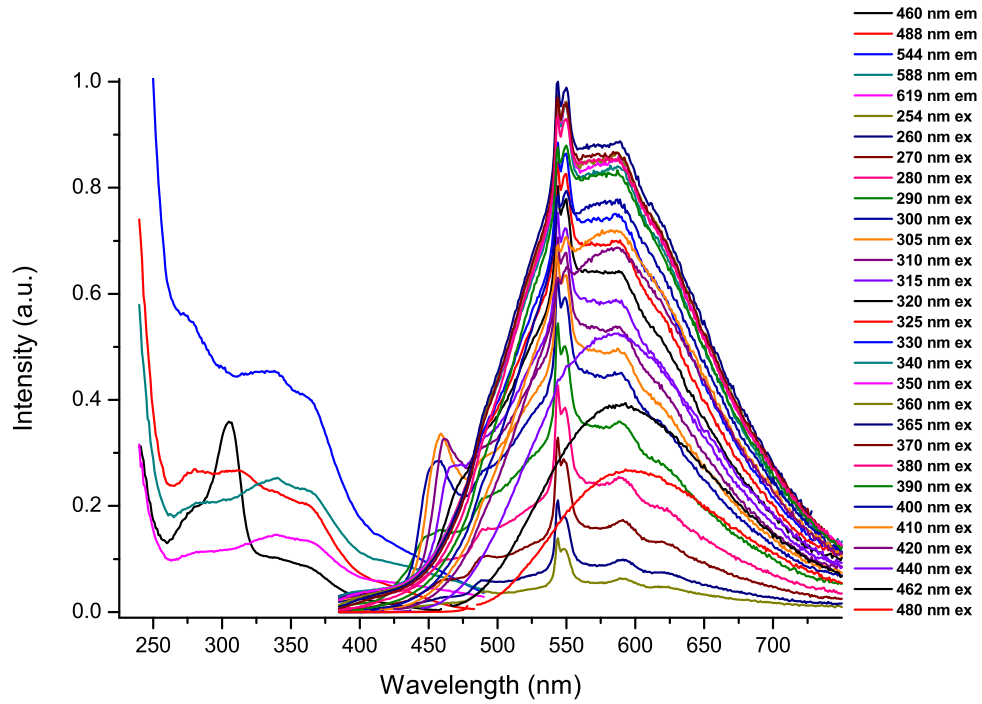


Figure 5.63.: Photoluminescence spectra of Tb³⁺/Eu²⁺ codoped amorphous Si₃B₃N₇ ceramic at different excitation and emission wavelengths.

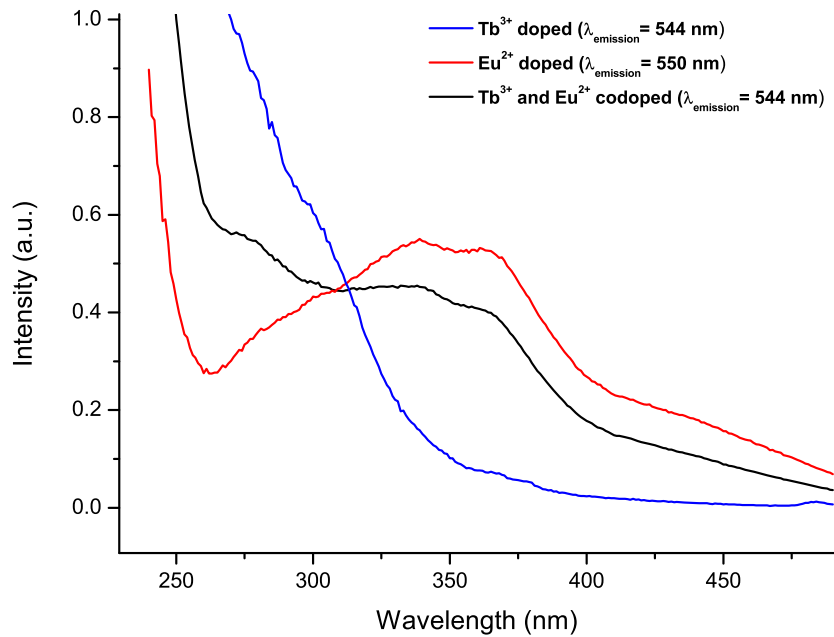


Figure 5.64.: Excitation spectra of Tb³⁺ doped, Eu²⁺ doped and Tb³⁺/Eu²⁺ codoped amorphous Si₃B₃N₇ ceramics measured at maximum emission wavelengths.

5. Phosphors Based on Amorphous $\text{Si}_3\text{B}_3\text{N}_7$ Matrix

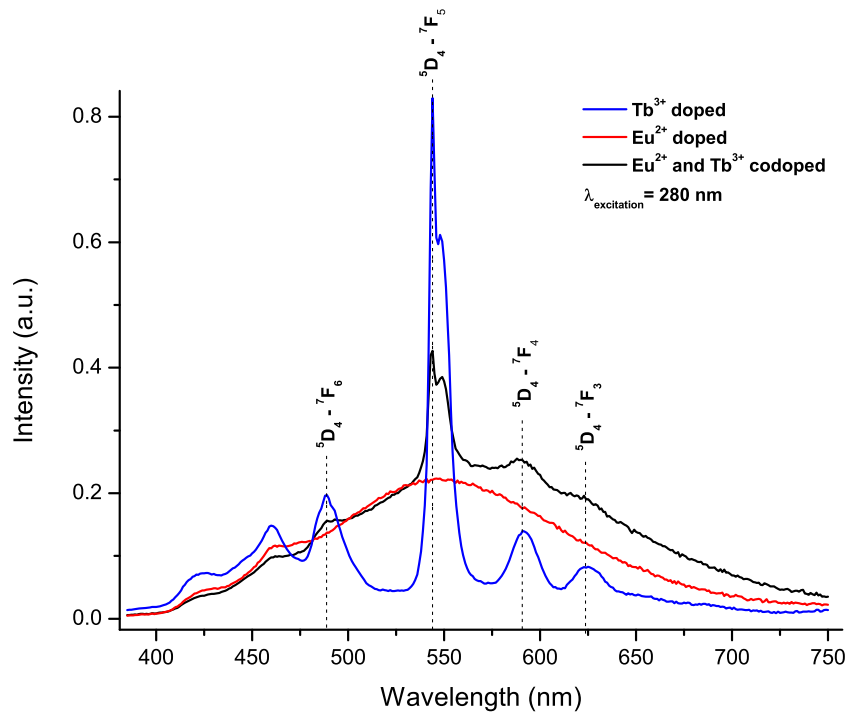


Figure 5.65.: Emission spectra of Tb^{3+} doped, Eu^{2+} doped and $\text{Tb}^{3+}/\text{Eu}^{2+}$ codoped amorphous $\text{Si}_3\text{B}_3\text{N}_7$ ceramics measured at 280 nm excitation wavelength.

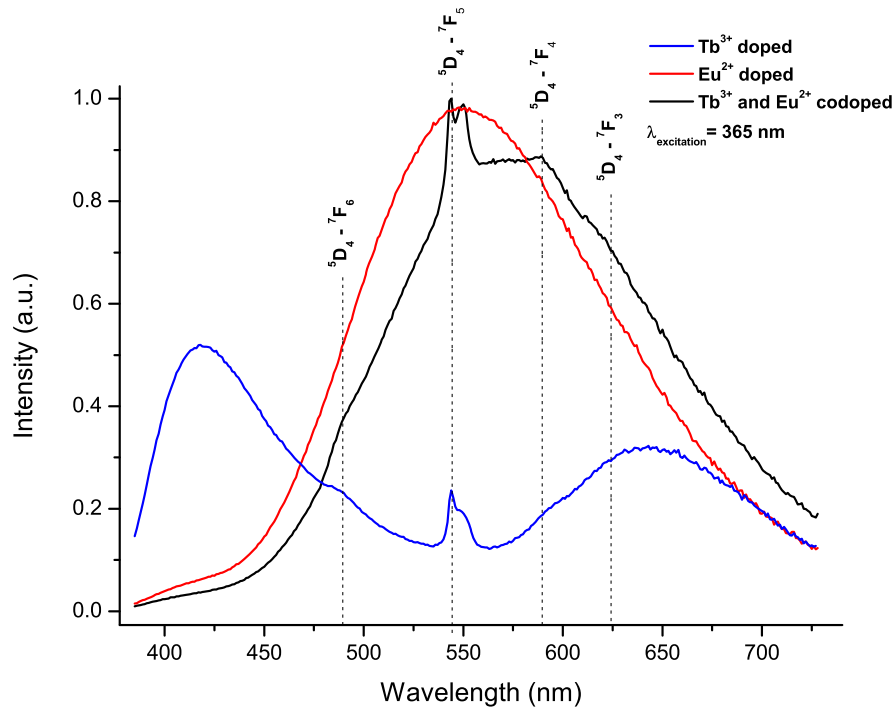


Figure 5.66.: Emission spectra of Tb^{3+} doped, Eu^{2+} doped and $\text{Tb}^{3+}/\text{Eu}^{2+}$ codoped amorphous $\text{Si}_3\text{B}_3\text{N}_7$ ceramics measured at 365 nm excitation wavelength.

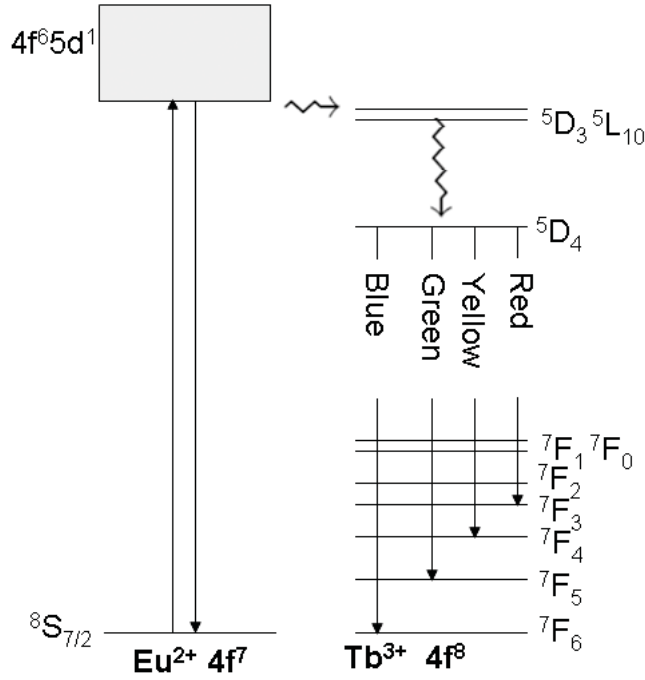


Figure 5.67.: Energy transfer mechanism from Eu^{2+} ions to Tb^{3+} ions in $\text{Tb}^{3+}/\text{Eu}^{2+}$ codoped amorphous $\text{Si}_3\text{B}_3\text{N}_7$ ceramic.

Figure 5.67 represents a possible energy transfer mechanism from Eu^{2+} to Tb^{3+} ions. The $4f^65d^1$ level of Eu^{2+} ions has been expected to have almost the same energy with $5D_3$ and $5L_{10}$ levels of Tb^{3+} ions. After excitation of the $4f^65d^1$ state of Eu^{2+} ions, some of the electrons can relax radiatively to the $4f^7$ ground state of Eu^{2+} ions, which produces the broad emission band at around 570 nm, while the other electrons can be transferred to the $5D_3$ and $5L_{10}$ levels of Tb^{3+} ions. Then, these electrons in the $5D_3$ and $5L_{10}$ levels of Tb^{3+} ions can decay non-radiatively to $5D_4$ level, from which they can decay radiatively to the $7F_6$, $7F_5$, $7F_4$ and $7F_3$ levels at 488 nm, 544 nm, 591 nm and 624 nm, respectively.

5.14. Tb/Ce Codoped Amorphous $\text{Si}_3\text{B}_3\text{N}_7$ Matrix

Green emission by Tb^{3+} ions usually results from the excitation by UV-light at rather short wavelengths. However, this is not appropriate for white emitters which use violet to blue LEDs for an excitation source. Therefore, it is of great interest for white-LED applications to sensitize Tb^{3+} emission ($5D_4 \rightarrow 7F_J$) through energy transfer from a sensitizer ion. In that respect, Ce^{3+} ions are the most widely applied sensitizers for Tb^{3+} ions [192]. Codoping of Tb^{3+} activated oxide-base phosphors with Ce^{3+} as a sensitizer has been well investigated for mercury gas-discharge lamps [192]. In these lamps, the 254 nm radiation of the mercury gas-discharge is absorbed by Ce^{3+} , which is then transferred to Tb^{3+} , and finally yields green emission. Generally, higher Tb^{3+} concentrations are

5. Phosphors Based on Amorphous $\text{Si}_3\text{B}_3\text{N}_7$ Matrix

required for efficient energy transfer in order to quench the $5d \rightarrow 4f$ emission of Ce^{3+} and $^5\text{D}_3 \rightarrow ^7\text{F}_J$ blue emissions (due to cross-relaxation process) of Tb^{3+} .

In the present study, the feasibility of using Ce^{3+} ions as sensitizers for Tb^{3+} doped amorphous $\text{Si}_3\text{B}_3\text{N}_7$ ceramic has been studied. It has been shown in Section 5.4 that Ce^{3+} ions in amorphous $\text{Si}_3\text{B}_3\text{N}_7$ host matrix show significant absorption between 340 nm and 450 nm. Accordingly, the challenging question is if Tb^{3+} emissions in amorphous $\text{Si}_3\text{B}_3\text{N}_7$ matrix can be sensitized by codoping with Ce^{3+} via the emission of UV-to-blue light like in InGaN LEDs.

Typical green emission of Tb^{3+} ions via short wavelength excitation has also been observed for Tb^{3+} doped amorphous $\text{Si}_3\text{B}_3\text{N}_7$ ceramic (see Figure 5.60). This was previously discussed in Section 5.12 and it was observed that excitation between 330 nm and 350 nm resulted a significant decrease in green emission with the intrinsic violet emission of $\text{Si}_3\text{B}_3\text{N}_7$ host matrix becoming dominant. It has also been shown that Ce^{3+} doped amorphous $\text{Si}_3\text{B}_3\text{N}_7$ ceramics have a broad emission band between 520 nm and 550 nm, and a wide excitation window ranging from 330 nm to 450 nm (see Section 5.4).

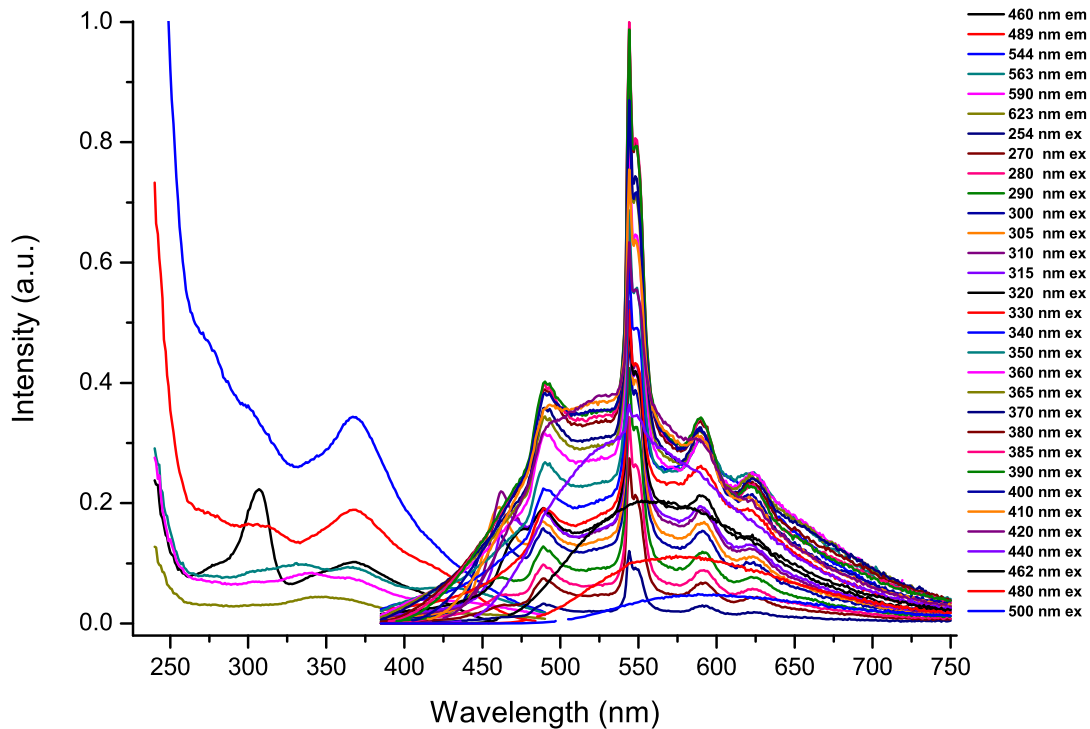


Figure 5.68.: Photoluminescence spectra of $\text{Tb}^{3+}/\text{Ce}^{3+}$ codoped amorphous $\text{Si}_3\text{B}_3\text{N}_7$ ceramic at different excitation and emission wavelengths.

Powder X-ray pattern and diffuse reflection spectrum of Tb³⁺/Ce³⁺ codoped amorphous Si₃B₃N₇ ceramic were presented in Figure 5.57 and Figure 5.59, respectively. In the diffuse reflection spectra, in addition to the strong drop in the reflection between 250 nm and 400 nm due to Si₃B₃N₇ host matrix, additional absorptions appeared between 280 nm and 320 nm due to Tb³⁺ ions in Tb³⁺ doped sample and between 350 nm and 400 nm due to Ce³⁺ ions in Ce³⁺ doped sample. In that context, the diffuse reflection spectrum of Tb³⁺/Ce³⁺ codoped amorphous Si₃B₃N₇ ceramic clearly showed the absorption bands belonging to both Tb³⁺ and Ce³⁺ ions. This was also confirmed by the excitation spectra of Tb³⁺/Ce³⁺ codoped amorphous Si₃B₃N₇ ceramic (Figure 5.68). In the excitation spectrum (emission at 544 nm) of Tb³⁺/Ce³⁺ codoped amorphous Si₃B₃N₇ ceramic, an additional excitation band between 330 nm and 400 nm is clearly visible, which was typical for the Ce³⁺ doped amorphous Si₃B₃N₇ ceramic (Figure 5.30).

Excitation below 330 nm, which was the starting wavelength of Ce³⁺ absorption band, resulted in emission spectra including mainly Tb³⁺ emissions together with a very weak Ce³⁺ emission band attributed to the fact that Tb³⁺ ions could be directly excited via the ⁷F₆ → ⁵D₃ transition (see Section 5.12). On the other hand, excitation above 330 nm resulted in a broad Ce³⁺ emission band (between 520 and 590 nm, see Section 5.4) superimposed with Tb³⁺ emissions (for clarity, some selected emissions are given in Figure 5.69). Based on the fact that hardly any Tb³⁺ emissions could be observed with excitation wavelengths above 420 nm in Tb³⁺ doped amorphous Si₃B₃N₇ ceramics (see Figure 5.60), it can be concluded that an efficient energy transfer really has occurred from Ce³⁺ to Tb³⁺ in Tb³⁺/Ce³⁺ codoped amorphous Si₃B₃N₇ ceramic. This is because for these wavelengths (> 420 nm) only direct excitation of Ce³⁺ ions is possible (see Figure 5.70). Furthermore, when the Ce³⁺ emission spectrum (at 420 nm excitation) is subtracted from the emission spectrum of Tb³⁺/Ce³⁺ codoped sample (at 420 nm excitation) in Figure 5.70, pure Tb³⁺ emissions are obtained (Figure 5.71), which indicates an efficient energy transfer from Ce³⁺ ions to Tb³⁺ ions. It is seen from the emission spectra in Figure 5.68 that both 5d → 4f emission of Ce³⁺ ions and ⁵D₄ → ⁷F_J emissions of Tb³⁺ ions occur at the same time. This can be explained by partial overlapping of the ⁷F₆ - ⁵D₄ energy level of Tb³⁺ ions with the Ce³⁺ emission band that results in energy transfer from the 5d band of Ce³⁺ ions to the ⁵D₄ level of Tb³⁺ ions. This kind of behavior was not observed for oxide phosphors but has been observed for YTbSi₄N₆C:Ce³⁺ crystalline compounds [337]. In Tb³⁺/Ce³⁺ codoped amorphous Si₃B₃N₇ ceramics, excitation energies, mostly greater than 330 nm, are absorbed by Ce³⁺ ions through the 4f → 5d transition. Then, after relaxation, Ce³⁺ ions transfer some of their energies to the nearest neighbor Tb³⁺ ions, which are pumped to the ⁵D₄ level, from which the ⁵D₄ → ⁷F_J emissions occurs. At the same time, Ce³⁺ ions also transfer the rest of their energy to themselves, from which the 4f → 5d broad emission takes place.

5. Phosphors Based on Amorphous $\text{Si}_3\text{B}_3\text{N}_7$ Matrix

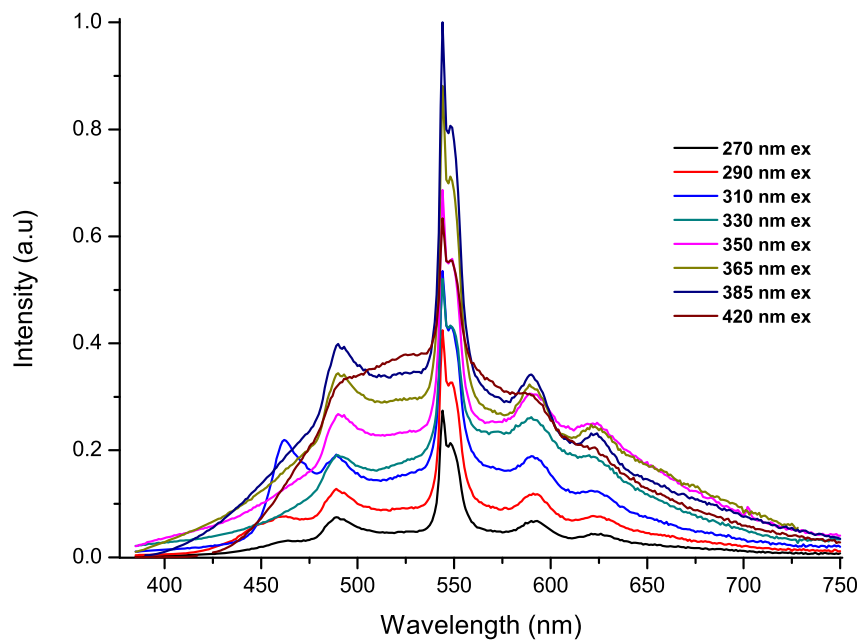


Figure 5.69.: Emission spectra of $\text{Tb}^{3+}/\text{Ce}^{3+}$ codoped amorphous $\text{Si}_3\text{B}_3\text{N}_7$ ceramic at some selected excitation wavelengths.

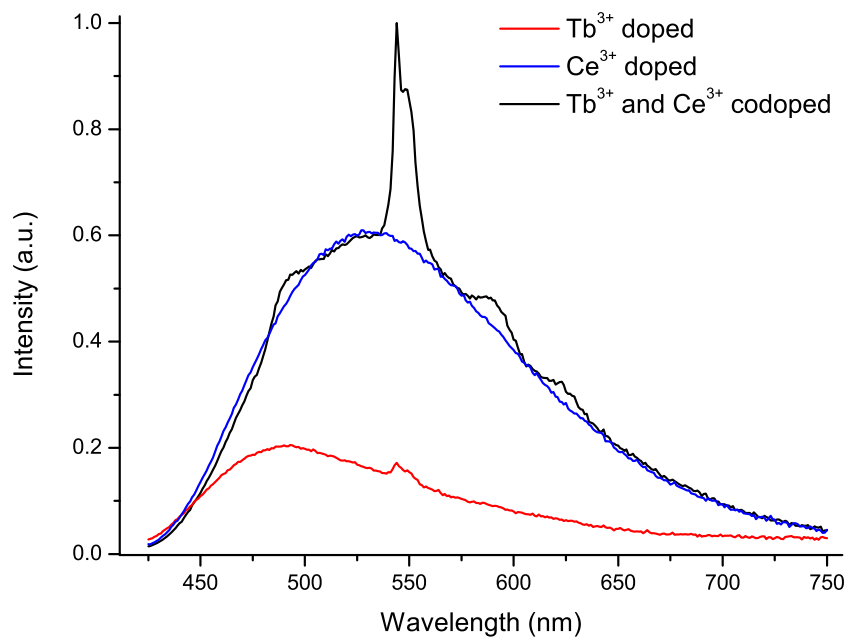


Figure 5.70.: Emission spectra of Tb^{3+} doped, Ce^{3+} codoped and $\text{Tb}^{3+}/\text{Ce}^{3+}$ codoped amorphous $\text{Si}_3\text{B}_3\text{N}_7$ ceramics measured at 420 nm excitation wavelength.

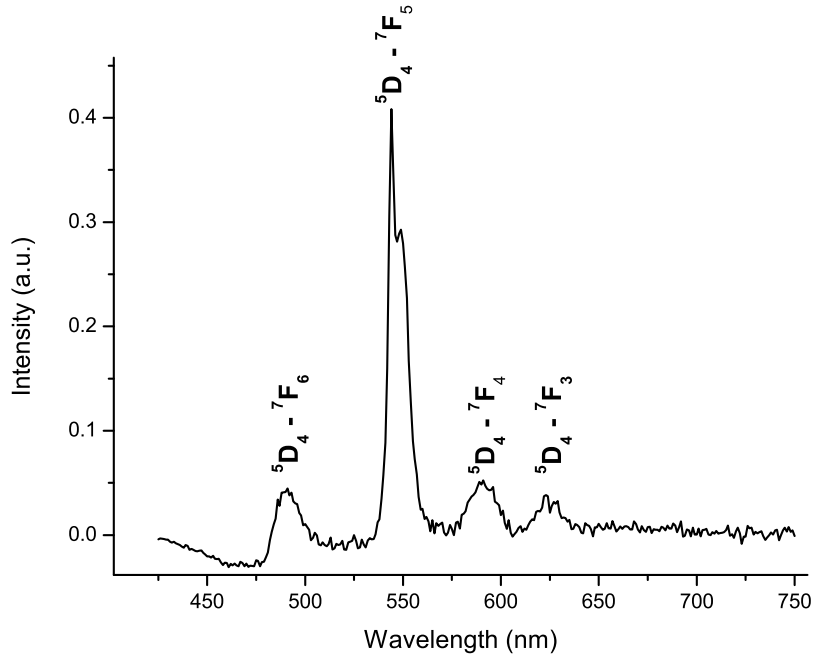


Figure 5.71.: Tb^{3+} emissions obtained by subtracting the emission spectrum of Ce^{3+} doped amorphous $\text{Si}_3\text{B}_3\text{N}_7$ ceramic (blue line) from the emission spectrum of $\text{Tb}^{3+}/\text{Ce}^{3+}$ codoped amorphous $\text{Si}_3\text{B}_3\text{N}_7$ ceramic (black line) in Figure 5.70 measured at 420 nm excitation wavelength.

Since Ce^{3+} and Eu^{2+} ions have very similar energy level schemes (Figure 5.34), one could expect that Eu^{2+} ions have a similar efficient energy transfer to Tb^{3+} ions as Ce^{3+} ions. However, the results showed that the energy transfer from Ce^{3+} to Tb^{3+} is much more efficient than that from Eu^{2+} to Tb^{3+} (compare Figure 5.63 and Figure 5.68). This implies that the excited energy level of Ce^{3+} is more suitable for an efficient energy transfer to Tb^{3+} than that of Eu^{2+} . Another important characteristic feature of the emission spectra of $\text{Tb}^{3+}/\text{Ce}^{3+}$ codoped amorphous $\text{Si}_3\text{B}_3\text{N}_7$ ceramic is that $4f \rightarrow 4f$ emissions of Tb^{3+} ions do not show any red shift due to the strong shielding of the $4f$ shell, even though the Red-Edge Effect is observed for the broad Ce^{3+} emission band.

5.15. Ho Doped Amorphous $\text{Si}_3\text{B}_3\text{N}_7$ Matrix

Efficient luminescence of Ho^{3+} ions has not been usually observed due to the presence of crowded energy levels (Figure 5.72). On the other hand, emissions of Ho^{3+} ions at 543 nm, 649 nm and 778 nm in Y_3GaO_6 [338], at 545 nm in Sr_2CeO_4 [339] and at 453 nm and 543 nm in LaAlO_3 [340] under UV excitation have recently been reported. In addition, Ho^{3+} ions have been widely used for infrared-to-visible up-conversion phosphors by codoping, for example, with Y^{3+} [341] and Yb^{3+} [342]. Moreover, codoping of Ho^{3+}

5. Phosphors Based on Amorphous $\text{Si}_3\text{B}_3\text{N}_7$ Matrix

with Eu^{2+} in SrAl_2O_4 [343], $\text{Sr}_3\text{Al}_{10}\text{SiO}_{20}$ [344] and CaGa_2S_4 [345] lattices resulted in phosphorescence (also known as long-lasting or afterglow phenomenon).

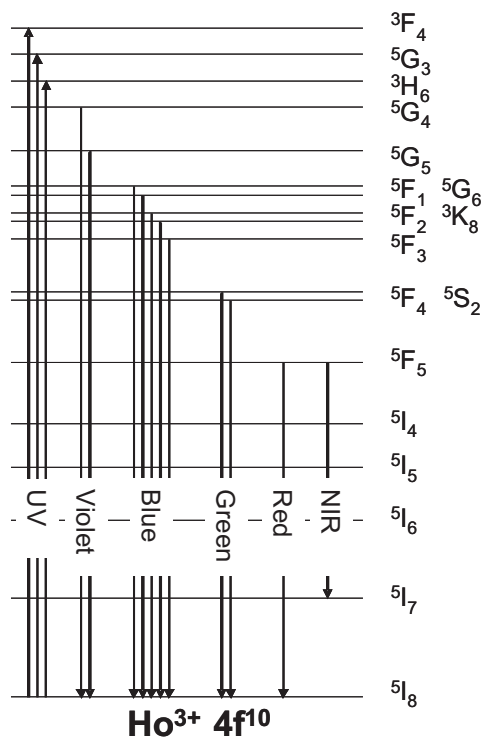


Figure 5.72.: Representation of energy level diagram of Ho^{3+} ions (for reasons of clarity not all levels have been shown).

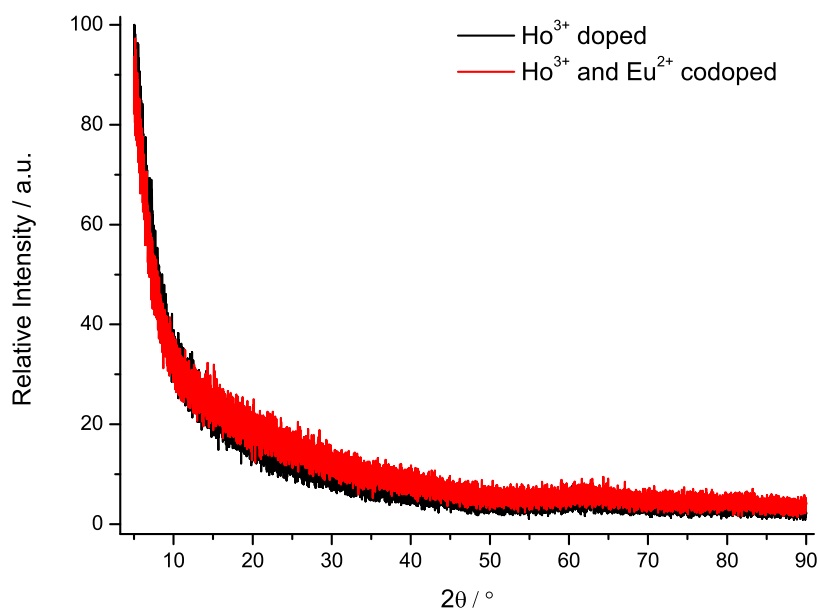


Figure 5.73.: Powder X-ray diffractograms of Ho^{3+} doped and $\text{Ho}^{3+}/\text{Eu}^{2+}$ codoped amorphous $\text{Si}_3\text{B}_3\text{N}_7$ ceramics.

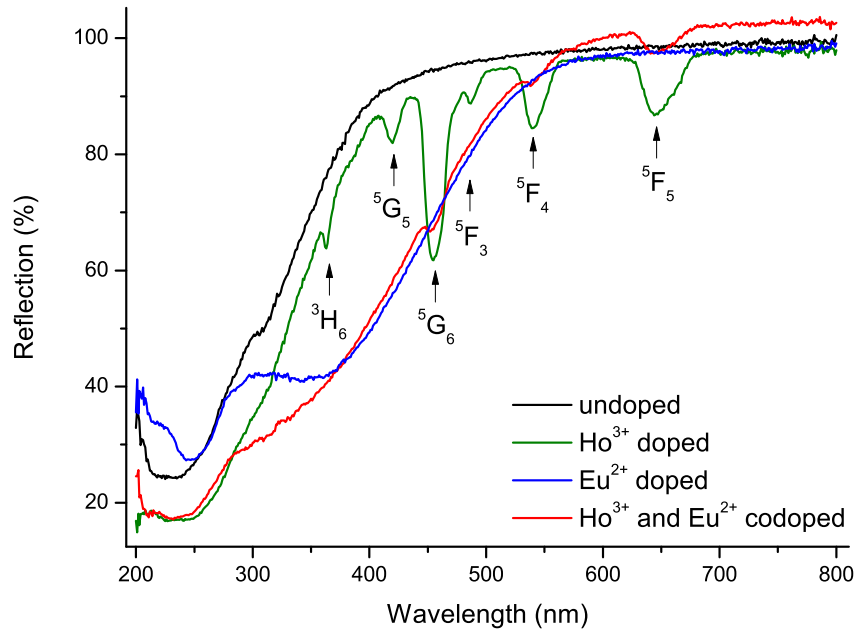


Figure 5.74.: Diffuse reflection spectra of undoped, Ho^{3+} doped, Eu^{2+} doped and $\text{Ho}^{3+}/\text{Eu}^{2+}$ codoped amorphous $\text{Si}_3\text{B}_3\text{N}_7$ ceramics.

Figure 5.73 shows the powder X-ray diffractograms for Ho^{3+} doped, and $\text{Ho}^{3+}/\text{Eu}^{2+}$ codoped amorphous $\text{Si}_3\text{B}_3\text{N}_7$ ceramics. In the diffuse reflection spectrum (Figure 5.74), incorporation of Ho^{3+} ions into the amorphous $\text{Si}_3\text{B}_3\text{N}_7$ matrix resulted in stronger absorption at 250 nm, which was shifted up to 350 nm with an additional absorption at 363 nm due to the $^5\text{I}_8 \rightarrow ^3\text{H}_6$ transition (Figure 5.74). In addition to this strong absorption in the UV region, there were also certain absorption bands in the visible region. All of the absorption bands in the visible region in the diffuse reflection spectrum can be assigned to transitions from the ground state level to higher energy levels which is well consistent with the literature data [338]. These transitions were assigned from the $^5\text{I}_8$ ground state level to $^5\text{G}_5$ at 420 nm, to $^5\text{G}_6$ at 455 nm, to $^5\text{F}_3$ at 487 nm, to $^5\text{F}_4$ at 540 nm and to $^5\text{F}_5$ at 645 nm. Due to these absorptions in the visible region, the Ho^{3+} doped amorphous $\text{Si}_3\text{B}_3\text{N}_7$ ceramic possesses a very light pink color.

Photoluminescence spectra of Ho^{3+} doped ceramic (Figure 5.75) exhibited the intrinsic excitation and emission peaks of the undoped amorphous $\text{Si}_3\text{B}_3\text{N}_7$ ceramic with additional peaks belonging to Ho^{3+} ions. In Figure 5.75, it is quite difficult to distinguish the absorption and emission bands due to Ho^{3+} ions. Therefore, for understand understanding, Figure 5.76 and Figure 5.77 are presented for some selected excitation and emission wavelengths together with the corresponding spectra of the undoped amorphous $\text{Si}_3\text{B}_3\text{N}_7$ ceramic. Excitation spectra of Ho^{3+} doped ceramic appear well consistent with the dif-

5. Phosphors Based on Amorphous $\text{Si}_3\text{B}_3\text{N}_7$ Matrix

fuse reflection spectra (Figure 5.76). Compared to undoped samples, incorporation of Ho^{3+} ions into amorphous $\text{Si}_3\text{B}_3\text{N}_7$ host matrix resulted in much stronger and broader excitation band (e.g. 58 nm FWHM measured at 400 nm emission wavelength) in the UV region at 348 nm due to the $^5\text{I}_8 \rightarrow ^5\text{G}_5$ transition, including a shoulder at 365 nm due to the $^5\text{I}_8 \rightarrow ^3\text{H}_6$ transition. This shoulder becomes a separate peak in the excitation spectra which are measured at longer emission wavelengths, e.g. at 440 nm and 480 nm.

Emission spectra of the Ho^{3+} doped amorphous $\text{Si}_3\text{B}_3\text{N}_7$ ceramic have generally resembled the emission pattern of the undoped amorphous $\text{Si}_3\text{B}_3\text{N}_7$ ceramic (Figure 5.77). In addition to the intrinsic emission bands of $\text{Si}_3\text{B}_3\text{N}_7$ host matrix, Ho^{3+} ions exhibited much stronger emissions in the violet region due to $^3\text{H}_6 \rightarrow ^5\text{I}_8$ and $^5\text{G}_5 \rightarrow ^5\text{I}_8$ transitions, and weaker emissions in the blue to green region due to $^5\text{F}_2$, $^5\text{F}_3$, $^3\text{K}_8$, $^5\text{G}_6$, $^5\text{F}_4$, $^5\text{S}_2 \rightarrow ^5\text{I}_8$ transitions and in the red region due to $^5\text{F}_5 \rightarrow ^5\text{I}_8$ transition. Excitation with 365 nm light yielded very intense violet emission. Furthermore, 4f \rightarrow 4f emission bands, which were assigned to Ho^{3+} ions, has appeared not to have a significant red shift due to the strong shielding of 4f shell, whereas a significant red shift was observed in the emission spectra from the bands assigned to the amorphous $\text{Si}_3\text{B}_3\text{N}_7$ host matrix.

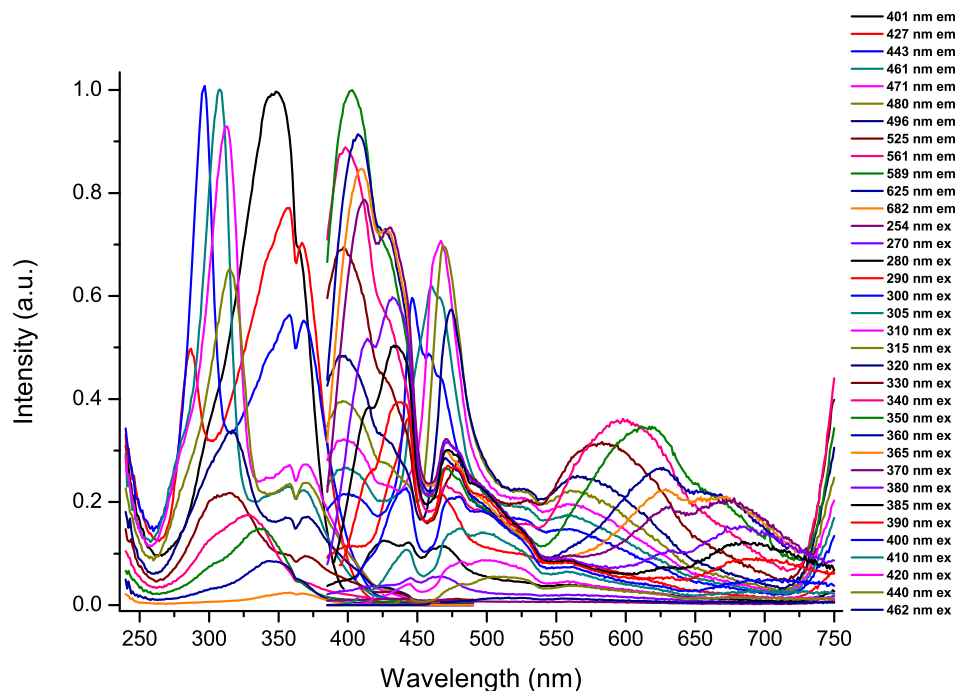


Figure 5.75.: Photoluminescence spectra of Ho^{3+} doped amorphous $\text{Si}_3\text{B}_3\text{N}_7$ ceramic at different excitation and emission wavelengths.

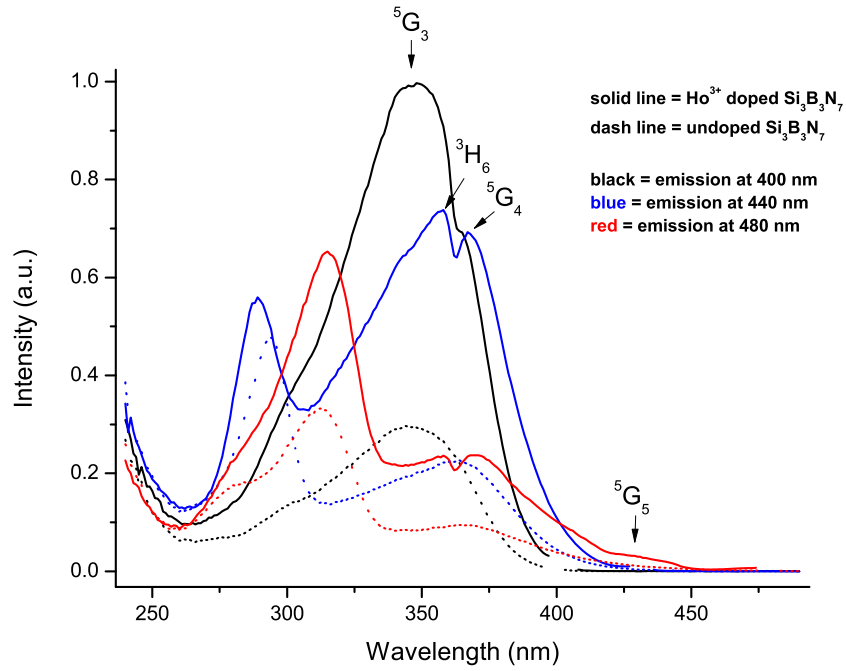


Figure 5.76.: Excitation spectra of undoped and Ho^{3+} doped amorphous $\text{Si}_3\text{B}_3\text{N}_7$ ceramics measured at 400 nm (black), 440 nm (blue) and 480 nm (red) emissions (solid lines = Ho^{3+} doped ceramic, dash lines = undoped ceramic).

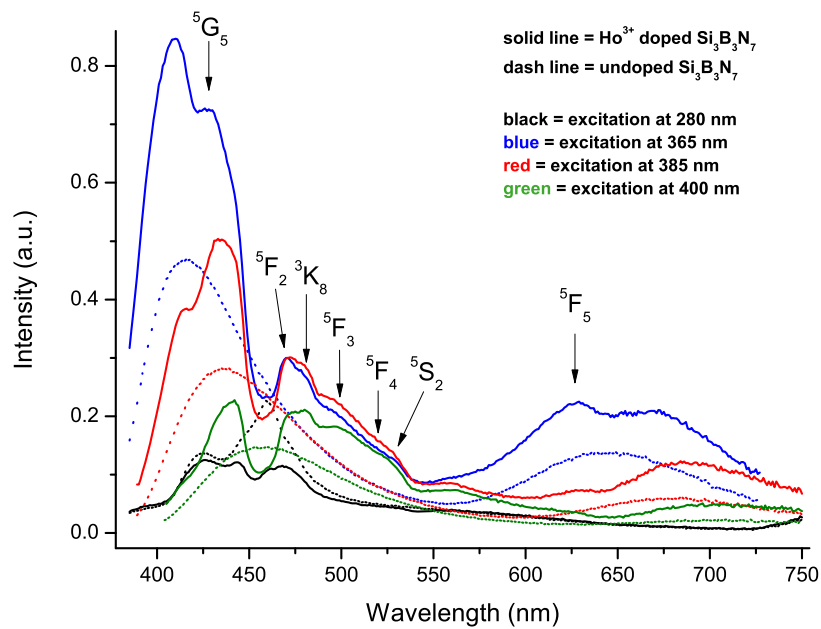


Figure 5.77.: Emission spectra of undoped and Ho^{3+} doped amorphous $\text{Si}_3\text{B}_3\text{N}_7$ ceramics measured at 280 nm (black), 365 nm (blue), 385 nm (red) and 400 nm (green) excitations (solid lines = Ho^{3+} doped ceramic, dash lines = undoped ceramic).

5.16. Ho³⁺/Eu²⁺ Codoped Amorphous $\text{Si}_3\text{B}_3\text{N}_7$ Matrix

Powder X-ray pattern and diffuse reflection spectrum of Ho³⁺/Eu²⁺ codoped amorphous $\text{Si}_3\text{B}_3\text{N}_7$ ceramic were presented in Figure 5.73 and Figure 5.74, respectively. In the diffuse reflection spectrum, it is seen that Ho³⁺/Eu²⁺ codoped sample has shifted the intrinsic strong drop in the reflection between 250 nm and 400 nm due to $\text{Si}_3\text{B}_3\text{N}_7$ matrix to around 520 nm because of the strong absorption of Eu²⁺ ions. In addition, the absorption bands belonging to Ho³⁺ ions at 646 nm due to $^5\text{I}_8 \rightarrow ^5\text{F}_5$, at 540 nm due to $^5\text{I}_8 \rightarrow ^5\text{F}_4$ and at 454 nm due to $^5\text{I}_8 \rightarrow ^5\text{G}_6$ transitions were observed. Absorptions due to $^5\text{I}_8 \rightarrow ^5\text{F}_3$, $^5\text{I}_8 \rightarrow ^5\text{G}_5$ and $^5\text{I}_8 \rightarrow ^3\text{H}_6$ transitions were overlapped with the strong absorption of Eu²⁺ ions below 520 nm.

Photoluminescence spectra of Ho³⁺/Eu²⁺ codoped amorphous $\text{Si}_3\text{B}_3\text{N}_7$ ceramic are shown in Figure 5.78. In addition to the structureless broad absorption band of Eu²⁺ ions, the excitation spectrum of the Ho³⁺/Eu²⁺ codoped sample included two additional broad bands at 440 nm and 470 nm due to $^5\text{I}_8 \rightarrow ^5\text{G}_5$ and $^5\text{I}_8 \rightarrow ^5\text{G}_6$ absorptions, respectively (Figure 5.79), that is consistent with the diffuse reflection spectrum (Figure 5.74). Moreover, Ho³⁺/Eu²⁺ codoped amorphous $\text{Si}_3\text{B}_3\text{N}_7$ ceramics exhibited a broad emission band in the visible region with a peak maximum at 580 nm.

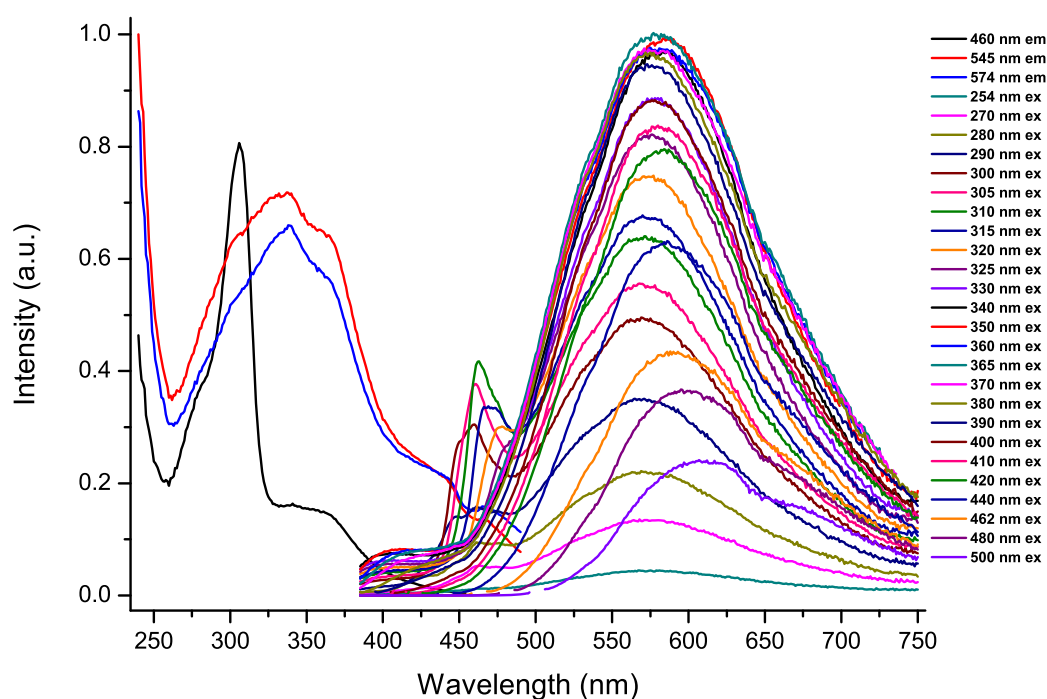


Figure 5.78.: Photoluminescence spectra of Ho³⁺/Eu²⁺ codoped amorphous $\text{Si}_3\text{B}_3\text{N}_7$ ceramic at different excitation and emission wavelengths.

Compared to the Eu^{2+} doped sample (see Figure 5.15), the most significant difference in the emission spectrum of the $\text{Ho}^{3+}/\text{Eu}^{2+}$ codoped sample is that the broad emission band is not symmetric. There are two broad shoulders at 535 nm and 650 nm, which are attributed to $^5\text{F}_4, ^5\text{S}_2 \rightarrow ^5\text{I}_8$ and $^5\text{F}_5 \rightarrow ^5\text{I}_8$ transitions, respectively. This effect can be better seen in Figure 5.80, in which emission spectra of Eu^{2+} doped and $\text{Ho}^{3+}/\text{Eu}^{2+}$ codoped samples are compared at 365 nm excitation wavelength. These shoulders increase the FWHM values from 150 nm to 167 nm and might result in better color rendering. The excitation band at 305 nm (measured at 460 nm emission wavelength) and the less intense blue emission peaks in Figure 5.78 resulted from the intrinsic emission of $\text{Si}_3\text{B}_3\text{N}_7$ host matrix.

Even though a significant Red-Edge Effect was observed in the emission spectra from the bands assigned to the Eu^{2+} ions, 4f \rightarrow 4f emission bands assigned to Ho^{3+} ions appear not to have a significant red shift due to the strong shielding of 4f shell. On the other hand, no afterglow phenomenon has been observed by naked eye, which had been reported for some compounds [343, 344, 345].

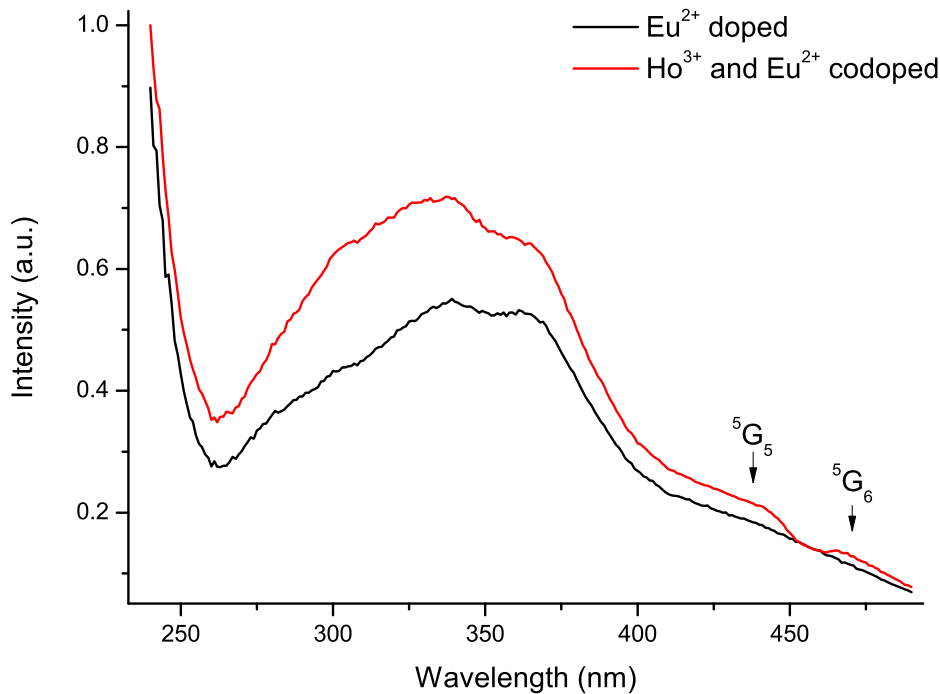


Figure 5.79.: Excitation spectra of Eu^{2+} doped and $\text{Ho}^{3+}/\text{Eu}^{2+}$ codoped amorphous $\text{Si}_3\text{B}_3\text{N}_7$ ceramics measured at 545 nm emission wavelength.

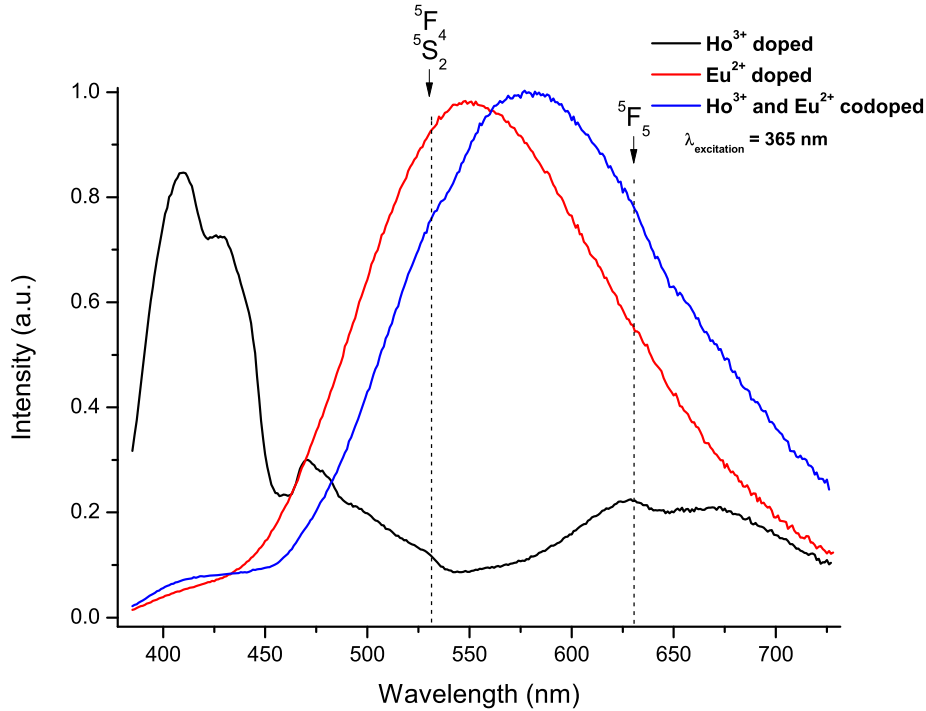


Figure 5.80.: Emission spectra of Ho^{3+} doped, Eu^{2+} doped and $\text{Ho}^{3+}/\text{Eu}^{2+}$ codoped amorphous $\text{Si}_3\text{B}_3\text{N}_7$ ceramics measured at 365 nm excitation wavelength.

5.17. Tm Doped Amorphous $\text{Si}_3\text{B}_3\text{N}_7$ Matrix

Tm^{3+} doped materials have recently attracted great attention. Having a rich energy level distribution (Figure 5.81) makes Tm^{3+} doped materials suitable for various hi-tech applications such as lasers [346], fiber amplifiers [347] and up- and down-conversion phosphors [348]. Solid state lasers operating in the eye-safe spectral region around $1.9 \mu\text{m}$ are demanded for various applications, including remote sensing (e.g. lidar (light detection and ranging)), medicine and environmental gas detection. In that respect, thulium ions exhibit significant advantages over the other rare earth ions as a laser operating at $1.9 \mu\text{m}$. The $^3\text{H}_4$ level of Tm^{3+} ion can be efficiently and directly excited by the high power and well-developed commercially available AlGaAs laser diodes around 800 nm [346]. On the other hand, in order to broaden the telecommunication range, the 1450-1480 nm band (S^+ band) has been developed. The best candidate for this has been found to be thulium doped glass fiber amplifiers due to the $^3\text{H}_4 \rightarrow ^3\text{F}_4$ transition of Tm^{3+} ions, which results in a broad emission band at $1.46 \mu\text{m}$ [347]. Thulium doped materials are also ideal candidates for up- and down-conversion processes because multiplets of the $4f^{12}$ configuration make up an energy level scheme such that sequential step-by-step excitations become possible. In this way, many down and up cross-relaxations become active [348]. Most frequently, Ho^{3+} , Er^{3+} and Yb^{3+} are codoped with Tm^{3+} in order to obtain improved up-

and down-conversion emissions.

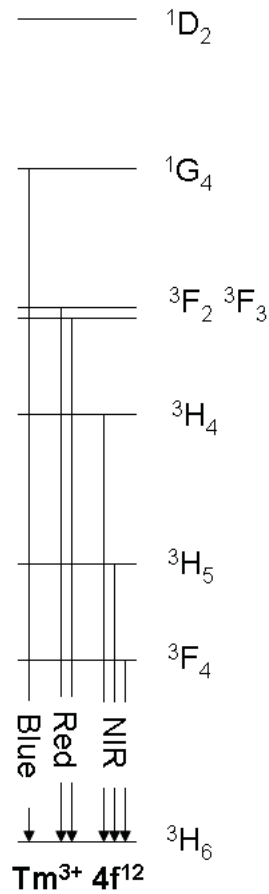


Figure 5.81.: Representation of energy level diagram of Tm^{3+} ions (for reasons of clarity not all levels have been shown).

In the present study, Tm^{3+} doping has been achieved via the organometallic route by using $\text{Tm}[\text{N}(\text{Si}(\text{CH}_3)_3)_2]_3$. Figure 5.82 presents powder X-ray diffractograms for Tm^{3+} doped, and $\text{Tm}^{3+}/\text{Eu}^{2+}$ codoped amorphous $\text{Si}_3\text{B}_3\text{N}_7$ ceramics. In addition to the strong absorption at around 230 nm due to the $\text{Si}_3\text{B}_3\text{N}_7$ host matrix, the characteristic $4f \rightarrow 4f$ transitions of Tm^{3+} ions were observed in the diffuse reflection spectrum (Figure 5.83). All of the absorption bands in the visible and the near-IR regions in the diffuse reflection spectrum were assigned to the transition from the ground state energy level to the higher energy levels of Tm^{3+} ions, which were consistent with the literature data [346]. These transitions were from $3H_6$ ground state level of Tm^{3+} ions to $1G_4$ at 467 nm, to $3F_2$ and $3F_3$ at 684 nm, to $5F_4$ at 786 nm, to $3H_5$ at 1213 nm and to $3H_4$ at 1625 nm. The transition from $3H_6$ ground state to $1D_2$, which was expected to be observed at around 360 nm, was covered by the strong absorption of the amorphous $\text{Si}_3\text{B}_3\text{N}_7$ host matrix.

5. Phosphors Based on Amorphous $\text{Si}_3\text{B}_3\text{N}_7$ Matrix

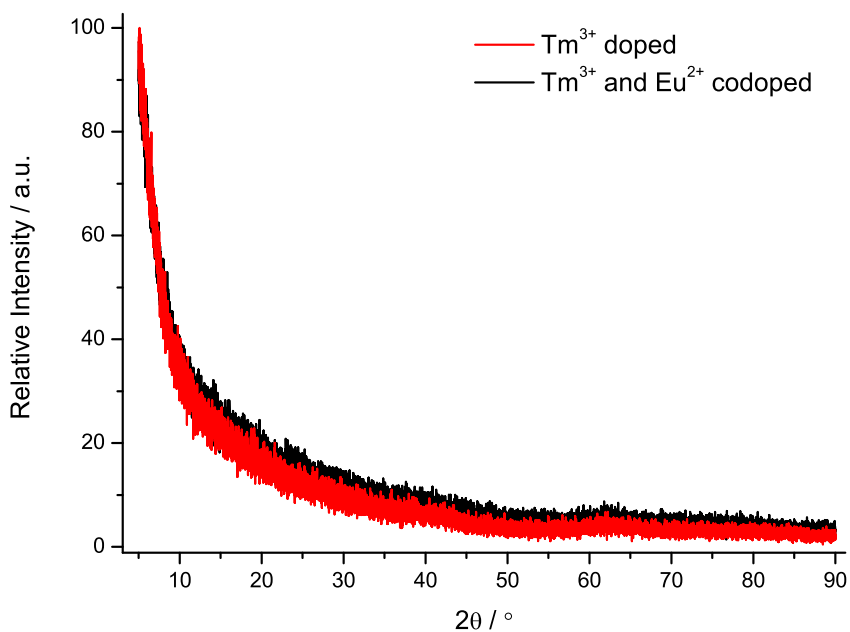


Figure 5.82.: Powder X-ray diffractograms of Tm^{3+} doped and $\text{Tm}^{3+}/\text{Eu}^{2+}$ codoped amorphous $\text{Si}_3\text{B}_3\text{N}_7$ ceramics.

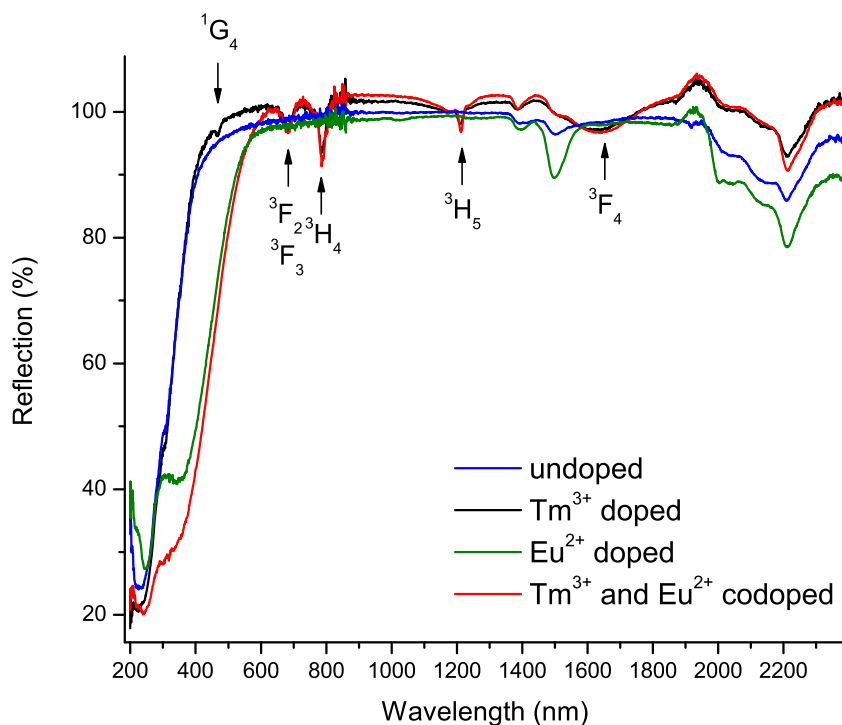


Figure 5.83.: Diffuse reflection spectra of undoped, Tm^{3+} doped, Eu^{2+} doped and $\text{Tm}^{3+}/\text{Eu}^{2+}$ codoped amorphous $\text{Si}_3\text{B}_3\text{N}_7$ ceramics.

Photoluminescence spectra of Tm³⁺ doped amorphous Si₃B₃N₇ ceramic are presented in Figure 5.84 and appeared almost the same as the undoped sample. Therefore, it is inferred that the same discussions for the photoluminescence properties of the undoped amorphous Si₃B₃N₇ ceramic are valid for the Tm³⁺ doped sample (see Section 5.2). Although the diffuse reflection spectrum of the Tm³⁺ doped amorphous Si₃B₃N₇ ceramic indicated the presence of significant amount of Tm³⁺ ions, possible blue emission due to ¹G₄ → ³H₆ transition was barely observed, deduced by comparing with the photoluminescence spectrum of the undoped amorphous Si₃B₃N₇ ceramic (Figure 5.2). The blue emission due to the ¹G₄ → ³H₆ transition of Tm³⁺ ions was so weak compared to intrinsic blue emission of Si₃B₃N₇ host matrix that only a very weak emission at 473 nm could be observed when the sample was excited with the 400 nm light (Figure 5.85).

Even though the blue emission obtained by UV excitation is inefficient, Tm³⁺ doped amorphous Si₃B₃N₇ ceramic might have promising laser and amplifier properties. On the other hand, it is also believed that codoping of amorphous Si₃B₃N₇ host matrix with Tm³⁺ and some other trivalent rare earth ions such as Ho³⁺, Er³⁺ and Yb³⁺ ions might yield efficient up- and down-conversion phosphors. Therefore, further investigations are necessary for Tm³⁺ (co)doped amorphous Si₃B₃N₇ ceramics.

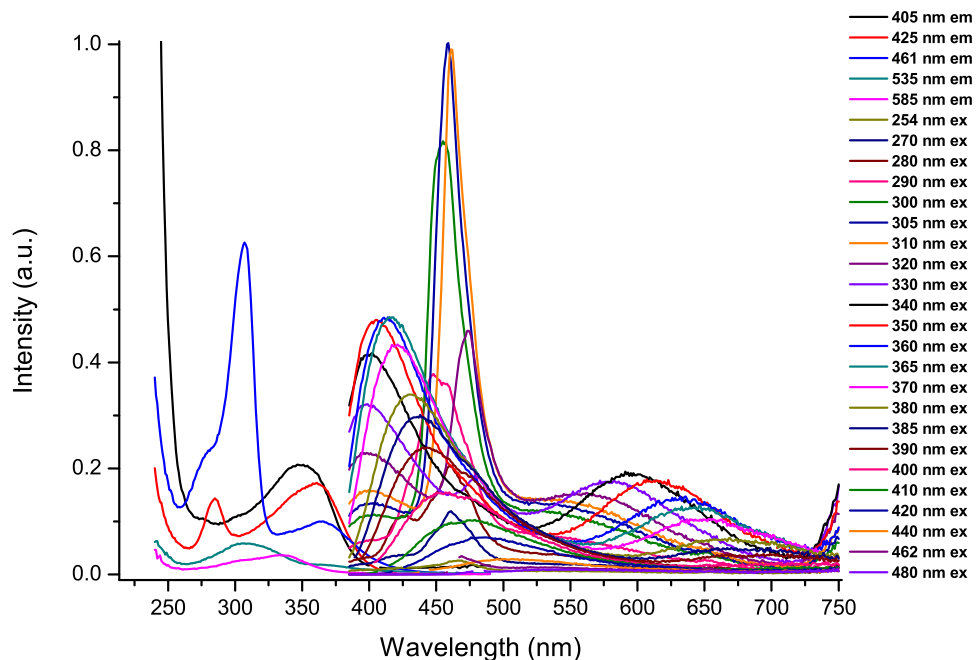


Figure 5.84.: Photoluminescence spectra of Tm³⁺ doped amorphous Si₃B₃N₇ ceramic at different excitation and emission wavelengths.

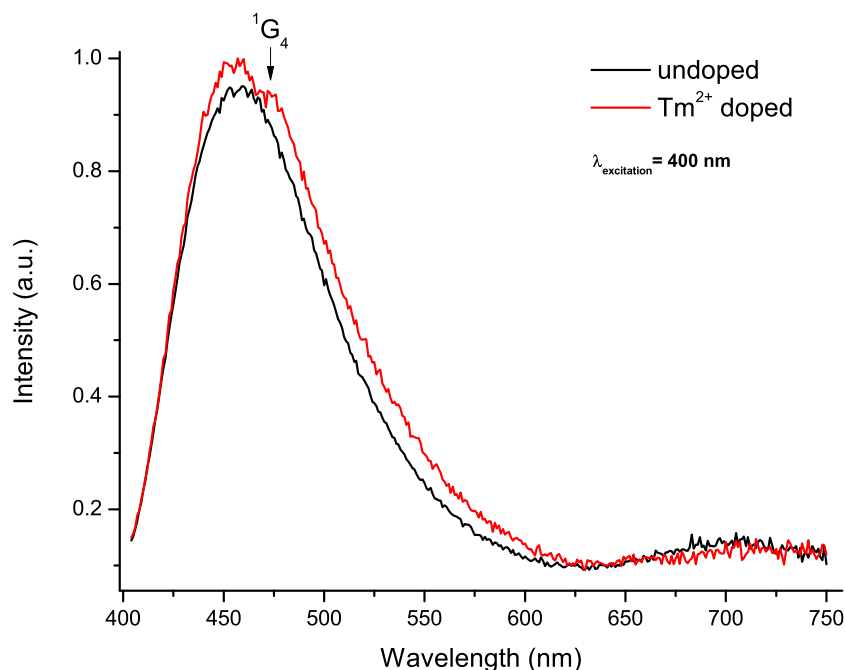


Figure 5.85.: Emission spectra of undoped and Tm^{3+} doped amorphous $\text{Si}_3\text{B}_3\text{N}_7$ ceramics measured at 400 nm excitation.

5.18. Tm/Eu Codoped Amorphous $\text{Si}_3\text{B}_3\text{N}_7$ Matrix

Powder X-ray pattern of $\text{Tm}^{3+}/\text{Eu}^{2+}$ codoped amorphous $\text{Si}_3\text{B}_3\text{N}_7$ ceramic was presented in Figure 5.82. In the diffuse reflection spectrum of $\text{Tm}^{3+}/\text{Eu}^{2+}$ codoped sample (Figure 5.83), typical Tm^{3+} absorption bands were obtained (see Section 5.17). On the other hand, as expected, codoping of Tm^{3+} and Eu^{2+} ions into amorphous $\text{Si}_3\text{B}_3\text{N}_7$ host matrix resulted in a shift of the intrinsic strong drop in the reflection between 250 nm and 400 nm to around 520 nm. Therefore, the ${}^3\text{H}_6 \rightarrow {}^1\text{G}_4$ and ${}^3\text{H}_6 \rightarrow {}^1\text{D}_2$ absorptions of Tm^{3+} ions were covered by the strong absorption of Eu^{2+} ions below 520 nm. The color of the $\text{Tm}^{3+}/\text{Eu}^{2+}$ codoped amorphous $\text{Si}_3\text{B}_3\text{N}_7$ ceramic is yellow.

Photoluminescence spectra of $\text{Tm}^{3+}/\text{Eu}^{2+}$ codoped amorphous $\text{Si}_3\text{B}_3\text{N}_7$ ceramic are shown in Figure 5.86. It is clear that the same emission profiles as in Eu^{2+} doped sample (see Figure 5.15) have been obtained for $\text{Tm}^{3+}/\text{Eu}^{2+}$ codoped sample. Therefore, the same discussions for the photoluminescence properties of Eu^{2+} doped amorphous $\text{Si}_3\text{B}_3\text{N}_7$ ceramic are valid for $\text{Tm}^{3+}/\text{Eu}^{2+}$ codoped sample (see Section 5.2). Since Tm^{3+} doped sample was already shown to have very weak blue emission due to ${}^1\text{G}_4 \rightarrow {}^3\text{H}_6$ transition in $\text{Si}_3\text{B}_3\text{N}_7$ host matrix, this blue emission in $\text{Tm}^{3+}/\text{Eu}^{2+}$ codoped sample is believed to be overlapped by the broad emission band of Eu^{2+} ions.

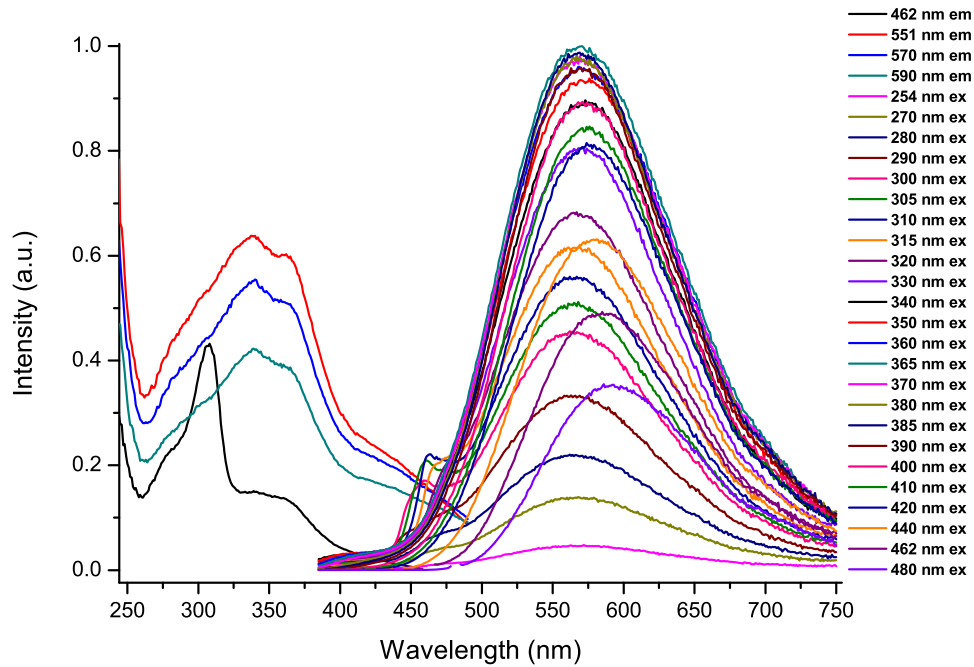


Figure 5.86.: Photoluminescence spectra of $\text{Tm}^{3+}/\text{Eu}^{2+}$ codoped amorphous $\text{Si}_3\text{B}_3\text{N}_7$ ceramic at different excitation and emission wavelengths.

5.19. Yb Doped Amorphous $\text{Si}_3\text{B}_3\text{N}_7$ Matrix

Yb doping has been achieved either via the metal route by using Yb metal or the organometallic route by using $\text{Yb}[\text{N}(\text{Si}(\text{CH}_3)_3)_2]_3$. Figure 5.87 shows the powder X-ray diffractograms for Yb doped amorphous $\text{Si}_3\text{B}_3\text{N}_7$ ceramics which were obtained via the two different routes. The diffuse reflection spectra have revealed that Yb ions are in both divalent and trivalent states. In addition to the strong absorption at around 230 nm due to $\text{Si}_3\text{B}_3\text{N}_7$ host matrix, the reflection spectra of all Yb doped samples have the characteristic $4f \rightarrow 4f$ transitions of Yb^{3+} ions (Figure 5.88).

Yb^{3+} ions have the simplest energy level scheme among the rare earth ions: only the $^2\text{F}_{7/2}$ ground state and the $^2\text{F}_{5/2}$ excited state, separated by 10000 cm^{-1} (Figure 5.88). These transitions are always located in the near-IR region regardless of the host material [349]. The $^2\text{F}_{7/2} \rightarrow ^2\text{F}_{5/2}$ transition of Yb^{3+} ions was clearly seen from the diffuse reflection spectra of Yb doped amorphous $\text{Si}_3\text{B}_3\text{N}_7$ ceramics at 920 nm and 982 nm (Figure 5.89). On the other hand, $4f^{13} \rightarrow 4f^{12}5d$ absorption band of Yb^{3+} ions is usually observed in the far-UV region, which could not be detected here as it is out of the measurement limit of the spectrometer. As Yb^{3+} ions do not have absorptions in the near-UV and the visible region, in Figure 5.89, the broad absorption band extended up to around 500 nm with respect to absorption of $\text{Si}_3\text{B}_3\text{N}_7$ host matrix is ascribed to the $4f^{14} \rightarrow 4f^{13}5d$ transition

5. Phosphors Based on Amorphous $\text{Si}_3\text{B}_3\text{N}_7$ Matrix

of Yb^{2+} ions. This extended absorption band is responsible for the light brown color of the Yb doped samples prepared via the metal route.

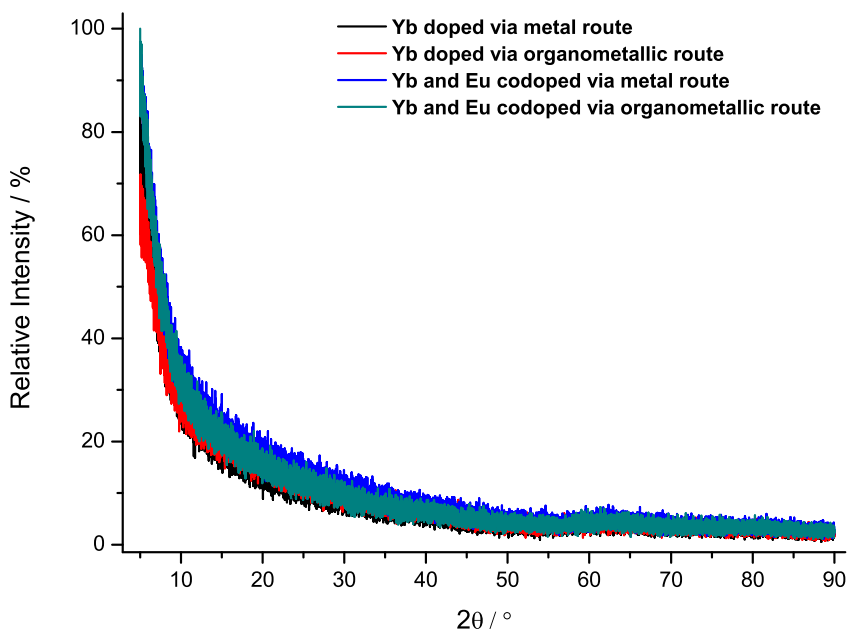


Figure 5.87.: Powder X-ray diffractograms of Yb doped and Yb/Eu codoped amorphous $\text{Si}_3\text{B}_3\text{N}_7$ ceramics obtained via both the metal and organometallic routes.

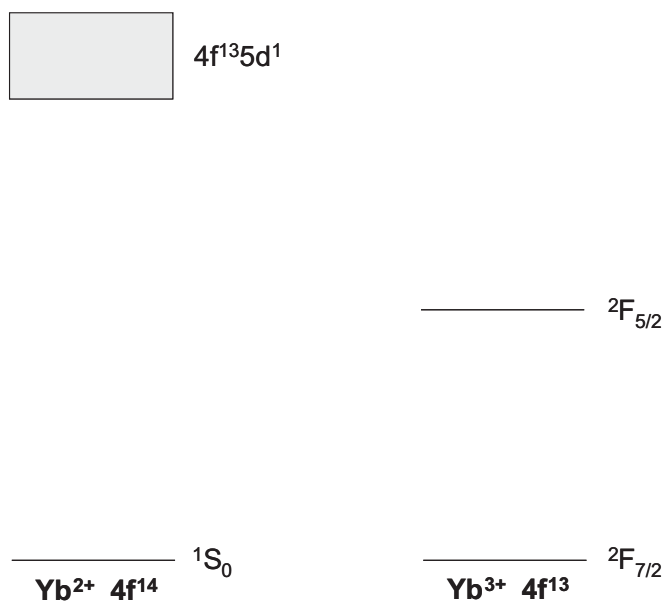


Figure 5.88.: Representation of energy level diagrams of Yb^{2+} and Yb^{3+} ions.

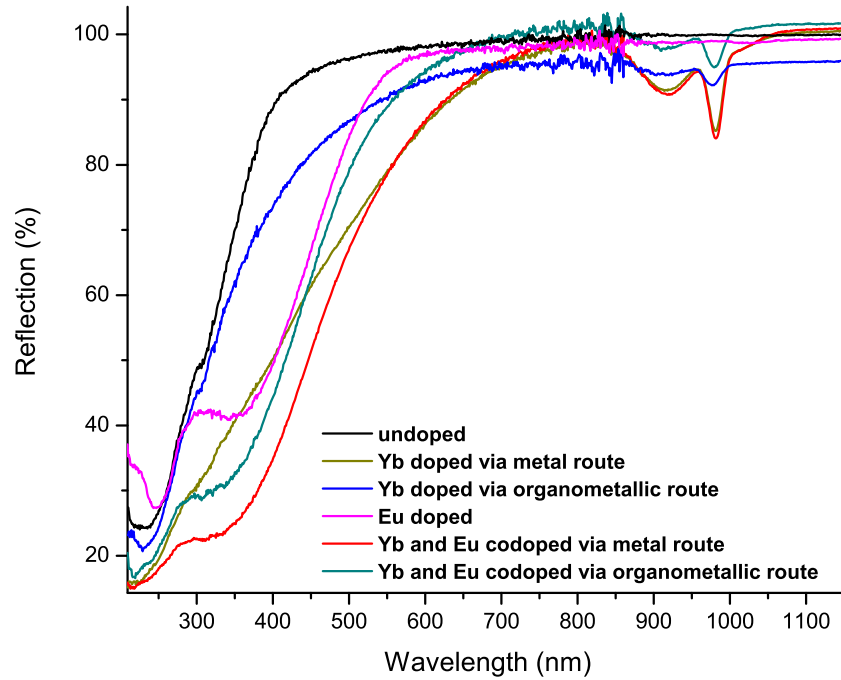
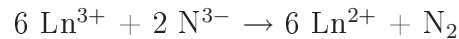


Figure 5.89.: Diffuse reflection spectra of undoped, Yb doped and Yb/Eu codoped amorphous $\text{Si}_3\text{B}_3\text{N}_7$ ceramics.

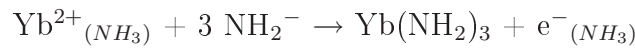
The presence of both divalent and trivalent Yb ions in the final ceramics via both routes can be rationalized by assuming two different mechanisms. First, in cases where trivalent lanthanides are used as starting compounds (i.e. the organometallic route in this study), chemically incorporated nitrogen reacts with trivalent lanthanides and reduces them to divalent state according to following general reaction:



This mechanism works quite well for Eu doped materials and, for example, no Eu^{3+} ions have been detected in SiAlON glasses [350] and amorphous $\text{Si}_3\text{B}_3\text{N}_7$ ceramics (see Section 5.2). It has also been shown that partial reduction to the divalent state has been observed for Sm^{3+} doped in SiAlON glasses [332, 351], though no reduction has been observed for amorphous $\text{Si}_3\text{B}_3\text{N}_7$ ceramics in this study (see Section 5.8). Furthermore, in the case of Yb^{3+} doping, partial reduction to Yb^{2+} has been reported for SiAlON glasses [351]. Similarly, in the present study, it has also been deduced from the diffuse reflection spectra that partial reduction of Yb^{3+} to Yb^{2+} has occurred in the amorphous $\text{Si}_3\text{B}_3\text{N}_7$ ceramic (Figure 5.89). Furthermore, more intense peaks in the near-IR region and greater shift of the intrinsic broad absorption of the $\text{Si}_3\text{B}_3\text{N}_7$ host matrix towards longer wavelengths in the diffuse reflection spectra are the result of higher Yb^{2+} concentrations.

5. Phosphors Based on Amorphous $\text{Si}_3\text{B}_3\text{N}_7$ Matrix

The second reason for the presence of both divalent and trivalent Yb ions in Yb doped amorphous $\text{Si}_3\text{B}_3\text{N}_7$ ceramics can be explained as follow: It is well known that Yb metal can be dissolved in liquid ammonia to form Yb^{2+} ions. Therefore, it would be expected that only Yb^{2+} ions exist in Yb doped amorphous $\text{Si}_3\text{B}_3\text{N}_7$ ceramics synthesized via the metal route. However, the diffuse reflection spectra in Figure 5.89 show that trivalent Yb ions are present in all cases (the absorptions in the near-IR region). A possible explanation for this has been reported such that Yb^{2+} ions have considerably less stability in liquid ammonia than Eu^{2+} ions. This results in a mixture of $\text{Yb}(\text{NH}_2)_2$ and $\text{Yb}(\text{NH}_2)_3$ according to following reaction [352]:



Therefore, according to this reaction, Yb^{2+} ions in liquid ammonia are partially converted to Yb^{3+} ions during preparation via the metal route, leading to the absorptions observed in the near-IR region in the diffuse reflection spectra (Figure 5.89).

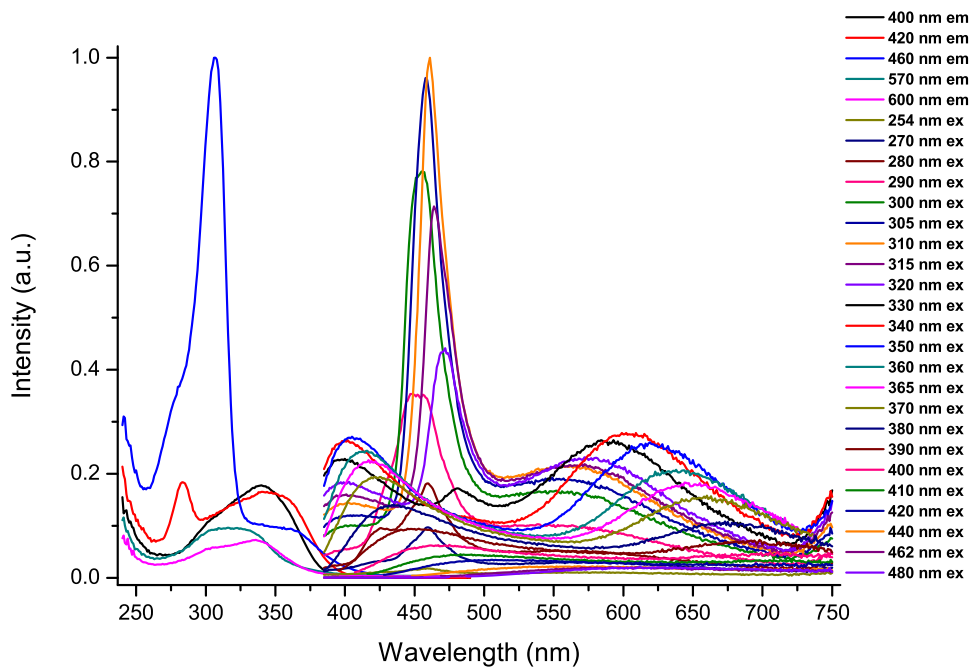


Figure 5.90.: Photoluminescence spectra of Yb doped amorphous $\text{Si}_3\text{B}_3\text{N}_7$ ceramic via the metal route at different excitation and emission wavelengths.

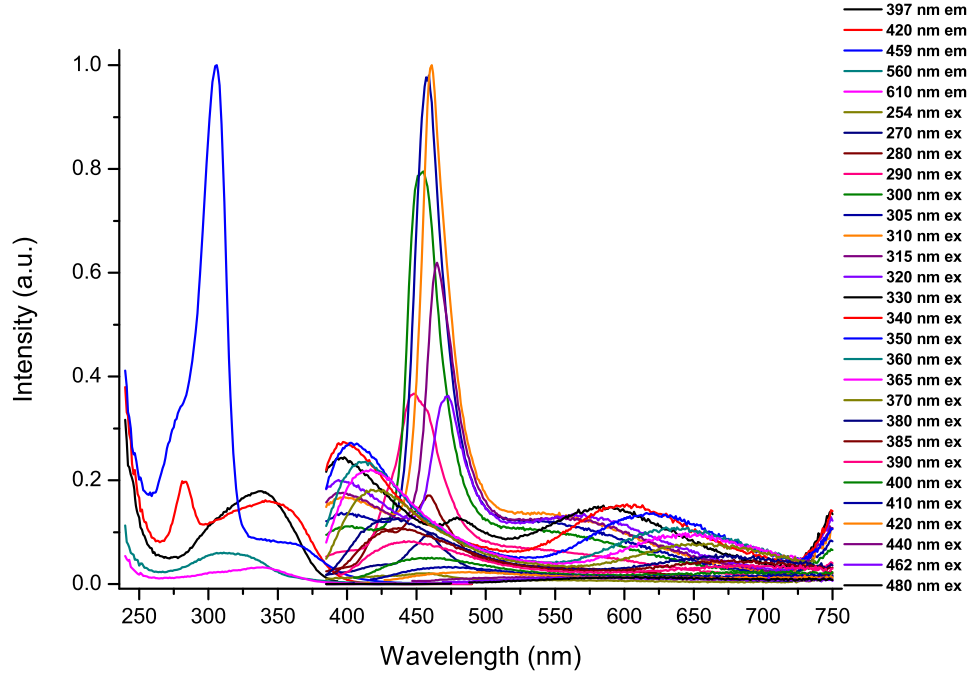


Figure 5.91.: Photoluminescence spectra of Yb doped amorphous $\text{Si}_3\text{B}_3\text{N}_7$ ceramic via the organometallic route at different excitation and emission wavelengths.

Photoluminescence spectra of Yb doped amorphous $\text{Si}_3\text{B}_3\text{N}_7$ ceramics prepared via both the metal and organometallic routes are presented in Figure 5.90 and Figure 5.91, respectively. Although the diffuse reflection spectra shows the presence of a substantial amount of Yb^{2+} ions, no Yb^{2+} emission due to the $4f^{13}5d \rightarrow 4f^{14}$ transition has been observed in the visible region of the spectrum for both routes, deduced from a comparison with the photoluminescence spectrum of undoped and Yb doped amorphous $\text{Si}_3\text{B}_3\text{N}_7$ ceramics. Moreover, photoluminescence spectra also show that all Yb doped samples exhibit the same excitation and emission behavior as the undoped $\text{Si}_3\text{B}_3\text{N}_7$ matrix. Therefore, it is inferred that the same discussions for the photoluminescence properties of the undoped amorphous $\text{Si}_3\text{B}_3\text{N}_7$ ceramic are valid for all Yb doped samples (see Section 5.2).

The lack of Yb^{2+} emission most probably resulted from the strong temperature quenching that is a common problem in Yb-doped materials. Yb^{2+} luminescence has been reported for some borates, sulphates and phosphates but no luminescence was reported for calcium oxides, alkaline-earth aluminates and silicates [353]. The lower quenching temperatures of Yb^{2+} luminescence can be explained by thermally activated photoionization at relatively low temperatures. This peculiar behavior of Yb^{2+} could be deduced by ionization from the lowest excited state to the conduction band at higher temperatures. Quite recently, similar behavior has been reported by Hintzen et al. such that no Yb^{2+} luminescence was observed for Yb doped Y-Si-Al-O-N glasses [351]. However,

Sekiguchi et al. have recently reported that when Y was replaced with Li, Mg and Ca in Si-Al-O-N glasses, broad emissions due to Yb^{2+} ions has been observed at 537 nm, 543 nm and 549 nm, respectively [354, 355, 356]. Furthermore, Bachmann et. al. have recently observed an anomalous Yb^{2+} emission at 615 nm in $\text{SrSi}_2\text{O}_2\text{N}_2$ host material, which was characterized by a large Stokes shift and low quenching temperature [357]. The authors claimed that when the fd state was at energies higher than the conduction band edge, excitation into the fd state was followed by photoionization and trapping of the electron close to the lanthanide impurity forming an impurity-trapped exciton state. Thus, this anomalous emission was ascribed to be an Yb^{2+} -trapped exciton luminescence.

5.20. Yb/Eu Codoped Amorphous $\text{Si}_3\text{B}_3\text{N}_7$ Matrix

Powder X-ray diffractograms and diffuse reflection spectra of Yb/Eu codoped amorphous $\text{Si}_3\text{B}_3\text{N}_7$ ceramics were presented in Figure 5.87 and Figure 5.89, respectively. Similar to Yb doped amorphous $\text{Si}_3\text{B}_3\text{N}_7$ ceramics, the diffuse reflection spectra in Figure 5.89 revealed that Yb ions are both in divalent and trivalent states in Yb/Eu codoped samples (see Section 5.19). The diffuse reflection spectra of the codoped samples, regardless of the preparation route, exhibited characteristic $4f \rightarrow 4f$ transitions of Yb^{3+} ions at 915 nm and 980 nm. In addition, the broad absorption band extended up to around 500 nm with respect to the absorption of $\text{Si}_3\text{B}_3\text{N}_7$ matrix, is ascribed to the $4f^{14} \rightarrow 4f^{13}5d$ transition of Yb^{2+} ions together with the $4f^7 \rightarrow 4f^65d$ transition of Eu^{2+} ions.

Photoluminescence spectra of Yb/Eu codoped amorphous $\text{Si}_3\text{B}_3\text{N}_7$ ceramics, prepared via both the organometallic ($\text{Yb}[\text{N}(\text{Si}(\text{CH}_3)_2)_3]_3$ and Eu metal were used) and the metal (Yb and Eu metals were used) routes, are shown in Figure 5.92 and Figure 5.93, respectively. As seen from Figure 5.92 and Figure 5.93, the same emission profiles with Eu^{2+} doped sample (see Figure 5.15) have been obtained for Yb/Eu codoped amorphous $\text{Si}_3\text{B}_3\text{N}_7$ ceramics. Therefore, the same discussions for the photoluminescence properties of Eu^{2+} doped amorphous $\text{Si}_3\text{B}_3\text{N}_7$ ceramic are valid for Yb/Eu codoped samples (see Section 5.2). It is implied that no emission has been obtained from Yb^{2+} ions in Yb/Eu codoped amorphous $\text{Si}_3\text{B}_3\text{N}_7$ ceramics as in the case for Yb doped samples. The same reasons are suggested for the lack of Yb^{2+} emissions in Yb/Eu codoped amorphous $\text{Si}_3\text{B}_3\text{N}_7$ ceramics as discussed for Yb doped samples in Section 5.19.

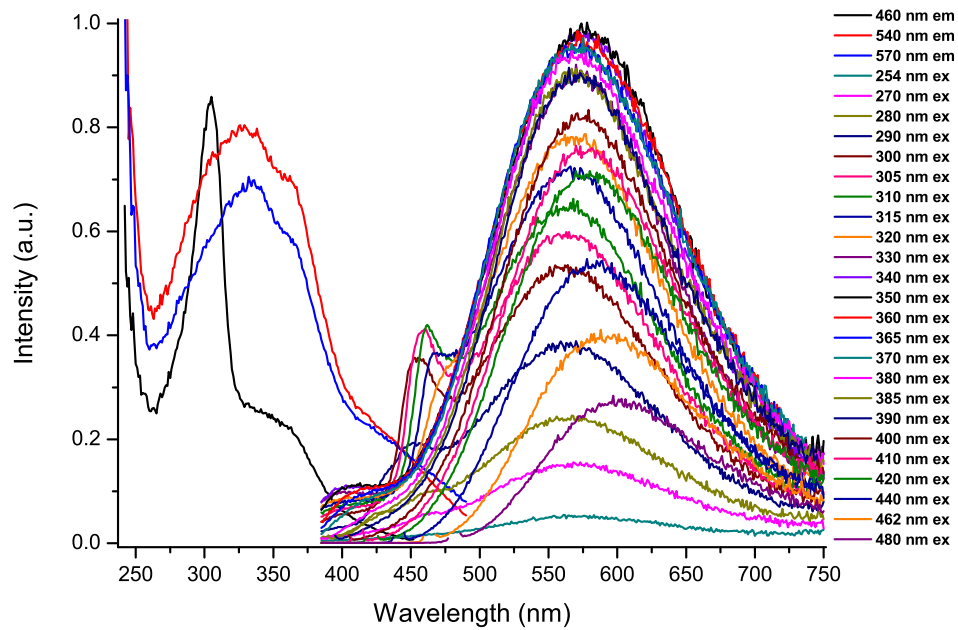


Figure 5.92.: Photoluminescence spectra of Yb/Eu codoped amorphous $\text{Si}_3\text{B}_3\text{N}_7$ ceramic prepared via the metal route at different excitation and emission wavelengths.

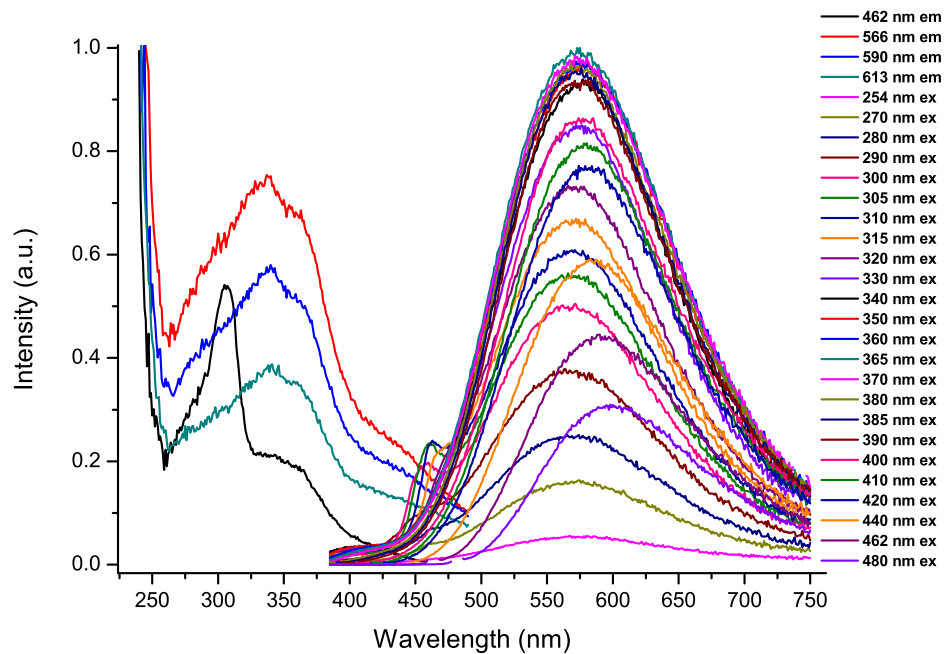


Figure 5.93.: Photoluminescence spectra of Yb/Eu codoped amorphous $\text{Si}_3\text{B}_3\text{N}_7$ ceramic prepared via the organometallic route at different excitation and emission wavelengths.

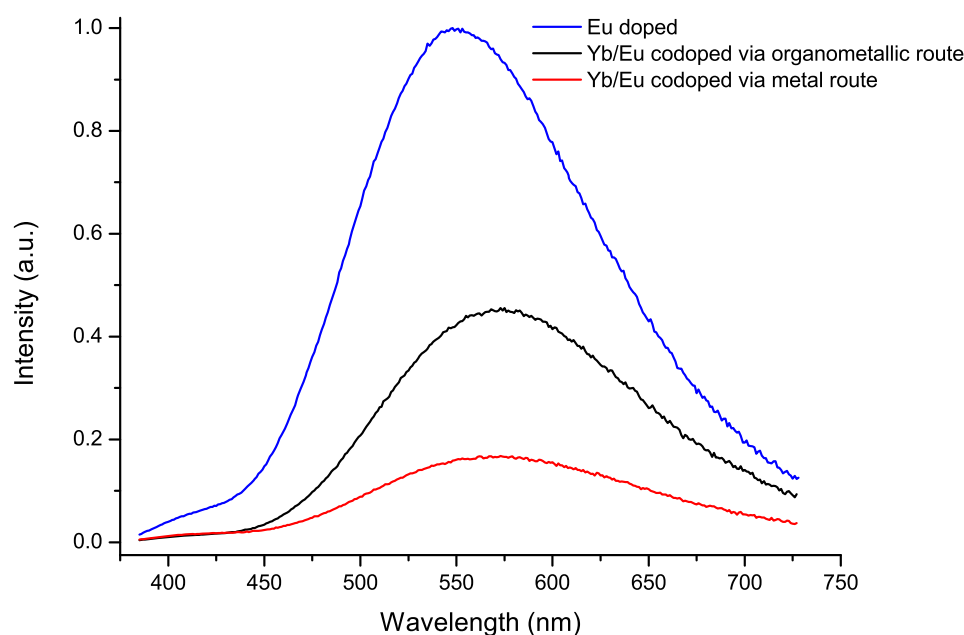


Figure 5.94.: Emission spectra of Eu doped and Yb/Eu codoped amorphous $\text{Si}_3\text{B}_3\text{N}_7$ ceramics measured at 365 nm excitation wavelength.

It has also been observed that codoping of Yb ions into the amorphous $\text{Si}_3\text{B}_3\text{N}_7$ host matrix together with the Eu^{2+} ions resulted a significant decrease in intensity of Eu^{2+} emission (Figure 5.94). The codoped sample synthesized via the metal route (obtained from 0.0535 g Eu metal and 0.1215 g Yb metal) had lower intensity, which included potentially more Yb^{2+} ions compared to the codoped sample obtained via the organometallic route (obtained from 0.055 g Eu metal and 0.1527 g $\text{Yb}[\text{N}(\text{Si}(\text{CH}_3)_3)_2]_3$). Furthermore, both codoped samples have lower emission intensities than Eu^{2+} doped sample (obtained from 0.0522 g Eu metal). This significant decrease in emission intensities was most probably caused by the absorption of some of the incident light by the Yb^{2+} ions, which resulted in non-radiative emissions.

5.21. Sn Doped Amorphous $\text{Si}_3\text{B}_3\text{N}_7$ Matrix

Sn^{2+} is a ns^2 -type luminescent center. This type of ion usually shows absorption bands labeled as A, B and C in the order of increasing energy, due to the transitions of $^1\text{S}_0 \rightarrow ^3\text{P}_1$, $^1\text{S}_0 \rightarrow ^3\text{P}_2$ and $^1\text{S}_0 \rightarrow ^1\text{P}_1$, respectively. The absorption band A is usually located in the UV range and the others are at shorter wavelengths. In ns^2 -type ions, luminescence in the visible region generally results from the transition in band A ($^3\text{P}_1 \rightarrow ^1\text{S}_0$). To illustrate, $\text{Sr}_2\text{P}_2\text{O}_7:\text{Sn}^{2+}$ has been reported to have excitation bands at 210 nm (band C), 233 nm

(band B) and 250 nm (band A), and exhibited an emission band at 464 nm with half-width of 105 nm measured at 250 nm excitation [192]. Similarly, $\text{SrB}_6\text{O}_{10}:\text{Sn}^{2+}$ had excitation bands at 260 nm (band B) and 325 nm (band A), and showed an emission band at 420 nm with half-width of 68 nm measured at 325 nm excitation [192].

Powder X-ray diffractogram for Sn^{2+} doped amorphous $\text{Si}_3\text{B}_3\text{N}_7$ ceramic is shown in Figure 5.95. Diffuse reflection and photoluminescence spectra of Sn^{2+} doped amorphous $\text{Si}_3\text{B}_3\text{N}_7$ ceramic are presented in Figure 5.96 and Figure 5.97, respectively. It is clearly seen in Figure 5.97 that emission profiles of Sn^{2+} doped sample appear different from that of undoped samples (see Figure 5.2). Comparing the excitation spectra of undoped and Sn^{2+} doped amorphous $\text{Si}_3\text{B}_3\text{N}_7$ ceramics, measured at 480 nm emission, an additional excitation band at 337 nm is assigned to the absorption band A ($^1\text{S}_0 \rightarrow ^3\text{P}_1$) of Sn^{2+} ions (Figure 5.98). This strong absorption has also been observed in the diffuse reflection spectrum in Figure 5.96. The $^3\text{P}_1 \rightarrow ^1\text{S}_0$ emission band was observed in the blue region of the spectrum ranging from 460 nm to 540 nm, depending on the excitation wavelength. To illustrate, excitation with 340 nm and 365 nm yielded broad emission bands at 481 nm and 504 nm, respectively (Figure 5.99). Furthermore, a significant red shift was observed, which might result from a strong interaction between the excited state particles and the local environment in amorphous $\text{Si}_3\text{B}_3\text{N}_7$ host matrix (see the discussion in Sections 5.1 and 5.2).

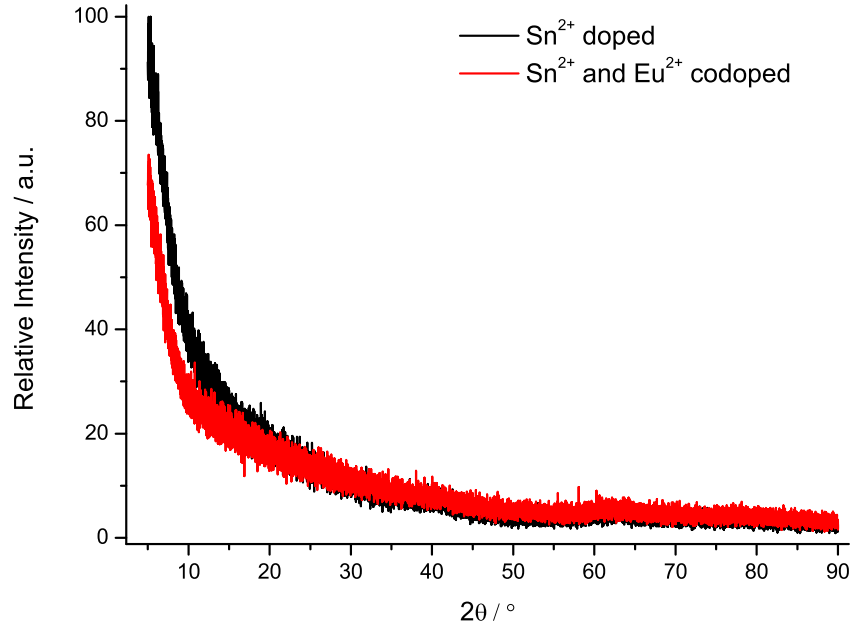


Figure 5.95.: Powder X-ray diffractograms of Sn^{2+} doped and $\text{Sn}^{2+}/\text{Eu}^{2+}$ codoped amorphous $\text{Si}_3\text{B}_3\text{N}_7$ ceramics.

5. Phosphors Based on Amorphous $\text{Si}_3\text{B}_3\text{N}_7$ Matrix

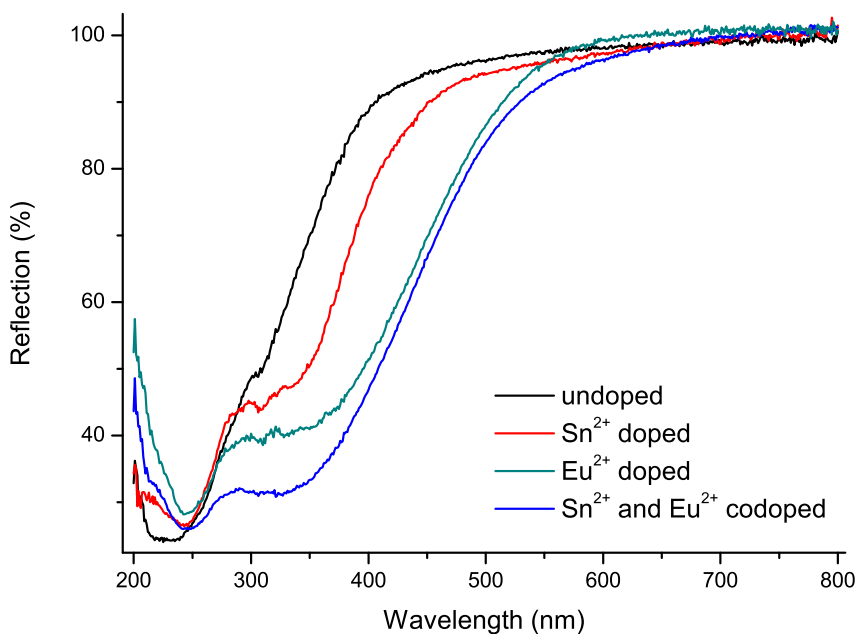


Figure 5.96.: Diffuse reflection spectra of undoped, Sn^{2+} doped, Eu^{2+} doped and $\text{Sn}^{2+}/\text{Eu}^{2+}$ codoped amorphous $\text{Si}_3\text{B}_3\text{N}_7$ ceramics.

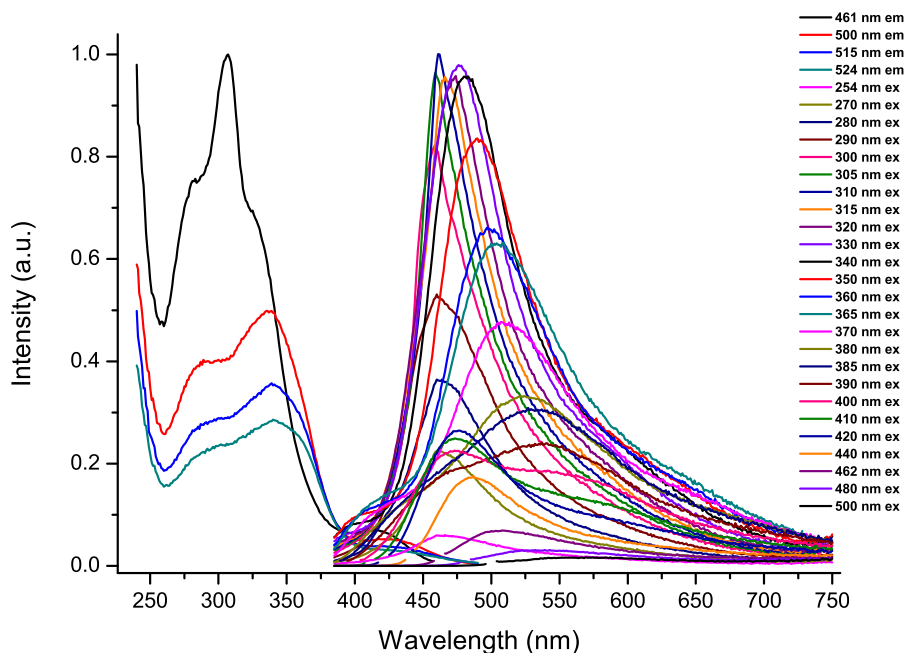


Figure 5.97.: Photoluminescence spectra of Sn^{2+} doped amorphous $\text{Si}_3\text{B}_3\text{N}_7$ ceramic at different excitation and emission wavelengths.

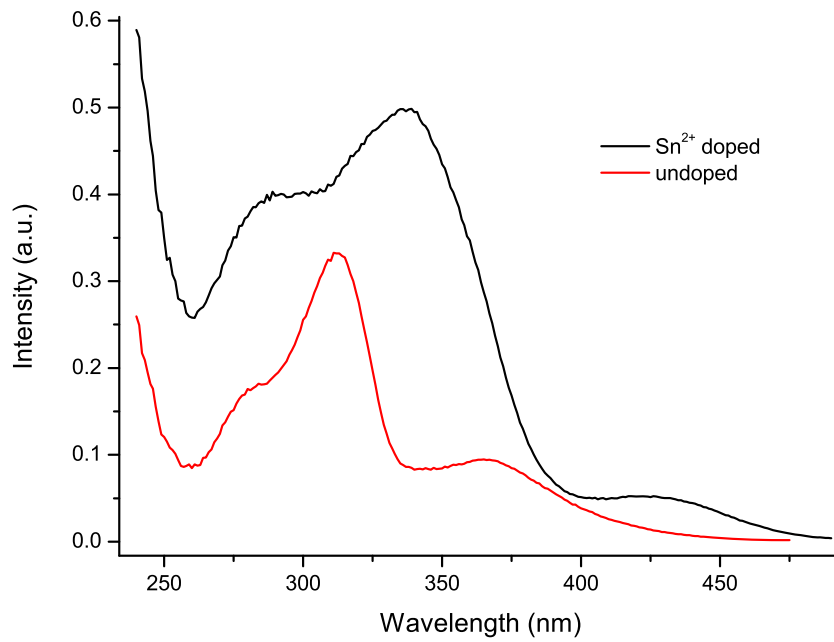


Figure 5.98.: Excitation spectra of undoped and Sn^{2+} doped amorphous $\text{Si}_3\text{B}_3\text{N}_7$ ceramics at 480 nm emission.

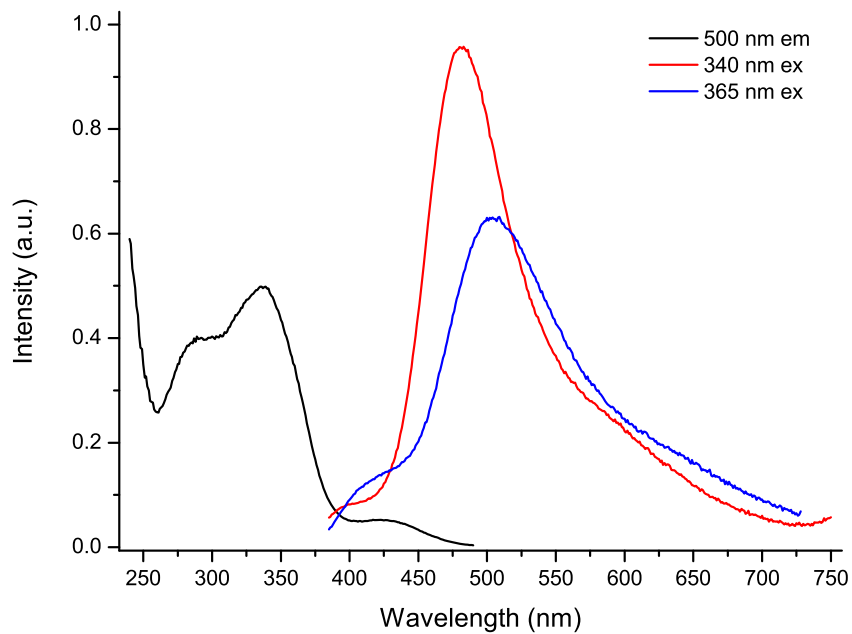


Figure 5.99.: Excitation spectrum at 500 nm emission wavelength (black line) and emission spectra at 340 nm (red line) and 365 nm (blue line) excitation wavelengths of Sn^{2+} doped amorphous $\text{Si}_3\text{B}_3\text{N}_7$ ceramic.

5.22. Sn/Eu Codoped Amorphous $\text{Si}_3\text{B}_3\text{N}_7$ Matrix

Powder X-ray pattern and diffuse reflection spectrum of $\text{Sn}^{2+}/\text{Eu}^{2+}$ codoped amorphous $\text{Si}_3\text{B}_3\text{N}_7$ ceramic were presented in Figure 5.95 and Figure 5.96, respectively. Diffuse reflection spectrum in Figure 5.96 indicates that $\text{Sn}^{2+}/\text{Eu}^{2+}$ codoped samples have broader absorption bands than Eu^{2+} doped, and Sn^{2+} doped samples. Photoluminescence spectra of $\text{Sn}^{2+}/\text{Eu}^{2+}$ codoped amorphous $\text{Si}_3\text{B}_3\text{N}_7$ ceramic are shown in Figure 5.100. It is clearly seen that the same emission profiles as in Eu^{2+} doped sample (see Figure 5.15) have been observed for $\text{Sn}^{2+}/\text{Eu}^{2+}$ codoped sample. Therefore, the same discussions for the photoluminescence properties of Eu^{2+} doped amorphous $\text{Si}_3\text{B}_3\text{N}_7$ ceramic are valid for $\text{Sn}^{2+}/\text{Eu}^{2+}$ codoped sample (see Section 5.2).

Figure 5.101 is presented to compare the photoluminescence properties of Sn^{2+} doped, Eu^{2+} doped, and $\text{Sn}^{2+}/\text{Eu}^{2+}$ codoped amorphous $\text{Si}_3\text{B}_3\text{N}_7$ ceramics (emission spectra were measured at 365 nm excitation wavelength and excitation spectra were measured at the corresponding maximum emission wavelengths). In comparison with the emission spectra of Sn^{2+} doped sample, $\text{Sn}^{2+}/\text{Eu}^{2+}$ codoped sample shows no emission at around 480 nm but rather exhibits a broad emission band similar to Eu^{2+} doped sample with lower intensity. A possible explanation for this phenomenon is that the blue emission due to Sn^{2+} ions is simultaneously absorbed by Eu^{2+} ions.

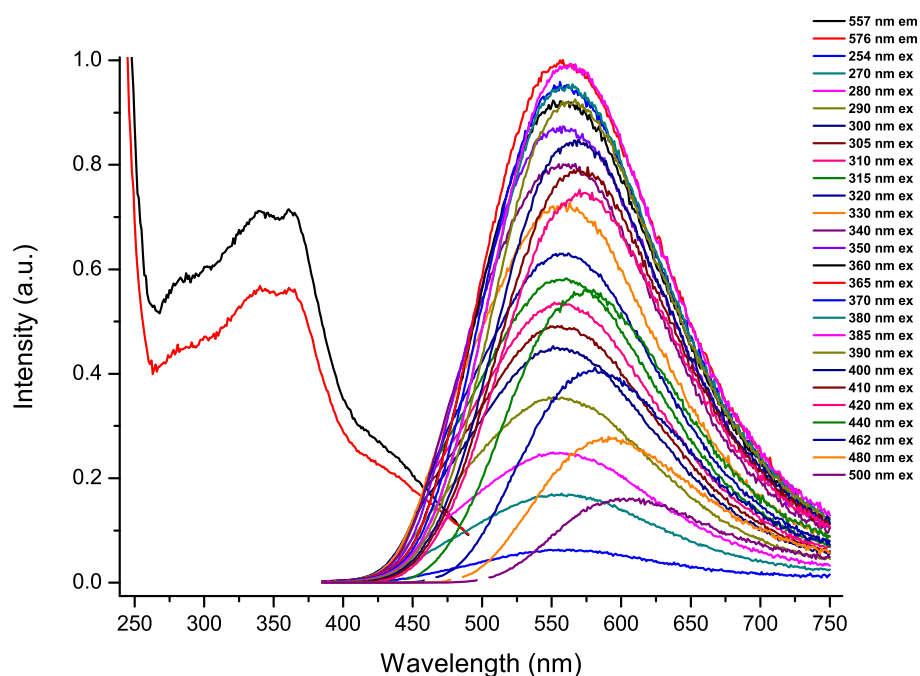


Figure 5.100.: Photoluminescence spectra of $\text{Sn}^{2+}/\text{Eu}^{2+}$ codoped amorphous $\text{Si}_3\text{B}_3\text{N}_7$ ceramic at different excitation and emission wavelengths.

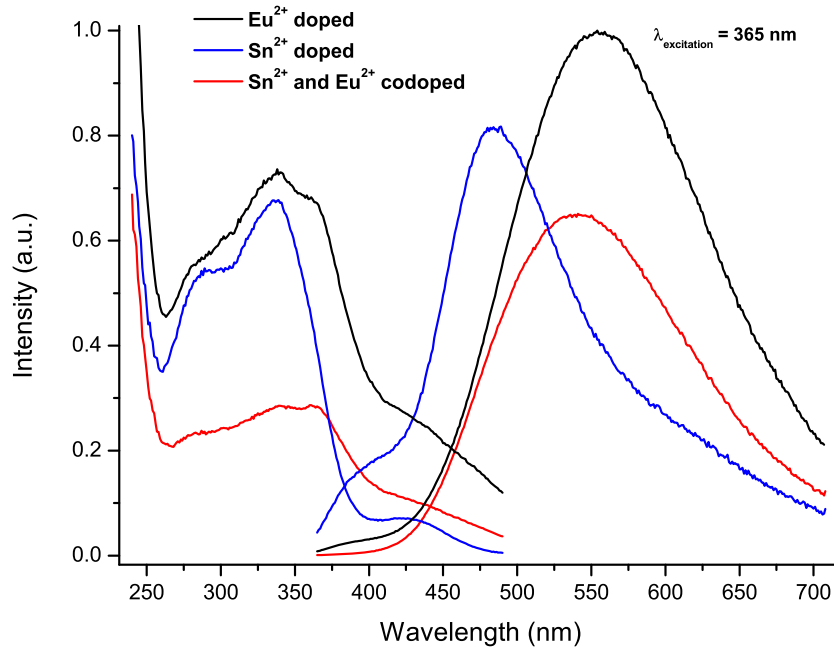


Figure 5.101.: Excitation spectra at maximum emission wavelengths and emission spectra at 365 nm excitation wavelength of Eu^{2+} doped, Sn^{2+} doped and $\text{Sn}^{2+}/\text{Eu}^{2+}$ codoped amorphous $\text{Si}_3\text{B}_3\text{N}_7$ ceramics.

5.23. M Doped Amorphous $\text{Si}_3\text{B}_3\text{N}_7$ Matrices, where $M = \text{Sr}, \text{Ba}, \text{Y}$ and La

Ca^{2+} , Sr^{2+} , Ba^{2+} , Y^{3+} and La^{3+} ions do not show luminescent properties but are widely applied as constituent cations in host materials to be substituted by or as charge compensator for activator ions. These ions have comparable diameters with lanthanide ions and thus allow replacement with lanthanide ions in the crystal structure. Crystals which constitute Ca^{2+} , Sr^{2+} and Ba^{2+} ions as building units are widely studied in order to obtain efficient luminescent materials, which are doped with divalent lanthanide ions. For example, Eu^{2+} doped $\text{M}_2\text{Si}_5\text{N}_8$ ($M = \text{Ca}, \text{Sr}$ and Ba) phosphors are one of the most promising red phosphors for pc-LEDs [257]. Similarly, crystal lattices which constitute Y^{3+} and La^{3+} ions are frequently considered to be doped with trivalent lanthanides. To illustrate, Ce^{3+} doped $\text{Y}_3\text{Al}_5\text{O}_{12}$ (YAG:Ce) is still one of the most widely used phosphor in pc-LEDs and Nd^{3+} doped $\text{Y}_3\text{Al}_5\text{O}_{12}$ (YAG:Nd) is still one of the best laser material. In the present study, Sr^{2+} , Ba^{2+} , Y^{3+} and La^{3+} ions are incorporated into amorphous $\text{Si}_3\text{B}_3\text{N}_7$ host matrix either alone or together with Eu^{2+} ions in order to investigate the luminescence properties.

5. Phosphors Based on Amorphous $\text{Si}_3\text{B}_3\text{N}_7$ Matrix

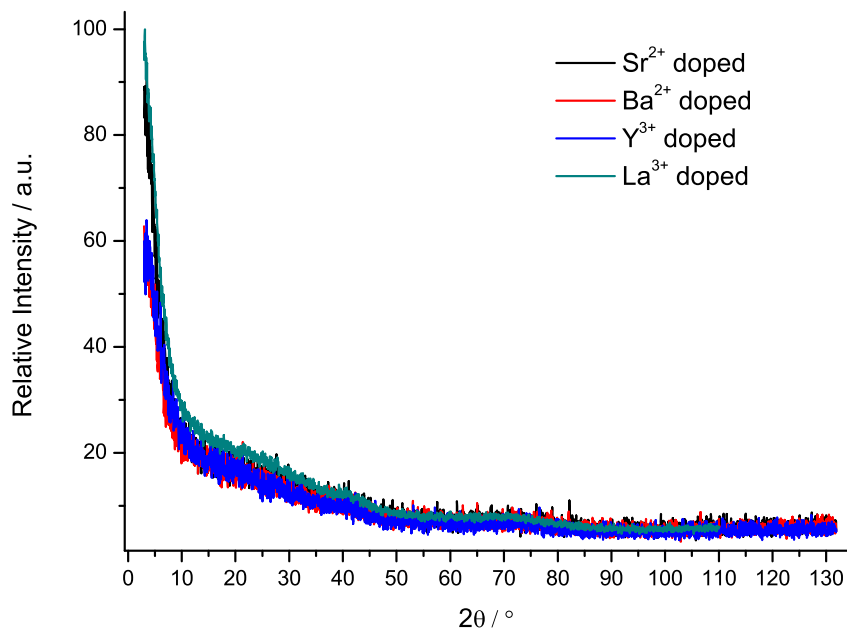


Figure 5.102.: Powder X-ray diffractograms of Sr²⁺ doped, Ba²⁺ doped, Y³⁺ doped and La³⁺ doped amorphous $\text{Si}_3\text{B}_3\text{N}_7$ ceramics.

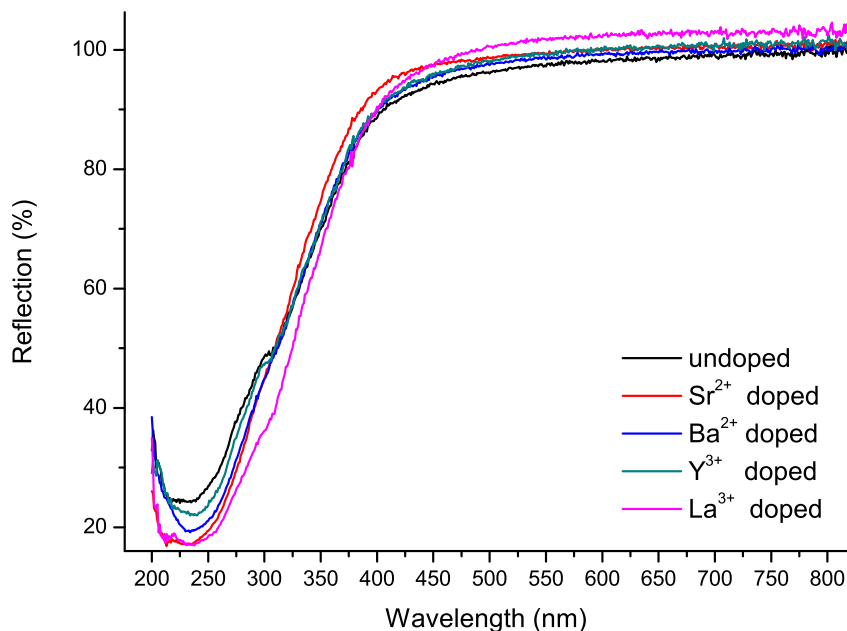


Figure 5.103.: Diffuse reflection spectra of undoped, Sr²⁺ doped, Ba²⁺ doped, Y³⁺ doped and La³⁺ doped amorphous $\text{Si}_3\text{B}_3\text{N}_7$ ceramics.

As Sr and Ba metals are soluble in liquid ammonia, these ions were incorporated into amorphous Si₃B₃N₇ host matrix via the metal route. On the other hand, Y³⁺ and La³⁺ ions were incorporated via the organometallic route. Powder X-ray diffractograms and diffuse reflection spectra of Sr²⁺ doped, Ba²⁺ doped, Y³⁺ doped and La³⁺ doped amorphous Si₃B₃N₇ host matrices are shown in Figure 5.102 and Figure 5.103, respectively. Diffuse reflection spectra of these amorphous samples have almost the same pattern with the undoped one. However, they all have stronger absorption at shorter wavelengths between 200 nm and 300 nm when compared to the undoped sample.

Photoluminescence spectra of Sr²⁺ doped, Ba²⁺ doped, Y³⁺ doped and La³⁺ doped amorphous Si₃B₃N₇ ceramics are presented in Figure 5.104, Figure 5.105, Figure 5.106 and Figure 5.107, respectively. As seen from those figures, all these samples show the same photoluminescence behavior as the undoped amorphous Si₃B₃N₇ ceramic (see Figure 5.2), indicating that they are not luminescent active centers. Therefore, it is inferred that the same discussions for the photoluminescence properties of the undoped amorphous Si₃B₃N₇ ceramic are valid for Sr²⁺ doped, Ba²⁺ doped, Y³⁺ doped and La³⁺ doped samples (see Section 5.2).

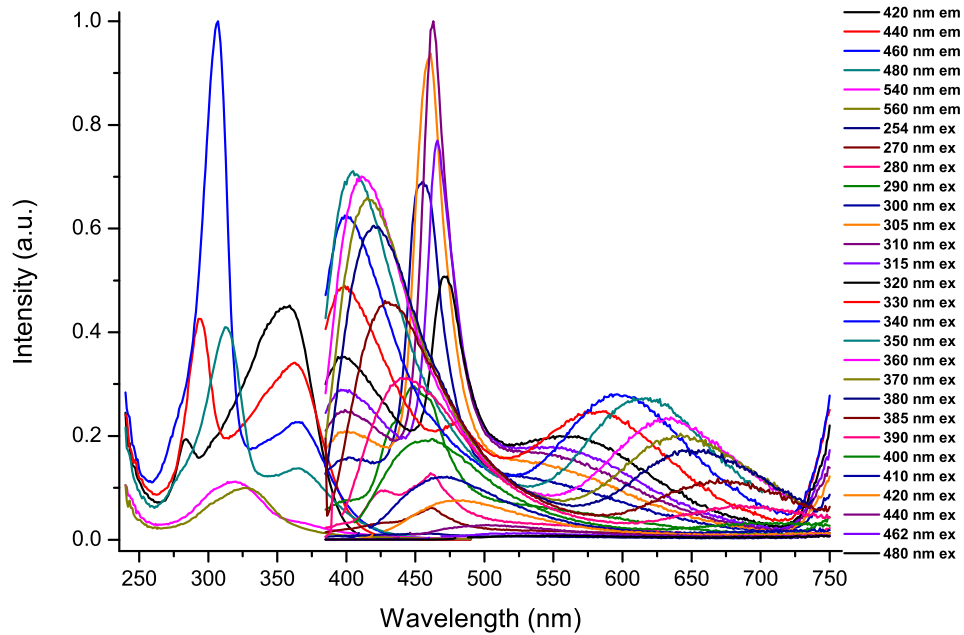


Figure 5.104.: Photoluminescence spectra of Sr²⁺ doped amorphous Si₃B₃N₇ ceramic at different excitation and emission wavelengths.

5. Phosphors Based on Amorphous $\text{Si}_3\text{B}_3\text{N}_7$ Matrix

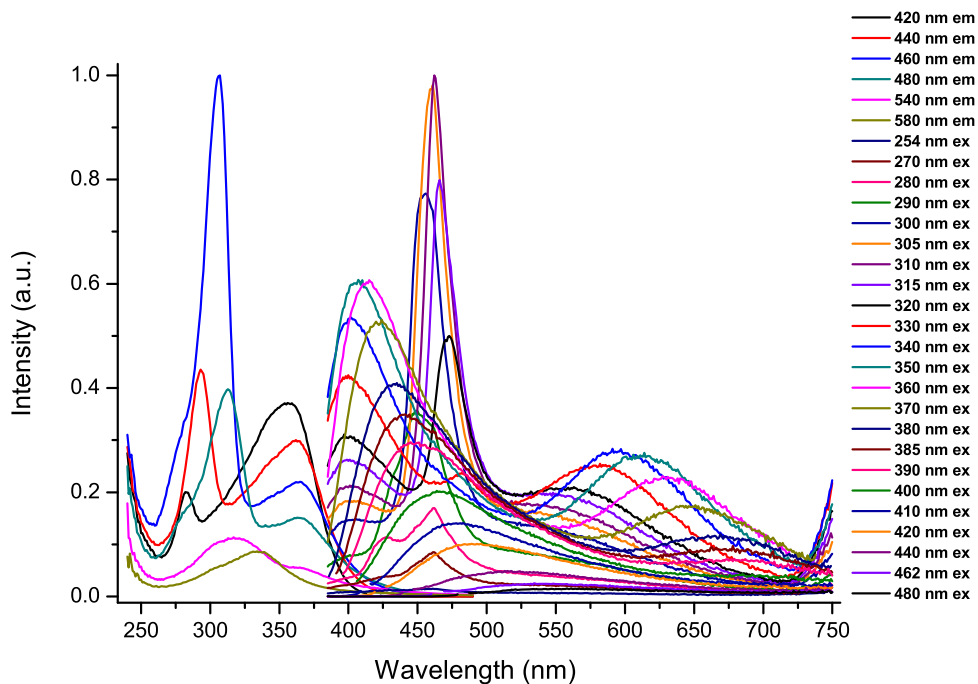


Figure 5.105.: Photoluminescence spectra of Ba²⁺ doped amorphous Si₃B₃N₇ ceramic at different excitation and emission wavelengths.

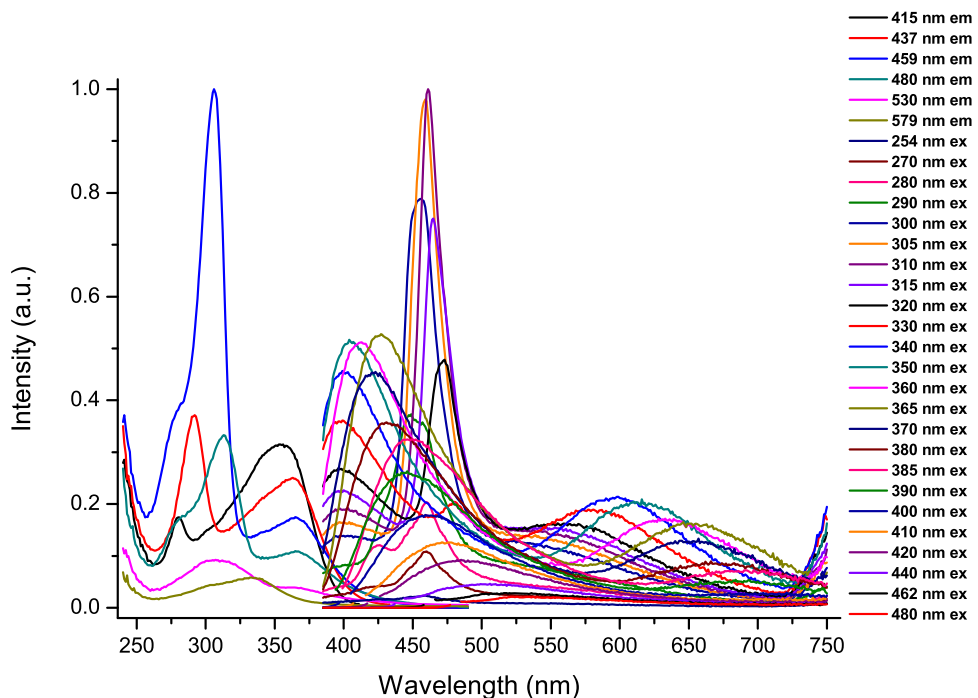


Figure 5.106.: Photoluminescence spectra of Y³⁺ doped amorphous Si₃B₃N₇ ceramic at different excitation and emission wavelengths.

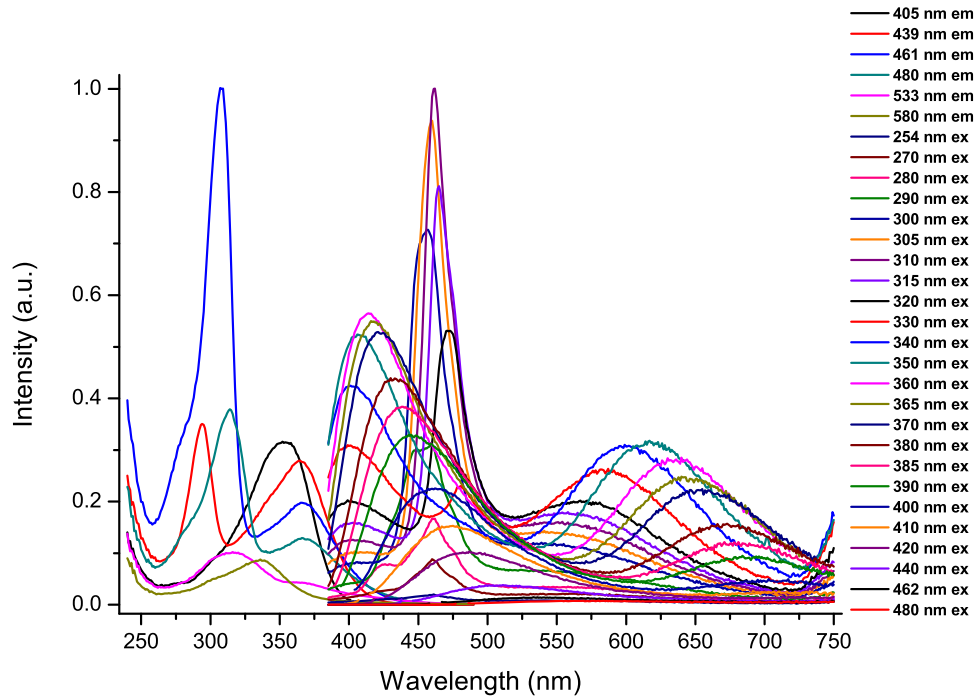


Figure 5.107.: Photoluminescence spectra of La^{3+} doped amorphous $\text{Si}_3\text{B}_3\text{N}_7$ ceramic at different excitation and emission wavelengths.

5.24. M/Eu Codoped Amorphous $\text{Si}_3\text{B}_3\text{N}_7$ Matrices, where $M = \text{Sr}, \text{Ba}, \text{Y}$ and La

As it has been discussed in Section 5.23, Sr^{2+} , Ba^{2+} , Y^{3+} and La^{3+} ions are not luminescent active centers but widely used as substituting ions with activator ions in crystal host lattices. Since, in the present work, an amorphous material has been chosen to host the activator ions, Sr^{2+} , Ba^{2+} , Y^{3+} and La^{3+} ions were not expected to act as substituting ions with Eu^{2+} ions but they are rather expected to be homogeneously distributed among the Eu^{2+} ions which might lead to reduce the self absorption of neighboring Eu^{2+} ions and thus might increase the overall efficiency. Therefore, the effects of Sr^{2+} , Ba^{2+} , Y^{3+} and La^{3+} ions on the luminescence of Eu^{2+} ions in the amorphous $\text{Si}_3\text{B}_3\text{N}_7$ host matrices are investigated.

Eu^{2+} , Sr^{2+} and Ba^{2+} ions were obtained by dissolving the respective metals in liquid ammonia (metal route). On the other hand, Y^{3+} and La^{3+} ions were obtained from the $\text{Y}[\text{N}(\text{Si}(\text{CH}_3)_2)_3]_3$ and $\text{La}[\text{N}(\text{Si}(\text{CH}_3)_2)_3]_3$ compounds, respectively (organometallic route). Powder X-ray diffraction and diffuse reflection spectra of M/ Eu^{2+} codoped amorphous $\text{Si}_3\text{B}_3\text{N}_7$ ceramics, where $M = \text{Sr}^{2+}$, Ba^{2+} , Y^{3+} and La^{3+} , are presented in Figure 5.108 and Figure 5.109, respectively. Diffuse reflection spectra of these amorphous codoped

5. Phosphors Based on Amorphous $\text{Si}_3\text{B}_3\text{N}_7$ Matrix

samples have almost the same pattern as the Eu^{2+} doped sample. They all show stronger absorption at shorter wavelengths between 200 nm and 350 nm than Eu^{2+} doped sample. $\text{Ba}^{2+}/\text{Eu}^{2+}$ codoped sample appears to extend the absorption band to longer wavelengths between 350 nm and 530 nm but this is attributed to higher amount of Eu^{2+} ions: the codoped sample was prepared with 0.0632 g Eu metal, whereas the Eu^{2+} doped sample was prepared with 0.0518 g Eu metal (see Section 5.25).

Photoluminescence spectra of $\text{Sr}^{2+}/\text{Eu}^{2+}$ codoped, $\text{Ba}^{2+}/\text{Eu}^{2+}$ codoped, $\text{Y}^{3+}/\text{Eu}^{2+}$ codoped and $\text{La}^{3+}/\text{Eu}^{2+}$ codoped amorphous $\text{Si}_3\text{B}_3\text{N}_7$ ceramics are presented in Figure 5.110, Figure 5.111, Figure 5.112 and Figure 5.113, respectively. As seen from those figures, all these samples show the same photoluminescence patterns as the Eu^{2+} doped amorphous $\text{Si}_3\text{B}_3\text{N}_7$ ceramic (Figure 5.15). Therefore, the same discussions for the photoluminescence properties of Eu^{2+} doped amorphous $\text{Si}_3\text{B}_3\text{N}_7$ ceramic are valid for M/Eu^{2+} codoped amorphous $\text{Si}_3\text{B}_3\text{N}_7$ ceramics, where $\text{M} = \text{Sr}^{2+}, \text{Ba}^{2+}, \text{Y}^{3+}$ and La^{3+} (see Section 5.2). Figure 5.114 compares the emission spectra of Eu^{2+} doped, and M/Eu^{2+} codoped amorphous $\text{Si}_3\text{B}_3\text{N}_7$ ceramics, where $\text{M} = \text{Sr}^{2+}, \text{Ba}^{2+}, \text{Y}^{3+}$ and La^{3+} , at 365 nm excitation wavelength. As seen from the Figure 5.114, none of these ions shows any significant improvement on the luminescence efficiency of the Eu^{2+} ions in amorphous $\text{Si}_3\text{B}_3\text{N}_7$ matrix.

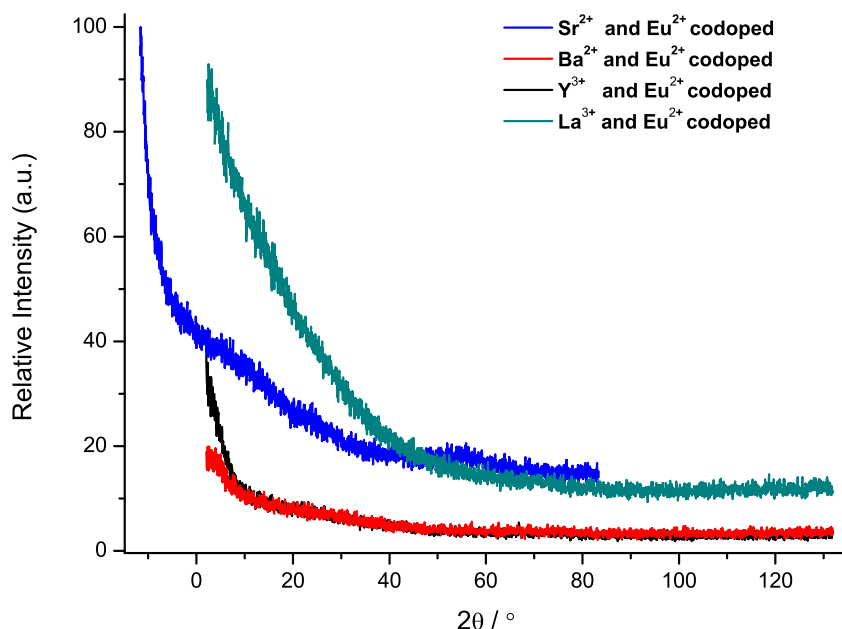


Figure 5.108.: Powder X-ray diffractograms of M/Eu^{2+} codoped amorphous $\text{Si}_3\text{B}_3\text{N}_7$ ceramics, where $\text{M} = \text{Sr}^{2+}, \text{Ba}^{2+}, \text{Y}^{3+}$ and La^{3+} .

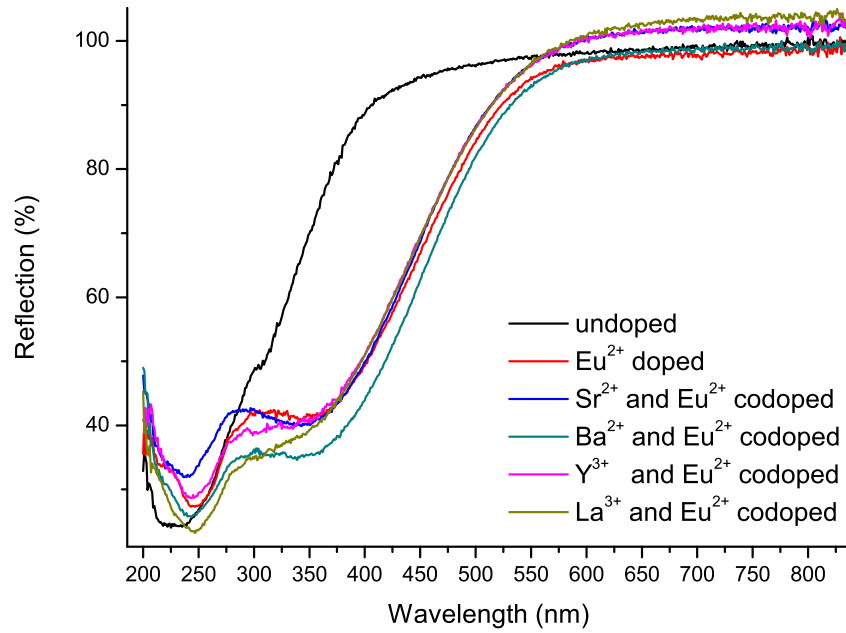


Figure 5.109.: Diffuse reflection spectra of undoped, Eu^{2+} doped and M/Eu^{2+} codoped amorphous $\text{Si}_3\text{B}_3\text{N}_7$ ceramics, where $\text{M} = \text{Sr}^{2+}$, Ba^{2+} , Y^{3+} and La^{3+} .

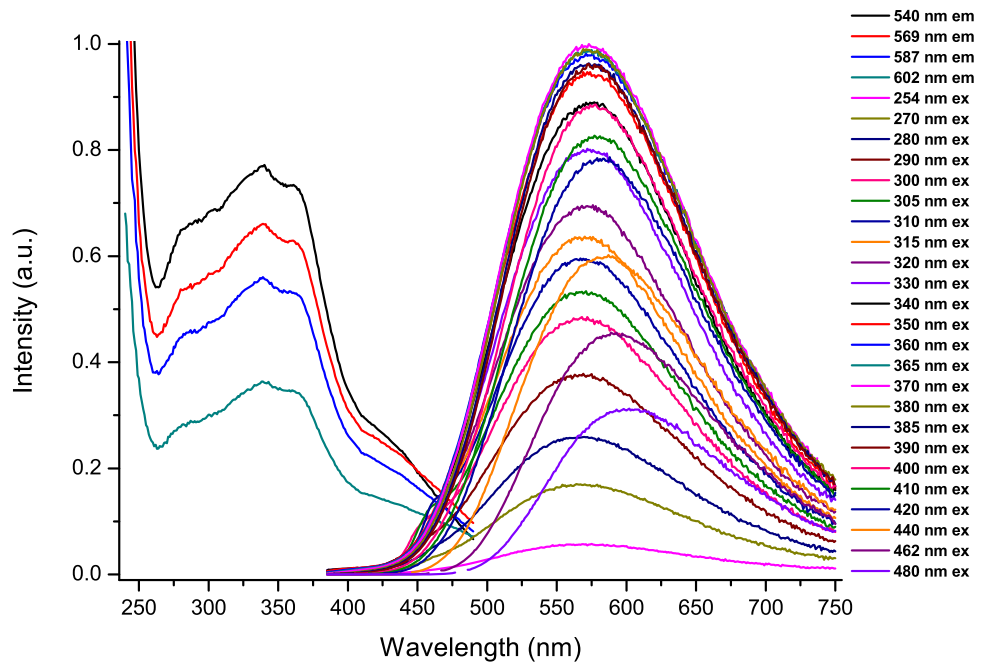


Figure 5.110.: Photoluminescence spectra of $\text{Sr}^{2+}/\text{Eu}^{2+}$ codoped amorphous $\text{Si}_3\text{B}_3\text{N}_7$ ceramic at different excitation and emission wavelengths.

5. Phosphors Based on Amorphous $\text{Si}_3\text{B}_3\text{N}_7$ Matrix

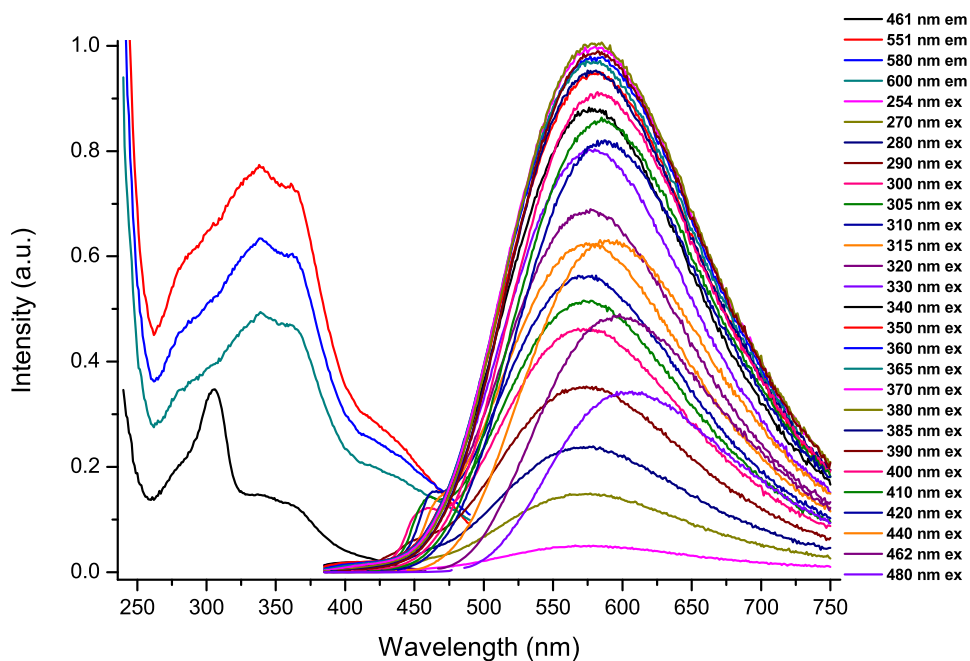


Figure 5.111.: Photoluminescence spectra of $\text{Ba}^{2+}/\text{Eu}^{2+}$ codoped amorphous $\text{Si}_3\text{B}_3\text{N}_7$ ceramic at different excitation and emission wavelengths.

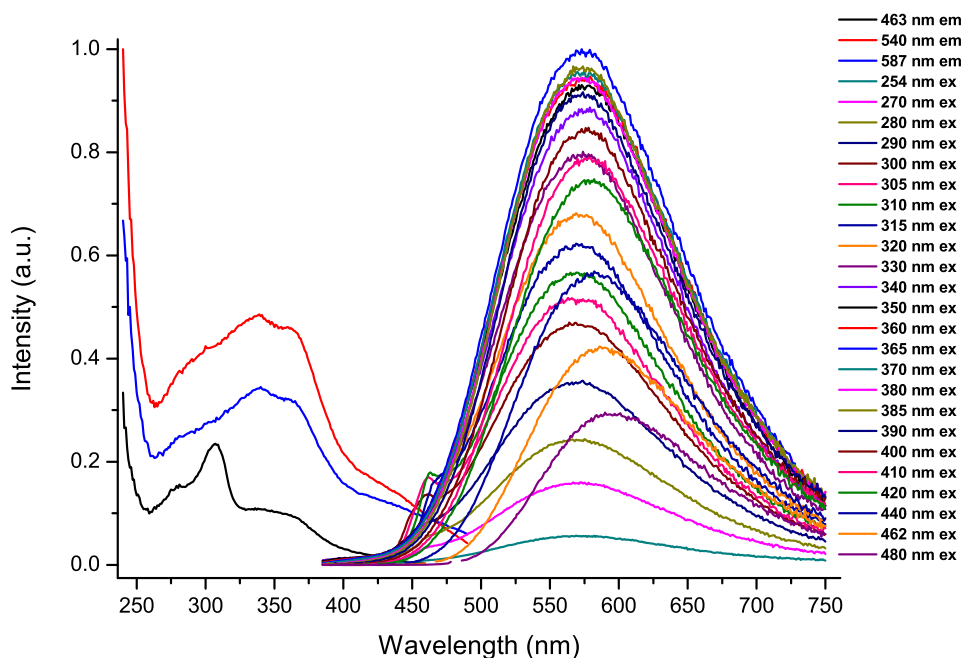


Figure 5.112.: Photoluminescence spectra of $\text{Y}^{3+}/\text{Eu}^{2+}$ codoped amorphous $\text{Si}_3\text{B}_3\text{N}_7$ ceramic at different excitation and emission wavelengths.

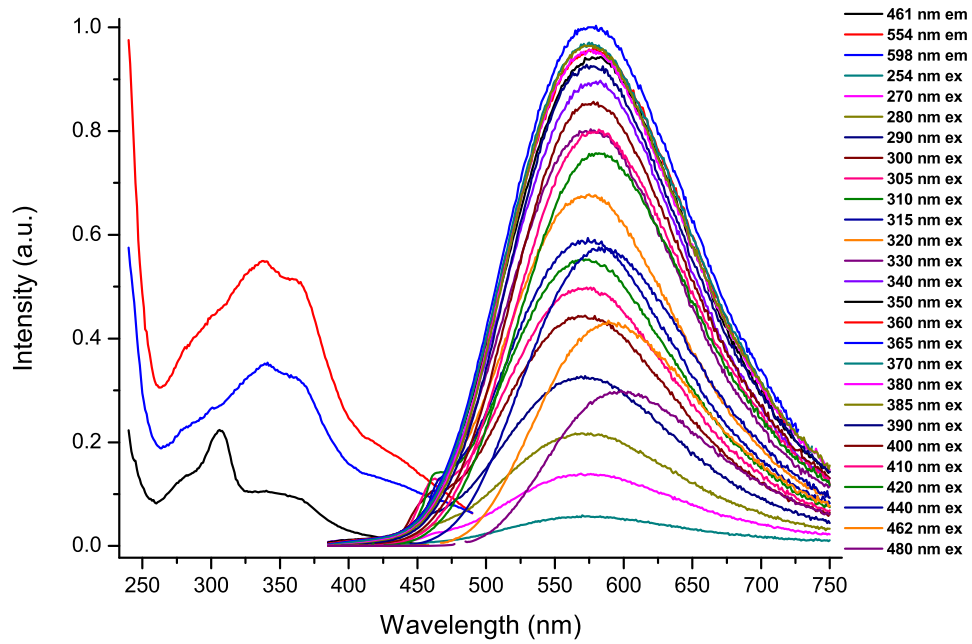


Figure 5.113.: Photoluminescence spectra of La^{3+}/Eu^{2+} codoped amorphous $Si_3B_3N_7$ ceramic at different excitation and emission wavelengths.

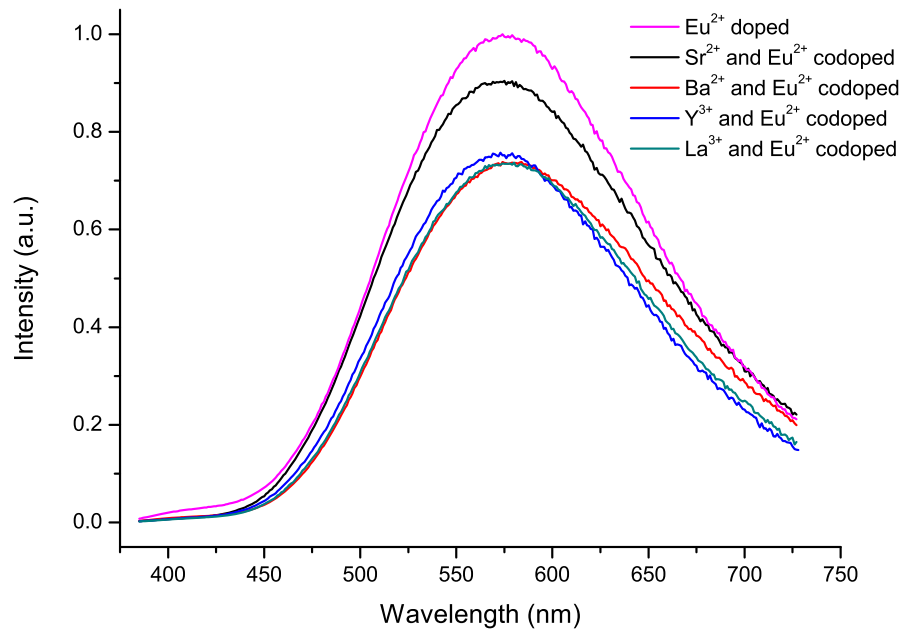


Figure 5.114.: Emission spectra of Eu^{2+} doped and M/Eu^{2+} codoped amorphous $Si_3B_3N_7$ ceramics, where $M = Sr^{2+}, Ba^{2+}, Y^{3+}$ and La^{3+} , at 365 nm excitation wavelength.

5.25. Dependence of Luminescence on the Concentration of Activators in Amorphous $\text{Si}_3\text{B}_3\text{N}_7$

Dependence of luminescence on the concentration of activator ions in amorphous $\text{Si}_3\text{B}_3\text{N}_7$ ceramics were studied for Eu^{2+} doped, Ce^{3+} doped, Tb^{3+} doped and $\text{Ce}^{3+}/\text{Eu}^{2+}$ codoped amorphous $\text{Si}_3\text{B}_3\text{N}_7$ ceramics. Eu metal or $\text{Eu}[\text{N}(\text{Si}(\text{CH}_3)_2)_3]_3$ were used as Eu^{2+} sources and $\text{Ce}[\text{N}(\text{Si}(\text{CH}_3)_2)_3]_3$ and $\text{Tb}[\text{N}(\text{Si}(\text{CH}_3)_2)_3]_3$ were used as Ce^{3+} and Tb^{3+} sources, respectively. Obviously, varying the amounts of rare earth ions incorporated into amorphous $\text{Si}_3\text{B}_3\text{N}_7$ host matrix will significantly change the local surroundings of the corresponding ions, which eventually may result in tuning the emission color of the samples.

Eu^{2+} doped amorphous $\text{Si}_3\text{B}_3\text{N}_7$ ceramics generally exhibit well developed broad emission spectra with a peak maximum value ranging from 540 nm and 640 nm and a wide excitation window between 260 nm to 480 nm, depending on the Eu^{2+} concentration (Figure 5.115). Increasing the Eu^{2+} content results in a red shift in the emission spectra (Figure 5.116). This can generally be explained by the configurational coordinate model. Figure 5.117 represents a configurational coordinate model for the energy transfer followed by reabsorption and reemission (red shift) processes between two neighboring luminescent active centers. The mechanism in this model is the same as that discussed in Figure 5.11 (see Section 5.1). The only difference is that the emitted energy from one active center is transferred and absorbed by another active center. Therefore, the degree of the red shift in emission wavelength strongly depends on the concentration of the active centers in host matrix, as the probability of energy transfer and thus the reabsorption process increases with decreasing the distance between neighboring active centers. In addition, a decrease in emission intensities was observed as Eu^{2+} concentration was increased, due to the concentration quenching (Figure 5.116). Figure 5.118 shows photos of Eu^{2+} doped amorphous $\text{Si}_3\text{B}_3\text{N}_7$ ceramics having various amounts of Eu^{2+} ions under day light and 366 nm light, indicating the red shift in emission clearly.

Similar to Eu^{2+} doped amorphous $\text{Si}_3\text{B}_3\text{N}_7$ ceramics, Ce^{3+} doped samples also exhibited well developed broad emission spectra with peak maximum value ranging from 520 nm and 580 nm and a wide excitation window between 260 nm to 480 nm, depending on the Ce^{3+} concentration (Figure 5.119). Excitation spectra of Ce^{3+} doped amorphous $\text{Si}_3\text{B}_3\text{N}_7$ ceramics generally have two peak maxima, one at 305 nm and other at 365 nm (Figure 5.119). The former is due to the absorption of the $\text{Si}_3\text{B}_3\text{N}_7$ matrix and the latter due to the absorption by Ce^{3+} ions. This was also confirmed by the diffuse reflection spectra in Figure 5.29, which showed strong absorption for all samples between 340 nm and 400 nm due to Ce^{3+} ions. Similar to Eu^{2+} doped samples, increasing the Ce^{3+}

content in amorphous $\text{Si}_3\text{B}_3\text{N}_7$ network results in a red shift in emission band (Figure 5.120). This is also considered due to an energy transfer followed by reabsorption and reemission (red shift) processes between two neighboring Ce^{3+} ions (see Figure 5.117). In addition, emission intensities also decreased when Ce^{3+} concentration was increased due to concentration quenching (Figure 5.120).

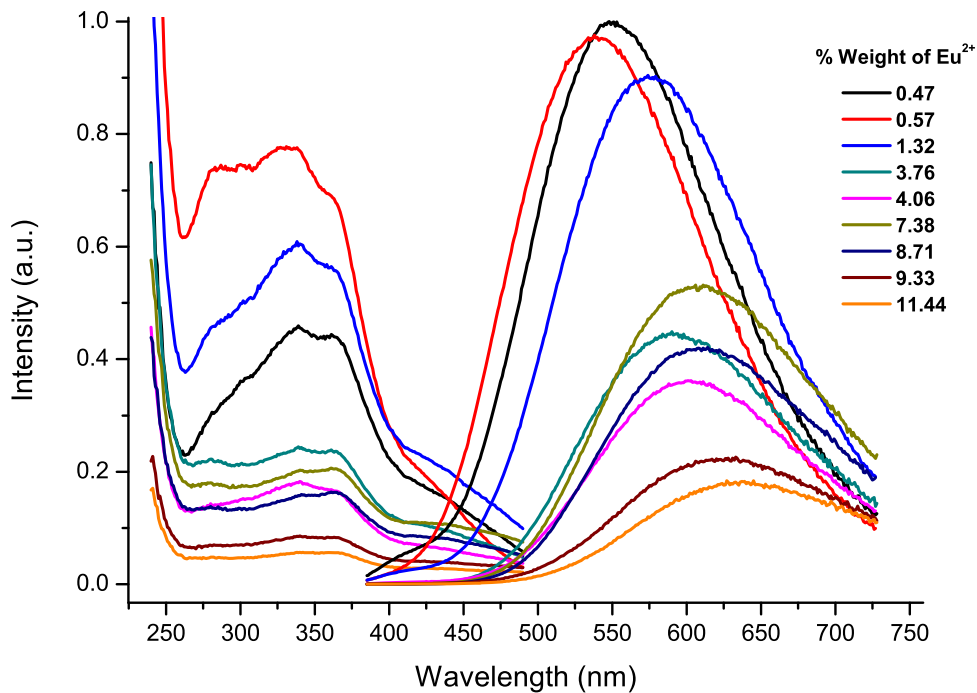


Figure 5.115.: Photoluminescence spectra of Eu^{2+} doped amorphous $\text{Si}_3\text{B}_3\text{N}_7$ ceramics having various Eu^{2+} concentration (Excitation spectra were measured at maximum emission wavelengths and emission spectra were measured at 365 nm excitation wavelength).

In the case of $\text{Ce}^{3+}/\text{Eu}^{2+}$ codoped amorphous $\text{Si}_3\text{B}_3\text{N}_7$ ceramics, the samples possess photoluminescence properties similar to single ion doped ones. As seen in Figure 5.121, the samples with more Eu^{2+} content tended to have a red shift, whereas the samples with more Ce^{3+} content exhibit a blue shift in emission. The FWHM values for $\text{Ce}^{3+}/\text{Eu}^{2+}$ codoped amorphous $\text{Si}_3\text{B}_3\text{N}_7$ ceramics were determined to be between 155 nm and 176 nm, which are the values between those of the single ion doped ceramics.

5. Phosphors Based on Amorphous $\text{Si}_3\text{B}_3\text{N}_7$ Matrix

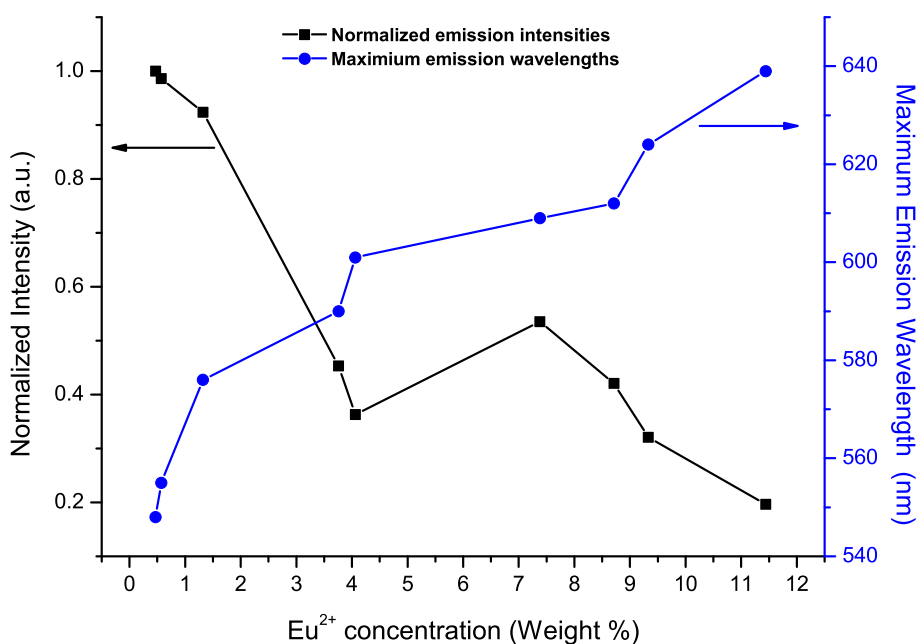


Figure 5.116.: Effect of the Eu^{2+} concentration on the maximum emission wavelength and intensities.

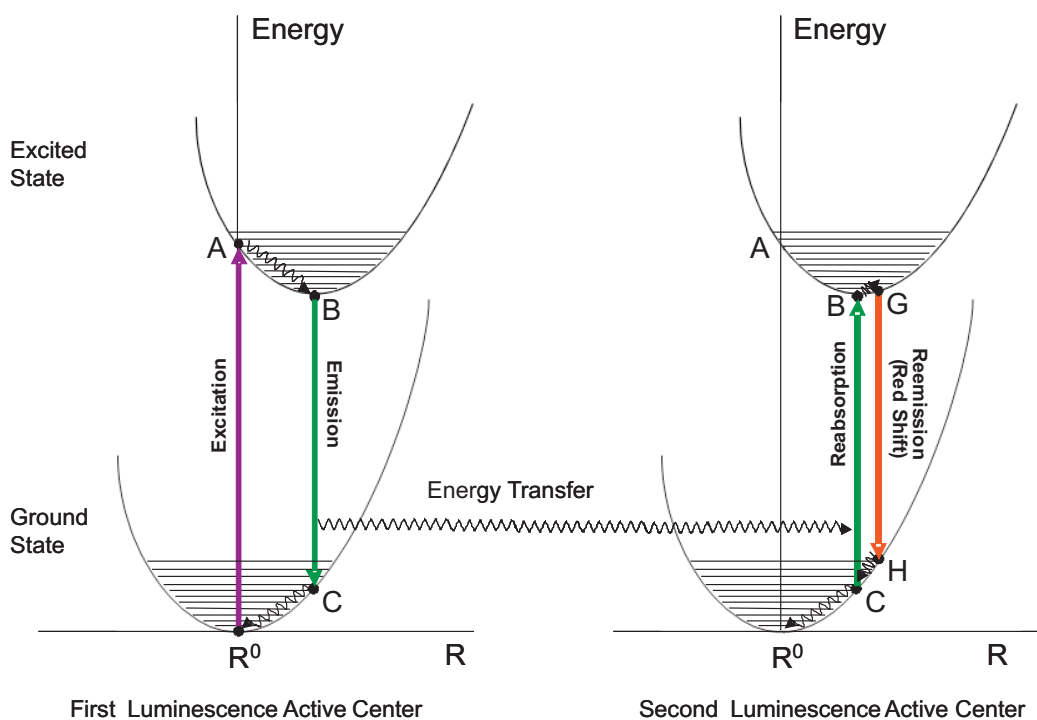


Figure 5.117.: Representation of a configurational coordinate model for the energy transfer followed by reabsorption and re-emission (red shift) processes between two neighboring luminescent active centers.

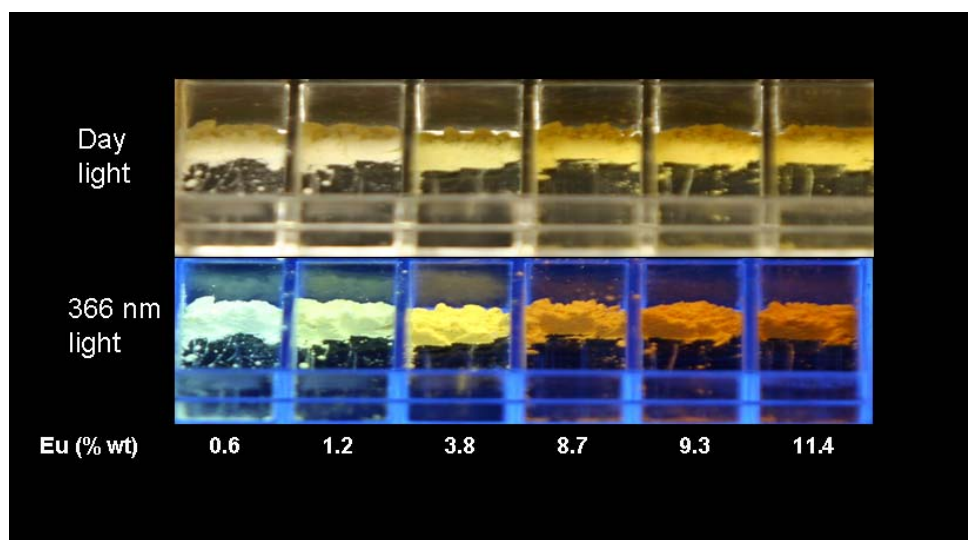


Figure 5.118.: Photos of Eu^{2+} doped amorphous $\text{Si}_3\text{B}_3\text{N}_7$ ceramics having various Eu^{2+} concentration under day light and 366 nm light.

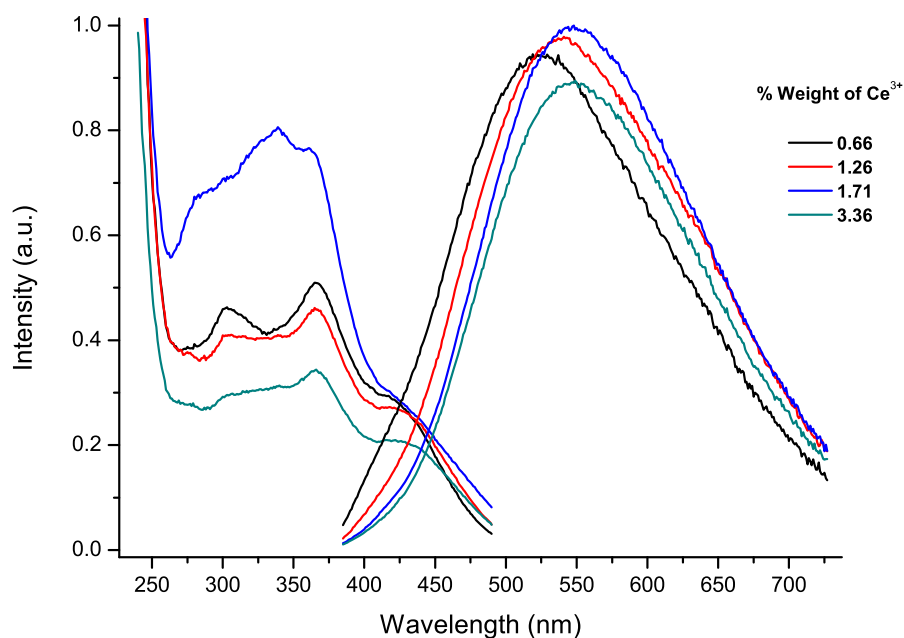


Figure 5.119.: Photoluminescence spectra of Ce^{3+} doped amorphous $\text{Si}_3\text{B}_3\text{N}_7$ ceramics at various Ce^{3+} concentration (Excitation spectra are measured at maximum emission wavelengths and emission spectra are measured at 365 nm excitation wavelength).

5. Phosphors Based on Amorphous $\text{Si}_3\text{B}_3\text{N}_7$ Matrix

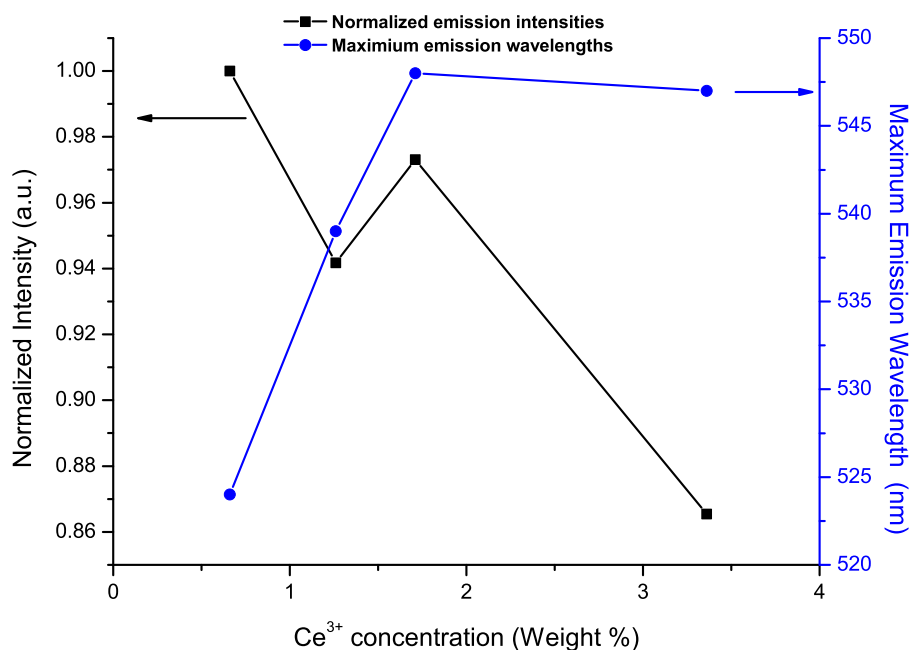


Figure 5.120.: Effect of the Ce^{3+} concentration on the maximum emission wavelength and intensities.

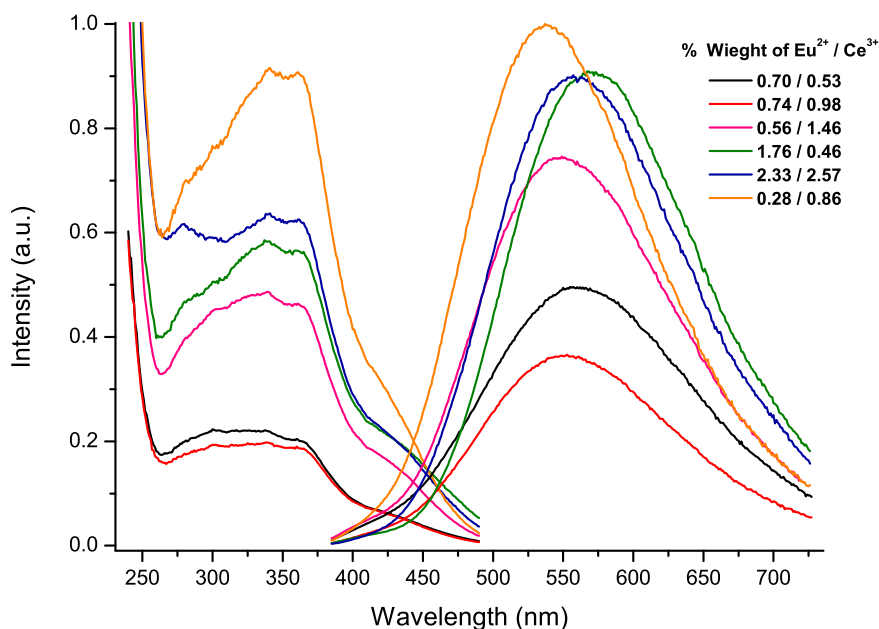


Figure 5.121.: Photoluminescence spectra of $\text{Ce}^{3+}/\text{Eu}^{2+}$ codoped amorphous $\text{Si}_3\text{B}_3\text{N}_7$ ceramics at various Ce^{3+} and Eu^{2+} concentrations (Excitation spectra are measured at maximum emission wavelengths and emission spectra are measured at 365 nm excitation wavelength).

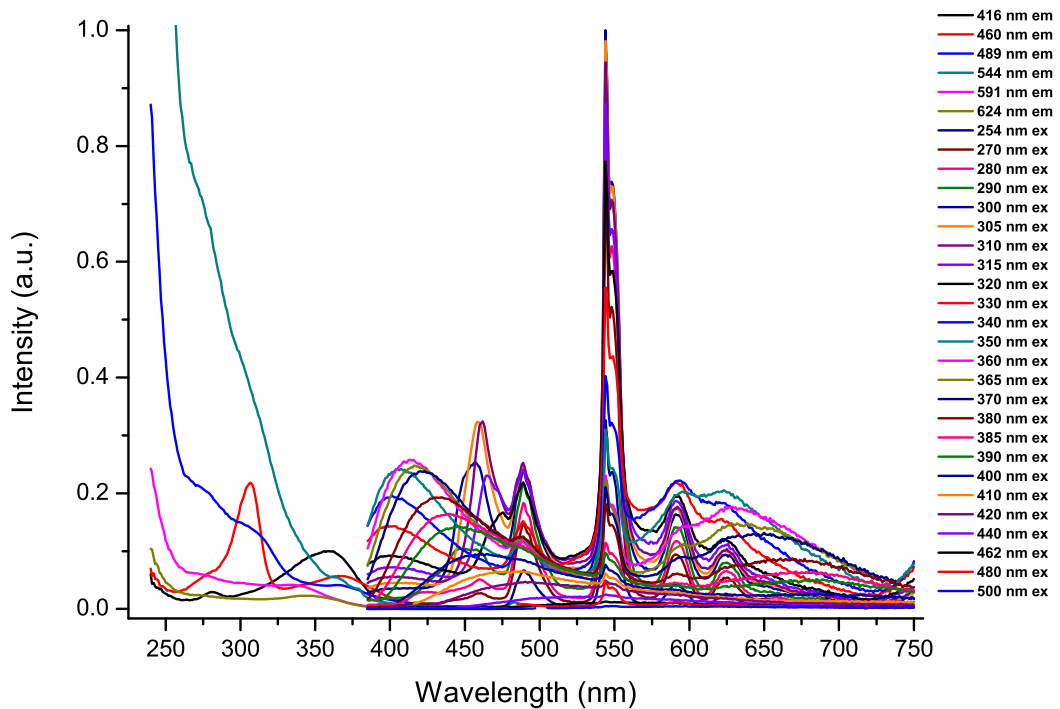


Figure 5.122.: Photoluminescence spectra of 2.25 % (wt) Tb^{3+} doped amorphous $\text{Si}_3\text{B}_3\text{N}_7$ ceramic at different excitation and emission wavelengths.

In contrast to Ce^{3+} and Eu^{2+} (co)doped amorphous $\text{Si}_3\text{B}_3\text{N}_7$ ceramics, no shift in the emission peak maximum values has been observed in Tb^{3+} doped amorphous $\text{Si}_3\text{B}_3\text{N}_7$ ceramics with Tb^{3+} concentration changes. This is assumed due to a strong shielding of the 4f shell (from which the emissions occur) via 5d shell, preventing the Tb^{3+} ions from being affected significantly by their local environment. Comparison of Figure 5.60 and Figure 5.122 clearly shows that at lower Tb^{3+} concentration, e.g. 0.6 % weight Tb^{3+} , the intrinsic emission peaks of the amorphous $\text{Si}_3\text{B}_3\text{N}_7$ host matrix are more dominant. On the other hand, at higher Tb^{3+} content, e.g. 2.25 % weight Tb^{3+} , the emissions due to the $\text{Si}_3\text{B}_3\text{N}_7$ host matrix have much lower intensities and Tb^{3+} emission peaks become more dominant, which results in more efficient green emission.

5.26. Conclusions

In the present work, photoluminescence analysis of the amorphous $\text{Si}_3\text{B}_3\text{N}_7$ reveals that this material possesses an intrinsic blue emission when excited with shorter wavelength lights, i.e. between 280 nm and 320 nm (where it also has a strong absorption), and violet emission when excited with longer wavelength lights, i.e. between 340 nm and 380 nm, resulting from the defects in the amorphous network. Additionally, amorphous $\text{Si}_3\text{B}_3\text{N}_7$

5. Phosphors Based on Amorphous $\text{Si}_3\text{B}_3\text{N}_7$ Matrix

ceramic has been considered as a host matrix for various ions, including Ce^{3+} , Nd^{3+} , Sm^{3+} , Eu^{2+} , Gd^{3+} , Tb^{3+} , Ho^{3+} , Tm^{3+} , Yb^{2+} , Yb^{3+} , La^{3+} , Y^{3+} , Sn^{2+} , Sr^{2+} and Ba^{2+} . Only Ce^{3+} , Nd^{3+} , Sm^{3+} , Eu^{2+} , Tb^{3+} , Ho^{3+} or Sn^{2+} ions incorporated into amorphous $\text{Si}_3\text{B}_3\text{N}_7$ matrix have resulted in luminescence in the visible range of the spectrum. While Nd^{3+} , Sm^{3+} , Tb^{3+} and Ho^{3+} exhibited line emissions due to the underlying $4f \rightarrow 4f$ transitions, broad emission bands were obtained by Ce^{3+} and Eu^{2+} ions because of the $5d \rightarrow 4f$ transitions and by Sn^{2+} ions because of the ${}^3\text{P}_1 \rightarrow {}^1\text{S}_0$ transition.

Among the line emitting species, the emission in Tb^{3+} doped samples vary considerably when excited with different wavelength light. To illustrate, intense green emission is obtained when excited with shorter wavelength light (254 nm - 280 nm). Furthermore, by combining the intrinsic blue emission of the host matrix, Tb^{3+} doped samples yield very intense white light, when excited with 280-320 nm light. On the other hand, excitation with a light longer than 340 nm results in intrinsic violet emission of the $\text{Si}_3\text{B}_3\text{N}_7$ host matrix. Therefore, Tb^{3+} doped $\text{Si}_3\text{B}_3\text{N}_7$ ceramics are very good candidates when combined with UV-LEDs to produce a white light. On the other hand, line emissions due to Nd^{3+} , Sm^{3+} and Ho^{3+} ions are not intense enough such that mainly the intrinsic emissions of the $\text{Si}_3\text{B}_3\text{N}_7$ host matrix are dominant.

Obviously, the most promising samples seem to be Ce^{3+} and Eu^{2+} (co)doped ones. As their first excited energy levels are comparable, they both produce similar broad emission bands in the visible region of the spectrum as well as structureless and wide excitation bands covering the UV-to-visible region of the spectrum. Emissions between 520 nm and 640 nm are obtained for Ce^{3+} and Eu^{2+} (co)doped amorphous $\text{Si}_3\text{B}_3\text{N}_7$ with FWHM values in the range between 150 nm and 200 nm, depending on the concentration. These results show that Ce^{3+} and Eu^{2+} (co)doped amorphous $\text{Si}_3\text{B}_3\text{N}_7$ ceramics are promising candidates as phosphor materials for blue-LEDs to obtain a white light.

When incorporated into amorphous $\text{Si}_3\text{B}_3\text{N}_7$ matrices, Gd^{3+} , Tm^{3+} , Yb^{2+} , Yb^{3+} , La^{3+} , Y^{3+} , Sr^{2+} and Ba^{2+} ions show no luminescence in the visible region of the spectrum. In addition, those ions together with Sn^{2+} ions have no significant improvement on the luminescence properties of Eu^{2+} when codoped in a $\text{Si}_3\text{B}_3\text{N}_7$ host matrix. On the other hand, codoping of Eu^{2+} together with Nd^{3+} , Sm^{3+} and Tb^{3+} into a $\text{Si}_3\text{B}_3\text{N}_7$ matrix results in a combined luminescence; that means in addition to the typical broad emission band of Eu^{2+} ions, emissions belonging to codopant ions have appeared. The additional signals belonging to the corresponding codopant ions will most probably result in higher CRI values compared to the Eu^{2+} doped ceramic. In addition to codoping with Eu^{2+} ions, Tb^{3+} ions have been codoped with Ce^{3+} ions. In this case, rather efficient energy transfer from Ce^{3+} to Tb^{3+} has been observed, which makes this sample among others one of the most prominent materials as a phosphor to be used on blue-LEDs for generating a white light.

Even though amorphous nitridic materials have not been previously considered seriously as a host material for activator ions, one can conclude in this study that amorphous $\text{Si}_3\text{B}_3\text{N}_7$ ceramic can indeed host various activator ions, providing a new class of phosphors. In addition, the production method of these amorphous luminescent ceramics, which is based on the polymer route, brings significant advantages over the conventional solid state syntheses as follow: 1) Highly pure starting materials can be applied, 2) solvent mediated one-pot synthesis results in a homogeneous distribution of the activator ions within the host matrix, 3) as there is no need to replace an ion from a lattice by an activator ion in amorphous $\text{Si}_3\text{B}_3\text{N}_7$ host matrix, various ions, even more than one, can easily be incorporated simultaneously into the network, 4) the preceramic polymers can be processed in various conventional polymer processing techniques, which is not possible along all solid state routes, 5) relatively low calcination temperatures, i.e. 1200 °C, and short heating times, i.e. dwelling for 4 hours, are required, and 6) all side-products can easily be recycled and reused.

5. *Phosphors Based on Amorphous Si₃B₃N₇ Matrix*

6. Ferromagnetic $\text{Si}_3\text{B}_3\text{N}_7$ Ceramics

As a new trend in polymer derived ceramics (PDCs), composite materials which combine the outstanding structural properties of PDCs with the functional properties of a metal or an alien ceramic dispersed phase are designed and processed. The production of respective novel ceramic composites via pyrolysis of the preceramic polymer containing reactive or inert fillers as the sensing or active element opens new markets in, for example, information technology, electronic, automotive and space industries. In the literature, two methods have mainly been applied to produce metal containing PDCs. In the first method, various metal powders, alloys or compounds (Fe, Mn, Co, Ni, Ni-Mn, Co-Mn, Fe-Mn, Fe_3O_4) were mixed with polysilazanes before any pyrolysis processes [358, 359, 360, 361]. In the second method, metal containing organosilicon or silazane monomers were polymerized [362, 363, 364]. Then, after pyrolysis in both cases various metal containing SiC, Si_3N_4 or SiCN ceramic composites sharing promising magnetic properties were obtained.

In the previous chapter, it has been shown that amorphous $\text{Si}_3\text{B}_3\text{N}_7$ matrix can host various activator, sensitizer or charge compensator ions in order to be used as efficient phosphors. In this chapter, the versatile amorphous $\text{Si}_3\text{B}_3\text{N}_7$ matrix is aimed to host Fe, Co and Ni particles in order to obtain ferromagnetic materials.

6.1. Fe Doped Amorphous $\text{Si}_3\text{B}_3\text{N}_7$ Matrix

Fe doping into $\text{Si}_3\text{B}_3\text{N}_7$ host matrix has been achieved by reacting TADB with liquid ammonia, in which Fe_2O_3 nanopowders were suspended. After purification and pyrolysis steps (see Section 10.2), α -Fe doped ferromagnetic $\text{Si}_3\text{B}_3\text{N}_7$ ceramic was obtained. Powder X-ray analyses of Fe_2O_3 nanopowders, SiBN: Fe_2O_3 polymer after 210 °C and $\text{Si}_3\text{B}_3\text{N}_7$:Fe ceramic after 1200 °C are presented in Figure 6.1. As it is seen from Figure 6.1, significant amount of Fe_2O_3 nanoparticles appeared not to react with TADB and NH_3 and survived even after sublimation of NH_4Cl at 210 °C. On the other hand, it was observed in the powder X-ray diffractogram of $\text{Si}_3\text{B}_3\text{N}_7$:Fe ceramic after 1200 °C that all of the Fe_2O_3 nanoparticles (Hematite, ICSD [73-2234]) were reduced to α -Fe (ICSD [6-696]) during the pyrolysis. Similar behavior was also reported by Saha et. al. The authors synthesized magnetic SiCN composites by mixing liquid polysilazane Ceraset[®] with 70 % (vol.) Fe_3O_4 particles, which were subsequently pyrolysed. It was described that the evolution of CH_4

6. Ferromagnetic $\text{Si}_3\text{B}_3\text{N}_7$ Ceramics

and H_2 between 600 °C and 900 °C range caused the reduction of Fe_3O_4 into α -iron [358].

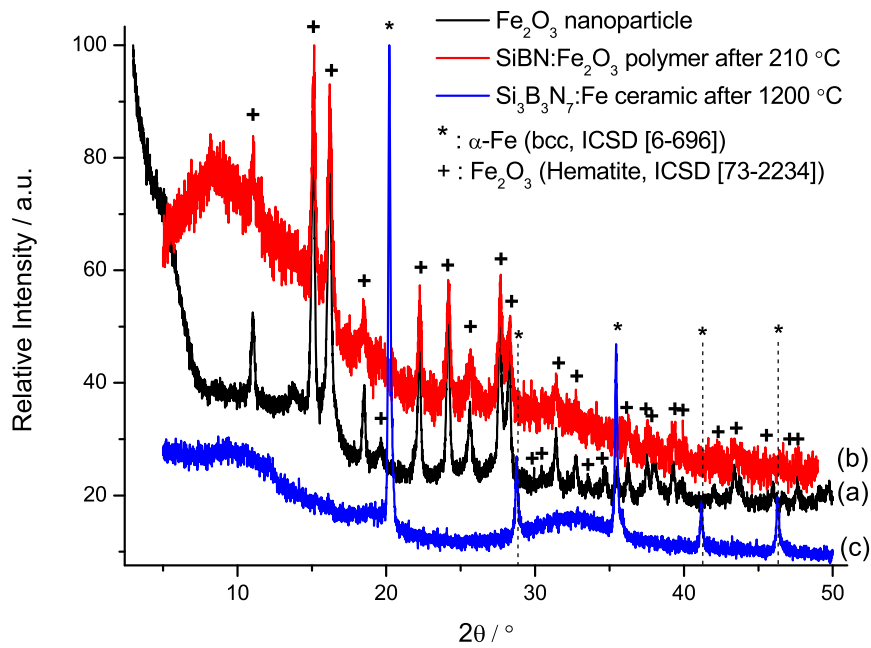


Figure 6.1.: Powder X-ray diffractograms of a) Fe_2O_3 nanoparticles, b) Fe_2O_3 doped SiBN polymer after 210 °C and c) Fe doped $\text{Si}_3\text{B}_3\text{N}_7$ ceramic after 1200 °C.

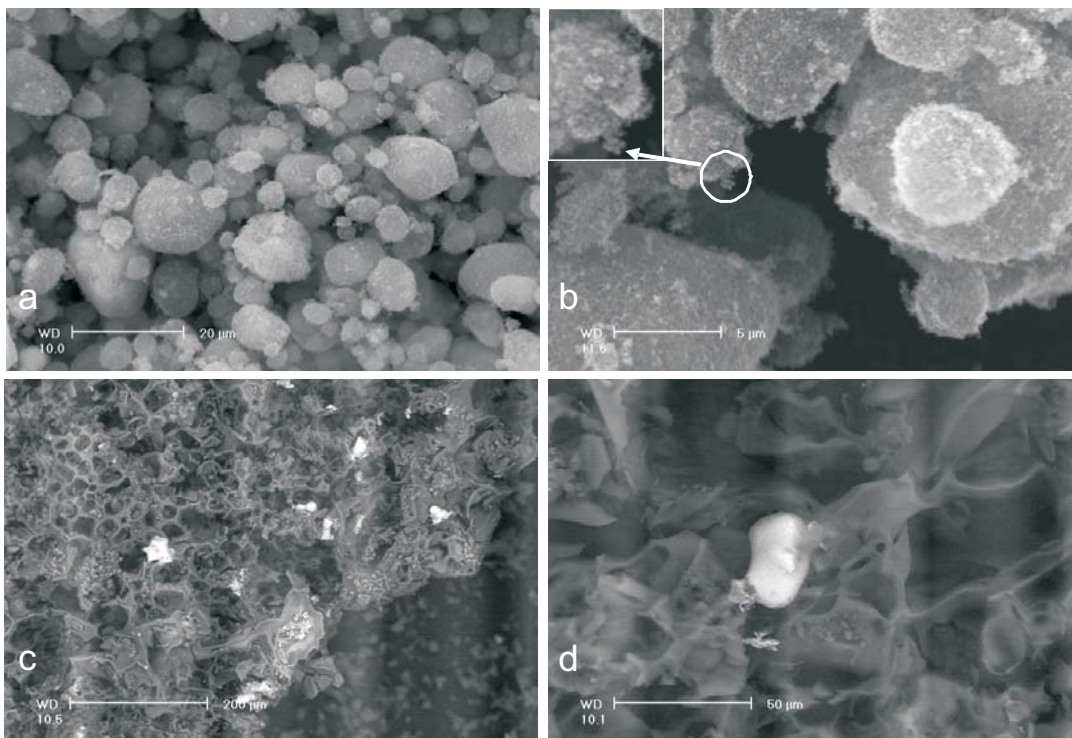


Figure 6.2.: SEM images of Fe_2O_3 nanoparticles (a and b) and $\text{Si}_3\text{B}_3\text{N}_7$:Fe ceramic (c and d) at different magnifications.

Figure 6.2-a and Figure 6.2-b represent the SEM images of Fe_2O_3 nanoparticles at different magnifications. These SEM images were obtained by secondary electron beam (SE) mode. It is clearly seen in Figure 6.2-a that Fe_2O_3 nanoparticles are agglomerated into bigger spheres (up to $20\ \mu\text{m}$ diameters). On the other hand, higher magnification SEM image of Fe_2O_3 nanoparticles in Figure 6.2-b shows that nano domains of Fe_2O_3 particles still remain. Figure 6.2-c and Figure 6.2-d exhibit the SEM images of Fe doped $\text{Si}_3\text{B}_3\text{N}_7$ ceramic after $1200\ ^\circ\text{C}$ at different magnifications. These SEM images were obtained by back scattered electron beam (BSE) mode. The white spots in the images correspond to the metallic iron phases, whereas the dark phases are assigned as $\text{Si}_3\text{B}_3\text{N}_7$ host matrix via energy dispersive X-ray (EDX) analysis. It is seen in those images that metallic Fe micro-domains (about $20 - 40\ \mu\text{m}$ diameter) are quite homogeneously distributed through the $\text{Si}_3\text{B}_3\text{N}_7$ host matrix.

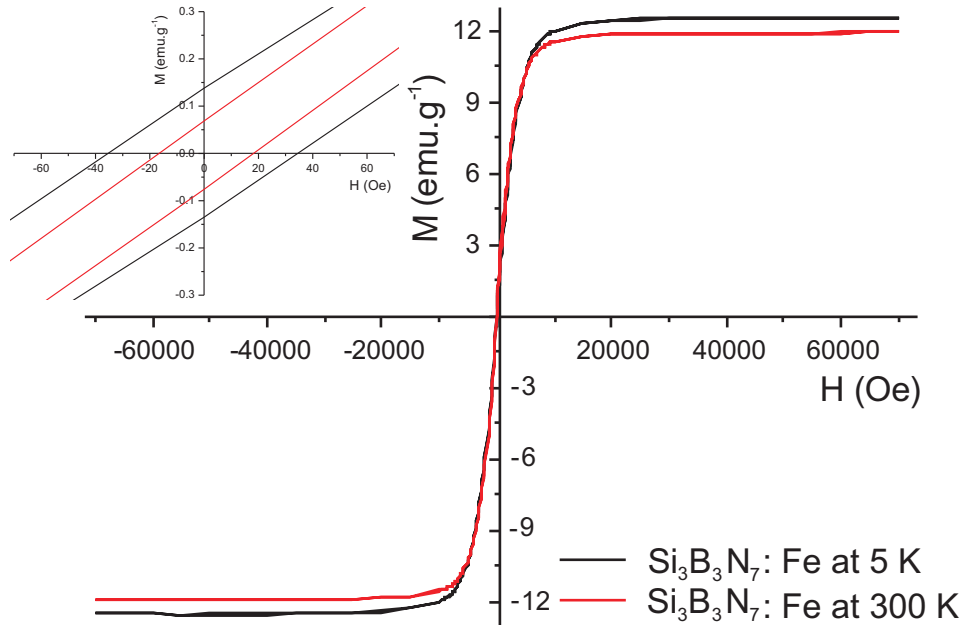


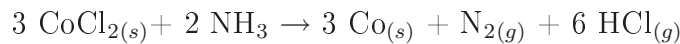
Figure 6.3.: Hysteresis loops of Fe doped $\text{Si}_3\text{B}_3\text{N}_7$ ceramic at 5 K and 300 K (The inset is an expanded region of the hysteresis loops depicting the small coercivity and remanence values).

The magnetization of Fe doped $\text{Si}_3\text{B}_3\text{N}_7$ ceramic was measured as a function of magnetic field and temperature (Figure 6.3). M-H curves represent the hysteresis loops of Fe doped $\text{Si}_3\text{B}_3\text{N}_7$ ceramic at 5 K and 300 K with saturation magnetization of $12.5\ \text{emu.g}^{-1}$ and $11.9\ \text{emu.g}^{-1}$, respectively, at $20000\ \text{Oe}$. Moreover, the hysteresis loops at 5 K and 300 K were characterized by narrow areas with small values of coercivities ($35\ \text{Oe}$ at 5 K and $17\ \text{Oe}$ at 300 K) and remanences ($0.14\ \text{emu.g}^{-1}$ at 5 K and $0.07\ \text{emu.g}^{-1}$ at 300 K) (see the inset in Figure 6.3). Therefore, Fe doped $\text{Si}_3\text{B}_3\text{N}_7$ ceramic can be classified as a soft ferromagnetic material.

6.2. Co Doped Amorphous $\text{Si}_3\text{B}_3\text{N}_7$ Matrix

Cobalt doping into the $\text{Si}_3\text{B}_3\text{N}_7$ host matrix has been achieved by reacting TADB with liquid ammonia in which either $\text{Co}(\text{NH}_3)_6\text{Cl}_3$ or $\text{Co}[\text{N}(\text{SiMe}_3)_2]_2$ was suspended. After purification and pyrolysis steps (see Section 10.2), elemental cobalt doped ferromagnetic $\text{Si}_3\text{B}_3\text{N}_7$ ceramics were obtained. $\text{Si}_3\text{B}_3\text{N}_7:\text{Co}$ ceramics were prepared in three different ways. Firstly, $\text{Co}(\text{NH}_3)_6\text{Cl}_3$ was used as a Co source and the corresponding polymer (SiBN:Co-1 polymer) was heated to 900 °C under NH_3 flow and 1200 °C under N_2 flow, and the ceramic is named as $\text{Si}_3\text{B}_3\text{N}_7:\text{Co-1}$. Secondly, $\text{Co}(\text{NH}_3)_6\text{Cl}_3$ was used as a Co source and the corresponding polymer (SiBN:Co-2 polymer) was heated to first 900 °C and then 1200 °C under Ar flow, and the ceramic is named as $\text{Si}_3\text{B}_3\text{N}_7:\text{Co-2}$. Thirdly, $\text{Co}[\text{N}(\text{SiMe}_3)_2]_2$ was used as a Co source and the corresponding polymer (SiBN:Co-3 polymer) was heated to 900 °C under NH_3 flow and 1200 °C under N_2 flow, and the ceramic is named as $\text{Si}_3\text{B}_3\text{N}_7:\text{Co-3}$.

Figure 6.4, Figure 6.5 and Figure 6.6 represent powder X-ray diffractograms of $\text{Si}_3\text{B}_3\text{N}_7:\text{Co-1}$, $\text{Si}_3\text{B}_3\text{N}_7:\text{Co-2}$ and $\text{Si}_3\text{B}_3\text{N}_7:\text{Co-3}$, respectively. In all cases, SiBN-Co polymers after sublimation at 210 °C had blue color. This is attributed to formation of CoCl_2 , which was further proven by powder X-ray analyses. In the cases of $\text{Si}_3\text{B}_3\text{N}_7:\text{Co-1}$ and $\text{Si}_3\text{B}_3\text{N}_7:\text{Co-2}$, which have $\text{Co}(\text{NH}_3)_6\text{Cl}_3$ as starting compound, thermal decomposition of $\text{Co}(\text{NH}_3)_6\text{Cl}_3$ at 190 °C results in the formation of CoCl_2 [365]. On the other hand, in the case of $\text{Si}_3\text{B}_3\text{N}_7:\text{Co-3}$, which has $\text{Co}[\text{N}(\text{SiMe}_3)_2]_2$ as starting compound, more acidic $-\text{BCl}_2$ group of TADB is believed to react with $\text{Co}[\text{N}(\text{SiMe}_3)_2]_2$, yielding CoCl_2 . It was also reported that CoCl_2 in presence of NH_3 yields metallic cobalt around 600 °C, according to following reaction [366]:



It is known that metallic cobalt forms two allotropes, which are α -Co (hexagonal close-packed, hcp) and β -Co (face centered cubic, fcc). The transition between hcp and fcc structures ideally occurs at 450 °C, but in practice, the energy difference is so small that random intergrowth of the two is quite common. For cobalt doped $\text{Si}_3\text{B}_3\text{N}_7$ ceramics, heating process to 900 °C (either under NH_3 or Ar atmosphere) resulted in the formation of only β -Co (face centered cubic, fcc) for all samples. Similarly, β -Co phases have been also observed for all samples after heating to 1200 °C (either under N_2 or Ar atmosphere). On the other hand, α -Co phases have additionally been observed for $\text{Si}_3\text{B}_3\text{N}_7:\text{Co-2}$ and $\text{Si}_3\text{B}_3\text{N}_7:\text{Co-3}$ ceramics, which were barely visible for $\text{Si}_3\text{B}_3\text{N}_7:\text{Co-1}$ in powder X-ray diffractograms.

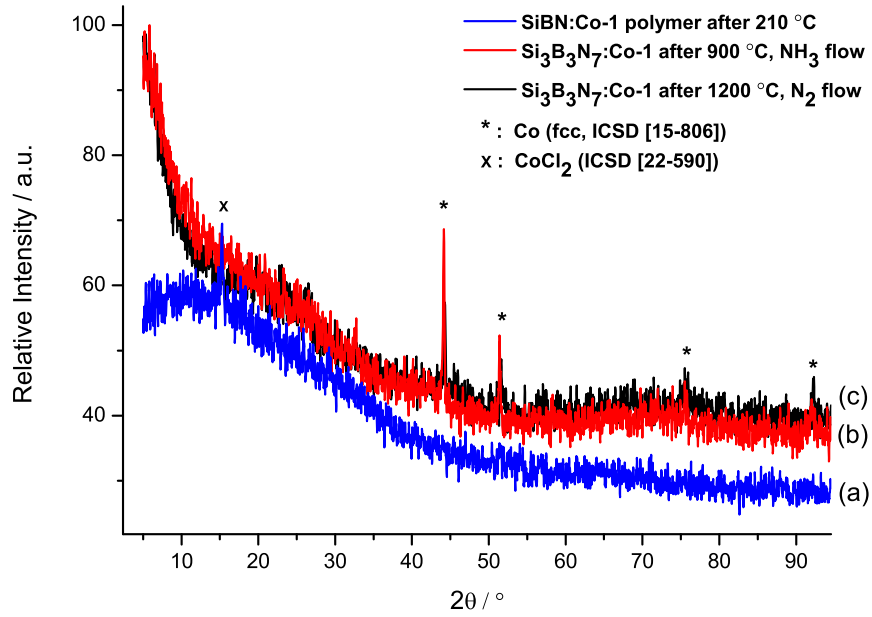


Figure 6.4.: Powder X-ray diffractograms of a) SiBN:Co-1 polymer after 210 °C, $\text{Si}_3\text{B}_3\text{N}_7$:Co-1 ceramics after b) 900 °C with NH_3 flow and c) 1200 °C with N_2 flow, starting with $\text{Co}(\text{NH}_3)_6\text{Cl}_3$ as Co source.

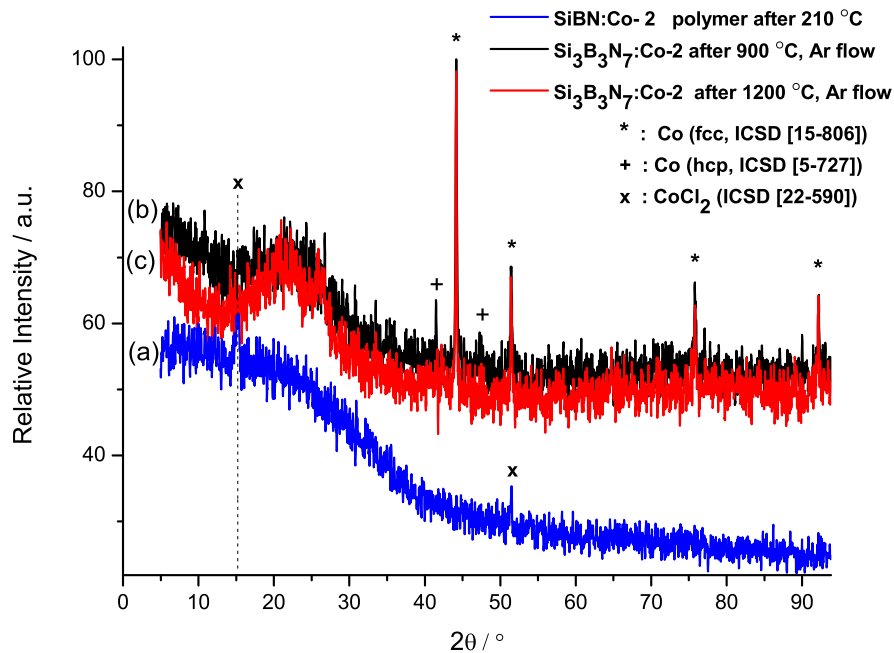


Figure 6.5.: Powder X-ray diffractograms of a) SiBN:Co-2 polymer after 210 °C, $\text{Si}_3\text{B}_3\text{N}_7$:Co-2 ceramics b) after 900 °C and c) 1200 °C with Ar flow, starting with $\text{Co}(\text{NH}_3)_6\text{Cl}_3$ as Co source.

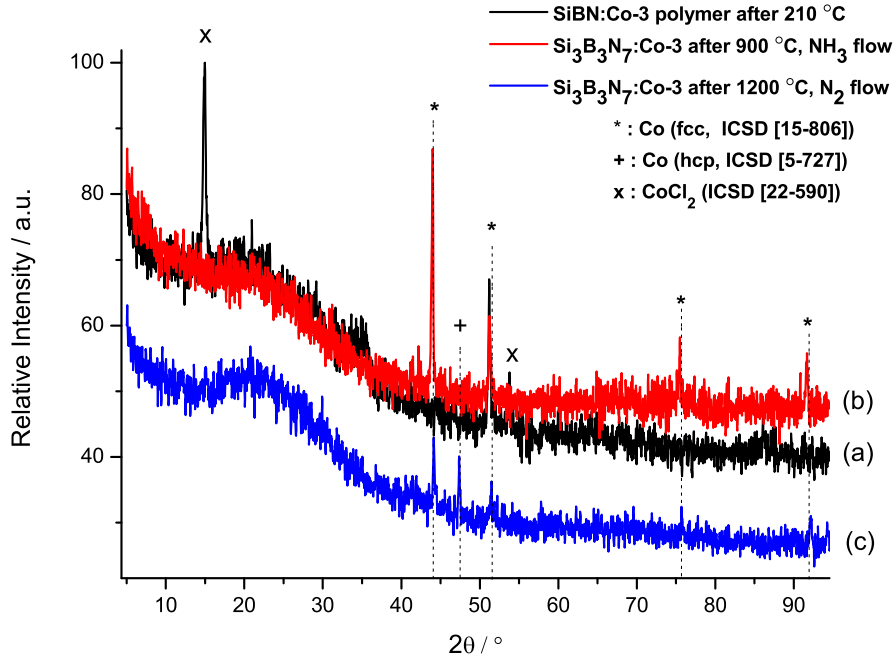


Figure 6.6.: Powder X-ray diffractograms of a) SiBN:Co-3 polymer after 210 °C, $\text{Si}_3\text{B}_3\text{N}_7$:Co-3 ceramic after b) 900 °C with NH_3 flow and c) 1200 °C with N_2 flow, starting with $\text{Co}[\text{N}(\text{SiMe}_3)_2]_2$ as Co source.

Figure 6.7-a and Figure 6.7-b represent the SEM images of $\text{Si}_3\text{B}_3\text{N}_7$:Co-1, whereas Figure 6.7-c and Figure 6.7-d are given for that of $\text{Si}_3\text{B}_3\text{N}_7$:Co-2, and Figure 6.7-e and Figure 6.7-f for that of $\text{Si}_3\text{B}_3\text{N}_7$:Co-3 at different magnifications. All given SEM images were obtained by back scattered electron beam (BSE) mode and the white spots in the images were determined as metallic cobalt phases, whereas the dark phases were assigned as $\text{Si}_3\text{B}_3\text{N}_7$ host matrix via energy dispersive X-ray (EDX) analysis. The metallic cobalt phases in all samples appeared as microspheres (submicron to micron sizes). It has been observed during the SEM analyses that metallic cobalt phases were quite homogeneously distributed through the $\text{Si}_3\text{B}_3\text{N}_7$ host matrix. $\text{Si}_3\text{B}_3\text{N}_7$:Co-1 and $\text{Si}_3\text{B}_3\text{N}_7$:Co-3 have almost the same morphology whereas the morphology of $\text{Si}_3\text{B}_3\text{N}_7$:Co-2, which was pyrolysed under Ar atmosphere, appeared differently. As it is seen in Figure 6.7-d, cobalt phases appear not only as spheres but also look like random-shaped droplets. It was also observed that the $\text{Si}_3\text{B}_3\text{N}_7$ host matrix in $\text{Si}_3\text{B}_3\text{N}_7$:Co-2 had smoother surface morphology than the other samples. Therefore, one can conclude that pyrolysis atmosphere has strong influence in the morphology of the final ceramic.

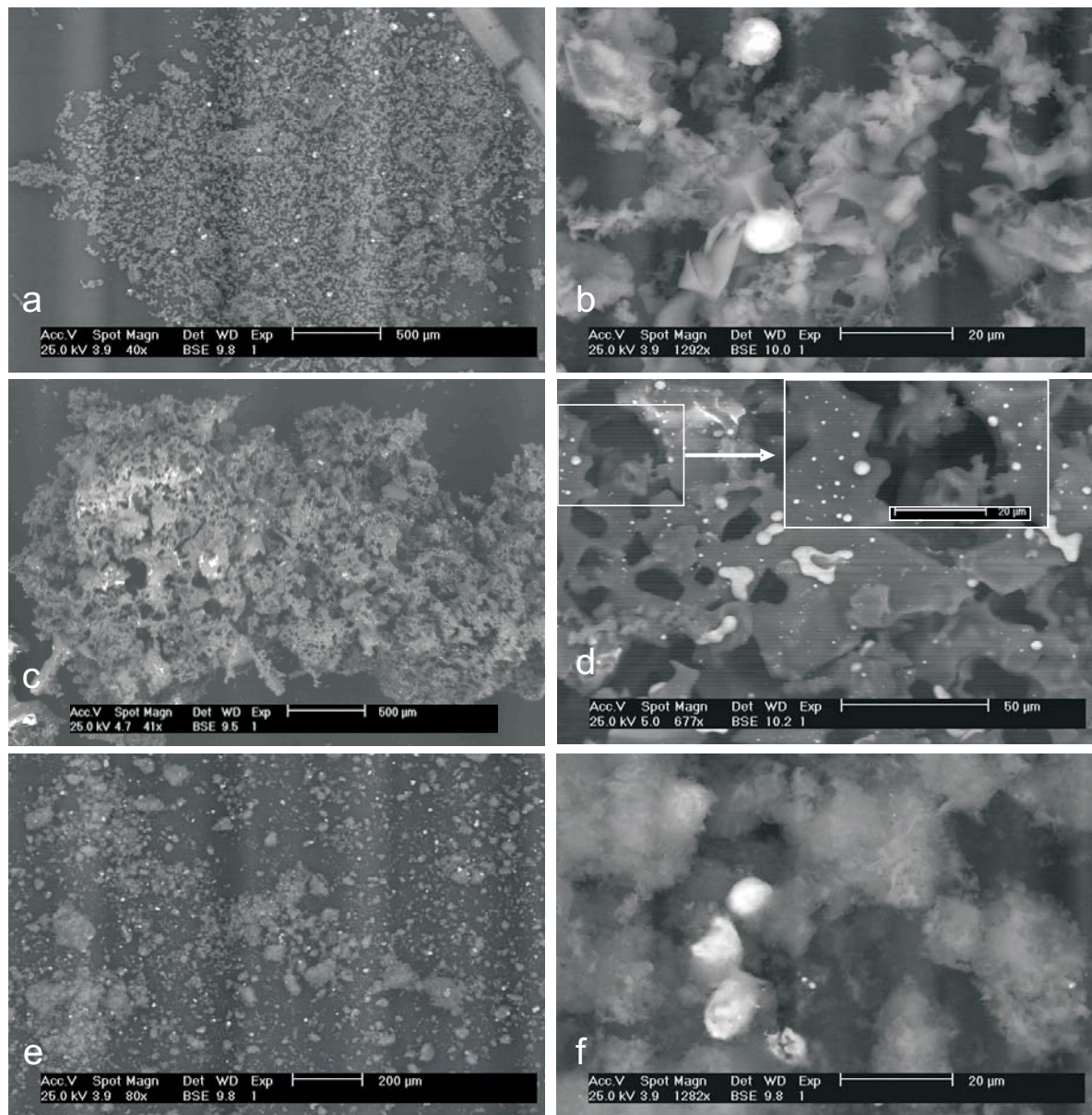


Figure 6.7.: The SEM images of SiBN:Co-1 (a and b), SiBN:Co-2 (c and d) and SiBN:Co-3 (e and f) ceramics after 1200 °C at different magnifications.

6. Ferromagnetic $\text{Si}_3\text{B}_3\text{N}_7$ Ceramics

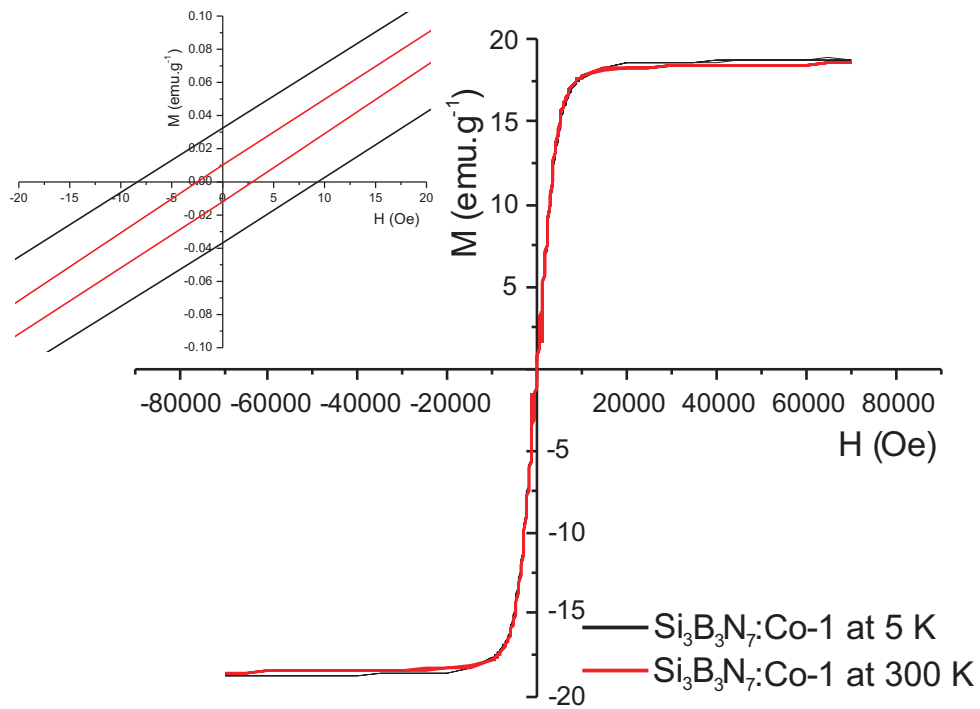


Figure 6.8.: Hysteresis loops for $\text{Si}_3\text{B}_3\text{N}_7\text{:Co-1}$ ceramic at 5 K and 300 K (The inset is an expanded region of the hysteresis loops depicting the small coercivity and remanence values).

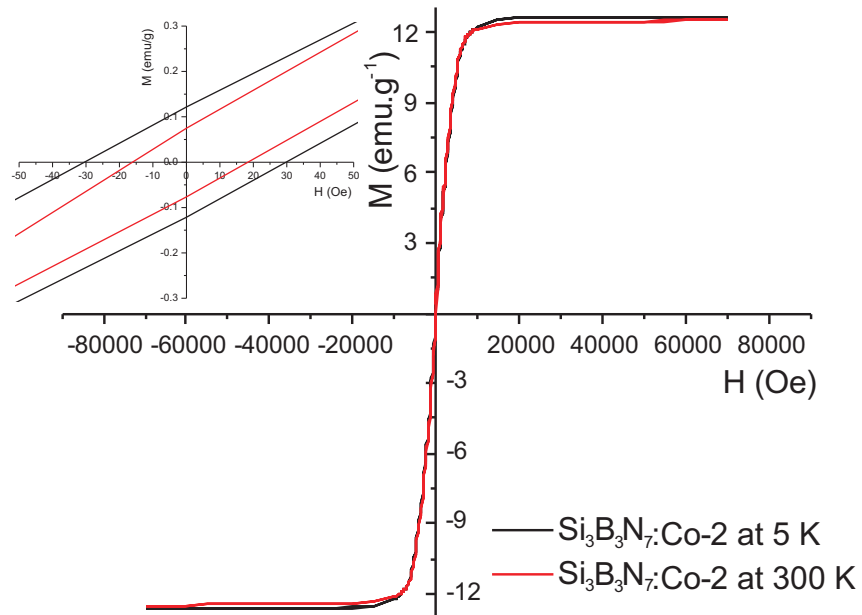


Figure 6.9.: Hysteresis loops for $\text{Si}_3\text{B}_3\text{N}_7\text{:Co-2}$ ceramic at 5 K and 300 K (The inset is an expanded region of the hysteresis loops depicting the small coercivity and remanence values).

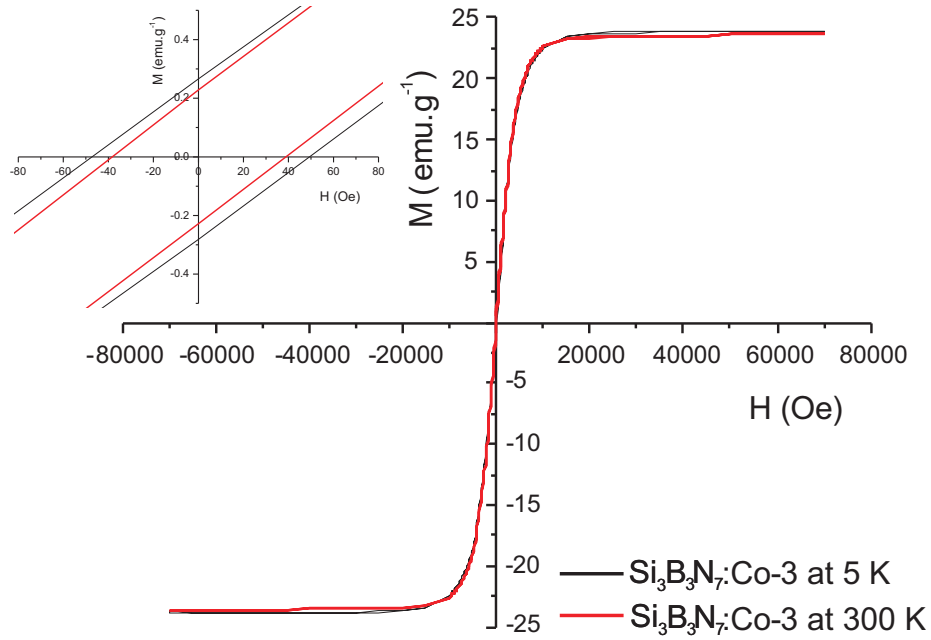


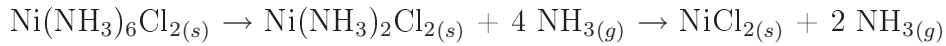
Figure 6.10.: Hysteresis loops for $\text{Si}_3\text{B}_3\text{N}_7\text{:Co-3}$ ceramic at 5 K and 300 K (The inset is an expanded region of the hysteresis loops depicting the small coercivity and remanence values).

The magnetizations of Co doped $\text{Si}_3\text{B}_3\text{N}_7$ ceramics have been measured as a function of magnetic field and temperature, and represented in Figure 6.8, Figure 6.9 and Figure 6.10 for $\text{Si}_3\text{B}_3\text{N}_7\text{:Co-1}$, $\text{Si}_3\text{B}_3\text{N}_7\text{:Co-2}$ and $\text{Si}_3\text{B}_3\text{N}_7\text{:Co-3}$, respectively. M-H curves show the hysteresis loops of Co doped $\text{Si}_3\text{B}_3\text{N}_7$ ceramics at 5 K and 300 K. The saturation magnetizations were achieved for all Co doped samples at around 20000 Oe with the values of 18.6 emu.g^{-1} at 5 K and 18.3 emu.g^{-1} at 300 K for $\text{Si}_3\text{B}_3\text{N}_7\text{:Co-1}$ ceramic, 12.6 emu.g^{-1} at 5 K and 12.4 emu.g^{-1} at 300 K for $\text{Si}_3\text{B}_3\text{N}_7\text{:Co-2}$ ceramic, and 23.7 emu.g^{-1} at 5 K and 23.3 emu.g^{-1} at 300 K for $\text{Si}_3\text{B}_3\text{N}_7\text{:Co-3}$ ceramic. Moreover, the hysteresis loops for all Co doped samples at 5 K and 300 K were characterized by narrow areas with small values of coercivities and remanences (see the insets in Figures 6.8, 6.9 and 6.10). The coercivity values are 7.8 Oe at 5 K and 2.4 Oe at 300 K for $\text{Si}_3\text{B}_3\text{N}_7\text{:Co-1}$ ceramic, 30 Oe at 5 K and 16 Oe at 300 K for $\text{Si}_3\text{B}_3\text{N}_7\text{:Co-2}$ ceramic, and 48 Oe at 5 K and 38.5 Oe at 300 K for $\text{Si}_3\text{B}_3\text{N}_7\text{:Co-3}$ ceramic. The remanence values are 0.034 emu.g^{-1} at 5 K and 0.01 emu.g^{-1} at 300 K for $\text{Si}_3\text{B}_3\text{N}_7\text{:Co-1}$ ceramic, 0.12 emu.g^{-1} at 5 K and 0.075 emu.g^{-1} at 300 K for $\text{Si}_3\text{B}_3\text{N}_7\text{:Co-2}$, and 0.27 emu.g^{-1} at 5 K and 0.23 emu.g^{-1} at 300 K for $\text{Si}_3\text{B}_3\text{N}_7\text{:Co-3}$ ceramic. Therefore, it can be concluded from those small coercivity and remanence values that all Co doped $\text{Si}_3\text{B}_3\text{N}_7$ ceramics can be classified as soft ferromagnetic materials.

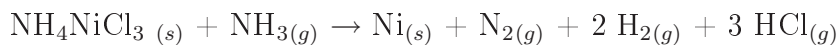
6.3. Ni Doped Amorphous $\text{Si}_3\text{B}_3\text{N}_7$ Matrix

Ni doping has been achieved by ammonolysis of TADB with liquid ammonia in which $\text{Ni}(\text{NH}_3)_6\text{Cl}_2$ was suspended. After purification and pyrolysis (see Section 10.2), elemental nickel doped ferromagnetic $\text{Si}_3\text{B}_3\text{N}_7$ ceramic were obtained. Figure 6.11 shows powder X-ray diffractograms of SiBN:Ni polymer after 210 °C and $\text{Si}_3\text{B}_3\text{N}_7:\text{Ni}$ ceramics after 900 °C with NH_3 flow and after 1200 °C with N_2 flow.

In the literature, thermal decomposition of $\text{Ni}(\text{NH}_3)_6\text{Cl}_2$ was reported to take place in two defined steps [367]:



These two steps were reported to occur at around 85 °C and 175 °C, respectively. Therefore, one could expect to see the NiCl_2 diffraction peaks in the powder X-ray diffractogram of SiBN:Ni polymer, which was heated to 210 °C under vacuum (10^{-3} mbar). However, as it is seen from Figure 6.11, powder X-ray diffractogram of SiBN:Ni polymer contains only NH_4NiCl_3 peaks. On the other hand, it was also reported that yellow-orange colored NH_4NiCl_3 is obtained when NiCl_2 is reacted with NH_4Cl at around 300 °C [368]. Therefore, this makes sense in the present case such that NH_4Cl is formed during the reaction between TADB and NH_3 , and NiCl_2 is formed due to the thermal decomposition of the $\text{Ni}(\text{NH}_3)_6\text{Cl}_2$. Then, the reaction between NiCl_2 and NH_4Cl results in the formation of NH_4NiCl_3 , which is also responsible for the yellow-orange color of the SiBN:Ni polymer. Moreover, heating the SiBN:Ni polymer either to 900 °C under NH_3 flow or subsequently to 1200 °C under N_2 flow resulted in the formation of metallic Ni (body centered cubic), most probably due to the following reaction:



The SEM images of nickel doped $\text{Si}_3\text{B}_3\text{N}_7$ ceramic are presented in Figure 6.12 at different magnifications. The SEM images were obtained by the back scattered electron beam (BSE) mode and the white spots in the images were determined as metallic nickel phases, whereas the dark phases were assigned to the $\text{Si}_3\text{B}_3\text{N}_7$ host matrix via energy dispersive X-ray (EDX) analysis. Similar to the cobalt doped $\text{Si}_3\text{B}_3\text{N}_7$ ceramic, the metallic nickel phases have appeared as microspheres (submicron to micron sizes). It has also been observed during the SEM analyses that nickel microspheres are very homogeneously distributed through the $\text{Si}_3\text{B}_3\text{N}_7$ host matrix.

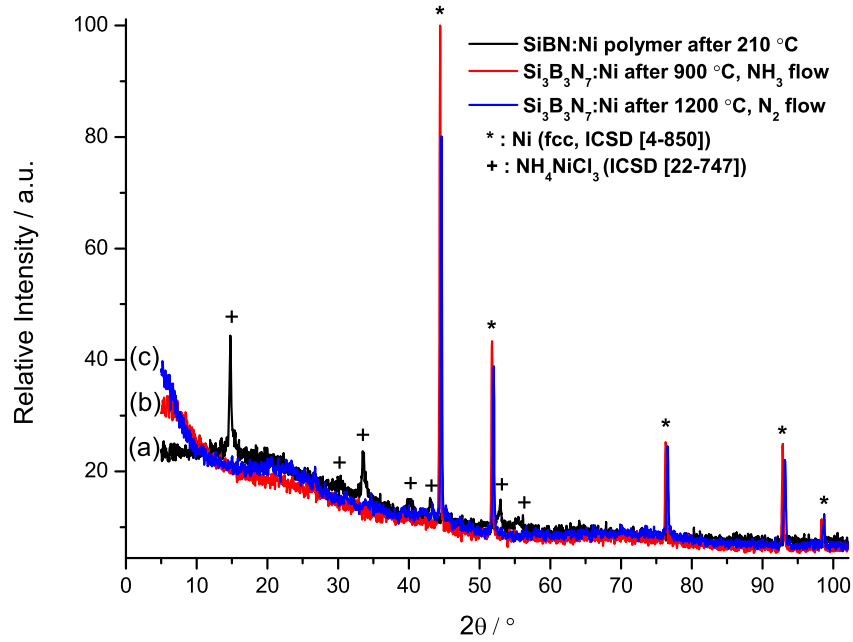


Figure 6.11.: Powder X-ray diffractograms of a) SiBN:Ni polymer after 210 °C, $\text{Si}_3\text{B}_3\text{N}_7$:Ni ceramics after b) 900 °C with NH_3 flow and c) 1200 °C with N_2 flow.

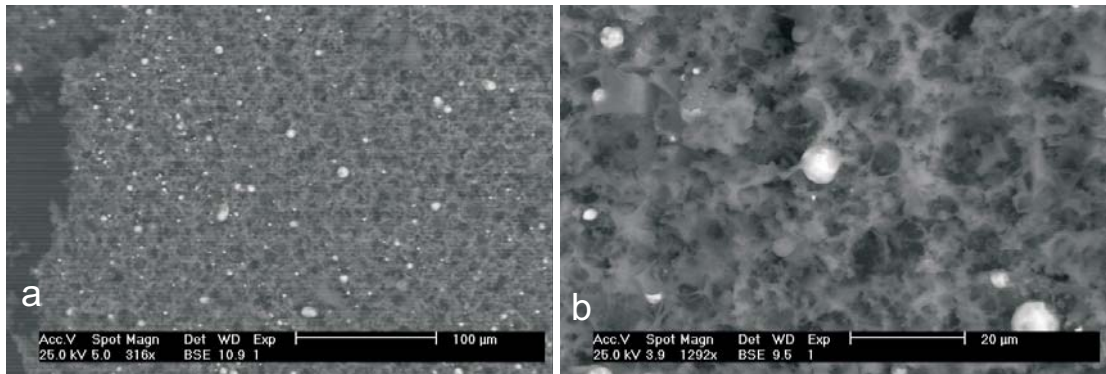


Figure 6.12.: The SEM images of $\text{Si}_3\text{B}_3\text{N}_7$:Ni ceramic after 1200 °C at different magnifications.

The magnetization of Ni doped $\text{Si}_3\text{B}_3\text{N}_7$ ceramic was measured as a function of magnetic field and temperature (Figure 6.13). M-H curves represent the hysteresis loops of Ni doped $\text{Si}_3\text{B}_3\text{N}_7$ ceramic at 5 K and 300 K with saturation magnetization of 4.7 emu.g^{-1} and 2.8 emu.g^{-1} , respectively, at 5000 Oe. Moreover, the hysteresis loops at 5 K and 300 K were characterized by narrow areas with small values of coercivities (8.7 Oe at 5 K and 12.3 Oe at 300 K) and remanences (0.036 emu.g^{-1} both at 5 K and 300 K) (see the inset in Figure 6.13). Therefore, Ni doped $\text{Si}_3\text{B}_3\text{N}_7$ ceramic can also be classified as a soft ferromagnetic material.

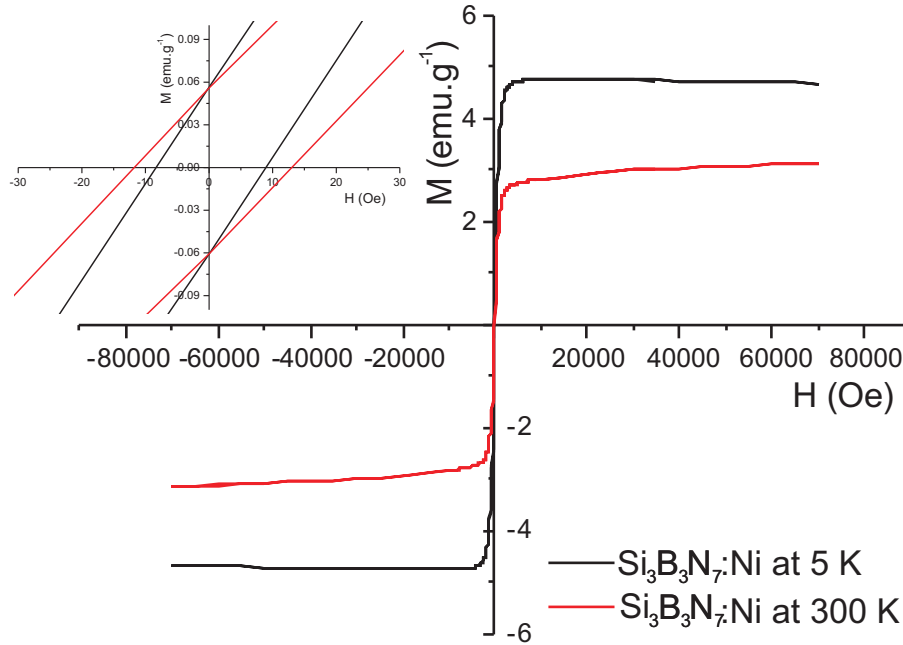


Figure 6.13.: Hysteresis loops of Ni doped $\text{Si}_3\text{B}_3\text{N}_7$ ceramic at 5 K and 300 K (The inset is an expanded region of the hysteresis loops depicting the small coercivity and remanence values).

6.4. Conclusions

As reported in Chapter 5, lanthanides, Y, Sn, Sr or Ba have been incorporated into the amorphous $\text{Si}_3\text{B}_3\text{N}_7$ host matrix as ions regardless of the form of the corresponding starting material, i.e., being a metal or a compound. This has been proven by various analytical methods including powder X-ray analysis (no any metallic phases have been observed), photoluminescence and diffuse reflection spectroscopies, and magnetic measurements. However, all attempts to dope Fe, Co or Ni into the amorphous $\text{Si}_3\text{B}_3\text{N}_7$ host matrix have resulted in incorporation of the corresponding elements as bulk metals rather than as isolated ions, as proven by powder X-ray analyses. Therefore, all of the Fe, Co or Ni doped $\text{Si}_3\text{B}_3\text{N}_7$ ceramics have appeared as grey-black colored due to containing the corresponding elements as metals. The SEM measurements have revealed that the metallic phases of Fe, Co or Ni into the $\text{Si}_3\text{B}_3\text{N}_7$ matrix appeared as microspheres (submicron to micron sizes) and were distributed quite homogeneously through the matrix. The results of the magnetic measurements have shown that Fe, Co and Ni doped $\text{Si}_3\text{B}_3\text{N}_7$ ceramics can be classified as soft ferromagnetic materials, which may find applications in microwave devices, magnetic shielding, transformers or recording heads. On the other hand, since Fe, Co and Ni doped $\text{Si}_3\text{B}_3\text{N}_7$ ceramics contain significant submicron domains, possible superparamagnetic or spin glass properties should be investigation.

7. A Novel Production Method for Crystalline Nitridosilicates

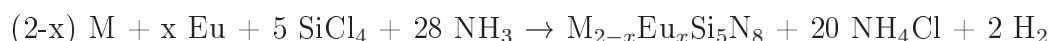
The nitride-based crystalline phosphors, especially the nitridosilicate types, have extensively been studied due to having outstanding thermal, chemical, and mechanical stabilities and structural diversities. Various M-Si-N phases have been investigated as host lattices for color conversion phosphors such as MSiN_2 , $\text{M}_5\text{Si}_2\text{N}_6$, $\text{M}_2\text{Si}_4\text{N}_7$, $\text{M}_3\text{Si}_6\text{N}_{11}$, M_4SiN_4 , MSi_3N_5 , $\text{M}_2\text{Si}_5\text{N}_8$ and $\text{MSi}_7\text{N}_{10}$, where M = Mg, Ca, Sr, Ba, Ln and Y [199]. All these compounds have been prepared by conventional solid state reactions, requiring extreme conditions, laborious handling and complex equipments like radio frequency furnace, which make the cost for mass-production significantly high. Therefore, it is extremely urgent to find an elegant method for the production of nitride-based phosphors, which can be easily up-scaled. For this purpose, the polymer route provides a promising approach. In the present work, various nitridosilicate type phosphors, such as CeSi_3N_5 , $\text{Sr}_{2-x}\text{Mn}_x\text{Si}_5\text{N}_8$, $\text{M}_{2-x}\text{Eu}_x\text{Si}_5\text{N}_8$, $\text{M}_{2-2x}\text{R}_x\text{Li}_x\text{Si}_5\text{N}_8$, and $\text{Ba}_{1-2x}\text{R}_x\text{Li}_x\text{Si}_7\text{N}_{10}$, where M = Ca and Sr, and R = Ce and Tb have been synthesized successfully by applying the polymer route [369], similar to the one which has already been applied for the synthesis of phosphors based on amorphous $\text{Si}_3\text{B}_3\text{N}_7$ ceramic (see Chapter 5). In this case, SiCl_4 has been ammonolysed with liquid NH_3 in which Eu, Ca, Sr, Ba and Li were dissolved (named as metal route) or $\text{Eu}[\text{N}(\text{Si}(\text{CH}_3)_2)_3]$, $\text{Ce}[\text{N}(\text{Si}(\text{CH}_3)_2)_3]$ and $\text{Tb}[\text{N}(\text{Si}(\text{CH}_3)_2)_3]$ were suspended (named as organometallic route). Details for preparations are presented in Section 10.3. The significant advantages of this novel method over the conventional solid state syntheses are that it does not require extreme conditions, laborious handling and complex equipments, and allows to obtain the desired compounds via a single step reaction in a solution by using commercially available reactants.

7.1. Synthesis and Characterization of $M_{2-x}Eu_xSi_5N_8$, where $M = Ca$ and Sr

The compounds $M_{2-x}Eu_xSi_5N_8$, where $M = Ca$ and Sr have previously been synthesized via different methods and investigated in details by various research groups. All these previous works have been described in Section 4.3. The $M_2Si_5N_8$ host lattices, where $M = Ca, Sr, Ba$ and Eu , contain M^{2+} ions as well as three-dimensional covalent network structure of corner-sharing SiN_4 tetrahedra. In addition, two crystallographically independent N atoms occur with molar ratio 1:1 which are bonded to two and three Si, respectively. Moreover, $Ca_2Si_5N_8$ has a monoclinic crystal system whereas $M_2Si_5N_8$, where $M = Sr, Ba$ and Eu , have orthorhombic one [245, 251, 252].

In the present study, the $M_{2-x}Eu_xSi_5N_8$ compounds, where $M = Ca$ and Sr , have been prepared via the polymer route in various compositions, including $x=0$ and $x=2$, by first ammonolysing the stoichiometric amounts of $SiCl_4$ with liquid ammonia in which Eu, Ca and Sr are dissolved or $Eu[N(Si(CH_3)_3)_2]_3$ is suspended, and then pyrolysing the obtained polymers at 1500 °C. The following reactions are proposed ($M = Ca$ and Sr):

a) For the metal route:



b) For the organometallic route:

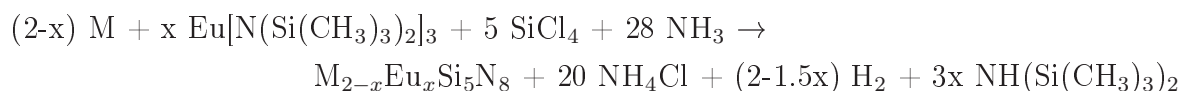


Figure 7.1 and Figure 7.2 represent the powder X-ray diffractograms of $Ca_2Si_5N_8$ and $Sr_2Si_5N_8$, respectively. In both cases, the powder X-ray pattern of the samples are agree well with their theoretical powder patterns as calculated from the data in Inorganic Crystal Structure Database (ICSD) with ICSD numbers [82-2489] and [85-101] for $Ca_2Si_5N_8$ and $Sr_2Si_5N_8$, respectively. In addition to the diffraction peaks belonging to the $Ca_2Si_5N_8$ or $Sr_2Si_5N_8$ phases, both samples include some Si_3N_4 and undefined phases. Since no metallic phases were observed, the Si_3N_4 phases might result from the unstoichiometric addition of $SiCl_4$, which has been observed in almost all nitridosilicates obtained via the polymer route. In addition, such unknown phases were also reported in previous works [257]. Therefore, Si_3N_4 and undefined phases will only be presented in the corresponding powder X-ray diffractograms through this chapter, in order to avoid the repetition.

Figure 7.3 and Figure 7.4 include the diffuse reflection spectra of $Ca_2Si_5N_8$ and $Sr_2Si_5N_8$, respectively. Since both of the host matrices have grayish-white appearance, they exhibit strong reflection in the visible region of the spectrum. In addition, both of the host matrices have strong absorption in the UV region between 200 nm and 300 nm.

7.1. Synthesis and Characterization of $M_{2-x}Eu_xSi_5N_8$, where $M = Ca$ and Sr

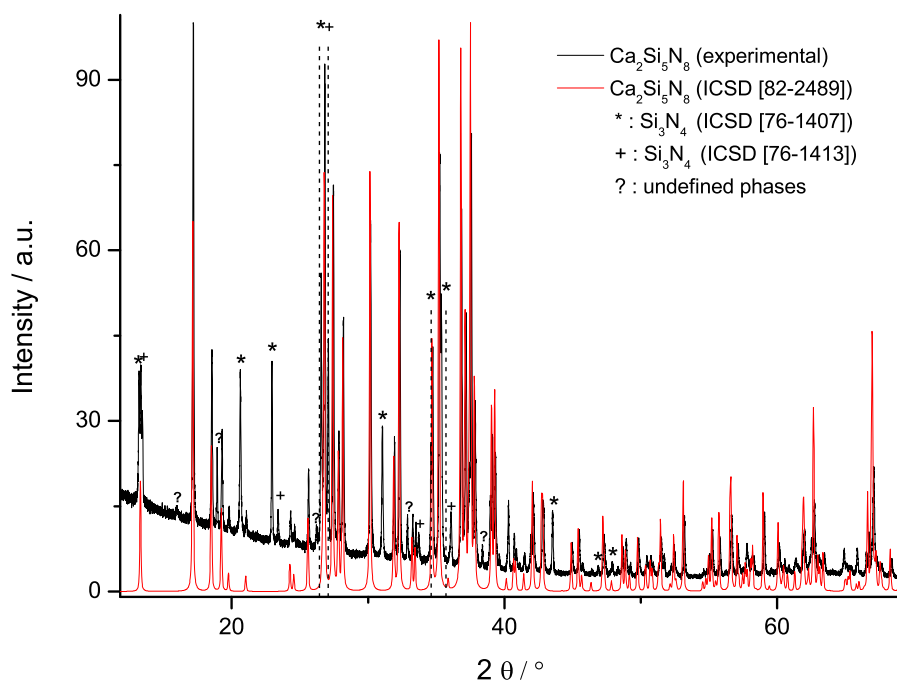


Figure 7.1.: Powder X-ray diffractogram of $Ca_2Si_5N_8$.

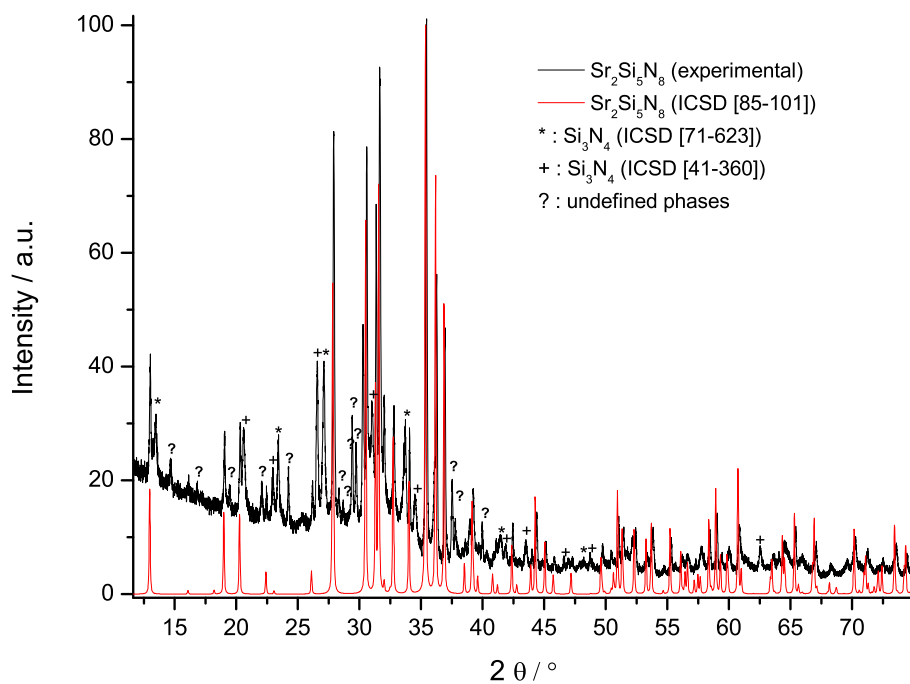


Figure 7.2.: Powder X-ray diffractogram of $Sr_2Si_5N_8$.

7. A Novel Production Method for Crystalline Nitridosilicates

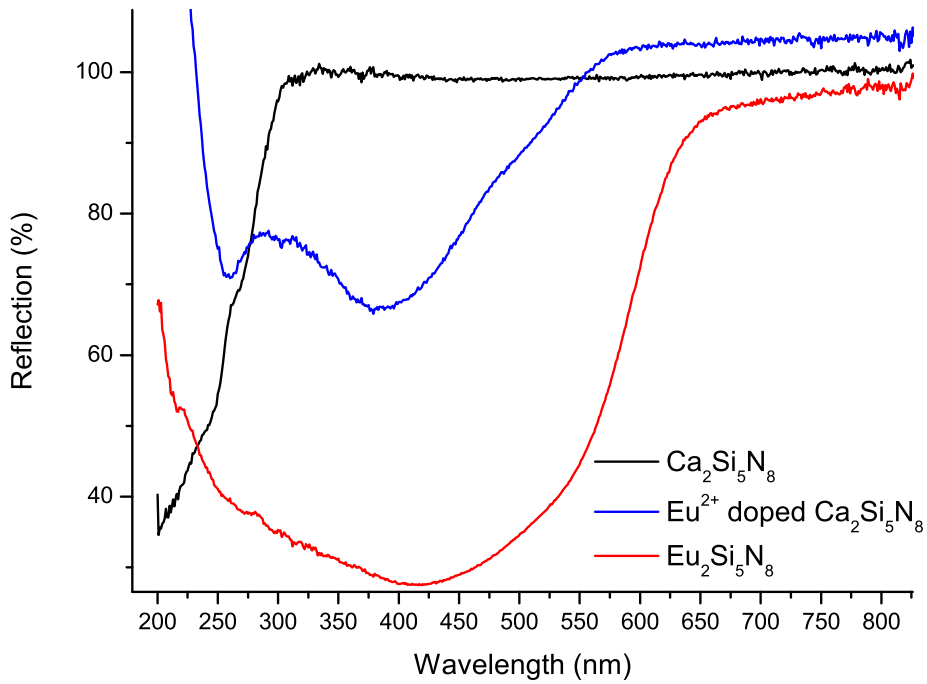


Figure 7.3.: Diffuse reflection spectra of $\text{Ca}_2\text{Si}_5\text{N}_8$, Eu^{2+} doped $\text{Ca}_2\text{Si}_5\text{N}_8$ and $\text{Eu}_2\text{Si}_5\text{N}_8$.

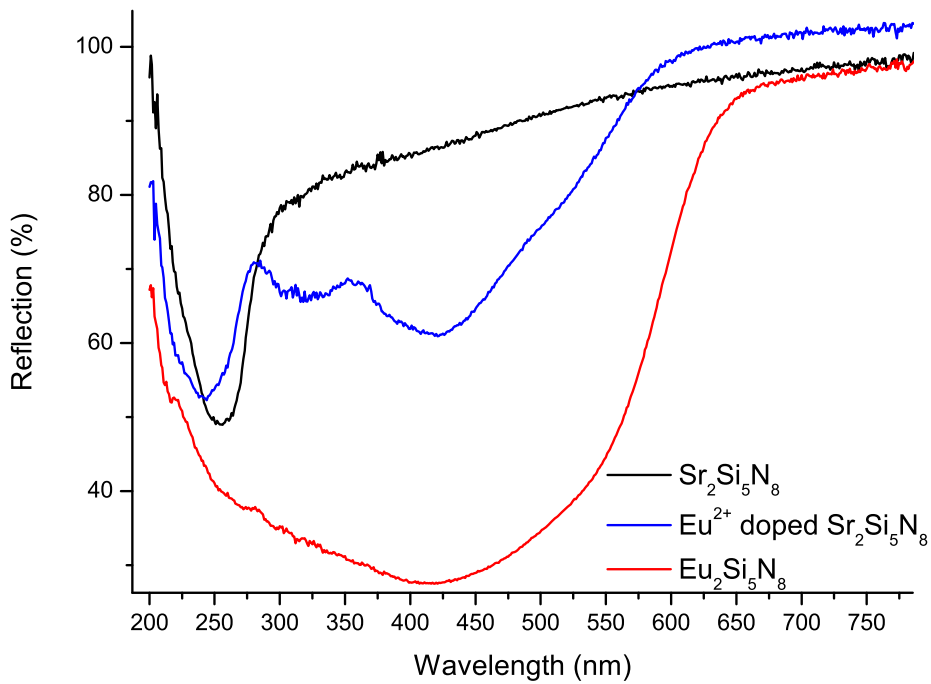


Figure 7.4.: Diffuse reflection spectra of $\text{Sr}_2\text{Si}_5\text{N}_8$, Eu^{2+} doped $\text{Sr}_2\text{Si}_5\text{N}_8$ and $\text{Eu}_2\text{Si}_5\text{N}_8$.

The powder X-ray diffractogram of Eu^{2+} doped $Ca_2Si_5N_8$ matrix is presented in Figure 7.5. It is seen in this figure that all of the $Ca_2Si_5N_8$ diffraction peaks in ICSD, [82-2489], are well matched by those of the Eu^{2+} doped $Ca_2Si_5N_8$ samples. The diffuse reflection spectrum of the Eu^{2+} doped $Ca_2Si_5N_8$ ceramic is depicted in Figure 7.3, which is well consistent with the literature values [257]. In the diffuse reflection spectrum, Eu^{2+} doped $Ca_2Si_5N_8$ exhibited two main absorption bands. The absorption band between 220 nm and 280 nm is assigned to the absorption of $Ca_2Si_5N_8$ host matrix. On the other hand, the absorption band between 300 nm and 450 nm, which gives rise to the orange color of the sample, is attributed to the absorption by Eu^{2+} ions because this band is absent in undoped $Ca_2Si_5N_8$. For comparison, the diffuse reflection spectrum of the end member of Eu^{2+} doped $Ca_2Si_5N_8$ system, which is $Eu_2Si_5N_8$, is also included in Figure 7.3. However, it has already been reported that the solubility limit of the Eu^{2+} ions in $Ca_2Si_5N_8$ host matrix is 7 mol % due to the fact that the two end members, $Ca_2Si_5N_8$ and $Eu_2Si_5N_8$, belong to different space groups (i.e. monoclinic versus orthorhombic crystal systems) [257].

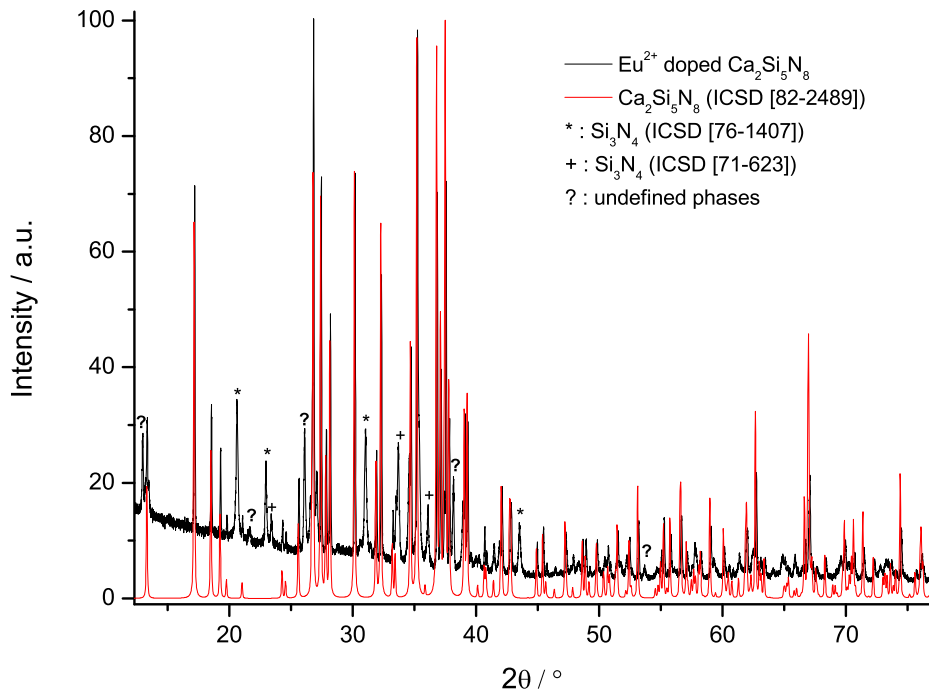


Figure 7.5.: Powder X-ray diffractogram of Eu^{2+} doped $Ca_2Si_5N_8$.

7. A Novel Production Method for Crystalline Nitridosilicates

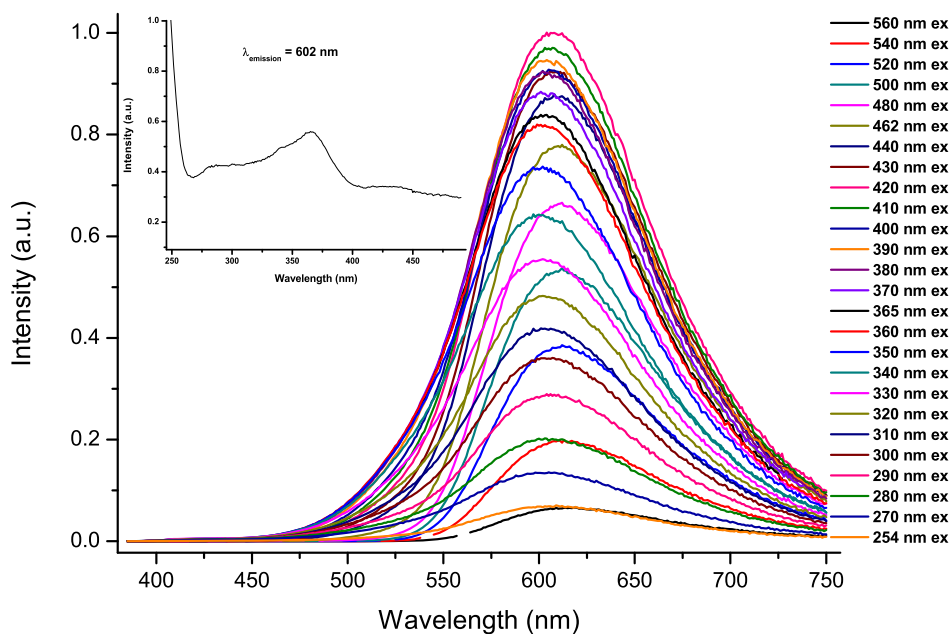


Figure 7.6.: Emission spectra of Eu^{2+} doped $\text{Ca}_2\text{Si}_5\text{N}_8$ at different excitation wavelengths (Inset: Excitation spectrum at 602 nm emission wavelength).

The emission spectra of Eu^{2+} doped $\text{Ca}_2\text{Si}_5\text{N}_8$ sample at different excitation wavelengths are shown in Figure 7.6 with an inset representing the excitation spectrum of the sample at 602 nm emission wavelength. These spectra are well consistent with the literature data [257]. The Eu^{2+} doped $\text{Ca}_2\text{Si}_5\text{N}_8$ sample exhibited a structureless very wide excitation spectrum ranging from 260 nm to 490 nm and a typical broad emission band due to the $4f^65d^1 \rightarrow 4f^7$ transition of Eu^{2+} ions at 607 nm (in [257], the emissions were reported to be between 605 nm and 615 nm, depending on Eu^{2+} concentration).

Figure 7.7 shows the powder X-ray diffractogram of Eu^{2+} doped $\text{Sr}_2\text{Si}_5\text{N}_8$ matrix and represents that all of the $\text{Sr}_2\text{Si}_5\text{N}_8$ diffraction peaks in ICSD, [85-101], perfectly match with those in the diffractogram of the sample. The diffuse reflection spectrum of Eu^{2+} doped $\text{Sr}_2\text{Si}_5\text{N}_8$ ceramic is exhibited in Figure 7.4, which is well consistent with the literature data [257]. In the diffuse reflection spectrum, Eu^{2+} doped $\text{Sr}_2\text{Si}_5\text{N}_8$ exhibited three distinct absorption bands. The absorption band between 220 nm and 280 nm is assigned to the absorption of the $\text{Sr}_2\text{Si}_5\text{N}_8$ host matrix. On the other hand, two absorption bands (the one between 280 nm and 360 nm, and the other between 360 nm and 580 nm) are attributed to the absorption by the Eu^{2+} ions because this band is absent in undoped $\text{Sr}_2\text{Si}_5\text{N}_8$. These absorptions in the visible region of the spectrum are responsible for the orange color of the samples. Similar behavior was also reported in [257]. The absorption band between 280 nm and 360 nm, which is assigned to the absorption of Eu^{2+} ions, was not significant in

the case of Eu^{2+} doped $Ca_2Si_5N_8$ sample. For comparison, the diffuse reflection spectrum of the end member of Eu^{2+} doped $Sr_2Si_5N_8$ system, which is $Eu_2Si_5N_8$, is also included in Figure 7.4. Since Eu^{2+} ions are completely soluble in $Sr_2Si_5N_8$ host lattice due to the fact that the two end members, $Sr_2Si_5N_8$ and $Eu_2Si_5N_8$, belong to the same space group (i.e. orthorhombic crystal systems), increasing the Eu^{2+} content into $Sr_2Si_5N_8$ matrix shifts the absorption band in reflection spectrum towards longer wavelengths [257].

The emission spectra of Eu^{2+} doped $Sr_2Si_5N_8$ sample at different excitation wavelengths are presented in Figure 7.8 with an inset representing the excitation spectrum of the sample at 632 nm emission wavelength. The spectra are well consistent with the literature value [257]. The Eu^{2+} doped $Sr_2Si_5N_8$ sample exhibited a structureless very wide excitation spectrum ranging from 260 nm to 490 nm, and a typical broad emission band due to the $4f^65d^1 \rightarrow 4f^7$ transition of Eu^{2+} ions at 632 nm (in [257], the emissions were reported to be between 609 nm and 680 nm, depending on Eu^{2+} concentration).

$Eu_2Si_5N_8$, the end member of the Eu^{2+} doped $Ca_2Si_5N_8$ and $Sr_2Si_5N_8$ systems, has been successfully synthesized via both the metal and organometallic polymer routes. Figure 7.9 and Figure 7.10 represent the powder X-ray diffractograms of $Eu_2Si_5N_8$ obtained via the metal and organometallic routes, respectively. As it is seen in both figures, all of the $Eu_2Si_5N_8$ diffraction peaks in ICSD, [87-0423], perfectly match by those of the $Eu_2Si_5N_8$ samples obtained via both the metal and organometallic routes. The $Eu_2Si_5N_8$ sample obtained via the metal route contains very few Si_3N_4 impurities without any other undefined phases (Figure 7.9) whereas the $Eu_2Si_5N_8$ sample obtained via the organometallic route contains both very few Si_3N_4 impurities and some undefined phases (Figure 7.10). The diffuse reflection spectrum of the $Eu_2Si_5N_8$ is given in both Figure 7.3 and Figure 7.4 and characterized with a strong and broad absorption between 200 nm and 600 nm, which is responsible for the orange-red appearance of the samples. The same result was also reported in [257].

The emission spectra of $Eu_2Si_5N_8$ via the metal route at different excitation wavelengths are presented in Figure 7.11 with an inset representing the excitation spectrum of the sample at 684 nm emission wavelength. Furthermore, photoluminescence spectra of $Eu_2Si_5N_8$ via the organometallic route at different excitation wavelengths are shown in Figure 7.12 with an inset representing the excitation spectrum of the sample at 681 nm emission wavelength. The photoluminescence spectra of $Eu_2Si_5N_8$ obtained via both routes are well consistent with the literature value [257]. Similar to the values in the literature, $Eu_2Si_5N_8$ samples exhibited a structureless very wide excitation spectrum ranging from 260 nm to 490 nm, and a typical broad emission band due to the $4f^65d^1 \rightarrow 4f^7$ transition of Eu^{2+} ions at 685 nm and 682 nm for the metal and organometallic routes, respectively (in [257], the emission was reported to be at 680 nm).

7. A Novel Production Method for Crystalline Nitridosilicates

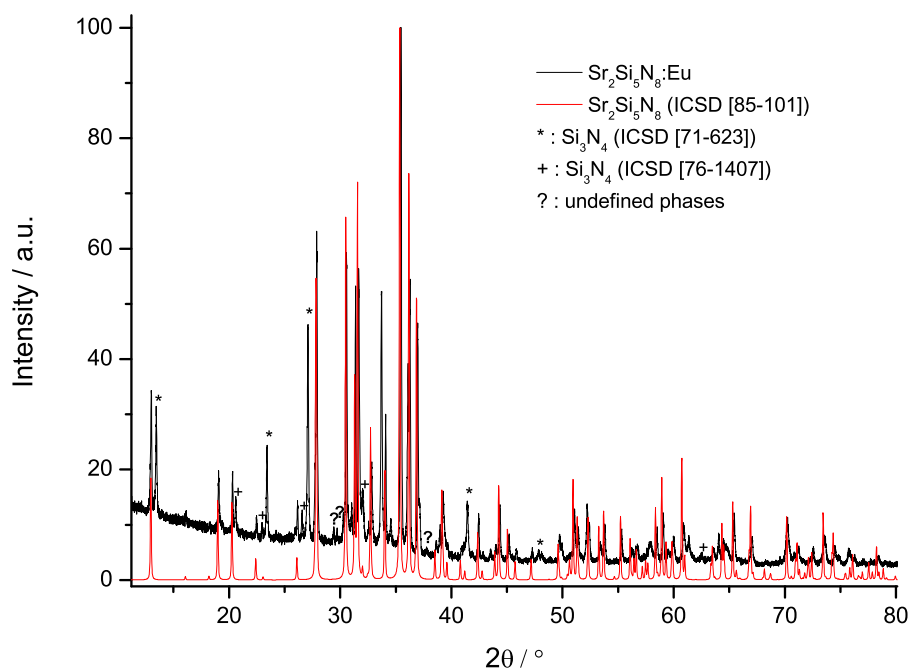


Figure 7.7.: Powder X-ray diffractogram of Eu²⁺ doped Sr₂Si₅N₈.

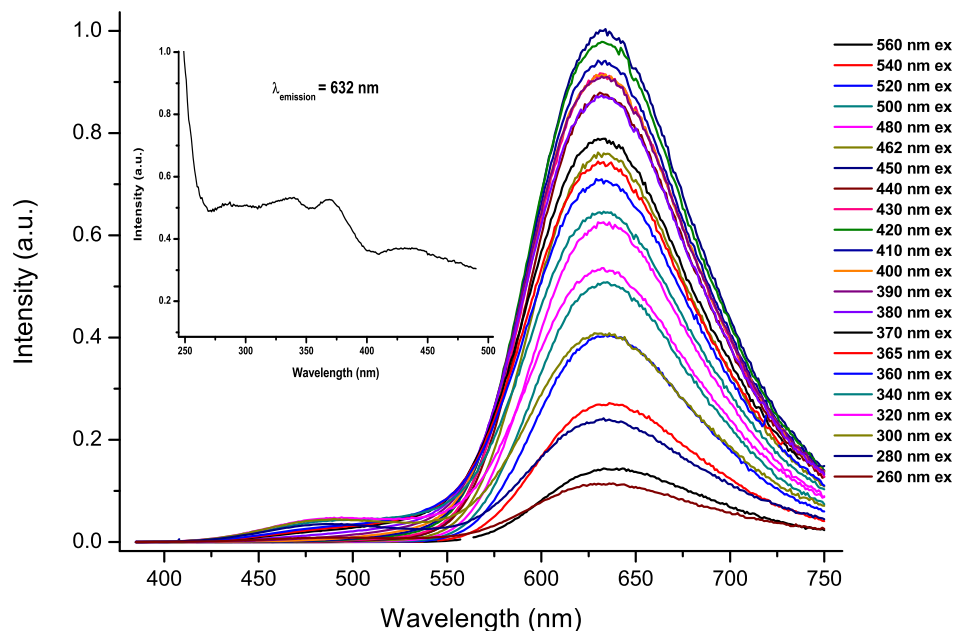


Figure 7.8.: Emission spectra of Eu²⁺ doped Sr₂Si₅N₈ at different excitation wavelengths (Inset: Excitation spectrum at 632 nm emission wavelength).

7.1. Synthesis and Characterization of $M_{2-x}Eu_xSi_5N_8$, where $M = Ca$ and Sr

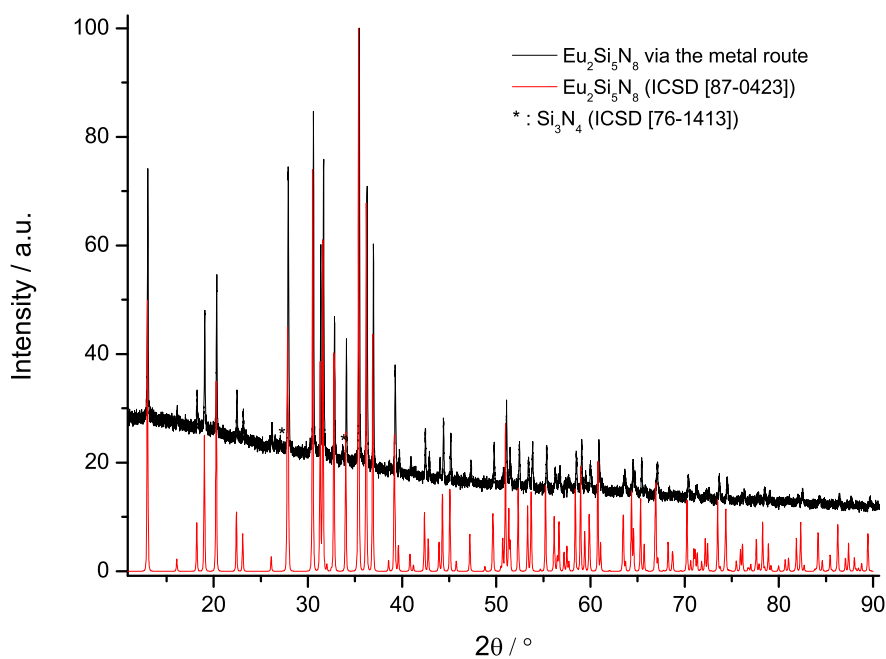


Figure 7.9.: Powder X-ray diffractogram of $Eu_2Si_5N_8$ synthesized via the metal route.

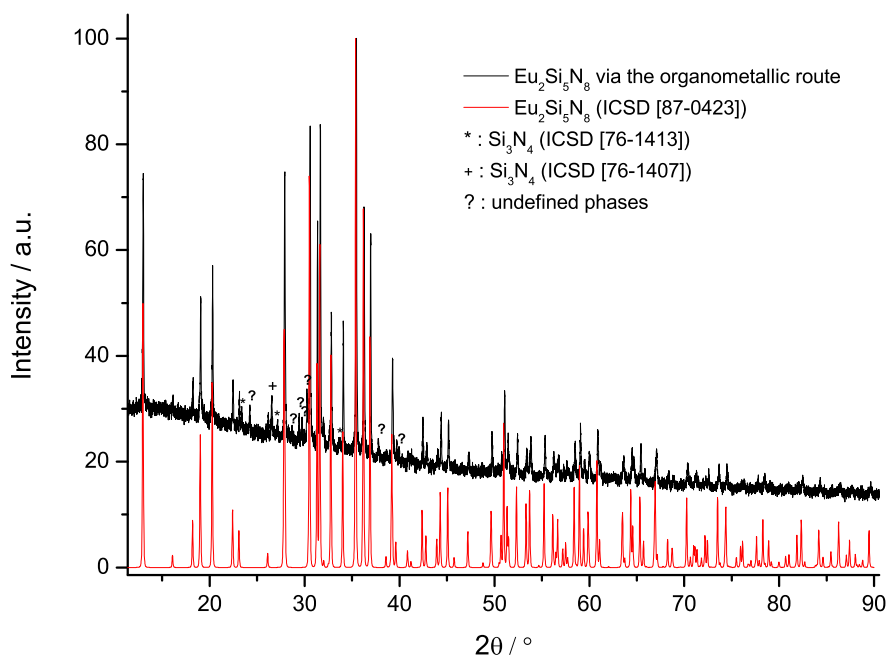


Figure 7.10.: Powder X-ray diffractogram of $Eu_2Si_5N_8$ synthesized via the organometallic route.

7. A Novel Production Method for Crystalline Nitridosilicates

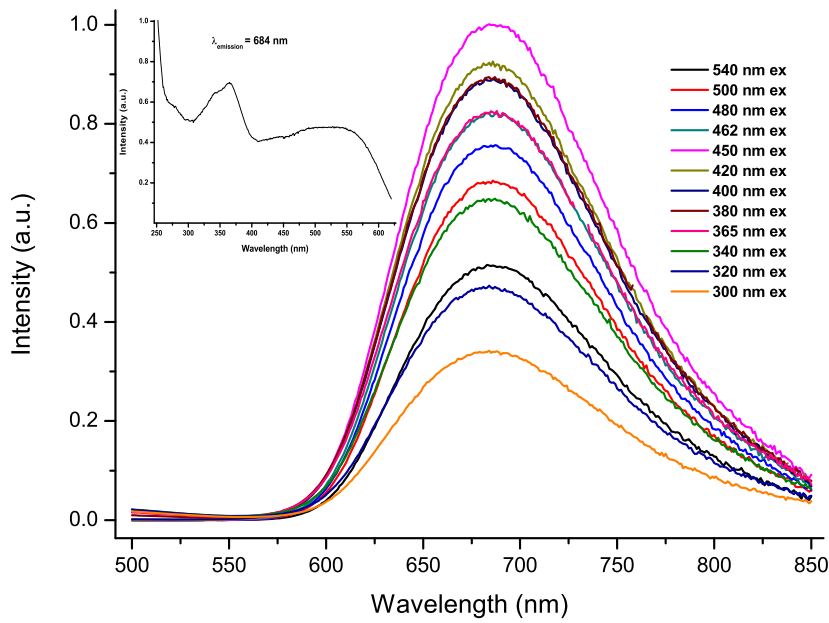


Figure 7.11.: Emission spectra of $\text{Eu}_2\text{Si}_5\text{N}_8$ synthesized via the metal route at different excitation wavelengths (Inset: Excitation spectrum at 684 nm emission wavelength).

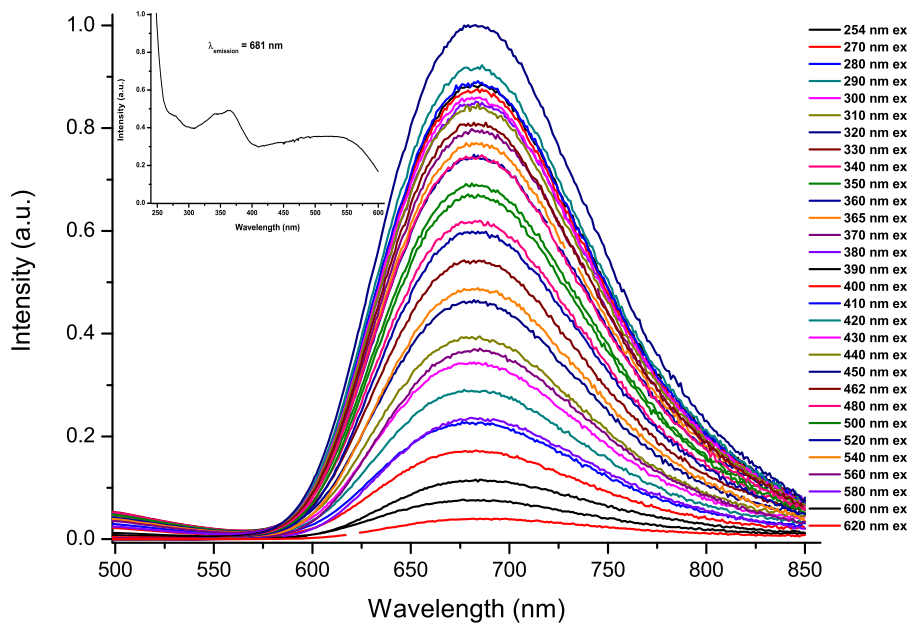


Figure 7.12.: Emission spectra of $\text{Eu}_2\text{Si}_5\text{N}_8$ synthesized via organometallic route at different excitation wavelengths (Inset: Excitation spectrum at 681 nm emission wavelength).

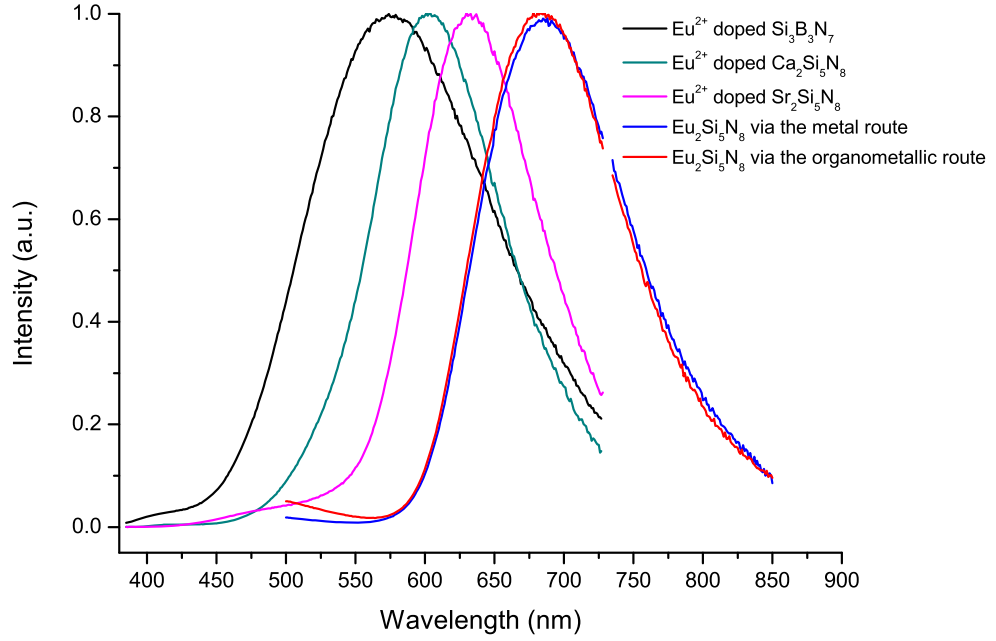


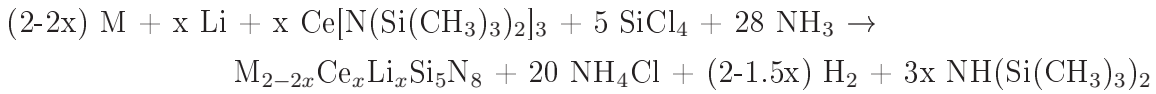
Figure 7.13.: Comparison of the emission spectra of Eu^{2+} doped $Ca_2Si_5N_8$ and $Sr_2Si_5N_8$, $Eu_2Si_5N_8$ synthesized via both the metal and the organometallic route, and Eu^{2+} doped amorphous $Si_3B_3N_7$ at 365 nm excitation wavelength.

Figure 7.13 compares the emission spectra of Eu^{2+} doped $Ca_2Si_5N_8$ and $Sr_2Si_5N_8$, $Eu_2Si_5N_8$ synthesized via both the metal and the organometallic routes, and Eu^{2+} doped amorphous $Si_3B_3N_7$ at 365 nm excitation wavelength. The FWHM values are determined as 160 nm for Eu^{2+} doped amorphous $Si_3B_3N_7$, 112 nm for Eu^{2+} doped $Ca_2Si_5N_8$, 107 nm for Eu^{2+} doped $Sr_2Si_5N_8$ and 126 nm for $Eu_2Si_5N_8$. The FWHM value of Eu^{2+} doped amorphous $Si_3B_3N_7$ ceramic is around 45 % higher than those of Eu^{2+} doped $Ca_2Si_5N_8$ and $Sr_2Si_5N_8$, and 27 % higher than those of $Eu_2Si_5N_8$ crystalline ceramics. In addition, it has been discussed in Chapter 5.25 that the emission wavelength of Eu^{2+} doped amorphous $Si_3B_3N_7$ ceramics can be tuned easily by adjusting the Eu^{2+} concentration in amorphous $Si_3B_3N_7$ matrix. Therefore, it is quite obvious that Eu^{2+} doped amorphous $Si_3B_3N_7$ ceramics might show better color rendering properties when combined with GaN-type LEDs in comparison to Eu^{2+} doped $Ca_2Si_5N_8$ and $Sr_2Si_5N_8$ crystalline ceramics.

7.2. Synthesis and Characterization of

$M_{2-2x}Ce_xLi_xSi_5N_8$, where $M = Ca$ and Sr

Ce^{3+}/Li^+ codoped $Ca_2Si_5N_8$ and $Sr_2Si_5N_8$ host lattices have previously been investigated by Hintzen et. al [258]. The authors applied conventional solid state synthesis, in which Ce and Li metals were fired together with the corresponding alkaline-earth nitrides and Si_3N_4 . In the present work, the polymer route has been applied for the synthesis of Ce^{3+}/Li^+ codoped $Ca_2Si_5N_8$ and $Sr_2Si_5N_8$ host lattices. The following reactions are proposed ($M = Ca$ and Sr):



The powder X-ray diffractogram of Ce^{3+}/Li^+ codoped $Ca_2Si_5N_8$ matrix is presented in Figure 7.14. It is seen in this figure that all of the $Ca_2Si_5N_8$ diffraction peaks in ICSD, [82-2489], are agree well with that of the Ce^{3+}/Li^+ codoped $Ca_2Si_5N_8$ samples. The diffuse reflection spectrum of Ce^{3+}/Li^+ codoped $Ca_2Si_5N_8$ is included in Figure 7.15. In addition to the absorption between 230 nm and 300 nm due to the $Ca_2Si_5N_8$ host lattice, a strong absorption of Ce^{3+} ions between 350 nm and 470 nm has clearly been observed.

The photoluminescence spectra of Ce^{3+}/Li^+ codoped $Ca_2Si_5N_8$ sample are presented in Figure 7.16. Excitation spectrum at 496 nm emission wavelength includes three main excitation bands at around 250 nm, 330 nm and 370 nm, and a shoulder peak at 400 nm. The excitation band at around 250 nm originates from the host matrix as can be concluded from the diffuse reflection spectrum. The remaining excitation bands including the shoulder peak are assigned to $4f \rightarrow 5d$ transition of Ce^{3+} ions separated by crystal field splitting of the 5d state. The emission spectra show a broad band with two maxima at around 500 nm and 580 nm, among which the former one is dominating. Even though there are two crystallographic Ca sites in $Ca_2Si_5N_8$ [251], Hintzen et. al reported only one highly symmetric emission band (between 470 nm to 480 nm, depending on the Ce^{3+} concentration) for the same compound [258]. The same authors also reported that the main excitation band occurred at around 400 nm whereas the excitation band at 370 nm appeared as a shoulder, which has appeared the other way around in the present study. Since our sample has some Si_3N_4 impurities, these slight differences are attributed to those impurities.

Figure 7.17 exhibits the powder X-ray diffractogram of Ce^{3+}/Li^+ codoped $Sr_2Si_5N_8$ matrix. All of the $Sr_2Si_5N_8$ diffraction peaks in ICSD, [82-2489], are agree well with that of the Ce^{3+}/Li^+ codoped $Sr_2Si_5N_8$ sample. Figure 7.15 contains the diffuse reflection spectrum of Ce^{3+}/Li^+ codoped $Sr_2Si_5N_8$, which has similar reflection pattern with the Ce^{3+}/Li^+ codoped $Ca_2Si_5N_8$ sample. The absorption between 230 nm and 300 nm is due

to the $Sr_2Si_5N_8$ host lattice and the strong absorption between 350 nm and 470 nm is assigned to the $4f \rightarrow 5d$ transition of Ce^{3+} ions.

The photoluminescence spectra of Ce^{3+}/Li^+ codoped $Sr_2Si_5N_8$ sample are shown in Figure 7.18. Excitation spectra at different emission wavelengths possessed four excitation bands at around 250 nm, 330 nm, 370 nm and 400 nm. The excitation band at around 250 nm is resulted from the host matrix, which is consistent with the diffuse reflection spectrum. The remaining excitation bands are assigned to $4f \rightarrow 5d$ transition of Ce^{3+} ions separated by crystal-field splitting of the 5d state. The emission spectra have an asymmetric broad band with a maximum at around 550 nm. The same emission behavior was reported by Hintzen et. al and this asymmetry in the emission band was assigned that Ce^{3+} ions occupied two different Sr sites in $Sr_2Si_5N_8$ [258]. The fact that the structural difference between the two cation sites is larger in $Sr_2Si_5N_8$ as compared to $Ca_2Si_5N_8$ [252] was given as an explanation for the above observation. The same authors also reported that the main excitation band occurred at around 395 nm whereas that in the present study appeared at 370 nm, most probably due to the Si_3N_4 impurities.

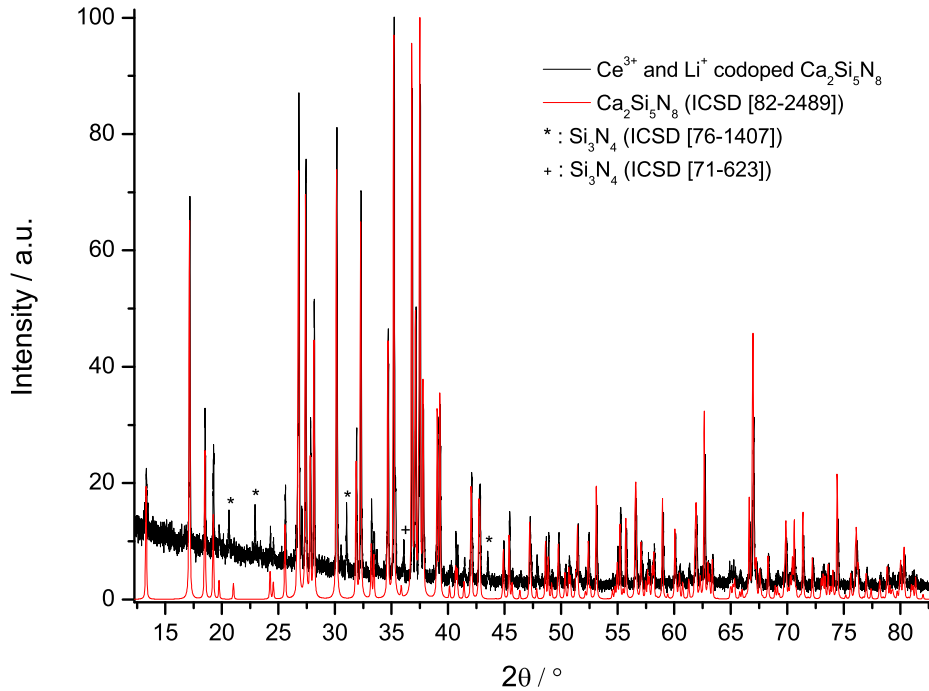


Figure 7.14.: Powder X-ray diffractogram of Ce^{3+}/Li^+ codoped $Ca_2Si_5N_8$.

7. A Novel Production Method for Crystalline Nitridosilicates

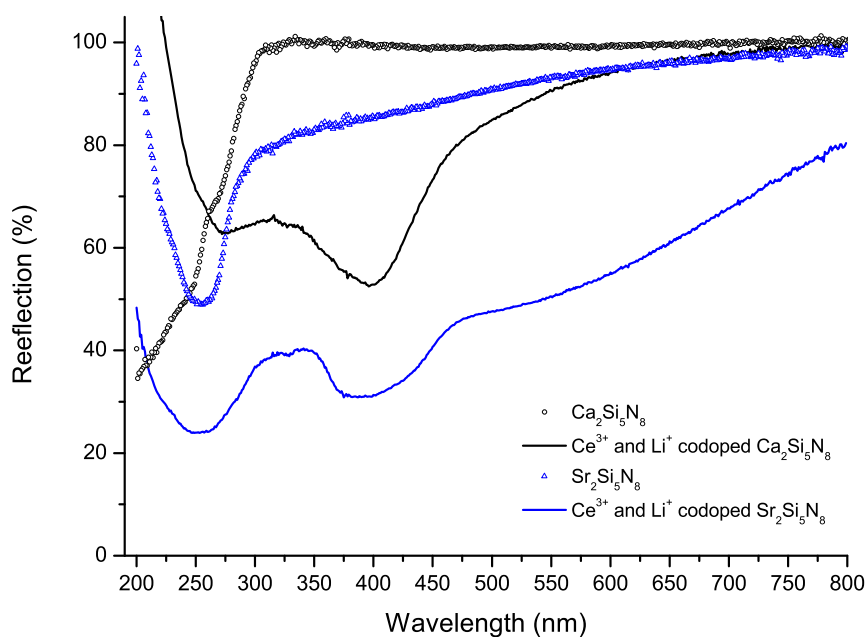


Figure 7.15.: Diffuse reflection spectra of $\text{Ca}_2\text{Si}_5\text{N}_8$, $\text{Ce}^{3+}/\text{Li}^+$ codoped $\text{Ca}_2\text{Si}_5\text{N}_8$, $\text{Sr}_2\text{Si}_5\text{N}_8$, and $\text{Ce}^{3+}/\text{Li}^+$ codoped $\text{Sr}_2\text{Si}_5\text{N}_8$.

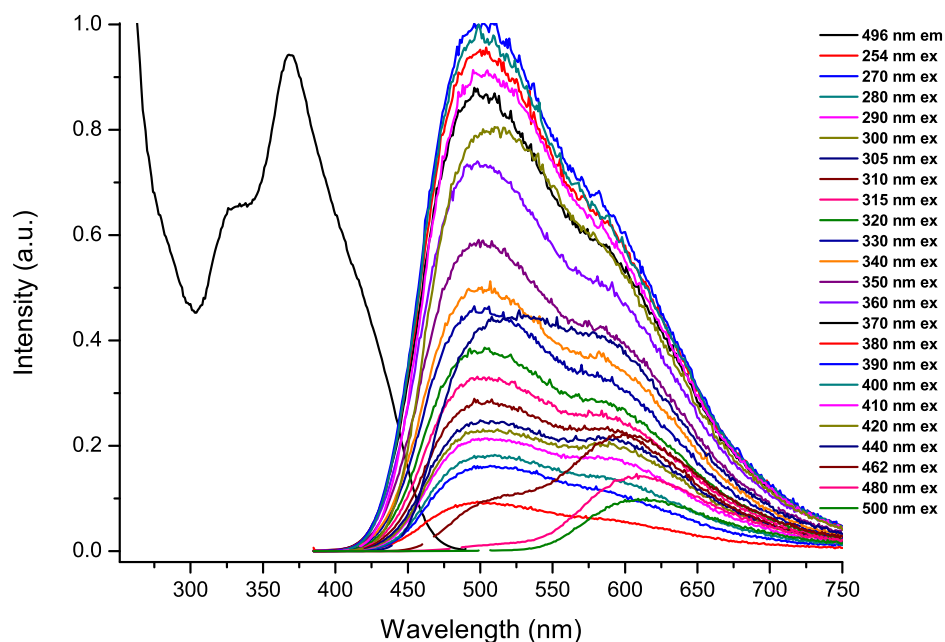


Figure 7.16.: Photoluminescence spectra of $\text{Ce}^{3+}/\text{Li}^+$ codoped $\text{Ca}_2\text{Si}_5\text{N}_8$ at different excitation and emission wavelengths.

7.2. Synthesis and Characterization of $M_{2-2x}Ce_xLi_xSi_5N_8$, where $M = Ca$ and Sr

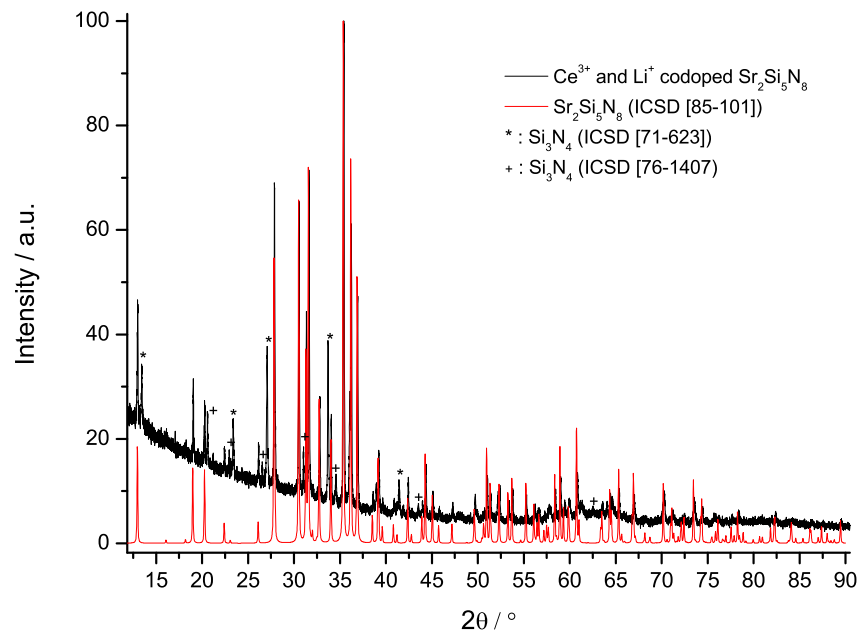


Figure 7.17.: Powder X-ray diffractogram of Ce^{3+}/Li^{+} codoped $Sr_2Si_5N_8$.

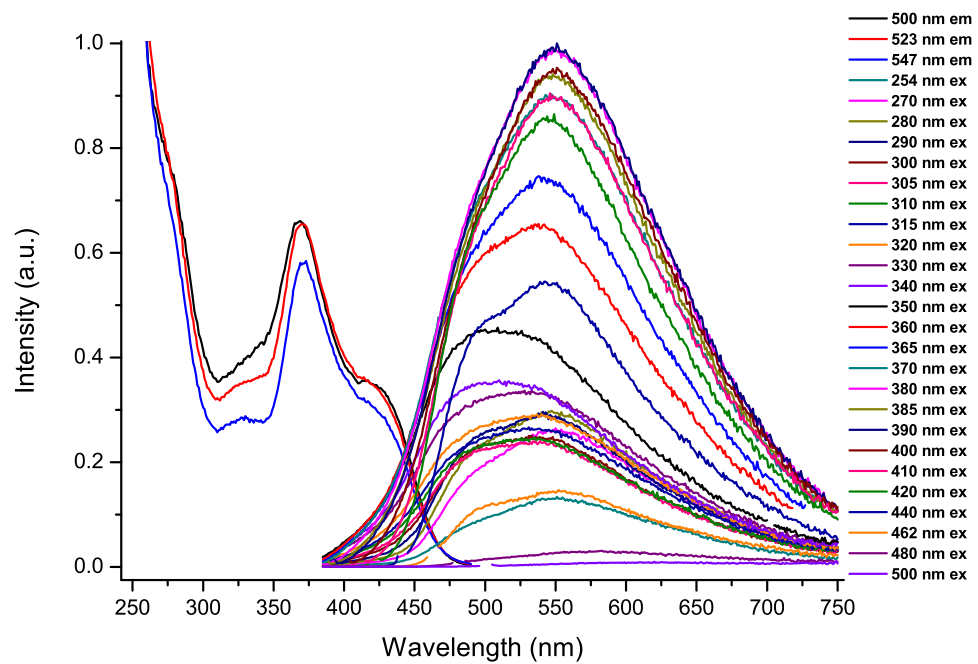


Figure 7.18.: Photoluminescence spectra of Ce^{3+}/Li^{+} codoped $Sr_2Si_5N_8$ at different excitation and emission wavelengths.

7.3. Synthesis and Characterization of

$M_{2-2x}Tb_xLi_xSi_5N_8$, where $M = Ca$ and Sr

To the best of our knowledge, Tb^{3+}/Li^+ codoped $Ca_2Si_5N_8$ and $Sr_2Si_5N_8$ host lattices have been prepared for the first time in the present work, via applying the polymer route. The following reactions are proposed ($M = Ca$ and Sr):



Both samples exhibited very intense characteristic Tb^{3+} green emission. The powder X-ray diffractogram of Tb^{3+}/Li^+ codoped $Ca_2Si_5N_8$ matrix is presented in Figure 7.19. It is seen in this figure that all of the $Ca_2Si_5N_8$ diffraction peaks in ICSD, [82-2489], are agree well with that of the Tb^{3+}/Li^+ codoped $Ca_2Si_5N_8$ samples. The diffuse reflection spectrum of Tb^{3+}/Li^+ codoped $Ca_2Si_5N_8$ is included in Figure 7.20. The absorption between 230 nm and 260 nm is assigned to the absorption of the $Ca_2Si_5N_8$ host lattice, and that between 270 nm and 320 nm is assigned to the $4f \rightarrow 5d$ transition of Tb^{3+} ions, which is consistent with the excitation spectrum of the sample.

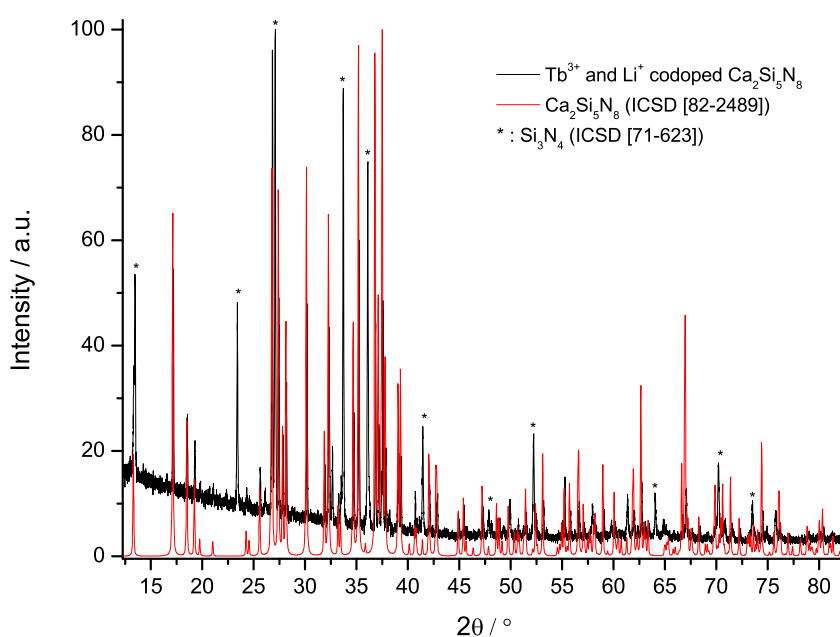


Figure 7.19.: Powder X-ray diffractogram of Tb^{3+}/Li^+ codoped $Ca_2Si_5N_8$.

7.3. Synthesis and Characterization of $M_{2-2x}Tb_xLi_xSi_5N_8$, where $M = Ca$ and Sr

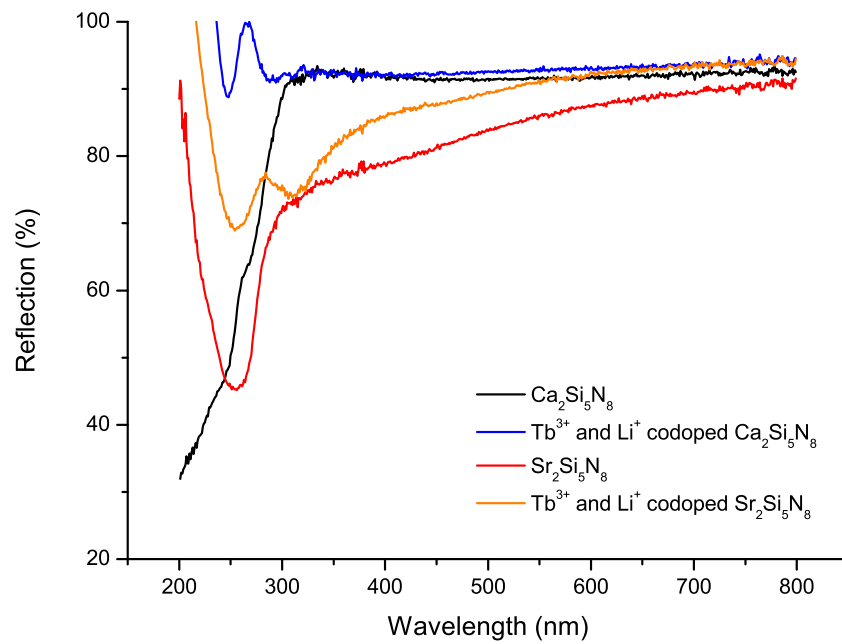


Figure 7.20.: Diffuse reflection spectra of $Ca_2Si_5N_8$, Tb^{3+}/Li^+ codoped $Ca_2Si_5N_8$, $Sr_2Si_5N_8$, and Tb^{3+}/Li^+ codoped $Sr_2Si_5N_8$.

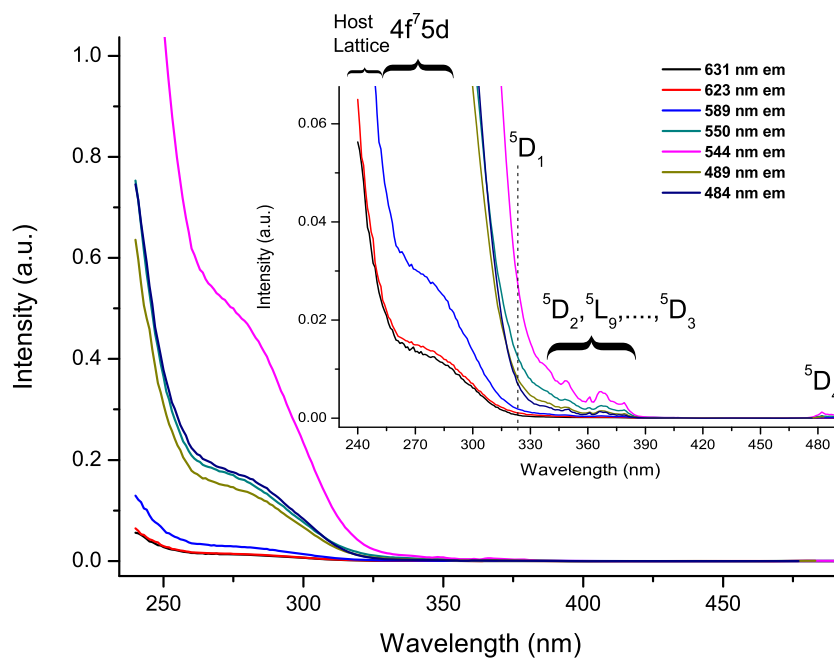


Figure 7.21.: Excitation spectra of Tb^{3+}/Li^+ codoped $Ca_2Si_5N_8$ at different emission wavelengths (Inset represents the zoomed spectra).

7. A Novel Production Method for Crystalline Nitridosilicates

Excitation spectra of $\text{Tb}^{3+}/\text{Li}^+$ codoped $\text{Ca}_2\text{Si}_5\text{N}_8$ sample are presented in Figure 7.21. All typical absorption bands of Tb^{3+} ions have been observed (see Figure 5.58). In addition to the strong absorption due to the host lattice at around 250 nm, Tb^{3+} ions showed strong absorption between 250 nm and 300 nm due to the $4f^8 \rightarrow 4f^75d^1$ transition. Moreover, absorptions from the ground state level ($4f^8$ or 7F_6) to excited states were depicted in the inset graph of Figure 7.21. All typical $4f \rightarrow 4f$ emission lines have been observed in the emission spectra of $\text{Tb}^{3+}/\text{Li}^+$ codoped $\text{Ca}_2\text{Si}_5\text{N}_8$ matrix and corresponding transitions are presented in Figure 7.22. All these emissions result in a very intense bright green light.

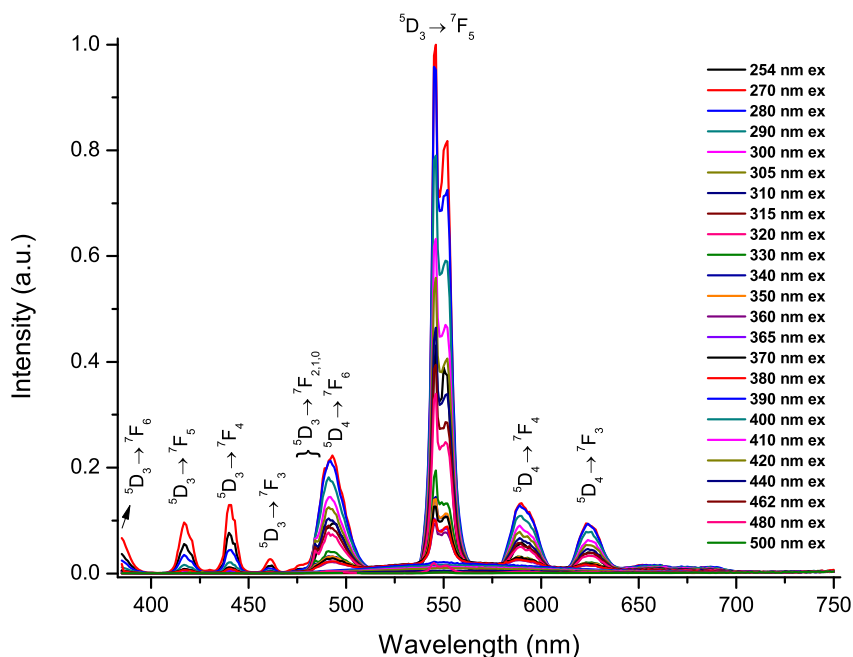


Figure 7.22.: Emission spectra of $\text{Tb}^{3+}/\text{Li}^+$ codoped $\text{Ca}_2\text{Si}_5\text{N}_8$ at different excitation wavelengths.

Figure 7.23 shows the powder X-ray diffractogram of $\text{Tb}^{3+}/\text{Li}^+$ codoped $\text{Sr}_2\text{Si}_5\text{N}_8$ matrix. This figure depicts that all of the $\text{Sr}_2\text{Si}_5\text{N}_8$ diffraction peaks in ICSD, [85-101], agree well with that of the $\text{Tb}^{3+}/\text{Li}^+$ codoped $\text{Sr}_2\text{Si}_5\text{N}_8$ sample. Different than the $\text{Tb}^{3+}/\text{Li}^+$ codoped $\text{Ca}_2\text{Si}_5\text{N}_8$ sample, some undefined phases have been detected in the X-ray diffractogram of the $\text{Tb}^{3+}/\text{Li}^+$ codoped $\text{Sr}_2\text{Si}_5\text{N}_8$ sample. Figure 7.20 contains the diffuse reflection spectrum of $\text{Tb}^{3+}/\text{Li}^+$ codoped $\text{Sr}_2\text{Si}_5\text{N}_8$, which has similar reflection pattern with the $\text{Tb}^{3+}/\text{Li}^+$ codoped $\text{Ca}_2\text{Si}_5\text{N}_8$ sample. Different than $\text{Tb}^{3+}/\text{Li}^+$ codoped $\text{Ca}_2\text{Si}_5\text{N}_8$ sample, $4f \rightarrow 4f$ transitions of Tb^{3+} ions in $\text{Tb}^{3+}/\text{Li}^+$ codoped $\text{Sr}_2\text{Si}_5\text{N}_8$ sample extends the $4f \rightarrow 5d$ absorption band to longer wavelengths. Excitation spectra of $\text{Tb}^{3+}/\text{Li}^+$ codoped $\text{Sr}_2\text{Si}_5\text{N}_8$ sample are presented in Figure 7.24. Similar to the $\text{Tb}^{3+}/\text{Li}^+$ codoped $\text{Ca}_2\text{Si}_5\text{N}_8$ sample, all typical absorption bands of Tb^{3+} ions are observed and de-

7.3. Synthesis and Characterization of $M_{2-2x}Tb_xLi_xSi_5N_8$, where $M = Ca$ and Sr

picted in the inset graph of Figure 7.24. Furthermore, an analogous emission pattern as Tb^{3+}/Li^+ doped $Ca_2Si_5N_8$ sample has been obtained for Tb^{3+}/Li^+ codoped $Sr_2Si_5N_8$ matrix and the corresponding transitions are depicted in Figure 7.25. All these emissions result in a very intense bright green light.

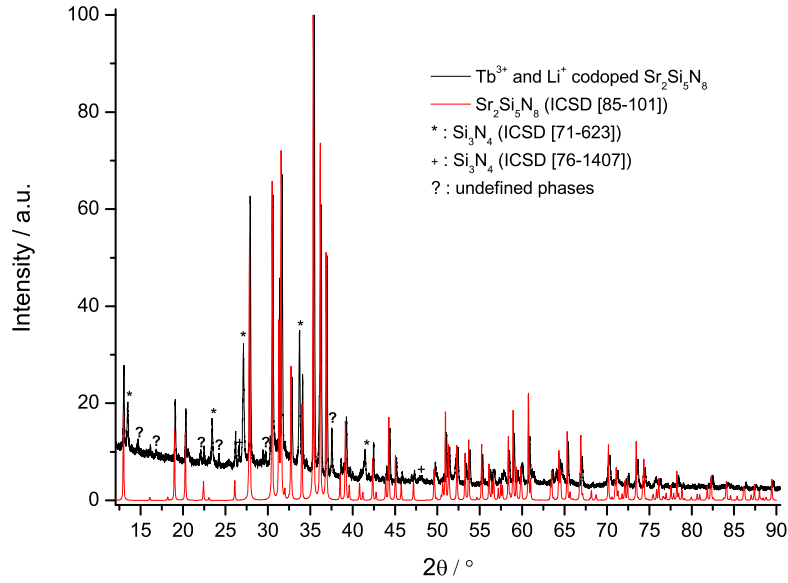


Figure 7.23.: Powder X-ray diffractogram of Tb^{3+}/Li^+ codoped $Sr_2Si_5N_8$.

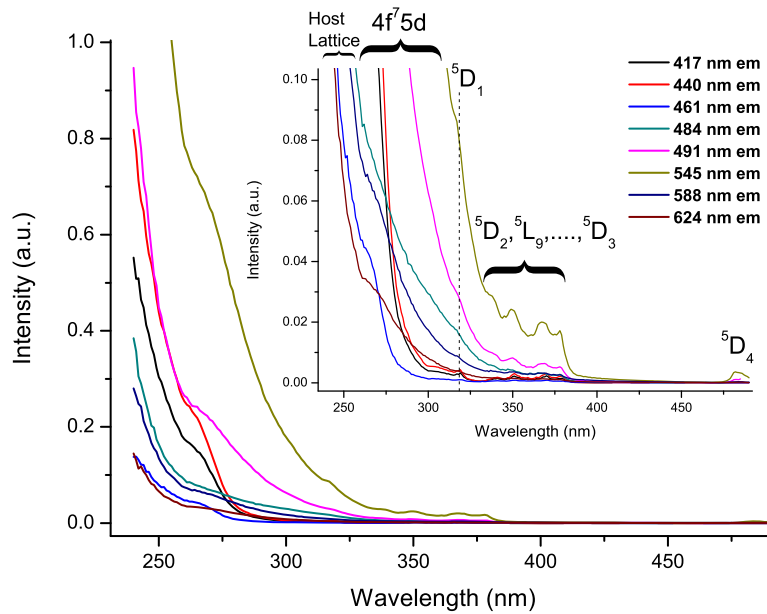


Figure 7.24.: Excitation spectra of Tb^{3+}/Li^+ codoped $Sr_2Si_5N_8$ at different emission wavelengths (Inset represents the zoomed spectra).

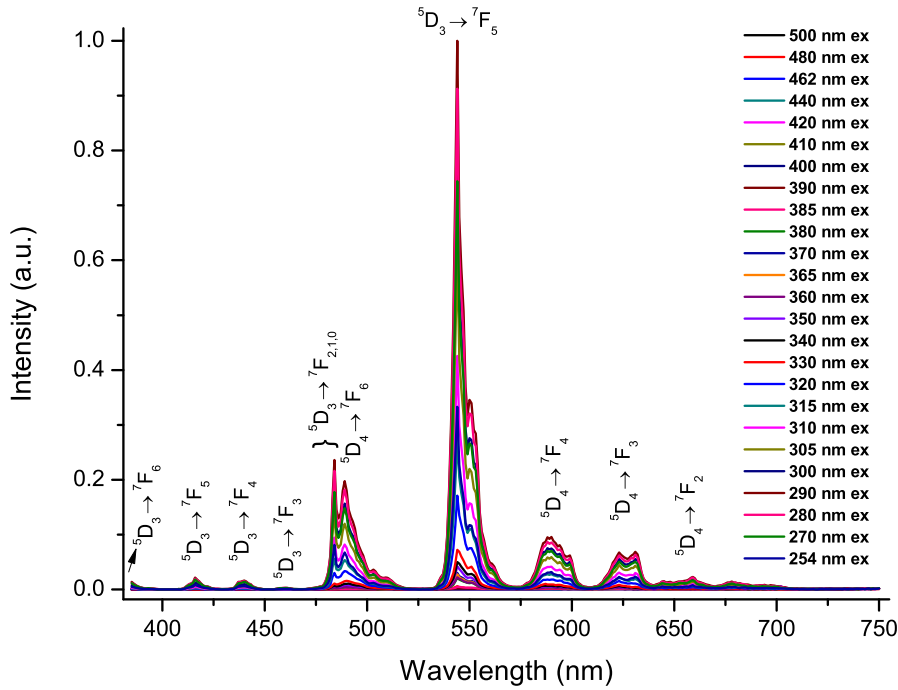


Figure 7.25.: Emission spectra of $\text{Tb}^{3+}/\text{Li}^{+}$ codoped $\text{Sr}_2\text{Si}_5\text{N}_8$ at different excitation wavelengths.

7.4. Synthesis and Characterization of $\text{Sr}_{2-x}\text{Mn}_x\text{Si}_5\text{N}_8$

Mn^{2+} doped $\text{Sr}_2\text{Si}_5\text{N}_8$ host lattices has previously been synthesized and investigated by Hintzen et. al [370]. The authors applied conventional solid state synthesis, in which Mn metal were fired together with SrN_x and Si_3N_4 powders. In the present work, the polymer route has been applied for the synthesis of Mn^{2+} doped $\text{Sr}_2\text{Si}_5\text{N}_8$. The following reaction is proposed:

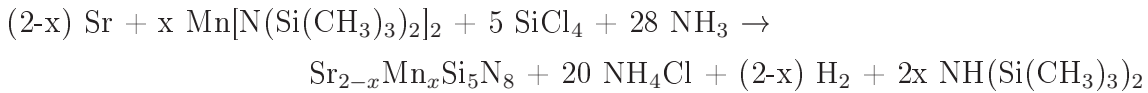


Figure 7.26 represents the powder X-ray diffractogram of Mn^{2+} doped $\text{Sr}_2\text{Si}_5\text{N}_8$ matrix. All of the $\text{Sr}_2\text{Si}_5\text{N}_8$ diffraction peaks in ICSD, [85-101], perfectly match by those of Mn^{2+} doped $\text{Sr}_2\text{Si}_5\text{N}_8$ sample. The diffuse reflection spectrum of Mn^{2+} doped $\text{Sr}_2\text{Si}_5\text{N}_8$ ceramic is exhibited in Figure 7.28, which is well consistent with the literature values [370]. The absorption between 200 nm and 300 nm is assigned to the absorption of the $\text{Sr}_2\text{Si}_5\text{N}_8$ host lattice, which is perfectly matching with the reflection spectrum of the undoped host lattice. Moreover, the absorption between 300 nm and 550 nm clearly resulted from the

transitions from the ground state ${}^6\text{A}_1$ (${}^6\text{S}$) energy level to higher energy levels of Mn^{2+} ions (see Figure 7.27), which is consistent with the excitation spectrum of the sample.

The emission spectra of Mn^{2+} doped $\text{Sr}_2\text{Si}_5\text{N}_8$ lattice at different excitation wavelengths and the excitation spectrum at 620 nm emission wavelength are presented in Figure 7.29, which is also well consistent with the literature data [370]. The excitation band at shorter wavelengths, around 250 nm, results from the host matrix as can be concluded from the diffuse reflection spectrum. The remaining excitation bands in the range between 280 nm and 500 nm are assigned to the transitions from the ground state, ${}^6\text{A}_1$ (${}^6\text{S}$), of Mn^{2+} ions to the following higher energy levels as depicted in Figure 7.29: ${}^4\text{E}$ (${}^4\text{D}$) and ${}^4\text{T}_2$ (${}^4\text{D}$) levels between 280 nm and 350 nm, ${}^4\text{A}_1$ (${}^4\text{G}$) and ${}^4\text{E}$ (${}^4\text{G}$) levels between 360 nm and 400 nm, and ${}^4\text{T}_2$ (${}^4\text{G}$) level between 410 nm and 450 nm (as illustrated in Figure 7.27). Similar to the values in the literature, Mn^{2+} doped $\text{Sr}_2\text{Si}_5\text{N}_8$ exhibits a single broad emission band due to the ${}^4\text{T}_2$ (${}^4\text{G}$) \rightarrow ${}^6\text{A}_1$ (${}^6\text{S}$) transition of Mn^{2+} ions at 617 nm (in [370], the emission was reported at 606 nm for 5 mol % Mn^{2+} concentration).

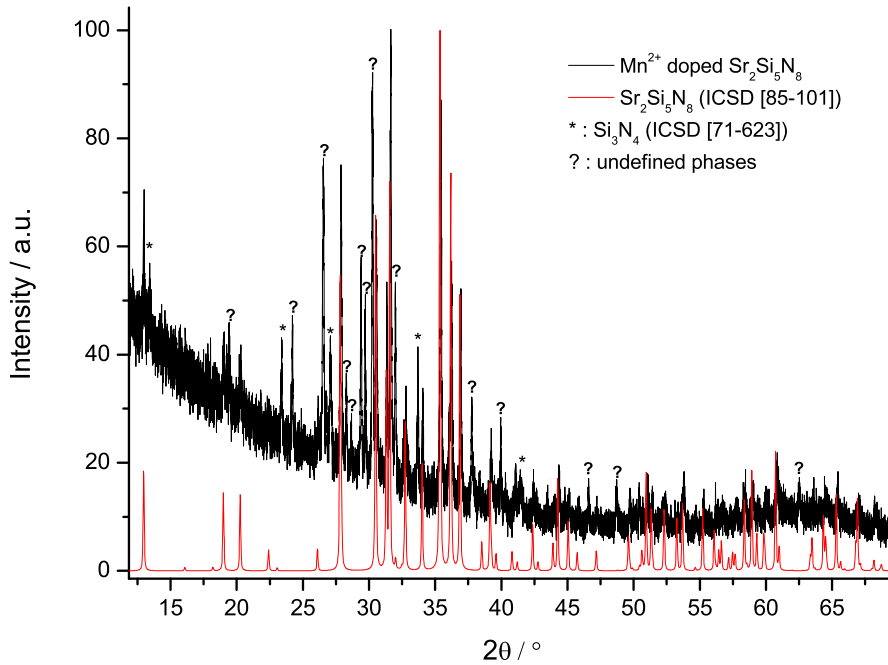


Figure 7.26.: Powder X-ray diffractogram of Mn^{2+} doped $\text{Sr}_2\text{Si}_5\text{N}_8$.

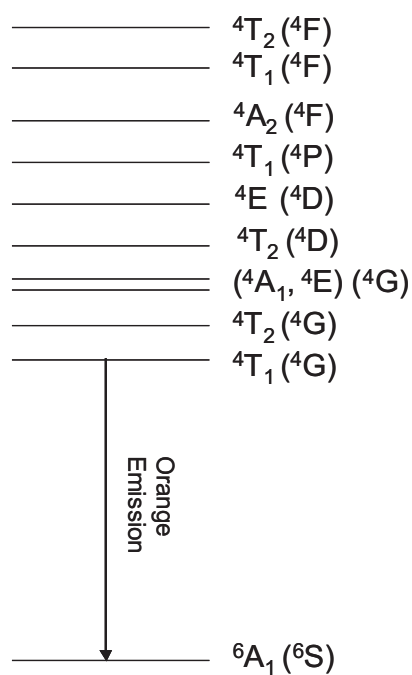


Figure 7.27.: Representation of the energy levels of Mn²⁺ ions.

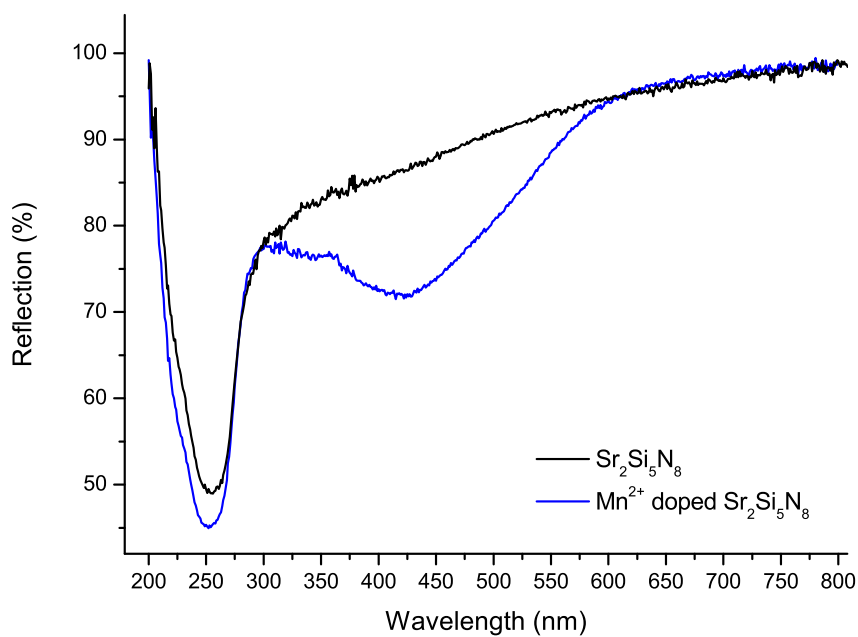


Figure 7.28.: Diffuse reflection spectra of $Sr_2Si_5N_8$ and Mn^{2+} doped $Sr_2Si_5N_8$.

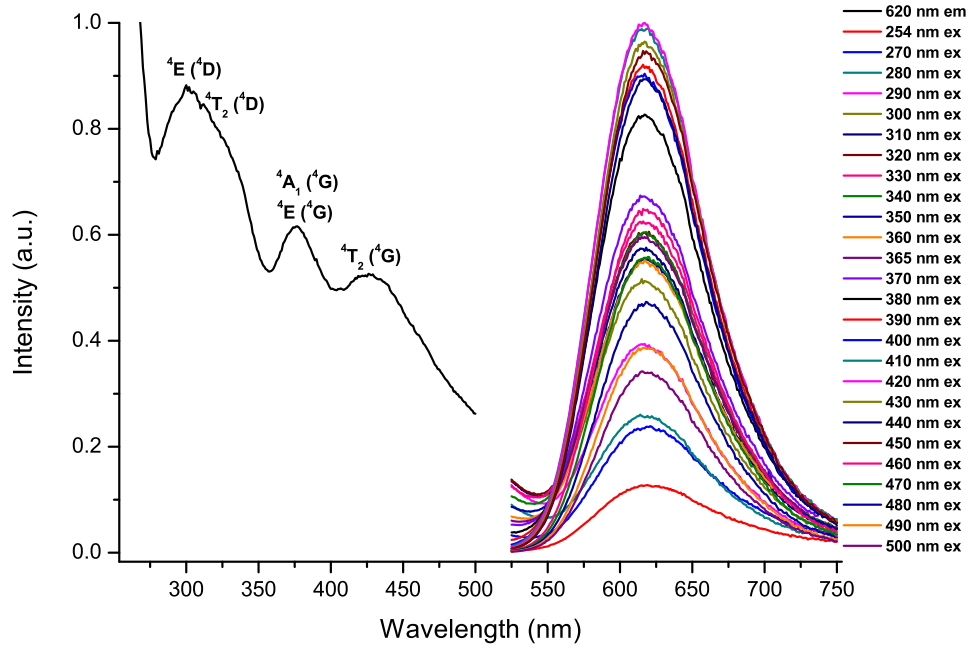


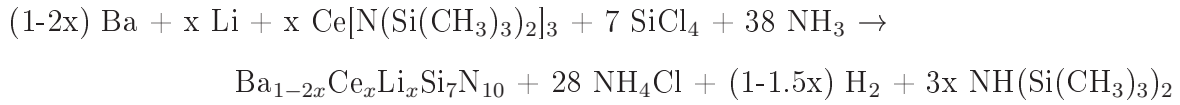
Figure 7.29.: Photoluminescence spectra of Mn^{2+} doped $Sr_2Si_5N_8$ at different excitation and emission wavelengths.

7.5. Synthesis and Characterization of $Ba_{1-2x}Ce_xLi_xSi_7N_{10}$

The host lattice $BaSi_7N_{10}$ has been first synthesized by Schnick et.al [250] via a solid state reaction of Ba metal and $Si(NH)_2$ powders in a radio frequency furnace. $BaSi_7N_{10}$ contains Ba^{2+} ions in a three-dimensional Si-N network, and it is the first nitridosilicate with both corner and edge-sharing SiN_4 tetrahedra, in which every fifth nitrogen connects two Si centers and the remaining nitrogen atoms bridge three Si atoms. Therefore, the three-dimensional SiN_4 network is more condensed than the network of the other nitridosilicates, resulting in more NSi_3 coordinations in comparison to $M_2Si_5N_8$, where $M = Ca, Sr, Ba$ and Eu . The Si:N molar ratio of 7:10 in $BaSi_7N_{10}$ nearly reaches the value for binary Si_3N_4 .

7. A Novel Production Method for Crystalline Nitridosilicates

To the best of our knowledge, $\text{Ce}^{3+}/\text{Li}^{+}$ codoped $\text{BaSi}_7\text{N}_{10}$ system has been synthesized for the first time in the present work by applying the polymer route. The following reaction is proposed:

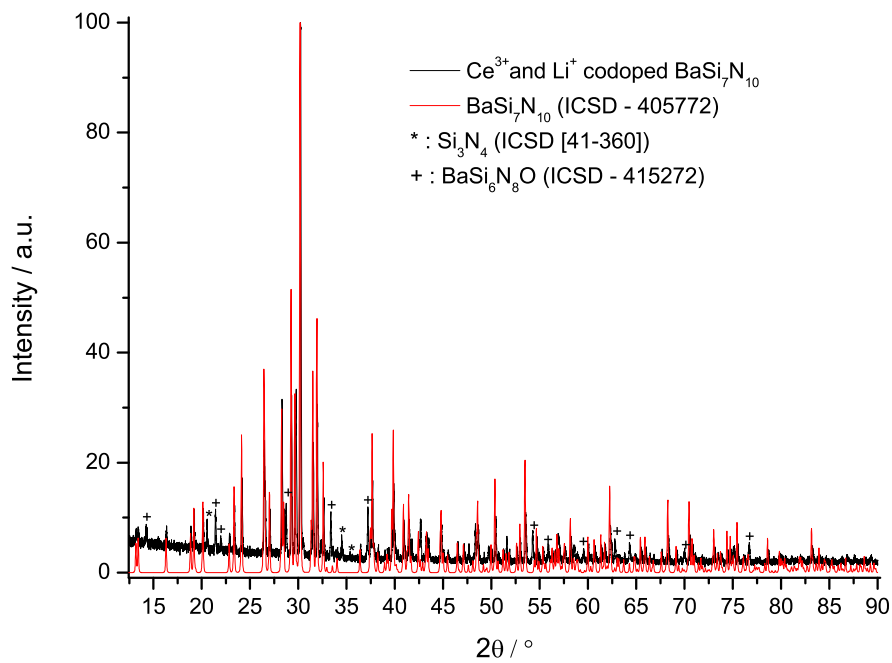
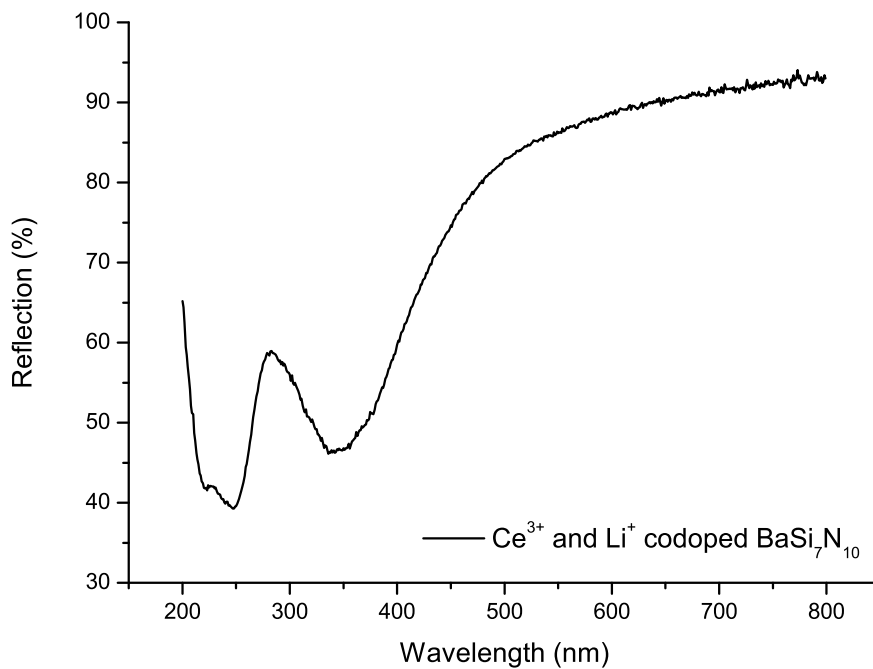


Powder X-ray diffractogram of $\text{Ce}^{3+}/\text{Li}^{+}$ codoped $\text{BaSi}_7\text{N}_{10}$ matrix is presented in Figure 7.30. This figure shows that all of the $\text{BaSi}_7\text{N}_{10}$ diffraction peaks in ICSD, 405772, agree well with that of the $\text{Ce}^{3+}/\text{Li}^{+}$ codoped $\text{BaSi}_7\text{N}_{10}$ sample. In addition, few $\text{BaSi}_6\text{N}_8\text{O}$ phases have been observed. It is well known that formation of an oxide compound is a common experience when Ba metal is used. As Ba is more reactive compared to Sr and Ca, it oxidizes very easily when exposed to air. Due to this property, Ba metal is widely applied as a "getter" in vacuum tubes, to remove the last traces of oxygen. Therefore, any trace amount of the oxygen impurity during the synthesis can be captured by Ba metal resulting in the formation of $\text{BaSi}_6\text{N}_8\text{O}$ phases. It has never been observed this kind of oxide phases in any other systems in the present study.

The diffuse reflection spectrum of $\text{Ce}^{3+}/\text{Li}^{+}$ codoped $\text{BaSi}_7\text{N}_{10}$ is represented in Figure 7.31. The absorption between 200 nm and 290 nm is assigned to the absorption of the $\text{BaSi}_7\text{N}_{10}$ host lattice whereas the absorption between 300 nm and 410 nm is attributed to the $4f \rightarrow 5d$ absorption of the Ce^{3+} ions.

The photoluminescence spectra of $\text{Ce}^{3+}/\text{Li}^{+}$ codoped $\text{BaSi}_7\text{N}_{10}$ lattice are shown in Figure 7.32. Excitation spectra at 480 nm emission wavelength possessed a single sharp excitation band at 280 nm and a shoulder at 360 nm. According to the diffuse reflection spectrum of the $\text{Ce}^{3+}/\text{Li}^{+}$ codoped $\text{BaSi}_7\text{N}_{10}$ sample, the excitation band at 280 nm seems to be the absorption of the $\text{BaSi}_7\text{N}_{10}$ host lattice. Moreover, the excitation band at 360 nm (as a shoulder) appears to be the $4f \rightarrow 5d$ transition of Ce^{3+} ions, which is also proven by the diffuse reflection spectrum. The emission spectra showed a broad band with a maximum at 480 nm when excited between 254 nm and 390 nm. Since the emission at 480 nm is very efficient at shorter excitation wavelengths (i.e. at 300 nm excitation), which are in the vicinity of the $\text{BaSi}_7\text{N}_{10}$ host lattice absorption, it seems that there is an efficient energy transfer from $\text{BaSi}_7\text{N}_{10}$ host lattice to the excited 5d level of Ce^{3+} ions.

The Red-Edge Effect has also been observed for $\text{Ce}^{3+}/\text{Li}^{+}$ codoped $\text{BaSi}_7\text{N}_{10}$ sample when excited with the light greater than 400 nm, which locate in the absorption edge. It is quite obvious in emission spectra that the impurity phases have no significant effect on emission when the sample is excited between 254 nm and 380 nm. Therefore, $\text{Ce}^{3+}/\text{Li}^{+}$ codoped $\text{BaSi}_7\text{N}_{10}$ lattices are perfectly matching with the radiation of UV-emitting LEDs for generating the blue light.

Figure 7.30.: Powder X-ray diffractogram of Ce^{3+}/Li^{+} codoped $BaSi_7N_{10}$.Figure 7.31.: Diffuse reflection spectrum of Ce^{3+}/Li^{+} codoped $BaSi_7N_{10}$.

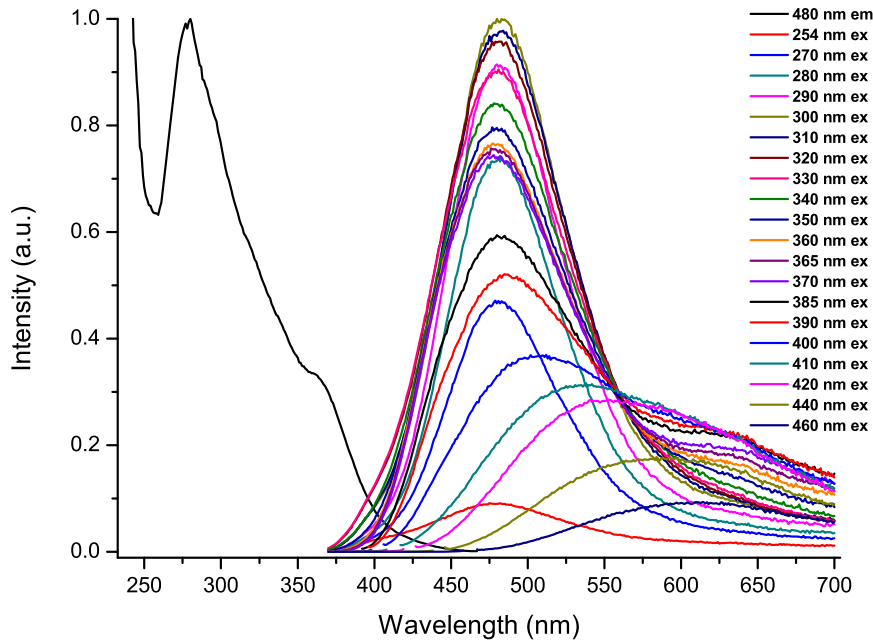
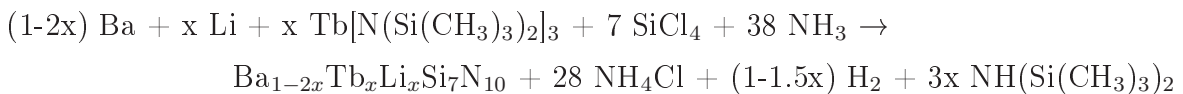


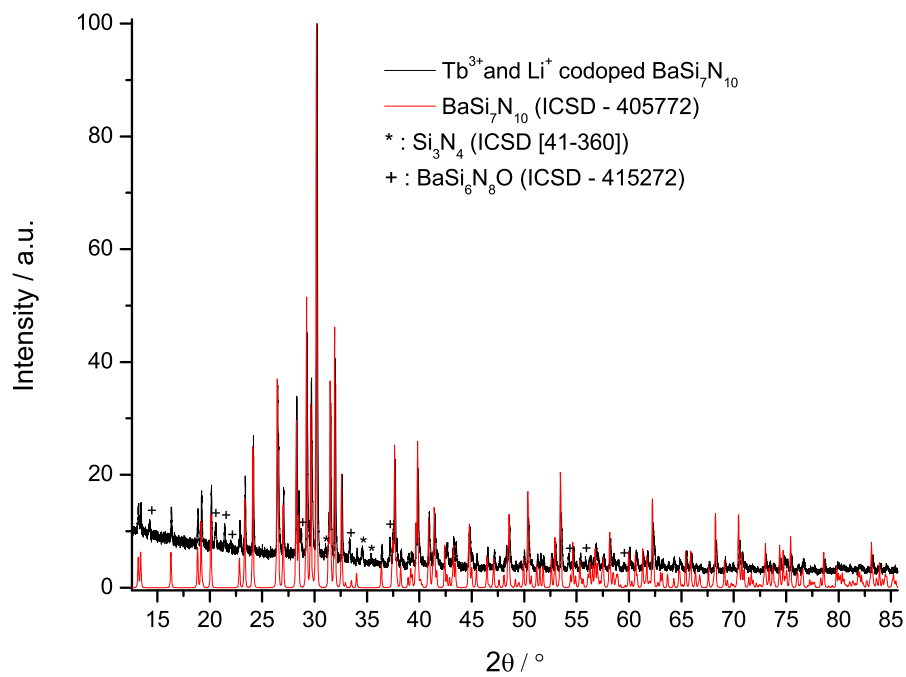
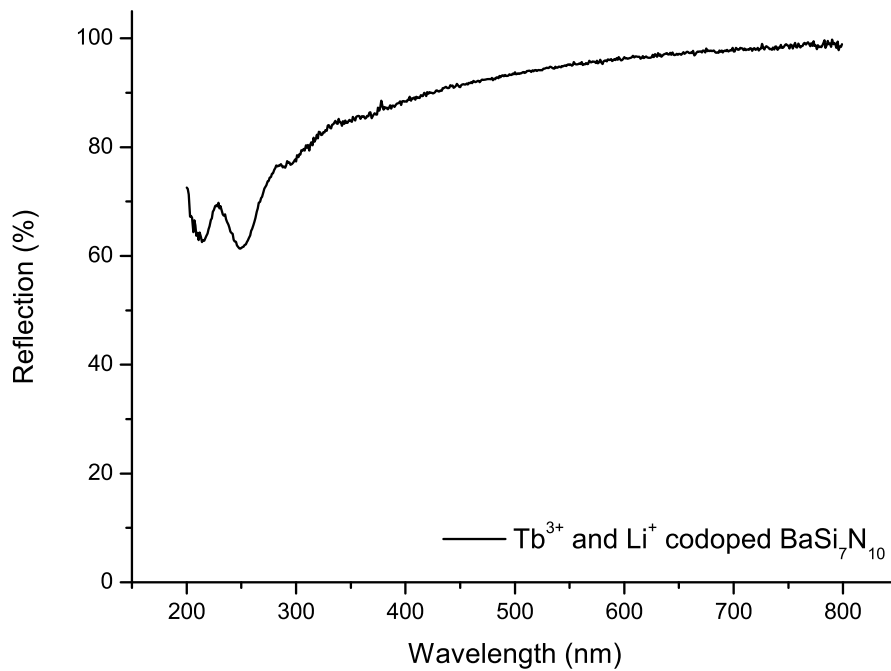
Figure 7.32.: Photoluminescence spectra of $\text{Ce}^{3+}/\text{Li}^{+}$ codoped $\text{BaSi}_7\text{N}_{10}$ at different excitation wavelengths.

7.6. Synthesis and Characterization of $\text{Ba}_{1-2x}\text{Tb}_x\text{Li}_x\text{Si}_7\text{N}_{10}$

To the best of our knowledge, $\text{Tb}^{3+}/\text{Li}^{+}$ codoped $\text{BaSi}_7\text{N}_{10}$ lattice has been synthesized for the first time in the present work by applying the polymer route. The following reaction is proposed:



The powder X-ray diffractogram of $\text{Tb}^{3+}/\text{Li}^{+}$ codoped $\text{BaSi}_7\text{N}_{10}$ matrix is presented in Figure 7.33. Similar to the $\text{Ce}^{3+}/\text{Li}^{+}$ codoped $\text{BaSi}_7\text{N}_{10}$ system, all of the $\text{BaSi}_7\text{N}_{10}$ diffraction peaks in ICSD, 405772, are agree well with that of the $\text{Tb}^{3+}/\text{Li}^{+}$ codoped $\text{BaSi}_7\text{N}_{10}$ samples. The diffuse reflection spectrum of $\text{Tb}^{3+}/\text{Li}^{+}$ codoped $\text{BaSi}_7\text{N}_{10}$ is presented in Figure 7.34. The absorption between 200 nm and 230 nm is assigned to the absorption of the $\text{BaSi}_7\text{N}_{10}$ host lattice, and that between 230 nm and 280 nm is assigned to the $4f^8 \rightarrow 4f^75d^1$ transition of Tb^{3+} ions, which is consistent with the excitation spectrum of the sample. Moreover, the weak absorptions between 280 nm and 350 nm can be assigned as the $4f \rightarrow 4f$ transitions of the Tb^{3+} ions.

Figure 7.33.: Powder X-ray diffractogram of Tb^{3+}/Li^{+} codoped $BaSi_7N_{10}$.Figure 7.34.: Diffuse reflection spectrum of Tb^{3+}/Li^{+} codoped $BaSi_7N_{10}$.

7. A Novel Production Method for Crystalline Nitridosilicates

Excitation spectra of $\text{Tb}^{3+}/\text{Li}^+$ codoped $\text{BaSi}_7\text{N}_{10}$ sample are presented in Figure 7.35. All typical absorption bands of Tb^{3+} ions were observed (see Figure 5.58). In addition to the strong absorption due to the host lattice at around 250 nm, Tb^{3+} ions showed strong absorption between 230 nm and 280 nm due to the $4f^8 \rightarrow 4f^75d^1$ transition.

All typical $4f \rightarrow 4f$ emission lines were observed in the emission spectra of $\text{Tb}^{3+}/\text{Li}^+$ codoped $\text{BaSi}_7\text{N}_{10}$ matrix and the corresponding transitions were depicted in Figure 7.36-a. The emission spectra excited at shorter wavelengths between 254 nm and 330 nm is depicted in Figure 7.36-b whereas Figure 7.36-c shows those excited at longer wavelengths between 340 nm and 480 nm. Excitation at shorter wavelengths resulted in strong Tb^{3+} emission.

On the other hand, excitation at longer wavelengths resulted in a gradual decrease in characteristic Tb^{3+} emissions. Moreover, in addition to the characteristic Tb^{3+} emissions, a broad band emission at around 560 nm was observed when the sample was excited at longer wavelengths, which might result from the Si_3N_4 impurities. Nevertheless, all these emissions result in a very intense bright green light.

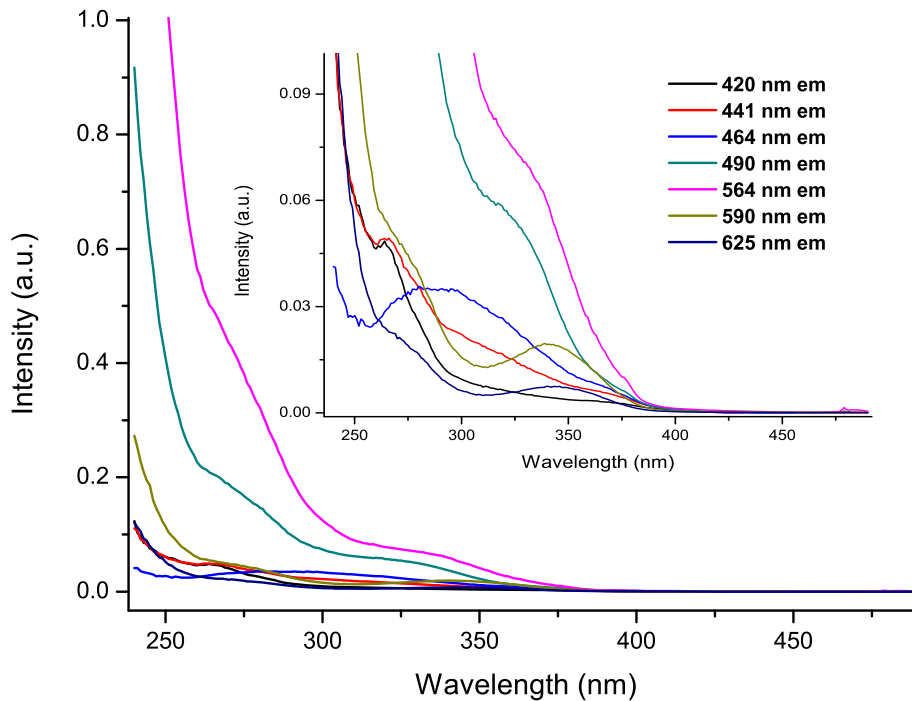
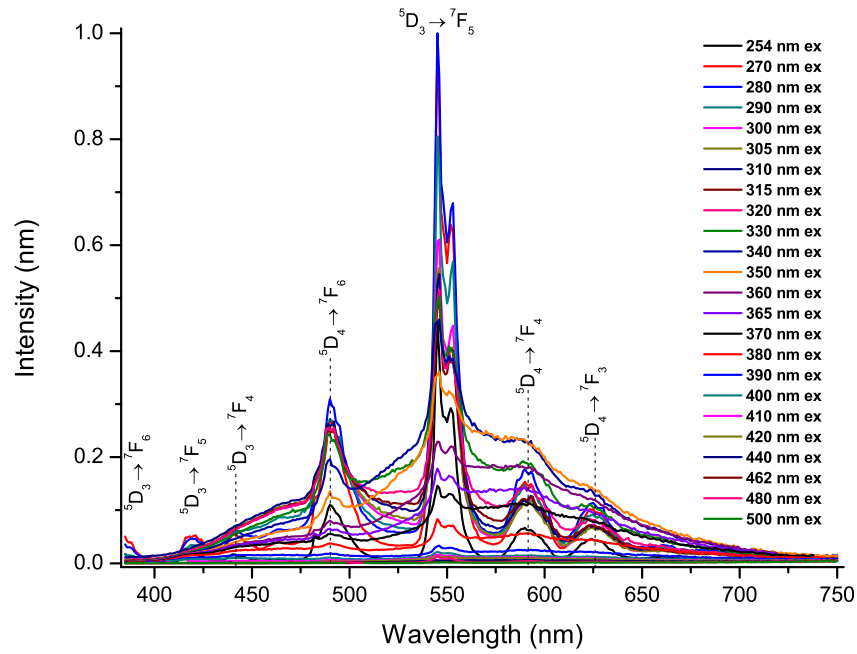
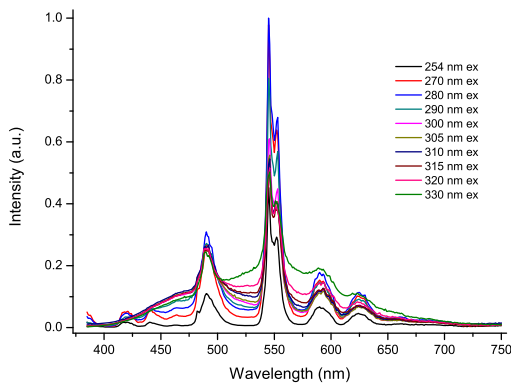


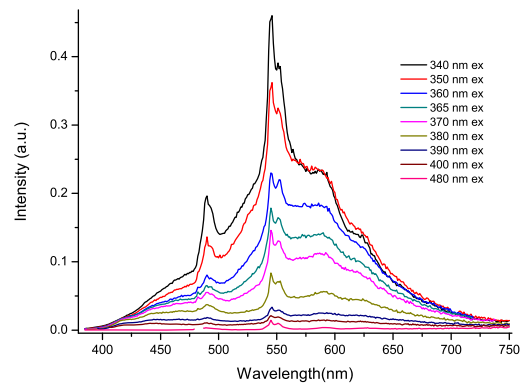
Figure 7.35.: Excitation spectra of $\text{Tb}^{3+}/\text{Li}^+$ codoped $\text{BaSi}_7\text{N}_{10}$ at different emission wavelengths (Inset represents the zoomed spectra).



(a)



(b)



(c)

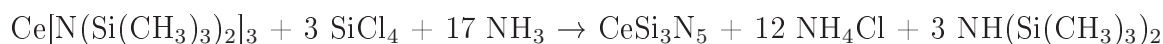
Figure 7.36.: Emission spectra of Tb^{3+}/Li^{+} doped $BaSi_7N_{10}$ at different excitation wavelengths.

7.7. Synthesis and Characterization of CeSi_3N_5

CeSi_3N_5 has previously been prepared by Jeitschko et. al [371, 372] in two different solid state reactions. In one method, the authors arc-melted elemental Ce and Si, which were successively heated under nitrogen atmosphere at 1500 °C for a week [371]. In another method, the same authors arc-melted a pellet of cerium fillings and Si_3N_4 powder, which was later sealed in an evacuated silica tube and annealed in a high-frequency furnace [372].

The crystal structure of CeSi_3N_5 was reported to contain the SiN_4 tetrahedra sharing only corners, thus forming a three-dimensional infinite network. The cerium atoms occupy cavities formed by the nitrogen atoms of that network, which is, therefore, related to those of framework silicates and zeolites. On the other hand, the authors have not discussed any optical properties of CeSi_3N_5 .

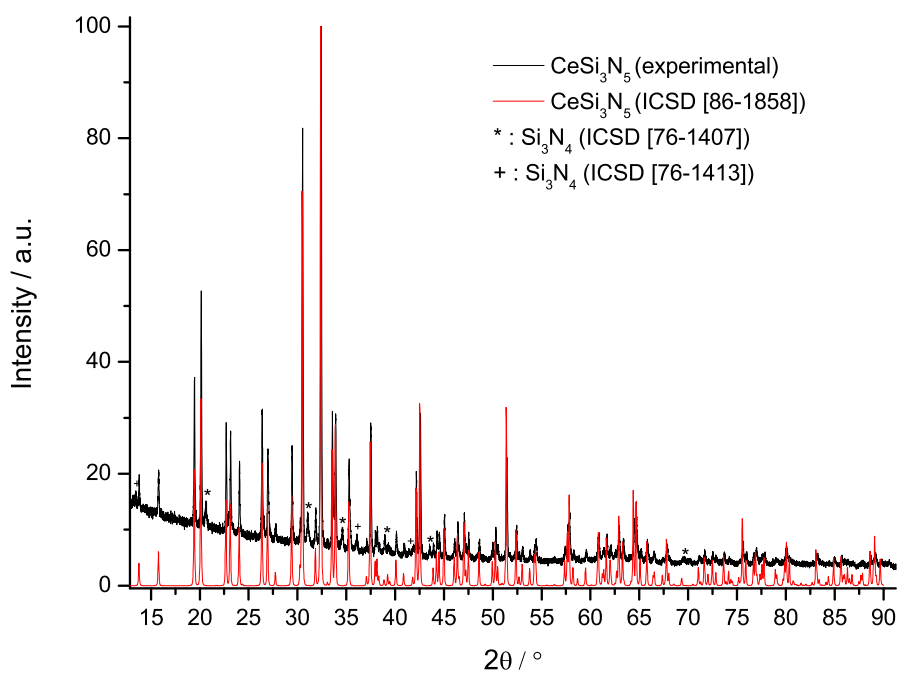
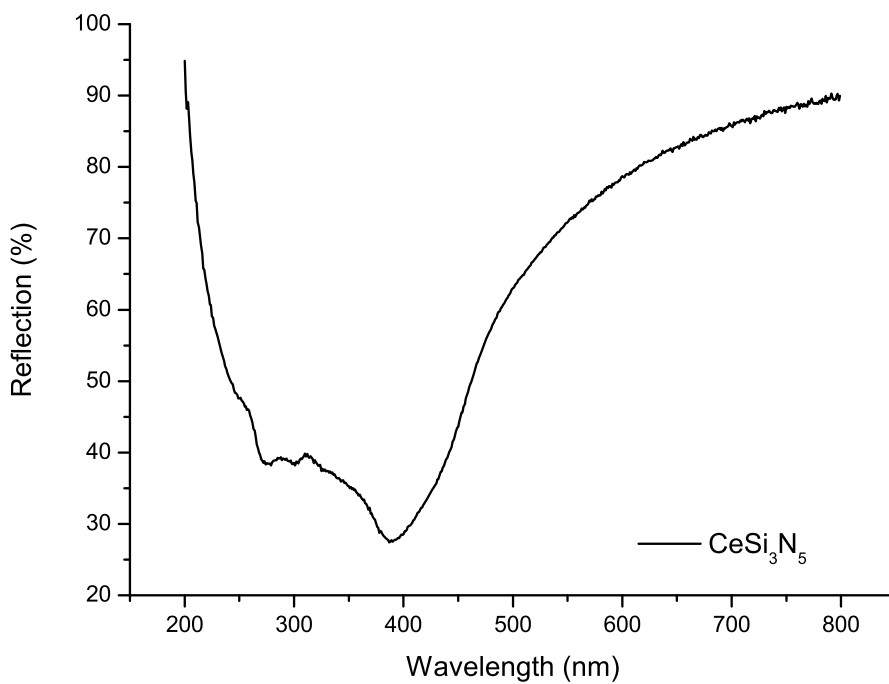
In the present work, the polymer route has been applied for the synthesis of CeSi_3N_5 and photoluminescence and diffuse reflection properties of CeSi_3N_5 have been investigated. The following reaction is proposed:



The powder X-ray diffractogram of CeSi_3N_5 is shown in Figure 7.37. This figure indicates that all of the calculated diffraction peaks for CeSi_3N_5 in ICSD, [86-1858], are agree well with that of the CeSi_3N_5 sample prepared in this work. The diffuse reflection spectrum of CeSi_3N_5 is presented in Figure 7.38. It is seen in the diffuse reflection spectrum that CeSi_3N_5 has a strong and broad absorption between 200 nm and 600 nm, which is responsible for the greenish-yellow body color.

The photoluminescence spectra of CeSi_3N_5 sample are displayed in Figure 7.39. Excitation spectrum included a broad excitation band between 270 nm and 380 nm, which is consistent with the diffuse reflection spectrum. CeSi_3N_5 showed strong blue emission at 468 nm as presented in the emission spectra.

The CeSi_3N_5 sample has also showed a strong red shift when it was excited with the light longer than 385 nm, which corresponds to the wavelengths at the absorption edge (Red-Edge Effect). Since this sample has maximum excitation at 365 nm, CeSi_3N_5 is very promising phosphor which can be used together with GaN based UV-LEDs to generate efficient blue light.

Figure 7.37.: Powder X-ray diffractogram of CeSi_3N_5 .Figure 7.38.: Diffuse reflection spectra of CeSi_3N_5 .

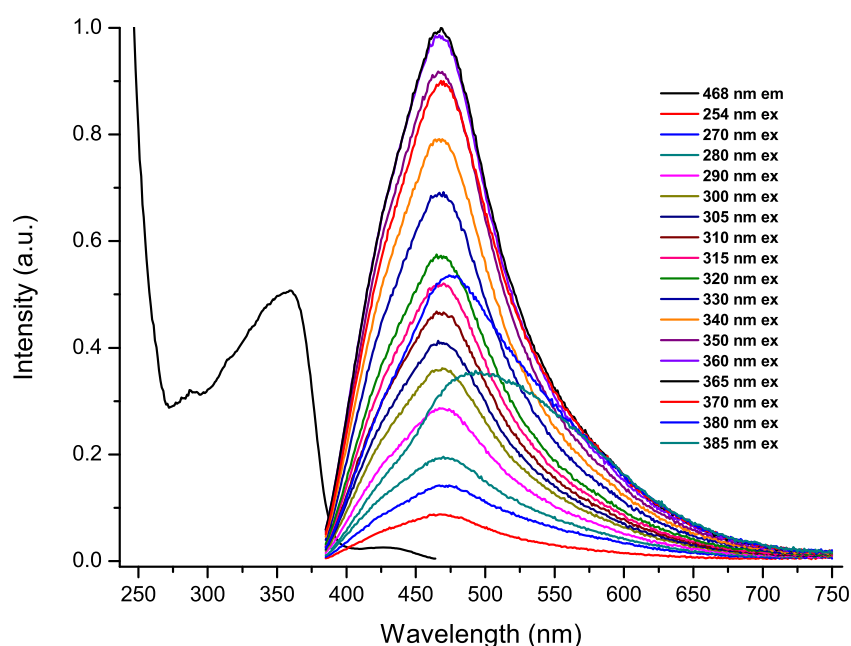


Figure 7.39.: Photoluminescence spectra of CeSi₃N₅ at different excitation and emission wavelengths.

7.8. Conclusions

Various nitridosilicate type phosphors, i.e. CeSi₃N₅, Sr_{2-x}Mn_xSi₅N₈, M_{2-x}Eu_xSi₅N₈, M_{2-2x}R_xLi_xSi₅N₈ and Ba_{1-2x}R_xLi_xSi₇N₁₀, where M = Ca and Sr, and R = Ce and Tb, have been successfully synthesized via the polymer route. To the best of our knowledge, Ca_{2-2x}Tb_xLi_xSi₅N₈, Sr_{2-2x}Tb_xLi_xSi₅N₈, Ba_{1-2x}Ce_xLi_xSi₇N₁₀ and Ba_{1-2x}Tb_xLi_xSi₇N₁₀ systems have been studied for the first time. Even though, in most cases, Si₃N₄ impurities and some unknown phases have been observed, the photoluminescence studies have revealed that those impurities had no significant negative effect on luminescence properties. It is believed that an optimization in the experimental conditions will yield single-phase products. Quite obviously, the polymer route for the production of nitridosilicate type phosphors have great advantageous over the conventional solid state syntheses such that 1) all required elements can be introduced homogeneously at once in a solution, which reduces significantly the handling processes in solid state reactions like intermediate grinding of ingredients, 2) no complicated heating system is necessary like radio frequency furnace, 3) any byproduct can be easily recovered such as excess NH₃, solvents and NH₄Cl, 4) commercially available starting materials are used and 5) it is very convenient for up-scaling.

8. A New Silaborazine-type Single Source Precursor for Si/B/N/C Ceramics

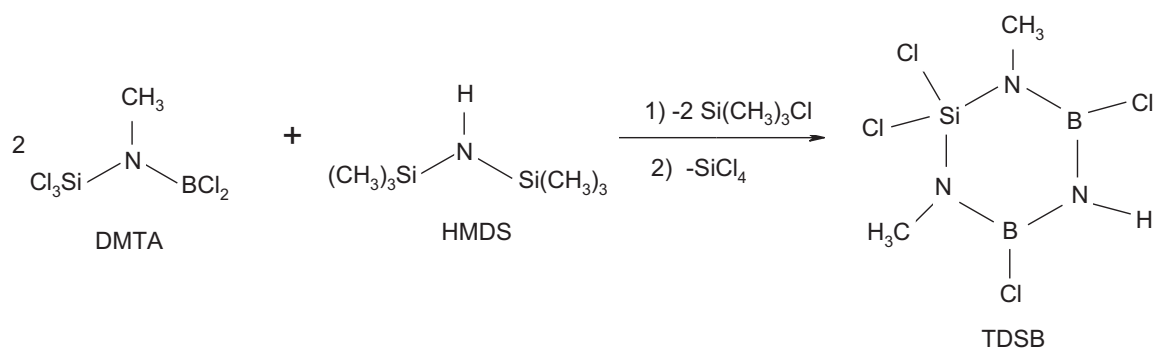
8.1. 1,1,3,5-tetrachloro-2,6-dimethyl-4-hydride-1-silaborazine (TDSB)

Silaborazines, six-membered heterocycles, are obtained when an R-B group in a borazine ring is replaced with one or two R₂-Si groups. Therefore, silaborazine derivatives are considered as transition compounds between borazines and cyclotrisilazanes. Unfortunately, there are only a few publications on alkyl substituted monocyclic silaborazines dating back to 1970s by German scientists [373, 374, 375, 376, 377, 378, 379]. Very recently, Epple et al. have synthesized chloro-substituted polycyclic silaborazines [151]. In the present study, a new silaborazine, namely 1,1,3,5-tetrachloro-2,6-dimethyl-4-hydride-1-silaborazine (TDSB) has been synthesized by reacting Cl₃Si-N(CH₃)-BCl₂ (DMTA) with hexamethyldisilazane (HMDS). The experimental details are presented in Section 10.4. TDSB is the first *halo-substituted monocyclic silaborazine* compound. The reactions and the proposed sequence of synthesis mechanism are presented in Figure 8.1.

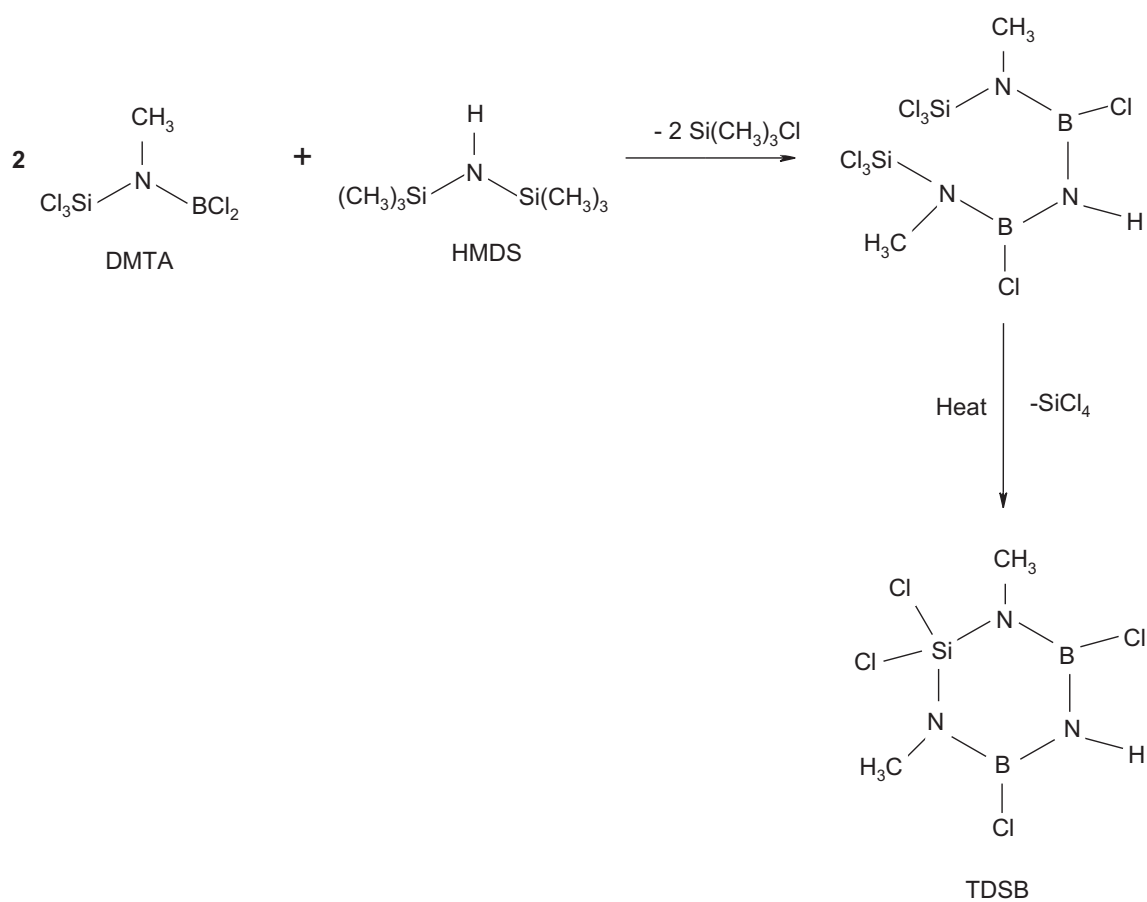
The prominent structural unit of TDSB is clearly the silaborazine ring, which is supposed to become a fixed part of the final covalent Si/B/N/C network after polymerization and pyrolysis. Due to chlorine atoms bonded to silicon and boron atoms, crosslinking of the TDSB single source precursor with nitrogen bases, such as methylamine or ammonia, is possible and should proceed very rapidly and quantitatively via dehydrohalogenation reactions. Crystals of TDSB have been obtained by sublimation at 100 °C, and have been characterized by single crystal X-ray diffraction, FT-IR, NMR and mass spectroscopy techniques.

The mass spectrum of the TDSB molecule is presented in Figure 8.2, which shows the expected molecular ion (M⁺) at m/z = 264. Further fragmentation of TDSB molecule is mainly characterized by the loss of some end groups such as -Cl and -CH₃, e.g. m/z = 235 for M - 2(CH₃) and m/z = 227 for M⁺ - HCl.

8. A New Silaborazine-type Single Source Precursor for Si/B/N/C Ceramics



(a)



(b)

Figure 8.1.: Synthesis of TDSB (a) and a proposed mechanism (b).

8.1. 1,1,3,5-tetrachloro-2,6-dimethyl-4-hydride-1-silaborazine (TDSB)

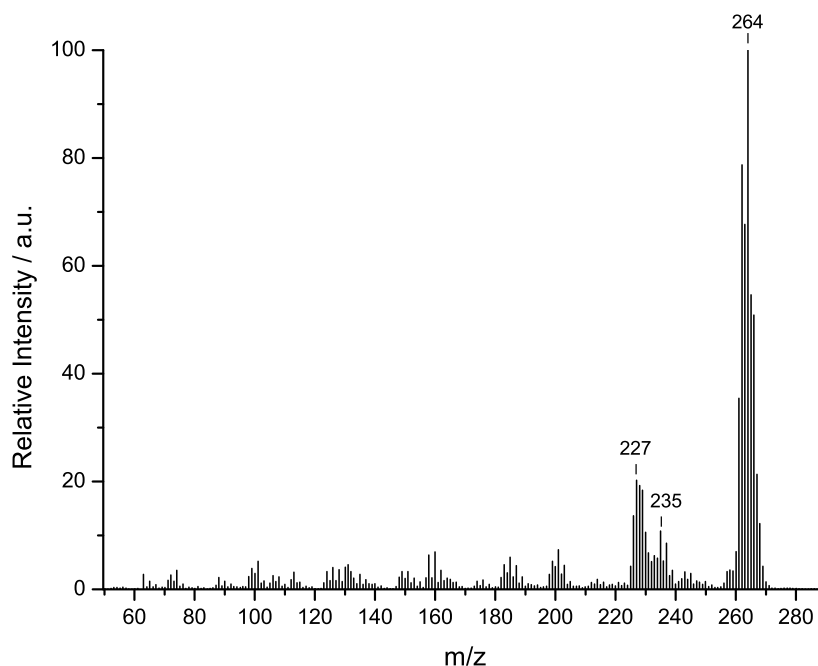


Figure 8.2.: Mass spectrum of TDSB.

The ^1H , ^{11}B , ^{13}C and ^{29}Si NMR spectra of TDSB molecule are shown in Figure 8.3 and the corresponding chemical shifts are listed in Table 8.1. In the ^1H -NMR spectrum (Figure 8.3-a), the equivalent protons in methyl groups (labelled as 7a, 7b, 7c, 8a, 8b and 8c in Figure 8.3-e) resulted in a strong singlet peak at 2.56 ppm whereas a broad signal at 4.23 ppm resulted from the proton bonded to N atom. Two equivalent C atoms (labelled as 7 and 8 in Figure 8.3-e) in TDSB molecule resulted in only one signal at 30.53 ppm in the ^{13}C -NMR spectrum (8.3-b). Furthermore, the Si atom in TDSB showed a single peak at -24.10 ppm in the ^{29}Si -NMR spectrum (8.3-c). Finally, the two equivalent B atoms (labelled as 3 and 5 in Figure 8.3-e) in TDSB molecule caused a strong signal at 30.23 ppm in the ^{11}B -NMR spectrum (8.3-d).

Table 8.1.: NMR spectroscopic data of TDSB.

Nucleus	Observed multiplicity	δ/ppm	Assignment
^1H	singlet	2.56	CH_3
^1H	singlet	4.23	NH
^{13}C	singlet	30.53	CH_3
^{11}B	singlet	30.23	
^{29}Si	singlet	-24.10	

8. A New Silaborazine-type Single Source Precursor for Si/B/N/C Ceramics

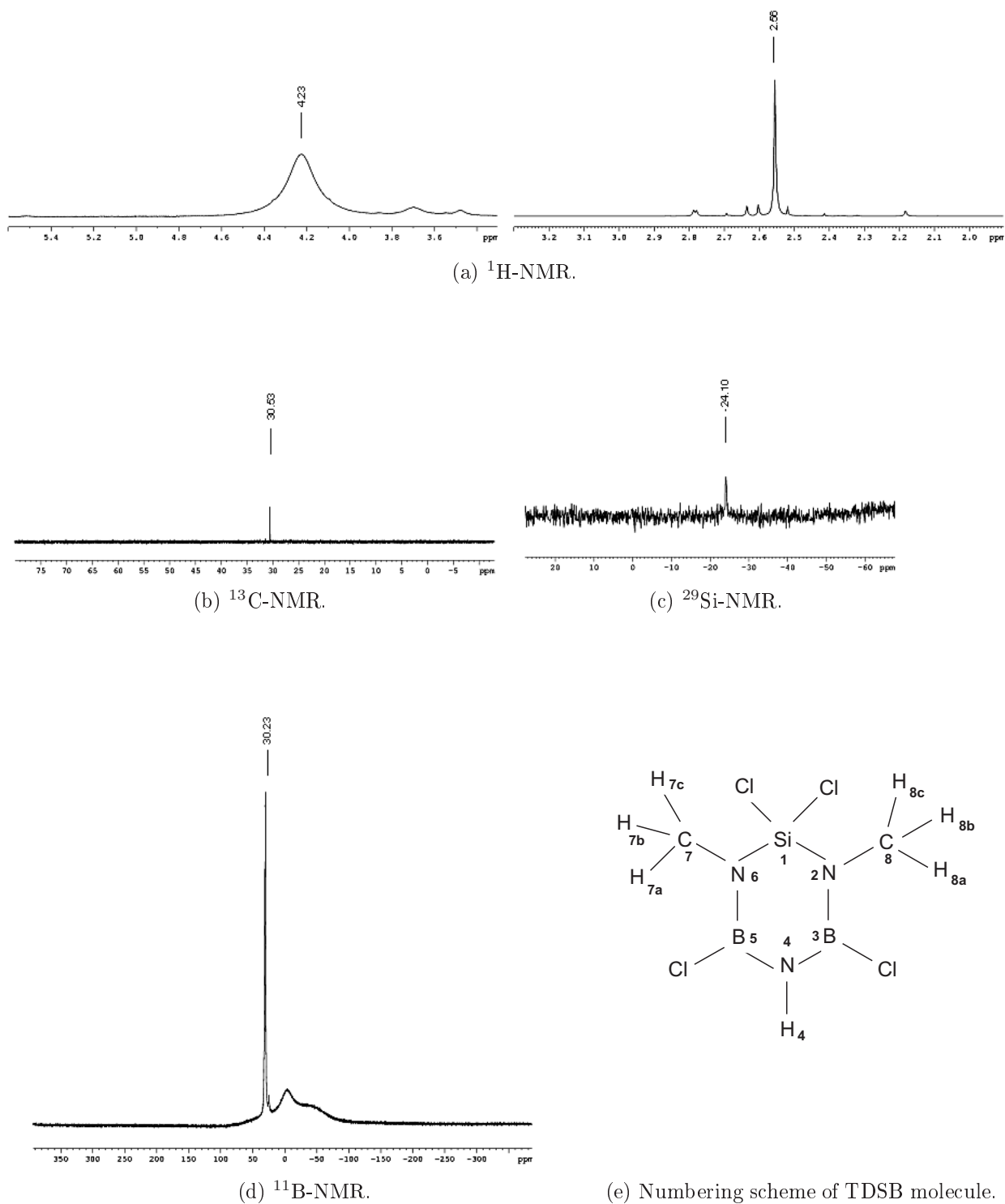


Figure 8.3.: a) ^1H -NMR, b) ^{13}C -NMR, c) ^{29}Si -NMR, d) ^{11}B -NMR spectra and e) numbering scheme of TDSB molecule.

8.1. 1,1,3,5-tetrachloro-2,6-dimethyl-4-hydrate-1-silaborazine (TDSB)

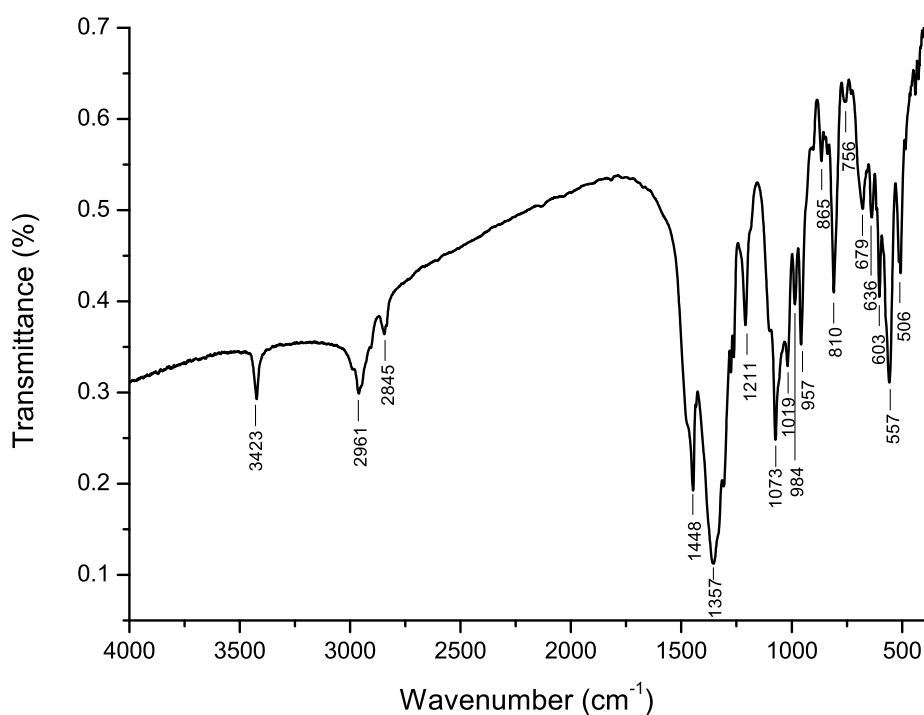


Figure 8.4.: FT-IR spectrum of TDSB.

Table 8.2.: IR absorptions of TDSB.

Wavenumber (cm ⁻¹)	Intensity ^a	Assignment
3423	m	$\nu_{as}(\text{NH})$
2961	m	$\nu_{as}(\text{CH}_3)$
2845	w	$\nu_s(\text{CH}_3)$
1448	vs	$\nu_{as}(\text{N-B-N})$ in SiB ₂ N ₃ ring
1357	vs	$\nu_{as}(\text{B-N-Si})$ in SiB ₂ N ₃ ring
1211	m	$\delta_s(\text{N-CH}_3)$ bending
1073	s	$\rho(\text{N-CH}_3)$ rocking
984	w	$\delta_s(\text{N-H})$ bending
957	m	$\nu_{as}(\text{B-Cl})$
810	m	$\nu_{as}(\text{Si-N})$ in SiB ₂ N ₃ ring
557	s	$\nu_{as}(\text{Si-Cl})$
506	m	$\nu_s(\text{Si-Cl})$

^avs: very strong, s: strong, m: medium, w: weak.

8. A New Silaborazine-type Single Source Precursor for Si/B/N/C Ceramics

The FT-IR spectrum of TDSB is shown in Figure 8.4. In the FT-IR spectrum, the strong stretching mode of the NH group appears at 3423 cm^{-1} and the typical bands for methyl groups appear in the range between 2800 cm^{-1} and 2980 cm^{-1} . In literature, a very strong absorption in the vicinity of 1400 cm^{-1} was reported as a characteristic band for borazine and its derivatives [97, 151, 380]. Similar values were also reported for the silaborazine derivatives, namely $\text{C}_6\text{H}_5\text{B}[\text{NHSi}(\text{CH}_3)_2]_2\text{NH}$ and $(\text{CH}_3)_2\text{Si}[\text{NHBC}_6\text{H}_5]_2\text{NH}$, at 1390 cm^{-1} and 1450 cm^{-1} , respectively [375]. Therefore, very intense absorptions of TDSB at 1448 cm^{-1} and 1357 cm^{-1} are assigned to the antisymmetric stretching B-N-B and B-N-Si vibrations of the six-membered silaborazine ring, respectively. The other functional groups can be identified by their characteristic stretching modes, e.g. B-Cl bond at 957 cm^{-1} and Si-Cl at 557 cm^{-1} . An overview of the most important IR absorptions of the TDSB together with the corresponding assignments is given in Table 8.2.

The crystallographic data and the results of the structure determination for TDSB are summarized in Table 8.3. In addition, atomic positions and anisotropic displacement parameters are tabulated in Table 8.4 and Table 8.5, while bond lengths, bond angles and torsion angles are presented in Table 8.7, Table 8.8 and Table 8.6, respectively. TDSB crystallizes in triclinic space group $P\bar{1}$ (Nr. 2, Pearson code $aP38$) with two formula units per unit cell. The structure of TDSB is composed of a SiB_2N_3 ring, which is essentially planar (Figure 8.5). The inner angles of the ring on B atoms are almost identical (i.e., $121.65(2)^\circ$ and $121.45(2)^\circ$ for B3 and B5, respectively) due to having the same environment, which are, however, both widened compared to the ideal 120° angle for a perfect hexagon. Similarly, the inner angles of the ring on N atoms bonded to methyl groups are $120.85(1)^\circ$ and $120.78(1)^\circ$ for N2 and N6, respectively, which are closer to the ideal angle. On the other hand, the N4 atom, bonded to H atom, has the widest inner angle as $126.22(2)^\circ$. The reason for this is clearly the Si atom on the ring, which has two Cl atoms resulting in narrowest inner angle of the ring (the N-Si-N angle is $109.05(7)^\circ$). Since the N4 atom is bonded to the smallest group (indeed only one H atom), it is the most flexible atom on the silaborazine ring, thus it compensates the decrease of the inner bond angle on Si atom by increasing its inner bond angle in order to maintain the planarity of the ring. Both Si1-N2 and Si1-N5 bond distances are equal as $1.696(1)\text{ \AA}$, whereas the B-N distances are ranging from $1.410(2)\text{ \AA}$ to $1.422(3)\text{ \AA}$. The B3 atom, which has slightly wider inner angle ($121.65(2)^\circ$), has slightly shorter B-N distances than the B4 atom in order to maintain the planarity of the ring. The bond distances and angles are well consistent with the literature data. To illustrate, $\text{C}_6\text{H}_5\text{Si}[\text{N}(\text{CH}_3)\text{B}(\text{CH}_3)]_2\text{N}(\text{CH}_3)$ and $(\text{H}_3\text{C})\text{B}[\text{N}(\text{CH}_3)\text{Si}(\text{C}_6\text{H}_5)]_2\text{N}(\text{CH}_3)$ have the average bond distances for Si-N as 1.728 \AA and 1.726 \AA , and for B-N as 1.441 \AA and 1.438 \AA together with the average N-Si-N angle as 104.4° and 107.1° , respectively [379].

8.1. 1,1,3,5-tetrachloro-2,6-dimethyl-4-hydride-1-silaborazine (TDSB)

Table 8.3.: Crystal data and structure refinement for TDSB at 273 K.

Empirical Formula	SiB ₂ N ₃ C ₂ H ₇ Cl ₄
Formula Weight / g.mol ⁻¹	264.62
Crystal System	Triclinic
Space Group (Nr.)	<i>P</i> $\bar{1}$ (2)
<i>a</i> / Å	7.2534(6)
<i>b</i> / Å	9.0788(7)
<i>c</i> / Å	9.1361(7)
α / °	66.839(2)
β / °	89.348(2)
γ / °	80.502(2)
Volume / Å ³	544.61(7)
<i>Z</i>	2
Density (calculated) / g.cm ⁻³	1.614
Diffractometer	Smart APEX CCD (Bruker AXS)
Monochromator	Graphite
X-ray radiation, λ / Å	Mo-K α , 0.71073
Absorption coefficient μ / mm ⁻¹	1.146
F(000)	264
θ range for collection / °	2.43 \leq θ \leq 30.99
Index range	-10 \leq <i>h</i> \leq 10, -13 \leq <i>k</i> \leq 13, -13 \leq <i>l</i> \leq 13
Reflections collected	7074
Independent reflections	3443
Internal residual value, <i>R</i> _{int}	0.0193
Completeness to $\theta = 30.99$	99.2 %
Absorption correction	semi-empirical
Structure refinement	SHELX97
Refinement method	Full-matrix least-squares on <i>F</i> ²
Data / restrain / parameters	3443 / 0 / 115
Goodness-of-fit on <i>F</i> ²	1.026
<i>R</i> ₁ [<i>F</i> ² > 2 σ (<i>F</i> ²)] ^a , <i>wR</i> (<i>F</i> ₂)	<i>R</i> ₁ = 0.0425, <i>wR</i> ₂ = 0.1232
<i>R</i> indices for all data	<i>R</i> ₁ = 0.0552, <i>wR</i> ₂ = 0.1384
Largest diff. peak and hole, $\Delta\rho_{max}$, $\Delta\rho_{min}$ / e.Å ³	0.359 , -0.450

^a $R_1 = \frac{\sum ||F_0| - |F_c||}{\sum |F_0|}$, $wR_2 = \sqrt{\frac{\sum w(F_0^2 - F_c^2)^2}{\sum w(F_0^2)^2}}$, where $w = 1/\sigma^2$

8. A New Silaborazine-type Single Source Precursor for Si/B/N/C Ceramics

In TDSB molecule, the B, Si, N, C atoms together with the two Cl atoms bonded to B atoms and one H atom bonded to the N atom are in a strictly planar arrangement. In addition, two neighboring molecules are inversely aligned such that the position of the B atoms in one ring superimpose with those in the neighboring ring and Si atoms stay farthest to each other. All of these features can be visualized when the TDSB molecules are viewed along the [001] direction (*c*-axis) as presented in Figure 8.6. Furthermore, the two methyl groups bonded to N atoms are in tetrahedral arrangement such that one of the H atoms, bonded to the C atom which has slightly longer C-N distance (labelled as H7B and C7 in Figure 8.5), is also located in the ring plane. In addition, two Cl atoms are tetrahedrally bonded to the Si atom and stay out of the ring plane about 127.83°.

Table 8.4.: Atomic coordinates ($\times 10^4$) and equivalent isotropic displacement parameters ($\text{\AA}^2 \times 10^3$) for TDSB. U_{eq} is defined as one third of the trace of the orthogonalized U^{ij} tensor.

	<i>x</i>	<i>y</i>	<i>z</i>	U_{eq}
Cl(1)	-328(1)	2605(1)	800(1)	77(1)
Cl(2)	4057(1)	2842(1)	687(1)	85(1)
Cl(3)	1966(1)	1951(1)	6913(1)	72(1)
Cl(4)	3375(1)	-3319(1)	5398(1)	80(1)
Si(1)	2107(1)	1809(1)	2192(1)	52(1)
N(2)	1924(2)	2429(2)	3721(2)	52(1)
B(3)	2181(3)	1289(2)	5317(2)	48(1)
N(4)	2617(2)	-407(2)	5708(2)	52(1)
B(5)	2846(3)	-1170(3)	4608(3)	52(1)
N(6)	2650(2)	-250(2)	2943(2)	55(1)
C(7)	2860(4)	-1034(3)	1781(3)	76(1)
C(8)	1479(4)	4198(2)	3303(3)	74(1)
H(4)	2830(30)	-1040(30)	6700(30)	61(6)
H(7A)	4089	-1677	1936	114
H(7B)	2691	-210	716	114
H(7C)	1937	-1719	1941	114
H(8A)	806	4397	4137	110
H(8B)	722	4716	2321	110
H(8C)	2619	4631	3181	110

8.1. 1,1,3,5-tetrachloro-2,6-dimethyl-4-hydrate-1-silaborazine (TDSB)

Table 8.5.: Anisotropic displacement parameters ($\text{\AA}^2 \times 10^3$) for TDSB. The anisotropic displacement factor exponent takes the form: $-2\pi[h^2a^{*2}U^{11} + \dots + 2hka^*b^*U^{12}]$

	U_{11}	U_{22}	U_{33}	U_{23}	U_{13}	U_{12}
Cl(1)	88(1)	83(1)	50(1)	-16(1)	-17(1)	-16(1)
Cl(2)	99(1)	99(1)	64(1)	-32(1)	30(1)	-41(1)
Cl(3)	96(1)	81(1)	52(1)	-41(1)	5(1)	-9(1)
Cl(4)	95(1)	50(1)	94(1)	-30(1)	-4(1)	-4(1)
Si(1)	64(1)	57(1)	38(1)	-22(1)	4(1)	-14(1)
N(2)	68(1)	47(1)	43(1)	-22(1)	1(1)	-8(1)
B(3)	52(1)	56(1)	43(1)	-26(1)	3(1)	-9(1)
N(4)	64(1)	51(1)	40(1)	-17(1)	2(1)	-9(1)
B(5)	52(1)	51(1)	59(1)	-27(1)	2(1)	-9(1)
N(6)	67(1)	58(1)	51(1)	-33(1)	4(1)	-11(1)
C(7)	95(2)	85(2)	70(1)	-55(1)	6(1)	-12(1)
C(8)	105(2)	48(1)	68(1)	-25(1)	-1(1)	-7(1)

Table 8.6.: Torsion angles ($^\circ$) of TDSB.

Atom contact	Angle	Atom contact	Angle
N(6)-Si(1)-N(2)-B(3)	-1.02(18)	B(3)-N(4)-B(5)-N(6)	0.1(3)
Cl(2)-Si(1)-N(2)-B(3)	-123.78(15)	B(3)-N(4)-B(5)-Cl(4)	-179.61(15)
Cl(1)-Si(1)-N(2)-B(3)	120.86(15)	N(4)-B(5)-N(6)-C(7)	-179.17(18)
N(6)-Si(1)-N(2)-C(8)	179.27(16)	Cl(4)-B(5)-N(6)-C(7)	0.5(3)
Cl(2)-Si(1)-N(2)-C(8)	56.52(17)	N(4)-B(5)-N(6)-Si(1)	-0.7(3)
Cl(1)-Si(1)-N(2)-C(8)	-58.85(17)	Cl(4)-B(5)-N(6)-Si(1)	179.00(10)
C(8)-N(2)-B(3)-N(4)	-179.72(18)	N(2)-Si(1)-N(6)-B(5)	1.06(19)
Si(1)-N(2)-B(3)-N(4)	0.6(3)	Cl(2)-Si(1)-N(6)-B(5)	123.70(15)
C(8)-N(2)-B(3)-Cl(3)	0.2(3)	Cl(1)-Si(1)-N(6)-B(5)	-120.91(15)
Si(1)-N(2)-B(3)-Cl(3)	-179.46(10)	N(2)-Si(1)-N(6)-C(7)	179.62(15)
N(2)-B(3)-N(4)-B(5)	0.0(3)	Cl(2)-Si(1)-N(6)-C(7)	-57.74(17)
Cl(3)-B(3)-N(4)-B(5)	-179.98(15)	Cl(1)-Si(1)-N(6)-C(7)	57.65(17)

8. A New Silaborazine-type Single Source Precursor for Si/B/N/C Ceramics

Table 8.7.: Bond lengths (pm) of TDSB.

Atom contact	Distance	Atom contact	Distance
Cl(1)-Si(1)	204.09(8)	N(4)-H(4)	86(3)
Cl(2)-Si(1)	203.69(8)	B(5)-N(6)	141.4(3)
Cl(3)-B(3)	177.83(18)	N(6)-C(7)	148.6(2)
Cl(4)-B(5)	176.8(2)	C(7)-H(7A)	96.00
Si(1)-N(6)	169.55(17)	C(7)-H(7B)	96.00
Si(1)-N(2)	169.56(14)	C(7)-H(7C)	96.00
N(2)-B(3)	141.0(2)	C(8)-H(8A)	96.00
N(2)-C(8)	147.6(2)	C(8)-H(8B)	96.00
B(3)-N(4)	141.7(3)	C(8)-H(8C)	96.00
N(4)-B(5)	142.2(3)		

Table 8.8.: Bond angles ($^{\circ}$) of TDSB.

Atom contact	Angle	Atom contact	Angle
N(6)-Si(1)-N(2)	109.05(7)	N(4)-B(5)-Cl(4)	117.57(16)
N(6)-Si(1)-Cl(2)	111.16(7)	B(5)-N(6)-C(7)	121.97(18)
N(2)-Si(1)-Cl(2)	110.95(6)	B(5)-N(6)-Si(1)	120.78(13)
N(6)-Si(1)-Cl(1)	110.57(6)	C(7)-N(6)-Si(1)	117.23(15)
N(2)-Si(1)-Cl(1)	110.73(6)	N(6)-C(7)-H(7A)	109.5
Cl(2)-Si(1)-Cl(1)	104.33(4)	N(6)-C(7)-H(7B)	109.5
B(3)-N(2)-C(8)	122.00(16)	H(7A)-C(7)-H(7B)	109.5
B(3)-N(2)-Si(1)	120.85(12)	N(6)-C(7)-H(7C)	109.5
C(8)-N(2)-Si(1)	117.15(13)	H(7A)-C(7)-H(7C)	109.5
N(2)-B(3)-N(4)	121.65(15)	H(7B)-C(7)-H(7C)	109.5
N(2)-B(3)-Cl(3)	120.51(14)	N(2)-C(8)-H(8A)	109.5
N(4)-B(3)-Cl(3)	117.85(14)	N(2)-C(8)-H(8B)	109.5
B(3)-N(4)-B(5)	126.22(16)	H(8A)-C(8)-H(8B)	109.5
B(3)-N(4)-H(4)	117.6(15)	N(2)-C(8)-H(8C)	109.5
B(5)-N(4)-H(4)	116.1(15)	H(8A)-C(8)-H(8C)	109.5
N(6)-B(5)-N(4)	121.45(17)	H(8B)-C(8)-H(8C)	109.5
N(6)-B(5)-Cl(4)	120.98(15)		

8.1. 1,1,3,5-tetrachloro-2,6-dimethyl-4-hydride-1-silaborazine (TDSB)

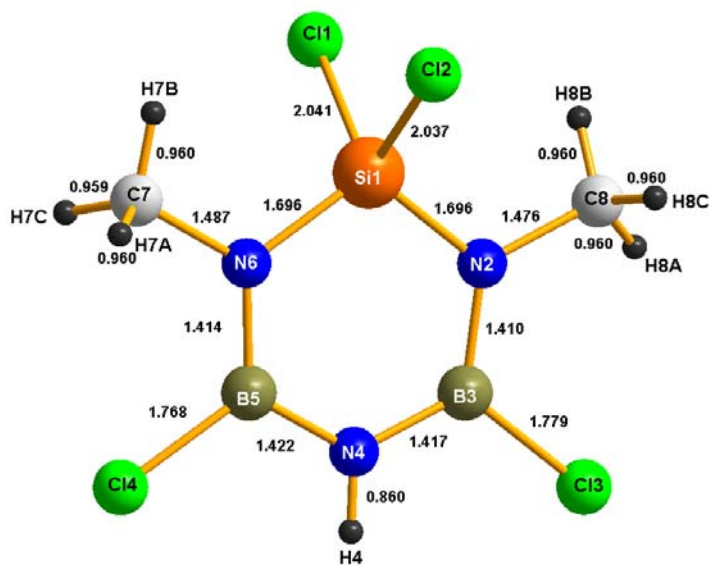


Figure 8.5.: Molecular structure of TDSB.

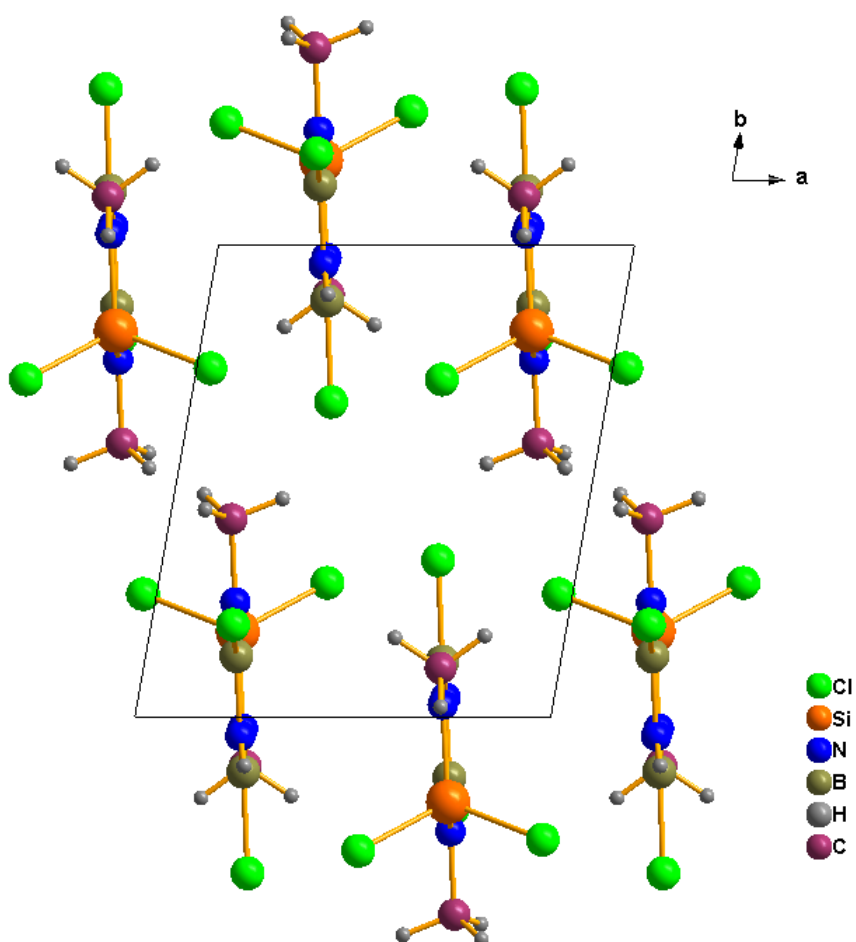


Figure 8.6.: A view of TDSB molecules along the [001] direction (*c*-axis).

8.2. Preceramic Polymers from TDSB

Preceramic polymers have been synthesized via dehydrohalogenation reactions of the new silaborazine-type single source precursor, TDSB, with ammonia (P-TDSB-1) and methylamine (P-TDSB-2). The details for the polymer syntheses are presented in Section 10.4. The as-synthesized P-TDSB-1 polymer is an insoluble solid in hexane whereas the as-synthesized P-TDSB-2 polymer is a viscous liquid. Both polymers have been characterized by powder X-ray diffraction (the viscous P-TDSB-2 polymer was annealed at 100 °C for about 5 hours to get a polymer powder), FT-IR spectroscopy and DTA/TG/MS techniques. The powder X-ray diffractograms of both polymers reveal that significant amount of the TDSB molecules are crosslinked via the corresponding nitrogen bases resulting in amorphous materials (Figure 8.7).

The FT-IR spectra of P-TDSB-1 and P-TDSB-2 are shown in Figure 8.8 and Figure 8.9, respectively. As one would expect, the absorptions in both polymers resemble the bands observed in the IR spectrum of the TDSB molecule, particularly with regard to the strong bands at 3380-3470 cm^{-1} , 2800-2980 cm^{-1} and 1350-1480 cm^{-1} , which are correlated to NH groups, methyl groups and silaborazine rings, respectively. A significant increase in intensity of the band at 3417 cm^{-1} (resulting from NH groups) for P-TDSB-1 polymer compared to the TDSB and P-TDSB-2 polymer clearly demonstrate the presence of the new terminal Si-NH₂ and B-NH₂, and bridging SiN(H)Si, SiN(H)B and BN(H)B groups, which were introduced during polycondensation with ammonia. Similarly, the absorption bands between 2800 cm^{-1} and 2980 cm^{-1} (resulting from CH₃ groups) in P-TDSB-2 polymer appear much stronger compared to the TDSB and P-TDSB-1 polymer, indicating the presence of the new terminal Si-NH(CH₃) and B-NH(CH₃), and bridging SiN(CH₃)Si, SiN(CH₃)B and BN(CH₃)B groups, which were introduced during polycondensation with methylamine. An overview of the most important IR absorption peaks of P-TDSB-1 and P-TDSB-2 together with the corresponding assignments are given in Table 8.9 and Table 8.10, respectively.

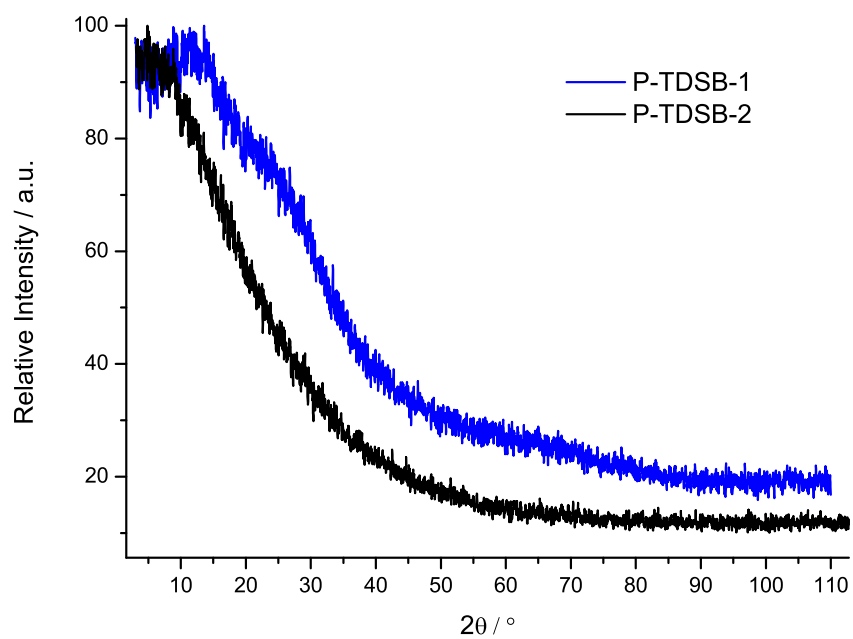


Figure 8.7.: Powder X-ray diffractograms of P-TDSB-1 and P-TDSB-2.

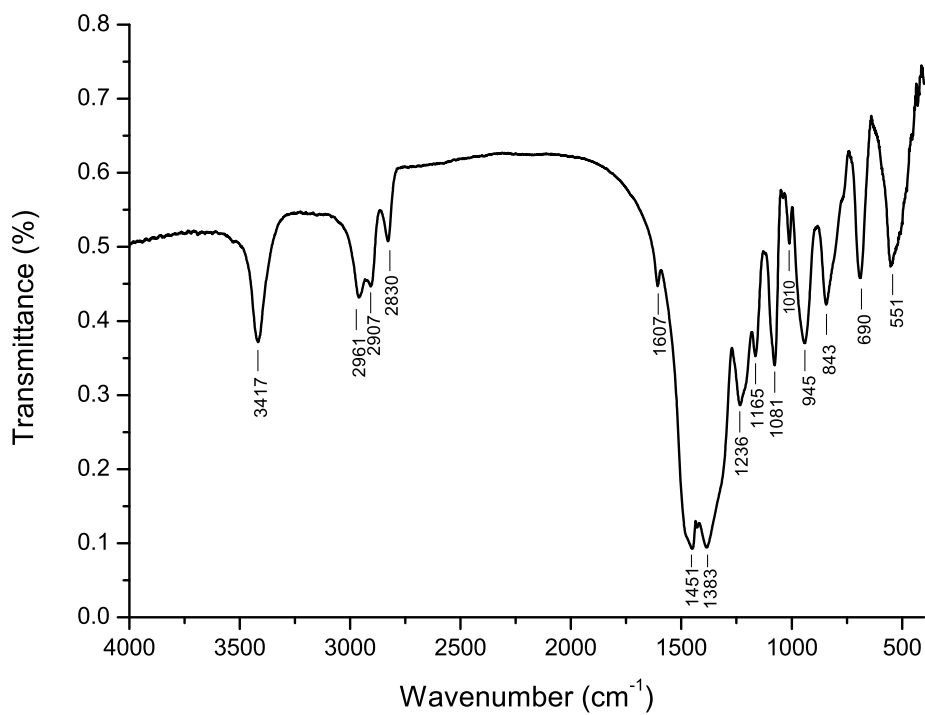


Figure 8.8.: FT-IR spectrum of P-TDSB-1.

Table 8.9.: IR absorptions of P-TDSB-1.

Wavenumber (cm ⁻¹)	Intensity ^a	Assignment
3417	s	$\nu_{as}(\text{NH})$
2961	m	$\nu_{as}(\text{CH}_3)$
2830	w	$\nu_s(\text{CH}_3)$
1451	vs	$\nu_{as}(\text{N-B-N})$ in SiB ₂ N ₃ ring
1383	vs	$\nu_{as}(\text{B-N-Si})$ in SiB ₂ N ₃ ring
1236	m	$\delta_s(\text{N-CH}_3)$ bending
1081	s	$\rho(\text{N-CH}_3)$ rocking
945	w	$\delta_s(\text{N-H})$ bending
843	m	$\nu_{as}(\text{Si-N})$ in SiB ₂ N ₃ ring
690	m	$\delta(\text{B-N})$ deformation vibration
551	m	$\delta(\text{Si-N})$ deformation vibration

^avs: very strong, s: strong, m: medium, w: weak.

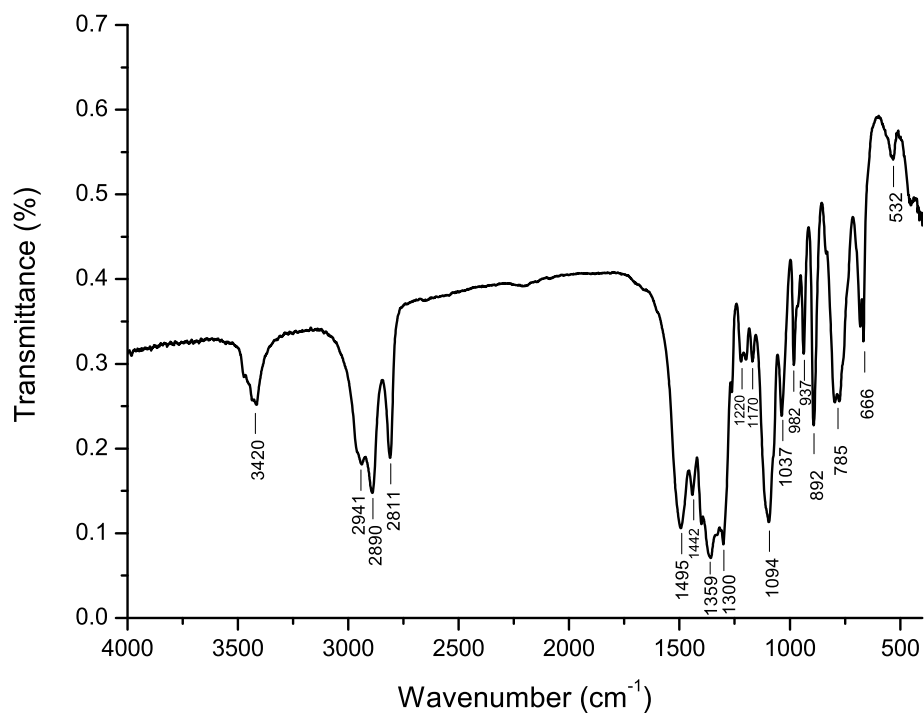


Figure 8.9.: FT-IR spectrum of P-TDSB-2.

Table 8.10.: IR absorptions of P-TDSB-2.

Wavenumber (cm ⁻¹)	Intensity ^a	Assignment
3420	m	$\nu_{as}(\text{NH})$
2890	s	$\nu_{as}(\text{CH}_3)$
2811	s	$\nu_s(\text{CH}_3)$
1495	vs	$\nu_{as}(\text{N-B-N})$ in SiB ₂ N ₃ ring
1359	vs	$\nu_{as}(\text{B-N-Si})$ in SiB ₂ N ₃ ring
1094	vs	$\rho(\text{N-CH}_3)$ rocking
937	w	$\delta_s(\text{N-H})$ bending
892	m	$\nu_{as}(\text{Si-N})$ in SiB ₂ N ₃ ring
785	s	$\rho_w(\text{N-H})$ wagging in -N(H)CH ₃
666	m	$\delta(\text{B-N})$ deformation vibration
532	m	$\delta(\text{Si-N})$ deformation vibration

^avs: very strong, s: strong, m: medium, w: weak.

The pyrolytic conversions of the P-TDSB-1 and P-TDSB-2 polymers into amorphous Si/B/N/(C) ceramics were monitored simultaneously by DTA/TG/MS technique. In analogy to the thermal degradation of previously reported preceramic polyboro(carbo)-silazanes, the pyrolyses of P-TDSB-1 and P-TDSB-2 preceramic polymers proceed in mainly two well-resolved stages, as presented in Figure 8.10 and Figure 8.11, respectively. In the first step between 200 °C and 600 °C, the P-TDSB-1 polymer loses 29.7 % of its initial mass under evolution of mainly ammonia, indicating further polycondensation and crosslinking of the corresponding polymer. The second step between 600 °C and 1090 °C is mainly characterized by the evolution of methane, probably originating from the methyl groups on the silaborazine ring of polymer. During this stage, a mass loss of 22.2 % was obtained for P-TDSB-1. Above 1090 °C, a slight decrease in mass of 7.6 % for P-TDSB-1 was observed, resulted from the evolution of nitrogen and hydrogen. Consequently, an overall ceramic yield of 40.5 % for P-TDSB-1 was obtained for the thermal conversion of the TDSB derived preceramic polymer into the corresponding Si/B/N/(C) ceramics. Similar to the P-TDSB-1 polymer, The P-TDSB-2 polymer loses 35.8 % of its initial weight between 200 °C and 380 °C, mainly by evolution of methylamine. Between 380 °C and 645 °C, P-TDSB-2 polymer loses additional 13.9 % weight mainly due to releasing of methyl groups both on the silaborazine rings and on the bridging nitrogen atoms. Further heating up to 1350 °C results in only 4.8 % weight loss. Finally, 54.5 % ceramic yield has been attained for P-TDSB-2 polymer at 1350 °C.

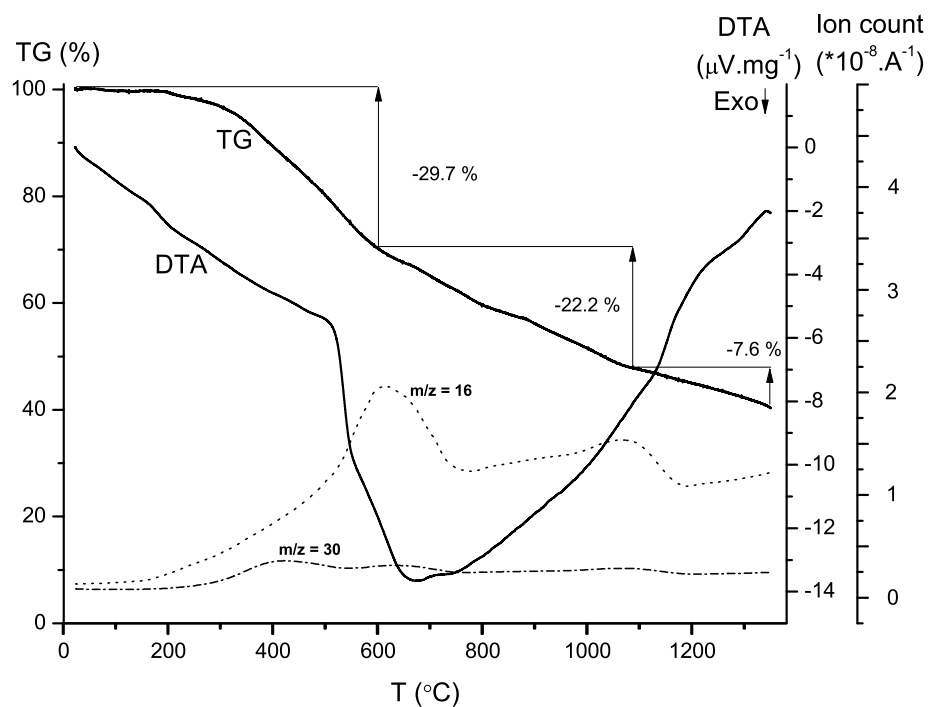


Figure 8.10.: DTA/TG/MS thermogram of P-TDSB-1 polymer.

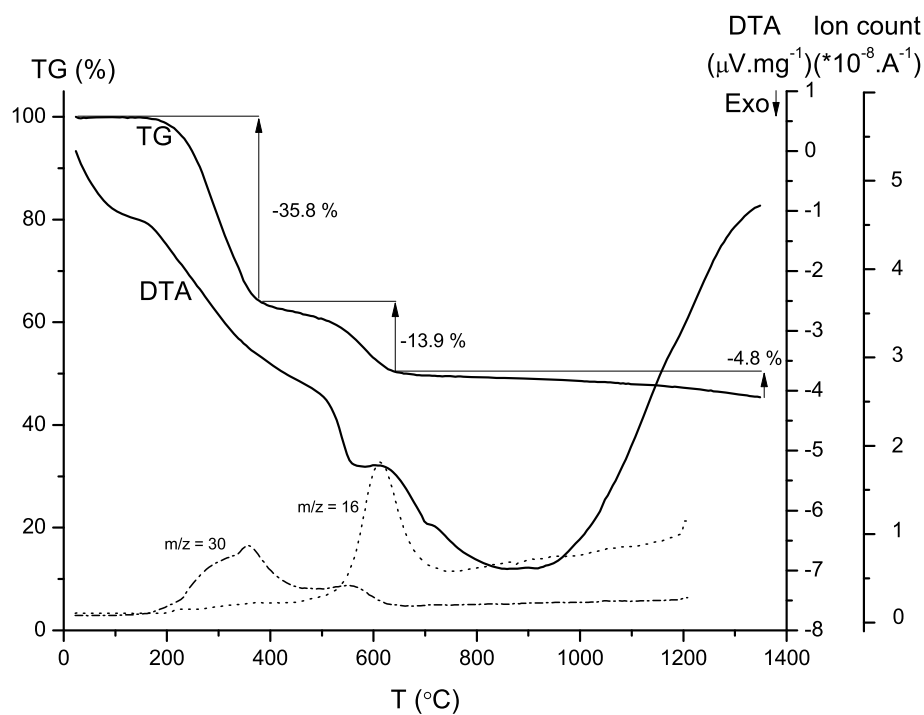


Figure 8.11.: DTA/TG/MS thermogram of P-TDSB-2 polymer.

8.3. New Si/B/N/(C) Ceramics

The amorphous Si/B/N/(C) ceramics have been prepared via the pyrolytic conversion of the preceramic polymers, P-TDSB-1 and P-TDSB-2, and subsequent calcinations. Three different Si/B/N/(C) ceramics were prepared. Two of them were obtained from P-TDSB-1 and P-TDSB-2 polymers through pyrolysis up to 900 °C and calcination at 1400 °C, both under Ar atmosphere, and called as C-TDSB-1 (grey) and C-TDSB-2 (black), respectively. The third one has been obtained from the P-TDSB-1 polymer via pyrolysis up to 900 °C under NH₃ (removing significant amount of methyl groups from structure) and calcination at 1400 °C under N₂ atmospheres, and called as C-TDSB-3 (white). The details for the pyrolyses and calcinations are presented in Section 10.4.

The amorphous character of the as-synthesized ceramics were determined by means of powder X-ray diffraction analysis, which clearly confirms random network structures for all ceramics (Figure 8.12). The chemical compositions of the all as-synthesized Si/B/N/C ceramics (Table 8.11) have the Si:B ratio as 1:2, which is exactly the same as in the precursor TDSB molecule. FT-IR spectra of C-TDSB-1, C-TDSB-2 and C-TDSB-3 ceramics are presented in Figure 8.13, Figure 8.14 and Figure 8.15, respectively. The broad but very strong IR absorption of all three ceramics between 1350 cm⁻¹ and 1450 cm⁻¹ can undoubtedly be assigned to the antisymmetric stretching mode of silaborazine ring, which was observed not only in other silaborazines in the literature [375] but also in both TDSB molecule and the polymers from TDSB. Thus, silaborazine rings introduced via the single source precursor TDSB have become a part of the final random networks. Other typical structural increments can also be identified from their corresponding broad bands, i.e. for Si-N between 1070 cm⁻¹ - 1130 cm⁻¹ and 440 cm⁻¹ - 480 cm⁻¹, and for B-N between 770 cm⁻¹ and 810 cm⁻¹. As the IR measurements were performed in air, broad water absorption bands are also observed between 3300 cm⁻¹ and 3600 cm⁻¹. An overview of the IR absorptions for the ceramics together with the corresponding assignments is given in Table 8.12. The high-temperature behavior of the ceramics from TDSB has also been investigated by DTA/TG analysis in helium flow with a rate of 10 K.min⁻¹ up to 1970 °C (Figure 8.16). Even though the decomposition of the amorphous network in all ceramics starts at around 1400 °C, only 2.5 % weight loss for C-TDSB-1, 1.2 % for C-TDSB-2 and 0.9 % for C-TDSB-3 were observed at 1910 °C. These very low amount of the weight losses are attributed to the silaborazine rings, which should be tightly integrated into the random network serving as a rigid structural element. X-ray powder diffractograms of C-TDSB-1, C-TDSB-2 and C-TDSB-3 ceramics after heating up to 1970 °C are presented in Figure 8.19, Figure 8.20 and Figure 8.21, respectively, indicating the formation of small Si₃N₄, SiC and Si domains, which are typical high-temperature decomposition crystalline phases of Si/B/N/C ceramics.

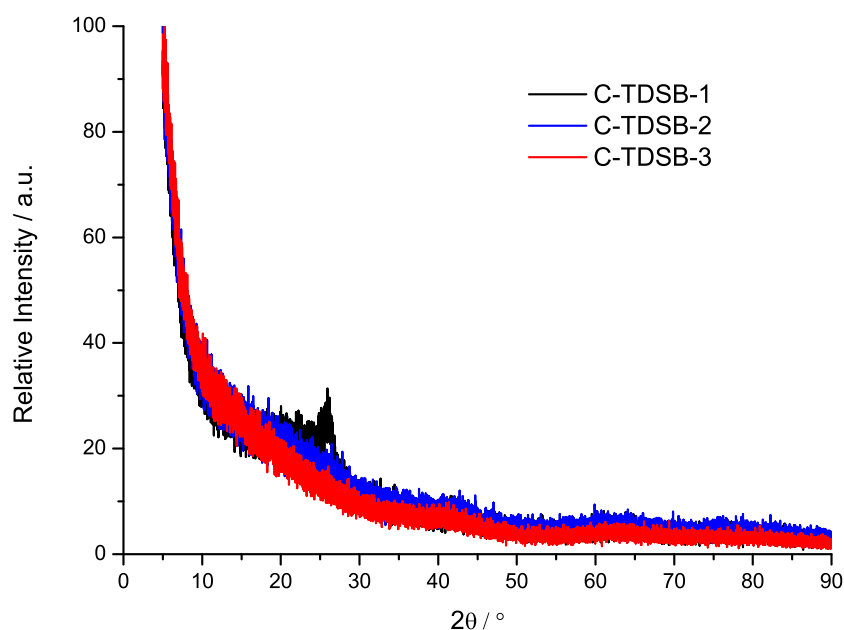


Figure 8.12.: Powder X-ray diffractograms of C-TDSB-1, C-TDSB-2 and C-TDSB-3 after 1400 °C.

Table 8.11.: Chemical compositions (% weight) of ceramics from TDSB after 1400 °C.

	Si	B	N	C	O	Σ	Empirical formula	Color
C-TDSB-1	31.91	24.97	37.96	3.71	0.60	99.15	exact: $\text{SiB}_2\text{N}_{2.4}\text{C}_{0.26}$ approx.: $\text{Si}_4\text{B}_8\text{N}_{10}\text{C}$	Grey
C-TDSB-2	23.52	17.84	34.76	19.96	0.38	96.46	exact: $\text{SiB}_2\text{N}_3\text{C}_2$	Black
C-TDSB-3	29.56	22.70	33.66	0.59	0.51	87.02	exact: $\text{SiB}_2\text{N}_{2.3}$ approx.: $\text{Si}_4\text{B}_8\text{N}_9$	White

Table 8.12.: IR absorptions of ceramics derived from P-TDSB polymers.

Assignment ^a	C-TDSB-1	C-TDSB-2	C-TDSB-3
$\nu_{as}(\text{B-N-Si})$ in SiB_2N_3 ring	1381 (vs)	1375 (vs)	1382 (vs)
$\nu(\text{Si-N})$	1094 (s)	1050-850 (s)	977 (s)
$\nu_s(\text{B-N})$	790 (s)	796 (s)	796 (m)
$\delta(\text{Si-N})$	464 (s)	454 (w)	471 (w)

^a Values are wavenumbers in cm^{-1} . vs: very strong, s: strong, m: medium, w: weak.

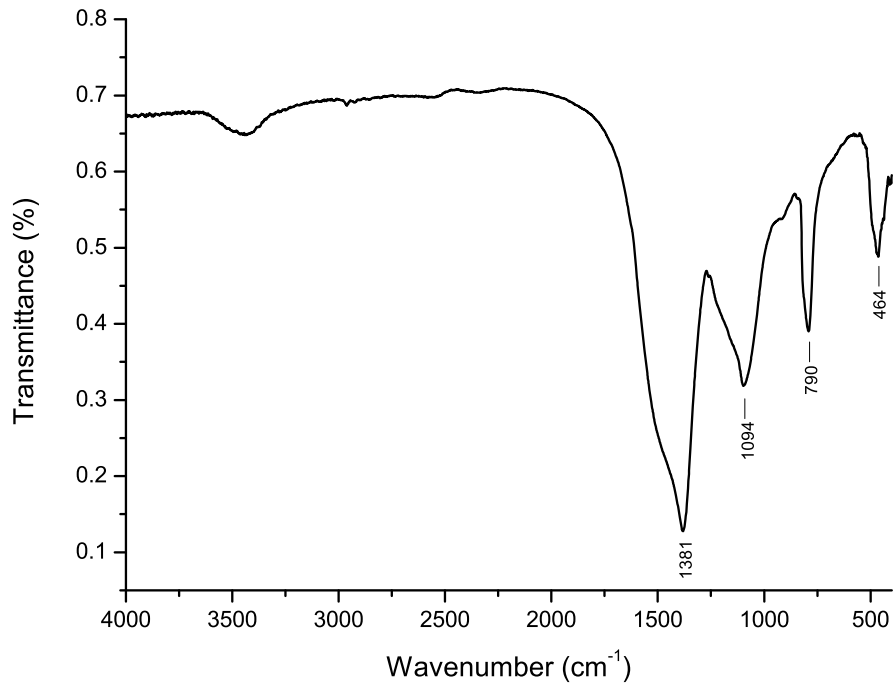


Figure 8.13.: FT-IR spectrum of C-TDSB-1.

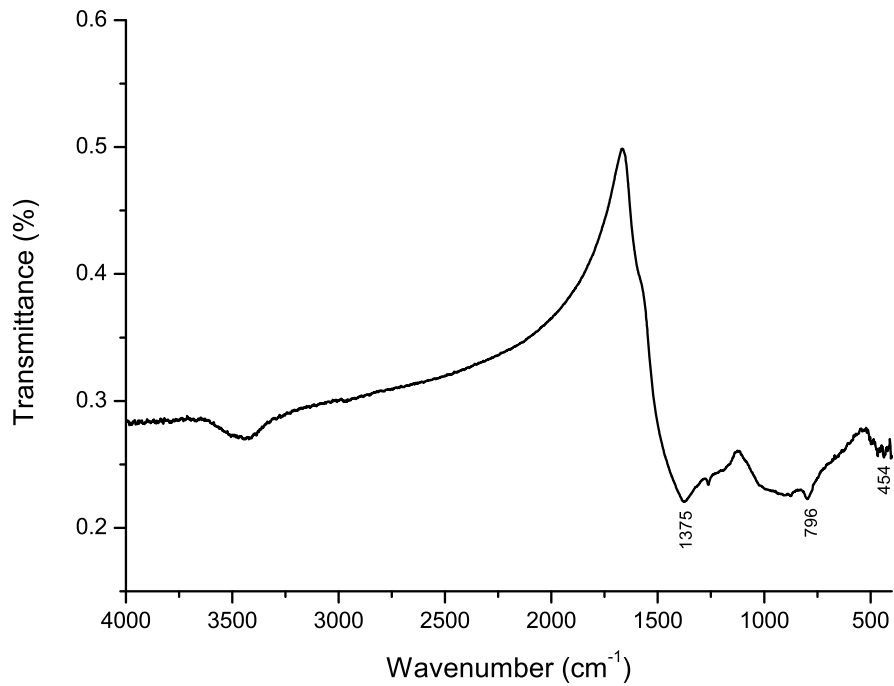


Figure 8.14.: FT-IR spectrum of C-TDSB-2.

8. A New Silaborazine-type Single Source Precursor for Si/B/N/C Ceramics

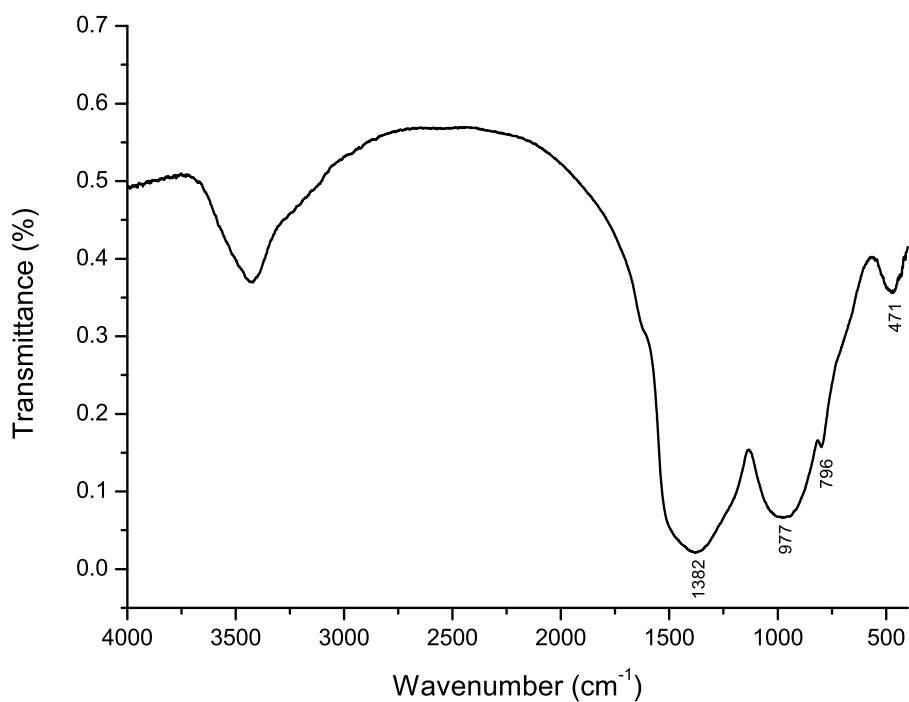


Figure 8.15.: FT-IR spectrum of C-TDSB-3.

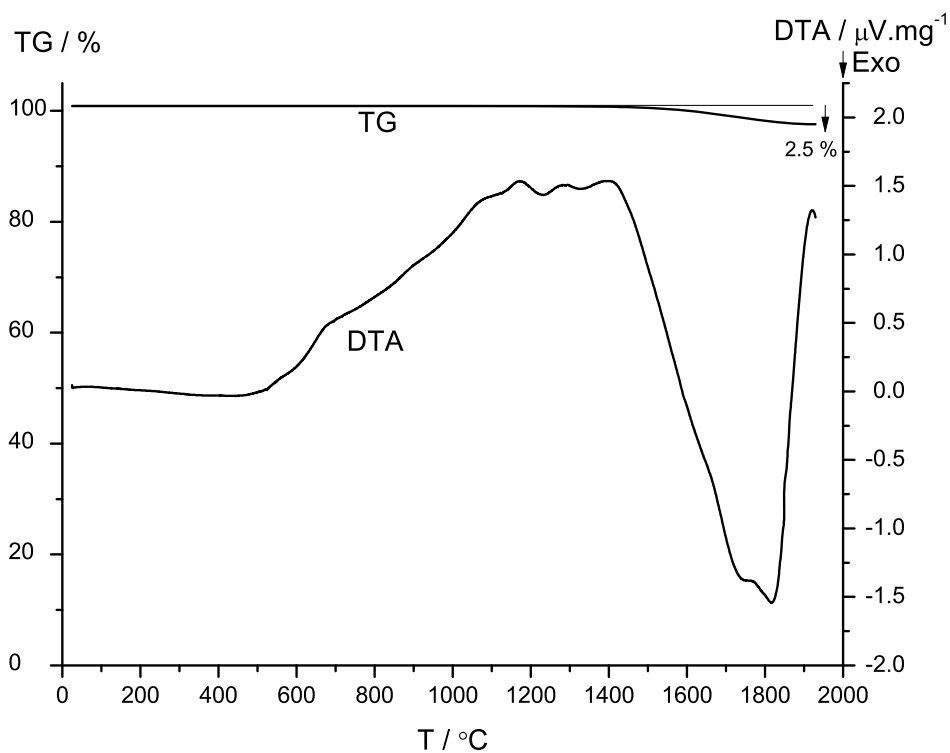


Figure 8.16.: High-temperature-DTA/TG thermogram (heating cycles) of of C-TDSB-1.

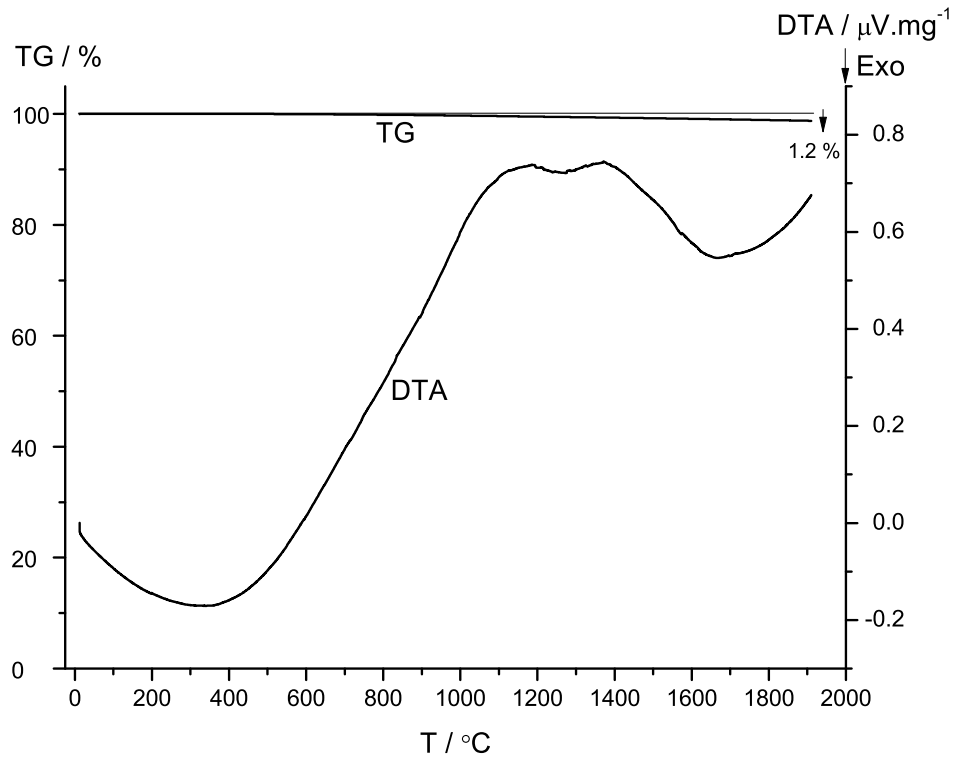


Figure 8.17.: High-temperature-DTA/TG thermogram (heating cycles) of C-TDSB-2.

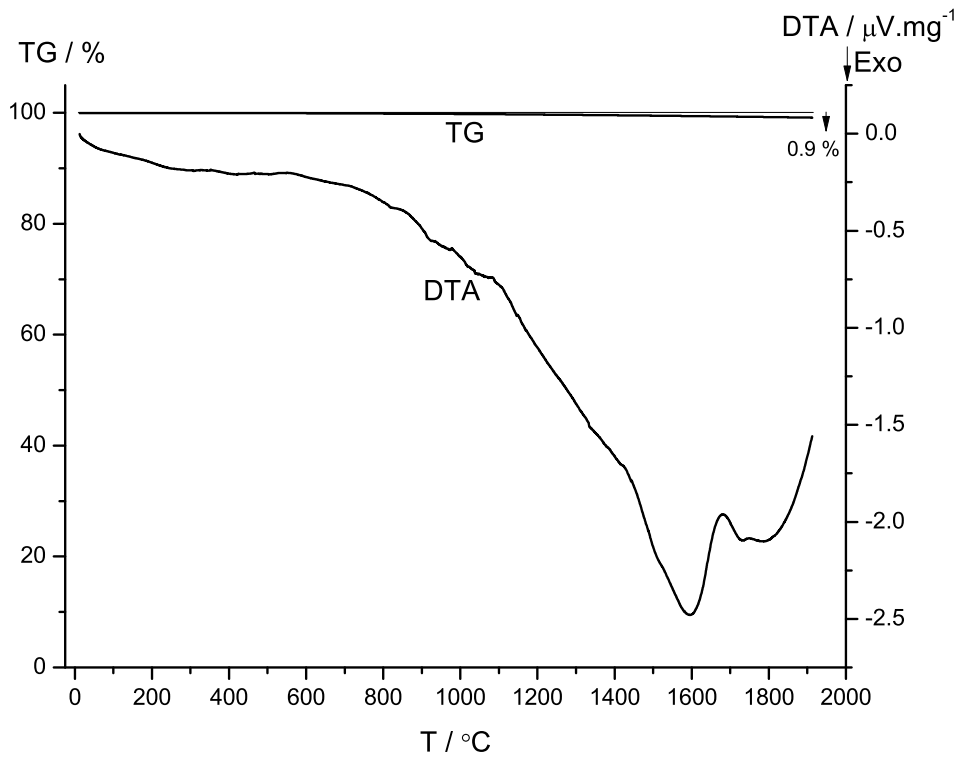


Figure 8.18.: High-temperature-DTA/TG thermogram (heating cycles) of C-TDSB-3.

8. A New Silaborazine-type Single Source Precursor for Si/B/N/C Ceramics

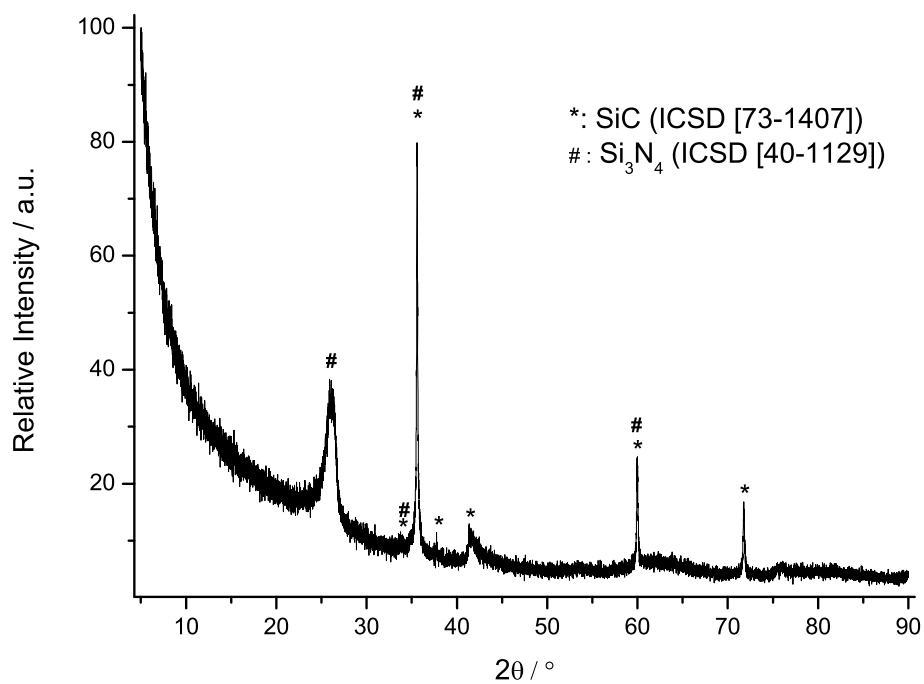


Figure 8.19.: Powder X-ray diffractogram of C-TDSB-1 after 1970 °C.

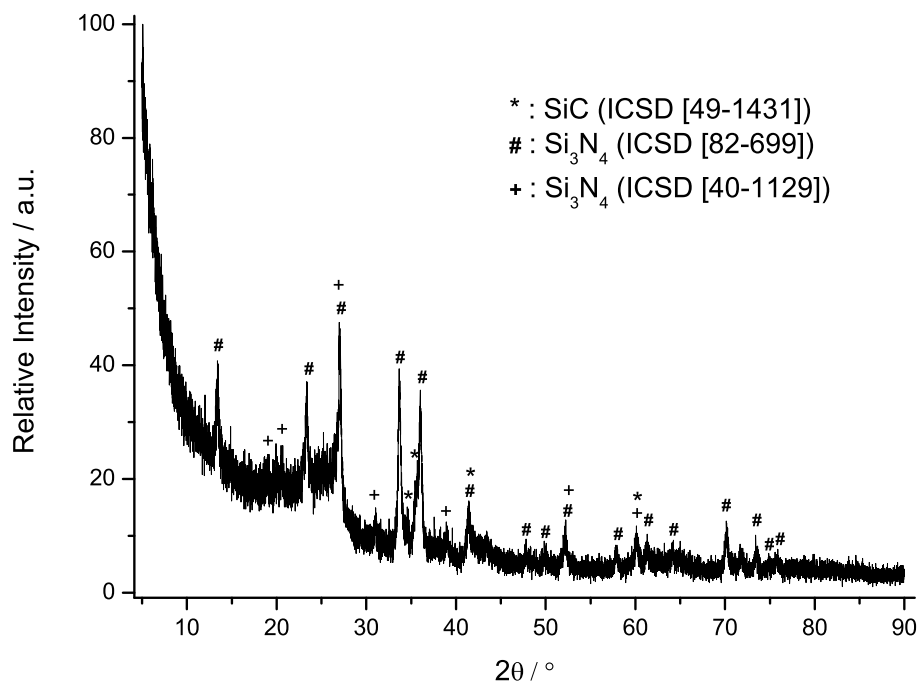


Figure 8.20.: Powder X-ray diffractogram of C-TDSB-2 after 1970 °C.

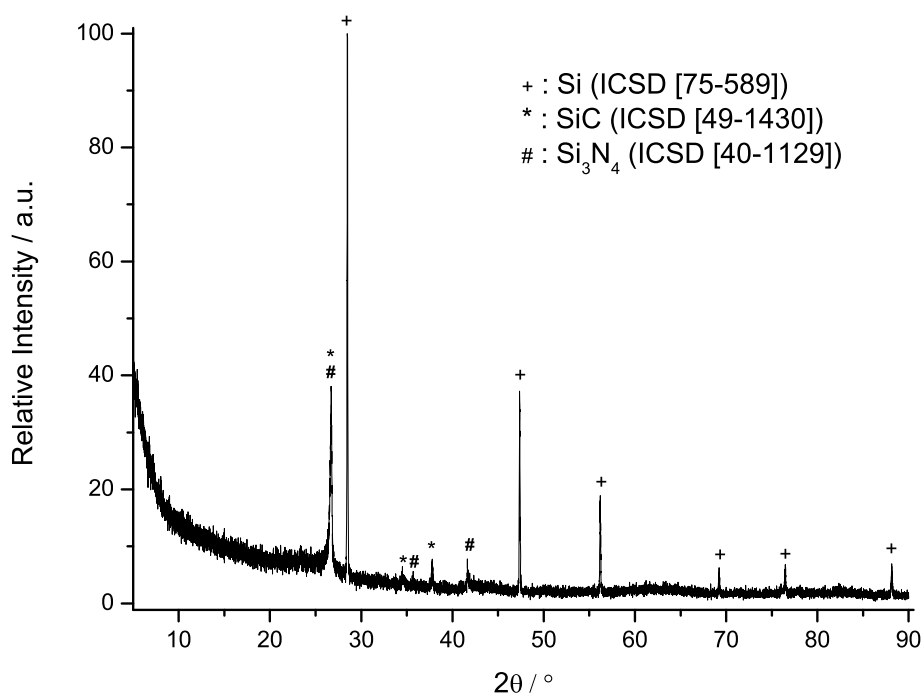


Figure 8.21.: Powder X-ray diffractogram of C-TDSB-3 after 1970 °C.

8.4. Conclusions

A new halo-substituted monocyclic silaborazine derivative, namely 1,1,3,5-tetrachloro-2,6-dimethyl-4-hydride-1-silaborazine (TDSB), has been synthesized and used as a single source precursor for the preparation of amorphous silicon boron (carbo)nitrides via the well-known polymer route. TDSB was polymerized with ammonia and methylamine to yield preceramic polymers, which provided amorphous ceramics after pyrolysis up to 1400 °C. New ceramic materials start to decompose at around 1400 °C with only very small weight losses at 1910 °C. The TDSB molecule comprises an important structural feature such that Si and B atoms on the monocyclic silaborazine ring are fully chlorinated, which allows direct crosslinking of the silaborazine rings through their constituent elements (Si and B) and a crosslinking agent (e.g. ammonia or amines). This makes the network stiffer and stronger against conformational changes of the structure, which results in very low weight loss at high temperatures. Furthermore, the results of elemental analysis indicates that the same Si:B ratio as in TDSB molecule is achieved. In addition, a very strong IR absorption in all ceramics between 1360 cm^{-1} and 1380 cm^{-1} reveals that the silaborazine rings are part of the final random network.

8. *A New Silaborazine-type Single Source Precursor for Si/B/N/C Ceramics*

9. Open Cell SiBNC Ceramic Foams

Open cell SiBNC ceramic foams have been prepared via the replica method, utilizing the commercially available melamine-based open cell Basotect[®] foam immersed into a polyborocarbosilazane polymer (experimental details are in Section 10.5). Since the open cell template foam (Basotect[®]) is melamine-based, it does not include oxygen as its constitutional unit. However, it may contain impurity level of oxygen which can be incorporated during manufacturing, such as from blowing agents or additives. On the other hand, this foam has relatively high thermal stability. As it is seen from DTA/TG thermogram, in both argon and oxygen atmosphere (Figure 9.1), there is almost no weight loss up to 200 °C and a very slow weight loss (10 % by weight) between 200 °C and 300 °C. Then a sudden weight loss, almost 30 % by weight occurs at 350 °C. The DTA curve also reveals that pristine Basotect[®] foam degrades at 350 °C. After that, it loses its weight gradually and only 10 % weight residue remains at 610 °C in oxygen atmosphere. In contrast, the foam degrades more slowly in argon atmosphere and retains almost 50 % of its weight at 610 °C and 30 % at 800 °C. This relatively high thermal stability allows polyborocarbosilazane polymer to crosslink sufficiently enough on the surface of open cell walls by tempering at around 300 °C, which result in keeping the same shape of the open cells in the final ceramic.

The SEM picture in Figure 9.2 shows clearly open cell structure of pure Basotect foam. The SEM picture in Figure 9.3 indicates the open cell structure formation of SiBNC ceramic, which is obtained by soaking the foam in polyborocarbosilazane polymer only once, centrifuging and pyrolysing subsequently. Due to centrifuging force at about 45° angle, some polymers stay inevitably at outer corner of the foam piece. Therefore, only in that corner, polyborocarbosilazane polymer is filled into the open cell, which are not able to be removed. After pyrolysis of this part of the sample, only cell walls of the foam is removed and bulk ceramics are remained in cell volume. This phenomenon can be clearly seen in the SEM picture in Figure 9.4. Other parts of the polymer-wetted foam are well centrifuged and open cell formations are obtained (Figure 9.3).

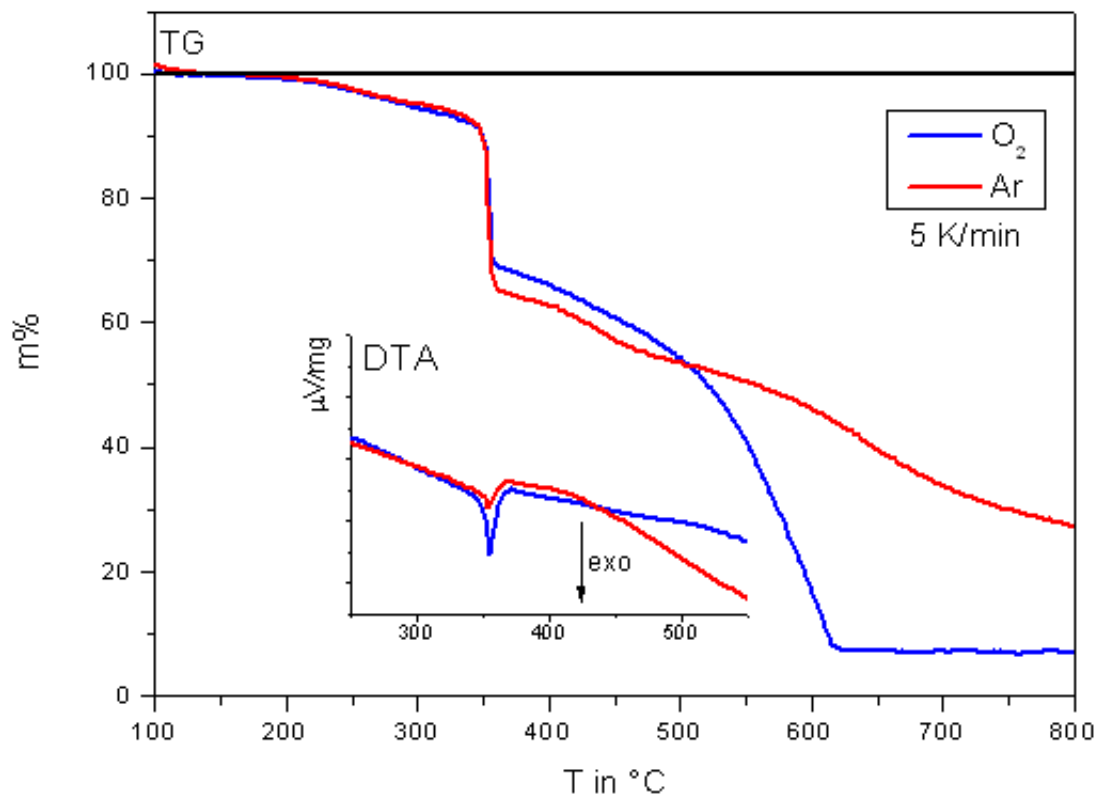


Figure 9.1.: TGA/DTA thermograms of pristine open cell Basotect® foam.

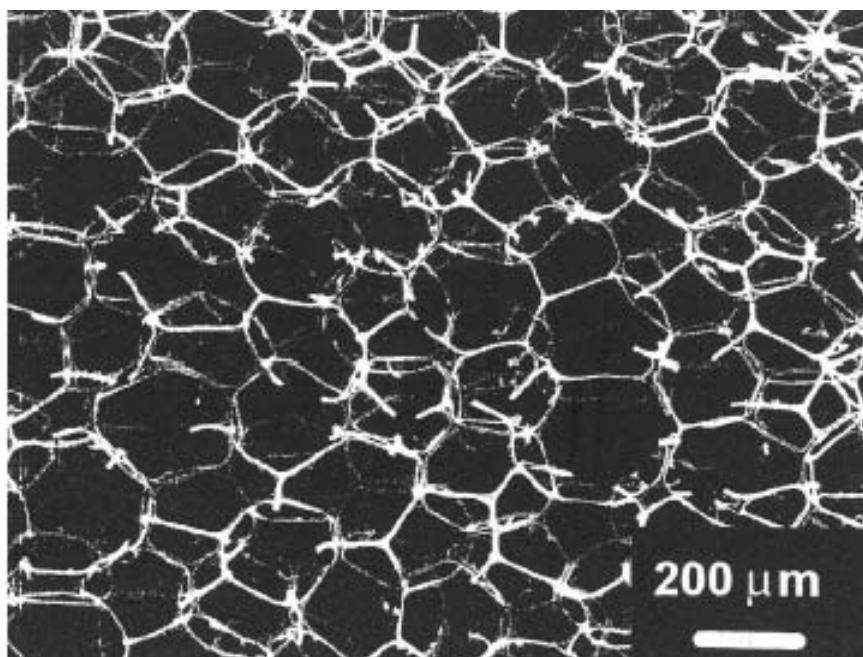


Figure 9.2.: SEM picture of pristine Basotect® foam.

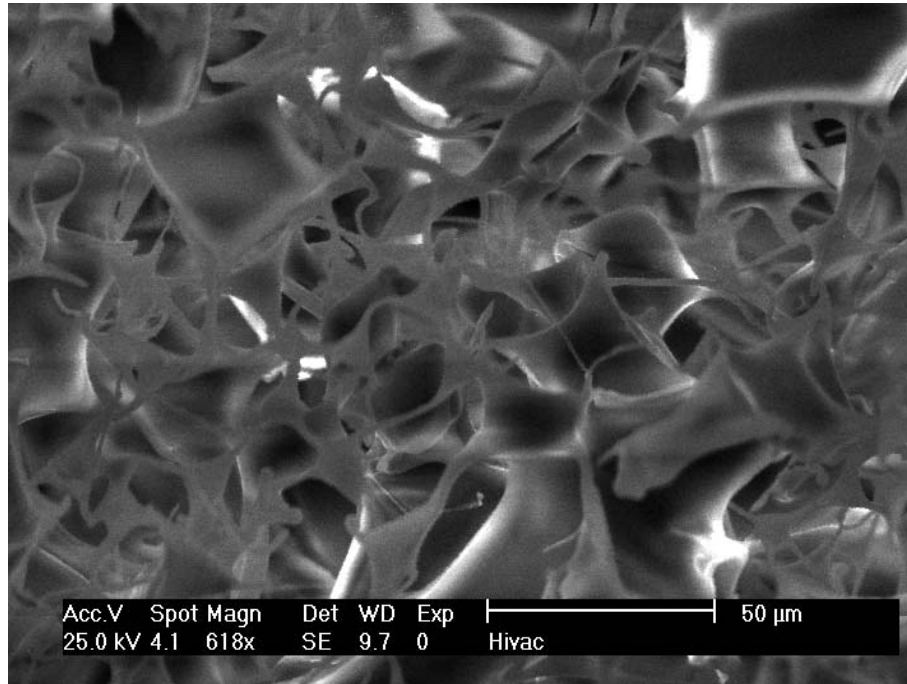


Figure 9.3.: SEM picture of the SiBNC ceramic foam obtained from preceramic polymer which is coated on the open cell walls of Basotect[®] foam once.

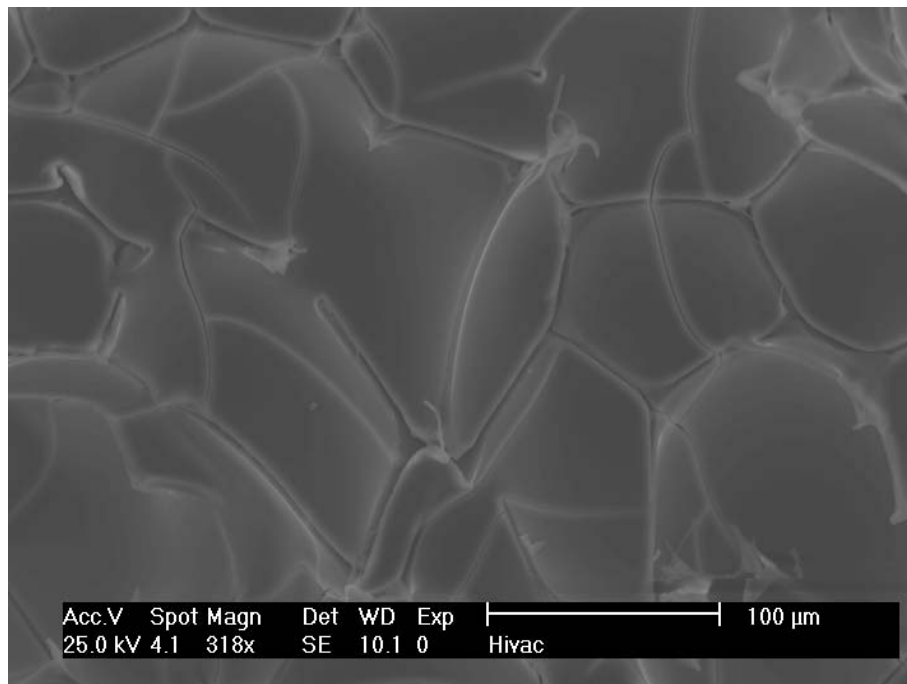


Figure 9.4.: SEM picture of the SiBNC ceramic foam obtained from preceramic polymer which is filled in the open cell volume of Basotect[®] foam.

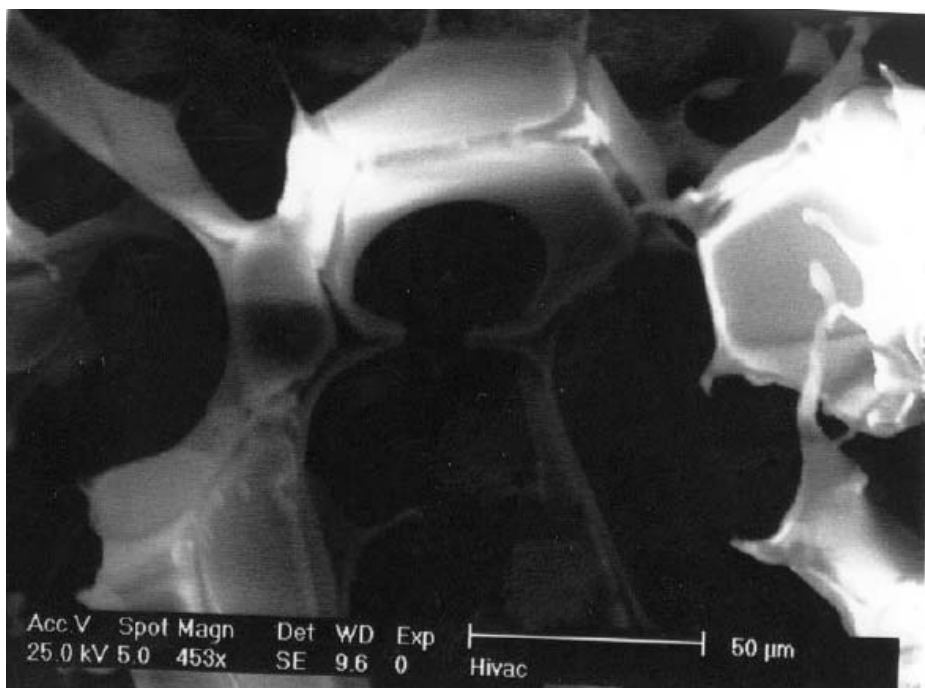


Figure 9.5.: SEM picture of the SiBNC ceramic foam obtained from preceramic polymer coated on the open cell walls of Basotect[®] foam twice.

Since the cell struts are the weakest points due to having unavoidable cracks after pyrolysis of the foam template, the final SiBNC open cell ceramic foams have weak mechanical strength, and are even touch sensitive. In order to improve its mechanical properties, it is considered to coat the open cell walls of the Basotect[®] foam twice with polyborocarbosilazane. The SEM picture in Figure 9.5 clearly presents thicker polymer coatings on the open cell walls compared to the previous one. This indicates that the second coating process is successful and there are still open cell formations in the final SiBNC ceramic. On the other hand, coating the polymer for the second time have not improved significantly the mechanical properties of the final open cell SiBNC ceramic foam.

In conclusion, the present work showed that the replica method is a promising technique for the production of open cell SiBNC ceramic foams. Therefore, further research is required for improving the mechanical properties, such as optimizing the experimental conditions and trying different open cell organic foam materials as templates.

10. General Experimental Methods

All reactions were carried out under an inert atmosphere (argon) in rigorously dried reaction apparatus and solvents. Before any manipulation, glassware systems, which were connected to a Schlenk line, were heated with the flame of a Bunsen burner under vacuum (10^{-3} regime) in order to remove air and moisture from the glass walls. After cooling down the glassware, the vessels were filled with dry argon. This procedure was repeated at least three times in order to be sure that the glassware system is inert. Freshly distilled commercially available hexamethyldisilazane (HMDS, > 98 %, Fluka), silicontetrachloride (SiCl_4 , > 99 %, Merck) and hexane (> 99 %, Merck) were used for the reactions. Moreover, commercially available borontrichloride (99.9%, Gerling Holz & Co, Hamburg, Germany), methylamine (99.5 %, Gerling Holz & Co, Hamburg, Germany) and ammonia (99.998 % and 99.999 %, Westfallen AG, Münster, Germany) were directly used without further purification. Ammonia with purity grade of 99.999 % and 99.998 % were used for the reactions and the pyrolyses, respectively. All the chemicals used for the present study are tabulated in Table 10.1.

10.1. Preparation of Phosphors Based on Amorphous $\text{Si}_3\text{B}_3\text{N}_7$ Ceramic

In the present work, syntheses of luminescent amorphous $\text{Si}_3\text{B}_3\text{N}_7$ ceramics were achieved by following the conventional synthesis method for amorphous $\text{Si}_3\text{B}_3\text{N}_7$ ceramics from the single source precursor molecule, (trichlorosilylamino)-dichloroborane (TADB), with some minor modifications [295]. First of all, TADB was synthesized according to the literature via a two-step reaction [43]. In the first step, HMDS was reacted with SiCl_4 to obtain an intermediate compound trichlorotrimethyldisilazane (TTDS). In the second step, TTDS was reacted with BCl_3 to obtain the desired single source precursor molecule, TADB. After that, the activators and/or sensitizers were incorporated into amorphous $\text{Si}_3\text{B}_3\text{N}_7$ ceramic mainly by following the two routes: the metal route and the organometallic route.

Table 10.1.: Commercially supplied chemicals.

Name	Purity (%)	Company
HMDS	> 98	Fluka
SiCl ₄	> 99	Merck
BCl ₃	99.9	Gerling Holz & Co
NH ₃	99.998 and 99.999	Westfallen AG
NH ₂ (CH ₃)	99.5	Gerling Holz & Co
Hexane	> 99	Merck
Eu, Yb, Li, Ca, Sr and Ba	99.99	Chempur
Ce[N(Si(CH ₃) ₃) ₂] ₃	96	ABCR
Nd[N(Si(CH ₃) ₃) ₂] ₃	97	Sigma-Aldrich
Sm[N(Si(CH ₃) ₃) ₂] ₃	98	Sigma-Aldrich
Eu[N(Si(CH ₃) ₃) ₂] ₃	98	ABCR
Gd[N(Si(CH ₃) ₃) ₂] ₃	98	Sigma-Aldrich
Ho[N(Si(CH ₃) ₃) ₂] ₃	97	Sigma-Aldrich
Tm[N(Si(CH ₃) ₃) ₂] ₃	98	Sigma-Aldrich
Yb[N(Si(CH ₃) ₃) ₂] ₃	98	Sigma-Aldrich
Y[N(Si(CH ₃) ₃) ₂] ₃	98	ABCR
Sn[N(Si(CH ₃) ₃) ₂] ₂	98	Sigma-Aldrich
Co(NH ₃) ₆ Cl ₃	99.999	Sigma-Aldrich
Ni(NH ₃) ₆ Cl ₂	99.999	Sigma-Aldrich
Fe ₂ O ₃	-	BASF
MnI ₂	99.99	Sigma-Aldrich
CoCl ₂	99.999	Sigma-Aldrich
TbCl ₃	99.99	Sigma-Aldrich
NaN(Si(CH ₃) ₃) ₂	1.0 M in THF	Sigma-Aldrich

10.1.1. Metal Route

In the metal route, elemental metals, such as Eu, Yb, Ca, Sr and Ba, which are soluble in liquid ammonia, were used. For the polymerization reaction, the single source precursor molecule, TADB (or, analogously, SiCl₄ for preparing Eu²⁺ doped amorphous Si₃N₄ ceramics), was ammonolysed with liquid ammonia in which elemental metals were dissolved. Mixing of these reactants was achieved in two different ways; either dropping of TADB

10.1. Preparation of Phosphors Based on Amorphous $\text{Si}_3\text{B}_3\text{N}_7$ Ceramic

into the flask containing liquid ammonia in which metals were dissolved or the other way around. Both methods yielded the same ceramics without any significant variation in properties; therefore the former method which is much easier to handle was preferred in most of the syntheses. On the other hand, addition of solvent, like hexane, has improved significantly the homogeneity in the final ceramic; thus, most of the syntheses have been performed in hexane medium. A typical experimental procedure in detail is presented below. All others, including the combination of the two methods in a single reaction, are tabulated in Table 10.2. The chemical composition of some rare-earth doped amorphous $\text{Si}_3\text{B}_3\text{N}_7$ ceramics were determined via elemental analysis and summarized in Table 10.3.

In a typical experiment, around 50 ml liquid ammonia was condensed on 0.051 g freshly distilled europium metal at $-76\text{ }^\circ\text{C}$ (dry ice and ethanol mixture) in a three-neck flask. Immediately, even after condensing some drops of liquid ammonia, a dark blue solution was obtained, which is the indications of both purity and solubility of Eu metal. Then, about 125 ml freshly distilled hexane, which is immiscible with liquid ammonia, was added into that flask. By the help of a single use injector and needle, 5 ml TADB was mixed with 25 ml hexane, which makes a miscible solution, in a graduated cylinder and then added dropwise into the flask containing the mixture of liquid ammonia, in which Eu metal were dissolved, and hexane under very slow of Ar flow. The reaction was quite aggressive and stirred vigorously at $-76\text{ }^\circ\text{C}$. Even the vapors of TADB and NH_3 are reacting and forms suddenly NH_4Cl salts all around the flask. After the reaction was completed, following common procedure was followed:

The flask was allowed to reach the room temperature under strong stirring, in which way the excess ammonia was removed under Ar flow. Then, hexane was removed under vacuum into a cold trap. After that, a white powder, which is a mixture of NH_4Cl and partially crosslinked polyborosilazane was obtained. The NH_4Cl salt was sublimed by heating at $210\text{ }^\circ\text{C}$ under vacuum ($P \approx 10^{-3}$ mbar) for almost 24 hours, which additionally removed all remaining volatile adducts, such that almost salt-free polymer was obtained. A clean BN crucible in a quartz tube was heated to $600\text{ }^\circ\text{C}$ in a horizontal furnace under vacuum ($P \approx 10^{-3}$ mbar) in order to make it moisture-free with the following heating program:

- heating from room temperature to $600\text{ }^\circ\text{C}$ with $100\text{ }^\circ\text{C}/\text{h}$ rate
- dwelling at $600\text{ }^\circ\text{C}$ for 5 hours
- cooling from $600\text{ }^\circ\text{C}$ to room temperature with $100\text{ }^\circ\text{C}/\text{h}$ rate

Almost salt-free polymer was loaded into a moisture-free BN crucible in an Ar filled glove-box and then heated to $900\text{ }^\circ\text{C}$ under ammonia flow inside a quartz tube in a horizontal furnace with the following temperature program:

10. General Experimental Methods

- heating from room temperature to 300 °C with 100 °C/h rate
- dwelling at 300 °C for 3 hours
- heating from 300 °C to 900 °C with 100 °C/h rate
- dwelling at 900 °C for 3 hours
- cooling from 900 °C to room temperature with 100 °C/h rate

Finally, the obtained material was further heated to 1200 °C in another horizontal furnace with a corundum tube under nitrogen flow in order to obtain the desired luminescent ceramic with the following temperature program:

- heating from room temperature to 1200 °C with 10 °C/min rate
- dwelling at 1200 °C for 3 hours
- cooling from 1200 °C to room temperature with 10 °C/min rate

10.1.2. Organometallic Route

In this route, activator and/or sensitizer elements which are not soluble in liquid ammonia are thought to be used as metal-complexes. The best candidates are found to be bis(trimethylsilylamido) (-N(Si(CH₃)₃)₂ or TMSA) complexes of the metal ions such as La³⁺, Ce³⁺, Nd³⁺, Sm³⁺, Eu³⁺, Gd³⁺, Tb³⁺, Ho³⁺, Tm³⁺, Yb³⁺, Y³⁺ and Sn²⁺. Only Tb[N(Si(CH₃)₃)₂]₃ was synthesized in the laboratory according to the literature [381], and all the others were supplied commercially (Table 10.1) and used without further purification. Similar to the metal route, the single source precursor TADB was ammonolysed with liquid ammonia in which the metal-complexes were suspended. For the same reasons as discussed for the metal route, a reaction way which is based on dropping of TADB and hexane mixture into the flask containing liquid ammonia, metal complex and hexane mixture was preferred for most of the syntheses. A typical experimental procedure in detail is presented below. All the others, including the combination of these two methods in a single reaction, are tabulated in Table 10.2.

In a typical experiment, around 50 ml liquid ammonia was condensed on 0.1496 g of Eu[N(Si(CH₃)₃)₂]₃ at -76 °C (dry ice and ethanol mixture) in a three-neck flask. Then about 125 ml freshly distilled hexane was added on the liquid ammonia mixture. By the help of a single use injector and needle, 5 ml TADB was mixed with 25 ml hexane in a graduated cylinder and was added dropwise into the flask containing the mixture of liquid ammonia, Eu[N(Si(CH₃)₃)₂]₃ and hexane under very slow of Ar flow. After the reaction was completed, the same procedure, as it was explained for the metal route, was followed (see Section 10.1.1).

10.1. Preparation of Phosphors Based on Amorphous $\text{Si}_3\text{B}_3\text{N}_7$ Ceramic

Table 10.2.: Experimental details, maximum emission wavelengths and full width at half maximum (FWHM) values for doped amorphous $\text{Si}_3\text{B}_3\text{N}_7$ ceramics.

Name	Amounts ^a	$\lambda_{\text{emission}}$ (nm) ^b	FWHM (nm)
s1	0.125 g Eu + 5 ml TADB + 50 ml NH_3	592	174
s2	0.2864 g Eu + 5 ml TADB + 50 ml NH_3	625	181
s6	0.0267 g Eu + 5 ml TADB + 50 ml NH_3	550	212
s7	0.0609 g Eu + 5 ml TADB + 50 ml NH_3	581	181
s8	0.0513 g Eu + 5 ml TADB + 50 ml NH_3	555	161
s9	0.223 g $\text{Eu}(\text{TMSA})_3$ + 10 ml TADB + 50 ml NH_3	554	160
s11	0.0052 g Eu + 5 ml TADB + 50 ml NH_3	522	152
s12	0.3377 g $\text{Ce}(\text{TMSA})_3$ + 10 ml TADB + 50 ml NH_3	492	202
s13	0.1493 g $\text{Eu}(\text{TMSA})_3$ + 0.1493 g $\text{Ce}(\text{TMSA})_3$ + 10 ml TADB + 50 ml NH_3	560	178
s14	0.1483 g $\text{Eu}(\text{TMSA})_3$ + 10 ml TADB + 50 ml NH_3	540	155
s15	0.1504 g $\text{Ce}(\text{TMSA})_3$ + 10 ml TADB + 50 ml NH_3	462	156
s16	0.0741 g $\text{Eu}(\text{TMSA})_3$ + 0.1447 g $\text{Ce}(\text{TMSA})_3$ + 5 ml TADB + 50 ml NH_3	552	163
s17	0.1483 g $\text{Eu}(\text{TMSA})_3$ + 0.0737 g $\text{Ce}(\text{TMSA})_3$ + 5 ml TADB + 50 ml NH_3	572	167
s18	0.3017 g $\text{Ce}(\text{TMSA})_3$ + 5 ml TADB + 50 ml NH_3	541	196
s19	0.4028 g Eu + 5 ml TADB + 50 ml NH_3	641	179
s20	0.7507 g Eu + 5 ml TADB + 50 ml NH_3	657	198
s21	0.5185 g Eu + 5 ml TADB + 50 ml NH_3	603	171
s22	0.2568 g Eu + 5 ml TADB + 50 ml NH_3	532	156
s23	0.2610 g Eu + 5 ml TADB + 100 ml hexane + 50 ml NH_3	592	168
s24	0.1173 g Eu + 5 ml TADB + 150 ml hexane + 50 ml NH_3	563	160
s25	0.0832 g Eu + 5 ml TADB + 150 ml hexane + 50 ml NH_3	592	161
s28	0.3268 g Eu + 5 ml TADB + 150 ml hexane + 50 ml NH_3	609	178
s29	0.4128 g Eu + 5 ml TADB + 150 ml hexane + 50 ml NH_3	640	189
s30	0.6195 g Eu + 5 ml TADB + 150 ml hexane + 50 ml NH_3	611	182
s31	0.4989 g Eu + 5 ml TADB + 150 ml hexane + 50 ml NH_3	640	187

10. General Experimental Methods

Table 10.2 continued

Name	Amounts ^a	$\lambda_{emission}$ (nm) ^b	FWHM (nm)
s33	0.0050 g Eu + 5 ml TADB + 150 ml hexane + 50 ml NH ₃	522	160
s35	0.2893 g Eu + 1 ml TADB + 150 ml hexane + 50 ml NH ₃	582	105
s36	0.5583 g Eu + 1 ml TADB + 150 ml hexane + 50 ml NH ₃	578	109
s37	0.1496 g Ce(TMSA) ₃ + 5 ml TADB + 150 ml hexane + 50 ml NH ₃	525	189
s38	0.4087 g Ce(TMSA) ₃ + 5 ml TADB + 150 ml hexane + 50 ml NH ₃	547	186
s39	0.7146 g Ce(TMSA) ₃ + 5 ml TADB + 150 ml hexane + 50 ml NH ₃	549	183
s40	0.0981 g Eu(TMSA) ₃ + 5 ml TADB + 150 ml hexane + 50 ml NH ₃	573	168
s41	1.0130 g Eu + 1 ml TADB + 150 ml hexane + 50 ml NH ₃	575	100
s42	0.1150 g Sr + 5 ml TADB + 150 ml hexane + 50 ml NH ₃	-	-
s43	0.0542 g Eu + 0.1067 Sr + 5 ml TADB + 150 ml hexane + 50 ml NH ₃	573	169
s44	0.1146 g Ba + 5 ml TADB + 150 ml hexane + 50 ml NH ₃	-	-
s45	0.0632 g Eu + 0.1108 Ba + 5 ml TADB + 150 ml hexane + 50 ml NH ₃	579	171
s46	0.1166 g Yb + 5 ml TADB + 150 ml hexane + 50 ml NH ₃	-	-
s47	0.0535 g Eu + 0.1215 Yb + 5 ml TADB + 150 ml hexane + 50 ml NH ₃	568	169
s49	0.07 g Eu(TMSA) ₃ + 0.2040 g Ce(TMSA) ₃ + 5 ml TADB + 150 ml hexane + 50 ml NH ₃	549	161
s50	0.1963 g Eu(TMSA) ₃ + 0.0654 g Ce(TMSA) ₃ + 5 ml TADB + 150 ml hexane + 50 ml NH ₃	570	159
s51	0.0518 g Eu + 5 ml TADB + 150 ml hexane + 50 ml NH ₃	574	162
s52	0.0503 g Eu + 0.1498 g Ce(TMSA) ₃ + 5 ml TADB + 150 ml hexane + 50 ml NH ₃	560	165
s53	0.0763 g Eu(TMSA) ₃ + 0.1495 g Ce(TMSA) ₃ + 5 ml TADB + 150 ml hexane + 50 ml NH ₃	537	153
s54	0.15 ml Sn(TMSA) ₂ + 5 ml TADB + 150 ml hexane + 50 ml NH ₃	504	115

10.1. Preparation of Phosphors Based on Amorphous $\text{Si}_3\text{B}_3\text{N}_7$ Ceramic

Table 10.2 continued

Name	Amounts ^a	$\lambda_{\text{emission}}$ (nm) ^b	FWHM (nm)
s55	0.0544 g Eu metal + 0.15 ml $\text{Sn}(\text{TMSA})_2$ + 5 ml TADB + 150 ml hexane + 50 ml NH_3	558	155
s56	0.1507 g $\text{Yb}(\text{TMSA})_3$ + 5 ml TADB + 150 ml hexane + 50 ml NH_3	-	-
s57	0.0550 g Eu + 0.1527g $\text{Yb}(\text{TMSA})_3$ + 5 ml TADB + 150 ml hexane + 50 ml NH_3	573	158
s58	0.1516 g $\text{Gd}(\text{TMSA})_3$ + 5 ml TADB + 150 ml hexane + 50 ml NH_3	-	-
s59	0.1484 g $\text{Y}(\text{TMSA})_3$ + 5 ml TADB + 150 ml hexane + 50 ml NH_3	-	-
s60	0.0508 g Eu + 5 ml SiCl_4 + 150 ml hexane + 50 ml NH_3	528	151
s61	0.05 g Eu + 0.1492g $\text{Y}(\text{TMSA})_3$ + 5 ml TADB + 150 ml hexane + 50 ml NH_3	573	157
s62	0.1015 g Eu + 5 ml SiCl_4 + 150 ml hexane + 50 ml NH_3	552	166
s64	0.0546 g Eu + 0.1516g $\text{Gd}(\text{TMSA})_3$ + 5 ml TADB + 150 ml hexane + 50 ml NH_3	568	157
s65	0.1507 g $\text{Sm}(\text{TMSA})_3$ + 5 ml TADB + 150 ml hexane + 50 ml NH_3	652	-
s67	0.0516 g Eu + 0.1505g $\text{Sm}(\text{TMSA})_3$ + 5 ml TADB + 150 ml hexane + 50 ml NH_3	566	163
s69	0.1499 g $\text{Nd}(\text{TMSA})_3$ + 5 ml TADB + 150 ml hexane + 50 ml NH_3	-	-
s70	0.1513 g $\text{Tm}(\text{TMSA})_3$ + 5 ml TADB + 150 ml hexane + 50 ml NH_3	-	-
s71	0.1552 g $\text{La}(\text{TMSA})_3$ + 5 ml TADB + 150 ml hexane + 50 ml NH_3	-	-
s72	0.1513 g $\text{Ho}(\text{TMSA})_3$ + 5 ml TADB + 150 ml hexane + 50 ml NH_3	-	-
s73	0.0577 g Eu + 0.1519 g $\text{Tm}(\text{TMSA})_3$ + 5 ml TADB + 150 ml hexane + 50 ml NH_3	570	149
s74	0.0530 g Eu + 0.1512 g $\text{La}(\text{TMSA})_3$ + 5 ml TADB + 150 ml hexane + 50 ml NH_3	576	162
s75	0.0504 g Eu + 0.1556 g $\text{Ho}(\text{TMSA})_3$ + 5 ml TADB + 150 ml hexane + 50 ml NH_3	579	167

10. General Experimental Methods

Table 10.2 continued

Name	Amounts ^a	$\lambda_{emission}$ (nm) ^b	FWHM (nm)
s77	0.0500 g Eu + 0.1526 g Nd(TMSA) ₃ + 5 ml TADB + 150 ml hexane + 50 ml NH ₃	561	183
s78	0.3007 g Eu + 5 ml TADB + 150 ml hexane + 50 ml NH ₃	623	181
s83	0.13 g Ho(TMSA) ₃ + 2 ml TADB + 150 ml hexane + 50 ml NH ₃	-	-
s84	0.1730 g Nd(TMSA) ₃ + 2 ml TADB + 150 ml hexane + 50 ml NH ₃	-	-
s90	0.1530 g Tb(TMSA) ₃ + 5ml TADB + 150 ml hexane + 50 ml NH ₃	544	-
s91	0.0502 g Eu + 0.1502 g Tb(TMSA) ₃ + 5 ml TADB + 150 ml hexane + 50 ml NH ₃	572	168
s93	0.5006 g Tb(TMSA) ₃ + 5ml TADB + 150 ml hexane + 50 ml NH ₃	544	-
s95	0.1518 g Tb(TMSA) ₃ + 0.1527 g Ce(TMSA) ₃ + 5 ml TADB + 150 ml hexane + 50 ml NH ₃	544	-
s96	0.1496 g Ce(TMSA) ₃ + 5ml TADB + 150 ml hexane + 50 ml NH ₃	534	209
s97	0.05 g Eu(TMSA) ₃ + 5ml TADB + 150 ml hexane + 50 ml NH ₃	566	190
s98	1.008g Eu(TMSA) ₃ + 5ml TADB + 150 ml hexane + 50 ml NH ₃	556	193
s99	0.2032 g Ce(TMSA) ₃ + 5ml TADB + 150 ml hexane + 50 ml NH ₃	492	176
s100	0.0516 g Ce(TMSA) ₃ + 5ml TADB + 150 ml hexane + 50 ml NH ₃	514	245
s101	0.0505 g Eu + 5 ml TADB + 150 ml hexane + 50 ml NH ₃	590	160
s102	0.2963 g Ce(TMSA) ₃ + 5ml TADB + 150 ml hexane + 50 ml NH ₃	585	169
s103	0.4978g Eu(TMSA) ₃ + 5ml TADB + 150 ml hexane + 50 ml NH ₃	609	175
s104	0.0051 g Eu + 5 ml TADB + 150 ml hexane + 50 ml NH ₃	542	200
s105	5 ml TADB + 150 ml hexane + 50 ml NH ₃	-	-
s106	0.2075 g Eu + 20 ml TADB + 600 ml hexane + 200 ml NH ₃	592	162

10.1. Preparation of Phosphors Based on Amorphous $\text{Si}_3\text{B}_3\text{N}_7$ Ceramic

Table 10.2 continued

Name	Amounts ^a	$\lambda_{\text{emission}}$ (nm) ^b	FWHM (nm)
s107	0.2080 g Eu + 20 ml TADB + 600 ml hexane + 200 ml NH_3	590	161
s108	0.6035 g $\text{Tb}(\text{TMSA})_3$ + 20 ml TADB + 600 ml hexane + 200 ml NH_3	544	-
s109	0.6034 g $\text{Tb}(\text{TMSA})_3$ + 20 ml TADB + 600 ml hexane + 200 ml NH_3	544	-
s110	0.1019 g Eu + 20 ml TADB + 600 ml hexane + 200 ml NH_3	575	160
s111	0.0522 g Eu + 20 ml TADB + 600 ml hexane + 200 ml NH_3	549	151
s112	0.0519 g Eu + 20 ml TADB + 600 ml hexane + 200 ml NH_3	562	172
s113	0.0267 g Eu + 20 ml TADB + 600 ml hexane + 200 ml NH_3	539	173
s114	0.0522 g Eu + 20 ml TADB + 600 ml hexane + 200 ml NH_3	563	162
s115	0.0271 g Eu + 20 ml TADB + 600 ml hexane + 200 ml NH_3	545	214

^aTADB = $\text{Cl}_3\text{SiN}(\text{H})\text{BCl}_2$ and TMSA = $[\text{N}(\text{Si}(\text{CH}_3)_3)_2]$

^b $\lambda_{\text{excitation}}=365$ nm for all samples except Tb doped ones (300 nm)

10. General Experimental Methods

Table 10.3.: Chemical compositions (weight %) of some luminescent rare earth doped amorphous $\text{Si}_3\text{B}_3\text{N}_7$ and Si_3N_4 ceramics.

	Si	B	N	O	Eu	Ce	Tb	Empirical Formulae
s18	25.62	11.54	37.73	1.70		1.26		$\text{SiB}_{1.2}\text{N}_3\text{Ce}_{0.01}$
s19	28.51	16.60	35.61	0.51	4.16			$\text{SiB}_{1.5}\text{N}_{2.5}\text{Eu}_{0.027}$
s20	24.93	14.36	38.64	0.51	7.90			$\text{SiB}_{1.5}\text{N}_{3.1}\text{Eu}_{0.058}$
s21	26.08	17.88	32.79	0.79	4.06			$\text{SiB}_{1.8}\text{N}_{2.3}\text{Eu}_{0.029}$
s22	27.29	20.80	30.66	0.83	0.70			$\text{SiB}_2\text{N}_{2.3}\text{Eu}_{0.005}$
s23	26.2	17.97	33.36	0.45	3.76			$\text{SiB}_{1.8}\text{N}_{2.7}\text{Eu}_{0.027}$
s24	30.39	15.67	34.36	-	0.82			$\text{SiB}_{1.3}\text{N}_{2.3}\text{Eu}_{0.005}$
s25	32.73	17.44	38.47	0.41	0.95			$\text{SiB}_{1.4}\text{N}_{2.4}\text{Eu}_{0.005}$
s28	23.87	14.86	40.32	1.03	7.38			$\text{SiB}_{1.6}\text{N}_{3.4}\text{Eu}_{0.057}$
s29	25.40	15.56	34.20	0.44	11.44			$\text{SiB}_{1.65}\text{N}_{2.7}\text{Eu}_{0.083}$
s30	21.85	13.04	29.82	0.68	8.71			$\text{SiB}_{1.6}\text{N}_{2.7}\text{Eu}_{0.073}$
s31	24.42	15.38	32.73	0.26	3.97			$\text{SiB}_{1.6}\text{N}_{2.7}\text{Eu}_{0.03}$
s33	34.09	12.92	36.25	0.39	0.14			$\text{SiBN}_{2.2}\text{Eu}_{0.0008}$
s37	23.47	14.86	34.54	0.34		0.66		$\text{SiB}_{1.6}\text{N}_3\text{Ce}_{0.006}$
s38	26.56	15.50	33.44	0.47		1.71		$\text{SiB}_{1.5}\text{N}_{2.5}\text{Ce}_{0.013}$
s39	26.38	11.85	39.95	0.30		3.36		$\text{SiB}_{1.2}\text{N}_3\text{Ce}_{0.026}$
s40	26.31	10.33	41.62	0.23	0.93			$\text{SiBN}_3\text{Eu}_{0.0065}$
s41	23.92	9.11	35.09	0.6	12.99			$\text{SiBN}_3\text{Eu}_{0.1}$
s49	26.72	11.27	39.49	0.46	0.56	1.46		$\text{SiBN}_3\text{Eu}_{0.004}\text{Ce}_{0.011}$
s50	26.86	10.71	39.48	0.44	1.76	0.46		$\text{SiBN}_3\text{Eu}_{0.012}\text{Ce}_{0.0034}$
s51	38.42	14.68	34.44	0.46	1.32			$\text{SiBN}_{1.8}\text{Eu}_{0.006}$
s52	24.53	10.82	31.44	0.95	2.33	2.57		$\text{SiB}_{1.2}\text{N}_{2.6}\text{Eu}_{0.018}\text{Ce}_{0.021}$
s53	25.43	11.76	37.71	0.47	0.28	0.86		$\text{SiB}_{1.1}\text{N}_3\text{Eu}_{0.002}\text{Ce}_{0.007}$
s60	45.74	-	37.53	1.35	1.07			$\text{Si}_3\text{N}_5\text{Eu}_{0.021}$
s62	45.87	-	37.38	1.31	2.14			$\text{Si}_3\text{N}_5\text{Eu}_{0.042}$
s78	24.19	10.65	33.69	0.40	9.93			$\text{SiB}_{1.2}\text{N}_{2.8}\text{Eu}_{0.08}$
s90	30.00	14.27	36.49	0.19			0.83	$\text{SiB}_{1.2}\text{N}_{2.4}\text{Tb}_{0.005}$
s93	31.43	13.65	37.99	0.39			2.25	$\text{SiBN}_{2.4}\text{Tb}_{0.013}$
s97	39.92	15.30	44.71	0.35	0.29			$\text{SiBN}_{2.3}\text{Eu}_{0.0013}$
s103	33.38	12.40	42.86	0.19	1.90			$\text{SiBN}_{2.7}\text{Eu}_{0.011}$
s108	32.62	12.69	38.45	0.49			0.60	$\text{SiBN}_{2.4}\text{Tb}_{0.003}$
s111	28.13	11.50	30.66	0.56	0.47			$\text{SiBN}_{2.2}\text{Eu}_{0.003}$

10.2. Preparation of Ferromagnetic $\text{Si}_3\text{B}_3\text{N}_7$ Ceramics

10.2.1. Preparation of Fe Doped $\text{Si}_3\text{B}_3\text{N}_7$ Ceramics

In the present work, Fe doped $\text{Si}_3\text{B}_3\text{N}_7$ ceramic has been prepared by reacting the single source precursor TADB with liquid ammonia in which Fe_2O_3 nanoparticles were suspended. Detailed description of the synthesis is as follow: Around 50 ml liquid ammonia was condensed on 0.5880 g Fe_2O_3 nanoparticles at -76°C (dry ice and ethanol mixture) in a three-neck flask. Then about 125 ml freshly distilled hexane was added in liquid ammonia mixture. By the help of a single use injector and needle, 5 ml TADB was mixed with 30 ml hexane in a graduated cylinder and added dropwise into the flask containing the mixture of liquid ammonia, Fe_2O_3 nanoparticles and hexane under very slow of Ar flow. After the reaction was completed, the same procedure as it was explained for the metal route of amorphous luminescent $\text{Si}_3\text{B}_3\text{N}_7$ ceramics was followed (Section 10.1.1).

10.2.2. Preparation of Co Doped $\text{Si}_3\text{B}_3\text{N}_7$ Ceramics

In the present work, cobalt doped $\text{Si}_3\text{B}_3\text{N}_7$ ceramics have been prepared by reacting the single source precursor TADB with liquid ammonia in which either $\text{Co}(\text{NH}_3)_6\text{Cl}_3$ or $\text{Co}[\text{N}(\text{Si}(\text{CH}_3)_3)_2]_2$ was suspended. Detailed descriptions of the syntheses are given below.

10.2.2.1. Reactions with $\text{Co}(\text{NH}_3)_6\text{Cl}_3$

$\text{Si}_3\text{B}_3\text{N}_7\text{:Co-1}$

Around 50 ml liquid ammonia was condensed on 1.1 g $\text{Co}(\text{NH}_3)_6\text{Cl}_3$ (orange color) at -76°C (dry ice and ethanol mixture) in a three-neck flask. Then, 5 ml of TADB was added dropwise into the flask containing the mixture of liquid ammonia and $\text{Co}(\text{NH}_3)_6\text{Cl}_3$ under very slow of Ar flow. After the reaction was completed, the flask was allowed to reach the room temperature under strong stirring, in which way the excess ammonia was removed under Ar flow. After that, an orange-white powder was obtained. The NH_4Cl salts were sublimed by heating at 300°C under vacuum ($P \approx 10^{-3}$ mbar) for almost 24 hours such that almost NH_4Cl -free blue colored polymer was obtained. This blue color was due to the formation of CoCl_2 , which was determined by powder X-ray analysis (see Figure 6.4). Afterwards, this blue polymer was pyrolysed with the same procedure as it was explained for the metal route of amorphous luminescent $\text{Si}_3\text{B}_3\text{N}_7$ ceramics (Section 10.1.1). The final ceramic was named as $\text{Si}_3\text{B}_3\text{N}_7\text{:Co-1}$.

Si₃B₃N₇:Co-2

5 ml TADB was added on 1.01 g Co(NH₃)₆Cl₃ (orange color) at -76 °C (dry ice and ethanol mixture) in a three-neck flask. Then, 50 ml of liquid ammonia was added dropwise into the flask containing the mixture of TADB and Co(NH₃)₆Cl₃ under very slow of Ar flow. After the reaction was completed, the flask was allowed to reach the room temperature under strong stirring, in which way the excess ammonia was removed under Ar flow. After that, an orange-white powder was obtained. The NH₄Cl salts were sublimed by heating at 210 °C under vacuum ($P \approx 10^{-3}$ mbar) for almost 24 hours such that almost NH₄Cl-free blue colored polymer was obtained. This blue color was due to the formation of CoCl₂, which was determined by powder X-ray analysis (see Figure 6.5). Afterwards, this blue polymer was pyrolysed with almost the same procedure as it was explained for the metal route of amorphous luminescent Si₃B₃N₇ ceramics with only minor changes (Section 10.1.1). The only difference was that the blue polymer was pyrolysed to 900 °C and then 1200 °C under Ar flow. The final ceramic was named as Si₃B₃N₇:Co-2.

10.2.2.2. Reactions with Co[N(Si(CH₃)₃)₂]₂

Si₃B₃N₇:Co-3

Co[N(Si(CH₃)₃)₂]₂ was synthesized according to the literature [382]. Then, 6.52 g of Co[N(Si(CH₃)₃)₂]₂ was dissolved in 100 ml freshly distilled hexane and 5 ml TADB was added on it at 0 °C. A reaction was observed and the dark green color of Co[N(Si(CH₃)₃)₂]₂ changed to light blue. Then around 50 ml liquid ammonia was added at -76 °C dropwise into the flask containing the mixture of TADB and Co[N(Si(CH₃)₃)₂]₂ under very slow of Ar flow. After the reaction was completed, the same procedure as it was explained for the metal route of amorphous luminescent Si₃B₃N₇ ceramics was followed (Section 10.1.1). The final ceramic was named as Si₃B₃N₇:Co-3.

10.2.3. Preparation of Ni Doped Si₃B₃N₇ Ceramics

In the present work, nickel doped Si₃B₃N₇ ceramic has been prepared by ammonolysis of the single source precursor TADB and Ni(NH₃)₆Cl₂ mixture with liquid ammonia. Detailed description of synthesis is as follow: 5 ml TADB was added on 1.3360 g Ni(NH₃)₆Cl₂ at room temperature in a three-neck flask. Then, about 50 ml liquid ammonia at -76 °C was dropwisely added on TADB and Ni(NH₃)₆Cl₂ mixture under very slow of Ar flow. After the reaction was completed, it was allowed to reach the room temperature and excess ammonia was removed by Ar flow. The NH₄Cl salt was removed via sublimation at 210 °C for 24 hours. Almost salt free product was heated slowly to 900 °C under NH₃ flow with the following heating program:

- heating from room temperature to 300 °C with 27 °C/h rate
- dwelling at 300 °C for 3 hours
- heating from 300 °C to 900 °C with 27 °C/h rate
- dwelling at 900 °C for 3 hours
- cooling from 900 °C to room temperature with 200 °C/h rate

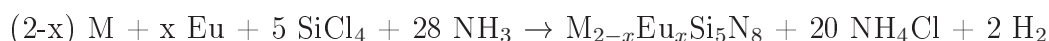
After that, the obtained material was heated to 1200 °C under N₂ flow with 10 °C/h heating rate and 3 hours dwelling time and then subsequent cooled to room temperature with the same rate.

10.3. Preparation of Crystalline Nitridosilicate Phosphors

In the present work, various nitridosilicate type phosphors, i.e. CeSi₃N₅, Sr_{2-x}Mn_xSi₅N₈, M_{2-x}Eu_xSi₅N₈, M_{2-2x}R_xLi_xSi₅N₈, and Ba_{1-2x}R_xLi_xSi₇N₁₀, where M = Ca and Sr, and R = Ce and Tb have been synthesized successfully by applying polymer route, similar to the one which has already been applied for the synthesis of phosphors based on amorphous Si₃B₃N₇ ceramics (see Chapter 10.1). In this case, SiCl₄ has been ammonolysed with liquid NH₃ in which Eu, Ca, Sr, Ba and Li were dissolved (named as the metal route) or Eu[N(Si(CH₃)₃)₂]₃, Ce[N(Si(CH₃)₃)₂]₃, Tb[N(Si(CH₃)₃)₂]₃ and Mn[N(Si(CH₃)₃)₂]₂ were suspended (named as the organometallic route). Following to the literature [381] and [383], only Tb[N(Si(CH₃)₃)₂]₃ and Mn[N(Si(CH₃)₃)₂]₂ were synthesized in the laboratory, respectively. All other chemicals have been commercially obtained (Table 10.1).

10.3.1. Metal Route

This route is based on a direct reaction of SiCl₄ in hexane medium with liquid NH₃ in which the metals M (M= Ca, Sr, Ba and/or Eu) are dissolved. The proposed reactions for the synthesis of M_{2-x}Eu_xSi₅N₈, where M = Ca and Sr, is as follow:



A typical experimental method is presented in detail below. The same procedure has been applied for all other nitride-based crystalline phosphors which were synthesized via the metal route. The amounts of the reactants and the solvent are tabulated in Table 10.4.

Around 100 ml liquid ammonia was condensed on 0.8797 g (0.0058 mol) freshly distilled europium metal at -76 °C (dry ice and ethanol mixture) in a three-neck flask. Then about

10. General Experimental Methods

220 ml freshly distilled hexane was added in liquid ammonia solution. By the help of a single use injector and needle, 1.6576 ml (0.0145 mol) SiCl_4 was mixed with 30 ml hexane in a graduated cylinder and was added dropwise into the flask containing the mixture of liquid ammonia, in which Eu was dissolved, and hexane under very slow of Ar flow. The reaction was quite aggressive and stirred vigorously at $-76\text{ }^\circ\text{C}$. Even the vapors of SiCl_4 and NH_3 were reacting and formed suddenly NH_4Cl salts all around the flask. After the reaction was completed, the following procedure was applied:

It was allowed to reach the room temperature, and, by this way, excess ammonia was removed under Ar flow. Then, hexane was removed under vacuum in a cold trap. After that, a white powder, which was a mixture of NH_4Cl salt and a polymer, containing Si and N, was obtained. The NH_4Cl salts were sublimed by heating at $210\text{ }^\circ\text{C}$ under vacuum ($P \approx 10^{-3}$ mbar) for almost 24 hours, which additionally removed all the remaining volatile adducts, such that almost salt-free polymer was obtained. A clean BN crucible in a quartz tube was heated to $600\text{ }^\circ\text{C}$ in a horizontal furnace under vacuum ($P \approx 10^{-3}$ mbar) in order to make it moisture-free with the following heating program:

- heating from room temperature to $600\text{ }^\circ\text{C}$ with $100\text{ }^\circ\text{C/h}$ rate
- dwelling at $600\text{ }^\circ\text{C}$ for 5 hours
- cooling from $600\text{ }^\circ\text{C}$ to room temperature with $100\text{ }^\circ\text{C/h}$ rate

Almost salt-free polymer was loaded into the moisture-free BN crucible in an Ar filled glove-box and then heated to $900\text{ }^\circ\text{C}$ under ammonia flow with the following temperature program:

- heating from room temperature to $300\text{ }^\circ\text{C}$ with $100\text{ }^\circ\text{C/h}$ rate
- dwelling at $300\text{ }^\circ\text{C}$ for 3 hours
- heating from $300\text{ }^\circ\text{C}$ to $900\text{ }^\circ\text{C}$ with $100\text{ }^\circ\text{C/h}$ rate
- dwelling at $900\text{ }^\circ\text{C}$ for 3 hours
- cooling from $900\text{ }^\circ\text{C}$ to room temperature with $100\text{ }^\circ\text{C/h}$ rate

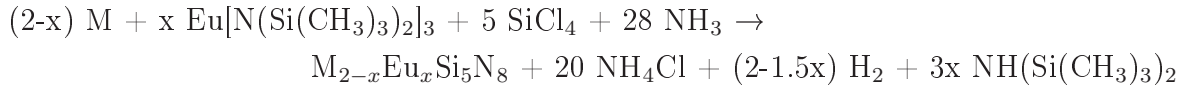
Finally, the obtained material was heated to $1500\text{ }^\circ\text{C}$ in another horizontal furnace with a corundum tube under nitrogen flow in order to obtain the desired crystalline compounds, in this case the $\text{Eu}_2\text{Si}_5\text{N}_8$, with the following temperature program:

- heating from room temperature to $1500\text{ }^\circ\text{C}$ with $10\text{ }^\circ\text{C/min}$ rate
- dwelling at $1500\text{ }^\circ\text{C}$ for 5 hours
- cooling from $1500\text{ }^\circ\text{C}$ to room temperature with $10\text{ }^\circ\text{C/min}$ rate

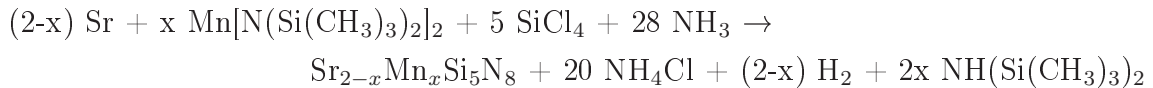
10.3.2. Organometallic Route

The organometallic route is based on a direct reaction of SiCl_4 with liquid ammonia in which $\text{Eu}[\text{N}(\text{Si}(\text{CH}_3)_3)_2]_3$, $\text{Ce}[\text{N}(\text{Si}(\text{CH}_3)_3)_2]_3$, $\text{Mn}[\text{N}(\text{Si}(\text{CH}_3)_3)_2]_2$ and $\text{Tb}[\text{N}(\text{Si}(\text{CH}_3)_3)_2]_3$ are suspended. The proposed reactions are presented below:

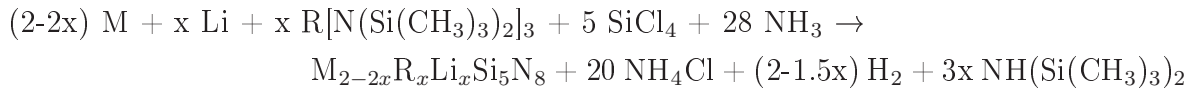
a) The reaction for the synthesis of $\text{M}_{2-x}\text{Eu}_x\text{Si}_5\text{N}_8$, where $\text{M} = \text{Ca}$ and Sr , is as follow:



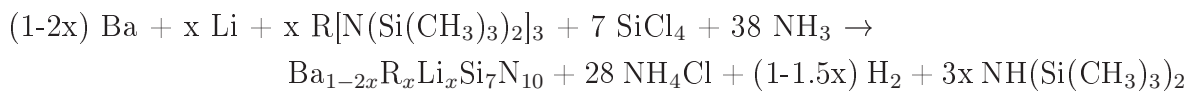
b) The reaction for the synthesis of $\text{Sr}_{2-x}\text{Mn}_x\text{Si}_5\text{N}_8$ is as follow:



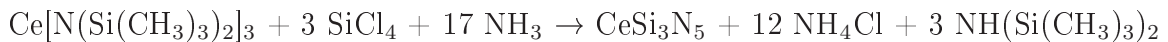
c) The reaction for the syntheses of $\text{M}_{2-2x}\text{R}_x\text{Li}_x\text{Si}_5\text{N}_8$, where $\text{M} = \text{Ca}$ and Sr , and $\text{R} = \text{Ce}$ and Tb , are as follow:



d) The reaction for the syntheses of $\text{Ba}_{(1-2x)}\text{R}_x\text{Si}_7\text{N}_{10}$, where $\text{R} = \text{Ce}$ and Tb , are as follow:



e) The reaction for the synthesis of CeSi_3N_5 is as follow:



A typical experimental procedure in detail is represented below. The same procedure has been applied for all other nitride-based crystalline phosphors which were synthesized via the organometallic route. In the cases where Li^+ ions were used as charge compensators, Li metal was dissolved in liquid ammonia, which contains suspended $\text{Ce}[\text{N}(\text{Si}(\text{CH}_3)_3)_2]_3$ or $\text{Tb}[\text{N}(\text{Si}(\text{CH}_3)_3)_2]_3$. The amounts of the reactants and the solvent are tabulated in Table 10.4.

Around 100 ml liquid ammonia was condensed in a three-neck flask, containing 1.0192 g (0.0016 mol) $\text{Eu}[\text{N}(\text{Si}(\text{CH}_3)_3)_2]_3$, at -76°C (dry ice and ethanol mixture). Then about 220 ml freshly distilled hexane was added in liquid ammonia solution. By the help of a single use injector and needle, 0.46 ml (0.004 mol) SiCl_4 was mixed with 30 ml hexane in a graduated cylinder and was added dropwise into the flask containing the mixture of liquid ammonia, $\text{Eu}[\text{N}(\text{Si}(\text{CH}_3)_3)_2]_3$ and hexane under very slow of Ar flow. After the reaction was completed, same procedure as it was explained for the metal route for nitride-based crystalline ceramics was followed (Section 10.3.1).

10. General Experimental Methods

Table 10.4.: Experimental details, maximum emission wavelengths and full width at half maximum (FWHM) values for crystalline nitridosilicate-type ceramics.

Name	Amounts ^a	$\lambda_{emission}$ (nm) ^b	FWHM (nm)
s76	0.8797 g Eu + 1.6576 ml SiCl ₄ + 250 ml hexane + 100 ml NH ₃	687	128
s80	0.3862 g Ca + 2.77 ml SiCl ₄ + 150 ml hexane + 50 ml NH ₃	-	-
s81	0.6854 g Ba + 1.43 ml SiCl ₄ + 150 ml hexane + 50 ml NH ₃	-	-
s82	1.2965 g Sr + 4.24 ml SiCl ₄ + 200 ml hexane + 100 ml NH ₃	-	-
s85	0.0312 g Eu + 1.007 Sr + 3.27 ml SiCl ₄ + 250 ml hexane + 100 ml NH ₃	625	113
s89	0.3770 g Ca + 2.699 ml SiCl ₄ + 150 ml hexane + 50 ml NH ₃	-	-
s117	0.0305 g Eu + 0.3995 g Ca + 2 ml SiCl ₄ + 150 ml hexane + 50 ml NH ₃	603	112
s118	0.4019 g Ca + 2 ml + SiCl ₄ + 150 ml hexane + 50 ml NH ₃	-	-
s119	0.0311 g Eu + 1.0011 g Sr + 2 ml SiCl ₄ + 250 ml hexane + 100 ml NH ₃	632	107
s120	1.0018 g Sr + 2 ml SiCl ₄ + 250 ml hexane + 100 ml NH ₃	-	-
s121	1.0009 g Eu + 1.4 ml SiCl ₄ + 250 ml hexane + 100 ml NH ₃	685	130
s122	1.0192 g Eu(TMSA) ₃ + 0.46 ml SiCl ₄ + 250 ml hexane + 50 ml NH ₃	685	129
s123	1.0028 g Sr + 0.1872 g Ce(TMSA) ₃ + 0.0025 g Li + 3 ml SiCl ₄ + 250 ml hexane + 100 ml NH ₃	539	179
s124	0.9141 g Ce(TMSA) ₃ + 1.01 ml + SiCl ₄ + 150 ml hexane + 30 ml NH ₃	468	107
s126	1.0007 g Sr + 0.1002 g Mn(TMSA) ₂ + 3.27 ml SiCl ₄ + 250 ml hexane + 100 ml NH ₃	617	91
s127	1.0028 g Sr + 0.1927 g Tb(TMSA) ₃ + 0.0020 g Li + 3.44 ml SiCl ₄ + 250 ml hexane + 100 ml NH ₃	544	-
s128	1.0052 g Ca + 0.4225 g Tb(TMSA) ₃ + 0.0045 g Li + 7.56 ml SiCl ₄ + 250 ml hexane + 100 ml NH ₃	544	-

Table 10.4 continued

Name	Amounts ^a	$\lambda_{emission}$ (nm) ^b	FWHM (nm)
s129	1.0313 g Ba + 0.1265 g Tb(TMSA) ₃ + 0.0018 g Li + 2.26 ml SiCl ₄ + 250 ml hexane + 100 ml NH ₃	544	-
s136	0.602 g Ca + 0.2461 g Ce(TMSA) ₃ + 0.0028 g Li + 4.54 ml SiCl ₄ + 250 ml hexane + 100 ml NH ₃	498	170
s137	1.506 g Ba + 0.179 g Ce(TMSA) ₃ + 0.002 g Li + 3.3 ml SiCl ₄ + 250 ml hexane + 100 ml NH ₃	479	110

^aTMSA = [N(Si(CH₃)₃)₂]

^b $\lambda_{excitation}$ =365 nm for all samples

10.4. Preparation of New Si/B/N/(C) Ceramics

10.4.1. Synthesis of TDSB

1,1,3,5-tetrachloro-1,6-dimethyl-4-hydride-1-silaborazine (TDSB) has been synthesized as a single source precursor by reacting dichloroboryl-methyl-trichlorosilyl-amine (DMTA) and hexamethyldisilazane (HMDS). DMTA for the reaction was supplied from Institut für Chemische Verfahrenstechnik, Universität Stuttgart, where it was synthesized according to the literature [81] via a continuous process system. HMDS was supplied commercially (Sigma-Aldrich). Both DMTA and HMDS were freshly distilled before the reaction. The reaction and the proposed mechanism was depicted in Figure 8.1.

In a typical experiment, 101.44 g (0.4137 mol) DMTA was dropwisely added on 66.78 g (0.4137 mol) HMDS at 0 °C. When the reaction mixture reached slowly to room temperature, a cloudy mixture was obtained, which was later filtered. Then, the volatile by-products including Si(CH₃)₃Cl and excess HMDS were removed in a cold trap under vacuum. The remaining viscous material was heated to 100 °C and 1.3x10⁻³ mbar, resulted in growing transparent TDSB crystals on the water cooled surfaces of a double-jacket sublimation tube. After that a sponge-like polymeric material has remained in the flask. The yield was about 2.35 g (4.3 %).

10.4.2. Preparation of Preceramic Polymers from TDSB

10.4.2.1. Preparation of P-TDSB-1 Polymer

The preceramic polymer P-TDSB-1 has been prepared by polycondensation reaction of TDSB with liquid ammonia. In a typical experiment, almost 100 times in excess of NH_3 (16.66 ml) was condensed in a flask at $-76\text{ }^\circ\text{C}$. Afterwards, 80 ml hexane was added. Then, 1.71 g (0.0065 mol) TDSB crystals were dissolved in 20 ml hexane and transferred into a graduated dropping funnel. Afterwards, it was slowly reacted with liquid ammonia via a vigorous stirring under Ar flow. The reaction mixture was slowly allowed to reach the room temperature. After removing all of the excess ammonia under Ar flow, the solid polymer and NH_4Cl salts were filtered and washed three times with hexane. Then, powder preceramic polymer, P-TDSB-1, has been obtained after removing the NH_4Cl salts via sublimation at $210\text{ }^\circ\text{C}$ and 1.3×10^{-3} mbar.

10.4.2.2. Preparation of P-TDSB-2 Polymer

The preceramic polymer P-TDSB-2 has been prepared by polycondensation reaction of TDSB with liquid methylamine. In a typical experiment, almost 100 times in excess of $\text{NH}_2(\text{CH}_3)$ (40 ml) was condensed in a flask at $-76\text{ }^\circ\text{C}$. Afterwards, 80 ml Hexane was added. Then 2.35 g (0.0089 mol) TDSB crystals were dissolved in 20 ml hexane and transferred in a graduated dropping funnel. Afterwards, it was slowly reacted with liquid methylamine via a vigorous stirring under Ar flow. The reaction mixture was slowly allowed to reach the room temperature. After removing of all excess methylamine under Ar flow, the NH_4Cl salts were filtered and washed three times with hexane. Then, pure viscous preceramic polymer, P-TDSB-2, has been obtained after removing hexane under vacuum (1.3×10^{-3} mbar) in a cold trap.

10.4.3. Preparation of Si/B/N/(C) Ceramics

The Si/B/N/(C) ceramics were obtained via a two-step heating process using the temperature program mentioned below. The C-TDSB-1 and C-TDSB-2 ceramics were prepared from the P-TDSB-1 and P-TDSB-2 polymers, respectively, through pyrolysis up to $900\text{ }^\circ\text{C}$ and calcination at $1400\text{ }^\circ\text{C}$ both under Ar atmosphere. On the other hand, the C-TDSB-3 ceramic was prepared from the P-TDSB-1 polymer via pyrolysis up to $900\text{ }^\circ\text{C}$ under ammonia and calcination at $1400\text{ }^\circ\text{C}$ under nitrogen atmospheres. In a typical experiment, some amount of polymer was loaded into a moisture-free BN crucible in an Ar filled glove-box and then heated to $900\text{ }^\circ\text{C}$ under Ar (for C-TDSB-1 and C-TDSB-2 ceramics) or NH_3 (for C-TDSB-3 ceramic) flow inside a quartz tube in a horizontal furnace with the following temperature program:

- heating from room temperature to 300 °C with 100 °C/h rate
- dwelling at 300 °C for 3 hours
- heating from 300 °C to 900 °C with 100 °C/h rate
- dwelling at 900 °C for 3 hours
- cooling from 900 °C to room temperature with 100 °C/h rate

Finally, the obtained material was calcined at 1400 °C in another horizontal furnace with a corundum tube under Ar (for C-TDSB-1 and C-TDSB-2 ceramics) or N₂ (for C-TDSB-3 ceramic) flow in order to obtain the desired Si/B/N/(C) ceramics according to the following temperature program:

- heating from room temperature to 1400 °C with 10 °C/min rate
- dwelling at 1400 °C for 3 hours
- cooling from 1400 °C to room temperature with 10 °C/min rate.

10.5. Preparation of Open Cell SiBNC Ceramic Foams

Preceramic polymer of polyborocarbosilazane was prepared according to previously described method by reacting single source precursor TADB with methylamine [43]. A melamine-based open cell Basotect[®] foam, which was supplied from BASF, was cut roughly 1 x 1 x 1 cm³ piece, and heated gently in a Schlenk tube with the flame of a Bunsen burner under vacuum in order to remove the moisture. Then, it was soaked in roughly 3 ml of viscous polyborocarbosilazane. Afterwards, excess polymer was removed via centrifuging with 4000 rpm/min for at least one hour in a special argon filled Schlenk tube with a glass filter in the middle. Then, polymer-wetted foam in a moisture-free BN crucible was gently heated in a horizontal furnace up to 900 °C under Ar flow with the following temperature program:

- heating from room temperature to 80 °C with 10 °C/h rate
- dwelling at 80 °C for 10 hours
- heating from 80 °C to 150 °C with 10 °C/h rate
- dwelling at 150 °C for 10 hours
- heating from 150 °C to 300 °C with 10 °C/h rate
- dwelling at 300 °C for 5 hours

10. General Experimental Methods

- heating from 300 °C to 400 °C with 1 °C/h rate
- dwelling at 400 °C for 2 hours
- heating from 400 °C to 900 °C with 10 °C/h rate
- dwelling at 900 °C for 3 hours
- cooling to room temperature with 20 °C/h rate.

After this heat treatment process, the foam was further heated to 1200 °C with 10 °C/min rate under Ar flow, dwelled at that temperature for 3 hours and cooled to room temperature with the same rate in order to obtain air stable open cell SiBNC ceramic foam.

For coating the Basotect[®] foam twice with polyborocarbosilazane, the following procedure was applied: The pristine moisture-free piece of Basotect[®] foam was immersed in polyborocarbosilazane, centrifuged to remove excess polymer and heated to 190 °C with the following program:

- heating from room temperature to 70 °C with 5 °C/h rate
- dwelling at 70 °C for 10 hours
- heating from 70 °C to 140 °C with 5 °C/h rate
- dwelling at 140 °C for 2 hours
- heating from 140 °C to 190 °C with 2 °C/h rate
- dwelling at 190 °C for 5 hours
- cooling to room temperature with 5 °C/h rate.

This preheated and polymer coated foam was soaked again into the polyborocarbosilazane in order to coat the open cell walls for second time. Then it was centrifuged again about 7 hours with 4000 rpm/min and heated to first 900°C and then 1200 °C with the same temperature programming given for sample which was coated with polymer only once.

11. Summary

High performance ceramics are key materials in our century in various high-tech applications. Among them, non-oxide ceramics have attracted particular attention due to their outstanding chemical, mechanical and thermal stability. Recently, various Si and N containing multinary non-oxide ceramics have been investigated. From these diverse systems, precursor derived amorphous Si/B/N/C ceramics show superior mechanical and thermal durability compared to their binary subsystems. The fact that makes these ceramics even more special is the preparation method based on *the polymer route*. In this route, a single source precursor molecule is polymerized by a suitable crosslinking agent yielding a polymer, which can be easily processed, e.g. via classical polymer processing techniques. The most prominent application of those preceramic polymers is producing the amorphous Si/B/N/C fibers, which are the only fibers that fulfill all the requirements as stated by the European turbine producers for energy and aerospace applications. Obviously, it is very challenging and urgent to find new single source precursors as well as new fields of application for amorphous Si/B/N/(C) ceramics. In this thesis, thus, amorphous $\text{Si}_3\text{B}_3\text{N}_7$ ceramic has been applied as a host matrix for various rare-earth ions (Chapter 5) in order to be used as a new class of phosphor materials and for Fe, Co and Ni elements (Chapter 6) to obtain ferromagnetic materials. Furthermore, a monocyclic silaborazine-type single source precursor molecule has been synthesized for new amorphous Si/B/N/(C) ceramics (Chapter 8). Additionally, an open cell Si/B/N/C ceramic foam has been prepared (Chapter 9). Apart from the amorphous Si/B/N/(C) ceramics, M/Si/N systems, where M = alkaline, alkaline earth or rare earth elements, are also considered as an important class of materials, which are widely applied as host lattices for efficient phosphors. Out of them, $\text{M}_2\text{Si}_5\text{N}_8$ and $\text{MSi}_7\text{N}_{10}$ materials, where M = Ca, Sr and Ba, are particularly interesting host lattices especially for Eu^{2+} and Ce^{3+} ions and have recently been studied extensively because of their exceptional photoluminescence properties. Different research groups in all over the world are struggling to find a reasonable synthesis method for the mass production of those kind of phosphors. In the present thesis, a novel production method based on the polymer route has been developed for the production of not only already known but also some new rare-earth doped $\text{M}_2\text{Si}_5\text{N}_8$ and $\text{BaSi}_7\text{N}_{10}$ host lattices, where M = Ca and Sr (Chapter 7).

Phosphors Based on Amorphous $\text{Si}_3\text{B}_3\text{N}_7$ Ceramic

Phosphor materials based on amorphous $\text{Si}_3\text{B}_3\text{N}_7$ ceramic have been prepared via the well-known polymer route. For the syntheses, the single source precursor molecule, $\text{Cl}_3\text{SiN}(\text{H})\text{BCl}_2$ (TADB), has been polymerized with liquid ammonia in which the desired ions are included. The following ions have been applied: Ce^{3+} , Nd^{3+} , Sm^{3+} , Eu^{2+} , Gd^{3+} , Tb^{3+} , Ho^{3+} , Tm^{3+} , Yb^{2+} , Yb^{3+} , La^{3+} , Y^{3+} , Sn^{2+} , Sr^{2+} and Ba^{2+} . Interestingly, undoped amorphous $\text{Si}_3\text{B}_3\text{N}_7$ ceramic shows intrinsic emissions in the visible region of the spectrum, i.e. blue emission via exciting with shorter wavelengths (280-320 nm) and violet emission when excited with longer wavelengths (> 340 nm). Furthermore, from this variety of ions, incorporation of Ce^{3+} , Nd^{3+} , Sm^{3+} , Eu^{2+} , Tb^{3+} , Ho^{3+} and Sn^{2+} into $\text{Si}_3\text{B}_3\text{N}_7$ matrix cause luminescence in the visible region of the spectrum. Especially, Nd^{3+} , Sm^{3+} , Tb^{3+} and Ho^{3+} doped samples exhibit line emissions due to the corresponding $4f \rightarrow 4f$ transitions whereas broad emission bands result from doping of Ce^{3+} and Eu^{2+} ($5d \rightarrow 4f$ transition) as well as Sn^{2+} ($^3\text{P}_1 \rightarrow ^1\text{S}_0$ transition). Newsworthy, the luminescence of the Tb^{3+} doped samples can be tuned by changing the excitation wavelength such that very intense green, white and violet emissions are obtained when excited with 280 nm or shorter, between 280 nm and 330 nm, and 330 nm or longer wavelengths, respectively. On the other hand, line emissions of Nd^{3+} , Sm^{3+} and Ho^{3+} ions are relatively weak and thus mainly the intrinsic emissions of $\text{Si}_3\text{B}_3\text{N}_7$ host matrices are observed. Both Ce^{3+} and Eu^{2+} doped amorphous $\text{Si}_3\text{B}_3\text{N}_7$ ceramics have been considered as very promising phosphors for pc-LEDs. Both ions in $\text{Si}_3\text{B}_3\text{N}_7$ result in structureless and wide excitation bands covering the UV-to-visible region of the spectrum together with broad emission bands due to $5d \leftrightarrow 4f$ transitions; i.e. emissions for Eu^{2+} doped samples are in between 540 nm and 640 nm, and for Ce^{3+} doped ones are in between 520 nm and 550 nm, depending on the concentration of the corresponding ions. On the other hand, neither La^{3+} , Y^{3+} , Sr^{2+} and Ba^{2+} ions, which are not luminescent active centers, nor Gd^{3+} , Tm^{3+} , Yb^{2+} and Yb^{3+} ions incorporated in $\text{Si}_3\text{B}_3\text{N}_7$ exhibit luminescence in the visible region of the spectrum. As a further investigation, all of the ions discussed above have been codoped together with Eu^{2+} ions into amorphous $\text{Si}_3\text{B}_3\text{N}_7$ matrix in order to investigate the effect of codoping on the luminescence of Eu^{2+} ions. In all cases, typical $5d \rightarrow 4f$ broad emission band due to Eu^{2+} ions are obtained. For Nd^{3+} , Sm^{3+} and Tb^{3+} codoped samples, this broad emission band superimposes with the $4f \rightarrow 4f$ emission lines of the corresponding codopant ions due to an energy transfer from Eu^{2+} ions to the codopant ions. All other codopant ions, including La^{3+} , Gd^{3+} , Ho^{3+} , Tm^{3+} , Yb^{3+} , Yb^{2+} , Y^{3+} , Sr^{2+} and Ba^{2+} , show no significant improvement on the luminescence properties of Eu^{2+} ions in $\text{Si}_3\text{B}_3\text{N}_7$ host matrix. Additionally, Tb^{3+} ions have been codoped with Ce^{3+} ions, resulting in a very efficient energy transfer from Ce^{3+} to Tb^{3+} compared to that from Eu^{2+} to Tb^{3+} . Therefore, this sample is regarded to be an auspicious candidate as a phosphor material,

which can be combined with a blue-LED to create a white light. Similar to amorphous $\text{Si}_3\text{B}_3\text{N}_7$ ceramics, the polymer route has been applied for the preparation of Eu^{2+} doped amorphous Si_3N_4 ceramics by employing SiCl_4 instead of TADB. Typical broad emission of Eu^{2+} ions due to the $5d \rightarrow 4f$ transition has also been observed in these samples.

Phosphors Based on Nitridosilicates

The versatile polymer route has also been applied for the synthesis of various nitridosilicate type crystalline phosphors, i.e. $\text{Sr}_{2-x}\text{Mn}_x\text{Si}_5\text{N}_8$, $\text{M}_{2-x}\text{Eu}_x\text{Si}_5\text{N}_8$, $\text{M}_{2-2x}\text{R}_x\text{Li}_x\text{Si}_5\text{N}_8$, $\text{Ba}_{1-2x}\text{R}_x\text{Li}_x\text{Si}_7\text{N}_{10}$ and CeSi_3N_5 where $\text{M} = \text{Ca}$ and Sr , and $\text{R} = \text{Ce}$ and Tb . Analogous to the preparation method for the phosphors based on amorphous $\text{Si}_3\text{B}_3\text{N}_7$, SiCl_4 has been used as a precursor molecule instead of TADB. $\text{Ca}_{2-2x}\text{Tb}_x\text{Li}_x\text{Si}_5\text{N}_8$, $\text{Sr}_{2-2x}\text{Tb}_x\text{Li}_x\text{Si}_5\text{N}_8$, $\text{Ba}_{1-2x}\text{Ce}_x\text{Li}_x\text{Si}_7\text{N}_{10}$ and $\text{Ba}_{1-2x}\text{Tb}_x\text{Li}_x\text{Si}_7\text{N}_{10}$ phosphors have been prepared and investigated for the first time.

Ferromagnetic $\text{Si}_3\text{B}_3\text{N}_7$ Ceramics

The same production method, applied for the synthesis of the phosphors based on amorphous $\text{Si}_3\text{B}_3\text{N}_7$, has been employed for incorporating some transition metals, including Fe, Co and Ni. In contrast to the cases for lanthanides, Y, Ca, Sr and Sn, all efforts for incorporation of Fe, Co and Ni into amorphous $\text{Si}_3\text{B}_3\text{N}_7$ host matrix have resulted in metallic form of the corresponding elements rather than isolated ions, resulting in a grey-black appearances. These metallic phases have homogeneously distributed as microspheres (submicron to micron sizes). According to the magnetic measurements, doping the amorphous $\text{Si}_3\text{B}_3\text{N}_7$ matrix with Fe, Co or Ni yields soft ferromagnetic materials.

A Silaborazine-type Single Source Precursor Molecule for Si/B/N/(C) Ceramics

The first halo-substituted monocyclic silaborazine derivative, namely 1,1,3,5-tetrachloro-2,6-dimethyl-4-hydride-1-silaborazine (TDSB) (space group: $P\bar{1}$, cell parameters: $a = 7.2534(6)$ Å, $b = 9.0788(7)$ Å, $c = 9.1361(7)$ Å, $\alpha = 66.839(2)^\circ$, $\beta = 89.348(2)^\circ$, $\gamma = 80.502(2)^\circ$), has been synthesized by a silazane cleavage of hexamethyldisilazane (HMDS) with a known precursor molecule dichloroboryl-methyl-trichlorosilyl-amine (DMTA). Not only having Si:B ratio as 1:2 in a six-membered monocyclic ring but also having fully chlorinated Si and B atoms on the ring make this compound particularly attractive. Pre-ceramic polymers from TDSB precursor molecule have easily been obtained via polymerization with ammonia or methylamine, which later have been converted into amorphous silicon boron (carbo)nitride ceramics at 1400 °C. Even

11. Summary

though decomposition of these new ceramic materials start around 1400 °C, only very small weight losses, i.e. 0.9 - 2.5 weight percent, at 1910 °C are attained. Direct crosslinking through the constituent elements of the ring, i.e. Si and B atoms, is attributed to these low weight losses at high temperature due to forming stronger and stiffer network resisting the conformational changes in network. IR absorptions between 1360 cm⁻¹ and 1380 cm⁻¹ in all as-obtained ceramics are clear evidences for assigning the silaborazine rings as being a part of the amorphous networks. Furthermore, elemental analysis results showed that Si:B ratio of 1:2 in the precursor TDSB molecule is precisely transferred through the polymer stage into the final ceramics, regardless of the crosslinking agents.

Preparation of Open Cell SiBNC Ceramic Foams

Apart from all those synthesized materials mentioned above, an open cell SiBNC ceramic foam has been prepared as a structural material. For this purpose, a viscose preceramic polymer has been synthesized by reacting the single source precursor molecule, TADB, with methylamine. Then the open cell walls of a commercially available foam (Basotect®, BASF) has been coated by soaking it in this preceramic polymer and a subsequent centrifuging processes. Further heat treatment removes the foam template (replica method), leaving an open cell SiBNC ceramic foam behind. Even though the formation of open cells in SiBNC ceramic foam has been observed by SEM analysis, the final material appears to have poor mechanical stability.

Concluding Remarks

- The polymer route for the synthesis of genuine Si₃B₃N₇ ceramics has been applied for the synthesis of a new class of phosphor materials based on amorphous Si₃B₃N₇ ceramics. Among them, Eu²⁺, Ce³⁺ and Tb³⁺ (co)doped samples are regarded promising phosphors, which can be used together with UV- and blue-LEDs to generate white light.
- Preparing Eu²⁺ doped amorphous Si₃N₄ matrices along an analogous path has indicated that the polymer route is a convenient method for the production of phosphors also in this case.
- New ferromagnetic SiBN ceramics have been prepared by incorporating Fe, Co and Ni into amorphous Si₃B₃N₇ matrices through the polymer route.
- The polymer route has additionally been utilized for the production of crystalline nitridosilicate-type phosphors. This route allows a real one-pot synthesis of nitridosilicate-type phosphors, eliminating various preparative and laborious handling steps.

Hence, it is believed that this route will make the mass production of nitridosilicate-type phosphors easy and cost effective, which is conventionally struggled for by several research groups in industry and academia.

- Using the halo-substituted monocyclic silaborazine-type molecule, TDSB, as a single source molecular precursor has resulted in amorphous ceramics having Si:B ratios as 1:2, through the polymer route.
- The replica method seems promising to develop open cell SiBNC ceramic foams.

11. Summary

12. Zusammenfassung

Hochleistungskeramiken stellen heutzutage Schlüsselmaterialien in zahlreichen High-tech-Anwendungen dar, wobei vor allem die nicht-oxidischen Keramiken, aufgrund ihrer hervorragenden chemischen, mechanischen und thermischen Stabilität, besondere Aufmerksamkeit erlangt haben. In letzter Zeit wurden verstärkt Si und N enthaltende, multinäre nicht-oxidische Keramiken untersucht, von denen besonders die über Vorläufermoleküle erhaltenen, amorphen Si/B/N/C-Keramiken im Vergleich zu den entsprechenden binären Systemen, eine verbesserte mechanische und thermische Beständigkeit aufweisen. Ein weiterer Punkt macht diese Art von keramischen Materialien sehr speziell, nämlich deren Synthese über eine Polymerroute. Bei diesem Verfahren wird ein Vorläufermolekül mit Hilfe eines geeigneten Vernetzungsreagenzes polymerisiert. Das entstandene Polymer lässt sich dann leicht über klassische Verarbeitungsschritte der Polymertechnik weiterverarbeiten.

Die bekannteste Anwendung für derartige präkeramische Polymere ist die Herstellung von amorphen Si/B/N/C-Fasern. Diese Fasern erfüllen als einzige die, von europäischen Turbinenherstellern vorgegebenen Voraussetzungen für den Einsatz in der Kraftwerks- und Raumfahrttechnik. Die Entdeckung neuer Vorläufermoleküle, sowie die Erschließung neuer Anwendungsgebiete für amorphe Si/B/N/C-Keramiken stellt demnach eine dringende Herausforderung dar.

Im Rahmen dieser Doktorarbeit wurde daher eine amorphe $\text{Si}_3\text{B}_3\text{N}_7$ -Keramik als Trägermaterial für verschiedene Seltenerdionen (Kapitel 5) zur Entwicklungen einer neuen Klasse von Leuchtstoffen, sowie durch Einbau von Elementen wie Fe, Co und Ni (Kapitel 6) zur Herstellung von ferromagnetischen Materialien eingesetzt. Außerdem wurde ein monozyklisches Silaborazinderivat als Vorläufermolekül für eine neuartige Si/B/N/(C) Keramik (Kapitel 8), sowie ein offenzellige Si/B/N/C-Schaumkeramik hergestellt (Kapitel 9).

Neben den amorphen Si/B/N/C-Keramiken wurden auch M/Si/N-Systeme mit $M = \text{Alkali-}, \text{Erdalkali- oder Seltenerdmetall}$ untersucht, die als Trägermaterial für effiziente Leuchtstoffe bereits weit verbreitete Verwendung finden. $\text{M}_2\text{Si}_5\text{N}_8$ und $\text{MSi}_7\text{N}_{10}$ Systeme mit $M = \text{Ca}, \text{Sr}, \text{Ba}$ sind dabei als Matrixmaterial, speziell für Eu^{2+} und Ce^{3+} , besonders interessant und werden seit kurzem intensiv hinsichtlich ihrer außergewöhnlichen Photolumineszenz untersucht. Verschiedene Forschungsgruppen auf der ganzen Welt bemühen sich sehr intensiv um eine rationale Synthesemethode zur großtechnischen

Herstellung dieser Art Leuchtstoffe. Im Rahmen dieser Arbeit wurde eine, auf der Polymerroute basierende, neue Synthesemethode entwickelt, die nicht nur zur Herstellung von bereits bekannten, sondern auch von neuartigen, mit Seltenerdionen dotierten $M_2Si_5N_8$ (mit $M = Ca$ und Sr) und $BaSi_7N_{10}$ -Matrizen verwendet werden kann (Kapitel 7).

Leuchtstoffe auf Basis von amorphen $Si_3B_3N_7$ Keramiken

Leuchtstoffe basierend auf $Si_3B_3N_7$ -Keramiken wurden über die bekannte Polymerroute dargestellt. Dabei wurde das Vorläufermolekül $Cl_3SiN(H)BCl_2$ (TADB) mit flüssigem Ammoniak und dem darin gelösten Kation polymerisiert. Auf diese Weise wurden folgende Ionen in die Matrix eingebaut: Ce^{3+} , Nd^{3+} , Sm^{3+} , Eu^{2+} , Gd^{3+} , Tb^{3+} , Ho^{3+} , Tm^{3+} , Yb^{2+} , Yb^{3+} , La^{3+} , Y^{3+} , Sn^{2+} , Sr^{2+} und Ba^{2+} . Interessanterweise zeigt undotiertes $Si_3B_3N_7$ eine intrinsische Emission im sichtbaren Bereich des Spektrums, speziell eine blaue Emission bei Anregung im kurzwelligen Spektralbereich (280 nm - 320 nm) und eine violette Emission bei längeren Anregungswellenlängen (> 340 nm). Weiterhin führt eine Dotierung mit Ce^{3+} , Nd^{3+} , Sm^{3+} , Eu^{2+} , Tb^{3+} , Ho^{3+} und Sn^{2+} in die $Si_3B_3N_7$ -Matrix zu Lumineszenz im sichtbaren Spektralbereich. Dabei weisen die mit Nd^{3+} , Sm^{3+} , Tb^{3+} und Ho^{3+} -ionen dotierten Proben schmale Emissionslinien aufgrund von $4f \rightarrow 4f$ Übergängen auf, wohingegen breite Emissionsbanden durch Dotierung mit Ce^{3+} und Eu^{2+} -ionen ($5d \rightarrow 4f$ Übergänge), und Sn^{2+} ($^3P_1 \rightarrow ^1S_0$ Übergang) entstehen.

Bemerkenswert ist, dass die Lumineszenz von Proben, die mit Tb^{3+} dotiert worden sind durch Änderung der Anregungswellenlänge so eingestellt werden kann, das bei Anregung mit Wellenlängen kleiner als 280 nm intensiv grünes, bei Anregung zwischen 280 nm und 300 nm weißes und bei Wellenlängen größer 330 nm intensiv violettes Licht erzeugt wird. Andererseits sind die Linienemissionen von Nd^{3+} , Sm^{3+} und Ho^{3+} relativ schwach, weshalb hauptsächlich die intrinsische Emission der $Si_3B_3N_7$ -Matrix beobachtet wird. Sowohl mit Ce^{3+} als auch mit Eu^{2+} dotiertes amorphes $Si_3B_3N_7$ wurde als vielversprechender Leuchtstoff für pc-LEDs untersucht. Die Dotierung von $Si_3B_3N_7$ mit beiden Ionen führt zu strukturlosen, breiten Anregungsbanden, die den UV-Vis-Bereich des Spektrums überdecken, sowie zu einer breiten Emissionsbande eines $5d \rightarrow 4f$ Übergangs. Die Emission der Eu^{2+} dotierten Proben liegt dabei zwischen 540 nm und 640 nm, die für Ce^{3+} -dotierte Proben zwischen 520 nm und 550 nm, jeweils abhängig von der Konzentration des entsprechenden Ions. Weder der Einbau von La^{3+} , Y^{3+} , Sr^{2+} und Ba^{2+} , die keine Lumineszenzzentren sind, noch der von Gd^{3+} , Tm^{3+} , Yb^{2+} und Yb^{3+} führen zu Lumineszenz im sichtbaren Bereich.

In einer weiteren Untersuchungsreihe wurden alle oben beschriebenen Ionen jeweils in Kombination mit Eu^{2+} , in die $Si_3B_3N_7$ -Keramik eingebaut, um den Einfluss der Codotierung auf die Lumineszenz von Eu^{2+} , zu untersuchen. In allen Fällen wurden die typischen breiten $5d \rightarrow 4f$ Emissionsbanden von Eu^{2+} , beobachtet. Bei den mit Nd^{3+} ,

Sm^{3+} und Tb^{3+} co-dotierten Proben waren deren breite Banden von der $4f \rightarrow 4f$ Emission des entsprechenden Co-dotierungsspezies überlagert. Dies resultiert aus einem Energietransfer von Eu^{2+} zur entsprechenden Co-dotierungsspezies. Alle andern Co-dotierungsspezies, La^{3+} , Gd^{3+} , Ho^{3+} , Tm^{3+} , Yb^{3+} , Yb^{2+} , Y^{3+} , Sr^{2+} und Ba^{2+} verbessern die Lumineszenz der Eu^{2+} -Ionen in der $\text{Si}_3\text{B}_3\text{N}_7$ -Matrix nicht signifikant. Zusätzlich wurden Tb^{3+} -Ionen zu Ce^{3+} -Ionen co-dotiert, was zu einem sehr effizienten Energietransfer von Ce^{3+} zu Tb^{3+} , verglichen mit dem von Eu^{2+} zu Tb^{3+} , führt. Dieses Material kann deshalb als ein vielversprechender Kandidat für ein Leuchtstoffmaterial betrachtet werden, das mit einer blauen LED kombiniert werden kann, um weißes Licht zu erzeugen. Ähnlich wie bei amorphem $\text{Si}_3\text{B}_3\text{N}_7$ wurde auch hier die Polymerroute zur Herstellung von Eu^{2+} dotierten Si_3N_4 -Keramiken verwendet, wobei statt TADB SiCl_4 eingesetzt wurde. Auch in diesen Proben wurden die für $5d \rightarrow 4f$ Übergänge typischen breiten Emissionsbanden des Eu^{2+} Ions beobachtet.

Leuchtstoffe auf Basis von Nitridosilikaten

Die vielseitige Polymerroute wurde auch auf die Synthese von kristallinen Nitridosilikat-Leuchtstoffen angewendet. Dies beinhaltet Verbindungen der Typen $\text{M}_{2-x}\text{Eu}_x\text{-Si}_5\text{N}_8$, $\text{M}_{2-2x}\text{R}_x\text{Li}_x\text{Si}_5\text{N}_8$, $\text{Ba}_{1-2x}\text{R}_x\text{Li}_x\text{Si}_7\text{N}_{10}$ und CeSi_3N_5 mit $\text{M} = \text{Ca}$ und Sr und $\text{R} = \text{Ce}$ und Tb . Analog zur Synthesemethode für die auf $\text{Si}_3\text{B}_3\text{N}_7$ basierenden Leuchtstoffe, wurde auch hier SiCl_4 statt TADB als Vorläufer eingesetzt. $\text{M}_{2-2x}\text{Tb}_x\text{Li}_x\text{Si}_5\text{N}_8$ (mit $\text{M} = \text{Ca}$ und Sr) und $\text{Ba}_{1-2x}\text{R}_x\text{Li}_x\text{Si}_7\text{N}_{10}$ (mit $\text{R} = \text{Ce}$ und Tb) Leuchtstoffe wurden so zum ersten Mal hergestellt und untersucht.

Ferromagnetische $\text{Si}_3\text{B}_3\text{N}_7$ -Keramiken

Die beschriebene Synthesemethode wurde auch zum Einbau von Übergangsmetallionen, einschließlich Fe , Co , und Ni , eingesetzt. Im Gegensatz zu den Lanthanoiden, Y , Ca , Sr und Sn , führten alle Versuche zum Einbau von Fe , Co und Ni in amorphes $\text{Si}_3\text{B}_3\text{N}_7$ statt des Einbaus ionischer Spezies, zu metallischen Einschlüssen dieser Elemente, was zu einer Grau-Schwarz-Färbung des Materials führt. Diese metallischen Phasen bestehen aus homogen verteilten Mikrokügelchen (Submikrometer bis Mikrometer Größe). Magnetische Messungen zeigen, dass auf diese Weise schwach ferromagnetische $\text{Si}_3\text{B}_3\text{N}_7$ Keramiken erhalten wurden.

Ein Silaborazinderivat als Vorläufermolekül für Si/B/N/(C)-Keramiken

Das erste halogen-substituierte monozyklische Silaborazinderivat, nämlich 1,1,3,5-tetra-chloro-2,6-dimethyl-4-hydrate-1-silaborazine (TDSB) (Raumgruppe: $P\bar{1}$, Gitterparametern: $a = 7.2534(6)$ Å, $b = 9.0788(7)$ Å, $c = 9.1361(7)$ Å, $\alpha = 66.839(2)^\circ$, $\beta = 89.348(2)^\circ$, $\gamma = 80.502(2)^\circ$), wurde durch eine Silazanspaltung von Hexamethyldisilazan mit dem bekannten Vorläufermolekül Dichloroboryl-methyl-trichlorosilyl-amine (DMTA) synthetisiert. Nicht nur das Si:B Verhältnis von 1:2 in einem sechs-gliedrigen Ring, sondern auch die Tatsache, dass die Si- und B-Atome des Rings vollständig chloriert sind, macht diese Verbindung besonders interessant. Präkeramische Polymere ausgehend von TDSB wurden durch einfache Polymerisation mit Ammoniak oder Methylamin erhalten und schließlich bei 1400 °C zu amorphen Silicium-Bor-Carbonitridkeramiken umgewandelt. Obwohl die Zersetzung dieser neuen Keramik bei ungefähr 1400 °C beginnt, bleibt der Gewichtsverlust von 0.9-2.5 Gewichtsprozent selbst bei 1910 °C sehr gering. Der Grund für diesen geringen Gewichtsverlust bei hohen Temperaturen liegt wahrscheinlich in der direkten Vernetzung der Ringatome Si und B, was zum Aufbau eines starken, starren Gerüsts führt, das Konformationsänderungen innerhalb des Netzwerks widersteht.

Das Auftreten von IR-Absorptionen zwischen 1360 cm^{-1} und 1380 cm^{-1} bei allen hergestellten Keramiken ist ein eindeutiger Hinweis darauf, dass Silaborazanringe Teil des amorphen Netzwerks sind. Die Ergebnisse von Elementaranalysen zeigen außerdem, dass das Si:B Verhältnis von 1:2 des Vorläufermoleküls TDSB über die Stufe des Polymers in die Keramik übertragen wird, unabhängig vom jeweiligen Vernetzungsreagenzes.

Ein offenzellige Si/B/N/C-Schaumkeramik

Anders als alle bereits erwähnten im Rahmen dieser Arbeit synthetisierten Materialien, wurde nun ein offenzellige Si/B/N/C-Schaumkeramik als Strukturmaterial hergestellt. Zu diesem Zweck wurde zunächst durch Reaktion des Vorläufers TADB mit Methylamin ein viskoses, präkeramisches Polymer hergestellt. Danach wurden die offenzelligen Wände eines kommerziell erhältlichen Schaumstoffs (Basotect[®], BASF) durch Eintauchen des Schaumstoffs in das präkeramische Polymer benetzt. Durch anschließendes Erhitzen wurde das Schaumstofftemplat entfernt (Replikaverfahren), wodurch ein offenzellige Si/B/N/C-Schaumstoff zurückblieb. Obwohl die Bildung von offenen Zellen im so erhaltenen Si/B/N/C-Schaumstoff mittels SEM Analyse nachgewiesen wurde, scheint das Endmaterial eine schlechte mechanische Stabilität aufzuweisen.

Abschließende Bemerkungen

- Die Polymerroute zur Synthese der ursprünglichen $\text{Si}_3\text{B}_3\text{N}_7$ -Keramik wurde zur Synthese einer neuartigen Klasse von Leuchtstoffen, basierend auf amorphem $\text{Si}_3\text{B}_3\text{N}_7$ eingesetzt. Unter den so erhaltenen neuen Verbindungen können die mit Eu^{2+} , Ce^{3+} und Tb^{3+} (co)dotierten Proben als vielversprechende, neue Leuchtstoffe betrachtet werden, die zusammen mit UV- und Blaulicht-LEDs zur Erzeugung von weißem Licht eingesetzt werden können.
- Die Herstellung von mit Eu^{2+} -dotierten amorphen Si_3N_4 -Matrizen mittels einer analogen Methode hat gezeigt, dass die Polymerroute auch in diesem Fall ein gut geeignetes Verfahren zur Herstellung von Leuchtstoffen ist.
- Neue ferromagnetische SiBN-Keramiken wurden durch Einbau von Fe, Co und Ni in amorphes $\text{Si}_3\text{B}_3\text{N}_7$, ebenfalls über die Polymerroute, hergestellt.
- Zusätzlich wurde die Polymerroute dazu benutzt, kristalline Leuchtstoffe auf Nitridosilikatbasis herzustellen. Diese Methode erlaubt die tatsächliche Ein-Topf-Synthese von Nitridosilikat-Leuchtstoffen und spart zahlreiche Arbeitsschritte ein. Aus diesem Grund sollte dieses Syntheseverfahren die großtechnische Darstellung von Nitridosilikat-Leuchtstoffen vereinfachen und effizienter machen, ein Ziel, um das sich bereits eine Reihe von Forschergruppen in der Industrie und in der akademischen Forschung bemühen.
- Die Verwendung des halogen-substituierten monozyklischen Silaborazinderivats, TDSB, als Vorläufermolekül führte über die Polymerroute, zu amorphen Keramiken mit einem Si:B-Verhältnis von 1:2.
- Die sogenannte Replikaverfahren scheint ein vielversprechendes Verfahren zur Synthese von offenzellige Si/B/N/C-Schaumstoffen zu sein.

12. Zusammenfassung

Bibliography

- [1] H. P. Baldus and M. Jansen. Novel High-Performance Ceramics - Amorphous Inorganic Networks from Molecular Precursors. (*Angewandte Chemie (1997) 109, 338*) *Angewandte Chemie International Edition in English*, 36:328, 1997.
- [2] P. S. Nicholson. Higher-Performance Ceramics - Towards 2000. *Key Engineering Materials*, 122-124:3, 1996.
- [3] H. P. Baldus, M. Jansen, and D. Sporn. Ceramic Fibers for Matrix Composites in High-Temperature Engine Applications. *Science*, 285:699, 1999.
- [4] M. Jansen, B. Jäschke, and T. Jäschke. Amorphous Multinary Ceramics in the Si-B-N-C System. In M. Jansen, editor, *High Performance Non-oxide Ceramics I*, volume 101 of *Structure and Bonding*, page 137. Springer, Berlin, 2002.
- [5] W. Schlenk and A. Tahl. Über Metallketyle, eine große Klasse von Verbindungen mit dreiwertigem Kohlenstoff II. *Berichte der Deutschen Chemischen Gesellschaft*, 46:2840, 1913.
- [6] D. F. Shriver, editor. *The Manipulation of Air-sensitive Compounds*. McGraw-Hill, 1969.
- [7] J. R. Lakowicz, editor. *Principle of Fluorescence Spectroscopy*. Springer, Singapore, 2006.
- [8] OPUS. Version 2.03, Bruker Optik 1999.
- [9] Stoe & Cie. WinXPOW, Version 1.2, Darmstadt 2001.
- [10] ICSD. Inorganic Crystal Structure Database, FIZ Karlsruhe.
- [11] ICDD-JCPDS. Joint Committee on Powder Diffraction Standards, Swartmore, USA.
- [12] Siemens Analytical X-ray Instruments. SMART32, Version 5.618: Program for Data Collection, Madison, WI, USA 1997.
- [13] G. M. Sheldrick. Bruker-AXS, Version 2.0: Area Detector Absorption Correction, Madison, WI, USA 2001.

Bibliography

- [14] G. M. Sheldrick. Bruker-AXS, SHELXTL, Version 6.12: Program for Solution of Structures, Madison, WI, USA 2001.
- [15] H. Lueken, editor. *Magnetochemie*. Teubner, Stuttgart, 1999.
- [16] Phoenix, EDAX Inc. 1998.
- [17] S. Mann, D. Geilenberg, J. A. C. Broekaert, and M. Jansen. Digestion Methods for Advanced Ceramic Materials and Subsequent Determination of Silicon and Boron by Inductively Coupled Plasma Atomic Emission Spectroscopy. *Journal of Analytical Atomic Spectrometry*, 12:975, 1997.
- [18] P. Muralt. Recent Progress in Materials Issues for Piezoelectric MEMS. *Journal of the American Ceramic Society*, 91:1385, 2008.
- [19] T. Takenaka, H. Nagata, and Y. Hiruma. Current Developments and Prospective of Lead-Free Piezoelectric Ceramics. *Japanese Journal of Applied Physics*, 47:3787, 2008.
- [20] H. Oesterreicher. Superconductivity and Structure. *Journal of Superconductivity and Novel Magnetism*, 20:201, 2007.
- [21] B. Raveau. The Perovskite History: More than 60 Years of Research from the Discovery of Ferroelectricity to Colossal Magnetoresistance via High Temperature Superconductivity. *Progress in Solid State Chemistry*, 35:171, 2007.
- [22] S. Tanaka. High-Temperature Superconductivity. *Japanese Journal of Applied Physics*, 45:9011, 2006.
- [23] R. J. Cava. Oxide Superconductors. *Journal of American Ceramic Society*, 83:5, 2000.
- [24] K. P. Kunz, V. K. Sarin, R. F. Davis, and S. R. Bryan. Self-Diffusion of Si-30 and N-15 in Alpha-Phase Silicon-Nitride. *Materials Science and Engineering A - Structural Materials Properties Microstructure and Processing*, 105:47, 1988.
- [25] K. Kijima and S. Shirasaki. Nitrogen Self-Diffusion in Silicon-Nitride. *Journal of Chemical Physics*, 65:2668, 1976.
- [26] G. Borchardt, K. Gömann, M. Kilo, and H. Schmidt. Diffusion in Ceramics. In R. Riedel and I-W. Chen, editors, *Ceramics Science and Technology*, volume 1. Wiley-VCH Verlag GmbH, Weinheim, 2008.
- [27] N. T. Andrianov. Sol-Gel Method in Oxide Material Technology. *Glass and Ceramics*, 60:320, 2003.

- [28] J. D. Mackenzie. Sol-Gel Research - Achievements Since 1981 and Prospects for the Future. *Journal of Sol-Gel Science and Technology*, 26:23, 2003.
- [29] G. Frenzer and W. F. Maier. Amorphous Porous Mixed Oxides: Sol-Gel Ways to a Highly Versatile Class of Materials and Catalysis. *Annual Review of Materials Research*, 36:281, 2006.
- [30] L. L. Hench and R. Orefice. Sol-Gel Technology. In A. Siedel, editor, *Kirk-Othmer Encyclopedia of Chemical Technology, 5th Ed.*, volume 23. John Wiley & Sons, New Jersey, 2007.
- [31] R. Riedel, E. Ionescu, and I-W. Chen. Modern Trends in Advanced Ceramics. In R. Riedel and I-W. Chen, editors, *Ceramics Science and Technology*, volume 1. Wiley-VCH Verlag GmbH, Weinheim, 2008.
- [32] M. V. Landau. Sol-Gel Process. In E. Gerhard, H. Knözinger, F. Schüth, and J. Weitkamp, editors, *Handbook of Heterogeneous Catalysis, 2nd Ed.*, volume 1. Wiley-WCH, Weinheim, 2008.
- [33] S. Yajima, M. Hayashi, and M. Omori. Continuous Silicon-Carbide Fiber of High-Tensile Strength. *Chemistry Letters*, 9:931, 1975.
- [34] S. Yajima, M. Hayashi, M. Omori, and K. Okamura. Development of a Silicon-Carbide Fiber with High-Tensile Strength. *Nature*, 261:683, 1976.
- [35] S. Yajima, K. Okamura, M. Hayashi, and M. Omori. Synthesis of Continuous SiC Fibers with High Tensile Strength. *Journal of American Ceramic Society*, 59:324, 1976.
- [36] R. T. Paine and C. K. Narula. Synthetic Routes to Boron Nitride. *Chemical Reviews*, 90:73, 1990.
- [37] D. A. Lindquist, J. F. Janik, A. K. Datye, and R. T. Paine. Boron Nitride Fibers Processed from Poly(borazinylamine) Solutions. *Chemistry of Materials*, 4:17, 1992.
- [38] D. Seyferth, G. H. Weisman, and C. Prudhomme. A Liquid Silazane Precursor to Silicon Nitride. *Journal of American Ceramic Society*, 66:C13, 1983.
- [39] D. Seyferth and G. H. Weisman. Polysilazane Routes to Silicon Nitride. *Polymer Preprints / American Chemical Society Division of Polymer Chemistry*, 25:10, 1984.
- [40] D. Seyferth and G. H. Weisman. Silazane Precursors to Silicon Nitride. *Ultrastructure Processing of Ceramics, Glasses, and Composites. Proceedings of the International Conference*, page 265, 1984.

Bibliography

- [41] D. Seyferth, C. Strohmann, H. J. Tracy, and J. L. Robinson. Synthesis and Useful Reactions of Organosilicon Polymeric Precursors for Ceramics. *Materials Research Society Symposium Proceedings*, 249:3, 1992.
- [42] M. Seher, J. Bill, R. Riedel, and F. Aldinger. Processing and Properties of Carbon-Containing Silicon-Nitride Ceramics Derived from the Pyrolysis of Polyhydrosilazanes. *Key Engineering Materials*, 89-91:101, 1994.
- [43] H. P. Baldus, O. Wagner, and M. Jansen. Synthesis of Advanced Ceramics in the System Si/B/N and Si/B/N/C Employing Novel Precursor Compound. *Materials Research Society Symposium Proceedings*, 271:821, 1992.
- [44] H. Schönfelder, F. Aldinger, and R. Riedel. Silicon Carbonitrides - A Novel Class of Materials. *Journal de Physique IV*, 3(C7, Part 2):1293, 1993.
- [45] R. M. Laine and F. Babonneau. Pre-ceramic Polymer Routes to Silicon Carbide. *Chemistry of Materials*, 5:260, 1993.
- [46] M. Birot, J. P. Pillot, and J. Dunogues. Comprehensive Chemistry of Polycarbosilanes, Polysilazanes, and Polycarbosilazanes as Precursors of Ceramics. *Chemical Reviews*, 95:1443, 1995.
- [47] A. Kienzle, K. Wurm, J. Bill, F. Aldinger, and R. Riedel. Polymeric Silylcarbodiimides - Novel Route to Si-C-N Ceramics. In N. Auner and J. Weis, editors, *Organosilicon Chemistry II - From Molecules to Materials*. Wiley-WCH, Weinheim, 1996.
- [48] R. J. P. Corriu. Keramiken und nanostrukturierte Materialien aus molekularen Vorstufen. *Angewandte Chemie*, 112:1432, 2000.
- [49] G. Winter, W. Verbeek, and M. Mansmann. Production of Shaped Articles of Silicon Carbide and Silicon Nitride. *US 3892583*, 1975.
- [50] H. Lange, G. Wötting, and G. Winter. Silicon Nitride - From Powder Synthesis to Ceramic Materials. *Angewandte Chemie International Edition in English*, 30:1579, 1991.
- [51] K. J. Wynee and R. W. Rice. Ceramics via Polymer Pyrolysis. *Annual Review of Materials Science*, 14:297, 1984.
- [52] R. Riedel, G. Mera, R. Hauser, and A. Klonczyński. Silicon-Based Polymer-Derived Ceramics: Synthesis, Properties and Applications - A review. *Journal of the Ceramic Society of Japan*, 114:425, 2006.

- [53] Y. G. Andreev and T. Lundström. High-Temperature Synthesis and Investigation of Hexagonal Boron Carbonitride. *Journal of Alloys and Compounds*, 210:311, 1994.
- [54] Y. G. Andreev, T. Lundström, S. W. Harris, D. C. Apperley, and D. P. Thompson. On the Nature of Boron-Carbon-Nitrogen Compounds Synthesised from Organic Precursors. *Journal of Alloys and Compounds*, 227:102, 1995.
- [55] J. Bill, M. Frieß, and R. Riedel. Conversion of Amine-Boranes to Boron Carbide Nitride. *European Journal of Solid State Chemistry*, 29:195, 1992.
- [56] J. Bill and R. Riedel. Boron Carbide Nitride Derived from Amine-Boranes. *Materials Research Society Symposium Proceedings*, 271:839, 1992.
- [57] J. Bill, R. Riedel, and G. Passing. Amine-Boranes as Precursors for Boron Carbonitride. *Zeitschrift für Anorganische und Allgemeine Chemie*, 610:83, 1992.
- [58] M. Weinmann, J. Schuhmacher, H. Kummer, S. Prinz, J. Q. Peng, H. J. Seifert, M. Christ, K. Müller, J. Bill, and F. Aldinger. Synthesis and Thermal Behavior of Novel Si-B-C-N Ceramic Precursors. *Chemistry of Materials*, 12(3):623, 2000.
- [59] P. G. Chantrell and E. P. Popper. Inorganic Polymers and Ceramics. In E. P. Popper, editor, *Special Ceramics*. Academic Press, New York, 1964.
- [60] H. Nöth. Zur Spaltung der Si-N-Bindung durch Lewis Acide Bor-Verbindungen. *Zeitschrift für Naturforschung*, B16:618, 1961.
- [61] G. Winter, W. Verbeek, and M. Mansmann. Formkörper aus homogenen Mischungen von Siliciumcarbide und Siliciumnitride und Verfahren zu ihrer Herstellung. *DE 2243527 A1*, 1974.
- [62] G. Winter, W. Verbeek, and M. Mansmann. Molded Bodies of Homogeneous Mixtures of Silicon Carbide and Silicon Nitride. *Chemical Abstracts*, 81:126134n, 1974.
- [63] D. Seyferth and G. H. Wiseman. Pre ceramic Organosilazane Polymers. *US 4482669*, 1984.
- [64] D. Seyferth. Synthesis of Some Organosilicon Polymers and Their Pyrolytic Conversion to Ceramics. *Advances in Chemistry Series*, 224:565, 1990.
- [65] M. Takamizawa, T. Kobayashi, A. Hayashida, and Y. Takeda. Organoborosilicon Polymer and a Method for the Preparation Thereof. *US 4550151*, 1985.
- [66] M. Takamizawa, T. Kobayashi, A. Hayashida, and Y. Takeda. Method for the Preparation of an Inorganic Fiber Containing Silicon, Carbon, Boron and Nitrogen. *DE 3447411 A1 (1985)*, *US 4604367 (1986)*.

Bibliography

- [67] M. Takamizawa, T. Kobayashi, A. Hayashida, and Y. Takeda. Borsiliciumorganisches Polymeres und Herstellungsverfahren dafür. *DE 3444306 C2*, 1985.
- [68] D. Seyferth. Borosilazane Polymeric Precursors for Borosilicon Nitride. *Journal of the American Ceramic Society*, 73:2131, 1990.
- [69] J. Löffelholz. *Neue präparative Zugänge zu nitrischen Mischkeramiken, Polymere und niedermolekulare Precursoren für Keramiken in den Systemen Si/B/N, Si/Al/N, Si/Ti/N und Si/Zr/N*. PhD thesis, Rheinische Friedrich-Wilhelms-Universität Bonn, 1994.
- [70] M. Jansen and H. Jüngermann. A New Class of Promising Ceramics Based on Amorphous Inorganic Networks. *Current Opinion in Solid State and Materials Science*, 2:150, 1997.
- [71] M. Jansen. Highly Stable Ceramics Through Single Source Precursors. *Solid State Ionics*, 101:1, 1997.
- [72] T. Jäschke and M. Jansen. Synthesis, Crystal Structure, and Spectroscopic Characterization of the Borazine Derivatives $[B\{CH_2(SiCl_3)\}NH]_3$ and $[B\{CH_2(SiCl_2CH_3)\}NH]_2$. *Zeitschrift für Anorganische und Allgemeine Chemie*, 630(2):239, 2004.
- [73] H. P. Baldus, M. Jansen, and O. Wagner. New Materials in the System Si-(N,C)-B and their Characterisation. *Key Engineering Materials*, 89:75, 1994.
- [74] O. Wagner, M. Jansen, and H. P. Baldus. $N(B(NMe_2)_2)(Si(NMe_2)_3)(Ti(NMe_2)_3)$, $[N(Si(NMe_2)_3)(Ti(NMe_2)_2)]_2$ and $N(SiMe_3)(Si(NMe_2)_3)(Ti(NMe_2)_3)$ - Synthesis and Characterisation of New Molecular Single-Source Precursors for Nitride and Carbonitride Ceramics. *Zeitschrift für Anorganische und Allgemeine Chemie*, 620(2):366, 1994.
- [75] M. Jansen and T. Jäschke. Preparation, Crystal Structure, and Spectroscopic Characterization of $[(H_3C)_3Si]NH(BCl_2)$. *Zeitschrift für Anorganische und Allgemeine Chemie*, 625(12):1957, 1999.
- [76] U. Müller. *Amorphe Keramiken im System Si/B/N(C) : Synthese neuer Einkomponentenvorläufer und Keramiken; Aufklärung neuer Strukturcharakteristika durch isotope Substitution*. PhD thesis, Rheinische Friedrich-Wilhelms-Universität Bonn, 2000.
- [77] U. Müller and M. Jansen. Siliciumborcarbonitridkeramiken und Vorläuferverbindungen, Verfahren zu deren Herstellung und Verwendung. *DE 10045427 A1*, 2000.

- [78] U. Müller, M. Weinmann, and M. Jansen. $\text{Cl}_2\text{MeSi-NH-BCl}_2$ and $\text{ClMe}_2\text{Si-NH-BCl}_2$: Novel Processable Single Source Precursors of Amorphous Si/C/B/N Ceramics. *Journal of Materials Chemistry*, 18(31):3671, 2008.
- [79] T. Gasparis-Ebeling and H. Nöth. Contributions to the Chemistry of Boron, 200. B-Functional Diboryl-silyl- and Boryl-silyl-stannyl-amines. *Chemische Berichte*, 123:261, 1990.
- [80] M. Kroschel. *Amorphe B/Si/C/N Hochleistungskeramiken aus Einkomponentenvorläufern*. PhD thesis, Rheinische Friedrich-Wilhelms-Universität Bonn, 2001.
- [81] M. Kroschel and M. Jansen. Silicium-Bor-Kohlenstoff-Stickstoff-Keramiken und Vorläuferverbindungen, Verfahren zu deren Herstellung sowie deren Verwendung. *DE 10045428 A1*, 2000.
- [82] U. Wannagat, H. Moretto, P. Schimdt, and M. Schulze. Beiträge zur Chemie der Silicium-Stickstoff-Verbindungen. C. Die partielle Ammonolyse des Siliciumtetrachlorids Hexachlordisilazan. Hexachlorocyclotrisilazan. *Zeitschrift für Anorganische und Allgemeine Chemie*, 381:288, 1971.
- [83] J. Haberecht, F. Krumeich, H. Gruetzmacher, and R. Nesper. High-Yield Molecular Borazine Precursors for Si-B-N-C Ceramics. *Chemistry of Materials*, 16:418, 2004.
- [84] R. N. Meals. Hydrosilation in the Synthesis of Organosilanes. *Pure and Applied Chemistry*, 13:141, 1966.
- [85] B. Kim, M. Cho, and H. Woo. Si-Si, Si-C, Si-O, Si-N Coupling of Hydrosilanes to Useful Silicon-Containing Materials. *Synlett*, 5:761, 2004.
- [86] Q. D. Ngheim, J. Perumal, and D. Kim. Moisture-Resistant Borazine-Carbosilane Polymers from Triethynylborazine and Carbosilane Derivatives using Pt-Catalyzed Hydrosilylation Polymerization. *Soft Materials*, 4:237, 2008.
- [87] Y. Chujo. Versatile Reactions of Organoboron Polymers Prepared by Hydroboration Polymerization. *Journal of Macromolecular Science, Part A: Pure and Applied Chemistry*, 31:1647, 1994.
- [88] M. Zeidlewicz. Hydroboration. In A. Siedel, editor, *Kirk-Othmer Encyclopedia of Chemical Technology, 5th Ed.*, volume 13. John Wiley & Sons, New Jersey, 2007.
- [89] P. R. Jones and J. K. Myers. The Hydroboration of Methylchlorosilylalkenes. *Journal of Organometallic Chemistry*, 34:C9, 1972.

Bibliography

- [90] S. R. Riccitiello, M. T. S. Hsu, and T. S. Chen. Boron-Carbon-Silicon Polymers and the Ceramic Thereof. *US 4987201*, 1991.
- [91] M. Weinmann, R. Haug, J. Bill, F. Aldinger, J. Schuhmacher, and K. Müller. Boron-Containing Polysilylcarbodiimides: A New Class of Molecular Precursors for Si-B-C-N Ceramics. *Journal of Organometallic Chemistry*, 541(1-2):345, 1997.
- [92] L. M. Ruwisch, P. Dürichen, and R. Riedel. Synthesis of Silyl Substituted Organoboranes by Hydroboration of Vinylsilanes. *Polyhedron*, 19:323, 2000.
- [93] R. Soundararajan and D. S. Matteson. Hydroboration with Boron Halides and Trialkylsilanes. *Journal of Organic Chemistry*, 55:2274, 1990.
- [94] R. Soundararajan and D. S. Matteson. Hydroboration with Haloborane/Trialkylsilane Mixtures. *Organometallics*, 14:4157, 1995.
- [95] H. Jüngermann and M. Jansen. Silylalkylboranes, Oligo or Polyborocarbosilazanes and Silicon Carbonitride Ceramics. *EP 0973781 A1*, 1998.
- [96] M. Gastreich, C. M. Marian, H. Jüngermann, and M. Jansen. Molecular Precursors to Ceramics - II - [(Trichlorosilyl)dichloroboryl]ethane: Synthesis and Characterisation by means of Experiment and Theory. *European Journal of Inorganic Chemistry*, (1):75, 1999.
- [97] T. Jäschke and M. Jansen. A New Borazine-Type Single Source Precursor for Si/B/N/C Ceramics. *Journal of Materials Chemistry*, 16(27):2792, 2006.
- [98] J. Y. Corey. Historical Overview and Comparison of Silicon with Carbon. In S. Patai and Z. Rappoport, editors, *The Chemistry of Organic Silicon Compounds, Part 1*. John Wiley & Sons Ltd., Chippenham, 1991.
- [99] C. Friedel and J. M. Crafts. Sur Quelques Nouvelles Combinaisons Organiques du Silicium et sur le Poids Atomique de cet Element. *Comptes Rendus Hebdomadaires des Seances de l'Academie des Sciences*, 56:590, 1863.
- [100] V. Grignard. Sur Quelques Nouvelles Combinaisons Organometalliques du Magnesium et Leur Application a des Synthese d'alcools et d'hydrocarbures. *Comptes Rendus Hebdomadaires des Seances de l'Academie des Sciences*, 130:1322, 1900.
- [101] F. S. Kipping. Organic Derivatives of Silicon. Preparation of Alkylsilicon Chlorides. *Proceedings of the Chemical Society, London*, 20:15, 1904.
- [102] E. G. Rochow. Preparation of Organosilicon Halides. *US 2380995*, 1941.

- [103] E. G. Rochow. The Direct Synthesis of Organosilicon Compounds. *Journal of American Chemical Society*, 67:963, 1945.
- [104] R. Müller. *Deutsches Reichspatent, Anm. C57411, DWP 5348*, June 1942.
- [105] W. Kalchauer and B. Pachaly. Müller-Rochow Synthesis: The Direct Process to Methylchlorosilanes. In E. Gerhard, H. Knözinger, F. Schüth, and J. Weitkamp, editors, *Handbook of Heterogeneous Catalysis, 2nd Ed.*, volume 5. Wiley-WCH, Weinheim, 2008.
- [106] J. J. Zuckerman. The Direct Synthesis of Organosilicon Compounds. *Advances in Inorganic Chemistry and Radiochemistry*, 6:383, 1964.
- [107] R. Müller and E. G. Rochow. One Hundred Years of Organosilicon Chemistry. *Journal of Chemical Education*, 42:41, 1965.
- [108] D. Seyferth. Dimethyldichlorosilane and the Direct Synthesis of Methylchlorosilanes. The Key to the Silicones Industry. *Organometallics*, 20:4978, 2001.
- [109] C. R. Krüger and E. G. Rochow. Polyorganosilazanes. *Journal of Polymer Science Part A: General Papers*, 2:3179, 1964.
- [110] E. G. Rochow. Die Polymerization von Silicium - Stickstoffverbindungen. *Monatshefte fuer Chemie*, 95:750, 1964.
- [111] M. Kumada, M. Yamaguchi, Y. Yamamoto, J. Nakajima, and K. Shiina. Synthesis of Some Methylidisilanes Containing Functional Groups. *Journal of Organometallic Chemistry*, 21:1264, 1956.
- [112] M. Kumada, J. Nakajima, M. Ishikawa, and Y. Yamamoto. Synthesis and Intramolecular Rearrangements of Chloromethylpentamethylidisilane and 1-Chloromethyl-2-chloromethylidisilane. *Journal of Organometallic Chemistry*, 23:292, 1958.
- [113] K. Shiina and M. Kumada. Thermal Rearrangement of Hexamethylidisilane to Trimethyl(dimethylsilylmethyl)silane. *Journal of Organometallic Chemistry*, 23:139, 1958.
- [114] M. Kumada. A Personal History Concerning a Chance Discovery of a Road Leading to Organopolysilane Chemistry. *Journal of Organometallic Chemistry*, 685:3, 2003.
- [115] W. Gerrard and M. F. Lappert. Reactions of Boron Trichloride with Organic Compounds. *Chemical Reviews*, 58:1081, 1958.

Bibliography

- [116] T. Jäschke and M. Jansen. Hochtemperaturostabile Siliciumcarbidnitridkeramiken aus Silylalkylborazinen, Verfahren zu deren Herstellung sowie deren Verwendung. *DE 10108069.7*, 2001.
- [117] Z. C. Wang, T. W. Kamphowe, S. Katz, J. Q. Peng, H. J. Seifert, J. Bill, and F. Aldinger. Effects of Polymer Thermolysis on Composition, Structure and High-Temperature Stability of Amorphous Silicoboron Carbonitride Ceramics. *Journal of Materials Science Letters*, 19(19):1701, 2000.
- [118] P. Gerstel, A. Müller, J. Bill, and F. Aldinger. Synthesis and High-Temperature Behavior of Si/B/C/N Precursor-derived Ceramics Without “Free Carbon”. *Chemistry of Materials*, 15(26):4980, 2003.
- [119] T. Jäschke and M. Jansen. Kohlenstoffreiche Siliciumcarbidnitridekeramiken und Vorläuferverbindungen, Verfahren zu deren Herstellung sowie deren Verwendung. *DE 10045050.4*, 2000.
- [120] J. W. Dietz. Amorphous Boron-Silicon-Nitride Materials. *US 3676343*, 1972.
- [121] J. Löffelholz, J. Engering, and M. Jansen. Sol-Gel-Process in the Ammono-System - A Novel Access to Silicon Based Nitrides. *Zeitschrift für Anorganische und Allgemeine Chemie*, 626(4):963, 2000.
- [122] J. Engering and M. Jansen. Pre-ceramic Polyazanes via Sol-Gel Route in the Ammono System and via Molecular Single Source Precursors - A Comparison of Performance. *Zeitschrift für Anorganische und Allgemeine Chemie*, 629(5):913, 2003.
- [123] F. Cheng, S. M. Kelly, S. Clark, N. A. Young, S. J. Archibald, and J. S. Bradley. Ammonothermal Synthesis of a Mesoporous Si-Ti-N Composite Material from a Single-Source Precursor. *Chemistry of Materials*, 17:5594, 2005.
- [124] A. L. Hector. Materials Synthesis Using Oxide Free Sol-Gel Systems. *Chemical Society Reviews*, 36:1745, 2007.
- [125] J. Löffelholz and M. Jansen. Novel Access to Polyborosilazanes and Polyalumosilazanes Suitable as Precursors for Ternary Nitride Ceramics. *Advanced Materials*, 7(3):289, 1995.
- [126] R. Riedel, A. Kienzle, V. Szabo, and J. Mayer. Hydroboration of Polymethylvinylsilane - A Novel Route to Silicon Boron Carbide Ceramics. *Journal of Materials Science*, 28:3931, 1993.

- [127] A. Müller, P. Gerstel, M. Weinmann, J. Bill, and F. Aldinger. Correlation of Boron Content and High Temperature Stability in Si-B-C-N Ceramics. *Journal of the European Ceramic Society*, 20(14-15):2655, 2000.
- [128] F. Aldinger, M. Weinmann, and J. Bill. Precursor-Derived Si-B-C-N Ceramics. *Pure and Applied Chemistry*, 70(2):439, 1998.
- [129] M. Weinmann, R. Haug, J. Bill, M. de Guire, and F. Aldinger. Boron-Modified Polysilylcarbodiimides as Precursors for Si-B-C-N Ceramics: Synthesis, Plastic-Forming and High-Temperature Behavior. *Applied Organometallic Chemistry*, 12(10-11):725, 1998.
- [130] M. Weinmann and F. Aldinger. High Temperature Stable Ceramics from Inorganic Polymers. In J. Bill, F. Wakai, and F. Aldinger, editors, *Precursor-Derived Ceramics*. Wiley-WCH, Weinheim, 1999.
- [131] Z. C. Wang, P. Gerstel, G. Kaiser, H. Kummer, J. Bill, F. Aldinger, and R. Riedel. $\{B[C_2H_4Si(CH_3)NH]_2[C_2H_4Si(CH_3)N(SiH_2Ph)]\}_n$: The First Polyborosilazane Precursor for Silicoboron Carbonitride Stable to 2200 °C. *Chemistry Letters*, (4):296, 2001.
- [132] N. Janakiraman, M. Weinmann, J. Schuhmacher, K. Müller, J. Bill, F. Aldinger, and P. Singh. Thermal Stability, Phase Evolution, and Crystallization in Si-B-C-N Ceramics Derived from a Polyborosilazane Precursor. *Journal of the American Ceramic Society*, 85(7):1807, 2002.
- [133] Y. Hasegawa. Preparation of Polyorganoborosilazanes and Conversion into Ultra-High-Temperature Borosilicon Carbonitrides. *Journal of the Ceramic Society of Japan*, 6:480, 2006.
- [134] T. Wideman, K. Su, E. E. Remsen, G. A. Zank, and L. G. Sneddon. Synthesis, Characterization, and Ceramic Conversion Reactions of Borazine/Silazane Copolymers: New Polymeric Precursors to SiNCB Ceramics. *Chemistry of Materials*, 7:2203, 1995.
- [135] T. Wideman, E. Cortez, E. E. Remsen, G. A. Zank, P. J. Carroll, and L. G. Sneddon. Reactions of Monofunctional Boranes with Hydridopolysilazane: Synthesis, Characterization, and Ceramic Conversion Reactions of New Processible Precursors to SiNCB Ceramic Materials. *Chemistry of Materials*, 9:2218, 1997.
- [136] K. Su, E. E. Remsen, G. A. Zank, and L. G. Sneddon. Synthesis, Characterization, and Ceramic Conversion Reactions of Borazine-Modified Hydridopolysilazanes:

Bibliography

- New Polymeric Precursors to Silicon Nitride Carbide Boride (SiNCB) Ceramic Composites. *Chemistry of Materials*, 5:547, 1993.
- [137] K. Su, E. E. Remsen, G. A. Zank, and L. G. Sneddon. Synthesis, Characterization and Ceramic Conversion Reactions of Borazine-Modified Hydridopolysilazanes. *Polymer Preprints (American Chemical Society, Division of Polymer Chemistry)*, 34:334, 1993.
- [138] O. Funayama, T. Kato, Y. Tashiro, and T. Isoda. Synthesis of a Polyborosilazane and its Conversion into Inorganic Compounds. *Journal of the American Ceramic Society*, 76:717, 1993.
- [139] O. Funayama, H. Nakahara, M. Okoda, Okumura M., and T. Isoda. Conversion Mechanism of Polyborosilazane into Silicon Nitride-Based Ceramics. *Journal of Materials Science*, 30:410, 1995.
- [140] O. Funayama, M. Arai, H. Aoki, Y. Tashiro, T. Katahata, K. Sato, T. Isoda, T. Suzuki, and I. Kohshi. Boron-Containing, Silicon Nitride-Based Ceramic Shaped Body. *EP 404503 A1*, 1990.
- [141] O. Funayama, M. Arai, Y. Tashiro, T. Isoda, and K. Sato. Polyborosilazane and Process for Producing the Same. *US 5030744*, 1991.
- [142] R. Riedel, A. Kienzle, W. Dressler, L. Ruwisch, J. Bill, and F. Aldinger. A Sili-coboron Carbonitride Ceramic Stable to 2000 °C. *Nature*, 382(6594):796, 1996.
- [143] R. Riedel, A. Kienzle, G. Petzow, M. Brück, and T. Vaahs. Borhaltige Polysiloxane, Verfahren zu ihrer Herstellung, aus ihnen herstellbare Bor und Silicium enthaltende keramische Materialien, sowie deren Herstellung. *DE 4320782 A1*, 1994.
- [144] H. Jüngermann and M. Jansen. Quaternare Keramiken im System Si/B/N/C aus polymeren Carbamidsaurederivaten. *Materialwissenschaft und Werkstofftechnik*, 29:573, 1998.
- [145] D. Srivastava, E. N. Duesler, and R. T. Paine. Synthesis of Silylborazines and Their Utilization as Precursors to Silicon-Containing Boron Nitride. *European Journal of Inorganic Chemistry*, 1998:855, 1998.
- [146] M. Weinmann, M. Horz, F. Berger, A. Müller, K. Müller, and F. Aldinger. Dehydrocoupling of Tris(hydridosilyl)boranes and Cyanamide: A Novel Access to Boron-Containing Polysilylcarbodiimides. *Journal of Organometallic Chemistry*, 659(1-2):29, 2002.

- [147] J. Haberecht, A. Krummland, F. Breher, B. Gebhardt, H. Rueegger, R. Nesper, and H. Gruetzmacher. Functionalized Borazines as Precursors for New Silica Gels. *Dalton Transactions*, 11:2126, 2003.
- [148] M. Shatnawi, W. Al-Mansi, and I. Arafa. Formation of Si-C-N Ceramics from Melamine-carbosilazane Single Source Precursors. *Journal of Solid State Chemistry*, 181:150, 2008.
- [149] M. Jansen and M. Kroschel. Die Umwandlung von N-Methylpolyborosilazan in amorphes Siliciumborcarbonitrid. *Zeitschrift für anorganische und allgemeine Chemie*, 626:1634, 2000.
- [150] T. Jäschke and M. Jansen. Synthesis and Characterization of New Amorphous Si/B/N/C Ceramics with Increased Carbon Content Through Single-Source Precursors. *Comptes Rendus Chimie*, 7(5):471, 2004.
- [151] A. Epple. *Darstellung und Characterisierung neuer Einkomponentenvorläufer und Keramiken im System Si/B/N/C und Festkörper-NMR-Untersuchungen an isotoopenmarkiertem SiBN₃C*. PhD thesis, Universität Stuttgart, 2006.
- [152] A. Hannemann, J. C. Schön, and M. Jansen. Thermodynamic Stability of Solid and Fluid Phases in the Si₃B₃N₇ System. *Philosophical Magazine*, 88(7):1037, 2008.
- [153] A. Hannemann, J. C. Schön, and M. Jansen. Stability of Nanovoids in Amorphous Si₃B₃N₇. *Philosophical Magazine*, 85(23):2621, 2005.
- [154] A. Hannemann, J. C. Schön, M. Jansen, and P. Sibani. Nonequilibrium Dynamics in Amorphous Si₃B₃N₇. *Journal of Physical Chemistry B*, 109(23):11770, 2005.
- [155] A. Hannemann, J. C. Schön, and M. Jansen. Modeling the Sol-Gel Synthesis Route of Amorphous Si₃B₃N₇. *Journal of Materials Chemistry*, 15(11):1167, 2005.
- [156] A. Hannemann, J. C. Schön, M. Jansen, H. Putz, and T. Lengauer. Modeling Amorphous Si₃B₃N₇: Structure and Elastic Properties. *Physical Review B*, 70(14), 2004.
- [157] J. C. Schön, A. Hannemann, and M. Jansen. Modeling the Synthesis of Amorphous Si₃B₃N₇ via a Sequence of Dynamically Well-Separated Steps. *Journal of Physical Chemistry B*, 108(7):2210, 2004.
- [158] M. Mühlhäuser, M. Gastreich, C. M. Marian, H. Jüngermann, and M. Jansen. Structural Properties of [(trichlorosilyl)amino]dichloroborane. *Journal of Physical Chemistry*, 100(41):16551, 1996.

Bibliography

- [159] R. M. Hagenmayer, U. Müller, C. J. Benmore, J. Neufeind, and M. Jansen. Structural Studies on Amorphous Silicon Boron Nitride $\text{Si}_3\text{B}_3\text{N}_7$: Neutron Contrast Technique on Nitrogen and High Energy X-ray Diffraction. *Journal of Materials Chemistry*, 9(11):2865, 1999.
- [160] J. Haug, P. Lamparter, M. Weinmann, and F. Aldinger. Diffraction Study on the Atomic Structure and Phase Separation of Amorphous Ceramics in the Si-(B)-C-N System. 2. Si-B-C-N Ceramics. *Chemistry of Materials*, 16(1):83, 2004.
- [161] R. Franke, St. Bender, H. Jüngermann, M. Kroschel, and M. Jansen. The Determination of Structural Units in Amorphous Si-B-N-C Ceramics by means of Si, B, N and C K-XANES Spectroscopy. *Journal of Electron Spectroscopy and Related Phenomena*, 641-645:101, 1999.
- [162] R. Franke, St. Bender, I. Arzberger, J. Hormes, M. Jansen, H. Juengermann, and J. Loeffelholz. The Determination of Local Structural Units in Amorphous SiBN_3C by means of X-ray Photoelectron and X-ray Absorption Spectroscopy. *Fresenius' Journal of Analytical Chemistry*, 354:874, 1996.
- [163] R. M. Hagenmayer, U. Müller, and M. Jansen. Neutron Contrast Technique on Nitrogen in $\text{Si}_3\text{B}_3\text{N}_7$. *Physica B: Condensed Matter*, 276-278:423, 2000.
- [164] D. Heinemann, W. Assenmacher, W. Mader, M. Kroschel, and M. Jansen. Structural Characterization of Amorphous Ceramics in the System Si-B-N-(C) by means of Transmission Electron Microscopy Methods. *Journal of Materials Research*, 14:3746, 1999.
- [165] L. van Wüllen, A. Roth, and M. Jansen. The Role of Carbon in the Nitridic High Performance Ceramics in the System Si-B-N-C (Erratum of vol 27, pg 90, 2005). *Solid State Nuclear Magnetic Resonance*, 27(4):271, 2005.
- [166] U. Müller, W. Hoffbauer, and M. Jansen. Short-Range Ordering in Amorphous $\text{Si}_3\text{B}_3\text{N}_7$ as Determined by Multinuclear NMR Spectroscopy. *Chemistry of Materials*, 12(8):2341, 2000.
- [167] J. Schuhmacher, M. Weinmann, J. Bill, F. Aldinger, and K. Müller. Solid-State NMR Studies of the Preparation of Si-C-N Ceramics from Polysilylcarbodiimide Polymers. *Chemistry of Materials*, 10(12):3913, 1998.
- [168] Y. Sehleier, A. Verhoeven, and M. Jansen. NMR Studies of Short and Intermediate Range Ordering of Amorphous Si-B-N-C-H Pre-ceramic at the Pyrolysis Stage of 600 °C. *Journal of Materials Chemistry*, 17(40):4316, 2007.

- [169] Y. Sehlleier, A. Verhoeven, and M. Jansen. Observation of Direct Bonds Between Carbon and Nitrogen in Si-B-N-C Ceramic After Pyrolysis at 1400 °C. *Angewandte Chemie International Edition*, 47(19):3600, 2008.
- [170] G. Jeschke, M. Kroschel, and M. Jansen. A Magnetic Resonance Study on the Structure of Amorphous Networks in the Si-B-N(-C) System. *Journal of Non-crystalline Solids*, 260(3):216, 1999.
- [171] L. van Wüllen and M. Jansen. Random Inorganic Networks: A Novel Class of High-Performance Ceramics. *Journal of Materials Chemistry*, 11(1):223, 2001.
- [172] L. van Wüllen, U. Müller, and M. Jansen. Understanding Intermediate-Range Order in Amorphous Nitridic Ceramics: A $^{29}\text{Si}\{^{11}\text{B}\}$ REDOR/REAPDOR and $^{11}\text{B}\{^{29}\text{Si}\}$ REDOR Study. *Chemistry of Materials*, 12(8):2347, 2000.
- [173] J. Lücke, H. P. Baldus, G. Passing, K. Rigby, and K. Vogt. Industrial Applications of SiBN(C) Ceramics Produced from Pre ceramic Polymers. *Ceramic Forum International/Ber DKG*, 75:18, 1998.
- [174] M. Haltrich, G. Wahl, J. Arndt, and R. Suchentrunk. Deposition of SiBCN Films from a Monomeric Borosilazane. *Proceedings of Electrochemical Society*, 97-25:1223, 1997.
- [175] M. A. Rooke and P. M. A. Sherwood. Surface Studies of Potentially Oxidation Protective Si-B-N-C Films for Carbon Fibers. *Chemistry of Materials*, 9:285, 1997.
- [176] R. Weisbarth and M. Jansen. Investigations on Reactive Coatings Applied to Siboramic (SiBN₃C) Fibers. *Journal of Materials Chemistry*, 13(8):1926, 2003.
- [177] G. B. Zheng, H. Sano, Y. Uchiyama, and K. Kobayashi. Effects of Boron Addition on the Mechanical Properties of Carbon Fiber Reinforced SiC Composites. *Key Engineering Materials*, 159-160:393, 1999.
- [178] G. Ziegler, J. Lücke, I. Richter, and D. Suttor. C-Fibre Reinforced Composites with Polymer-Derived Matrix: Microstructure, Thermal Properties, Strength. *Key Engineering Materials*, 132-136:1870, 1997.
- [179] M. Weinmann, T. W. Kamphowe, J. Schuhmacher, K. Müller, and F. Aldinger. Design of Polymeric Si-B-C-N Ceramic Precursors for Application in Fiber-reinforced Composite Materials. *Chemistry of Materials*, 12(8):2112, 2000.
- [180] T. W. Kamphowe, M. Weinmann, J. Bill, and F. Aldinger. Preparation of Fibre-Reinforced Si-B-C-N Ceramics by Polymer Precursor Infiltration. *Silicates Industries*, 63(11-12):159, 1998.

Bibliography

- [181] H. Yang, P. Deschatelets, S. T. Brittain, and G. M. Whitesides. Fabrication of High Performance Ceramic Microstructures from a Polymeric Precursor Using Soft Lithography. *Advanced Materials*, 13:54, 2001.
- [182] H. P. Baldus, N. Percheneck, A. Thierauf, R. Herborn, and D. Sporn. Neue keramische Fasern im System Silicium-Bor-Stickstoff-Kohlenstoff. *DE 19530404 A1*, 1997.
- [183] H. P. Baldus, G. Passing, H. Scholz, D. Sporn, M. Jansen, and J. Goring. Properties of Amorphous SiBNC-Ceramic Fibres. *Key Engineering Materials*, 127-131:177, 1997.
- [184] S. Bernard, M. Weinmann, D. Cornu, P. Miele, and F. Aldinger. Preparation of High-Temperature Stable Si-B-C-N Fibers from Tailored Single Source Polyborosilazanes. *Journal of European Ceramic Society*, 25(2-3):251, 2005.
- [185] S. Bernard, M. Weinmann, P. Gerstel, P. Miele, and F. Aldinger. Boron-Modified Polysilazane as a Novel Single-Source Precursor for SiBCN Ceramic Fibers: Synthesis, Melt-Spinning, Curing and Ceramic Conversion. *Journal of Materials Chemistry*, 15(2):289–299, 2005.
- [186] P. Miele, S. Bernard, and B. Toury. Recent Developments in Polymer-Derived-Ceramic Fibers (PDCFs): Preparation, Properties and Applications - A Review. *Soft Materials*, 4:249, 2007.
- [187] R. Weisbarth and M. Jansen. SiBN₃C Ceramic Workpieces by Pressureless Pyrolysis without Sintering Aids: Preparation, Characterization and Electrical Properties. *Journal of Materials Chemistry*, 13(12):2975, 2003.
- [188] R. Weisbarth. *Formkörper, Mechanische Eigenschaften und Verbundwerkstoffe Amorpher Si/B/N/C Keramiken sowie Studien zur Synthese von Phosphorcarbiden über Precursorrouten*. PhD thesis, Rheinische Friedrich-Wilhelms-Universität Bonn, 2003.
- [189] G. Blasse and B. C. Grabmaier, editors. *Luminescent Materials*. Springer-Verlag, Berlin, 1994.
- [190] K. A. Franz, W. G. Kehr, A. Siggel, J. Wiczoreck, and W. Adam. Luminescent Materials. In *Ullmann's Encyclopedia of Industrial Chemistry*, volume 20. Wiley-WCH, Weinheim, 2003.
- [191] C. R. Ronda, editor. *Luminescence: From Theory to Application*. Wiley-WCH, Weinheim, 2008.

- [192] W. M. Yen, S. Shinoya, and H. Yamamoto, editors. *Phosphor Handbook*. CRC Press, Boca Raton, 2007.
- [193] H. J. Queisser and U. Heim. Optical Emission from Semiconductors. *Annual Review of Materials Research*, 4:125, 1974.
- [194] G. H. Dieke, editor. *Spectra and Energy Levels of Rare Earth Ions in Crystals*. John Wiley and Sons, Inc., New York, 1968.
- [195] W. T. Carnall, G. L. Goodman, K. Rajnak, and R. S. Rana. A systematic Analysis of the Spectra of Lanthanides Doped into Single Crystal LaF_3 . *Journal of Chemical Physics*, 90:3443, 1989.
- [196] P. Dorenbos. f - d Transition Energies of Divalent Lanthanides in Inorganic Compounds. *Journal of Physics: Condensed Matter*, 15:575, 2003.
- [197] A. Lakshmanan, editor. *Luminescence and Display Phosphors: Phenomena and Applications*. Springer-Verlag, Berlin, 1994.
- [198] E. F. Schubert, editor. *Light-Emitting Diodes, 2nd Edition*. Cambridge University Press, New York, 2006.
- [199] A. Kitai, editor. *Luminescent Materials and Applications*. John Wiley & Sons Ltd., West Sussex, 2008.
- [200] S. Nakamura and G. Fasol, editors. *The Blue Laser Diode: GaN Based Light Emitters and Lasers*. Springer-Verlag, Berlin, 1997.
- [201] S. Nakamura and S. F. Chichibu, editors. *Introduction to Nitride Semiconductor Blue Lasers and Light Emitting Diodes*. Taylor & Francis, London, 2000.
- [202] S. Nakamura, T. Mukai, and M. Senoh. Candela Class High-Brightness InGaN/AlGaIn Double-Heterostructure Blue-Light-Emitting Diodes. *Applied Physics Letters*, 64:1687, 1994.
- [203] S. Nakamura, M. Senoh, N. Iwasa, S. Nagahama, T. Yamada, and T. Mukai. Superbright Green InGaIn Single-Quantum-Well-Structure Light-Emitting Diodes. *Japanese Journal of Applied Physics*, 34:L1332, 1995.
- [204] S. Nakamura. InGaIn/AlGaIn Blue-Light-Emitting Diodes. *Journal of Vacuum Science and Technology A*, 13:705, 1995.
- [205] S. Nakamura, M. Senoh, N. Iwasa, and S. Nagahama. High Brightness InGaIn Blue, Green and Yellow Light-Emitting Diodes with Quantum Well Structures. *Japanese Journal of Applied Physics*, 34:L797, 1995.

Bibliography

- [206] S. Nakamura. InGaN-based Blue/Green LEDs and Laser Diodes. *Advanced Materials*, 8:689, 1996.
- [207] S. Nakamura. III-V Nitride-Based Light-Emitting Diodes. *Diamond and Related Materials*, 5:496, 1996.
- [208] S. Nakamura. III-V Nitride-Based Light-Emitting Devices. *Solid State Communications*, 102:237, 1996.
- [209] S. Nakamura. Present and Future Aspects of Blue Light Emitting Devices. *Applied Surface Sciences*, 113-114:689, 1997.
- [210] G. Bogner, A. Debray, G. Heidel, K. Höhn, U. Müller, and P. Schlotter. White LED. *Society of Photo-Optical Instrumentation Engineers Conference on Light Emitting Diodes: Research, Manufacturing and Applications*, 3621:143, 1999.
- [211] S. C. Allen and A. J. Steckl. A Nearly Ideal Phosphor-Converted White Light Emitting Diode. *Applied Physics Letters*, 92:143309, 2008.
- [212] E. Bailey and E. S. Tormey. High Color Rendering Index White LED Light System Using Multi-Wavelength Pump Sources and Mixed Phosphors. *WO 2008/101156 A2*, 2008.
- [213] N. Farchtchian, B. Braune, and H. Brunner. Phosphor-Converted LEDs Take on Industrial Applications. *Laser Focus World*, page 99, 2004.
- [214] G. Denis, P. Deniard, E. Gautron, F. Clabau, A. Garcia, and S. Jobic. Structure and White Luminescence of Eu-Activated $(\text{Ba,Sr})_{13-x}\text{Al}_{22-2x}\text{Si}_{10+2x}\text{O}_{66}$ Materials. *Inorganic Chemistry*, 47:4226, 2008.
- [215] T. Fiedler, T. Fries, F. Jermann, M. Zachau, and F. Zwaschka. Phosphor and Light Source Comprising Such a Phosphor. *US 7267786 B2*, 2007.
- [216] E. C. Fuchs and K. Gatterer. White Light Emitting Phosphors. *WO 2007/128016 A2*, 2007.
- [217] S. Nayama and K. Itoh. Case Study on Combination of Fluorescent Materials for White LED to Obtain High Color Rendering Index. *Journal of Light and Visual Environment*, 30:39, 2006.
- [218] W. Oberleithner and H. Kawaguchi. Phosphor Converted Light Emitting Diode. *WO 2008/043519 A1*, 2008.

- [219] J. C. Kyoung, J. K. Park, K. M. Kim, C. H. Kim, and H. K. Kim. Phosphor-Conversion White Light Emitting Diode Using InGaN Near-Ultraviolet Chip. *Solid State Phenomena*, 124-126:499, 2007.
- [220] P. Li, Z. Yang, Z. Wang, and Q. Guo. White Light Emitting Diodes of UV-Based $\text{Sr}_3\text{Y}_2(\text{BO}_3)_4:\text{Dy}^{3+}$ and Luminescent Properties. *Materials Letters*, 62:1455, 2008.
- [221] T. Masaaki, H. Uetake, R. Hiramatsu, K. Ootsuka, Y. Hattori, and N. Shida. Luminescent Material. *US 2008/0017831 A1*, 2008.
- [222] T. Miyoshi, T. Yanamoto, T. Kozaki, S. Nagahama, Y. Narukawa, M. Sano, T. Yamada, and T. Mukai. Recent Status of White LEDs and Nitride LDs. *Proceeding of SPIE*, 6894:689414-1, 2008.
- [223] R. Müller-Mach, G. O. Müller, M. R. Krames, and T. Trottier. High Power Phosphor Converted Light Emitting Diodes Based on III-Nitrides. *IEEE Journal on Selected Topics in Quantum Electronics*, 8:339, 2002.
- [224] R. Müller-Mach, G. O. Müller, and G. M. Craford. Light Emitting Diode (LED) Device That Produces White Light by Performing Phosphor Conversion on All of the Primary Radiation Emitted by the Light Emitting Structure of the LED Device. *US 6501102 B2*, 2002.
- [225] G. O. Müller, R. B. Müller-Mach, T. Jüstel, P. Huppertz, D. U. Wiechert, and D. Uhlich. Phosphor Converted Light Emitting Device. *WO 2007/080555 A1*, 2007.
- [226] P. Schmidt, T. Jüstel, W. Mayr, H. D. Bausen, W. Schinck, and H. Höppe. Light-Emitting Device Comprising an Eu(II)-Activated Phosphor. *US 7061024 B2*, 2006.
- [227] A. A. Setlur, J. Shiang, H. A. Comanza, C. A. Becker, S. Duclos, A. M. Srivastava, S. Weaver, and T. F. Soules. Rules for Efficient Light Sources Using Phosphor Converted LEDs. *WO 2005/083036 A1*, 2005.
- [228] A. A. Setlur and E. Radkov. Ce^{3+} and Eu^{2+} Doped Phosphors for Light Generation. *US 7229573 B2*, 2007.
- [229] A. A. Setlur, A. M. Srivastava, and H. A. Comanza. Red Phosphor for LED Based Lighting. *US 7329371 B2*, 2008.
- [230] K. Shunichi, Y. Kim, and S. Im. Phosphor for White Light Emitting Device and White Light Emitting Device Including the same. *US 2008/0020236 A1*, 2008.

Bibliography

- [231] T. Taguchi. Present Status of Energy Saving Technologies and Future Prospect in White LED Lighting. *IEEJ Transactions on Electrical and Electronic Engineering*, 3:21, 2008.
- [232] M. Zachau, D. Becker, D. Berben, T. Fiedler, F. Jermann, and F. Zwaschka. Phosphors for Solid State Lighting. *Proceeding of SPIE*, 6910:691010–1, 2008.
- [233] K. Bando, Y. Noguchi, K. Sakano, and Y. Shimizu. Development and Applications of Highbright White LED Lamps. *Technical Digest, Phosphor Research Society, 264th Meeting Proceedings*, page 5, 1996.
- [234] K. Bando, K. Sakano, Y. Noguchi, and Y. Shimizu. Development of High-Bright and Pure-White LED Lamps. *Journal of Light and Visual Environment*, 22:2, 1998.
- [235] Y. Shimizu, K. Sakano, Y. Noguchi, and T. Moriguchi. Light Emitting Device Having a Nitride Compound Semiconductor and a Phosphor Containing a Garnet Fluorescent Material. *US 5998925*, 1999.
- [236] H. Jang, W. Im, D. C. Lee, D. Y. Jeon, and S. S. Kim. Enhancement of Red Spectral Emission Intensity of $\text{Y}_3\text{Al}_5\text{O}_{12}:\text{Ce}^{3+}$ Phosphor via Pr Codoping and Tb Substitution for the Application to White LEDs. *Journal of Luminescence*, 126:371, 2007.
- [237] H. Yang and Y. Kim. Energy Transfer-Based Spectral Properties of Tb-, Pr-, or Sm-codoped YAG:Ce Nanocrystalline Phosphors. *Journal of Luminescence*, 128:1570, 2008.
- [238] Y. Shimomura, T. Honma, M. Shigeiwa, T. Akai, K. Okamoto, and N. Kijima. Photoluminescence and Crystal Structure of Green-Emitting $\text{Ca}_3\text{Sc}_2\text{Si}_3\text{O}_{12}:\text{Ce}^{3+}$ Phosphor for White Light Emitting Diodes. *Journal of the Electrochemical Society*, 154:J35, 2007.
- [239] J. S. Kim, P. E. Jeon, J. C. Choi, and H. L. Park. Emission Color Variation of $\text{M}_2\text{SiO}_4:\text{Eu}^{2+}$ (M=Ba, Sr, Ca) Phosphors for Light-Emitting Diode. *Solid State Communications*, 133:187, 2005.
- [240] J. S. Kim, Y. H. Park, S. M. Kim, J. C. Choi, and H. L. Park. Temperature-Dependent Emission Spectra of $\text{M}_2\text{SiO}_4:\text{Eu}^{2+}$ (M=Ca, Sr, Ba) Phosphors for Green and Greenish White LEDs. *Solid State Communications*, 133:445, 2005.
- [241] W. J. Park, M. K. Jung, and D. H. Yoon. Enhanced Luminescence Efficiency for Bi, Eu Doped Y_2O_3 Red Phosphors for White LEDs. *Solid State Phenomena*, 124-126:379, 2007.

- [242] Y. Hu, W. Zhuang, H. Ye, S. Zhang, Y. Fang, and X. Huang. Preparation and Luminescent Properties of $(\text{Ca}_{1-x}\text{Sr}_x)\text{S}:\text{Eu}^{2+}$ Red-Emitting Phosphor for White LED. *Journal of Luminescence*, 111:139, 2005.
- [243] M. Nazarov, D. Y. Noh, and H. Kim. Structural and Luminescent Properties of Calcium, Strontium and Barium Thiogallates. *Materials Chemistry and Physics*, 107:456, 2008.
- [244] R.-J. Xie and N. Hirosaki. Silicon-based oxynitride and nitride phosphors for white-LEDs - a review. *Science and Technology of Advanced Materials*, 8:588, 2007.
- [245] H. Huppertz and W. Schnick. $\text{Eu}_2\text{Si}_5\text{N}_8$ and $\text{EuYbSi}_4\text{N}_7$. The First Nitridosilicates with a Divalent Rare Earth Metal. *Acta Crystollographica Section C*, C53:1751, 1997.
- [246] R. Mueller-Mach, G. Mueller, M. R. Krames, H. A. Höpfe, F. Stadler, W. Schnick, T. Jüstel, and P. Schmidt. Highly Efficient All-Nitride Phosphor-Converted White Light Emitting Diode. *Physica Status Solidi (a)*, 202:1727, 2005.
- [247] P. Schmidt, T. Jüstel, H. Höpfe, W. Schnick, and W. Mayr. Illumination System Comprising a Radiation Source and a Fluorescent Material. *WO 2005/116163 A1*, 2005.
- [248] W. Schnick, H. Huppertz, and R. Lauterbach. High Temperature Syntheses of Novel Nitrido- and Oxonitrido-Silicates and SiAlONs Using RF Furnaces. *Journal of Materials Chemistry*, 9:289, 1999.
- [249] H. A. Höpfe, H. Trill, B. D. Mosel, H. Eckert, G. Kotzyba, R. Pöttgen, and W. Schnick. Hyperfine Interactions in the 13 K Ferromagnet $\text{Eu}_2\text{Si}_5\text{N}_8$. *Journal of Physics and Chemistry of Solids*, 63:853, 2002.
- [250] H. Huppertz and W. Schnick. Edge-Sharing SiN_4 Tetrahedra in the Highly Condensed Nitridosilicate $\text{BaSi}_7\text{N}_{10}$. *Chemistry - A European Journal*, 3:249, 1997.
- [251] T. Schlieper and W. Schnick. Nitrido Silicates. I. High Temperature Synthesis and Crystal Structure of $\text{Ca}_2\text{Si}_5\text{N}_8$. *Zeitschrift für Anorganische und Allgemeine Chemie*, 621:1037, 1995.
- [252] T. Schlieper, W. Milius, and W. Schnick. Nitrido Silicates. II. High Temperature Syntheses and Crystal Structures of $\text{Sr}_2\text{Si}_5\text{N}_8$ and $\text{Ba}_2\text{Si}_5\text{N}_8$. *Zeitschrift für Anorganische und Allgemeine Chemie*, 621:1380, 1995.

Bibliography

- [253] H. A. Höpfe, H. Lutz, P. Morys, W. Schnick, and A. Seilmeier. Luminescence in Eu^{2+} Doped $\text{Ba}_2\text{Si}_5\text{N}_8$: Fluorescence, Thermoluminescence, and Upconversion. *Journal of Physics and Chemistry of Solids*, 61:2001, 2000.
- [254] M. Zeuner, H. Frauke, and W. Schnick. Low Temperature Precursor Route for Highly Efficient Spherically Shaped LED-Phosphors $\text{M}_2\text{Si}_5\text{N}_8:\text{Eu}^{2+}$ (M=Eu, Sr, Ba). *Chemistry of Materials*, 21:336, 2009.
- [255] H. T. Hintzen, J. W. H. van Krevel, and G. Botty. Red Emitting Luminescent Material. *EP 1104799 A1*, 2001.
- [256] C. M. Fang, H. T. Hintzen, G. de With, and R. A. de Groot. Electronic Structure of the Alkaline-Earth Silicon Nitrides $\text{M}_2\text{Si}_5\text{N}_8$ (M= Ca and Sr) Obtained from First-Principle Calculations and Optical Reflectance Spectra. *Journal of Physics: Condensed Matter*, 13:67, 2001.
- [257] Y. Q. Li, J. E. J. van Steen, J. W. H. van Krevel, G. Botty, A. C. A. Delsing, F. J. DiSalvo, G. de With, and H. T. Hintzen. Luminescence Properties of Red Emitting $\text{M}_2\text{Si}_5\text{N}_8:\text{Eu}^{2+}$ (M=Ca, Sr, Ba) LED Conversion Phosphors. *Journal of Alloys and Compounds*, 417:273, 2006.
- [258] Y. Q. Li and H. T. Hintzen. Luminescence Properties of Ce^{3+} Activated Alkaline Earth Silicon Nitride $\text{M}_2\text{Si}_5\text{N}_8$ (M=Ca, Sr, Ba) Materials. *Journal of Luminescence*, 116, 2006.
- [259] S. Oshio. Method for Producing Nitridosilicate-Based Compound, Nitridosilicate Phosphor, and Light-Emitting Apparatus Using the Nitridosilicate Phosphor. *WO 2005/049763 A1*, 2005.
- [260] O. G. Müller, R. B. Müller-Mach, J. Meyer, P. J. Schmidt, and D. U. Wiechert. Phosphor Converted Light-Emitting Device. *EP 1669429 A1*, 2006.
- [261] X. Piao, T. Horikawa, H. Hanzawa, and K. Machida. Characterization and Luminescence Properties of $\text{Sr}_2\text{Si}_5\text{N}_8:\text{Eu}^{2+}$ Phosphor for White Light-Emitting-Diode Illumination. *Applied Physics Letters*, 88:161908, 2006.
- [262] X. Piao, T. Horikawa, H. Hanzawa, and K. Machida. Preparation of $(\text{Sr}_{1-x}\text{Ca}_x)_2\text{Si}_5\text{N}_8:\text{Eu}^{2+}$ Solid Solutions and Their Luminescence Properties. *Journal of the Electrochemical Society*, 153:H232, 2006.
- [263] X. Piao, K. Machida, T. Horikawa, and H. Hanzawa. Synthesis of Nitridosilicate $\text{CaSr}_{1-x}\text{Eu}_x\text{Si}_5\text{N}_8$ Phosphor by Calcium Cyanamide Reduction for White Light-Emitting Diode Applications. *Journal of the Electrochemical Society*, 155:J17, 2008.

- [264] J. W. H. van Krevel. *On New Rare-earth Doped M-Si-Al-O-N Materials: Luminescence Properties and Oxidation Resistance*. PhD thesis, Technical University of Eindhoven, 2000.
- [265] X. Piao, K. Machida, T. Horikawa, and H. Hanzawa. Self-Propagating High Temperature Synthesis of Yellow-Emitting $\text{Ba}_2\text{Si}_5\text{N}_8:\text{Eu}^{2+}$ Phosphor for White Light-Emitting-Diode Illumination. *Applied Physics Letters*, 91:041908, 2007.
- [266] R. Xie, N. Hirosaki, T. Suehiro, F. Xu, and M. Mitomo. A Simple, Efficient Synthetic Route to $\text{Sr}_2\text{Si}_5\text{N}_8:\text{Eu}^{2+}$ Based Red Phosphors for White Light-Emitting Diodes. *Chemistry of Materials*, 18:5578, 2006.
- [267] R. Xie, N. Hirosaki, N. Kimura, K. Sakuma, and M. Mitomo. 2-Phosphor-Converted White Light-Emitting Diodes Using Oxynitride/Nitride Phosphors. *Applied Physics Letters*, 90:191101, 2007.
- [268] R. Le Toquin and A. K. Cheetham. Red-emitting Cerium-based Phosphor Materials for Solid-state Lighting Applications. *Chemical Physics Letters*, 131:65, 2004.
- [269] K. Uheda, N. Hirosaki, Y. Yamamoto, A. Naito, T. Nakajima, and H. Yamamoto. Luminescence Properties of a Red Phosphor, $\text{CaAlSiN}_3:\text{Eu}^{2+}$, for White Light Emitting Diodes. *Electrochemical and Solid-State Letters*, 9:H22, 2006.
- [270] H. Watanabe, H. Yamane, and N. Kijima. Crystal Structure and Luminescence of $\text{Sr}_{0.99}\text{Eu}_{0.01}\text{AlSiN}_3$. *Journal of Solid State Chemistry*, 181:1848, 2008.
- [271] H. Watanabe and N. Kijima. Crystal Structure and Luminescence Properties of $\text{Sr}_x\text{Ca}_{1-x}\text{AlSiN}_3:\text{Eu}^{2+}$ Mixed Nitride Phosphors. *Journal of Alloy and Compounds*, 475:434, 2009.
- [272] K. Sakuma, N. Hirosaki, N. Kimura, M. Ohashi, R. Xie, Y. Yamamoto, T. Suehiro, K. Asano, and D. Tanaka. White Light Emitting Diode Lamps Using Oxynitride and Nitride Phosphor Materials. *IEICE Transactions on Electronics*, E88-C:2057, 2005.
- [273] Y. Zhou, Y. Yoshizawa, K. Hirao, Z. Lences, and P. Sajgalik. Preparation of Eu-Doped Beta-SiAlON Phosphors by Combustion Synthesis. *Journal of the American Ceramic Society*, 91:3082, 2008.
- [274] R.-J. Xie, M. Mitomo, and N. Hirosaki. Luminescence Properties of Rare-Earth Doped Alpha-SiAlONs. *Key Engineering Materials*, 317-318:797, 2006.

Bibliography

- [275] R. Mueller-Mach, G. O. Mueller, P. J. Schmidt, D. U. Wiechert, and J. Meyer. Nitridosilicates, A New Family of Phosphors for Color Conversion of LEDs. *Proceedings of SPIE-The International Society for Optical Engineering*, 5941:59410Z-1, 2005.
- [276] S. N. Jayasinghe and M. J. Edirisinghe. A Novel Method of Forming Open Cell Ceramic Foams. *Journal of Porous Materials*, 9:265, 2002.
- [277] J. Adler and G. Standke. Offenzellige Schaumkeramik, Teil 1. *Keramische Zeitschrift*, 55:694, 2003.
- [278] J. Adler and G. Standke. Offenzellige Schaumkeramik, Teil 2. *Keramische Zeitschrift*, 55:786, 2003.
- [279] A. R. Studart, U. T. Gonzenbach, E. Tervoort, and L. J. Gauckler. Processing Routes to Macroporous Ceramics: A Review. *Journal of American Ceramic Society*, 89:1771, 2006.
- [280] K. Schwartzwalder and A. Somers. Method of Making Porous Ceramic Articles. *US 3090094*, 1963.
- [281] F. F. Lange and K. T. Miller. Open-Cell, Low Density Ceramics Fabricated from Reticulated Polymer Substrates. *Advanced Ceramic Materials*, 2:827, 1987.
- [282] H. Wang, S. Zheng, X. Li, and D. Kim. Preparation of Three-Dimensional Ordered Macroporous SiCN Ceramic Using Sacrificing Template Method. *Microporous and Mesoporous Materials*, 80:357, 2005.
- [283] J. Luyten, W. Wandermöhlen, S. Mullens, B. Wallaey, and R. Mortelmans. Strong Ceramic Foams from Polyurethane Templates. *Advances in Applied Ceramics*, 104:4, 2005.
- [284] P. Quadbeck, G. Stephani, K. Kümmel, J. Adler, and G. Standke. Synthesis and Properties of Open-Celled Metal Foams. *Materials Science Forum*, 534-536:1005, 2007.
- [285] P. Colombo and J. R. Hellmann. Ceramic Foams from Pre-ceramic Polymers. *Materials Research Innovations*, 6:260, 2002.
- [286] J. Adler and J. Ihle. Porous Silicon Carbide Ceramic Material and Method for the Production thereof. *WO 2003/070661*, 2003.
- [287] J. Adler and G. Standke. Open-Celled Silicon Carbide Foam Ceramic Method for Production thereof. *WO 2002/020426*, 2002.

- [288] M. F. Grandey and J. F. Kulp. Method of Preparing Silicon Nitride Foam Material. *US 3085886*, 1963.
- [289] H. M. Dess. Method of Making Foamed Silicon Nitride. *US 30849986*, 1963.
- [290] M. R. Nangrejo, X. Bao, and M. J. Edirisinghe. Preparation of Silicon Carbide - Silicon Nitride Composite Foams from Preceramic Polymers. *Journal of the European Ceramic Society*, 20:1777, 2000.
- [291] P. Colombo, M. Griffoni, and M. Modesti. Ceramic Foams from a Preceramic Polymer and Polyurethanes: Preparation and Morphological Investigations. *Journal of Sol-Gel Science and Technology*, 13:195, 1998.
- [292] P. Colombo and M. Modesti. Silicon Oxycarbide Ceramic Foams from a Preceramic Polymer. *Journal of the American Ceramic Society*, 82:573, 1999.
- [293] P. Colombo. Engineering Porosity in Polymer-Derived Ceramics. *Journal of the European Ceramic Society*, 28:1389, 2008.
- [294] J. Adler, M. Teichgräber, G. Standke, H. Jaunich, H. Stöver, and R. Stötzel. Open-Cell Expanded Ceramic With a High Level of Strength, and Process for the Production thereof. *WO 97/45381*, 1997.
- [295] M. Jansen and H. Cakmak. Leuchtstoffe. *DE 102006051757.1 A1*, *WO 2008/052771 A1*, 2006.
- [296] M. Lannoo. The Role of Dangling Bonds in the Properties of Surfaces and Interfaces of Semiconductors. *Revue de Physique Appliquée*, 25:887, 1990.
- [297] W. L. Warren, J. Kanicki, J. Robertson, and P. M. Lenahan. Energy Level of the Nitrogen Dangling Bond in Amorphous Silicon Nitride. *Applied Physics Letters*, 59:1699, 1991.
- [298] J. M. Shannon and B. A. Morgan. Hole Transport Via Dangling-Bond States in Amorphous Hydrogenated Silicon Nitride. *Journal of Applied Physics*, 86:1548, 1999.
- [299] S-Y. Lin. Electronic Defect States of Amorphous Silicon Nitride. *Optical Materials*, 23:93, 2003.
- [300] S. I. Simdyankin and S. R. Elliot. *Theory of Defects in Semiconductors*, chapter Light Induced Effects in Amorphous and Glassy Solids. Springer-Verlag, Berlin, 2007.

Bibliography

- [301] M. S. Brandt and M. Stutzmann. Excitons and Light-Induced Degradation of Amorphous Hydrogenated Silicon. *Applied Physics Letters*, 58:1620, 1991.
- [302] S. Ismail-Beigi and S. G. Louie. Self-Trapped Excitons in Silicon Dioxide: Mechanism and Properties. *Physical Review Letters*, 95:156401, 2005.
- [303] R. M. Van Gihoven, H. Jonsson, and L. R. Corrales. Characterization of Exciton Self-Trapping in Amorphous Silica. *Journal of Non-Crystalline Solids*, 352:2589, 2006.
- [304] D. L. Staebler and C. R. Wronski. Reversible Conductivity Changes in Discharge-Produced Amorphous Si. *Applied Physics Letter*, 31:292, 1977.
- [305] T. Shimizu. Staebler-Wronski Effect in Hydrogenated Amorphous Silicon and Related Alloy Films. *Japanese Journal of Applied Physics*, 43:3257, 2004.
- [306] A. P. Demchenko. The Red-Edge Effects: 30 Years of Exploration. *Luminescence*, 17:19, 2002.
- [307] S. I. Vavilov. The Fluorescence Yield of Dye Solutions as a Function of the Wave Length of the Exciting Light. *Zeitschrift für Physik*, 42:311, 1927.
- [308] M. Kasha. Characterization of Electronic Transition in Complex Molecules. *Discussions of the Faraday Society*, 9:14, 1950.
- [309] W. C. Galley and R. M. Purkey. Role of Heterogeneity of the Solvation Site in Electronic Spectra in Solution. *Proceedings of the National Academy of Sciences*, 67:1116, 1970.
- [310] A. N. Rubinov and V. I. Tomin. Bathochromic Luminescence in Solutions of Organic Dyes at Low Temperatures. *Optics and Spectroscopy*, 29:578, 1970.
- [311] G. Weber and M. Shinitzky. Failure of Energy Transfer Between Identical Aromatic Molecules on Excitation at the Long Wave Edge of the Absorption Spectrum. *Proceedings of the National Academy of Sciences*, 65:823, 1970.
- [312] G. Jones, D. Yan, J. Hu, J. Wan, B. Xia, and V. I. Vullev. Photoinduced Electron Transfer in Arylacridinium Conjugates in a Solid Glass Matrix. *The Journal of Physical Chemistry B*, 111:6921, 2007.
- [313] M. Jansen, J. C. Schoen, and L. van Wüllen. The Route to the Structure Determination of Amorphous Solids: A Case Study of the Ceramic $\text{Si}_3\text{B}_3\text{N}_7$. *Angewandte Chemie (2006) 118, 4350) Angewandte Chemie International Edition in English*, 45:4244, 2006.

- [314] S. Larach and R. E. Shrader. Multiband Luminescence in Boron Nitride. *Physical Review*, 104:68, 1956.
- [315] K. Watanabe, T. Taniguchi, and H. Kanda. Direct-Bandgap Properties and Evidence for Ultraviolet Lasing of Hexagonal Boron Nitride Single Crystal. *Nature Materials*, 3:404, 2004.
- [316] R. T. Williams, K. B. Ucer, D. L. Carroll, B. Berzina, L. Trinkler, V. Korsak, and R. Krut'okhstov. Photoluminescence of Self-Trapped Excitons in Boron Nitride Nanotubes. *Journal of Nanoscience and Nanotechnology*, 8:6504, 2008.
- [317] V. A. Nadolinnyi, V. V. Vasilev, and I. P. Mikhailovskii. Photo-Induced Metastable States in Silicon Nitride Amorphous Layers. *Physica Status Solidi (A)*, 116:K105, 1989.
- [318] C. Savall, J. C. Bruyere, and J. Krautwurm. Correlations Between ESR and Photoluminescence in Slightly Hydrogenated Silicon Nitride. *Journal of Physics D: Applied Physics*, 28:565, 1995.
- [319] V. I. Belyi and A. A. Rastorguev. Luminescence and Electronic Structure of Amorphous Silicon Nitride. Silicon Subsystem. *Journal of Structural Chemistry*, 41:526, 2000.
- [320] V. I. Belyi and A. A. Rastorguev. Luminescence and Electronic Structure of Amorphous Silicon Nitride. Nitrogen Subsystem. *Journal of Structural Chemistry*, 41:529, 2000.
- [321] V. A. Gritsenko, D. V. Gritsenki, Y. N. Novikov, R. W. M. Kwok, and I. Bello. Short-Range Order, Large-Scale Potential Fluctuations, and Photoluminescence in Amorphous SiN_x . *Journal of Experimental and Theoretical Physics*, 98:760, 2004.
- [322] L-W. Yin, Y. Bando, Y-C. Zhu, and Y-B. Li. Synthesis, Structure, and Photoluminescence of Very Thin and Wide α Silicon Nitride Single-Crystalline Nanobelts. *Applied Physics Letters*, 83:3584, 2003.
- [323] L. Zhang, H. Jin, W. Yang, Z. Xie, H. Miao, and L. An. Optical Properties of Single-Crystalline α - Si_3N_4 Nanobelts. *Applied Physics Letters*, 86:061908, 2005.
- [324] K. Sakuma, N. Hirosaki, and R-J. Xie. Red-Shift of Emission Wavelength Caused by Reabsorption Mechanism of Europium Activated Ca- α -SiAlON Ceramic Phosphors. *Journal of Luminescence*, 126:843, 2007.

Bibliography

- [325] W. A. Hollerman, N. P. Bergeron, F. N. Womack, S. M. Goedeke, and S. W. Allison. Changes in Half Brightness Dose due to Preparation Pressure for YAG:Ce. *IEEE Transactions on Nuclear Science*, 51:1080, 2004.
- [326] H. S. Jang and D. Y. Jeon. Yellow Emitting $\text{Sr}_3\text{SiO}_5\text{:Ce}^{3+}$, Li^+ Phosphor for White Light Emitting Diodes and Yellow Light Emitting Diodes. *Applied Physics Letters*, 90:041906, 2007.
- [327] J. Etourneau, J. Portier, and F. Menil. The Role of the Inductive Effect in Solid State Chemistry: How the Chemist Can Use It to Modify Both the Structural and Physical Properties of the Materials. *Journal of Alloys and Compounds*, 188:1, 1992.
- [328] C. Fouassier, B. Latourrette, J. Portier, and P. Hagenmuller. Nature de la Fluorescence de l'euporium Divalent Dans les Fluorures. *Materials Reserach Bulletin*, 11:933, 1976.
- [329] G. Gauthier, S. Jobic, M. Evain, H.-J. Koo, M.-H. Whangbo, C. Fouassier, and R. Brec. Syntheses, Structures, and Optical Properties of Yellow $\text{Ce}_2\text{Si}_5\text{S}_{17}$, $\text{Ce}_6\text{Si}_4\text{S}_{17}$, and $\text{Ce}_4\text{Si}_3\text{S}_{12}$ Materials. *Chemistry of Materials*, 15:828, 2003.
- [330] J. X. Meng, J. Q. Li, Z. P. Shi, and K. W. Cheah. Efficient Energy Transfer for Ce to Nd in Nd/Ce Codoped Yttrium Aluminum Garnet. *Applied Physics Letters*, 93:221908, 2008.
- [331] M. D. Ward. Transition-Metal Sensitised Near-Infrared Luminescence from Lanthanides in d-f Heteronuclear Arrays. *Coordination Chemistry Reviews*, 251:1663, 2007.
- [332] D. de Graaf. *Chemistry, Structure and Properties of Rare-Earth Containing Si-Al-O-N Glasses*. PhD thesis, Technical University of Eindhoven, 2000.
- [333] A. Gros, F. Gaume, and J. C. Gacon. Synthesis of New Luminescent Materials Activated with Divalent Samarium. *Journal of Solid State Chemistry*, 324:36, 1981.
- [334] A. Meijerink and G. J. Dirksen. Spectroscopy of Divalent Samarium in LiBaF_3 . *Journal of Luminescence*, 189:63, 1995.
- [335] A. G. Souza Filho, J. Mendes Filho, F. E. A. Melo, M. C. C. Custodio, R. Lebulenger, and A. C. Hernandez. Optical Properties of Sm^{3+} Doped Lead Fluoroborate Glasses. *Journal of Physics and Chemistry of Solids*, 61:1535, 2000.
- [336] W. F. van der Weg, Th. J. A. Popma, and A. T. Vink. Concentration Dependence of UV and Electron-Excited Tb^{3+} Luminescence in $\text{Y}_3\text{Al}_5\text{O}_{12}$. *Journal of Applied Physics*, 57:5450, 1985.

- [337] Y. Q. Li. *Structure and Luminescence Properties of Novel Rare-Earth Doped Silicon Nitride Based Materials*. PhD thesis, Technical University of Eindhoven, 2005.
- [338] F. S. Liu, Q. L. Liu, J. K. Liang, J. Luo, L. T. Yang, G. B. Song, Zhang Y., L. X. Wang, J. N. Yao, and G. H. Rao. Optical Spectra of Ln³⁺ (Nd³⁺, Sm³⁺, Dy³⁺, Ho³⁺, Er³⁺)-Doped Y₃GaO₆. *Journal of Luminescence*, 111:61, 2005.
- [339] T. Hirai and Y. Kawamura. Preparation of Sr₂CeO₄ Blue Phosphor Particles and Rare Earth (Eu, Ho, Tm, or Er)-Doped Sr₂CeO₄ Phosphor Particles, Using an Emulsion Membrane System. *Journal of Physical Chemistry B*, 108:12763, 2004.
- [340] V. Singh, D. T. Naidu, R. P. S. Chakradhar, Y. C. Ratnakaram, J-J. Zhu, and M. Soni. Synthesis, Characterization and Optical Properties of LaAlO₃:Ho³⁺ Phosphor. *Physica B*, 403:3781, 2008.
- [341] J. Silver, E. Barret, P. J. Marsch, and R. Withnall. Yttrium Oxide Upconverting Phosphors. 5. Upconversion Luminescent Emission from Holmium-Doped Yttrium Oxide under 632.8 nm Light Excitation. *Journal of Physical Chemistry B*, 107:9236, 2003.
- [342] X-X. Luo and W-H. Cao. Upconversion Luminescence of Holmium and Ytterbium Codoped Yttrium Oxysulfide Phosphor. *Materials Letters*, 61:3696, 2007.
- [343] M. Otha and M. Takami. Influence of Codoping Rare-Earth Ion on Long Lasting Phenomena of Eu-Doped Strontium Aluminate Phosphor. *Journal of the Electrochemical Society*, 151:G171, 2004.
- [344] J. Y. Kuang and J. X. Zhang. Effects of RE³⁺ as a Codopant in Blue Emitting Long Lasting Phosphors, Sr₃Al₁₀SiO₂₀:Eu²⁺. *Journal of Material Science*, 41:5500, 2006.
- [345] C. Guo, Q. Tang, D. Huang, C. Zhang, and Q. Su. Tunable color emission and afterglow in CaGa₂S₄:Eu²⁺, Ho³⁺ Phosphor. *Materials Research Bulletin*, 42:2032, 2007.
- [346] W. Guo, Y. Chen, Y. Lin, X. Gong, Z. Luo, and Y. Huang. Spectroscopic Analysis and Laser Performance of Tm³⁺:NaGd(MoO₄)₂ Crystal. *Journal of Physics D: Applied Physics*, 41:115409, 2008.
- [347] S. Tanabe, H. Hayashi, and T. Hanada. Improved Fluorescence from Tm-Ho- and Tm-Ho-Eu-Codoped Transparent PbF₂ Glass-Ceramics for S⁺ Band Amplifiers. *Journal of American Ceramic Society*, 85:839, 2002.

Bibliography

- [348] P. J. Deren, P. Goldner, and O. Guillot-Noel. Anti-Stokes Emission in LaAlO_3 Crystal Doped with Tm^{3+} Ions. *Journal of Alloys and Compounds*, 461:58, 2008.
- [349] D. L. DeLoach, S. A. Payne, L. L. Chase, K. Smith, W. L. Kway, and W. F. Krupke. Evaluation of Absorption and Emission Properties of Yb^{3+} Doped Crystals for Laser Application. *IEEE Journal of Quantum Electronics*, 29:1179, 1993.
- [350] D. de Graaf, H. T. Hintzen, S. Hampshire, and G. de With. Long Wavelength Eu^{2+} Emission in Eu-Doped YSiAlON Glasses. *Journal of European Ceramic Society*, 23:1093, 2003.
- [351] D. de Graaf, S. Le Rol, H. T. Hintzen, L. Le Gendre, and G. de With. Mixed oxidation States of Yb and Sm in SiAlON Glasses. *Journal of European Ceramic Society*, 26:2497, 2006.
- [352] J. C. Warf. Chemistry of Lanthanides in Liquid Ammonia. *Angewandte Chemie Internatinal Edition in English*, 9:383, 1970.
- [353] S. Lizzo, E. P. K. Nagelvoort, R. Erens, A. Meijerink, and G. Blasse. On the Quenching of the Yb^{2+} Luminescence in Different Host Lattices. *Journal of Physical Chemistry of Solids*, 6:963, 1997.
- [354] R.-J. Xie, N. Hirosaki, M. Mitomo, K. Uheda, T. Suehiro, X. Xu, Y. Yamamoto, and T. Sekiguchi. Strong Green Emission from $\alpha\text{-SiAlON}$ Activated by Divalent Ytterbium under Blue Light Irradiation. *Journal of Physical Chemistry B*, 109:9490, 2005.
- [355] B. Dierre, X. L. Yuan, N. Hirosaki, R.-J. Xie, and T. Sekiguchi. Luminescence Properties of Ca and Yb Codoped SiAlON Phosphors. *Materials Science and Engineering B*, 146:80, 2008.
- [356] B. Dierre, X. L. Yuan, N. Hirosaki, T. Kimura, R.-J. Xie, and T. Sekiguchi. Luminescence Distribution of Yb Doped Ca- $\alpha\text{-SiAlON}$ Phosphors. *Journal of Materials Research*, 23:1701, 2008.
- [357] V. Bachmann, T. Jüstel, A. Meijerink, C. Ronda, and P. J. Schmidt. Luminescence Properties of $\text{SrSi}_2\text{O}_2\text{N}_2$ Doped with Divalent Rare Earth Ions. *Journal of Luminescence*, 121:441, 2006.
- [358] A. Saha, S. R. Shah, R. Raj, and S. E. Russek. Polymer-Derived SiCN Composites with Magnetic Properties. *Journal of Materials Research*, 18:2549, 2003.

- [359] J. H. Park, K. H. Park, and D. P. Kim. Superparamagnetic Si_3N_4 -Fe-Containing Ceramics Prepared from a Polymer-Metal Complex. *Journal of Industrial and Engineering Chemistry*, 13:27, 2007.
- [360] X. Yan, X. Cheng, G. Han, R. Hauser, and R. Riedel. Synthesis and Magnetic Properties of Polymer Derived Metal/SiCN Ceramic Composites. *Key Engineering Materials*, 353-358:1485, 2007.
- [361] R. Hauser, A. Francis, R. Theismann, and R. Riedel. Processing and Magnetic Properties of Metal-Containing SiCN Ceramic Micro- and Nano-Composites. *Journal of Materials Science*, 43:4042, 2008.
- [362] M. J. MacLachlan, M. Ginzburg, N. Coombs, T. W. Coyle, P. N. Raju, J. E. Greedan, G. A. Ozin, and I. Manners. Shaped Ceramics with Tunable Magnetic Properties from Metal-Containing Polymers. *Science*, 287:1460, 2000.
- [363] Y. Li, Z. Zheng, C. Reng, Z. Zhang, S. Gao, W. Yang, and Z. Xie. Preparation of Si-C-N-Fe Magnetic Ceramics from Iron-Containing Polysilazane. *Applied Organometallic Chemistry*, 17:120, 2003.
- [364] A. Dumitru, I. Stamatina, A. Morozan, C. Mirea, and V. Ciupina. Si-C-N-Fe Nanostructured Ceramics from Inorganic Polymer Precursors Obtained by Plasma Polymerization. *Materials Science and Engineering, C*, 27:1331, 2007.
- [365] E. L. Simmons and W. W. Wendlandt. The Thermal Decomposition of Metal Complexes-XVIII Intermediates Formed in the Decomposition of Hexaaminocobalt (III) Chloride. *Journal of Inorganic and Nuclear Chemistry*, 28:2187, 1966.
- [366] E. Ingier-Stocka and A. Bogacz. Thermal Decomposition of $[\text{Co}(\text{NH}_3)_6]\text{Cl}_3$ Part I. Non-Isothermal, Quasi-Isothermal and Scanning Electron Microscopy Studies. *Journal of Thermal Analysis*, 35:1373, 1989.
- [367] T. D. George and W. W. Wendlandt. The Thermal Decomposition of Metal Complexes-II, Some Ammine and Ethylenediamine complexes of Nickel(II). *Journal of Inorganic and Nuclear Chemistry*, 25:395, 1963.
- [368] H. E. Swanson, H. F. McMurdie, M. C. Morris, and E. H. Evans. Standard X-Ray Diffraction Powder Patterns, Section 6., Data for 60 Substances. *National Bureau of Standards (U.S.) Monograph*, 25:6, 1968.
- [369] H. Cakmak and M. Jansen. Production of Nitride-based Phosphors. *Application Number EP08016232.4*, 2008.

Bibliography

- [370] C. J. Duan, W. M. Otten, A. C. A. Delsing, and H. T. Hintzen. Preparation and Photoluminescence Properties of Mn^{2+} -Activated $\text{M}_2\text{Si}_5\text{N}_8$ (M= Ca, Sr, Ba) Phosphors. *Journal of Solid State Chemistry*, 181:751, 2008.
- [371] M. Woike and W. Jeitschko. Preparation and Crystal Structure of the Nitridosilicates $\text{Ln}_3\text{Si}_6\text{N}_{11}$ (Ln = La, Ce, Pr, Nd, Sm) and LnSi_3N_5 (Ln = Ce, Pr, Nd). *Inorganic Chemistry*, 34:5105, 1995.
- [372] M. Woike and W. Jeitschko. Crystal Structure of Cerium Silicon Nitride (1/3/5), CeSi_3N_5 . *Zeitschrift für Kristallographie*, 211:813, 1996.
- [373] U. Wannagat, E. Bogusch, and R. Braun. Cyclosilazane mit Bor, Germanium, Zinn, Arsen oder Antimon als weiteren Ringgliedern. *Journal of Organometallic Chemistry*, 19:367, 1969.
- [374] I. Geisler and H. Nöth. Derivate von Silaborazolen. *Chemische Berichte*, 103:2234, 1970.
- [375] H. Nöth, W. Tinhof, and T. Taeger. Silaborazine aus Cyclosilazanen. *Chemische Berichte*, 107:3113, 1974.
- [376] H. Nöth and W. Tinhof. Synthese und NMR-Untersuchung von Silaborazin-Derivaten. *Chemische Berichte*, 108:3109, 1975.
- [377] K. Barlos and H. Nöth. Synthese und Reaktionen von Sila- und Phosphaborazinen. *Zeitschrift für Naturforschung*, 35b:415, 1979.
- [378] M. Hesse, U. Klingebiel, and L. Skoda. Silaborazine und Fluorborylsubstituierte Cyclotrisilazane. *Chemische Berichte*, 114:2287, 1981.
- [379] E. Hanecker and H. Nöth. Die Molekülstruktur zweiter Silaborazine. *Zeitschrift für Naturforschung*, 40b:717, 1985.
- [380] H. Watanabe, M. Narisada, T. Nakagawa, and M. Kubo. Infrared Absorption of borazole Derivatives. *Spectrochimica Acta*, 16:78, 1960.
- [381] H. G. Brittain, A. L. Wayda, and I. Mukerji. Luminescence Studies of Tris(bis(trimethylsilyl)amido)terbium(III) and of Its Adduct Complexes. *Inorganic Chemistry*, 26:2742, 1987.
- [382] H. Bürger and U. Wannagat. Silylamido-Derivate von Eisen und Kobalt. *Monatshefte für Chemie*, 94:1007, 1963.
- [383] H. Bürger and U. Wannagat. Silylamido-Verbindungen von Chrom, Mangan, Nickel und Kupfer. *Monatshefte für Chemie*, 95:1099, 1964.

13. Acknowledgments

I would like to express my deepest gratitude to my supervisor Prof. Dr. Dr. h. c. Martin Jansen for providing me with the opportunity to work in very interesting and challenging topics under his guidance, motivation, advice, encouragement and endless support. My sincere thanks to my Ph.D. examination committee members Prof. Dr. Thomas Schleid and Prof. Dr. Helmut Bertagnolli for their evaluation of my Ph.D. thesis.

My hearty thanks to Priv. Doz. Dr. Markus Weinmann and Dr. Thomas Jäschke for their valuable comments and discussions. I would like to thank Dr. Angelika Epple for her valuable support during the initial stages of my Ph.D. Special thanks to Ms. Marie-Luise Schreiber for her excellent technical support in the laboratory as well as for elemental analysis. Many thanks to Prof. Claudia Wickleder from Universität Siegen for providing us the initial photoluminescence spectra and valuable discussions. I am grateful to Prof. Dr Joachim Spatz from Max Planck Institute for Metals Research for kindly allowing me to use the fluorescence spectrometer in his department. I would also like to thank Dr. Christian Oberndorfer, Jakob Wilfert (also for SEM-EDX analysis) and Thomas Pilz for DTA/TG/MS measurements. Thanks to Mrs. Eva-Maria Peters for crystal structure solution, to Werner Giering for crystal picking, to Mr. Wolfgang König for IR and diffuse reflection spectroscopy measurements, to Mrs. Eva Brücher for magnetic measurements. I would especially to thank Dr. Hanne Nuss for her priceless helps and discussions. I am very grateful to Dr. Ayse Turak for her precious helps and comments. Many thanks to Evangelos Krokos for taking excellent pictures of my phosphors. Special thanks to the early and present ceramic group members for keeping a cool and friendly working atmosphere in the laboratory. I deeply appreciated the scientific and social atmosphere within the Jansen group. I also owe my special thanks to my Turkish friends in Stuttgart and to Dr. Timo Sörgel for their excellent friendship and creating a nice environment. Many thanks are due to the Max Planck Society for the doctoral fellowship during my entire Ph.D. tenure.

My sincere thanks to my beloved parents and parents-in-law for their encouragement, endless support and being always with us, no matter what their physical conditions and coordinates are. Finally, I would like to thank with all my heart to my wife, Güliz, for her love, understanding, moral support and help, without whom this study would never be finished.

13. Acknowledgments

14. List of Publication

Related Publications

1. H. Cakmak, M. Jansen, New class of phosphors for LED-based emitters, in *Annual Report 2009, Max Planck Institute for Solid State Research*.
2. H. Cakmak, M. Jansen, Intrinsic photoluminescence properties of amorphous $\text{Si}_3\text{B}_3\text{N}_7$ ceramic, *to be published*.
3. H. Cakmak, M. Jansen, C. Wickleder, F.J. Hormes, New phosphors based on amorphous $\text{Si}_3\text{B}_3\text{N}_7$ ceramics, *to be published*.
4. H. Cakmak, M. Jansen, Luminescence properties of Eu^{2+} and Tb^{3+} (co)doped amorphous $\text{Si}_3\text{B}_3\text{N}_7$ ceramics, *to be published*.
5. H. Cakmak, M. Jansen, Luminescence properties of Ce^{3+} and Tb^{3+} (co)doped amorphous $\text{Si}_3\text{B}_3\text{N}_7$ ceramics, *to be published*.
6. H. Cakmak, M. Jansen, Luminescence properties of Nd^{3+} and Eu^{2+} (co)doped amorphous $\text{Si}_3\text{B}_3\text{N}_7$ ceramics, *to be published*.
7. H. Cakmak, M. Jansen, Luminescence properties of Sm^{3+} and Eu^{2+} (co)doped amorphous $\text{Si}_3\text{B}_3\text{N}_7$ ceramics, *to be published*.
8. H. Cakmak, M. Jansen, Luminescence properties of Ho^{3+} and Eu^{2+} (co)doped amorphous $\text{Si}_3\text{B}_3\text{N}_7$ ceramics, *to be published*.
9. H. Cakmak, M. Jansen, Luminescence properties of Sn^{2+} doped amorphous $\text{Si}_3\text{B}_3\text{N}_7$ ceramics, *to be published*.
10. H. Cakmak, M. Jansen, Luminescence properties of Eu^{2+} doped amorphous Si_3N_4 ceramics, *to be published*.
11. H. Cakmak, M. Jansen, A novel production method for $\text{M}_{2-x}\text{Eu}_x\text{Si}_5\text{N}_8$ (M= Ca, Sr and Eu) phosphors, *to be published*.
12. H. Cakmak, M. Jansen, Synthesis of Mn^{2+} doped $\text{Sr}_2\text{Si}_5\text{N}_8$ phosphor through precursor route, *to be published*.

14. List of Publication

13. H. Cakmak, M. Jansen, Synthesis of Ce^{3+} doped $\text{M}_2\text{Si}_5\text{N}_8$ (M= Ca and Sr) phosphors through precursor route, *to be published*.
14. H. Cakmak, M. Jansen, New green phosphors: Tb^{3+} doped $\text{M}_2\text{Si}_5\text{N}_8$ (M= Ca and Sr), *to be published*.
15. H. Cakmak, M. Jansen, A new green phosphor: Tb^{3+} doped $\text{BaSi}_7\text{N}_{10}$, *to be published*.
16. H. Cakmak, M. Jansen, Luminescence properties of Ce^{3+} doped $\text{BaSi}_7\text{N}_{10}$, *to be published*.
17. H. Cakmak, M. Jansen, Synthesis of CeSi_3N_5 through precursor route and its luminescence properties, *to be published*.
18. H. Cakmak, M. Jansen, Soft ferromagnetic $\text{Si}_3\text{B}_3\text{N}_7$ ceramics, *to be published*.
19. H. Cakmak, M. Jansen, Open cell SiBNC ceramic foams, *to be published*.
20. H. Cakmak, M. Jansen, The first halo-substituted monocyclic silaborazine-type single source precursor molecule, *to be published*.
21. H. Cakmak, M. Jansen, Synthesis of new Si/B/N/C ceramics from a monocyclic silaborazine-type single source precursor, *to be published*.

Other Publications

1. G. Cakmak, Z. Kucukyavuz, S. Kucukyavuz, H. Cakmak, Mechanical, electrical and thermal properties of carbon fiber reinforced poly(dimethylsiloxane)/polypyrrole composites, Composites Part A: Applied Science and Manufacturing, 2004, 35, 417.

Patents

1. M. Jansen, H. Cakmak, Leuchstoffe, *DE 102006051757 A1, WO200805277*, 2006.
2. H. Cakmak, M. Jansen, Production of Nitride-based Phosphors, *Application number EP08016232.4*, 2008.

Attended Meetings

1. Down-conversion Phosphors based on Amorphous $\text{Si}_3\text{B}_3\text{N}_7$ Ceramics, 6th International Conference on Inorganic Materials, 2008, Dresden, Germany (oral presentation).

2. New Class of Phosphors based on Amorphous $\text{Si}_3\text{B}_3\text{N}_7$ Ceramics, New Frontiers in Material Synthesis and Characterization, Solid State Chemistry, Gordon Research Conferences, 2009, Oxford, United Kingdom (poster presentation).
3. Eu^{2+} and Tb^{3+} (co)doped Amorphous $\text{Si}_3\text{B}_3\text{N}_7$ Ceramics, 12th European Conference on Solid State Chemistry, 2009, Münster, Germany (poster presentation).

14. *List of Publication*

15. Curriculum Vitae

Personal

Name	Hasan Cakmak
Date of Birth	24.01.1977
Place of Birth	Sakarya/Türkiye
Marital Status	Married

Education

09/1996 – 06/2000	Bachelor Degrees in Chemistry, Department of Chemistry, Middle East Technical University, Ankara, Türkiye.
09/2000 – 09/2002	Master of Science in Chemistry, Department of Chemistry, Middle East Technical University, Ankara, Türkiye.
Title of the Thesis:	Melt Blending of High Density Polyethylene and Poly(ethyleneteraphtalate) in the Presence of Carbon Black.
08/2004 – 07/2009	Ph.D. research in the group of Prof. Martin Jansen, Max-Planck-Institute for Solid State Research, Stuttgart, Germany, and Ph.D. Degree from the Department of Chemistry, University of Stuttgart, Stuttgart, Germany.
Title of the Thesis:	New Applications of Amorphous $\text{Si}_3\text{B}_3\text{N}_7$ Ceramics and a Novel Production Method for Crystalline Nitridosilicates.

15. *Curriculum Vitae*

16. Explanation

Hiermit versichere ich an Eides statt, dass ich diese Dissertation unter Verwendung der angegebenen Hilfsmittel selbstständig angefertigt und bisher noch keinen Promotionversuch unternommen habe.